



**HAL**  
open science

# Development of single site catalysts based on Gallium and Vanadium for the dehydrogenation/aromatization of light alkanes

Jessy Abou Nakad

► **To cite this version:**

Jessy Abou Nakad. Development of single site catalysts based on Gallium and Vanadium for the dehydrogenation/aromatization of light alkanes. Catalysis. Université de Lyon, 2022. English. NNT : 2022LYSE1129 . tel-04719164

**HAL Id: tel-04719164**

**<https://theses.hal.science/tel-04719164v1>**

Submitted on 3 Oct 2024

**HAL** is a multi-disciplinary open access archive for the deposit and dissemination of scientific research documents, whether they are published or not. The documents may come from teaching and research institutions in France or abroad, or from public or private research centers.

L'archive ouverte pluridisciplinaire **HAL**, est destinée au dépôt et à la diffusion de documents scientifiques de niveau recherche, publiés ou non, émanant des établissements d'enseignement et de recherche français ou étrangers, des laboratoires publics ou privés.



N°d'ordre NNT : 2022LYSE1129

## **THESE de DOCTORAT DE L'UNIVERSITE DE LYON**

opérée au sein de  
**L'Université Claude Bernard Lyon 1**

**Ecole Doctorale N° 206**  
**Chimie, Procédés, Environnement**

**Spécialité de doctorat** : Chimie  
**Discipline** : Catalyse et applications

Soutenue publiquement le 08/07/2022, par :  
**Jessy ABOU NAKAD**

---

### **Development of single site catalysts based on Gallium and Vanadium for the dehydrogenation/aromatization of light alkanes**

---

Devant le jury composé de :

GODARD, Cyril	Professeur, Universitat Rovira i Virgili, Tarragona	Rapporteur
SAUTHIER, Mathieu	Professeur, Université de Lille	Rapporteur
DANIELLE, Stéphane	Professeur, Université de Lyon I Claude Bernard	Président
LAURENTI, Dorothée	Directrice de Recherche CNRS, IRCE-Lyon	Examinatrice
SCOTT, Susannah	Professeure, Université Santa Barbara, California	Examinatrice
TAOUFIK, Mostafa	Ingénieur de Recherche CNRS, Laboratoire CP2M, Université de Lyon	Directeur de thèse
GAUVIN, Régis	Directeur de Recherche CNRS, Institut de Recherche de Chimie, Paris	Invité



## Université Claude Bernard – LYON 1

Président de l'Université	M. Frédéric FLEURY
Président du Conseil Académique	M. Hamda BEN HADID
Vice-Président du Conseil d'Administration	M. Didier REVEL
Vice-Président du Conseil des Etudes et de la Vie Universitaire	M. Philippe CHEVALLIER
Vice-Président de la Commission de Recherche	M. Jean-François MORNEX
Directeur Général des Services	M. Damien VERHAEGHE

### **COMPOSANTES SANTE**

Faculté de Médecine Lyon-Est – Claude Bernard	Doyen : M. Gilles RODE
Faculté de Médecine et Maïeutique Lyon Sud Charles. Mérieux	Doyenne : Mme Carole BURILLON
UFR d'Odontologie	Doyenne : Mme Dominique SEUX
Institut des Sciences Pharmaceutiques et Biologiques	Directrice : Mme Christine VINCIGUERRA
Institut des Sciences et Techniques de la Réadaptation	Directeur : M. Xavier PERROT
Département de Formation et Centre de Recherche en Biologie Humaine	Directrice : Mme Anne-Marie SCHOTT

### **COMPOSANTES & DEPARTEMENTS DE SCIENCES & TECHNOLOGIE**

UFR Biosciences	Directrice : Mme Kathrin GIESELER
Département Génie Electrique et des Procédés (GEP)	Directrice : Mme Rosaria FERRIGNO
Département Informatique	Directeur : M. Behzad SHARIAT
Département Mécanique	Directeur : M. Marc BUFFAT
UFR - Faculté des Sciences	Directeur : M. Bruno ANDRIOLETTI
UFR (STAPS)	Directeur : M. Yannick VANPOULLE
Observatoire de Lyon	Directrice : Mme Isabelle DANIEL
Ecole Polytechnique Universitaire Lyon 1	Directeur : Emmanuel PERRIN
Ecole Supérieure de Chimie, Physique, Electronique (CPE Lyon)	Directeur : Gérard PIGNAULT
Institut Universitaire de Technologie de Lyon 1	Directeur : M. Christophe VITON
Institut de Science Financière et d'Assurances ESPE	Directeur : M. Nicolas LEBOISNE
	Directeur : M. Pierre CHAREYRON



“Follow your dreams, believe in yourself and never, never give up”



## Acknowledgement

At first, I want to praise and thank God who made all this experience possible for me.

I sincerely acknowledge the financial sponsorship and study leave grant received from the BiZeolCat Project, funded by the European Union's Horizon 2020 research and innovation program under grant agreement No. 814671. Moreover, I would like to thank our project coordinator, Dr. Ana Villacampa Del Tiempo, and in particular for accepting me as a member within her team. Indeed, it was an honour working with you. I would also like to thank all the partners involved in the project especially for their fruitful scientific conversations and advice during our meetings.

Throughout this journey, I appreciated the positive working environment and the team spirit at the Catalyse, Polymérisation, Procédés et Matériaux (CP2M) laboratory and Université de Lyon1.

My first and foremost thanks goes to my supervisor, Dr. Mostafa TAOUFIK for all the scientific guidance behind this work. His support has been instrumental in the pursuit of this research. He offered me the opportunity to work in his team and helped me gain solid technical and scientific skills. Also, I would like to thank Dr. Kai Chung SZETO for his contributions and for always being available. Dr. Aimery DE MALLMANN, thank you for all the help you provided, at scientific and administrative level.

To all those who were involved and contributed to the success of this PhD thesis especially Prof. Susannah Scott and Dr Li Li of University of California Santa Barbara, Dr Unni Oslebye and Dr Daniel Firth, of UiO lab, Oslo, thank you for your valuable support.

My deepest gratitude goes to the laboratory director, Dr. Timothy Mckenna and to the director of the doctoral school, Professor Stéphane Daniele. Thank you to the entire staff of CP2M. Many thanks for Dr Christine Lucas and Dr Nesrine Ouslati for all the knowledge you offered as well as your help in the NMR. Besides, I would like to thank Emmanuelle Fouillhe and Nathalie Jouglard as well, for assisting me in the administrative work, for all the interesting chats we had and for your kindness.

To my lab mates who turned into family, with whom I worked day (and sometimes night) for the past three years, a 'thank you' for all the moments we shared is not enough. I feel indeed

so lucky that I have met all of you: Isah, Paolo, CC, Felipe, Anthony and Sarah. Thank you from the bottom of my heart.

Since my arrival in Lyon, I feel blessed to be surrounded by people who also turned into family. You played a very important role in my life, and for that I am forever grateful. I am afraid there is not enough space to mention you all, but make sure that you have a special place in my heart.

To all my friends and family in Lebanon, France and worldwide; thank you for every thought, prayer or conversation we shared.

To my friend, who I can even call a sister, Nour Obeid. You are a true definition of a best friend, of someone who is always there, no matter the distance nor the time. Thank you for your constant support and love. I Love you.

To my cousin, Dr Jessica Eid, who is my role model and mentor, thank you for believing in me since the beginning. I am very honoured and glad I (almost) share your name. I love you.

My final words are reserved for my dearest: Dad, mom, Georges and Jad, I have no words to describe how grateful I am to have you as my family. I deeply thank you for all the continuous love, support and encouragement. Nothing I can say or do could ever be enough to you the love I have for you.

## Abbreviations

$\Delta$	Thermal treatment
$\delta$	Chemical shift
$\delta(\text{AB})$	Deformation frequencies of A-B bond
$\nu(\text{AB})$	Stretching frequencies of A-B Bond
$\text{\AA}$	Angstrom
BET	Brunauer, Emmett, Teller
<i>t</i> Bu	<i>tert</i> iobutyl group -C-(CH <sub>2</sub> ) <sub>3</sub>
DRIFT	Diffuse Reflectance Infrared Fourier Transform
EXAFS	Extended X-Ray Absorption Fine Structure
GC	Gas Chromatography
IR	InfraRed
NMR	Nuclear Magnetic Resonance
SOMC	Surface Organometallic Chemistry
<i>t</i> BuOH	<i>tert</i> iobutanol
DFT	Density Functional Theory
XAFS	X-ray absorption fine structure
XAS	X-ray absorption spectroscopy
EXAFS	Extended X-ray absorption fine structure
XANES	X-ray absorption near edge structure
ppm	part per million
nm	nanometre
cm <sup>-1</sup>	per centimetre
a.u.	atomic unit



## Table of contents

Acknowledgement.....	7
Abbreviations.....	9
General introduction.....	17
<b>CHAPTER I.....</b>	<b>23</b>
<b>Bibliographic study .....</b>	<b>23</b>
I.    Production of propylene .....	24
I.1.Uses and resources of propylene:.....	24
I.2.Industrial processes .....	27
II.   Production of butadiene.....	35
II.1 Uses and resources of 1,3-butadiene.....	35
II.2.Industrial process:.....	37
III.  Production of aromatics.....	39
III.1 Uses and resources of aromatics .....	39
III.2 Industrial process:.....	41
IV.   Propane dehydrogenation reaction.....	44
V.    Catalytic development of metal oxide catalyst in the non-oxidative PDH.....	45
V.1. Supported gallium oxide-based catalysts.....	46
V.2 Vanadium oxide-based catalysts .....	52
VI.   Preparation of single site catalysts using Surface Organometallic Chemistry.....	60
VI.1. Gallium catalysts prepared by SOMC .....	62
VI.2. Vanadium catalysts prepared by SOMC.....	66
VII.  General conclusion and objective of the thesis.....	70
References .....	72
<b>CHAPTER II. PART A .....</b>	<b>84</b>
<b>Direct conversion of trans-2-butene into a mixture of monomers with different composition over vanadium supported catalysts.....</b>	<b>84</b>

Abstract .....	85
Graphical abstract .....	85
Keywords: .....	85
List of abbreviations.....	85
Introduction .....	86
Experimental Section .....	88
Results and Discussions .....	91
Preparation and characterization of [V(=O)(OtBu) <sub>3</sub> ] on silica dehydroxylated at 200 °C(I).....	91
Preparation and characterization of [V(=O)(OtBu) <sub>3</sub> ] on alumina dehydroxylated at 500 °C (II) .	95
Catalytic properties .....	96
Conclusion.....	99
Acknowledgements.....	100
References .....	100
Supplementary Material .....	104
<b>CHAPTER II. PART B.....</b>	<b>111</b>
<b>Preparation of tripodal Vanadium Oxo-Organometallic Species Supported on Silica, [(≡SiO)<sub>3</sub>V(=O)], for Selective Non-Oxidative Dehydrogenation of Propane .....</b>	<b>111</b>
Abstract .....	112
Introduction .....	112
Experimental Section .....	115
Results and Discussions .....	117
Preparation and characterization of [V(=O)(OtBu) <sub>3</sub> ], (1) .....	117
Reactivity of [V(=O)(OtBu) <sub>3</sub> ], (1),with a silica dehydroxylated at 200 °C, synthesis of material (2).....	118
Reactivity of [V(=O)(OtBu) <sub>3</sub> ] with a silica dehydroxylated at 700 °C, material (3) synthesis...	123
Tripodal species .....	126
Catalytic properties .....	131

Conclusion.....	135
Acknowledgements.....	135
References .....	135
Supporting information .....	143
<b>CHAPTER III. PART A.....</b>	<b>146</b>
<b>Non-oxidative propane dehydrogenation over well-defined gallium catalysts prepared by surface organometallic chemistry .....</b>	<b>146</b>
Abstract.....	147
Introduction .....	147
Experimental Methods .....	151
Results and discussion.....	154
Grafting [Ga(O <i>t</i> Bu) <sub>3</sub> ] <sub>2</sub> with alumina dehydroxylated at 500 °C (I) .....	154
Grafting [Ga(O <i>t</i> Bu) <sub>3</sub> ] <sub>2</sub> onto silica dehydroxylated at 700 °C (II) .....	159
Catalytic propane dehydrogenation.....	163
Thermal treatment .....	165
Catalytic performance of (≡AlO) <sub>3</sub> Ga .....	168
EXAFS analysis of as-prepared Ga( <i>i</i> Bu) <sub>3</sub> /Al <sub>2</sub> O <sub>3-500</sub> .....	170
Conclusion.....	180
Acknowledgments .....	181
References .....	181
Supporting Information .....	189
<b>CHAPTER III. PART B.....</b>	<b>198</b>
<b>Influence of coke formation on supported Ga tripodal species during trans-2-butene conversion to butadiene.....</b>	<b>198</b>
Abstract .....	199
Introduction .....	199
Experimental Section .....	202
Results and Discussions .....	204

Preparation and characterization of tripodal species .....	204
Catalytic properties .....	209
Conclusion.....	212
Acknowledgements.....	213
References .....	213
Supporting information .....	217
<b>CHAPTER IV. PART A.....</b>	<b>219</b>
<b>The effect of local structure of Ga supported on meso H-ZSM-5 on the activity, stability, and selectivity in propane aromatization.....</b>	<b>219</b>
Abstract .....	220
Introduction .....	220
Experimental section.....	222
Results and discussion.....	225
Preparation and characterization of [Ga( <i>Or</i> Bu) <sub>3</sub> ] <sub>2</sub> supported on meso H-ZSM-5-250 (I).....	225
Preparation and characterization of supported tripodal Ga on meso H-ZSM-5-250 (II) .....	229
Preparation and characterization of [Ga( <i>i</i> Bu) <sub>3</sub> ] supported on meso H-ZSM-5-250 (III).....	231
Reactivity toward propane aromatization.....	235
Conclusion.....	238
Acknowledgments .....	239
References .....	239
Supporting information .....	242
<b>CHAPTER IV. PART B .....</b>	<b>245</b>
<b>Ga(<i>i</i>Bu)<sub>3</sub> supported on meso H-ZSM-5: Effect of Si/Al ratio on the activity and selectivity in propane aromatization.....</b>	<b>245</b>
Abstract .....	246
Introduction .....	246
Experimental Section .....	248
Results and discussion.....	251

Preparation and characterization of meso-H-ZSM-5 with Si/Al ratio (from 25 to $\infty$ ) .....	251
Catalytic properties of meso H-ZSM-5-250 in propane aromatization .....	257
Preparation and characterization of [Ga( <i>i</i> Bu) <sub>3</sub> ] supported on meso H-ZSM-5-250.....	258
Catalytic activity of [Ga( <i>i</i> Bu) <sub>3</sub> ] catalysts on meso H-ZSM-5-250 .....	264
Conclusion.....	268
Acknowledgments .....	269
References .....	269
<b>CHAPTER V</b> .....	<b>284</b>
<b>Conclusions and perspectives</b> .....	<b>284</b>
Perspectives .....	297



## General introduction

This PhD was carried out as a part of the BiZeolCat European project (H2020). The main objective of this project is to obtain light olefins and aromatics from light hydrocarbons by implementing new procedures, involving innovative catalysts synthesis methodologies, novel reactor design and processing and by demonstrating their improvement in sustainability and economic scalability compared to existing industrial processes. In this context, the main goal of this PhD is the preparation of well-defined supported single-site catalysts based on Ga and V, using an innovative synthesis process, for propane dehydrogenation (PDH) into propylene, butane/butenes dehydrogenation (BDH) into butadiene and propane aromatization (PAr) into aromatics (BTX = Benzene, Toluene, Xylenes).

The demand toward propylene, butadiene and BTX, has been increasing over the years and it is estimated to keep on growing.<sup>1-3</sup> Thus, this created an expanding gap between the supply and demand toward the market. The traditional routes such as steam cracking (for PDH and BDH), fluid catalytic cracking (for PDH) and catalytic reforming of naphta (for PAr) seem incapable of satisfying the rising demand.<sup>4-7</sup> Thus, alternative on-purpose routes,<sup>2,8,9</sup> like propane and butane/butenes dehydrogenation and propane aromatization were used in industry via three major processes: Catofin® and Oleflex® for PDH, Catadiene® for BDH and Cyclar® for PAr. The advantage of these processes is the availability of an abundant feedstock of light alkanes. However, platinum catalysts used in Oleflex® process require regeneration steps by using chlorine, a dangerous and environment unfriendly gas, in order to disperse the large metal particles formed. Besides, while chromium oxide based catalysts used in Catofin® and Catadiene® are cheaper, they suffer from a serious coking deactivation and are considered toxic and environmentally hostile, due to the presence of chromium in their composition.<sup>10</sup> Therefore, the development of alternative non-toxic and cheap efficient catalysts for improving the Pt and Cr stability remains a great challenge.

Many studies reported the development of the existing Pt and Cr catalysts and the investigation of novel alternative catalysts based on Ga, Zn, V, Zr, Co and many other metals for the targeted reactions.<sup>11</sup> Despite all these intensive studies, the nature of the active species on supported metal oxides, responsible of the dehydrogenation reaction, considered as the common step for all the targeted reactions (PDH, BDH and PAr) is still a matter of debate. This is due to the traditional preparation methods that yields a variety of surface species

(mono-, di-, oligomers and oxides particles) on the surface, which hampers the characterization and identification of the active sites and the establishment of a reliable structure-activity relationship. It was indeed demonstrated that the synthesis of isolated species is essential to limit or cancel the coke formation and deactivation processes and to obtain an active, selective and stable catalyst during the catalytic tests.

Thus, a judicious choice of innovative preparation methods of these catalytic systems is of a paramount importance in order to access to well-defined and highly active catalysts for these targeted reactions. The surface organometallic approach (SOMC) has demonstrated to be a powerful method for the immobilization of organometallic precursors via a protonolysis of a metal-ligand bond via the surface hydroxyl groups of an oxide, also called the grafting reaction of an organometallic precursor on an oxide support.<sup>12</sup> Generally, the support has a large influence on the structure of the resulting species and their catalytic performances. For alkane dehydrogenation, alumina and silica are generally used as supports for gallium and vanadium, while a highly acidic mesoporous zeolite is required in the case of propane aromatization, known to be a bifunctional reaction: dehydrogenation on the particles of the supported metal and aromatization on the acidic sites.

This work covers the preparation and characterization of site-single catalysts based on Ga and V for PDH, BDH and PAr. More importantly, the development of tripodal metal species was investigated for the first time and thus high activity and stability were obtained for dehydrogenation reactions. Moreover, a monopodal Ga bis alkyl species supported on a mesoporous zeolites displayed a high activity and selectivity for BTX synthesis. These results have been obtained upon a thorough investigation on the catalyst preparation methods and an intensive catalytic testing of all the prepared catalysts by evaluating several parameters such as the effects of the support, the ligands around the metal (coordination sphere), the podality from the surface, the temperature and gas composition.

The bibliographic study and all the experimental results of this work are presented in five main parts, including the introduction, three experimental chapters each divided in two parts followed by the conclusions and perspectives.

Chapter I draws up the generalities on propane and butane/butenes dehydrogenation as well as propane aromatization. The state of the art of the existing catalytic systems and the proposed mechanisms are also described. This section will be limited particularly on propane

dehydrogenation, a common step for the three-targeted reactions. After the bibliographic study, our goals and strategies employed for the proposed challenges are presented.

Chapter II reveals the preparation and characterization of the supported species resulting from the grafting of  $[V(=O)(OtBu)_3]$  on a silica dehydroxylated at different temperatures, 200 °C ( $SiO_{2-200}$ ) and 700 °C ( $SiO_{2-700}$ ) and on alumina dehydroxylated at 500 °C ( $Al_2O_{3-500}$ ). In addition, an original catalyst, containing tripodal vanadium species obtained by a thermal treatment of the grafted species on silica is described. The characterization and the catalytic performances of all these catalysts in propane and butenes dehydrogenation are presented. The mechanism for these catalytic reactions is discussed at the end of this chapter.

Chapter III is devoted to the preparation and extensive characterization of isolated Ga catalysts supported on alumina and silica by using surface organometallic chemistry (SOMC) method. Preparations using  $[Ga(iBu)_3]$  and  $[Ga(OtBu)_3]_2$  as precursors are compared in terms of structure of the supported species obtained onto  $Al_2O_{3-500}$  or  $SiO_{2-700}$ . Additionally, for the first time, the formation of tripodal Ga species from those obtained after the grafting of  $[Ga(OtBu)_3]_2$  onto these oxides are detailed and the resulting catalysts reveal an unprecedented stability during propane dehydrogenation. The catalytic performance as a function of the support and the ligands bonded to the metal center are also studied. The reason of the deactivation observed in the case of the catalyst prepared from  $[Ga(iBu)_3]$  compared to those containing the stable tripodal Ga species is furthermore explained via Operando XAFS. The catalytic activity of these materials is also evaluated in the direct trans-2-butene conversion in absence and presence of  $CO_2$  as co-feed.

Chapter IV is dedicated to propane aromatization with a Ga based catalyst supported on meso zeolites. Using the knowledge acquired in chapter III on Ga catalysts used for propane dehydrogenation, and especially on tripodal Ga species, our work is extended in Chapter IV to the supported species obtained on meso zeolites (Si/Al= 40) and their activity for propane aromatization (PAr). Supported species on meso zeolites are prepared as well from  $[Ga(iBu)_3]$  molecular precursor in order to study the effect of ligand on the activity and selectivity in PAr. Interestingly, in that case, in a continuous-flow reactor, the catalysts prepared from  $[Ga(iBu)_3]$  grafted on a meso zeolite reveal a better activity, stability and selectivity, as function of time on stream, compared to tripodal Ga species supported on a meso zeolite. In addition,  $[Ga(iBu)_3]$  can be selectively grafted on the Si-OH groups located within the mesopores and at the external surface of the meso zeolites with different ratio (Si/Al= 25, 40,

100, 200 and  $\infty$ ). The resulting materials are characterized by different techniques and are tested for propane aromatization as a function of the Si/Al ratio. The effect of the Si/Al ratio on the catalytic activity, selectivity and product distribution can thus be estimated. The influence of temperature and propane concentration in the feed are also studied.

Chapter V is a general conclusion that sums up the results of this PhD work and considers the study perspectives.

## References

- (1) Corma, A.; Melo, F. V.; Sauvanaud, L.; Ortega, F. Light Cracked Naphtha Processing: Controlling Chemistry for Maximum Propylene Production. *Catal. Today* **2005**, *107–108*, 699–706. <https://doi.org/10.1016/j.cattod.2005.07.109>.
- (2) V. Makshina, E.; Dusselier, M.; Janssens, W.; Degève, J.; A. Jacobs, P.; F. Sels, B. Review of Old Chemistry and New Catalytic Advances in the On-Purpose Synthesis of Butadiene. *Chem. Soc. Rev.* **2014**, *43* (22), 7917–7953. <https://doi.org/10.1039/C4CS00105B>.
- (3) Yang, L.; Liu, Z.; Liu, Z.; Peng, W.; Liu, Y.; Liu, C. Correlation between H-ZSM-5 Crystal Size and Catalytic Performance in the Methanol-to-Aromatics Reaction. *Chin. J. Catal.* **2017**, *38* (4), 683–690. [https://doi.org/10.1016/S1872-2067\(17\)62791-8](https://doi.org/10.1016/S1872-2067(17)62791-8).
- (4) Akah, A.; Al-Ghrami, M. Maximizing Propylene Production via FCC Technology. *Appl. Petrochem. Res.* **2015**, *5* (4), 377–392. <https://doi.org/10.1007/s13203-015-0104-3>.
- (5) Anabtawi, J. A.; Redwan, D. S.; Al-Jarallah, A. M.; Aitani, A. M. Advances in the Chemistry of Catalytic Reforming of Naphtha. *Fuel Sci. Technol. Int.* **1991**, *9* (1), 1–23. <https://doi.org/10.1080/08843759108942250>.
- (6) Corma, A.; Mengual, J.; Miguel, P. J. Steam Catalytic Cracking of Naphtha over ZSM-5 Zeolite for Production of Propene and Ethene: Micro and Macroscopic Implications of the Presence of Steam. *Appl. Catal. Gen.* **2012**, *417–418*, 220–235. <https://doi.org/10.1016/j.apcata.2011.12.044>.
- (7) Zeng, D.; Zhu, G.; Xia, C. Recent Advances of Aromatization Catalysts for C4 Hydrocarbons. *Fuel Process. Technol.* **2022**, *226*, 107087. <https://doi.org/10.1016/j.fuproc.2021.107087>.
- (8) Rochlitz, L.; Searles, K.; Alfke, J.; Zemlyanov, D.; V. Safonova, O.; Copéret, C. Silica-Supported, Narrowly Distributed, Subnanometric Pt–Zn Particles from Single Sites with High Propane Dehydrogenation Performance. *Chem. Sci.* **2020**, *11* (6), 1549–1555. <https://doi.org/10.1039/C9SC05599A>.
- (9) Choudhary, V. R.; Sivadinarayana, C.; Kinage, A. K.; Devadas, P.; Guisnet, M. H-Gallosilicate (MFI) Propane Aromatization Catalyst Influence of Calcination Temperature on Acidity, Activity and Deactivation Due to Coking. *Appl. Catal. Gen.* **1996**, *136* (2), 125–142. [https://doi.org/10.1016/0926-860X\(95\)00277-4](https://doi.org/10.1016/0926-860X(95)00277-4).
- (10) Qiao, K.; Peng, P.; Hu, C.; Bai, P.; Yan, Z. Synthesis of Vanadium-Based Catalysts and Their Excellent Catalytic Behaviors on Dehydrogenation of C4 Hydrocarbons. *Appl. Petrochem. Res.* **2015**, *5* (4), 321–327. <https://doi.org/10.1007/s13203-015-0118-x>.

- (11) Feng, B.; Wei, Y.-C.; Song, W.-Y.; Xu, C.-M. A Review on the Structure-Performance Relationship of the Catalysts during Propane Dehydrogenation Reaction. *Pet. Sci.* **2021**. <https://doi.org/10.1016/j.petsci.2021.09.015>.
- (12) Basset, J.-M.; Psaro, R.; Roberto, D.; Ugo, R. *Modern Surface Organometallic Chemistry*; John Wiley & Sons, 2009.



# **CHAPTER I**

---

## **Bibliographic study**

---

# I. Production of propylene

## I.1. Uses and resources of propylene:

Propylene is considered as a key component for the chemical industry, due to its role as a starting material to produce polypropylene, acrylonitrile, propylene oxide, cumene, phenol, iso-propylic alcohol and others.<sup>1,2</sup> Polypropylene is the most important and widely consumed product issued from the conversion of propylene (Figure 1).<sup>3</sup> Since its discovery in 1954, polypropylene gained a lot of attention as a thermoplastic due to its low density among commodity plastics for several applications in fibers, strapping, films, automotive and many others.<sup>3,4</sup> Therefore, propylene demand has been increasing since 1990,<sup>1</sup> and over 100 millions of tons of world consumption has been noted in 2017.<sup>5</sup> The demand is expected to reach 135 million tons of worldwide consumption in 2025,<sup>6</sup> with 35 million tons increase in only 8 years compared to 70 million tons consumed in 27 years (between 1990 and 2017). Moreover, the outgrowth in propylene market is outpacing the one toward ethylene market and is expected to rise over the following years.<sup>7</sup>

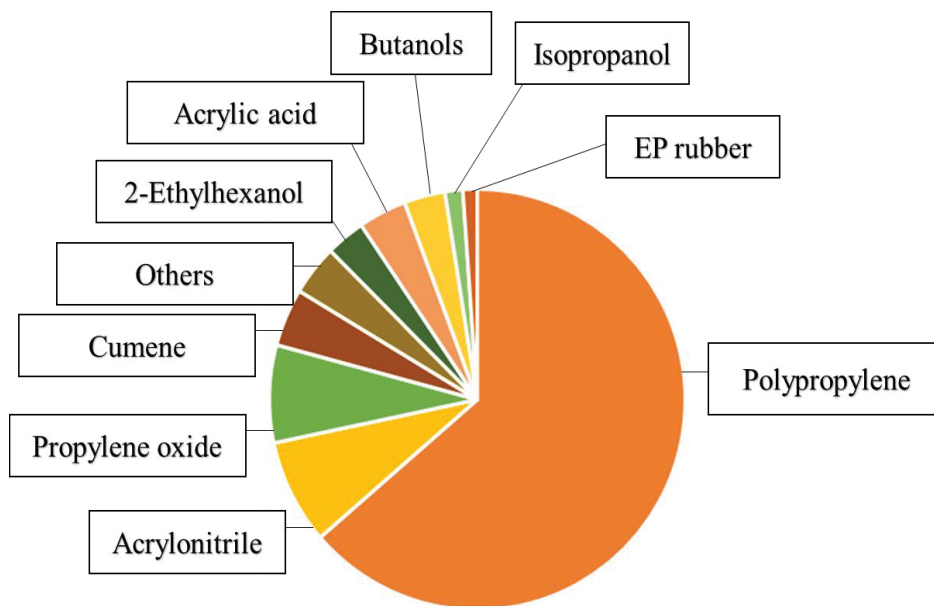


**Figure 1.** Global propylene consumption<sup>3</sup>

Propylene is mostly produced as a co-product from fluid catalytic cracking (FCC), but predominantly from steam cracking (SC) of naphta. With the increasing consumption of fossil fuels and the high demand for propylene, the aforementioned processes seem insufficient to satisfy the anticipated growth in the upcoming years.<sup>8-11</sup> Moreover, it is important to note that the high temperature used in the case of SC for alkene's production, leads to the formation of

significant amounts of undesirable CO<sub>2</sub> (more than 300 million tons of CO<sub>2</sub> per year).<sup>12</sup> Although lower temperature are used in the case of FCC, many by-products are generated, hence, additional high-cost steps are required to separate propylene.<sup>12</sup> Therefore, it is of vital importance to develop cost-effective, efficient and environmental-friendly routes for the production of propylene, that can address the increasing market demand. Consequently, many attempts have been developed in order to boost propylene's yield such as on-purpose technologies (OPT).<sup>13</sup> The latter includes several novel technologies like methanol to olefins (MTO),<sup>14</sup> olefin cross-metathesis between ethylene and 2-butenes<sup>15</sup> and propane dehydrogenation (PDH).<sup>16</sup> In addition to OPT, direct CO<sub>2</sub> conversion to light olefins<sup>17</sup> and Fisher-Tropsh to olefins<sup>18</sup> are also possible approaches to obtain propylene, but these processes are still under investigation. Figure 2 summarizes the main technologies used for propylene's production.

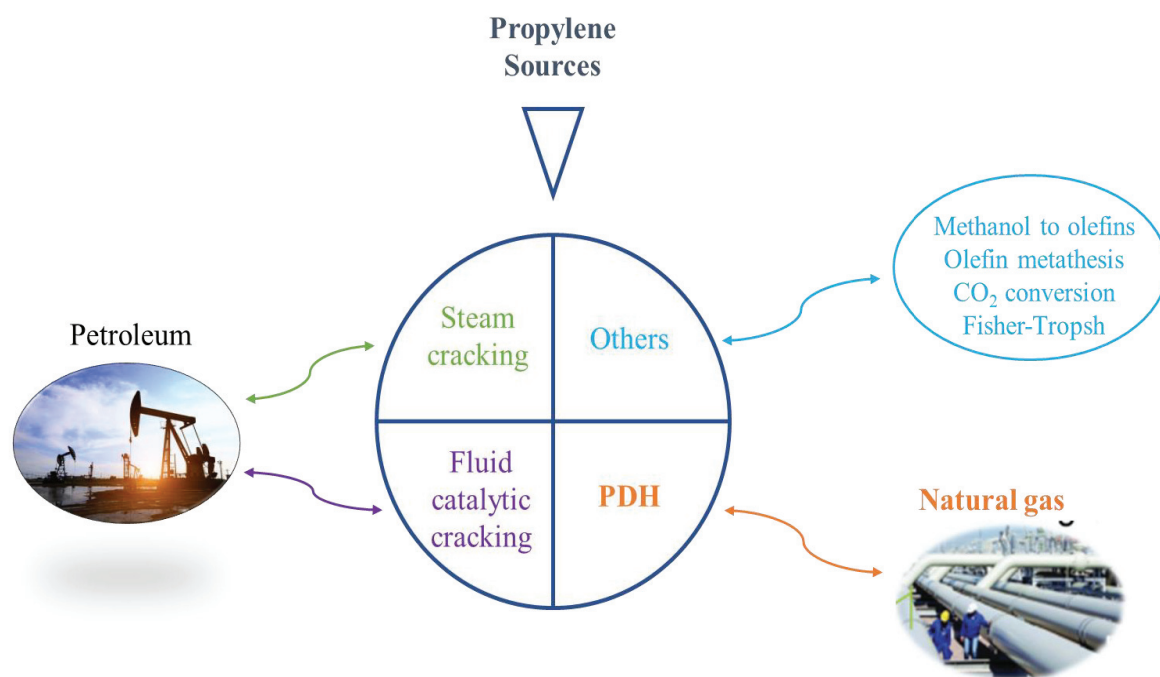


**Figure 2.** Existing processes for propylene production

In methanol to olefins reaction, methanol can be produced from syngas, that is produced by steam reforming of natural gas or gasification of coal. The mixture of carbon monoxide and hydrogen (syngas) can be converted into methanol and then into propylene or other olefins depending on the nature of the catalyst and/or the operating conditions. Usually, a zeolite-based catalyst is used in the MTO reaction.<sup>19–21</sup> Olefin metathesis, commercialized by ABB

Lummus, consists in converting a mixture of ethene and 2-butenes. This process includes three steps: a) dimerization of ethylene into 1-butene, b) isomerization of 1-butene into 2-butene and c) cross-metathesis of the mixture 2-butene and ethene.<sup>22</sup> This reaction uses  $\text{WO}_3$  on silica catalyst at high temperature and pressure. Fisher-Tropsh to olefins consists in converting syngas ( $\text{CO}/\text{H}_2$ ) into alkenes by using a catalyst based on Fe or Co that enables the formation of C-C and C-H bonds along with the cleavage of C-O bonds.<sup>23</sup> Recently, the direct conversion of  $\text{CO}_2$  into olefins gained lot of attention due to reducing the quantity of  $\text{CO}_2$  by converting it into high value chemicals like propylene. The bifunctional catalysts are required to transform the  $\text{CO}_2$  to propylene via methanol or via reverse water gas shift (RWGS), followed by further conversion of the intermediates (methanol and CO) by MTO or Fisher-Tropsh.<sup>24,25</sup> The direct propane dehydrogenation is a catalytic route involved in the conversion of propane into propylene in presence or absence of oxidants.<sup>26</sup> In other terms, propane dehydrogenation can be a non-oxidative or an oxidative reaction. In the case of non-oxidative propane dehydrogenation, propylene and hydrogen are mainly produced with some minor amounts of methane, ethane and ethylene. However, in the case of oxidative propane dehydrogenation, methane, ethane, ethylene and undesired oxygenated molecules (CO and  $\text{CO}_2$ ) are produced in addition to propylene.

Compared to SC and FCC, all the aforementioned processes do not require oil-feeding as a reactant and display better selectivity towards propylene. However, among these technologies, the non-oxidative PDH (NOPDH) is considered as a very promising route for two main reasons: the availability of a low-cost feedstock (propane) and the production of the targeted olefin along with hydrogen, considered as a valuable product for many applications.<sup>27</sup> With the discovery of shale reserves and their use as a source for the easy extraction of propane, this light hydrocarbon became widely available and cheap. Hence, it is of a great interest to use propane as a low-cost feedstock for propylene production.<sup>28</sup> It is important to note that since 2010, the PDH units are increasingly deployed worldwide and are predicted to keep on expanding. Additionally, NOPDH does not produce  $\text{CO}_2$ , contrarily to most of the aforementioned processes. Thus, propane dehydrogenation is considered as a high atom-economy reaction and respects many principles of green chemistry compared to the other processes.

## I.2. Industrial processes

To date, industrial processes for propane dehydrogenation are carried out in the absence of oxidant, and the catalysts used are based on supported Pt-Sn nanoparticles and Cr oxide. The recent development of new processes resulted in nine propane dehydrogenation technologies which differ in the catalyst composition, the operation and regeneration and the provided heat for the reaction.<sup>29</sup> The following section will be divided in two parts:

- The description of all the industrial processes for PDH using platinum-based catalysts, the active sites and the mechanism's reaction
- The description of all the industrial processes for PDH using chromium-based catalysts, the active sites and the mechanism's reaction

### I.2.a Industrial processes based on Pt for PDH:

Among the nine technologies, six of them use platinum-based catalysts to produce propylene: Oleflex® (UOP), PDH® (Linde-BASF), STAR® (Krupp-Uhde), FLOTU® (Tsinghua), SABIC® and FCDh® (Dow Chemical Company). For the KBR® process, no information was disclosed on the nature of the catalyst nor the design of the reactor. The main information related to these processes are shown in Table 1; however, only the commercialized Oleflex® and STAR® processes used for PDH will be fully detailed.<sup>29</sup>

**Table 1.** Summary of the technologies used for propane dehydrogenation

Technology	Reactor	Operation	Catalyst	Heat management	T (°C)	P (bar)	Cycle time
Catofin® (ABB LUMMUS)	Adiabatic fixed bed	Cyclic	CrO <sub>x</sub> /Al <sub>2</sub> O <sub>3</sub> + alkali	Pre-heaters, Regeneration	565-650	0.3-0.5	15-30 min
Oleflex® (UOP)	Adiabatic moving bed	Continuous	Pt-Sn/Al <sub>2</sub> O <sub>3</sub> + alkali	Interstage heating, regenerated catalyst	550-620	2-3	5-10 days
STAR® (Krupp-Uhde)	Adiabatic	Cyclic	Pt-Sn/Zn-Al <sub>2</sub> O <sub>3</sub> /Ca-Al <sub>2</sub> O <sub>3</sub>	Furnace and ODH	DH: 550-590, ODH: ~600	5-6	8h
FBD® (Yarsintez-Snamprogetti)	Fluidized bed	Continuous	CrO <sub>x</sub> /Al <sub>2</sub> O <sub>3</sub> + alkali	Regenerated catalyst	535-590	0.5-1.5	-
PDH® Linde-BASF-Statoil	Isothermal fixed bed	Cyclic	Pt/hydrotralcite Mg(Al)O; Pt-	Furnace	~590	~1	9h

(Sintef)			Sn/ZrO <sub>2</sub>				
FLOTU®/Tsinghua	Bimodal fluidized bed	Continuous	Pt-Sn/SAPO-34	Regenerated secondary catalyst	570-610	0.5-1.5	-
FCDh™ ® (Dow)	Fluidized bed	Continuous	Pt-Ga-K/Si-Al <sub>2</sub> O <sub>3</sub>	-	~600	1	-
SABIC®	Fluidized bed	Continuous	Pt-Sn/K/SAPO-34	Integrated FBR with internal regenerator	560-600	0.1-6	15-30 min
K-PRO™ ® (KBR)	Fluidized bed	Continuous	-	-	~600	1.5	-

### **Oleflex® process:**

Oleflex® process, commercialized by UOP in 1990, employs a Pt-Sn catalyst (with <1 wt % of Pt and 1-2 wt% of Sn) supported on modified alumina by Na or K (0-1 wt%) for the direct conversion of propane to propylene. A moving bed type reactor is used with a semi-continuous interstage heater, a catalyst regeneration unit, and a product recovery section (Figure 3). Pt-Sn supported catalyst requires the presence of hydrogen in the feed to reveal a high activity and stability (propane conversion between 30 - 40 %) and selectivity towards propylene (up to 88 %), while operating at high pressure (1 to 3 bar) and temperature in the range of 525 and 705 °C. Although this catalyst is highly active thanks to its good performance in the non-oxidative propane dehydrogenation, its lifetime is affected by coke formation and sintering of the platinum leading to a deactivation. Hence, the reactivation of the catalyst is required in the regeneration unit connected to the installation (CCR). The regeneration occurs by burning the carbon's deposition on the surface followed by the treatment of the catalysts by a chlorine-air mixture in order to redisperse the large platinum particles.<sup>30-32</sup>

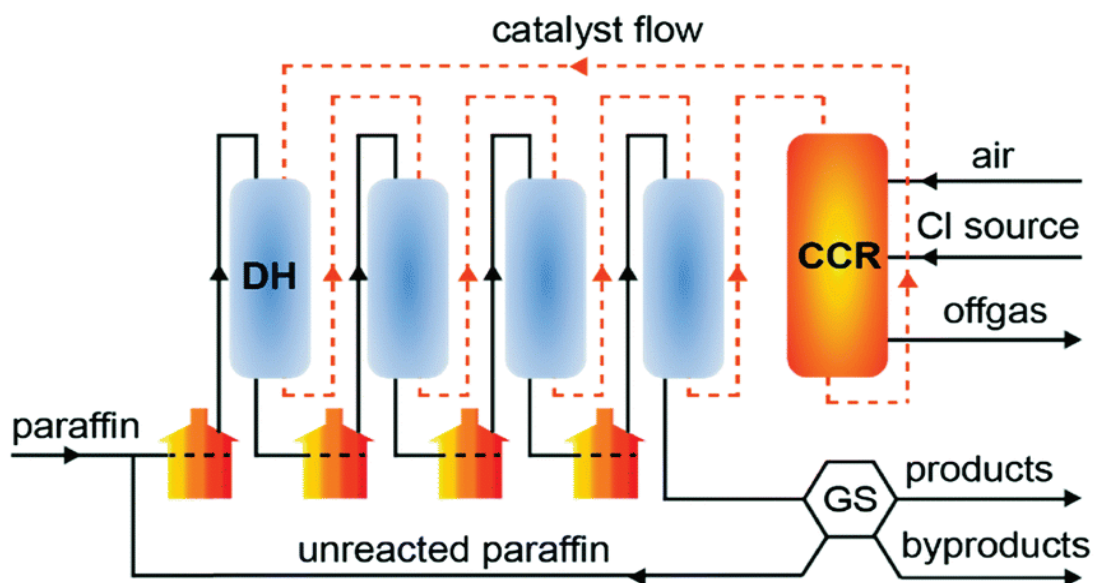


**Figure 3.** Schematic representation of Oleflex® process<sup>29</sup>

**STAR® process:**

The Steam Active Reforming (STAR)® technology (Figure 4) was developed by Philipps in 1990. It is the only process that can use the advantage of oxidative dehydrogenation in order to selectively combust the hydrogen (in the oxyreactor) formed during the non-oxidative propane dehydrogenation, thus shifting the equilibrium towards high selectivity to propylene. Additionally, it can generate heat that is beneficial for the endothermic PDH reaction. This technology uses a Pt-Sn catalyst supported on Zn-Ca aluminate in a tubular fixed bed reactor and can operate at lower temperature range (480-620 °C) compared to the other processes due to the aforementioned reason and high pressure between 5-6 bar. These conditions can afford a 35 % propane conversion with a selectivity between 80-90 %, with a catalyst lifetime exceeding 5 years compared to Oleflex® process (2-3 years). Another advantage of this process is the operating conditions resulting in a lower investment and expenses associated with coarse gas compression.

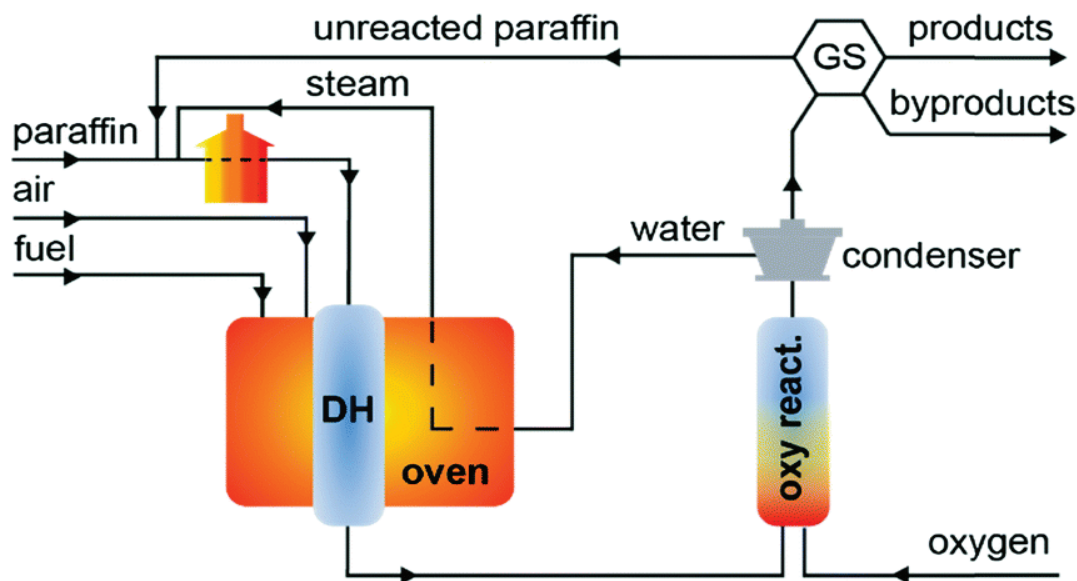
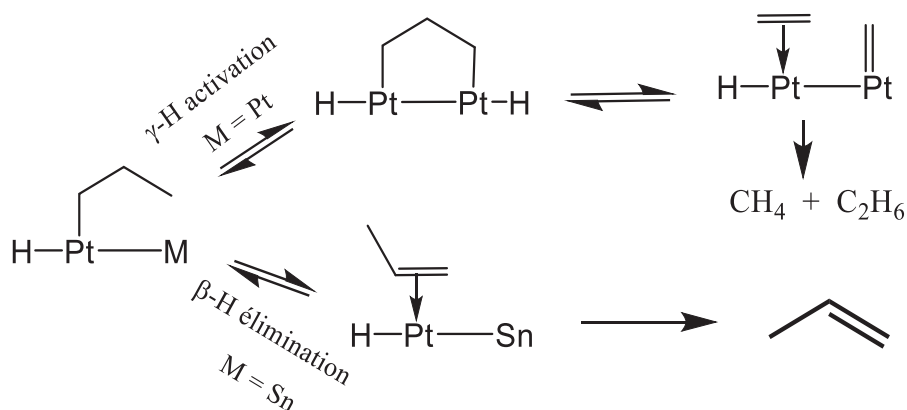


**Figure 4.** Schematic representation of STAR® process<sup>29</sup>

### **I.2.b Active sites and mechanism for PDH on Pt-Sn based catalysts:**

For all the studies concerning the development of Pt based catalyst used in the commercial processes, the continuity and the coordination environment of the platinum active sites play important roles in the catalytic performance. The nature of active sites in metal catalysts could be controlled by the interaction of other components such as promoters and supports. The addition of a second metal that could alloy with the active metal results in metal-metal bonds that would adjust the catalytic performance. In that manner, many promoters have been studied<sup>30</sup> where the promising catalytic behavior of Pt-Sn catalysts due to the geometric and electronic effects of Sn has been demonstrated.<sup>33</sup> In fact, the addition of Sn has a beneficial effect on reducing the sites for coke formation and separating large Pt clusters resulting in a better selectivity towards propylene. Despite their promising activity and use in industries, the active sites of Pt-Sn catalysts responsible for PDH are still unclear but are generally reported to be isolated Pt by Sn in the bimetallic nanoparticles. PtSn and Pt<sub>3</sub>Sn were proposed as active sites in many studies, while other works reported that partially modified platinum with reduced Sn exhibited higher and better activity in PDH compared to catalysts prepared with high amount of Sn.<sup>34</sup> In the case of bimetallic Pt-Sn catalyst, the reaction mechanism of PDH is widely known as a reverse Horiuti-Polanyi (HP) mechanism, consisting in three steps:<sup>35</sup> i) adsorption of propane on the isolated Pt through a Van der Waals interaction, ii) dissociation

of two adjacent C-H bond of propane, and iii) desorption of propylene and H<sub>2</sub> from metal surface.<sup>30</sup> While undesired reactions such as deep dehydrogenation and cleave of C-C bonds are susceptible to happen on Pt-Pt adjacent sites, the main reaction occurs on single Pt atom, surrounded by a Sn used as a promoter. The role of the latter has been widely studied revealing that its presence limits the secondary reactions (cracking) occurring via  $\gamma$ -H activation and favors the  $\beta$ -H elimination pathway leading to the production of the targeted product, propylene (Scheme 1).



**Scheme 1.** Proposed mechanism for bimetallic nanoparticles in PDH

### I.2.c Industrial processes based on Cr for PDH:

Among the aforementioned technologies, Catofin® (ABB Lummus) and FBD® (Snamprogetti-Yarsinez) employ a chromium oxide catalyst (Table 1); both of these processes are commercialized.

#### Catofin® process:

Catofin® uses a chromium oxide catalyst (18-20 wt%) supported on modified alumina by Na and K (1-2 wt%). This process occurs in several fixed adiabatic bed reactors (from 5 to 8) containing the catalyst, and propane is heated before the catalytic bed (Figure 5). These reactors alternate between three units: propane dehydrogenation, regeneration and purge steps. In other terms, while some reactors perform dehydrogenation, others will undergo regeneration or purge, leading to a constant flow of products, resulting in a cycle that lasts for 15 to 25 min. To achieve a selectivity of 87 % toward propylene, a high temperature of 650 °C and low pressure of 0.5 bar are required. It is important to note that the temperature gradually increases with time on stream to afford a constant activity during the catalyst's

lifespan. These operating conditions induce severe side reactions that result in a quick deactivation and sintering of the alumina, requiring a frequent regeneration every 15-25 min to maintain a high yield in propylene.<sup>30</sup> Although the regeneration process can partially restore the catalyst's activity, it causes an irreversible deactivation over the time due to the migration of chromium atoms in the framework of alumina leading to a decrease in the active sites concentration. The catalyst's lifetime in this process is estimated to be between 2-3 years.

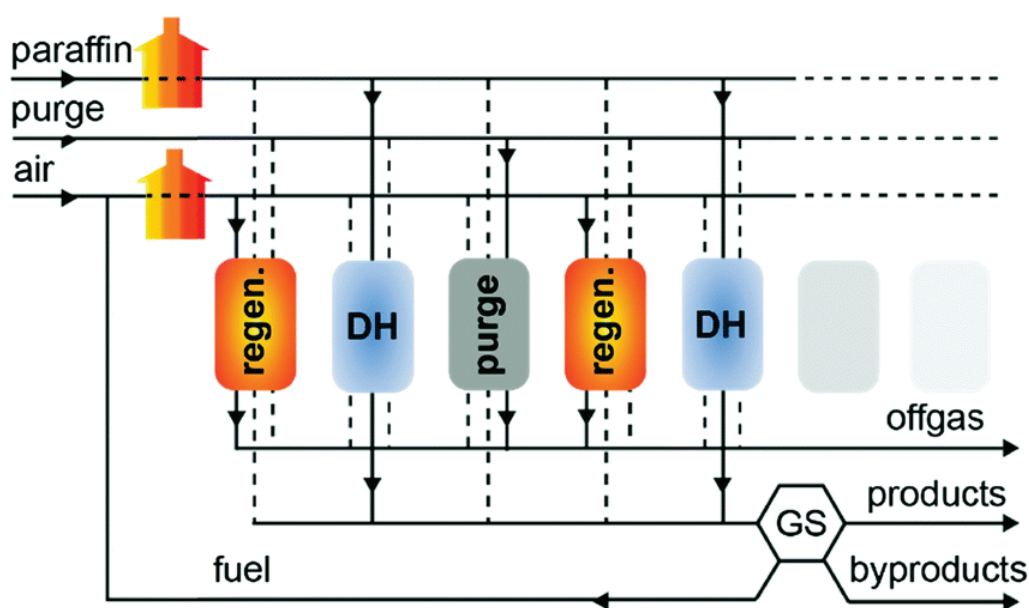


**Figure 5.** Schematic representation of Catofin® process<sup>29</sup>

### **FBD® process:**

The FBD® process is based on Fluidized Bed Dehydrogenation (FBD) technology and was developed by Yarsintez–Snamprogetti in the 1960's. The catalyst employed in FBD® process is similar to the Catofin®, a chromium oxide-based catalyst with a lower metal loading (around 15–19 wt%) that operates in a temperature range from 535 to 590 °C and between 0.5-1.5 bar. The catalysts particles are suspended by the gas and air flow using a distributor. In addition, due to the deactivation of chromium oxide under the operating conditions, the catalyst is regenerated, and the total cycle (reactor and regenerator) lasts for 10–30 min (Figure 6). Notably, less coke is formed in the case of FBD® process compared to Oleflex®, thus some fuel is introduced in the generator to supply the needed heat in order to satisfy the overall thermal balance. The catalyst's lifetime depends on the loss of the active catalyst

during the process, on the circulation rate and the catalyst mechanical strength. In order to compensate such loss and maintain the same conversion to propylene, new catalyst is introduced in the regenerator during the operation.

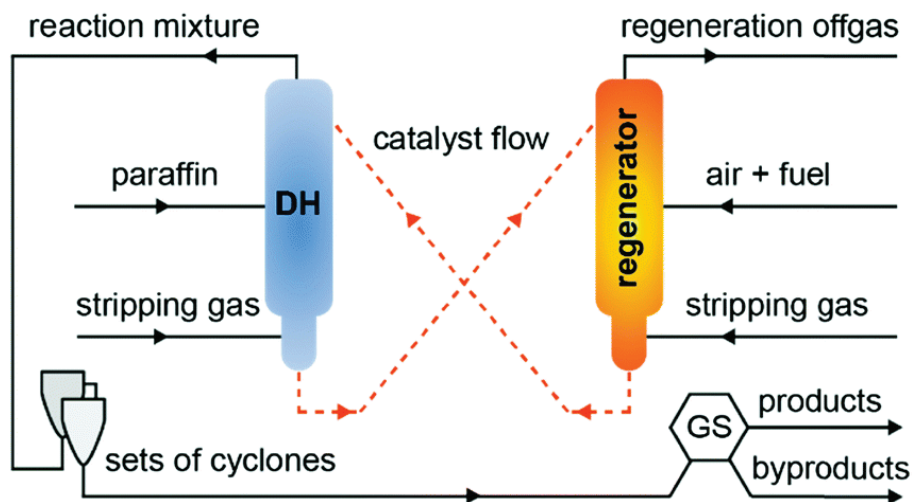


Figure 6. Schematic representation of FBD® process<sup>29</sup>

#### I.2.d Active sites and mechanism for PDH on Cr based catalysts:

CrOx based catalysts used in the processes are prepared via conventional methods (i.e using salts) with high loading of Cr (18-20 wt%) resulting in a low concentration of active sites and a mixture of isolated and chromium clusters on the surface (Figure 7).<sup>36</sup> Hence, it is difficult to characterize the nature of the active species responsible for the activity during the non-oxidative propane dehydrogenation.

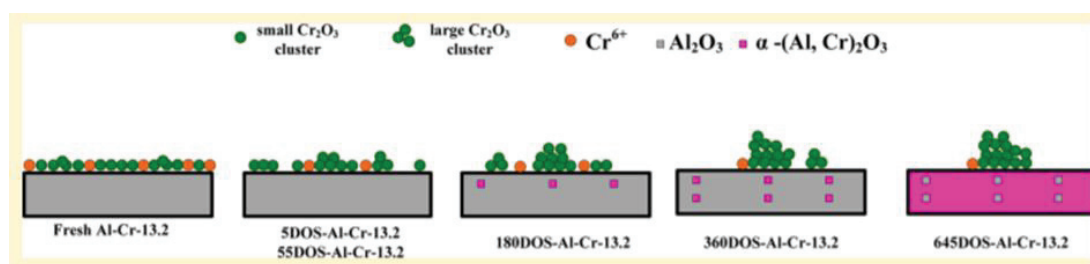
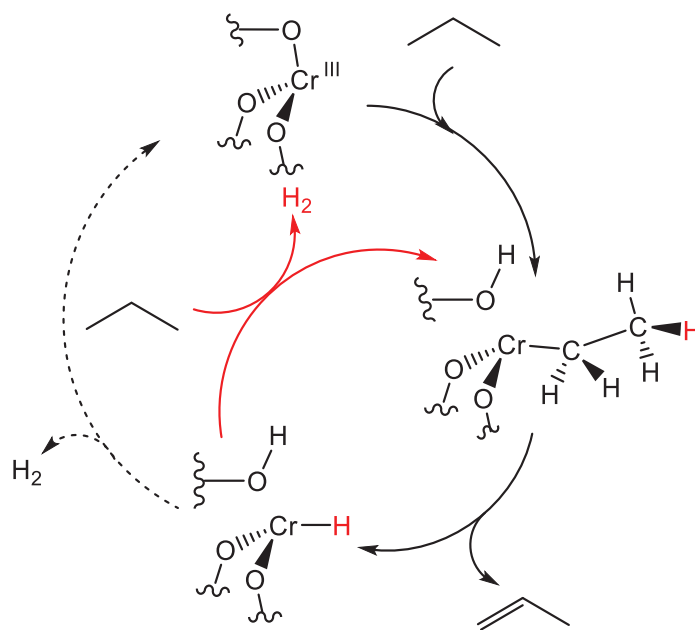


Figure 7. Different chromium species on the surface of alumina<sup>36</sup>

However, in-situ characterization of these catalysts revealed the presence of several oxidation states of chromium, like  $\text{Cr}^{2+}$ ,  $\text{Cr}^{3+}$ ,  $\text{Cr}^{5+}$  and  $\text{Cr}^{6+}$ ,<sup>26,37,38</sup> making it more complex to identify

the active species and to establish the mechanism for the reaction. Although the mechanism is still a matter of debate because of all the mentioned reasons,  $\text{Cr}^{3+}$  are considered as the active species for this reaction, due to their formation during the initiation step and the decrease of  $\text{Cr}^{6+}$  concentration.<sup>30,39</sup> In fact, Sattler et al. demonstrated by using in situ X-ray absorption near edge structure (XANES) and UV-vis spectra the reduction of  $\text{Cr}^{6+}$  to  $\text{Cr}^{3+}$  at early times during the reaction.<sup>40</sup> The proposed catalytic mechanism in PDH of isolated chromium oxide catalyst is based on metal-oxygen pairs, considered to be the source of active sites. The reduction-activation process of the catalyst results in a loss of a part of oxygen atoms and produce unsaturated chromium (III) bonded to three oxygens from the surface,  $(\equiv\text{AlO})_3\text{Cr}$ . The unsaturated Cr-O pairs support the coordination of carbon and hydrogen atoms of propane leading to the reduction of activation energy of C-H cleavage.<sup>41,42</sup> This step leads to the formation of a M-propyl intermediate and an OH group. Propylene is formed via a  $\beta$ -hydride elimination, resulting in a Cr-H species. The tripodal Cr active sites are regenerated after release of propene and  $\text{H}_2$  (Scheme 2). A parallel possible pathway consists in a C-H activation of Cr-H intermediate followed by a  $\beta$ -H elimination. This mechanism was supported by DFT calculations by Lillehaug et al.<sup>43</sup>



**Scheme 2.** Proposed PDH mechanism for isolated chromium catalysts

## II. Production of butadiene

### II.1 Uses and resources of 1,3-butadiene

1,3-Butadiene ( $C_4H_6$  or BD) is used in the industrial production of a variety of products, due to its high reactivity related to the presence of a conjugated double bond (Figure 8). The biggest consumption of BD is in the production of synthetic-elastomers such as styrene-butadiene rubber, polybutadiene, styrene-butadiene latex, chloroprene rubber and nitril rubber.<sup>44,45</sup> Thus, the global demand towards BD was anticipated to surpass 9 million metric tons in 2004. In 2012, the global demand was estimated to be 10 million metric tons,<sup>46</sup> while it was predicted to be 15.91 million tons in 2020, with an incremental growth of 3 % per year.

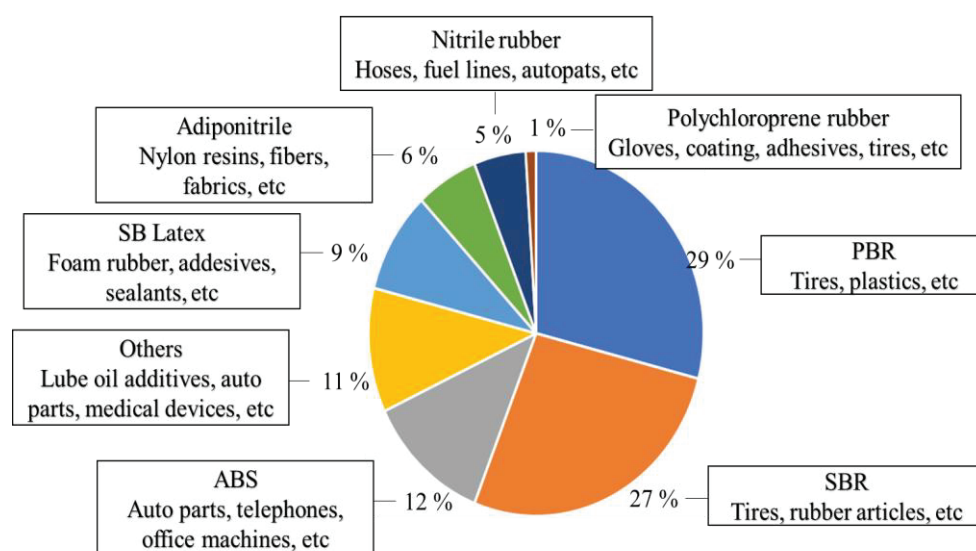


**Figure 8.** Various applications of 1,3 butadiene

Butadiene is usually obtained as a by-product from the production of ethylene via steam cracking (SC). Thus, the supply as well as the price of BD is highly dependent on the demand/production of ethylene.<sup>47</sup> In fact, the high production of ethylene over the years resulted in an oversupply in BD and the decrease in the development of some on purpose technologies. However, the recent discovery of new shale gas reserves has shifted the production of ethylene from SC to lighter material like ethane (for ethane dehydrogenation). Consequently, the market stability in BD is threatened which might lead to some shortage in its production and subsequent increase of its price. Thus, alternative processes are required to address the market need and on-purpose routes are proposed for this target, such as the

conversion of bio-sources molecules (dehydration of 2,3 butanediol and dehydrogenation of bioethanol)<sup>48,49</sup> and the catalytic oxidative or non-oxidative dehydrogenation of butane or a mixture of butane/butenes<sup>50–53</sup> (Figure 9).

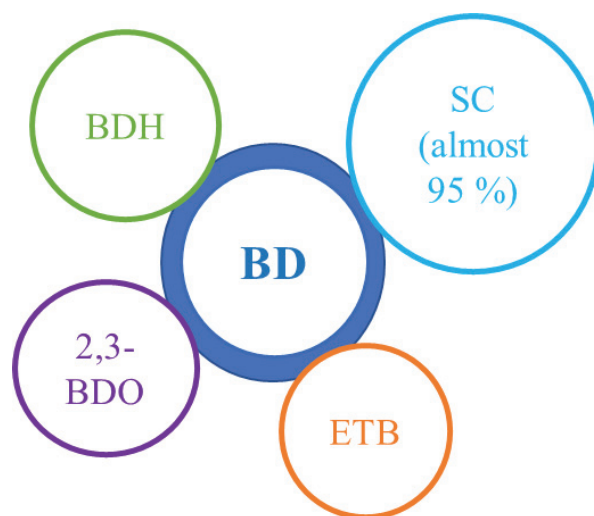


**Figure 9.** Various processes for 2,3 butadiene (BD) production

The dehydration of 2,3 butanediol (2,3-BDO) requires two steps: dehydration of 2,3-BDO into 3-butenes-2-ol, followed by another dehydration at a higher temperature to obtain BD. To our knowledge, Winfield revealed that BD in this process was obtained over  $\text{ThO}_2$  catalyst.<sup>54</sup> The dehydrogenation of bioethanol to butadiene (ETB) is covered by two different processes. The one step process that converts directly ethanol into butadiene over  $\text{ZnO}/\text{Al}_2\text{O}_3$ . This process is called the Lebedev® process,<sup>55</sup> whereas Ostromislensky® process refers to a two-step process: a partial dehydrogenation of ethanol into a mixture of ethanol/acetaldehyde over a  $\text{CuO}/\text{Cr}_2\text{O}_3$  followed by a conversion to butadiene catalyzed by  $\text{Ta}_2\text{O}_5/\text{SiO}_2$ .<sup>56</sup> The oxidative dehydrogenation of a mixture of n-butenes into butadiene is commercialized under the name of Oxo-D or O-X-D® process. Beside the formation of butadiene, the side reactions result in the formation of oxygenated by-products such as  $\text{CO}_2$ ,  $\text{CO}$  and  $\text{C}_4\text{H}_4\text{O}$  due to the overoxidation of butenes.<sup>57</sup> The non-oxidative dehydrogenation of butane/butenes is widely used at industrial scale for the production of BD and is commercialized under the name of the Catadiene® process.<sup>46</sup> The latter is catalyzed by a chromium on alumina catalyst and involves two steps: dehydrogenation of butane into a mixture of butenes followed by a further dehydrogenation into butadiene, or a dehydrogenation of butane into butenes and butadiene where butene is re-injected with butane in order to increase the selectivity in BD.<sup>9,26,58</sup> Among these processes, Catadiene® seems, until now, the most promising and established route to

produce butadiene. In fact, the non-oxidative dehydrogenation of C4 mixture has many advantages. First, it does not involve the use of the naphtha cracking unit nor the limited ethanol manufacturing as a feedstock. Second, it does not produce oxygenated and toxic molecules (CO<sub>2</sub> and CO).

## **II.2.Industrial process:**

To date, there is only one commercial process used by the industry that employs the non-oxidative butane/butenes dehydrogenation (Catadiene® process).

### **II.2.a Industrial process for BDH based on Cr:**

Catadiene® process was initially established by Houdry using one step for the formation of BD and was improved later by ABB Lummus to produce BD in two steps (Figure 10).<sup>26,59</sup>

#### **Catadiene® process:**

The Catadiene-Houdry® process uses a chromium supported catalyst on modified alumina produced by Clariant for the conversion of n-butane to 1.3 butadiene. This catalyst operates under a pressure between 0.1-0.4 atm and around 600 °C and displays a conversion between 30-40 % and a selectivity of 63 % towards butadiene accompanied with the formation of light hydrocarbons. It is important to note that besides BD, this reaction yields to the formation of butenes which after their separation from the targeted product, are recycled with fresh butane. Moreover, due to the high formation of coke under the operating conditions, the catalyst requires frequent regeneration.

In order to optimize the selectivity towards the targeted product, this process was extended by ABB Lummus, and more importantly operates in two separate steps. The first one consists in the dehydrogenation of n-butane to butenes, leading to a selectivity of 80 to 85 % while operating at 600 °C and atmospheric pressure. The second step catalyzed by a mixed iron-magnesium-potassium-chromium oxide catalyst, involves the further dehydrogenation of the recovered butenes resulting from the first step, leading to a selectivity of 65 % towards butadiene. Contrarily to PDH, the selectivity in the case of butadiene in both cases remains moderate and needs the development of new catalysts in order to improve it.

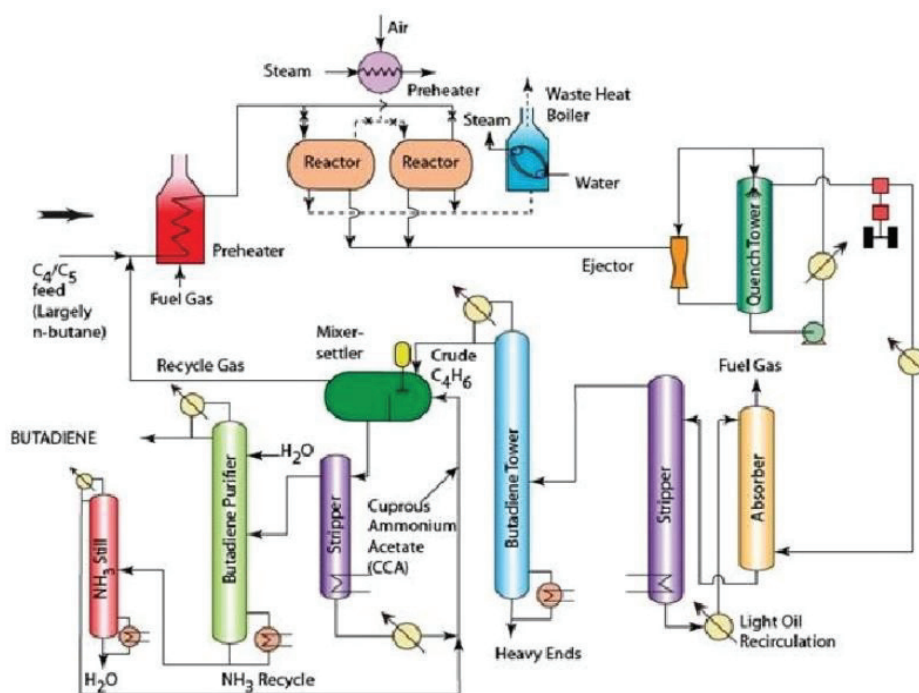
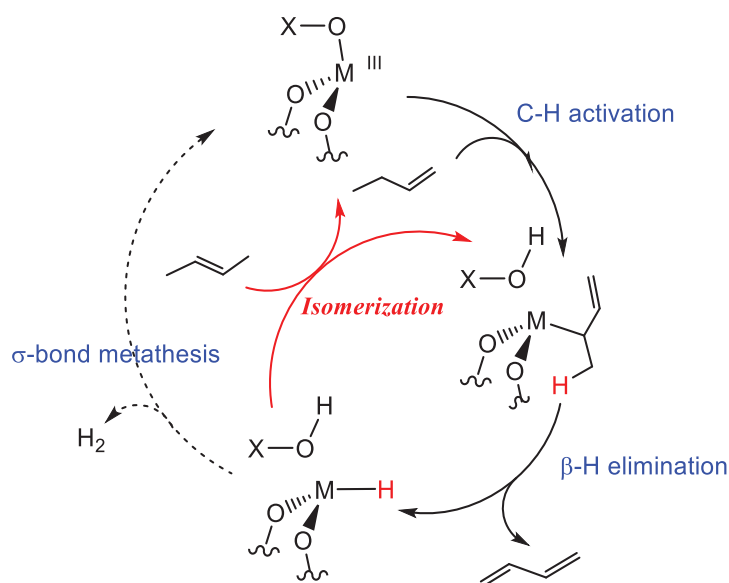


**Figure 10.** Schematic representation of Catadiene® process<sup>60</sup>

### II.2.b Active sites and mechanism

Catadiene® uses a chromium oxide supported catalyst and thus the active sites are proposed to be similar to PDH, unsaturated tripodal  $\text{Cr}^{3+}$ . The mechanism of the production from butane or butane/butenes occurs via two catalytic cycles (Scheme 3). The first cycle involves the dehydrogenation of butane into a mixture of butenes via three different steps: a C-H activation of butane on M-O followed by a  $\beta$ -H elimination and the release of butenes. The resulting species is a Cr-H which can either release hydrogen and regenerate the tripodal species or undergo C-H activation of butane to produce further butenes by  $\beta$ -H elimination. The conversion of butenes into butadiene occurs through a second cycle consisting in the activation of C-H bond of 1-butenes in an allylic position after trans-2-butenes isomerization, followed by a  $\beta$ -H elimination leading to the release of butadiene and hydrogen (Scheme 3).



**Scheme 3.** Proposed mechanism for butenes dehydrogenation

### III. Production of aromatics

#### III.1 Uses and resources of aromatics

Aromatics are referred in this context to benzene, toluene and xylene (BTX) and are considered as high valuable feedstocks for the chemical industry for the production of pigment dyes, surfactants and pesticides.<sup>61</sup> They are used for the production of rubbers, cosmetics and adhesives, but are mainly employed as gasoline blending components.<sup>62</sup> Thus, the global demand towards BTX and especially towards benzene and toluene has been increasing over the last years due to their high consumption and utilizations. Additionally, this demand is estimated to keep on rising over the next years (Figure 11, Left).

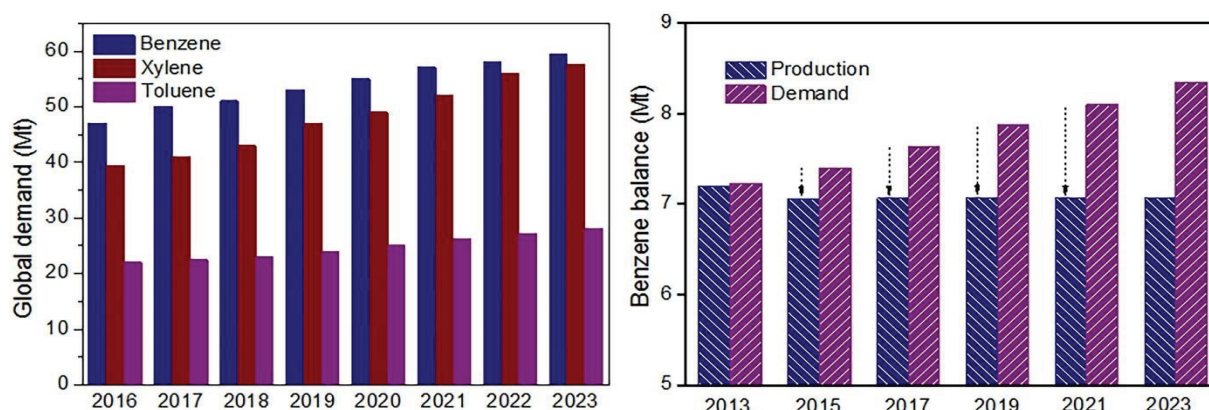


**Figure 11.** Left: Global demand towards BTX between 2016 and 2023 and Right: Benzene production vs demand between 2013 and 2023.<sup>63</sup>

The several pathways for the production of aromatics are summarized in Figure 12. BTX are mainly obtained from steam catalytic cracking of naphta.<sup>64</sup> However, it is obvious from Figure 11, Right that benzene's supply is unable to satisfy the market demand. With the huge development of the petrochemical industry and the high dependency on fossil fuels, the above-mentioned traditional route seems inadequate to fill the expanding gap between the production and the supply of BTX. Thus, it is urgent to develop alternative ways for the production of aromatics. In that manner, industrial and academic investigations in order to develop new process based on methanol to aromatics (MTA), syngas to aromatics (STA) and CO<sub>2</sub> hydrogenation have been also proposed and studied.<sup>65-67</sup> Moreover, alkane aromatization emerged as a promising and alternative synthetic method to produce aromatics and is used industrially.

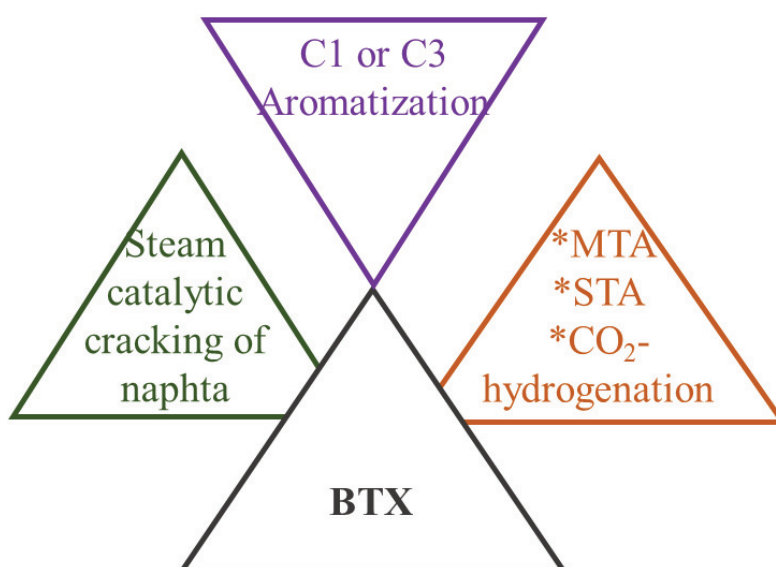


**Figure 12.** Various ways for the BTX production

Typically, Zn or Cu or Ga supported on ZSM-5 are used in methanol to aromatic's (MTA) reaction yielding a conversion around 50-70 % of aromatics coupled with light hydrocarbons and coke formation.<sup>68-70</sup> Two approaches are employed for the production of aromatics from syngas (STA): the first one is a direct transformation of syngas into aromatics over modified Fisher-Tropsch catalysts, while the second one occurs through two steps using composite catalysts that produce some intermediates, which are then transformed into aromatics.<sup>71</sup> Recently, more attention has been paid to transform CO<sub>2</sub>, a greenhouse gas, into valuable chemicals, such as selective CO<sub>2</sub> hydrogenation into aromatics. During this reaction, a

bifunctional (methanol synthesis catalyst/ H-ZSM-5) or multifunctional catalyst (Fe-based catalyst/ H-ZSM-5) has been employed. The selectivity towards aromatics as well as undesirable CO is highly dependent on the nature of the catalyst.<sup>72,73</sup> Replacing crude oil such as naphtha with a more available source (alkanes) results in a low cost and efficient process. For that reason, alkane aromatization has succeeded to attract the researchers focus from both an industrial and an academic point of view.<sup>74-79</sup> Methane and propane aromatization (MAr and PAr, respectively) have been intensively studied during the last years. MAr requires higher temperature than PAr, leading to the formation of coke and therefore reducing the lifetime of the catalyst.<sup>80</sup> PAr occurs through several steps: dehydrogenation, oligomerization, cyclization and aromatization. For that reason, a bifunctional catalyst is essential in order to catalyze propane into aromatics, without the production of oxygenated molecules or toxic by-products.

Based on the limitations and challenges that each of the above processes represents, propane aromatization remains a cost effective and environmental friendly technology to produce aromatics. In fact, PAr has been commercialized and a bifunctional catalyst (a gallium supported catalyst on an acidic micro-zeolite (ZSM-5)) is adopted by Cyclar®. In addition to Cyclar®, four other processes are being deployed for the production of BTX using a variety of feedstock such as M2-Mobil®, Aroforming®, Z-Forming® and Alpha® process. However, Cyclar® remains the most potential process to date and will be discussed in the following section.

## **III.2 Industrial process:**

### **III.2.a Industrial process for PAr based on Ga:**

The Cyclar® process is the result of a joint development between BP and UOP for the conversion of propane into aromatics. It involves a gallium-based catalyst on a commercial zeolite, ZSM-5.<sup>81</sup> This process includes several reactors: a main section consisting in a series of adiabatic reactors and a product recovery section ensuring the continuous production of aromatics and hydrogen, while another continuous catalyst regeneration (CCR) technology is designed in order to restore the catalyst's activity over the time on stream (Figure 13).<sup>82</sup> Thus, this results in a catalyst lifetime of two years. However, the highest selectivity obtained in this process after the product recovery section is moderate and estimated to be around 63.1 wt%.<sup>83</sup>

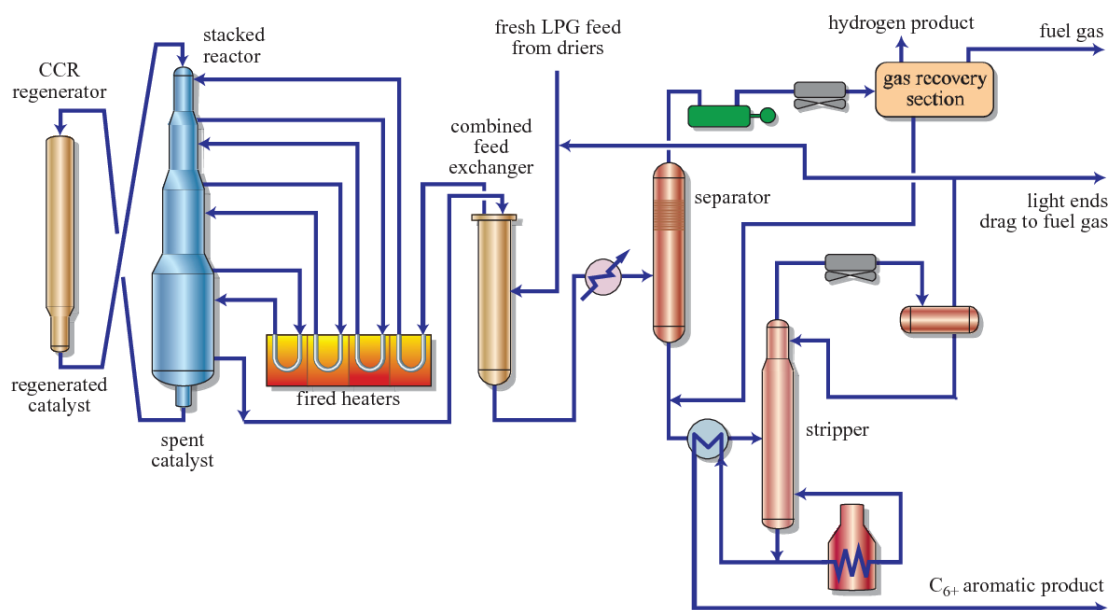
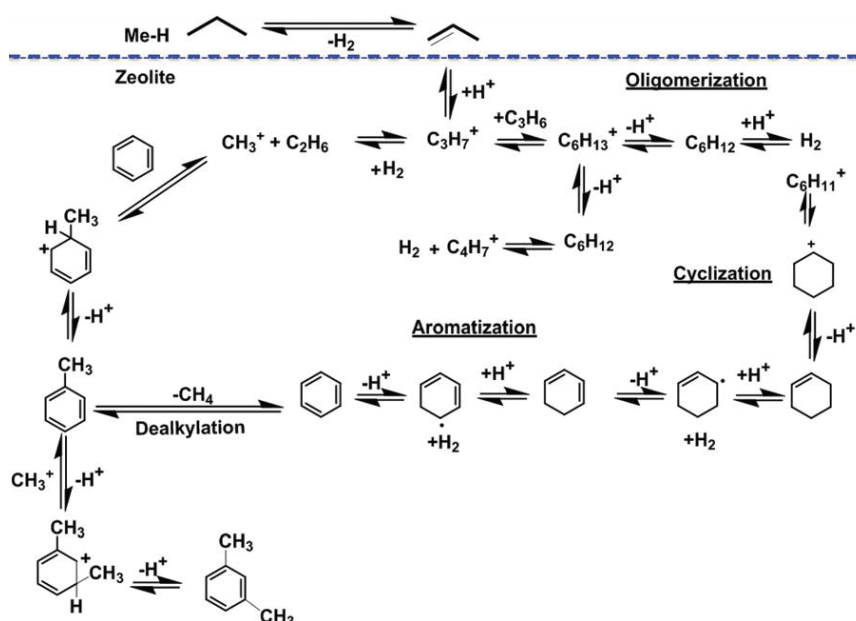


**Figure 13.** Schematic representation of Cyclar® process<sup>84</sup>

### III.2.b Active sites and mechanism:

As propane aromatization occurs in two main reactions (dehydrogenation and aromatization), a bifunctional catalyst displaying the active metal sites for dehydrogenation and acidic sites for oligomerization, cyclization and aromatization is required.<sup>85</sup> The complexity of the aromatization reactions makes it hard to control the activity and selectivity during aromatization reaction. It was reported that in Cyclar® process, the dehydrogenation activity is attributed to the gallium species, which leads to an increase in the selectivity toward aromatics by increasing the rate of the first reaction (dehydrogenation). However, the aromatization of propene intermediate is known to be catalyzed on the acidic sites in the micropores of the zeolite. The mechanism of the propene aromatization occurs by protonation of the double bond leading to the formation of C<sub>4</sub>-C<sub>10</sub> through oligomerization reaction. The transformation of the latter products into the corresponding dienes occurs via hydrogen transfer reaction, followed by a cyclization to form cyclic alkenes, which are furthermore converted into cyclic dienes. The last step corresponding to the formation of aromatics is due to the transfer of hydrogen from cyclic dienes in order to recover the active sites (Scheme 4). The exact nature of the gallium active sites in the case of the dehydrogenation step is still unclear (see section V.1).



**Scheme 4.** Proposed mechanism for propane aromatization<sup>86</sup>

## Conclusion

In summary, of all the aforementioned technologies, Oleflex<sup>®</sup>, STAR<sup>®</sup> (both platinum-based catalysts), Catofin<sup>®</sup> and Catadiene<sup>®</sup> (both chromium-based catalysts) have been used industrially for the propane and butane/butenes dehydrogenation while the Cyclar<sup>®</sup> process has been industrially used for the propane aromatization (Ga/ZSM-5). However, the issues related to both environmental (high toxicity of chromium) and economical (high cost of noble metal Pt) challenges and the lifetime (deactivation of the catalysts) require further development and optimization of the existing Cr and Pt catalysts. For aromatization, the high concentration of gallium related to the preparation method, results in an expensive catalyst and a remarkable deactivation and cracking due to the formation of undesired oligomeric GaOx species on the surface.

Thus, the need for alternative non-toxic, cheap and active candidates for the targeted reactions with low loading of metal compared to the existing industrial catalytic systems that can tackle the aforementioned issues is justified and remains an important focus for the research community. Several metal oxides such as Ga, V, Zn, Zr, Co, and noble metals have been investigated and reported widely, due to their high affinity for C-H bonds and low activity toward C-C cleavage. In the case of noble metals, platinum exhibited the best catalytic performance, while Ni, Rd and Ru lead to a low activity and selectivity in dehydrogenation

reaction. However, the metal oxides and mixed oxides of non-noble metals are equally important in catalyst technologies due to their low cost, abundant availability and a great flexibility in tailoring their properties. Among them, bulk and supported Ga and V oxides based catalysts have been widely studied and represent some competitive advantages for several applications in the future.

In addition, in all processes (PDH, BDH and PAr), the dehydrogenation step is reported to be the common reaction to obtain propylene, diene and aromatics. For this reason, in the following section, we will limit our literature review to the development of catalysts based on Ga and V oxides for the non-oxidative PDH, and particularly, on the supported metal (Ga and V) oxides catalysts.

#### IV. Propane dehydrogenation reaction

The non-oxidative propane dehydrogenation (NOPDH) is a catalytic process based on the direct conversion of propane into propylene and hydrogen. This reaction is endothermic and is limited by equilibrium at low temperature and high pressure. To overcome this limitation, high process temperature and low pressure are required to achieve high conversion (Figure 14).<sup>87,88</sup> According to the literature, a temperature of 550 °C and a pressure of 1 bar at least are used in conventional reactors to secure a conversion up to 30% (Figure 14).<sup>30</sup>

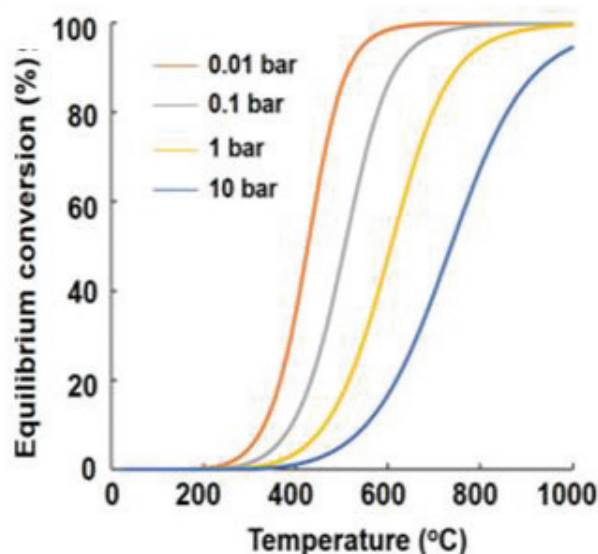
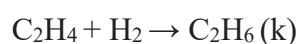
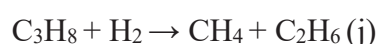


**Figure 14.** Equilibrium conversion as function of temperature and pressure<sup>30</sup>

At high temperature in the NOPDH process, cleavage of C-C bonds competes with the cleavage of C-H bonds, resulting in the cracking of propane and the formation of undesired products like methane and ethylene (i) in addition to the main reaction (h). Further side reactions explain the formation of ethane and methane by hydrogenolysis of propane (j), the hydrogenation of ethylene into ethane (k) and the coke formation (l).<sup>89</sup> These side reactions are proposed to be encouraged by the acidity of the support and due to the presence of hydrogen produced from the direct conversion of propane (h) and from coke formation (l). At high operating temperature, the formation and adsorption of coke on the catalyst's surface leads to a quick deactivation that affects its lifetime, thus frequent regeneration is necessary. For example, in the case of the Catofin® industrial process, the continuous regeneration of the catalyst occurs every 15-25 min.<sup>30</sup>



In order to limit the undesired reactions, many attempts were proposed such as using a membrane to selectively remove H<sub>2</sub>, and shifts the reaction toward producing more propylene by decreasing the working temperature.<sup>90</sup> Membranes were and still an interesting subject for researchers. They are not only beneficial to remove one product from a field and separate it from the mixture, but are also interesting to provide pure and valuable hydrogen for several catalytic applications.<sup>91-93</sup> However, this technology is still under investigation since the most used Pd-Ag membrane is expensive due to the high price of Pd and deactivates quickly during the dehydrogenation reaction.

## **V. Catalytic development of metal oxide catalyst in the non-oxidative PDH**

Currently, several studies are dedicated to the development of novel and potential metal oxide catalysts in propane dehydrogenation (PDH), such as zirconia, zinc, gallium oxide-based catalysts,<sup>94,95</sup> vanadium-oxide based catalysts<sup>96</sup> and so on. Among these, gallium and

vanadium oxide-based catalysts have been recognized as very promising alkane dehydrogenation materials due to their unique capacity to activate hydrocarbon species and excellent catalytic efficiency as compared to conventional Cr<sub>2</sub>O<sub>3</sub>. An exhaustive literature review will report next the systems describing the Ga and V catalyst's structure as well as their active species, their lifetime, their deactivation, the effect of the support and their activity toward propane conversion.

### **V.1. Supported gallium oxide-based catalysts**

Although commercial Ga<sub>2</sub>O<sub>3</sub> has shown to be far superior for the dehydrogenation reaction compared with Cr<sub>2</sub>O<sub>3</sub> and V<sub>2</sub>O<sub>5</sub> catalysts, some recent studies have demonstrated that supported gallium oxides can be more active and stable for the dehydrogenation of light alkanes.<sup>97-99</sup>

Supported gallium oxide-based catalysts have been a promising applicant for the non-oxidative dehydrogenation reaction for years since the discovery of Ga/ZSM-5 for propane aromatization in the 80's. Ever since, many studies were conducted in order to elucidate the reasons behind this high catalytic performance and to determine the active species responsible for its activity in PDH. Although propane dehydrogenation over supported Ga oxide have been studied for decades, the structure of the active species and the mechanism are still unclear. The active sites responsible for this reaction were debated for years, but it has been reported that they strongly depend on the nature of the support, the preparation methods and the metal loading.<sup>100</sup>

The effects of the surface area and the nature of the support (neutral, acidic or basic) on the catalyst's structure and activity have been reported and widely studied in literature.<sup>100</sup> In this context, gallium oxide was grafted on several supports like Al<sub>2</sub>O<sub>3</sub>, SiO<sub>2</sub>, MgO, ZrO<sub>2</sub>, TiO<sub>2</sub>, ZSM-5, ITQ-2, MCM-22 and others (Table 2). These studies revealed that the acidity of the support clearly influence the surface morphology, the gallium oxide dispersion on the surface and coke formation, which impacts the catalytic performance. Although this acidity can basically influence and determine the dispersion of gallium oxide active sites to obtain a high activity and selectivity in PDH, it can induce secondary cracking reactions, affecting the stability of the catalyst by formation of coke and the selectivity toward propylene. Thus, targeting a well-balanced concentration of acidic sites to maintain a good catalytic performance is essential.<sup>101</sup> Xu et al reported that the catalytic performance of Ga<sub>2</sub>O<sub>3</sub>

supported on TiO<sub>2</sub>, Al<sub>2</sub>O<sub>3</sub> and ZrO<sub>2</sub> was better compared to Ga<sub>2</sub>O<sub>3</sub> supported on SiO<sub>2</sub> and MgO in propane dehydrogenation. This behavior was attributed to the presence of a higher concentration of acid sites in medium to strong strength.<sup>97</sup>

**Table 2.** Comparison of the effect of supports on gallium oxide-based catalysts in propane dehydrogenation reaction

Catalysts	Ga <sub>2</sub> O <sub>3</sub> content(wt%)	T (° C)	WHSV (h <sup>-1</sup> )	X propane <sup>ab</sup> (%)	S propylene <sup>ab</sup> (%)	Ref
Ga <sub>2</sub> O <sub>3</sub> /MCM-22	5	600	0.6	57.8(20.6) <sup>c</sup>	37.5(64.1) <sup>c</sup>	102
Ga <sub>2</sub> O <sub>3</sub> /ITQ-2	5	600	0.6	30.0(19.3) <sup>c</sup>	72.0(78.4) <sup>c</sup>	102
Ga <sub>2</sub> O <sub>3</sub> /HZSM-48	5	600	0.6	40.0(36.3) <sup>c</sup>	53.8(54.5) <sup>c</sup>	95
Ga <sub>2</sub> O <sub>3</sub> /ZSM-5	5	600	0.6	76.3(25.0) <sup>c</sup>	—	103
Ga <sub>2</sub> O <sub>3</sub> /TiO <sub>2</sub>	5	600	0.6	23.0(3.0) <sup>d</sup>	85.0(—) <sup>d</sup>	97
Ga <sub>2</sub> O <sub>3</sub> /Al <sub>2</sub> O <sub>3</sub>	5	600	0.6	33.0(18.0) <sup>d</sup>	92.0(—) <sup>d</sup>	97
Ga <sub>2</sub> O <sub>3</sub> /ZrO <sub>2</sub>	5	600	0.6	39.0(5.0) <sup>d</sup>	74.0(—) <sup>d</sup>	97
Ga <sub>2</sub> O <sub>3</sub> /SiO <sub>2</sub>	5	600	0.6	7.2(6.5) <sup>d</sup>	92.0(—) <sup>d</sup>	97
Ga <sub>2</sub> O <sub>3</sub> /MgO	5	600	0.6	5.3(4.0) <sup>d</sup>	34.0(—) <sup>d</sup>	97
Ga <sub>2</sub> O <sub>3</sub> /Al <sub>2</sub> O <sub>3</sub>	5	620	0.6	46.0(15.6) <sup>c</sup>	95.2(93.1) <sup>c</sup>	100
Ga <sub>2</sub> O <sub>3</sub> /ZSM-5	5	620	0.6	78.1(28.8) <sup>c</sup>	60.2(86.1) <sup>c</sup>	100
Ga <sub>2</sub> O <sub>3</sub> /SiO <sub>2</sub>	5	620	0.6	6.7(5.1) <sup>c</sup>	90.1(91.1) <sup>c</sup>	100
Ga <sub>2</sub> O <sub>3</sub> /SBA-15	5	620	0.6	28.5(22.1) <sup>c</sup>	92.5(91.6) <sup>c</sup>	100

<sup>a</sup> Note: the given data of X propane and S propylene are estimated according to the given curves in the literatures. <sup>b</sup> The values outside and inside the parenthesis are the data obtained in the initial and terminal times, respectively. <sup>c</sup> The propane conversion (%) and corresponding propylene selectivity (%) after reaction for 8 h. <sup>d</sup> The propane conversion (%) and corresponding propylene selectivity (%) after reaction for 3 h

Additionally, the catalytic activity, stability and selectivity of Ga<sub>2</sub>O<sub>3</sub> on acidic microporous H-ZSM-5 were improved by the modification of the acidity of the support.<sup>104</sup> The high stability and higher selectivity toward propylene obtained in the case of Ga supported on high surface area, ITQ-2, was assigned to the high dispersion of gallium and consequently to a lower concentration of strong acid sites.<sup>102</sup> A higher amount of coke formation was reported in the case of Ga<sub>2</sub>O<sub>3</sub> on ZSM-5 than on neutral SBA-15, triggered by the presence of strong

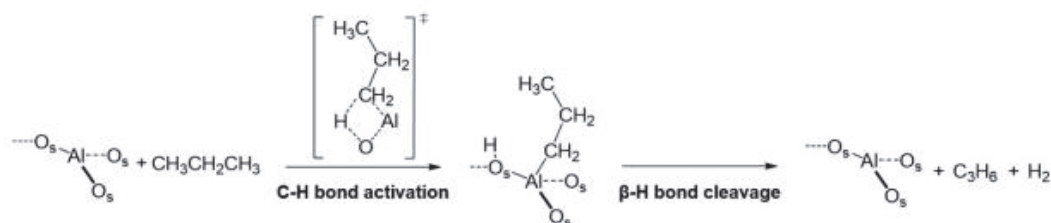
acid sites on ZSM-5 support (Table 3).<sup>100</sup> The acidity of these catalysts has been determined by NH<sub>3</sub>-TPD and revealed that Ga<sub>2</sub>O<sub>3</sub>/SBA-15 exhibits a very weak surface acidity with the increase of Ga<sub>2</sub>O<sub>3</sub> coverage. In fact, the lowest loading, 1Ga<sub>2</sub>O<sub>3</sub>/SBA-15, exhibited the highest TOF value and low coke amount, which is assigned to the high dispersion of gallium species. Increasing the gallium oxide loading to 3, 5, 7 and 9 results in a decrease in TOF values (Table 3).<sup>100</sup> This observation can be probably attributed to the formation of bulk Ga<sub>2</sub>O<sub>3</sub> at high loading, which decrease the efficiency of the gallium oxide catalyst during the dehydrogenation.

**Table 3.** Amount of coke as function of support and metal loading in PDH

Catalysts	Coke amount <sup>b</sup> (%)	TOF (s <sup>-1</sup> )(x10 <sup>-2</sup> )
5Ga <sub>2</sub> O <sub>3</sub> /ZSM-5 <sup>c</sup>	12.6	1.81
5Ga <sub>2</sub> O <sub>3</sub> /SBA-15 <sup>c</sup>	4.55	2.91
5Ga <sub>2</sub> O <sub>3</sub> /SiO <sub>2</sub> <sup>c</sup>	0.96	0.80
1Ga <sub>2</sub> O <sub>3</sub> /SBA-15 <sup>d</sup>	3.97	6.92
3Ga <sub>2</sub> O <sub>3</sub> /SBA-15 <sup>d</sup>	5.85	3.72
5Ga <sub>2</sub> O <sub>3</sub> /SBA-15 <sup>d</sup>	3.11	4.20
7Ga <sub>2</sub> O <sub>3</sub> /SBA-15 <sup>d</sup>	6.32	2.08
9Ga <sub>2</sub> O <sub>3</sub> /SBA-15 <sup>d</sup>	6.52	1.64
SBA-15	0.82	-

In addition to the effect of the acidity and the metal loading, the nature of the support has been studied. Among all the supports (Table 2), alumina is widely employed as support, notably in the commercial processes for PDH catalysts, due to its desirable textural properties: high surface area, high mechanical strength and thermal stability.<sup>100</sup> These properties are beneficial to have a highly dispersed gallium on the surface, and thus improve the catalyst's stability. Indeed, we recently demonstrated that dehydroxylated alumina at 500 °C displays a low activity around 3 % with high selectivity in propene.<sup>105</sup> This was attributed to the Lewis acid rising from Al<sup>3+</sup> site, contributing to the catalytic cycle, as reported in the case of Cr<sup>3+</sup> tripodal. Scheme 5 shows the proposed mechanism over Al<sub>2</sub>O<sub>3</sub> during propane

dehydrogenation. It includes an initial C-H bond via the abstraction of a proton by a surface oxygen, leading to a tetrahedral  $\text{Al}^{3+}\text{C}_3\text{H}_7$  surface species. Consequently, the  $\beta$ -hydrogen elimination results in the release of  $\text{H}_2$  and propylene.<sup>106</sup>



**Scheme 5.** Proposed mechanism for  $\text{Al}_2\text{O}_3$  in PDH<sup>106</sup>

The high activity of supported  $\text{Ga}_2\text{O}_3$  on alumina is related to the presence of tetracoordinated Lewis acidic  $\text{Ga}^{3+}$  sites, active sites for PDH.<sup>30,107,108</sup> In fact,  $\text{Ga}_2\text{O}_3$  on alumina has several polymorphs:  $\alpha$ -,  $\epsilon$ -,  $\gamma$ -,  $\delta$ -, and  $\beta$ - $\text{Ga}_2\text{O}_3$ . Among these,  $\beta$ - $\text{Ga}_2\text{O}_3$  structure is the most stable and exhibits the best activity in propane dehydrogenation.<sup>109</sup> The lattice is a monoclinic structure of  $\text{Ga}_2\text{O}_3$  where the Ga atoms are divided on the tetrahedral and octahedral sites.<sup>110</sup>

The atomic-scale understanding of active sites in supported  $\text{Ga}_2\text{O}_3$  catalysts was crucial in order to develop highly active catalysts in PDH.<sup>111</sup> It has been reported that the tetracoordinated Lewis acidic  $\text{Ga}^{3+}$  surface sites,<sup>30,107</sup> is associated with weak Lewis acid sites (LAS).<sup>112,113</sup> Chen et al. studied the catalysts  $\text{Ga}_2\text{O}_3\text{-Al}_2\text{O}_3$  prepared with several compositions ( $\text{Ga}_x\text{Al}_{10-x}\text{O}_{15}$ ) through a colloidal synthesis approach and demonstrated that the maximum propane activity and propene selectivity were observed at  $x=8$ . However, for the  $\text{Ga}_5\text{Al}_5\text{O}_{15}$  catalyst, the authors found a high stability at high conversion related to the abundant specific surface area sites due to the presence of tetrahedral  $\text{Ga}^{3+}$  sites. The presence of this latter species has been confirmed by  $^{71}\text{Ga}$  MAS NMR exhibiting a signal at 180 ppm as opposite to the trend of  $\text{Ga}^{3+}$  octahedral ion at 10 ppm. The increase of the aluminum content leads to an increase in the active  $\text{Ga}^{3+}$  tetrahedral sites.<sup>107</sup> More recently, Fernandez et al. confirmed the same findings by using  $^{71}\text{Ga}$  MAS NMR, XANES and EXAFS spectroscopy on  $(\text{Ga},\text{Al})_2\text{O}_3$  prepared with different Ga:Al molar ratios, (1 : 6; 1 : 3; 3 : 1 and 1 : 0) via a colloidal synthetic method. The  $^{71}\text{Ga}$  MAS NMR spectrum exhibited two signals at 150 and 30 ppm, assigned to distorted Ga tetrahedral and Ga octahedral sites, respectively.<sup>114</sup> In addition, XANES spectroscopy of the prepared  $(\text{Ga},\text{Al})_2\text{O}_3(x : y)$  series revealed additional information

on the relative abundance of Ga tetrahedral and octahedral sites. The two features at ca. 10 375 eV and 10 380 eV are related to tetrahedral Ga and octahedral Ga, respectively.<sup>115</sup> Moreover, as reported in the case of Chen et al earlier, the increase in aluminum content resulting in a higher concentration of tetrahedral Ga was confirmed by the increase of the white line feature of tetrahedral Ga sites as shown in Figure 15.A, and consequently leads to a decrease in those for octahedral Ga. The evaluation of the local environment of Ga by EXAFS provided additional information on the Ga coordination. Two distinct peaks were observed for Ga-O and Ga-Ga/Al (Figure 15.B). The authors demonstrated that the high activity and selectivity are related to the presence of tetrahedral Ga-O-Al(VI) surface linkage. In addition, the catalysts prepared with high loading of Ga exhibits a higher presence of bulk octahedral Ga sites, responsible for a fast deactivation by coke deposition.

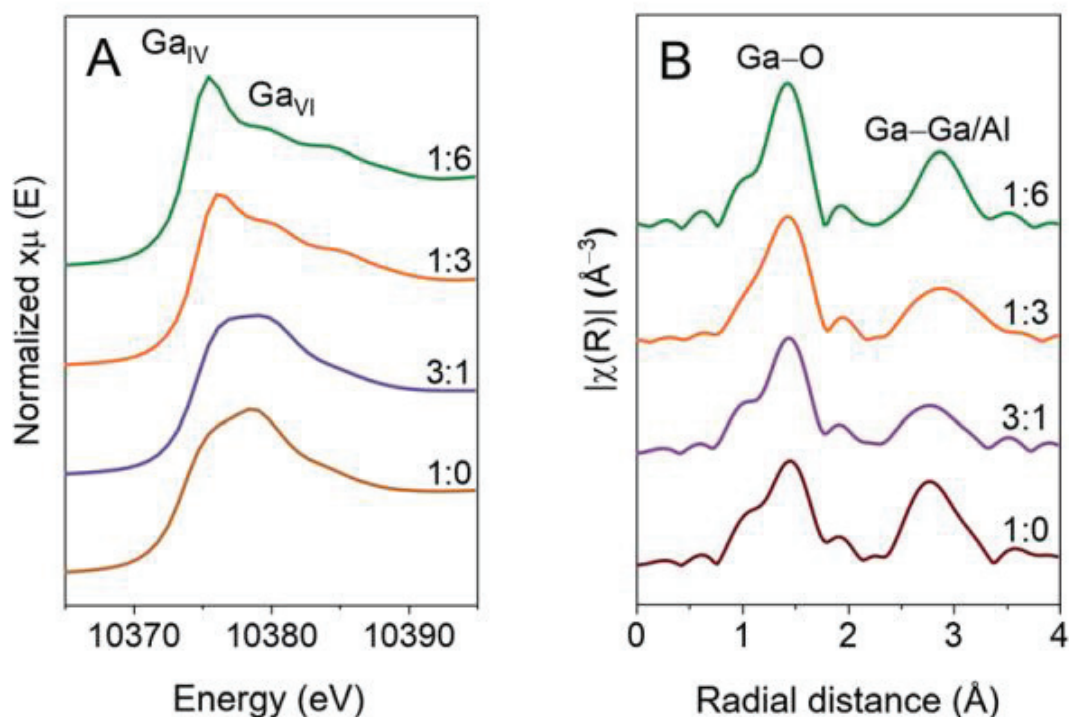


**Figure 15.** (A) Ga K-edge XANES spectra, and (B) Fourier transform of the EXAFS data of  $(Ga,Al)_2O_3(x : y)$ ; Captions in (A) indicate features corresponding to Ga(IV) and Ga(VI) sites and captions of the peaks in (B) indicate the Ga– O and Ga–Ga/Al coordination sphere<sup>115</sup>

All these preparation methods described in literature for supported gallium oxide catalysts are generally based on conventional techniques such as wetness impregnation of aqueous gallium nitrate on alumina. This preparation method is usually followed by calcination in order to

obtain a high dispersion of the metal sites on the surface.<sup>97,98,100,116,117</sup> Although these methods are easy and don't require previous treatments or synthesis step, they yield to a large distribution of MO<sub>x</sub> species on the surface, resulting in lower active sites and catalytic activity in PDH.

Due to the presence of a mixture of surface species on gallium oxide-based catalysts prepared by classical methods, the mechanism of PDH is still unclear and matter of debate. Generally, the active sites of supported gallium oxides are considered to be a tetrahedral Ga<sup>3+</sup>-oxygen pairs.<sup>35</sup> The latter usually tends to coordinate with carbon atoms and hydrogen atoms of propane, which reduce the activation energy of C-H cleavage. The Horiuty-Polanyi (HP) mechanism is widely employed to explain the dehydrogenation of propane into propylene over metal oxide catalysts. The first step involves an heterolytic C-H activation on Ga-O, leading to the alkyl fragment's adsorption on unsaturated metal atoms, while hydrogen adsorbs on oxygen atom near these metal atoms (Figure 16). This step is followed by a hydrogen transfer and coordination of propylene to the metal ion.<sup>118</sup> Then, hydrogen is desorbed by protonation of Ga-H and Al-OH and formation of Ga-O bond. Propylene is furthermore desorbed by a de-coordination from the metal.<sup>119</sup> However, recently, Schreiber et al. found that the aforementioned HP mechanism, may not be appropriate in the case of Ga/H-ZSM-5 catalysts for PDH.<sup>120</sup> In fact, they reported that beside the common heterolytically dissociation process considered a first step of dehydrogenation, the second one should occur via an intermediate state of carbenium instead of direct cleaver of C-H bond in propane (Figure 16).

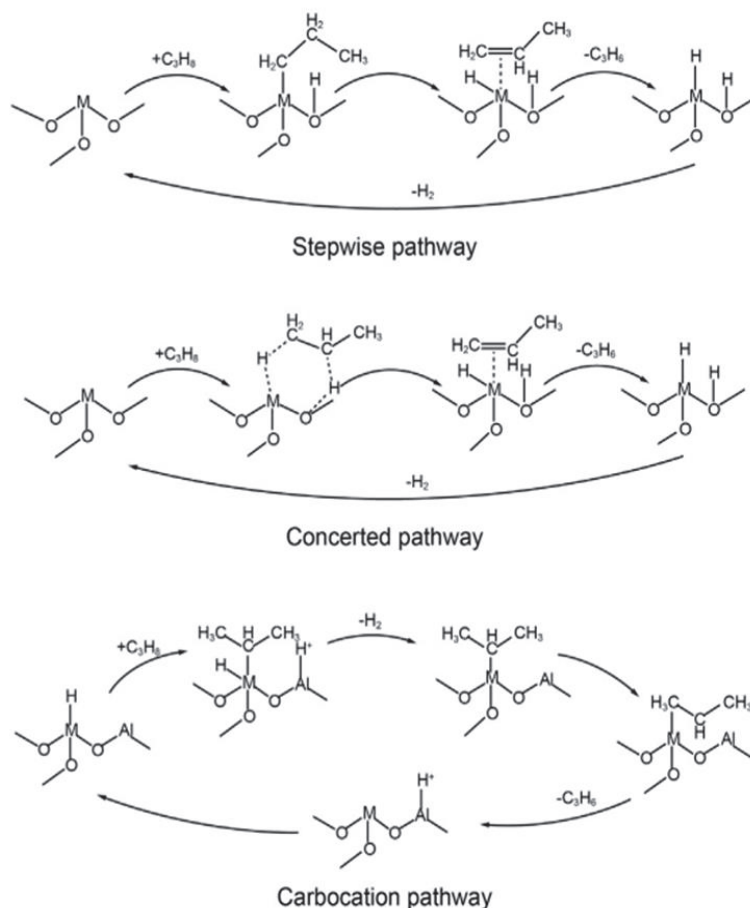


**Figure 16.** Proposed mechanism in the case of gallium oxide catalysts<sup>35</sup>

## V.2 Vanadium oxide-based catalysts

The chemistry of supported vanadium oxide catalysts has perceived remarkable research activities in the last decades due to their low cost, available V precursors and promising catalytic performance in propane dehydrogenation.<sup>121</sup> Since 1980s, extensive research started on vanadium-based catalysts with a main focus on the oxidative dehydrogenation on vanadium-magnesium mixed oxides.<sup>122,123</sup> Nevertheless, the overoxidation of propylene and other hydrocarbons during this reaction resulted in a lower olefin selectivity.<sup>124,125</sup> Later on, vanadium oxide catalysts have been developed for the non-oxidative propane dehydrogenation due to their high selectivity toward propylene. Similar to gallium, the nature of the vanadium species (monomeric, oligomeric and crystalline) present on the surface is still matter of debate. The intensive studies for the development of highly active catalysts have been reported in literature describing the effect of the support (type and surface area), the metal loading, the structure of vanadium species and the preparation methods. These

parameters have been demonstrated to influence the nature of these species and results in different catalytic activity.<sup>124</sup>

The nature and the surface area of the support play an important role in supported vanadium oxide catalysts for PDH reaction, in particular, in the structure of the active species and their dispersion on the surface. For example, vanadium supported on mesoporous alumina with high surface area and large pore volume exhibits a superior catalytic activity in PDH than a alumina with moderate surface area. The authors claimed that these mesoporous alumina materials with more surface acid sites favor the formation of oligomeric VO<sub>x</sub> species reported by Bai et al.<sup>126</sup> to be more active than the isolated ones. The presence of these VO<sub>x</sub> oligomeric species were identified by Raman and <sup>51</sup>V magnetic angle spinning nuclear magnetic resonance. Different supports such as Al<sub>2</sub>O<sub>3</sub>, SiO<sub>2</sub>, MCM-41, and modified alumina with MgO, SiO<sub>2</sub> and K<sub>2</sub>O were investigated in order to study the dispersion of vanadium oxide on the activity and selectivity in PDH. For example, Sokolow et al. reported that doping alumina with silica offers advantageous effects on the catalyst's stability and activity.<sup>127</sup> In fact, increasing SiO<sub>2</sub> content in Al<sub>2</sub>O<sub>3</sub>-SiO<sub>2</sub> from 0 to 70 wt % influenced the stability of the catalyst over the time on stream: at lower concentration of SiO<sub>2</sub> in the support (1 and 10 wt%) exhibited the highest yield in propylene with a 30 % of propane conversion. However, for the catalyst prepared with highest loading of SiO<sub>2</sub> (70 wt%), a high amount of coke was observed and attributed to the high acidity of this catalyst, resulting in its deactivation. Additionally, the modification of alumina by basic promoters such as MgO or K on alumina, enhances the catalytic activity and stability by reduction of the coke formation (Table 4). VO<sub>x</sub> on silica show also a high conversion and selectivity in PDH at 580 °C, related to the presence of isolated species,<sup>128</sup> contrarily to what was reported in the case of alumina by Bai et al.<sup>126</sup> These results revealed that the neutral and basic supports based on alumina and silica are the most used in order to develop highly active catalyst based on vanadium oxide.

**Table 4.** Catalytic data of VO<sub>x</sub> supported catalysts in PDH <sup>101</sup>

Catalysts	T °C	WHSV.h <sup>-1</sup>	Conversion (%)	Selectivity (%)	Lifetime.h <sup>-1</sup>	References
VO <sub>x</sub> /γ-Al <sub>2</sub> O <sub>3</sub>	600	0.88	32-16	93	28	129
VO <sub>x</sub> /γ-Al <sub>2</sub> O <sub>3</sub>	600	8.25	25-15	72-80	-	130
VO <sub>x</sub> /MgO-γ-Al <sub>2</sub> O <sub>3</sub>	600	3.3	33-24	83-91	-	131

VOx/ Al <sub>2</sub> O <sub>3</sub>	K-meso	610	2.85	70-25	87-83	40	126
VOx/Siral 10		550	0.94	35-12	80-95	25	96
VOx/Siral 10		550	1.78	31-11	90-94	60	127
VOx/SiO <sub>2</sub> (5.26 wt%)		580	0.59	65-43	90	32	132
VOx/SiO <sub>2</sub> (3.7 wt%)		580	0.59	65-43	90	36	128
VOx/MCM-41		550	1.78	22-16	92-93	22.5	133
VOx/MCM-41		550	0.57	<10	87-95	100	134

The nature of the active vanadium sites remains vague and elusive due to the classical preparation methods used similar to the case of gallium, leading to a mixture of oligomeric species on the surface.<sup>135,136</sup> However, numerous studies have been reported in literature and revealed the presence of three different types of VOx species: monovanadate, polyvanadate, and V<sub>2</sub>O<sub>5</sub> crystallite on the surface of the oxide, depending initially on the support surface area and metal loading.<sup>124,137</sup> Liu et al.<sup>129</sup> studied a series of vanadium oxide catalysts supported on alumina with different metal loading, 1, 6, 12 and 20 wt% corresponding to a vanadium density of 0.7, 3.9, 7.9, 13.1 V.nm<sup>-2</sup>, respectively. The characterization of these materials by XRD patterns confirmed the formation of well dispersed vanadium on the surface of alumina for all samples except for 20 %, where crystalline V<sub>2</sub>O<sub>5</sub> phase was identified. UV-Vis spectroscopy of these materials supported as well these findings. In fact, the decrease in the edge energy from 3.9 to 2.5 eV while increasing vanadium loading, represents a rise in the polymerization degree and in the size of vanadium oxides.<sup>96,138,139</sup> UV Raman is a highly sensitive technique allowing the identification of isolated and polymerized VOx species, while visible Raman is more suitable to detect crystalline V<sub>2</sub>O<sub>5</sub>.<sup>124,140</sup>

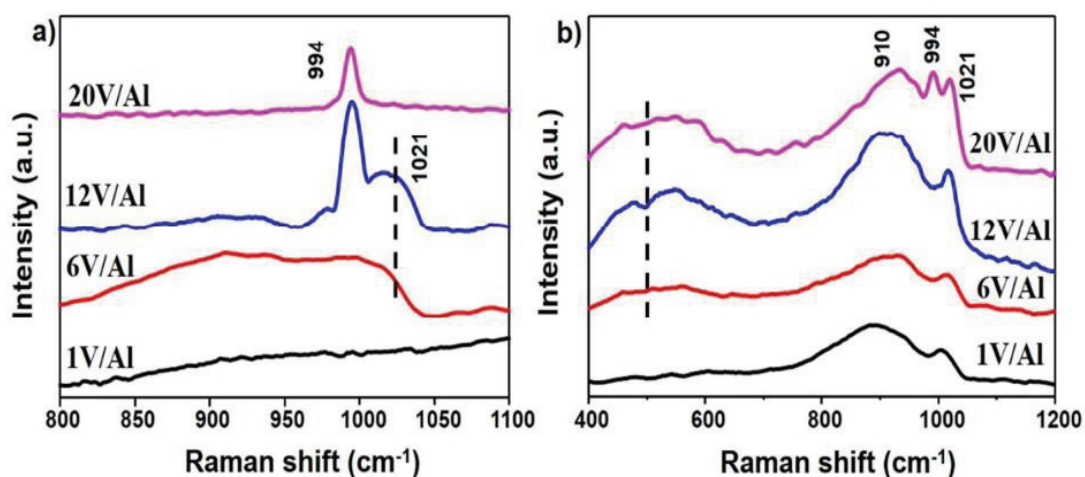
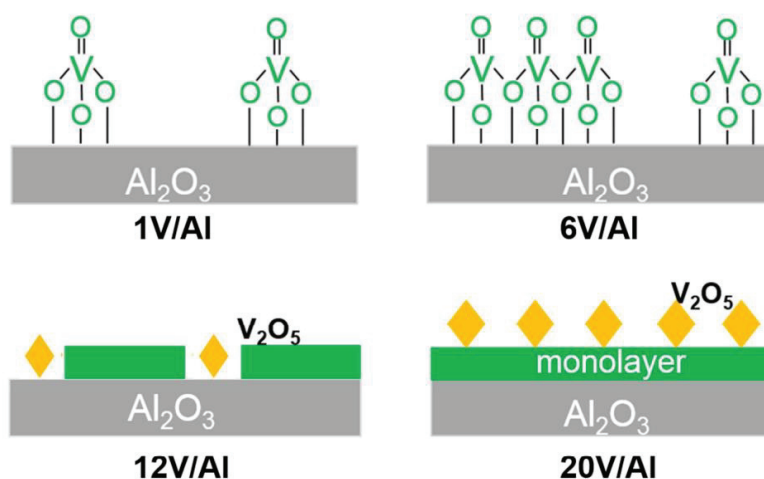


**Figure 17.** Visible ( $\lambda_{\text{excitation}}=532$  nm) and b) UV ( $\lambda_{\text{excitation}}=325$  nm) Raman spectra of the VO<sub>x</sub>/Al<sub>2</sub>O<sub>3</sub> catalysts<sup>129</sup>

A series of bands are visible for these samples in the range of 500-700 cm<sup>-1</sup>, 910 cm<sup>-1</sup>, 994 cm<sup>-1</sup>, and at around 1021 cm<sup>-1</sup>, assigned to V-O-V, V-O-Al, crystalline V<sub>2</sub>O<sub>5</sub> and V=O modes, respectively (Figure 17).<sup>136,140</sup> Importantly, the absence of V-O-V and crystalline V<sub>2</sub>O<sub>5</sub> modes in the UV Raman spectra for the 1% catalyst, indicates that only isolated VO<sub>4</sub> species are present on the surface. For the catalysts prepared with 6 and 12 % of V, in addition to V-O-Al and V=O bands, UV Raman spectra exhibits a broad band in the range of 500~700 cm<sup>-1</sup> assigned to polyvanadate V-O-V species. UV Raman of the 12 % V sample featured a supplementary band at 994 cm<sup>-1</sup>, indicating the presence of V<sub>2</sub>O<sub>5</sub> crystalline. The sharp band at 994 cm<sup>-1</sup> in UV Raman and visible Raman spectra for the catalyst prepared with highest loading (20 %), implies the predominance of V<sub>2</sub>O<sub>5</sub> crystals in this catalyst compared to the others. These results conclude that the metal loading plays a major role in the resulting structure on the surface. At lowest loading (1 % of V), isolated VO<sub>x</sub> species predominates, at 6 % a mixture of monovanadates and polyvanadates are present on the surface, at 12 %, monovanadates, polymerized VO<sub>x</sub> and small V<sub>2</sub>O<sub>5</sub> crystal coexist while at highest loading of 20 % a large concentration of V<sub>2</sub>O<sub>5</sub> is formed (Scheme 6).



**Scheme 6.** Proposed vanadium species of  $\text{VO}_x/\text{Al}_2\text{O}_3$  as function of metal loading (the green part represent isolated and polymerized  $\text{VO}_x$  species, while the yellow parts are for  $\text{V}_2\text{O}_5$  nanoparticles)<sup>129</sup>

In addition, XPS measurements for all these materials allowed the identification of the vanadium valence distribution of the surface. The results exhibited three different binding energies at around 517.6, 516.6 and 515.7 eV, corresponding to  $\text{V}^{5+}$ ,  $\text{V}^{4+}$ ,  $\text{V}^{3+}$  ion, respectively. In addition, the catalytic performance of all these catalysts were evaluated in propane dehydrogenation at 600 °C and all of them exhibited a high selectivity of 87 % toward propylene. However, the catalytic activity depends strongly on the metal loading. The propane conversion was proportional to the metal loading up to 12 %, while it decreased for the catalyst with the highest vanadium content (20 %). The amount of coke formation on the 12 % catalyst was measured using TGA after 4h of reaction and exhibited  $0.054 \text{ g.gcat}^{-1}$ . At that time the propane conversion dropped from 32 to around 16 %.

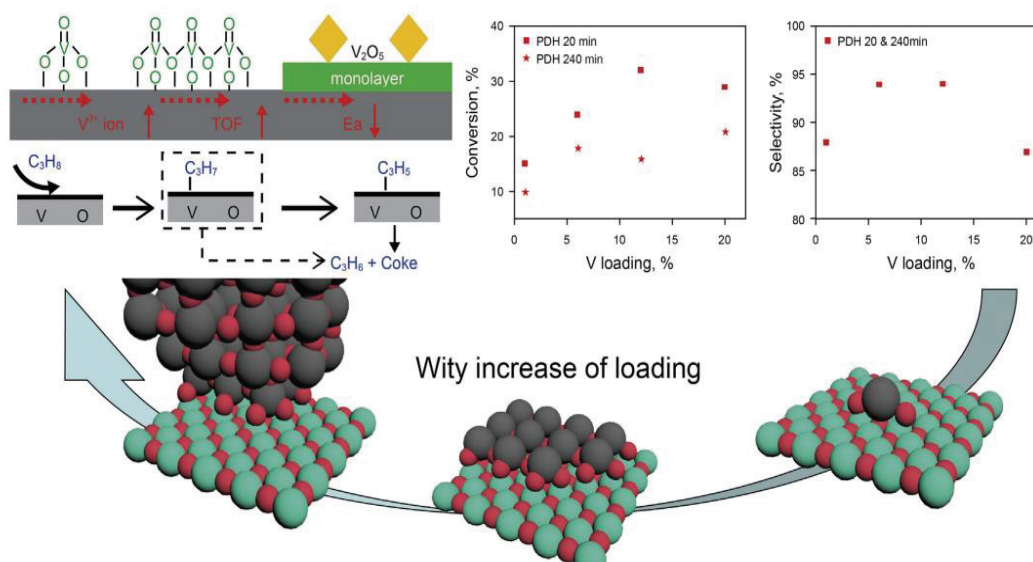
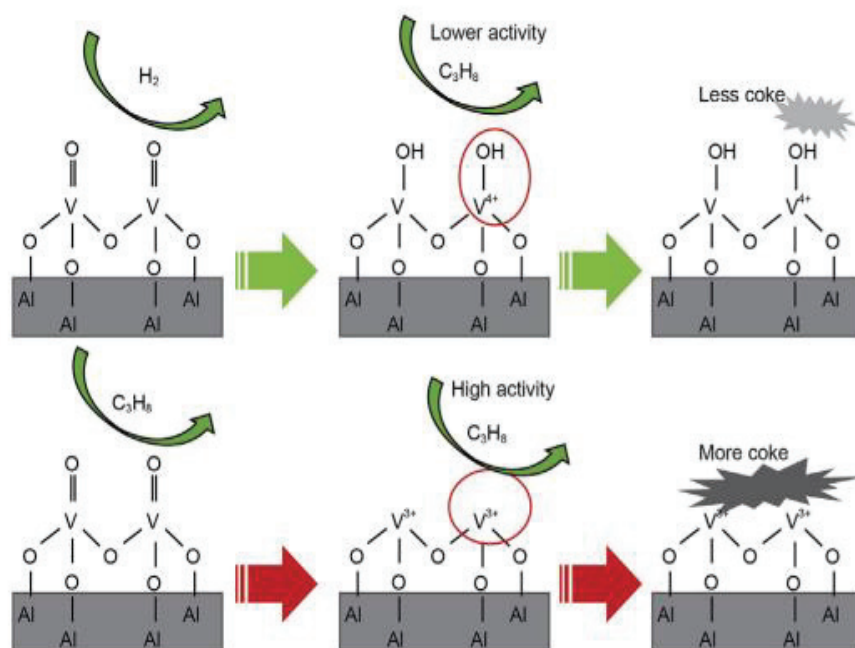


**Figure 18.** Effect of the metal loading on the structure and catalytic activity <sup>129</sup>

From the previous results, the surface species of  $VO_x$  bearing  $V^{5+}$ ,  $V^{4+}$  and  $V^{3+}$  ions on the catalysts, reveal different activity for propane dehydrogenation, and isolated  $V^{3+}$  ions were considered as the most active species compared to  $V^{5+}$  and  $V^{4+}$  ions. Although the mechanism is still unclear, two mechanisms were proposed for vanadium oxide-based catalysts. The first one suggested by Zhao et al.<sup>130</sup> involves a reduction of  $V=O$  into  $V^{4+}$  hydroxy in the presence of hydrogen, followed by a propane activation and leads to a relative low activity and coke formation. The second mechanism consists of a  $C_3H_8$  activation on a  $V^{5+}=O$ , which induces a reduction into  $V^{3+}$  and displays higher activity in PDH but with more coke formation compared to the previous mechanism. Several studies have been reported in order to elucidate the active species and the mechanism of the initiation step. In fact, the activation of the supported tetrahedral  $V^{5+}$  during the dehydrogenation reaction suggests the reduction of this species by propane. This step leads to the formation of supported  $V^{4+}$  and  $V^{3+}$ .<sup>141-143</sup> The difference in coke formation was attributed to the presence of hydroxyl groups: in fact, the presence of a high concentration of vanadium hydroxy (first mechanism) blocks exposed V ion, which improve  $C_3H_6$  desorption, avoids coke formation, and leads to a more stable catalyst compared to the second mechanism.



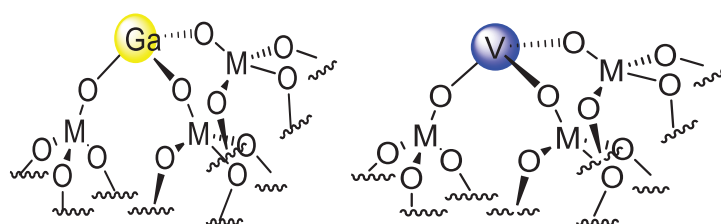
**Scheme 7.** Proposed mechanism for PDH based on vanadium oxide catalysts<sup>129</sup>

## Conclusion

In conclusion, the abundance of light alkanes due to the discovery of new shales gas reserves, opens the door to alternative technologies for the manufacturing of light alkenes, dienes and aromatics, such as on-purpose propane and butane/butene dehydrogenation and propane aromatization. The most developed and commercialized processes for PDH, BDH and PAR are Catofin® for PDH and Catadiene® for BDH, employing supported chromium on promoted alumina, while Cyclar® for PAR uses supported gallium on zeolites. The dehydrogenation reaction remains the common step among all these processes and was widely documented. Regarding the most commonly used PDH catalysts so far, the Ga and V-based catalysts exhibit many advantages in comparison with CrOx based catalysts, for instance, higher reaction rate, higher stability for longer process time before regeneration, and better environmental-friendliness. In that manner, several efforts were conducted in order to develop a highly active and stable catalyst, based on the knowledge of the structure–performance relationship and the catalytic mechanism. Supported vanadium-based catalysts have proven to be promising alternatives to CrOx-based catalyst, due to their low toxicity and price and high reactivity in propane dehydrogenation. It is important to note that numerous studies have focused on the catalytic activity of VOx in the oxidative propane dehydrogenation, while few describes the structure-reactivity relationship and catalytic performance in the non-oxidative

propane dehydrogenation over VO<sub>x</sub> supported catalysts. More recently, Ga as well became an important candidate for the non-oxidative propane dehydrogenation due to their efficient catalytic performance and their easy regeneration.

The reported catalytic systems based on Ga and V are generally prepared by classical methods using gallium or vanadium salts that lead to a mixture of monomeric, oligomeric and polymeric (GaO<sub>x</sub> or VO<sub>x</sub>) surface species. Thus, it is difficult to extend the knowledge of structure-activity relationship and the mechanism of PDH. This is due to the low concentration of active sites, resulting in a difficult or an incomplete determination of the active species. However, based on DFT calculations, there is a consensus that the structure of the active species is an isolated tetrahedral Ga or V bonded to three oxygen pairs from the support and that C-H activation of propane occurs on Ga<sup>3+</sup> or V<sup>3+</sup> on oxygen pair (Scheme 8). The low concentration of these active sites influences the catalytic activity and selectivity, and the presence of oligomeric species leads to severe cracking side reactions causing the deactivation of the catalyst by coke formation and a shorter lifespan.



**Scheme 8.** Structure of the active tripodal Ga or V species (M= Al, Si..)

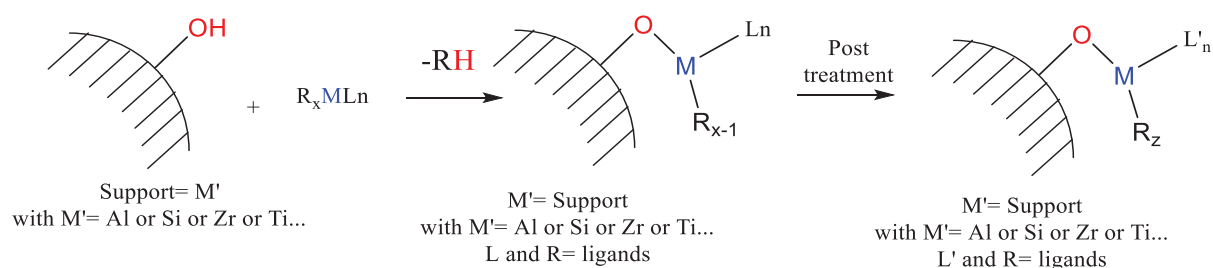
In this context, the development of more accurate catalytic systems is highly favored and required, aiming to identify the nature of the active sites and the elementary steps behind the mechanism of the targeted reaction. Advanced synthesis strategies are necessary to finely tune the structure of Ga and V oxide sites on the support in PDH. Thus, a powerful preparation method yielding to a high concentration of active species is extremely desired to access to well defined catalysts. Surface Organometallic Chemistry (SOMC) is a powerful approach providing the necessary tools to design well-defined single site catalysts. SOMC consists in grafting of organometallic species on the supports leading to well-defined single sites allowing to their better characterization which helps to establish the structure-activity

relationship. In addition, this strategy can lead to the development of highly active and stable catalyst for the targeted reaction.

The next section will be divided in three main parts: i) the SOMC methodology, (ii) a review on isolated Ga sites on oxide supports for PDH and PAr, and (iii) and a review on isolated V sites on oxide supports for PDH.

## VI. Preparation of single site catalysts using Surface Organometallic Chemistry

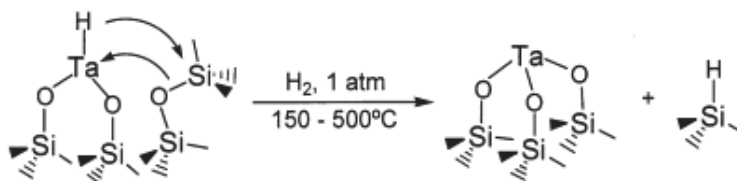
Surface Organometallic Chemistry is a field of surface science that has been developed by a pioneer in catalysis J.M Basset<sup>144</sup>, used since early 1980s and is considered as a bridge between homogenous and heterogenous catalysis. It is an effective method for the preparation of well-defined surface site species by immobilizing organometallic precursors on oxide surfaces (silica, alumina, zirconia...) or on metals (to form nanoparticles on oxides). More importantly, this tool allows a rigorous characterization during the different steps of the synthesis and grafting reactions. In the following section, we will only detail SOMC on oxide surfaces.



**Scheme 9.** Preparation of well-defined single site catalysts using SOMC

With careful thermal treatment of the support followed by characterization, it is possible to identify the type, concentration, and density of the hydroxyl groups M'-OH (M'= Si, Al, Zr, Ti...) present on the surface of the oxide support, that are considered as potential sites for reaction with organometallic complexes (Scheme 9). In fact, depending on the properties of the support, different reactivity can be observed leading to different species and different catalytic applications. Hence, the pre-treatment of the oxides results in a controlled grafting of the organometallic complex. It allows also to tune the concentration of grafting sites per area

of the support. With controlling the coordination sphere of the metal, it is possible to establish a structure-activity relationship for the catalyst by modification of the ligand. Upon grafting of the organometallic complex  $R_xML_n$  (R and L= ligands) on the support, the resulting species can be used directly as a catalyst for the targeted reaction or be subject for further post-treatment (like thermal treatment, hydrogenation, calcination...). By using SOMC on oxides, it is difficult to access in one step to tripodal metal catalysts. However, our group developed an innovative synthetic method in order to access to catalysts bearing a metal bonded with three oxygens from the support. For example, the controlled post-treatment allows in the case of oxophilic metal to access to active sites with different podality. For group IV, the reaction of silica with  $M-Np_4$  (M= Ti, Zr, Hf) leads to the formation of tripodal Zr-H,  $[(\equiv SiO)_3ZrH]$ , resulting from the grafting of  $ZrNp_4$  on silica followed by thermal treatment under  $H_2$  of monopodal Zr species intermediate,  $[(\equiv SiO)ZrNp_3]$ .<sup>145</sup> In fact, the mechanism of the formation of tripodal Zr-H is based on the transfer of hydride from Zr to Si by opening of the siloxane fragments from the surface. This strategy was also extended for the preparation of Ta tripodal systems.<sup>146</sup> The bipodal Ta-H,  $(\equiv SiO)_2Ta-H$ , is converted under hydrogen to tripodal Ta,  $(\equiv SiO)_3Ta$  at high temperature by transfer of hydride from Ta to Si (Scheme 10). Several applications of SOMC have been reported in literature based on the control of the coordination sphere of the metal and the establishment of the relationship structure-activity. For example, supported metal hydride of group IV, V and VI, were used in the hydrogenolysis of light alkanes and depolymerization of wax and polyethylene, alkane or olefin metathesis, direct conversion of ethylene to propylene and methane coupling to ethane.<sup>147</sup>



**Scheme 10.** Strategy to obtain highly unsaturated tripodal Ta systems<sup>146</sup>

Thus, there is a possibility to establish the relationship between the structure and activity by indentifying the structure of the surface organometallic species. The coordination sphere of a single site catalyst (where usually all sites are almost similar and isolated from each other), must be completely characterized via the combination of several techniques: mass balance

analysis, DRIFT, UV-visible, solid-state NMR spectroscopy, XAS (X-ray absorption spectroscopy), EXAFS (extended X-ray absorption fine structure) and XANES (X-ray absorption near edge structure). These characterizations can be coupled with in-situ techniques such as Operando DRIFT, XAS in-situ in order to identify the active species and to determine the mechanism of the catalytic reaction.

The following section will be focused on the description of the catalysts prepared by SOMC for PDH, BDH and PAr reactions. However, to our knowledge, no example was reported in the case of BDH using catalysts prepared by SOMC, hence, we will limit the next literature review to PDH and PAr and in particular to the preparation and characterization of the catalysts based on Ga and V prepared by SOMC. The effect of ligands, the nature of the support and the podality on the activity and selectivity in propane dehydrogenation and aromatization will be addressed.

### VI.1. Gallium catalysts prepared by SOMC

Catalytic systems based on Gallium are being intensively studied due to the high activity on Ga particularly in alkane dehydrogenation. In fact, this activity was demonstrated in the Cyclar® commercial process for propane aromatization, where Ga<sup>III</sup> sites are used to catalyze the dehydrogenation of propane into propene as first step in this process. To our knowledge, only few examples reported in literature describing the preparation of supported Ga single sites for propane dehydrogenation by SOMC.<sup>148</sup> The first example was reported by our group based on the grafting of [Ga(*i*Bu)<sub>3</sub>] on dehydroxylated alumina at 500 °C affording species **(I)**, and dehydroxylated silica at 700 °C affording **(II)**.<sup>105</sup> The resulting materials were characterized by DRIFT, solid-state NMR (<sup>1</sup>H and <sup>13</sup>C) and mass balance analysis and suggested the formation of a different structure on alumina and on silica. EXAFS spectroscopy of species **(I)** and **(II)** confirmed the previous findings and concluded that an isolated monomeric Ga species with 1.97 wt% of Ga on the surface of alumina, [(≡AlO)Ga(*i*Bu)<sub>2</sub>], **(I)** was formed, while a dimeric Ga species with 3.3 wt% of Ga was formed on the surface of silica, [(≡SiO)<sub>3</sub>Ga<sub>2</sub>(*i*Bu)<sub>3</sub>], **(II)**, (Table 5, Table 6, Scheme 11).

**Table 5.** Curve-fit parameters<sup>a</sup> for Ga K-edge EXAFS of Ga(*i*Bu)<sub>3</sub>/Al<sub>2</sub>O<sub>3-500</sub>

Type of neighbors	Number of neighbors	R / Å	10 <sup>3</sup> σ <sup>2</sup> / Å <sup>2</sup>
<b>Ga-O<sub>1</sub></b>	1	1.89(1)	1.3 (7) <sup>b</sup>
<b>Ga-C<sub>1</sub></b>	2	2.07(2)	1.3 (7) <sup>b</sup>

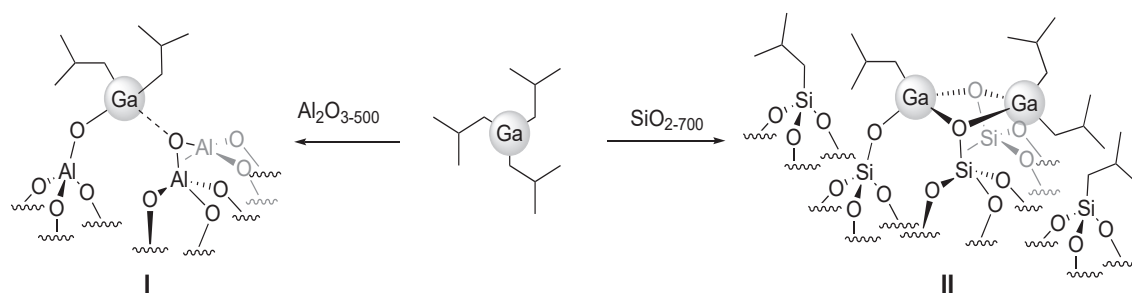
<b>Ga-O<sub>2</sub></b>	1	2.51(3)	7 (2) <sup>c</sup>
<b>Ga-C<sub>2</sub></b>	2	3.01(5)	7 (2) <sup>c</sup>
<b>Ga-Al</b>	1	3.23(3)	7 (2) <sup>c</sup>

<sup>a</sup>The data ranges used in the fit are  $3.0 \leq k \leq 13.0 \text{ \AA}^{-1}$  and  $1.0 \leq R \leq 3.2 \text{ \AA}$ . S0 2 was fixed at 1 and N was fixed at the integer values shown;  $\Delta E0$  was refined as a global fit parameter, returning a value of  $(1 \pm 2) \text{ eV}$ . The  $\sigma^2$  values were constrained in order to decrease the number of fit parameters and the correlations between them. The total number of variable parameters in the fit is 8, out of a total of 13.8 independent data points. Uncertainties in the last digit are shown in parentheses. The R-factor for this fit is 0.022. <sup>b</sup>Constrained to the same value. <sup>c</sup>Constrained to the same value.

**Table 6.** Curve-fit parameters<sup>a</sup> for Ga K-edge EXAFS of  $[\text{Ga}(i\text{Bu})_3]_2/\text{SiO}_{2-700}$

Type of neighbors	Number of neighbors <sup>b</sup>	R / $\text{\AA}$	$10^3 \sigma^2 / \text{\AA}^2$
<b>Ga-O<sub>1</sub></b>	1	1.92(2)	4.7 (5) <sup>b</sup>
<b>Ga-C<sub>1</sub>/O<sub>2</sub></b>	3	2.04(3)	4.7 (5) <sup>b</sup>
<b>Ga-C<sub>2</sub></b>	1.5	3.03(1)	4.7 (5) <sup>b</sup>
<b>Ga-Ga</b>	0.8 (1)	2.97(1)	8 (1) <sup>b</sup>

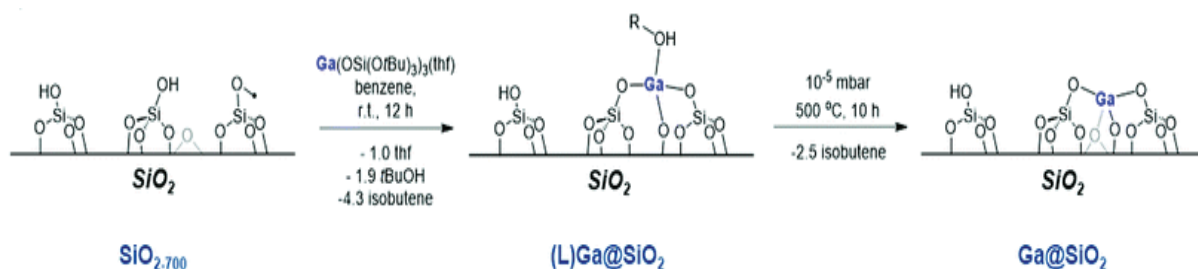
<sup>a</sup>The data ranges used in the fit are  $3.0 \leq k \leq 13.0 \text{ \AA}^{-1}$  and  $1.0 \leq R \leq 3.2 \text{ \AA}$ . S0 2 was fixed at 1 and N was fixed at the integer values shown;  $\Delta E0$  was refined as a global fit parameter, returning a value of  $(1 \pm 2) \text{ eV}$ . The  $\sigma^2$  values were constrained in order to decrease the number of fit parameters and the correlations between them. The total number of variable parameters in the fit is 8, out of a total of 13.8 independent data points. Uncertainties in the last digit are shown in parentheses. The R-factor for this fit is 0.022. <sup>b</sup>Constrained to the same value. <sup>b</sup>Constrained to the same value.



**Scheme 11.** Grafting of  $[\text{Ga}(i\text{Bu})_3]$  onto  $\text{Al}_2\text{O}_{3-500}$  and  $\text{SiO}_{2-700}$  leads to structurally distinct surface species.

Importantly and for the first time, we demonstrated that the catalytic performance of these catalysts depends on the nature of the support and the structure on the active species (Figure 19). In fact, the isolated monomeric  $[\text{Ga}(i\text{Bu})_3]$  on alumina is more active and selective than dimeric  $[\text{Ga}(i\text{Bu})_3]$  on silica. The difference in the activity was attributed to the structurally

different Ga species on the surface and the facility of activation [Ga-O-Al] compared to [Ga-O-Si] bond. However, catalyst **(I)** shows a fast deactivation at the beginning of the catalytic test, related to either coke formation or reduction of gallium. Later on, another catalyst was reported in literature using an approach combining SOMC and thermal treatment of the resulting species. It is important to note that after heating, the siloxy ligands around the metal lead to the formation of silanols and water after decomposition and formation of isobutene. The condensation of these silanols with Ga-OH intermediate gives a mixed oxide as reported in the case of non-hydrolytic sol gel synthetic method. The authors claim the formation of Ga tripodal sites. In fact, using this combination, the grafting of  $[\text{Ga}(\text{OSi}(\text{O}t\text{Bu})_3)(\text{THF})]$  on dehydroxylated silica at  $700\text{ }^\circ\text{C}$  was followed by a thermal treatment at  $500\text{ }^\circ\text{C}$  and reduced pressure in order to eliminate the organic ligands (Scheme 12).<sup>149</sup>



**Scheme 12.** Depiction of synthetic procedure employed for the generation of isolated  $\text{Ga}^{3+}$  sites supported on silica<sup>149</sup>

The characterization of the resulting species by EXAFS confirmed the formation of isolated tetracoordinate Ga sites with 1.6 wt% of Ga. This catalyst exhibited an initial propane conversion of 9.3 % which decreased to 6.5 % after 1200 min at  $550\text{ }^\circ\text{C}$  with very low GHSV (3.3% of C3 in Ar) and the selectivity toward propene was 93 %. In order to compare this catalyst with  $[\text{Ga}(i\text{Bu})_3]$  supported on silica and alumina, our group found that this species exhibits low activity as observed in the case of  $[\text{Ga}(i\text{Bu})_3]_2/\text{SiO}_2\text{-700}$  when tested in the same conditions in propane dehydrogenation (Figure 19).

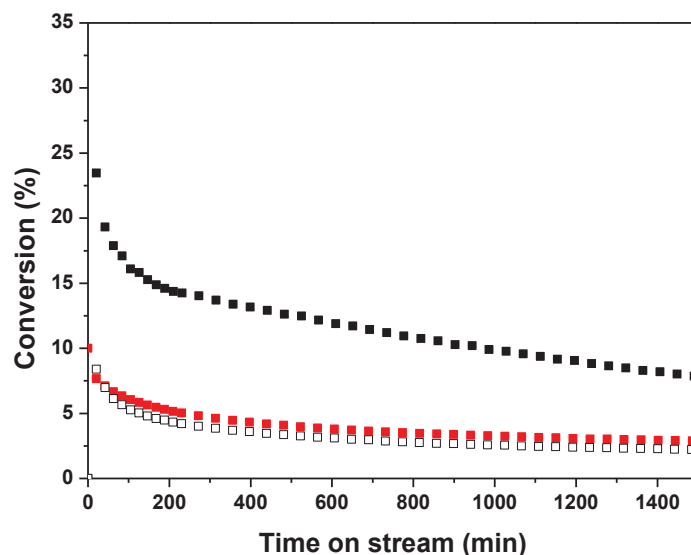
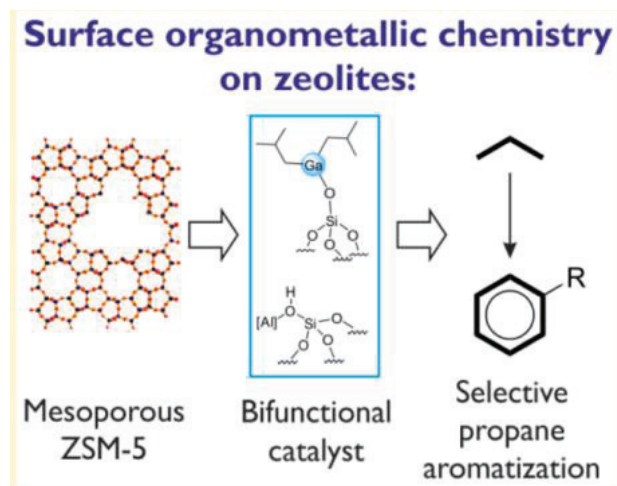


**Figure 19.** Comparison of propane conversion at 550 °C catalyzed by  $\text{Ga}(i\text{Bu})_3/\text{Al}_2\text{O}_{3-500}$  (**I**, solid black symbols),  $\text{Ga}(i\text{Bu})_3/\text{SiO}_{2-700}$  (**II**, open black symbols), and thermally treated  $\text{Ga}[\text{OSi}(\text{O}-t\text{-Bu})_3]_3/\text{SiO}_2$  (solid red symbols).<sup>105</sup>

From these results, we can conclude that isolated  $\text{Ga}^{\text{III}}$  species are highly desired for a better catalytic activity compared to dimeric Ga oxide species that results in a deactivation and a decrease in the selectivity as function of time. It is important to note that the catalysts prepared by SOMC had a significant higher catalytic activity and selectivity in propane dehydrogenation compared to conventional Ga catalysts prepared by impregnation of gallium nitrate on alumina. The latter displayed 2.64 wt% of Ga and exhibited a conversion of 9.8 % with 97 % of selectivity toward propene when tested at very low concentration of propane (2.3 % of C<sub>3</sub> in Ar) and at 1.4 bar.<sup>117</sup> The studies from the literature suggested that gallium catalysts prepared by impregnation from nitrates may contain isolated  $\text{Ga}^{\text{III}}$  sites. However, comparing the catalytic performance between both preparation methods implies the presence of a different species (di or oligomeric) on the surface exhibiting a difference in the catalytic performance and a lower activity in PDH.

From the knowledge gathered in PDH, the study on Ga catalysts was extended for the first time to propane aromatization by using SOMC synthetic method. The latter is known to catalyze propane into aromatics via a bifunctional catalyst (Scheme 13), where the metal sites are responsible for the dehydrogenation (first step) and the acidic sites from the zeolitic support perform oligomerization, cyclization and aromatization of propylene intermediate.<sup>150</sup>



**Scheme 13.** Bifunctional catalyst based on  $\text{Ga}(i\text{Bu})_3/\text{meso H-ZSM-5}$  for propane aromatization<sup>150</sup>

Thus, our group reported the immobilization of isolated  $[\text{Ga}(i\text{Bu})_3]$  sites selectively on the silanol groups located in the mesopores while leaving the Bronsted acid sites in the micropores unreacted. As a result, the formation of a well-defined monopodal species with 1.36 wt% of Ga with significant Bronsted acidity was characterized by EXAFS, DRIFT, solid state NMR and mass balance analysis.<sup>150</sup> The resulting bifunctional  $\text{Ga}(i\text{Bu})_3/\text{meso H-ZSM-5-250}$  ( $\text{Si}/\text{Al}=20$ ) catalyst exhibited a high conversion of 74 % with a selectivity of 64 wt% toward aromatics at 550 °C and with 2.5 % of  $\text{C}_3$  in Ar. This result confirms that by using SOMC, the grafting occurs selectively in the mesopores, and more importantly, that a judicious choice of the precursor's size is essential to avoid the access to the micropores and the grafting on the acidic sites. However, the size should not also be too bulky in order to avoid blocking access to the micropores. In fact, Kazansky et al. demonstrated that grafting small precursor  $[\text{GaMe}_3]$  than  $[\text{Ga}(i\text{Bu})_3]$  consumed the acidic sites as well in the zeolites, evidenced by characterization and most importantly by the absence of aromatics during propane aromatization due to the passivation of acidic sites.<sup>151</sup>

## VI.2. Vanadium catalysts prepared by SOMC

In parallel to Ga, vanadium-based catalyst has attracted a lot of attention due to their high use in the oxidative propane dehydrogenation. Their evaluation was extended to the non-oxidative propane dehydrogenation where isolated  $\text{V}^{3+}$  was proposed as active species in that case.<sup>152</sup> To our knowledge, only few examples describing the preparation of vanadium supported catalysts by SOMC for the non-oxidative propane dehydrogenation. The first example was

reported by our group concerning the grafting of vanadium oxo organometallic precursor on silica dehydroxylated at different temperatures. It was demonstrated that the dehydroxylation temperature of silica influences directly the structure of the resulting species on the surface. In fact, the grafting of  $[V(=O)(Mes)_3]$  on silica dehydroxylated at 200 and 700 °C, leads to a bipodal  $[(\equiv SiO)_2V(=O)(Mes)]$  (**I**) and monopodal  $[(\equiv SiO)V(=O)(Mes)_2]$  (**II**) species, by protonolysis between V-Mes and SiOH, respectively.<sup>152</sup> These structures were characterized by using DRIFT, Raman,  $^1H$ ,  $^{13}C$ , and  $^{51}V$  solid state NMR, and XAS spectroscopy. In this work, the  $^{51}V$  MAS NMR technique was instrumental to characterize these catalysts. In fact, the  $^{51}V$  MAS NMR spectrum of  $V(=O)(Mes)_3/SiO_{2-700}$  exhibited a signal at 412 ppm as determined by variation of the spinning frequency, which represents an upfield shift of 408 ppm compared to the molecular complex,  $[V(=O)(Mes)_3]$ , which resonates at 879 ppm. This result is in agreement with the formation of a monopodal surface species in the case of  $SiO_{2-700}$ . In fact, such an upfield shift has been previously reported in the homogeneous chemistry of  $V(=O)-(CH_2SiMe_3)_3$ , which shifted from 1205.7 to 627 ppm upon reaction with triphenylsilanol to form  $V(=O)-(CH_2SiMe_3)_2(OSiPh_3)$ .<sup>153</sup> In addition, XANES and EXAFS confirmed the formation of the structure of these catalysts. For complexes  $[V(=O)(Mes)_3]$ , (**II**) and (**III**), the position at 4.1 to 4.7 eV of the intense pre-edge peak from the energy of the foil K-edge, and its high intensity (1.19 to 0.71), are in line with the reported results in the case of four coordinated V(V) materials.<sup>154</sup> Moreover, the main K-edge of the  $VO(mesityl)_3/silica$  samples are shifted by ca. 18 eV to higher energy relative to the foil, which is also in the range of K-edge energies described for known V(V) compounds.<sup>155</sup>

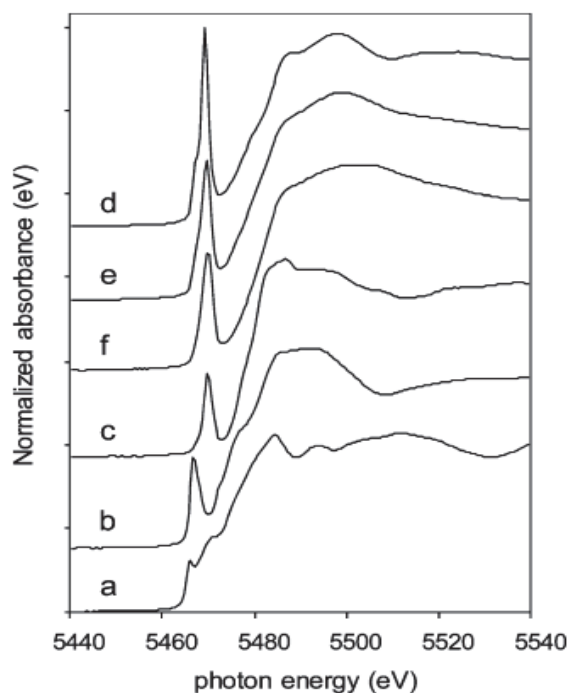


**Figure 20.** Comparison of vanadium K-edge XANES regions for (a) vanadium metal calibration foil, (b)  $[\text{V}^{\text{III}}(\text{Mes})_3 \cdot \text{THF}]$ , (c)  $\text{V}^{\text{IV}}(\text{O})\text{-SO}_4(\text{H}_2\text{O})_x$ , (d)  $[\text{V}^{\text{V}}(\text{=O})(\text{Mes})_3]$ , (e) supported complex **(II)**  $[(=\text{SiO})\text{V}(\text{=O})(\text{Mes})_2]$ , and (f) supported complex **(I)**,  $[(=\text{SiO})_2\text{V}(\text{=O})(\text{Mes})]$ .

To evaluate the effect of the structure on the catalytic activity, species **(I)** and **(II)** were tested in propane dehydrogenation at 500 °C. Both of these complexes were active and exhibited similar initial activity of 17 % followed by a slow deactivation leading to 9 and 12% after one week on stream for **(I)** and **(II)**, respectively (Figure 21). Additionally, the reaction is very selective toward propene where the selectivity ranges from 83 to 90 %. The mechanism of this reaction has been proposed. The first step involves an activation of C-H bond of propane on V-mesityl leads to the formation of a V-propyl intermediate. Followed by a  $\beta$ -H elimination, the latter species give a V-H with a coordinated propylene. A new activation of C-H bond leads to the release of propylene and hydrogen. Simultaneously, a parallel pathway was proposed involving a cleavage and reconstruction of V-H species with propylene coordinated. A second mechanism has been also proposed based on the formation of tripodal  $\text{V}^{\text{III}}$  systems after activation of propane on the pre-catalyst  $\text{V}=\text{O}$ . The formation of propylene occurs via heterolytic C-H activation of propane on V-O pairs, as described in the case of chromium based catalysts.<sup>156</sup>

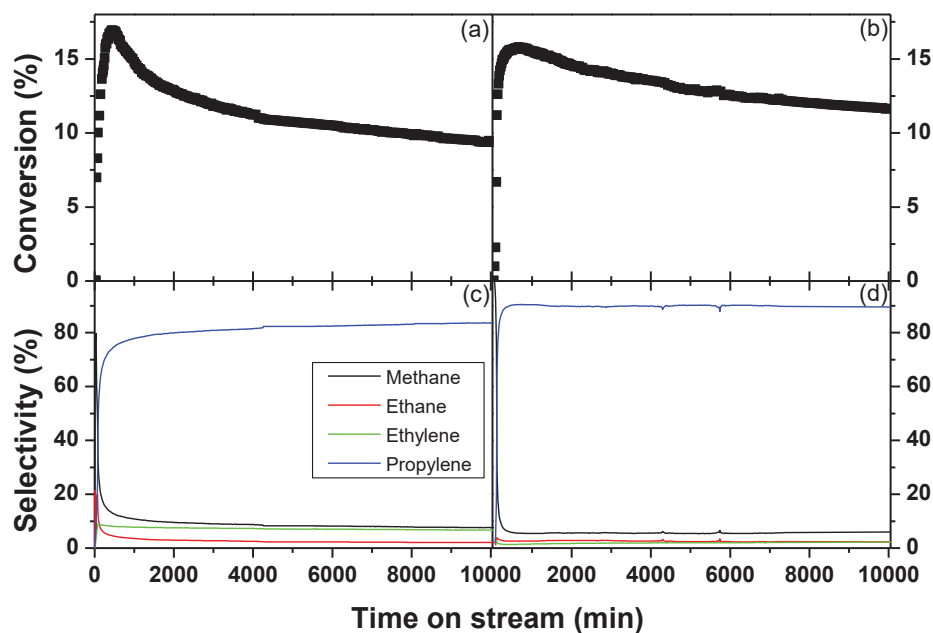


**Figure 21.** Conversion of non-oxidative propane dehydrogenation of (a) **(II)** and (b) **(I)**, and the corresponding product selectivity (part c and d for **(II)** and **(I)**, respectively).<sup>152</sup>

Kaphan et al reported a second example for the preparation of vanadium supported catalyst in PDH. In fact, the grafting of  $[V^{3+}(\text{Mes})_3(\text{THF})]$  on  $\text{SiO}_{2-200}$  affords a bipodal species,  $[(\equiv\text{SiO})_2V^{3+}(\text{Mes})(\text{THF})]$ .<sup>157</sup> The catalytic performance of this catalyst in propane dehydrogenation was evaluated at 550 °C. Compared to catalysts **(I)** and **(II)**, this catalyst showed a modest activity with an initial conversion of 8.1 % with a slow deactivation leading to 4.6 % after 200 h on stream. A high selectivity of around 94 % was obtained as function of time on stream. The induction period is not observed in this case compared to the results stated above with  $[V(=O)(\text{Mes})_3]$  precursor. This phenomenon was attributed to the reduction of  $V^{5+}$  into  $V^{3+}$  by propane at the beginning of catalytic reaction, which is in agreement with what was described above (section V.2).

These results showed that the vanadium-based catalysts prepared by SOMC had a significant higher catalytic activity and selectivity in propane dehydrogenation compared to classical V catalysts prepared by impregnation of ammonium metavanadate on oxides. In fact, conventional  $V_2O_5$  on silica reported by Takahara et al. and prepared by aqueous impregnation method exhibits a lower catalytic activity in PDH, attributed to the presence of a mixture of undesired and multiple inactive species on the surface.<sup>143</sup>

## VII. General conclusion and objective of the thesis

The main objective of this work is to obtain light olefins and aromatics from light hydrocarbons by implementing new procedures, involving innovative catalysts synthesis methodologies, novel reactor design and processing and by demonstrating their improvement toward sustainability and economic scalability compared to existing industrial processes. In this context, the main goal of this PhD is the preparation of well-defined supported single-site catalysts based on Ga and V, using an innovative synthesis process, for propane dehydrogenation (PDH) into propylene, butane/butenes dehydrogenation (BDH) into butadiene and propane aromatization (PAr) into aromatics (BTX = Benzene, Toluene, Xylenes).

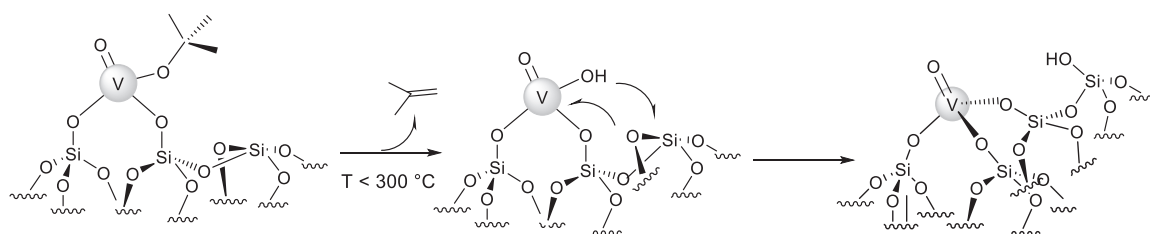
In this chapter, we described the uses and resources of propene, butadiene and aromatics. It is clear that propane dehydrogenation, 2-butenes conversion and propane aromatization are still to date undergoing a surge of research interest from the industrial and academic players. This interest is due to the increasing demand toward propene, butadiene and aromatics over the years, and the necessity to put in place alternative economic and ecofriendly routes to manufacture these products selectively. More particularly, we detailed the current commercialized processes for the non-oxidative PDH (Oleflex®, STAR®, Catofin®, FBD®), BDH (Catadiene®) and PAr (Cyclar®), their advantages, and limitations along with the catalysts employed, their active sites and proposed mechanisms. We can agree that all these processes suffer from the deactivation of the catalyst by coke formation due to the high operating temperature which requires a continuous regeneration. In addition, due to the high price of platinum-based catalysts (used in Oleflex® and STAR®) and its regeneration by dangerous chlorine to redisperse the particles, and to the environment hostility of chromium-based catalysts (employed in Catofin®, FBD® and Catadiene®), it is important to develop alternative non-toxic and cheap efficient catalysts.

According to this thorough prior art, dehydrogenation was demonstrated as a common reaction between these three targeted reactions. Thus, the literature was limited on the catalytic systems developed and described as promising candidates compared to Pt and Cr based catalysts in the common dehydrogenation reaction. Hence, the exploitation and development of new catalytic systems to improve the aforementioned issues and to establish a structure-activity relationship is of a great challenge and interest. Supported gallium and

vanadium-based catalysts have proven to be promising alternatives to CrOx-based catalyst, due to their low toxicity and price and high reactivity in propane dehydrogenation.

The reported catalytic systems based on Ga and V are generally prepared by conventional methods using gallium or vanadium salts resulting in a mixture of monomeric, oligomeric and polymeric (GaOx or VOx) species on the surface. Thus, the characterization attempts of these catalytic systems have failed to date to identify the active species for the targeted reactions and to establish a structure-activity relationship for the catalysts allowing to improve the catalytic performance. As mentioned previously, DFT calculations proposed that the active species for the dehydrogenation process is an isolated tetrahedral tripodal  $M^{3+}$  species. In addition, the low concentration of these active sites along with a mixture of oligomeric species leads to cracking reactions and thus a deactivation of the catalyst due to the formation of coke. Thus, an essential parameter is a judicious choice of the preparation method of the new catalysts based on Ga and V with large number of active sites and a tripodal structure. The research conducted in our laboratory using Surface Organometallic Chemistry (SOMC) has proven that it is a powerful method, which allow access to well-defined single site catalysts by control of the coordination sphere of the metal, resulting in high performing catalytic systems in terms of activity and selectivity. The preparation of supported tripodal metal species is very challenging by grafting of organometallic precursors since it needs three adjacent hydroxyl groups, which is difficult to access in commercial dehydroxylated support. However, our research group reported on a strategy allowing to access to tripodal metal systems by transfer of H from metal to support by ring opening in presence of hydrogen (Scheme 10).

In this PhD, this approach was extended for the preparation of tripodal Ga and V sites immobilized and well dispersed on the surface of oxide supports by using SOMC followed by a thermal treatment and transfer of hydroxy group from the metal to the support (Scheme 14).



**Scheme 14.** Example on the formation of tripodal species based on V after thermal treatment of  $V(=O)(OtBu)_3/SiO_{2-200}$

The outcome of this PhD work is presented into 3 major parts:

Chapter II describes the grafting of vanadium complex,  $[V(=O)(OtBu)_3]$  on the surface of dehydroxylated alumina at 500 °C and silica dehydroxylated at 200 and 700 °C. Tripodal vanadium species was obtained by thermal treatment of the resulting grafted species and characterized by different techniques DRIFT, solid-state NMR, UV-vis, XANES and mass balance analysis. Using these new catalysts, we studied the effect of the support and the effect of temperature on the catalytic activity in PDH and BDH. Thus, we were able to propose a mechanism based on vanadium for 2-butenes conversion.

Chapter III reveals the preparation of isolated Ga catalysts by grafting  $[Ga(iBu)_3]$  and  $[Ga(OtBu)_3]_2$  supported on alumina dehydroxylated at 500 °C and silica dehydroxylated at 700 °C. In addition, the formation of tripodal Ga species from those obtained after the grafting of  $[Ga(OtBu)_3]_2$  onto alumina is shown and characterized by DRIFT, solid-state NMR, EXAFS and mass balance analysis. The catalytic performance as a function of the support and the ligands bonded to the metal center were also evaluated. The deactivation observed in the case  $Ga(iBu)_3/Al_2O_{3-500}$  was explained via Operando XAFS. The catalytic activity of these materials is also similarly evaluated in the direct 2-butenes conversion and in the presence of CO<sub>2</sub> as co-feed.

Using the knowledge obtained in PDH in chapter III, we extended our study to propane aromatization. Hence, in the last chapter, we described the preparation and characterization of tripodal Ga on meso H-ZSM-5-250 (Si/Al= 40). In order to study the effect of ligand on the activity and selectivity in propane aromatization, we also prepared and characterized  $[Ga(iBu)_3]$  on meso H-ZSM-5-250 (Si/Al= 40). Moreover, we prepared a series of Ga based catalysts on different meso H-ZSM-5 with several ratios (Si/Al= 25, 40, 100, 200 and ∞) in order to evaluate the effect of the acidity on the catalytic activity and selectivity. The effect of temperature and propane concentration on the catalytic performance in PAr were also studied.

## References

- (1) Corma, A.; Melo, F. V.; Sauvanaud, L.; Ortega, F. Light Cracked Naphtha Processing: Controlling Chemistry for Maximum Propylene Production. *Catal. Today* **2005**, *107–108*, 699–706. <https://doi.org/10.1016/j.cattod.2005.07.109>.
- (2) Liu, Q.; Luo, M.; Zhao, Z.; Zhao, Q. K-Modified Sn-Containing Dendritic Mesoporous Silica Nanoparticles with Tunable Size and SnOx-Silica Interaction for the Dehydrogenation of Propane to Propylene. *Chem. Eng. J.* **2020**, *380*, 122423. <https://doi.org/10.1016/j.cej.2019.122423>.

- (3) Polypropylene, UNIPOL Technology, Dow, Applications, Properties, Plastic, Polymer, Thermoplastic. *Am. J. Polym. Sci.* **2016**, 11.
- (4) Andrady, A. L.; Neal, M. A. Applications and Societal Benefits of Plastics. *Philos. Trans. R. Soc. B Biol. Sci.* **2009**, 364 (1526), 1977–1984. <https://doi.org/10.1098/rstb.2008.0304>.
- (5) *Propylene Global Supply Demand Analytics Service*. <https://www.woodmac.com/news/editorial/propylene-global-supply-demand-analytics-service/> (accessed 2020-03-24).
- (6) Ahmed, M. H. M.; Masuda, T.; Muraza, O. The Role of Acidity, Side Pocket, and Steam on Maximizing Propylene Yield from Light Naphtha Cracking over One-Dimensional Zeolites: Case Studies of EU-1 and Disordered ZSM-48. *Fuel* **2019**, 258, 116034. <https://doi.org/10.1016/j.fuel.2019.116034>.
- (7) Farshi, A.; Shaiyegh, F.; Burogerdi, S. H.; Dehgan, A. FCC Process Role in Propylene Demands. *Pet. Sci. Technol.* **2011**, 29 (9), 875–885. <https://doi.org/10.1080/10916460903451985>.
- (8) Bhasin, M. M.; McCain, J. H.; Vora, B. V.; Imai, T.; Pujadó, P. R. Dehydrogenation and Oxydehydrogenation of Paraffins to Olefins. *Appl. Catal. Gen.* **2001**, 221 (1–2), 397–419. [https://doi.org/10.1016/S0926-860X\(01\)00816-X](https://doi.org/10.1016/S0926-860X(01)00816-X).
- (9) Wang, G.; Zhu, X.; Li, C. Recent Progress in Commercial and Novel Catalysts for Catalytic Dehydrogenation of Light Alkanes. *Chem. Rec.* **2020**, 20 (6), 604–616. <https://doi.org/10.1002/tcr.201900090>.
- (10) Corma, A.; Mengual, J.; Miguel, P. J. Steam Catalytic Cracking of Naphtha over ZSM-5 Zeolite for Production of Propene and Ethene: Micro and Macroscopic Implications of the Presence of Steam. *Appl. Catal. Gen.* **2012**, 417–418, 220–235. <https://doi.org/10.1016/j.apcata.2011.12.044>.
- (11) Akporiaye, D.; Jensen, S. F.; Olsbye, U.; Rohr, F.; Rytter, E.; Rønnekleiv, M.; Spjelkavik, A. I. A Novel, Highly Efficient Catalyst for Propane Dehydrogenation. *Ind. Eng. Chem. Res.* **2001**, 40 (22), 4741–4748. <https://doi.org/10.1021/ie010299+>.
- (12) Carter, J. H.; Bere, T.; Pitchers, J. R.; Hewes, D. G.; Vandegehuchte, B. D.; Kiely, C. J.; Taylor, S. H.; Hutchings, G. J. Direct and Oxidative Dehydrogenation of Propane: From Catalyst Design to Industrial Application. *Green Chem.* **2021**, 23 (24), 9747–9799. <https://doi.org/10.1039/D1GC03700E>.
- (13) Blay, V.; Epelde, E.; Miravalles, R.; Perea, L. A. Converting Olefins to Propene: Ethene to Propene and Olefin Cracking. *Catal. Rev.* **2018**, 60 (2), 278–335. <https://doi.org/10.1080/01614940.2018.1432017>.
- (14) Agarwal, A.; Sengupta, D.; El-Halwagi, M. Sustainable Process Design Approach for On-Purpose Propylene Production and Intensification. *ACS Sustain. Chem. Eng.* **2018**, 6 (2), 2407–2421. <https://doi.org/10.1021/acssuschemeng.7b03854>.
- (15) Zhu, X.; Li, X.; Xie, S.; Liu, S.; Xu, G.; Xin, W.; Huang, S.; Xu, L. Two New On-Purpose Processes Enhancing Propene Production: Catalytic Cracking of C4 Alkenes to Propene and Metathesis of Ethene and 2-Butene to Propene. *Catal. Surv. Asia* **2008**, 13 (1), 1. <https://doi.org/10.1007/s10563-008-9055-3>.
- (16) Medrano, J.-A.; Julián, I.; Herguido, J.; Menéndez, M. Pd-Ag Membrane Coupled to a Two-Zone Fluidized Bed Reactor (TZFBR) for Propane Dehydrogenation on a Pt-Sn/MgAl<sub>2</sub>O<sub>4</sub> Catalyst. *Membranes* **2013**, 3 (2), 69–86. <https://doi.org/10.3390/membranes3020069>.
- (17) Wang, S.; Zhang, L.; Zhang, W.; Wang, P.; Qin, Z.; Yan, W.; Dong, M.; Li, J.; Wang, J.; He, L.; Olsbye, U.; Fan, W. Selective Conversion of CO<sub>2</sub> into Propene and Butene. *Chem* **2020**, 6 (12), 3344–3363. <https://doi.org/10.1016/j.chempr.2020.09.025>.

- (18) Zhang, Z.; Zhang, J.; Wang, X.; Si, R.; Xu, J.; Han, Y.-F. Promotional Effects of Multiwalled Carbon Nanotubes on Iron Catalysts for Fischer-Tropsch to Olefins. *J. Catal.* **2018**, *365*, 71–85. <https://doi.org/10.1016/j.jcat.2018.05.021>.
- (19) Olsbye, U.; Svelle, S.; Bjørgen, M.; Beato, P.; Janssens, T. V. W.; Joensen, F.; Bordiga, S.; Lillerud, K. P. Conversion of Methanol to Hydrocarbons: How Zeolite Cavity and Pore Size Controls Product Selectivity. *Angew. Chem. Int. Ed.* **2012**, *51* (24), 5810–5831. <https://doi.org/10.1002/anie.201103657>.
- (20) Vora, B. V.; Pujado, P. R.; Miller, L. W.; Barger, P. T.; Nilsen, H. R.; Kvisle, S.; Fuglerud, T. Production of Light Olefins from Natural Gas. In *Studies in Surface Science and Catalysis*; Elsevier, 2001; Vol. 136, pp 537–542.
- (21) Vora, B. V.; Marker, T. L.; Barger, P. T.; Nilsen, H. R.; Kvisle, S.; Fuglerud, T. Economic Route for Natural Gas Conversion to Ethylene and Propylene. In *Studies in Surface Science and Catalysis*; de Pontes, M., Espinoza, R. L., Nicolaidis, C. P., Scholtz, J. H., Scurrill, M. S., Eds.; Natural Gas Conversion IV; Elsevier, 1997; Vol. 107, pp 87–98. [https://doi.org/10.1016/S0167-2991\(97\)80321-7](https://doi.org/10.1016/S0167-2991(97)80321-7).
- (22) Mol, J. Industrial Applications of Olefin Metathesis. *J. Mol. Catal. Chem.* **2004**, *213* (1), 39–45. <https://doi.org/10.1016/j.molcata.2003.10.049>.
- (23) Biloen, P.; Sachtler, W. M. H. Mechanism of Hydrocarbon Synthesis over Fischer-Tropsch Catalysts. In *Advances in Catalysis*; Eley, D. D., Pines, H., Weisz, P. B., Eds.; Academic Press, 1981; Vol. 30, pp 165–216. [https://doi.org/10.1016/S0360-0564\(08\)60328-4](https://doi.org/10.1016/S0360-0564(08)60328-4).
- (24) Liu, X.; Wang, M.; Zhou, C.; Zhou, W.; Cheng, K.; Kang, J.; Zhang, Q.; Deng, W.; Wang, Y. Selective Transformation of Carbon Dioxide into Lower Olefins with a Bifunctional Catalyst Composed of ZnGa<sub>2</sub>O<sub>4</sub> and SAPO-34. *Chem. Commun.* **2018**, *54* (2), 140–143. <https://doi.org/10.1039/c7cc08642c>.
- (25) Pawelec, B.; Guil-Lopez, R.; Mota, N.; Fierro, J. L. G.; Navarro Yerga, R. M. Catalysts for the Conversion of CO<sub>2</sub> to Low Molecular Weight Olefins-A Review. *Materials* **2021**, *14* (22), 6952. <https://doi.org/10.3390/ma14226952>.
- (26) Nawaz, Z. Light Alkane Dehydrogenation to Light Olefin Technologies: A Comprehensive Review. *Rev. Chem. Eng.* **2015**, *31* (5), 413–436. <https://doi.org/10.1515/revce-2015-0012>.
- (27) Qin, J.; Pei, C.; Zhao, C.; Lu, Z.; Sun, G.; Gong, J. Techno-Economic Analysis of a Hybrid Process for Propylene and Ammonia Production. *ACS Sustain. Chem. Eng.* **2022**. <https://doi.org/10.1021/acssuschemeng.2c00347>.
- (28) Sattler, J. J. H. B.; Gonzalez-Jimenez, I. D.; Luo, L.; Stears, B. A.; Malek, A.; Barton, D. G.; Kilos, B. A.; Kaminsky, M. P.; Verhoeven, T. W. G. M.; Koers, E. J.; Baldus, M.; Weckhuysen, B. M. Platinum-Promoted Ga/Al<sub>2</sub>O<sub>3</sub> as Highly Active, Selective, and Stable Catalyst for the Dehydrogenation of Propane. *Angew. Chem.* **2014**, *126* (35), 9405–9410. <https://doi.org/10.1002/ange.201404460>.
- (29) Monai, M.; Gambino, M.; Wannakao, S.; Weckhuysen, B. Propane to Olefins Tandem Catalysis: A Selective Route towards Light Olefins Production. *Chem. Soc. Rev.* **2021**, *50* (20), 11503–11529. <https://doi.org/10.1039/D1CS00357G>.
- (30) Sattler, J. J. H. B.; Ruiz-Martinez, J.; Santillan-Jimenez, E.; Weckhuysen, B. M. Catalytic Dehydrogenation of Light Alkanes on Metals and Metal Oxides. *Chem. Rev.* **2014**, *114* (20), 10613–10653. <https://doi.org/10.1021/cr5002436>.
- (31) Liu, J.; Liu, C.; Ma, A.; Rong, J.; Da, Z.; Zheng, A.; Qin, L. Effects of Al<sub>2</sub>O<sub>3</sub> Phase and Cl Component on Dehydrogenation of Propane. *Appl. Surf. Sci.* **2016**, *368*, 233–240. <https://doi.org/10.1016/j.apsusc.2016.01.282>.

- (32) Zangeneh, F. T.; Taeb, A.; Gholivand, K.; Sahebdehfar, S. The Effect of Mixed HCl–KCl Competitive Adsorbate on Pt Adsorption and Catalytic Properties of Pt–Sn/Al<sub>2</sub>O<sub>3</sub> Catalysts in Propane Dehydrogenation. *Appl. Surf. Sci.* **2015**, *357*, 172–178. <https://doi.org/10.1016/j.apsusc.2015.08.235>.
- (33) Dong, S.; Altvater, N. R.; Mark, L. O.; Hermans, I. Assessment and Comparison of Ordered & Non-Ordered Supported Metal Oxide Catalysts for Upgrading Propane to Propylene. *Appl. Catal. Gen.* **2021**, *617*, 118121. <https://doi.org/10.1016/j.apcata.2021.118121>.
- (34) Gao, X.; Xu, W.; Li, X.; Cen, J.; Xu, Y.; Lin, L.; Yao, S. Non-Oxidative Dehydrogenation of Propane to Propene over Pt–Sn/Al<sub>2</sub>O<sub>3</sub> Catalysts: Identification of the Nature of Active Site. *Chem. Eng. J.* **2022**, *443*, 136393. <https://doi.org/10.1016/j.cej.2022.136393>.
- (35) Feng, B.; Wei, Y.-C.; Song, W.-Y.; Xu, C.-M. A Review on the Structure-Performance Relationship of the Catalysts during Propane Dehydrogenation Reaction. *Pet. Sci.* **2022**, *19* (2), 819–838. <https://doi.org/10.1016/j.petsci.2021.09.015>.
- (36) Fridman, V. Z.; Xing, R. Deactivation Studies of the CrOx/Al<sub>2</sub>O<sub>3</sub> Dehydrogenation Catalysts under Cyclic Redox Conditions. *Ind. Eng. Chem. Res.* **2017**, *56* (28), 7937–7947. <https://doi.org/10.1021/acs.iecr.7b01638>.
- (37) Gao, X.-Q.; Lu, W.-D.; Hu, S.-Z.; Li, W.-C.; Lu, A.-H. Rod-Shaped Porous Alumina-Supported Cr<sub>2</sub>O<sub>3</sub> Catalyst with Low Acidity for Propane Dehydrogenation. *Chin. J. Catal.* **2019**, *40* (2), 184–191. [https://doi.org/10.1016/S1872-2067\(18\)63202-4](https://doi.org/10.1016/S1872-2067(18)63202-4).
- (38) Puurunen, R. L.; Beheydt, B. G.; Weckhuysen, B. M. Monitoring Chromia/Alumina Catalysts in Situ during Propane Dehydrogenation by Optical Fiber UV–Visible Diffuse Reflectance Spectroscopy. *J. Catal.* **2001**, *204* (1), 253–257. <https://doi.org/10.1006/jcat.2001.3372>.
- (39) Derossi, S.; Ferraris, G.; Fremiotti, S.; Garrone, E.; Ghiotti, G.; Campa, M. C.; Indovina, V. Propane Dehydrogenation on Chromia/Silica and Chromia/Alumina Catalysts. *J. Catal.* **1994**, *148* (1), 36–46. <https://doi.org/10.1006/jcat.1994.1183>.
- (40) Sattler, J. J. H. B.; Mens, A. M.; Weckhuysen, B. M. Real-Time Quantitative Operando Raman Spectroscopy of a CrOx/Al<sub>2</sub>O<sub>3</sub> Propane Dehydrogenation Catalyst in a Pilot-Scale Reactor. *ChemCatChem* **2014**, *6* (11), 3139–3145. <https://doi.org/10.1002/cctc.201402649>.
- (41) Chen, S.; Pei, C.; Sun, G.; Zhao, Z.-J.; Gong, J. Nanostructured Catalysts toward Efficient Propane Dehydrogenation. *Acc. Mater. Res.* **2020**, *1* (1), 30–40. <https://doi.org/10.1021/accountsmr.0c00012>.
- (42) Schweitzer, N. M.; Hu, B.; Das, U.; Kim, H.; Greeley, J.; Curtiss, L. A.; Stair, P. C.; Miller, J. T.; Hock, A. S. Propylene Hydrogenation and Propane Dehydrogenation by a Single-Site Zn<sup>2+</sup> on Silica Catalyst. *ACS Catal.* **2014**, *4* (4), 1091–1098. <https://doi.org/10.1021/cs401116p>.
- (43) Lillehaug, S.; Jensen, V. R.; Børve, K. J. Catalytic Dehydrogenation of Ethane over Mononuclear Cr(III)–Silica Surface Sites. Part 2: C–H Activation by Oxidative Addition. *J. Phys. Org. Chem.* **2006**, *19* (1), 25–33. <https://doi.org/10.1002/poc.990>.
- (44) Shylesh, S.; Gokhale, A. A.; Scown, C. D.; Kim, D.; Ho, C. R.; Bell, A. T. From Sugars to Wheels: The Conversion of Ethanol to 1,3-Butadiene over Metal-Promoted Magnesia-Silicate Catalysts. *ChemSusChem* **2016**, *9* (12), 1462–1472. <https://doi.org/10.1002/cssc.201600195>.
- (45) Pomalaza, G.; Ponton, P. A.; Capron, M.; Dumeignil, F. Ethanol-to-Butadiene: The Reaction and Its Catalysts. *Catal. Sci. Technol.* **2020**, *10* (15), 4860–4911. <https://doi.org/10.1039/D0CY00784F>.

- (46) V. Makshina, E.; Dusselier, M.; Janssens, W.; Degreè, J.; A. Jacobs, P.; F. Sels, B. Review of Old Chemistry and New Catalytic Advances in the On-Purpose Synthesis of Butadiene. *Chem. Soc. Rev.* **2014**, *43* (22), 7917–7953. <https://doi.org/10.1039/C4CS00105B>.
- (47) White, Wm. C. Butadiene Production Process Overview. *Chem. Biol. Interact.* **2007**, *166* (1), 10–14. <https://doi.org/10.1016/j.cbi.2007.01.009>.
- (48) Nakazono, K.; Takahashi, R.; Yamada, Y.; Sato, S. Dehydration of 2,3-Butanediol to Produce 1,3-Butadiene over Sc<sub>2</sub>O<sub>3</sub> Catalyst Prepared through Hydrothermal Aging. *Mol. Catal.* **2021**, *516*, 111996. <https://doi.org/10.1016/j.mcat.2021.111996>.
- (49) Pomalaza, G.; Capron, M.; Ordonsky, V.; Dumeignil, F. Recent Breakthroughs in the Conversion of Ethanol to Butadiene. *Catalysts* **2016**, *6* (12), 203. <https://doi.org/10.3390/catal6120203>.
- (50) Qureshi, Z. S.; Tanimu, G.; Aitani, A. M.; Asaoka, S.; Alasiri, H. Production of Butadiene and Lower Olefins via Oxidative Conversion of N-Butane over Ni-Bi-O/Zeolite Catalysts. *Mol. Catal.* **2022**, *522*, 112224. <https://doi.org/10.1016/j.mcat.2022.112224>.
- (51) Camacho-Bunquin, J.; Ferrandon, M. S.; Sohn, H.; Kropf, A. J.; Yang, C.; Wen, J.; Hackler, R. A.; Liu, C.; Celik, G.; Marshall, C. L.; Stair, P. C.; Delferro, M. Atomically Precise Strategy to a PtZn Alloy Nanocluster Catalyst for the Deep Dehydrogenation of N-Butane to 1,3-Butadiene. *ACS Catal.* **2018**, *8* (11), 10058–10063. <https://doi.org/10.1021/acscatal.8b02794>.
- (52) Zeng, T.; Sun, G.; Miao, C.; Yan, G.; Ye, Y.; Yang, W.; Sautet, P. Stabilizing Oxidative Dehydrogenation Active Sites at High Temperature with Steam: ZnFe<sub>2</sub>O<sub>4</sub>-Catalyzed Oxidative Dehydrogenation of 1-Butene to 1,3-Butadiene. *ACS Catal.* **2020**, *10* (21), 12888–12897. <https://doi.org/10.1021/acscatal.0c03405>.
- (53) Dumez, F. J.; Froment, G. F. Dehydrogenation of 1-Butene into Butadiene. Kinetics, Catalyst Coking, and Reactor Design. *Ind. Eng. Chem. Process Des. Dev.* **1976**, *15* (2), 291–301. <https://doi.org/10.1021/i260058a014>.
- (54) Winfield, M. E. The Catalytic Dehydration of 2,3-Butanediol to Butadiene. II. Adsorption Equilibria. *Aust. J. Chem.* **1950**, *3* (2), 290–305. <https://doi.org/10.1071/ch9500290>.
- (55) Lebedev, S. V. Preparation of Bivinyll Directly from Alcohol. I. *Zh Obshch Khim* **1933**, *3*, 698–717.
- (56) Dimian, A. C.; Bezedeà, N. I.; Bildea, C. S. Novel Two-Stage Process for Manufacturing Butadiene from Ethanol. *Ind. Eng. Chem. Res.* **2021**, *60* (23), 8475–8492. <https://doi.org/10.1021/acs.iecr.1c00958>.
- (57) Xingan, W.; Huiqin, L. Comparison of the Technology of Oxidative Dehydrogenation in a Fluidized-Bed Reactor with Those of Other Reactors for Butadiene. *Ind. Eng. Chem. Res.* **1996**, *35* (8), 2570–2575. <https://doi.org/10.1021/ie950347o>.
- (58) Samanta, C.; Bharaga, D. *FIPI 2020 On-Purpose Butadiene*; 2020.
- (59) Weissermel, K.; Arpe, H.-J. *Industrial Organic Chemistry*; John Wiley & Sons, 2008.
- (60) *Butadien Production Scribd File.pdf*. [dokumen.tips. https://dokumen.tips/documents/butadien-production-scribd-filepdf.html](https://dokumen.tips/documents/butadien-production-scribd-filepdf.html) (accessed 2022-05-24).
- (61) Li, Q.; Zhang, F.; Jarvis, J.; He, P.; Yung, M. M.; Wang, A.; Zhao, K.; Song, H. Investigation on the Light Alkanes Aromatization over Zn and Ga Modified HZSM-5 Catalysts in the Presence of Methane. *Fuel* **2018**, *219*, 331–339. <https://doi.org/10.1016/j.fuel.2018.01.104>.

- (62) Guisnet, M.; Gnep, N. S.; Alario, F. Aromatization of Short Chain Alkanes on Zeolite Catalysts. *Appl. Catal. Gen.* **1992**, *89* (1), 1–30. [https://doi.org/10.1016/0926-860X\(92\)80075-N](https://doi.org/10.1016/0926-860X(92)80075-N).
- (63) Zeng, D.; Zhu, G.; Xia, C. Recent Advances of Aromatization Catalysts for C4 Hydrocarbons. *Fuel Process. Technol.* **2022**, *226*, 107087. <https://doi.org/10.1016/j.fuproc.2021.107087>.
- (64) Ciapetta, F. G.; Wallace, D. N. Catalytic Naphtha Reforming. *Catal. Rev.* **1972**, *5* (1), 67–158. <https://doi.org/10.1080/01614947208076866>.
- (65) Wang, K.; Dong, M.; Li, J.; Liu, P.; Zhang, K.; Wang, J.; Fan, W. Facile Fabrication of ZSM-5 Zeolite Hollow Spheres for Catalytic Conversion of Methanol to Aromatics. *Catal. Sci. Technol.* **2017**, *7* (3), 560–564. <https://doi.org/10.1039/C6CY02476A>.
- (66) Zhou, W.; Zhou, C.; Yin, H.; Shi, J.; Zhang, G.; Zheng, X.; Min, X.; Zhang, Z.; Cheng, K.; Kang, J.; Zhang, Q.; Wang, Y. Direct Conversion of Syngas into Aromatics over a Bifunctional Catalyst: Inhibiting Net CO<sub>2</sub> Release. *Chem. Commun.* **2020**, *56* (39), 5239–5242. <https://doi.org/10.1039/D0CC00608D>.
- (67) Wei, Z.; Chen, L.; Cao, Q.; Wen, Z.; Zhou, Z.; Xu, Y.; Zhu, X. Steamed Zn/ZSM-5 Catalysts for Improved Methanol Aromatization with High Stability. *Fuel Process. Technol.* **2017**, *162*, 66–77. <https://doi.org/10.1016/j.fuproc.2017.03.026>.
- (68) Zaidi, H. A.; Pant, K. K. Catalytic Conversion of Methanol to Gasoline Range Hydrocarbons. *Catal. Today* **2004**, *96* (3), 155–160. <https://doi.org/10.1016/j.cattod.2004.06.123>.
- (69) Lopez-Sanchez, J. A.; Conte, M.; Landon, P.; Zhou, W.; Bartley, J. K.; Taylor, S. H.; Carley, A. F.; Kiely, C. J.; Khalid, K.; Hutchings, G. J. Reactivity of Ga<sub>2</sub>O<sub>3</sub> Clusters on Zeolite ZSM-5 for the Conversion of Methanol to Aromatics. *Catal. Lett.* **2012**, *142* (9), 1049–1056. <https://doi.org/10.1007/s10562-012-0869-2>.
- (70) Wang, T.; Tang, X.; Huang, X.; Qian, W.; Cui, Y.; Hui, X.; Yang, W.; Wei, F. Conversion of Methanol to Aromatics in Fluidized Bed Reactor. *Catal. Today* **2014**, *233*, 8–13. <https://doi.org/10.1016/j.cattod.2014.02.007>.
- (71) Yang, X.; Su, X.; Chen, D.; Zhang, T.; Huang, Y. Direct Conversion of Syngas to Aromatics: A Review of Recent Studies. *Chin. J. Catal.* **2020**, *41* (4), 561–573. [https://doi.org/10.1016/S1872-2067\(19\)63346-2](https://doi.org/10.1016/S1872-2067(19)63346-2).
- (72) Cui, X.; Gao, P.; Li, S.; Yang, C.; Liu, Z.; Wang, H.; Zhong, L.; Sun, Y. Selective Production of Aromatics Directly from Carbon Dioxide Hydrogenation. *ACS Catal.* **2019**, *9* (5), 3866–3876. <https://doi.org/10.1021/acscatal.9b00640>.
- (73) Ni, Y.; Chen, Z.; Fu, Y.; Liu, Y.; Zhu, W.; Liu, Z. Selective Conversion of CO<sub>2</sub> and H<sub>2</sub> into Aromatics. *Nat. Commun.* **2018**, *9* (1), 3457. <https://doi.org/10.1038/s41467-018-05880-4>.
- (74) Mechanistic Studies through H–D Exchange Reactions: Propane Aromatization in HZSM5 and Ga/HZSM5 Catalysts. *J. Catal.* **2016**, *344*, 252–262. <https://doi.org/10.1016/j.jcat.2016.09.009>.
- (75) Mehdad, A.; Lobo, R. F. Ethane and Ethylene Aromatization on Zinc-Containing Zeolites. *Catal. Sci. Technol.* **2017**, *7* (16), 3562–3572. <https://doi.org/10.1039/C7CY00890B>.
- (76) Xiang, Y.; Wang, H.; Cheng, J.; Matsubu, J. Progress and Prospects in Catalytic Ethane Aromatization. *Catal. Sci. Technol.* **2018**, *8* (6), 1500–1516. <https://doi.org/10.1039/C7CY01878A>.
- (77) Meng, X.; Wang, Z.; Zhang, R.; Xu, C.; Liu, Z.; Wang, Y.; Guo, Q. Catalytic Conversion of C<sub>4</sub> Fraction for the Production of Light Olefins and Aromatics. *Fuel Process. Technol.* **2013**, *116*, 217–221. <https://doi.org/10.1016/j.fuproc.2013.06.002>.

- (78) Su, X.; Zan, W.; Bai, X.; Wang, G.; Wu, W. Synthesis of Microscale and Nanoscale ZSM-5 Zeolites: Effect of Particle Size and Acidity of Zn Modified ZSM-5 Zeolites on Aromatization Performance. *Catal. Sci. Technol.* **2017**, *7* (9), 1943–1952. <https://doi.org/10.1039/C7CY00435D>.
- (79) Rodrigues, V. de O.; Faro Júnior, A. C. On Catalyst Activation and Reaction Mechanisms in Propane Aromatization on Ga/HZSM5 Catalysts. *Appl. Catal. Gen.* **2012**, *435–436*, 68–77. <https://doi.org/10.1016/j.apcata.2012.05.036>.
- (80) Spivey, J. J.; Hutchings, G. Catalytic Aromatization of Methane. *Chem. Soc. Rev.* **2014**, *43* (3), 792–803. <https://doi.org/10.1039/C3CS60259A>.
- (81) Bhan, A.; Delgass, W. N. Propane Aromatization over HZSM-5 and Ga/HZSM-5 Catalysts. *Catal. Rev.* **2008**, *50* (1), 19–151. <https://doi.org/10.1080/01614940701804745>.
- (82) Al-Zahrani, S. M. Catalytic Conversion of LPG to High-Value Aromatics: The Current State of the Art and Future Predictions. *Dev. Chem. Eng. Miner. Process.* **1998**, *6* (1–2), 101–120. <https://doi.org/10.1002/apj.5500060107>.
- (83) Giannetto, G.; Monque, R.; Galiasso, R. Transformation of LPG into Aromatic Hydrocarbons and Hydrogen over Zeolite Catalysts. *Catal. Rev.* **1994**, *36* (2), 271–304. <https://doi.org/10.1080/01614949408013926>.
- (84) Koval, C. A.; Lercher, J.; Scott, S. L.; Coates, G. W.; Iglesia, E.; Bullock, R. M.; Jaramillo, T. F.; Flytzani-Stephanopoulos, M.; Resasco, D.; Tway, C. L.; Batista, V.; Chapman, K. W.; Dai, S.; Dumesic, J.; Friend, C.; Hille, R.; Johnson, K.; Nørskov, J.; Rekoske, J.; Sarkar, R.; Bradley, C.; Garrett, B.; Henderson, C.; Miranda, R.; Peden, C.; Schwartz, V.; Runkles, K.; Fellner, K.; Jenks, C.; Nelson, M.; Appel, A. M.; Bare, S.; Bartlett, B. M.; Bligaard, T.; Chandler, B. D.; Davis, R. J.; Glezakou, V.-A.; Gregoire, J.; Hille, R.; Hock, A. S.; Kitchin, J.; Kung, H. H.; Rousseau, R.; Sadow, A. D.; Schaak, R. E.; Shaw, W. J.; Stacchiola, D. J.; Delferro, M.; Bunel, E.; Holladay, J.; Houle, F.; Jenks, C.; Krause, T.; Marshall, C.; Neale, N.; Parks, J.; Schaidle, J.; VandeLagemaat, J.; Wang, Y.; Weber, R. *Basic Research Needs for Catalysis Science to Transform Energy Technologies: Report from the U.S. Department of Energy, Office of Basic Energy Sciences Workshop May 8–10, 2017, in Gaithersburg, Maryland*; USDOE Office of Science (SC) (United States), 2017. <https://doi.org/10.2172/1616260>.
- (85) Guisnet, M.; Gnep, N. S. Aromatization of Propane over GaHMF1 Catalysts. Reaction Scheme, Nature of the Dehydrogenating Species and Mode of Coke Formation. *Catal. Today* **1996**, *31* (3), 275–292. [https://doi.org/10.1016/S0920-5861\(96\)00018-1](https://doi.org/10.1016/S0920-5861(96)00018-1).
- (86) Maksoud, W. A.; E. Gevers, L.; Vittenet, J.; Ould-Chikh, S.; Telalovic, S.; Bhatte, K.; Abou-Hamad, E.; H. Anjum, D.; N. Hedhili, M.; Vishwanath, V.; Alhazmi, A.; Almusaiter, K.; Marie Basset, J. A Strategy to Convert Propane to Aromatics (BTX) Using TiNp 4 Grafted at the Periphery of ZSM-5 by Surface Organometallic Chemistry. *Dalton Trans.* **2019**, *48* (19), 6611–6620. <https://doi.org/10.1039/C9DT00905A>.
- (87) Zhang, Y.; Zhou, Y.; Qiu, A.; Wang, Y.; Xu, Y.; Wu, P. Propane Dehydrogenation on PtSn/ZSM-5 Catalyst: Effect of Tin as a Promoter. *Catal. Commun.* **2006**, *7* (11), 860–866. <https://doi.org/10.1016/j.catcom.2006.03.016>.
- (88) Rezai, S. A. S.; Traa, Y. Equilibrium Shift in Membrane Reactors: A Thermodynamic Analysis of the Dehydrogenative Conversion of Alkanes. *J. Membr. Sci.* **2008**, *319* (1), 279–285. <https://doi.org/10.1016/j.memsci.2008.03.051>.
- (89) Bobrov, V. S.; Digurov, N. G.; Skudin, V. V. Propane Dehydrogenation Using Catalytic Membrane. *J. Membr. Sci.* **2005**, *253* (1), 233–242. <https://doi.org/10.1016/j.memsci.2004.11.037>.

- (90) Gbenedio, E.; Wu, Z.; Hatim, I.; Kingsbury, B. F. K.; Li, K. A Multifunctional Pd/Alumina Hollow Fibre Membrane Reactor for Propane Dehydrogenation. *Catal. Today* **2010**, *156* (3), 93–99. <https://doi.org/10.1016/j.cattod.2010.04.044>.
- (91) Kikuchi, E. Membrane Reactor Application to Hydrogen Production. *Catal. Today* **2000**, *56* (1–3), 97–101. [https://doi.org/10.1016/S0920-5861\(99\)00256-4](https://doi.org/10.1016/S0920-5861(99)00256-4).
- (92) Paglieri, S. N.; Way, J. D. Innovations in Palladium Membrane Research. *Sep. Purif. Methods* **2002**, *31* (1), 1–169. <https://doi.org/10.1081/SPM-120006115>.
- (93) Buxbaum, R. E.; Kinney, A. B. Hydrogen Transport through Tubular Membranes of Palladium-Coated Tantalum and Niobium. *Ind. Eng. Chem. Res.* **1996**, *35* (2), 530–537. <https://doi.org/10.1021/ie950105o>.
- (94) Liu, L.; Deng, Q.-F.; Agula, B.; Ren, T.-Z.; Liu, Y.-P.; Zhaorigetu, B.; Yuan, Z.-Y. Synthesis of Ordered Mesoporous Carbon Materials and Their Catalytic Performance in Dehydrogenation of Propane to Propylene. *Catal. Today* **2012**, *186* (1), 35–41. <https://doi.org/10.1016/j.cattod.2011.08.022>.
- (95) Ren, Y.; Wang, J.; Hua, W.; Yue, Y.; Gao, Z. Ga<sub>2</sub>O<sub>3</sub>/HZSM-48 for Dehydrogenation of Propane: Effect of Acidity and Pore Geometry of Support. *J. Ind. Eng. Chem.* **2012**, *18* (2), 731–736. <https://doi.org/10.1016/j.jiec.2011.11.134>.
- (96) Sokolov, S.; Bychkov, V. Yu.; Stoyanova, M.; Rodemerck, U.; Bentrup, U.; Linke, D.; Tyulenin, Y. P.; Korchak, V. N.; Kondratenko, E. V. Effect of VO<sub>x</sub> Species and Support on Coke Formation and Catalyst Stability in Nonoxidative Propane Dehydrogenation. *ChemCatChem* **2015**, *7* (11), 1691–1700. <https://doi.org/10.1002/cctc.201500151>.
- (97) Xu, B.; Zheng, B.; Hua, W.; Yue, Y.; Gao, Z. Support Effect in Dehydrogenation of Propane in the Presence of CO<sub>2</sub> over Supported Gallium Oxide Catalysts. *J. Catal.* **2006**, *239* (2), 470–477. <https://doi.org/10.1016/j.jcat.2006.02.017>.
- (98) Saito, M.; Watanabe, S.; Takahara, I.; Inaba, M.; Murata, K. Dehydrogenation of Propane Over a Silica-Supported Gallium Oxide Catalyst. *Catal. Lett.* **2003**, *89* (3), 213–217. <https://doi.org/10.1023/A:1025754413131>.
- (99) Nakagawa, K.; Kajita, C.; Okumura, K.; Ikenaga, N.; Nishitani-Gamo, M.; Ando, T.; Kobayashi, T.; Suzuki, T. Role of Carbon Dioxide in the Dehydrogenation of Ethane over Gallium-Loaded Catalysts. *J. Catal.* **2001**, *203* (1), 87–93. <https://doi.org/10.1006/jcat.2001.3306>.
- (100) Shao, C.-T.; Lang, W.-Z.; Yan, X.; Guo, Y.-J. Catalytic Performance of Gallium Oxide Based-Catalysts for the Propane Dehydrogenation Reaction: Effects of Support and Loading Amount. *RSC Adv.* **2017**, *7* (8), 4710–4723. <https://doi.org/10.1039/C6RA27204E>.
- (101) Chen, S.; Chang, X.; Sun, G.; Zhang, T.; Xu, Y.; Wang, Y.; Pei, C.; Gong, J. Propane Dehydrogenation: Catalyst Development, New Chemistry, and Emerging Technologies. *Chem. Soc. Rev.* **2021**, *50* (5), 3315–3354. <https://doi.org/10.1039/D0CS00814A>.
- (102) Wang, J.; Zhang, F.; Hua, W.; Yue, Y.; Gao, Z. Dehydrogenation of Propane over MWW-Type Zeolites Supported Gallium Oxide. *Catal. Commun.* **2012**, *18*, 63–67. <https://doi.org/10.1016/j.catcom.2011.11.023>.
- (103) Xu, B.; Li, T.; Zheng, B.; Hua, W.; Yue, Y.; Gao, Z. Enhanced Stability of HZSM-5 Supported Ga<sub>2</sub>O<sub>3</sub> Catalyst in Propane Dehydrogenation by Dealumination. *Catal. Lett.* **2007**, *119* (3), 283–288. <https://doi.org/10.1007/s10562-007-9232-4>.
- (104) Shen, Z.; Liu, J.; Xu, H.; Yue, Y.; Hua, W.; Shen, W. Dehydrogenation of Ethane to Ethylene over a Highly Efficient Ga<sub>2</sub>O<sub>3</sub>/HZSM-5 Catalyst in the Presence of CO<sub>2</sub>.

- Appl. Catal. Gen.* **2009**, *356* (2), 148–153. <https://doi.org/10.1016/j.apcata.2008.12.038>.
- (105) Szeto, K. C.; Jones, Z. R.; Merle, N.; Rios, C.; Gallo, A.; Le Quemener, F.; Delevoye, L.; Gauvin, R. M.; Scott, S. L.; Taoufik, M. A Strong Support Effect in Selective Propane Dehydrogenation Catalyzed by Ga(i-Bu)<sub>3</sub> Grafted onto  $\gamma$ -Alumina and Silica. *ACS Catal.* **2018**, *8* (8), 7566–7577. <https://doi.org/10.1021/acscatal.8b00936>.
- (106) Wang, P.; Xu, Z.; Wang, T.; Yue, Y.; Bao, X.; Zhu, H. Unmodified Bulk Alumina as an Efficient Catalyst for Propane Dehydrogenation. *Catal. Sci. Technol.* **2020**, *10* (11), 3537–3541. <https://doi.org/10.1039/D0CY00779J>.
- (107) Chen, M.; Xu, J.; Su, F.-Z.; Liu, Y.-M.; Cao, Y.; He, H.-Y.; Fan, K.-N. Dehydrogenation of Propane over Spinel-Type Gallia–Alumina Solid Solution Catalysts. *J. Catal.* **2008**, *256* (2), 293–300. <https://doi.org/10.1016/j.jcat.2008.03.021>.
- (108) Michorczyk, P.; Góra-Marek, K.; Ogonowski, J. Dehydrogenation of Propane in the Presence and Absence of CO<sub>2</sub> Over  $\beta$ -Ga<sub>2</sub>O<sub>3</sub> Supported Chromium Oxide Catalysts. *Catal. Lett.* **2006**, *109* (3), 195–198. <https://doi.org/10.1007/s10562-006-0077-z>.
- (109) Zheng, B.; Hua, W.; Yue, Y.; Gao, Z. Dehydrogenation of Propane to Propene over Different Polymorphs of Gallium Oxide. *J. Catal.* **2005**, *232* (1), 143–151. <https://doi.org/10.1016/j.jcat.2005.03.001>.
- (110) Binet, L.; Gourier, D.; Minot, C. Relation between Electron Band Structure and Magnetic Bistability of Conduction Electrons in  $\beta$ -Ga<sub>2</sub>O<sub>3</sub>. *J. Solid State Chem.* **1994**, *113* (2), 420–433. <https://doi.org/10.1006/jssc.1994.1390>.
- (111) Otroshchenko, T.; Jiang, G.; A. Kondratenko, V.; Rodemerck, U.; V. Kondratenko, E. Current Status and Perspectives in Oxidative, Non-Oxidative and CO<sub>2</sub>-Mediated Dehydrogenation of Propane and Isobutane over Metal Oxide Catalysts. *Chem. Soc. Rev.* **2021**, *50* (1), 473–527. <https://doi.org/10.1039/D0CS01140A>.
- (112) Nesterenko, N. S.; Ponomoreva, O. A.; Yuschenko, V. V.; Ivanova, I. I.; Testa, F.; Di Renzo, F.; Fajula, F. Dehydrogenation of Ethylbenzene and Isobutane over Ga- and Fe-Containing Mesoporous Silicas. *Appl. Catal. Gen.* **2003**, *254* (2), 261–272. [https://doi.org/10.1016/S0926-860X\(03\)00488-5](https://doi.org/10.1016/S0926-860X(03)00488-5).
- (113) Jiang, P.; Fu, H.; Ma, H.; Qian, W.; Zhang, H.; Ying, W. Dehydrogenation of Propane over Sugar Foams Templated Ga<sub>2</sub>O<sub>3</sub> Nanoparticles Catalysts. *Catal. Lett.* **2021**, *151* (7), 1894–1901. <https://doi.org/10.1007/s10562-020-03452-0>.
- (114) Areán, C. O.; Delgado, M. R.; Montouillout, V.; Massiot, D. Synthesis and Characterization of Spinel-Type Gallia-Alumina Solid Solutions. *Z. Für Anorg. Allg. Chem.* **2005**, *631* (11), 2121–2126. <https://doi.org/10.1002/zaac.200570027>.
- (115) Nishi, K.; Shimizu, K.; Takamatsu, M.; Yoshida, H.; Satsuma, A.; Tanaka, T.; Yoshida, S.; Hattori, T. Deconvolution Analysis of Ga K-Edge XANES for Quantification of Gallium Coordinations in Oxide Environments. *J. Phys. Chem. B* **1998**, *102* (50), 10190–10195. <https://doi.org/10.1021/jp982704p>.
- (116) Cybulskis, V. J.; Pradhan, S. U.; Lovón-Quintana, J. J.; Hock, A. S.; Hu, B.; Zhang, G.; Delgass, W. N.; Ribeiro, F. H.; Miller, J. T. The Nature of the Isolated Gallium Active Center for Propane Dehydrogenation on Ga/SiO<sub>2</sub>. *Catal. Lett.* **2017**, *147* (5), 1252–1262. <https://doi.org/10.1007/s10562-017-2028-2>.
- (117) Andrew “Bean” Getsoian; Das, U.; Camacho-Bunquin, J.; Zhang, G.; R. Gallagher, J.; Hu, B.; Cheah, S.; A. Schaidle, J.; A. Ruddy, D.; E. Hensley, J.; R. Krause, T.; A. Curtiss, L.; T. Miller, J.; S. Hock, A. Organometallic Model Complexes Elucidate the Active Gallium Species in Alkane Dehydrogenation Catalysts Based on Ligand Effects in Ga K-Edge XANES. *Catal. Sci. Technol.* **2016**, *6* (16), 6339–6353. <https://doi.org/10.1039/C6CY00698A>.

- (118) Huš, M.; Kopač, D.; Likozar, B. Kinetics of Non-Oxidative Propane Dehydrogenation on Cr<sub>2</sub>O<sub>3</sub> and the Nature of Catalyst Deactivation from First-Principles Simulations. *J. Catal.* **2020**, *386*, 126–138. <https://doi.org/10.1016/j.jcat.2020.03.037>.
- (119) Estes, D. P.; Siddiqi, G.; Allouche, F.; Kovtunov, K. V.; Safonova, O. V.; Trigub, A. L.; Koptuyug, I. V.; Copéret, C. C–H Activation on Co<sub>2</sub>O Sites: Isolated Surface Sites versus Molecular Analogs. *J. Am. Chem. Soc.* **2016**, *138* (45), 14987–14997. <https://doi.org/10.1021/jacs.6b08705>.
- (120) Schreiber, M. W.; Plaisance, C. P.; Baumgärtl, M.; Reuter, K.; Jentys, A.; Bermejo-Deval, R.; Lercher, J. A. Lewis–Brønsted Acid Pairs in Ga/H-ZSM-5 To Catalyze Dehydrogenation of Light Alkanes. *J. Am. Chem. Soc.* **2018**, *140* (14), 4849–4859. <https://doi.org/10.1021/jacs.7b12901>.
- (121) Wu, Y.-L.; Han, Z.-F.; Yan, X.; Lang, W.-Z.; Guo, Y.-J. Effective Synthesis of Vanadium-Doped Mesoporous Silica Nanospheres by Sol-Gel Method for Propane Dehydrogenation Reaction. *Microporous Mesoporous Mater.* **2022**, *330*, 111616. <https://doi.org/10.1016/j.micromeso.2021.111616>.
- (122) Chaar, M. A.; Patel, D.; Kung, M. C.; Kung, H. H. Selective Oxidative Dehydrogenation of Butane over V□Mg□O Catalysts. *J. Catal.* **1987**, *105* (2), 483–498. [https://doi.org/10.1016/0021-9517\(87\)90076-5](https://doi.org/10.1016/0021-9517(87)90076-5).
- (123) Wachs, I. E.; Weckhuysen, B. M. Structure and Reactivity of Surface Vanadium Oxide Species on Oxide Supports. *Appl. Catal. Gen.* **1997**, *157* (1), 67–90. [https://doi.org/10.1016/S0926-860X\(97\)00021-5](https://doi.org/10.1016/S0926-860X(97)00021-5).
- (124) Weckhuysen, B. M.; Keller, D. E. Chemistry, Spectroscopy and the Role of Supported Vanadium Oxides in Heterogeneous Catalysis. *Catal. Today* **2003**, *78* (1), 25–46. [https://doi.org/10.1016/S0920-5861\(02\)00323-1](https://doi.org/10.1016/S0920-5861(02)00323-1).
- (125) Ganduglia-Pirovano, M. V.; Popa, C.; Sauer, J.; Abbott, H.; Uhl, A.; Baron, M.; Stacchiola, D.; Bondarchuk, O.; Shaikhutdinov, S.; Freund, H.-J. Role of Ceria in Oxidative Dehydrogenation on Supported Vanadia Catalysts. *J. Am. Chem. Soc.* **2010**, *132* (7), 2345–2349. <https://doi.org/10.1021/ja910574h>.
- (126) Bai, P.; Ma, Z.; Li, T.; Tian, Y.; Zhang, Z.; Zhong, Z.; Xing, W.; Wu, P.; Liu, X.; Yan, Z. Relationship between Surface Chemistry and Catalytic Performance of Mesoporous γ-Al<sub>2</sub>O<sub>3</sub> Supported VOX Catalyst in Catalytic Dehydrogenation of Propane. *ACS Appl. Mater. Interfaces* **2016**, *8* (39), 25979–25990. <https://doi.org/10.1021/acsami.6b07779>.
- (127) Sokolov, S.; Stoyanova, M.; Rodemerck, U.; Linke, D.; Kondratenko, E. V. Effect of Support on Selectivity and On-Stream Stability of Surface VO<sub>x</sub> Species in Non-Oxidative Propane Dehydrogenation. *Catal. Sci. Technol.* **2014**, *4* (5), 1323–1332. <https://doi.org/10.1039/C3CY01083J>.
- (128) Hu, P.; Lang, W.-Z.; Yan, X.; Chen, X.-F.; Guo, Y.-J. Vanadium-Doped Porous Silica Materials with High Catalytic Activity and Stability for Propane Dehydrogenation Reaction. *Appl. Catal. Gen.* **2018**, *553*, 65–73. <https://doi.org/10.1016/j.apcata.2018.01.014>.
- (129) Liu, G.; Zhao, Z.-J.; Wu, T.; Zeng, L.; Gong, J. Nature of the Active Sites of VO<sub>x</sub>/Al<sub>2</sub>O<sub>3</sub> Catalysts for Propane Dehydrogenation. *ACS Catal.* **2016**, *6* (8), 5207–5214. <https://doi.org/10.1021/acscatal.6b00893>.
- (130) Zhao, Z.-J.; Wu, T.; Xiong, C.; Sun, G.; Mu, R.; Zeng, L.; Gong, J. Hydroxyl-Mediated Non-Oxidative Propane Dehydrogenation over VO<sub>x</sub>/γ-Al<sub>2</sub>O<sub>3</sub> Catalysts with Improved Stability. *Angew. Chem. Int. Ed.* **2018**, *57* (23), 6791–6795. <https://doi.org/10.1002/anie.201800123>.
- (131) Wu, T.; Liu, G.; Zeng, L.; Sun, G.; Chen, S.; Mu, R.; Agbotse Gbonfoun, S.; Zhao, Z.-J.; Gong, J. Structure and Catalytic Consequence of Mg-Modified VO<sub>x</sub>/Al<sub>2</sub>O<sub>3</sub>

- Catalysts for Propane Dehydrogenation. *AIChE J.* **2017**, *63* (11), 4911–4919. <https://doi.org/10.1002/aic.15836>.
- (132) Hu, P.; Lang, W.-Z.; Yan, X.; Chu, L.-F.; Guo, Y.-J. Influence of Gelation and Calcination Temperature on the Structure-Performance of Porous VOX-SiO<sub>2</sub> Solids in Non-Oxidative Propane Dehydrogenation. *J. Catal.* **2018**, *358*, 108–117. <https://doi.org/10.1016/j.jcat.2017.12.004>.
- (133) Sokolov, S.; Stoyanova, M.; Rodemerck, U.; Linke, D.; Kondratenko, E. V. Comparative Study of Propane Dehydrogenation over V-, Cr-, and Pt-Based Catalysts: Time on-Stream Behavior and Origins of Deactivation. *J. Catal.* **2012**, *293*, 67–75. <https://doi.org/10.1016/j.jcat.2012.06.005>.
- (134) Rodemerck, U.; Stoyanova, M.; Kondratenko, E. V.; Linke, D. Influence of the Kind of VO<sub>x</sub> Structures in VO<sub>x</sub>/MCM-41 on Activity, Selectivity and Stability in Dehydrogenation of Propane and Isobutane. *J. Catal.* **2017**, *352*, 256–263. <https://doi.org/10.1016/j.jcat.2017.05.022>.
- (135) Wegener, S. L.; Marks, T. J.; Stair, P. C. Design Strategies for the Molecular Level Synthesis of Supported Catalysts. *Acc. Chem. Res.* **2012**, *45* (2), 206–214. <https://doi.org/10.1021/ar2001342>.
- (136) Carrero, C. A.; Schloegl, R.; Wachs, I. E.; Schomaecker, R. Critical Literature Review of the Kinetics for the Oxidative Dehydrogenation of Propane over Well-Defined Supported Vanadium Oxide Catalysts. *ACS Catal.* **2014**, *4* (10), 3357–3380. <https://doi.org/10.1021/cs5003417>.
- (137) Haber, J. Fifty Years of My Romance with Vanadium Oxide Catalysts. *Catal. Today* **2009**, *142* (3), 100–113. <https://doi.org/10.1016/j.cattod.2008.11.007>.
- (138) Scholz, J.; Walter, A.; Ressler, T. Influence of MgO-Modified SBA-15 on the Structure and Catalytic Activity of Supported Vanadium Oxide Catalysts. *J. Catal.* **2014**, *309*, 105–114. <https://doi.org/10.1016/j.jcat.2013.08.031>.
- (139) Tian, H.; Ross, E. I.; Wachs, I. E. Quantitative Determination of the Speciation of Surface Vanadium Oxides and Their Catalytic Activity. *J. Phys. Chem. B* **2006**, *110* (19), 9593–9600. <https://doi.org/10.1021/jp055767y>.
- (140) Wu, Z.; Kim, H.-S.; Stair, P. C.; Rugmini, S.; Jackson, S. D. On the Structure of Vanadium Oxide Supported on Aluminas: UV and Visible Raman Spectroscopy, UV-Visible Diffuse Reflectance Spectroscopy, and Temperature-Programmed Reduction Studies. *J. Phys. Chem. B* **2005**, *109* (7), 2793–2800. <https://doi.org/10.1021/jp046011m>.
- (141) Harlin, M. E.; Niemi, V. M.; Krause, A. O. I.; Weckhuysen, B. M. Effect of Mg and Zr Modification on the Activity of VO<sub>x</sub>/Al<sub>2</sub>O<sub>3</sub> Catalysts in the Dehydrogenation of Butanes. *J. Catal.* **2001**, *203* (1), 242–252. <https://doi.org/10.1006/jcat.2001.3329>.
- (142) Harlin, M. E.; Niemi, V. M.; Krause, A. O. I. Alumina-Supported Vanadium Oxide in the Dehydrogenation of Butanes. *J. Catal.* **2000**, *195* (1), 67–78. <https://doi.org/10.1006/jcat.2000.2969>.
- (143) Takahara, I.; Saito, M.; Inaba, M.; Murata, K. Dehydrogenation of Propane over a Silica-Supported Vanadium Oxide Catalyst. *Catal. Lett.* **2005**, *102* (3), 201–205. <https://doi.org/10.1007/s10562-005-5856-4>.
- (144) Basset, J.-M.; Psaro, R.; Roberto, D.; Ugo, R. *Modern Surface Organometallic Chemistry*; John Wiley & Sons, 2009.
- (145) Rataboul, F.; Baudouin, A.; Thieuleux, C.; Veyre, L.; Copéret, C.; Thivolle-Cazat, J.; Basset, J.-M.; Lesage, A.; Emsley, L. Molecular Understanding of the Formation of Surface Zirconium Hydrides upon Thermal Treatment under Hydrogen of

- [(SiO)Zr(CH<sub>2</sub>tBu)<sub>3</sub>] by Using Advanced Solid-State NMR Techniques. *J. Am. Chem. Soc.* **2004**, *126* (39), 12541–12550. <https://doi.org/10.1021/ja038486h>.
- (146) Saggio, G.; de Mallmann, A.; Maunders, B.; Taoufik, M.; Thivolle-Cazat, J.; Basset, J.-M. Synthesis, Characterization, and Reactivity of the Highly Unsaturated Silica-Supported Trisiloxy Tantalum: (SiO)<sub>3</sub>Ta(III). *Organometallics* **2002**, *21* (24), 5167–5171. <https://doi.org/10.1021/om020376g>.
- (147) Popoff, N.; Mazoyer, E.; Pelletier, J.; Gauvin, R. M.; Taoufik, M. Expanding the Scope of Metathesis: A Survey of Polyfunctional, Single-Site Supported Tungsten Systems for Hydrocarbon Valorization. *Chem. Soc. Rev.* **2013**, *42* (23), 9035–9054. <https://doi.org/10.1039/C3CS60115C>.
- (148) R. Docherty, S.; Rochlitz, L.; Payard, P.-A.; Copéret, C. Heterogeneous Alkane Dehydrogenation Catalysts Investigated via a Surface Organometallic Chemistry Approach. *Chem. Soc. Rev.* **2021**, *50* (9), 5806–5822. <https://doi.org/10.1039/D0CS01424A>.
- (149) Searles, K.; Siddiqi, G.; V. Safonova, O.; Copéret, C. Silica-Supported Isolated Gallium Sites as Highly Active, Selective and Stable Propane Dehydrogenation Catalysts. *Chem. Sci.* **2017**, *8* (4), 2661–2666. <https://doi.org/10.1039/C6SC05178B>.
- (150) Szeto, K. C.; Gallo, A.; Hernández-Morejudo, S.; Olsbye, U.; De Mallmann, A.; Lefebvre, F.; Gauvin, R. M.; Delevoye, L.; Scott, S. L.; Taoufik, M. Selective Grafting of Ga(i-Bu)<sub>3</sub> on the Silanols of Mesoporous H-ZSM-5 by Surface Organometallic Chemistry. *J. Phys. Chem. C* **2015**, *119* (47), 26611–26619. <https://doi.org/10.1021/acs.jpcc.5b09289>.
- (151) Kazansky, V. B.; Subbotina, I. R.; van Santen, R. A.; Hensen, E. J. M. DRIFTS Study of the Nature and Chemical Reactivity of Gallium Ions in Ga/ZSM-5: II. Oxidation of Reduced Ga Species in ZSM-5 by Nitrous Oxide or Water. *J. Catal.* **2005**, *233* (2), 351–358. <https://doi.org/10.1016/j.jcat.2005.05.004>.
- (152) Szeto, K. C.; Loges, B.; Merle, N.; Popoff, N.; Quadrelli, A.; Jia, H.; Berrier, E.; De Mallmann, A.; Delevoye, L.; Gauvin, R. M.; Taoufik, M. Vanadium Oxo Organometallic Species Supported on Silica for the Selective Non-Oxidative Dehydrogenation of Propane. *Organometallics* **2013**, *32* (21), 6452–6460. <https://doi.org/10.1021/om400795s>.
- (153) Feher, F. J.; Blanski, R. L. Lewis Acid Adducts Oxovanadium (V) Alkyl and Triphenylsiloxy Complexes: Synthesis, Characterization, and Reactivity toward Ethylene. *Organometallics* **1993**, *12* (3), 958–963.
- (154) Nabavi, M.; Taulelle, F.; Sanchez, C.; Verdagner, M. Xanes and 51V Nmr Study of Vanadium-Oxygen Compounds. *J. Phys. Chem. Solids* **1990**, *51* (12), 1375–1382. [https://doi.org/10.1016/0022-3697\(90\)90020-G](https://doi.org/10.1016/0022-3697(90)90020-G).
- (155) Wong, J.; Lytle, F. W.; Messmer, R. P.; Maylotte, D. H. K<sub>2</sub>V-Edge Absorption Spectra of Selected Vanadium Compounds. *Phys. Rev. B* **1984**, *30* (10), 5596–5610. <https://doi.org/10.1103/PhysRevB.30.5596>.
- (156) Olsbye, U.; Virnovskaia, A.; Prytz, Ø.; Tinnemans, S. J.; Weckhuysen, B. M. Mechanistic Insight in the Ethane Dehydrogenation Reaction over Cr/Al<sub>2</sub>O<sub>3</sub> Catalysts. *Catal. Lett.* **2005**, *103* (1), 143–148. <https://doi.org/10.1007/s10562-005-6521-7>.
- (157) Kaphan, D. M.; Ferrandon, M. S.; Langeslay, R. R.; Celik, G.; Wegener, E. C.; Liu, C.; Niklas, J.; Poluektov, O. G.; Delferro, M. Mechanistic Aspects of a Surface Organovanadium(III) Catalyst for Hydrocarbon Hydrogenation and Dehydrogenation. *ACS Catal.* **2019**, *9* (12), 11055–11066. <https://doi.org/10.1021/acscatal.9b02800>.

## CHAPTER II. PART A

---

# Direct conversion of trans-2-butene into a mixture of monomers with different composition over vanadium supported catalysts

---



Jessy Abou Nakad,<sup>a</sup> Nicolas Berthet,<sup>a</sup> Kai Szeto,<sup>a</sup> Aimery De Mallman,<sup>a</sup> Mostafa Taoufik <sup>\*a</sup>

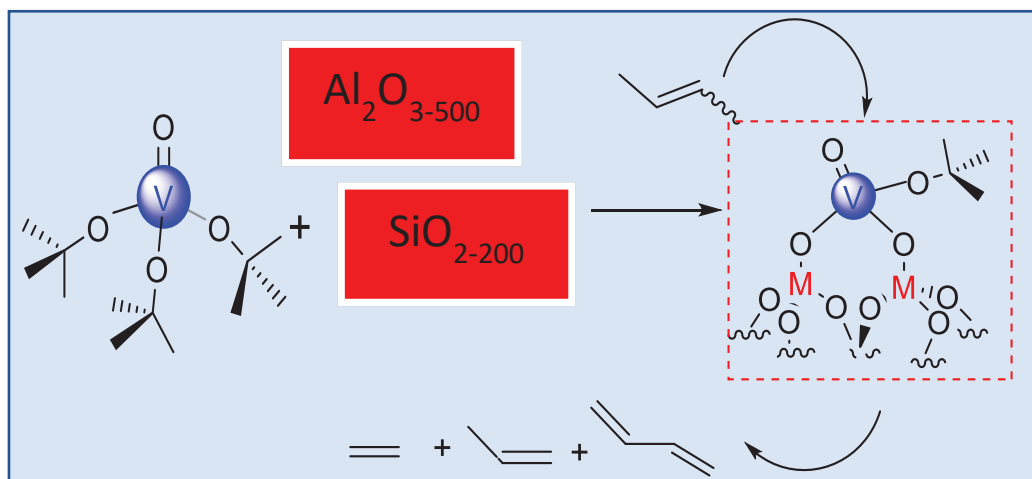
<sup>a</sup> Université de Lyon 1, CPE Lyon, CNRS-UMR 5128 – laboratoire Catalyse, Polymérisation, Procédés et Matériaux (CP2M), F-69616 Villeurbanne, France. Email: [mostafa.taoufik@univ-lyon1.fr](mailto:mostafa.taoufik@univ-lyon1.fr)

Article accepted in *Catalysis Communications*

## Abstract

Terpolymerization of 1,3-butadiene, ethylene and propylene became an important process to access EPDM rubbers materials with unique properties. Having a mixture of these monomers is preferred rather than mixing them from separated sources. Hence, we developed for the first time, well defined single-site V based-catalysts by SOMC of  $[V(=O)(OtBu)_3]$  on  $SiO_{2-200}$  and on  $Al_2O_{3-500}$  affording  $[(\equiv MO)_2V(=O)(OtBu)]$ , (M= Si or Al). The catalytic activity of these materials in 2-butenes conversion into different composition of monomers depends on the support and the working temperature. A mechanism for the formation of these monomers has been proposed based on  $\beta$ -H elimination and  $\beta$ -alkyl transfer as elementary steps.

## Graphical abstract



**Keywords:** trans-2-butenes conversion, vanadium, dehydrogenation,  $\beta$ -alkyl transfer,  $\beta$ -H elimination

## List of abbreviations

**EPDM:** Ethylene, Propylene, Diene, Monomer

**SOMC:** Surface Organometallic Chemistry

**DRIFT:** Diffuse Reflectance Infrared Fourier Transform spectroscopy

**NMR:** Nuclear Magnetic Resonance

**XANES:** X-ray Absorption Near Edge Spectroscopy

**IR:** Infrared spectroscopy

**FT-IR:** Fourier Transform Infrared

**UV-Vis:** Ultraviolet Visible

**UV-Vis-NIR:** Ultraviolet Visible Near Infrared spectrophotometry

**CP MAS:** Cross Polarization Magic Angle Spinning

**ESRF:** European Synchrotron Radiation Facility

**GC:** Gas Chromatography

**FID:** Flame-Ionization Detection

## **Introduction**

The demand for light olefins has constantly increased during the last decades [1]. Such monomers, particularly ethylene, propylene and 1,3-butadiene are important building blocks for unlimited conventional materials after being polymerized over proper catalysts [2]. Polymerizations of the aforementioned monomers are matured technologies and produce light weighted plastic materials from packing to construction, as well as elastomers. The main source of those monomers is derived from fossil fuels, notably by cracking. Due to the high demand for particularly ethylene and propylene, several on-purpose technologies have been commercialized [3–6] and remain to date active subjects for academic research. The dominating technology is the non-oxidative alkane (ethane or propane) dehydrogenation from natural gas, shale gas and recovered fractions of the cracking unit. On the other hand, on-purpose production of 1,3-butadiene has surprisingly received far less attention both in academy and industry taking into account that the availability of this monomer is expected to be limited in the future due to saturation of the cracking units [7].

As mentioned, polymerization and even co-polymerization of light olefins and dienes have already been widely studied [8]. Recently, polyolefin thermoplastic elastomers (TPO) have become important materials of various polyolefin polymers, semicrystalline thermoplastics, and amorphous elastomers [9]. Due to their properties such as high impact strength, low density and their chemical resistance, they have found applications for the production of

fillers, reinforcements, lubricants, heat stabilizers, antioxidants, ultraviolet stabilizers, colorants, and processing aids [10]. Most TPOs are formed by ethylene–propylene with or without diene rubber [11]. A highly potential field of research for the production of this rubber is terpolymerization of linear conjugated diene, for example 1,3-butadiene, with ethylene and propylene. Moreover, dependent on the composition of monomers, the final material can be tuned to fall in the range from conventional elastomer to highly crystalline [12]. For economical and safety reasons, it is preferable to simplify the process scheme of terpolymerization reaction in gas or liquid phase, by starting with a mixture of these monomers instead of mixing three different monomers. For example, in the case of the production of polyethylene and polypropylene, the monomers are generally produced in the refinery situated close to the polymerization unit. Hence, accessing to a mixture of ethylene, propylene and 1,3-butadiene from a low value reactant has a potential interest. However, the latter process faces several challenges, such as finding a suitable catalyst with the ability to selectively convert the given reactant into the desired monomers in a single reactor, preferably under continuous flow. Browsing through the low value hydrocarbons, it turns out that trans-2-butene are suitable candidates. Trans-2-butene are the thermodynamical most stable molecules and are the majority among the n-butene isomers [13]. Nevertheless, their practical application and chemistry are less exploited compared to the other isomers (1-butene and isobutene) [14,15]. Trans-2-butene is used for on-purpose propylene production by cross metathesis reaction with ethylene and for the production of alkylated gasoline [6,16]. The development of a simple catalytic system capable to convert directly 2-butenes into a mixture of valuable products such as ethylene, propylene and butadiene is a new scientific challenge. Hence, it is essential to design a supported metal active site with a reactive ligand able to undergo simultaneously a dehydrogenation step of trans-2-butene to form butadiene and hydrogen, and a  $\beta$ -alkyl transfer to produce ethylene and propylene from trans-2-butene using the released hydrogen (Scheme S1). On these premises, depending on the targeted catalytic reactions, and the postulated active intermediates in the catalytic cycle, one may select the appropriate surface organometallic precursors to carry out such transformations with optimal performances. Among different known catalytic systems, single-site catalysts offer a broad combination of different elements and coordinative ligands for C-H activation, olefin insertion, dehydrogenation through  $\beta$ -H elimination and  $\beta$ -alkyl transfer. As a first approach, the active species can be selected according to their abilities: (i) to form a metal-hydride for dehydrogenation reaction (Eq 1, Scheme S1) via C–H activation in an allylic position of trans-

2-butene followed by a  $\beta$ -H elimination and release of hydrogen; (ii) insertion of trans-2-butene on the same reactive ligand leading to two species, M-sec-butyl and M-n-butyl intermediates. In presence of released hydrogen from Eq 1,  $\beta$ -alkyl transfer of M-sec-butyl intermediate gives propylene and methane (Eq. 2, Scheme S1), while M-n-butyl intermediate gives ethylene and ethane (Eq. 3, Scheme S1). Supported metal hydrides from group (IV), (V) and (VI), have shown to be extremely versatile to transform hydrocarbons to valuable products via the aforementioned elementary steps [17]. Recapitulating these requirements of the catalyst, a promising candidate is supported single site species based on group (V) [18]. In fact, it has been reported in the literature that single site catalysts based on vanadium bearing oxo-alkyl ligands, show high activity in propane dehydrogenation to propylene via V-H as active species. In addition to propylene, minor, but substantial amounts of methane and ethane were observed and are probably originated from  $\beta$ -methyl transfer [19,20]. Thus, this supported bipodal V-H catalyst can perform simultaneously the dehydrogenation reactions of trans-2-butene to butadiene with the concomitant production of hydrogen, and the hydrogenolysis of 2-butenes by  $\beta$ -alkyl transfer to form propylene or ethylene and methane.

Herein, we report for the first time a bifunctional single-site catalyst based on vanadium, prepared through the grafting of  $[V(=O)(OtBu)_3]$  onto partially dehydroxylated silica or alumina for the conversion of trans-2-butene into a mixture of monomers (ethylene, propylene and butadiene). The catalysts were characterized by DRIFT, solid state NMR, XANES, elemental analysis and were tested in trans-2-butene conversion to evaluate the effect of the support. The effect of the temperature in the feed was evaluated on vanadium supported on silica. These parameters (support and temperature) can highly influence the monomers composition.

## Experimental Section

**General Procedure.** All experiments were carried out using standard air-free methodology in an argon-filled glovebox, on a Schlenk line or in a Schlenk-type apparatus interfaced to a high-vacuum line ( $10^{-5}$  mbar). Solvents were purified and dried according to standard procedures.  $[V(=O)(OtBu)_3]$  was synthesized in two steps. Elemental analyses were performed at Mikroanalytisches Labor Pascher. Diffuse reflectance infrared spectra were collected in a Nicolet 6700 FT-IR spectrophotometer in  $4\text{ cm}^{-1}$  resolutions with a SMART module. An air-tight IR cell with a  $CaF_2$  window was applied and the final spectra comprised

64 scans. Diffuse reflectance UV-Vis spectra in the range of 200-850 nm were recorded on a Perkin Elmer  $\lambda$ 1050 UV-Vis-NIR spectrophotometer adapted with the Praying Mantis optical unit provided by Harrick. The samples were diluted in dry BaSO<sub>4</sub> and the spectra were recorded against a BaSO<sub>4</sub> baseline. An air-tight cell with quartz windows was used.

Solution NMR spectra were recorded on an Avance-300 Bruker spectrometer. All chemical shifts were measured relative to residual <sup>1</sup>H or <sup>13</sup>C resonance in the deuterated C<sub>6</sub>D<sub>6</sub> solvent;  $\delta$  7.15 ppm for <sup>1</sup>H and 128 ppm for <sup>13</sup>C. Solid-state NMR spectra were acquired with a Bruker Avance 500 spectrometer (<sup>1</sup>H: 500.1 MHz, <sup>13</sup>C: 125.7 MHz). For <sup>1</sup>H experiments, the spinning frequency was 10 kHz, the recycle delay was 5 s and 8 scans were collected using a 90° pulse excitation of 3  $\mu$ s. The <sup>13</sup>C CP MAS spectrum was obtained at a spinning frequency of 10 kHz, with a recycle delay of 5 s and 12288 scans were collected. Chemical shifts were given in ppm with respect to TMS as external reference for <sup>1</sup>H and <sup>13</sup>C NMR. The <sup>51</sup>V MAS NMR spectrum was acquired in a Bruker DSX 300 spectrometer (<sup>51</sup>V: 78.9 MHz) using a single pulse excitation. The signal was optimized with crystalline V<sub>2</sub>O<sub>5</sub> ( $\delta$  = - 609 ppm) as external standard with a pulse angle of  $\pi/2$ . Two spinning rates were used to determine the isotropic chemical shift (10 kHz and 12 kHz). X-ray absorption spectra were acquired at ESRF on BM23 beam-line, at room temperature at the vanadium K edge. A double crystal Si(111) was used as monochromator and a system based on a total reflection through a double X-ray mirror with an incidence angle variable from 2 to 5 mrad allowed harmonic rejection to better than the 10<sup>-5</sup> level.[21] The spectra were recorded in the transmission mode between 5.4 to 5.65 KeV at room temperature (295 K). Each data set was collected simultaneously with a V metal foil reference and was later aligned according to that reference (first maximum of the derivative of the V foil spectrum set at 5465.1 eV). The molecular complexes and vanadyl sulfate were homogeneously mixed with dry BN and the supported V samples were packaged as pellets within a nitrogen filled dry box in a double air-tight sample holder equipped with kapton windows. The data analyses were performed by standard procedures using the program "Athena".[22]

**Preparation of the complex.** The vanadium precursor [V(=O)(*O**t*Bu)<sub>3</sub>] was synthesized by reaction of V<sub>2</sub>O<sub>5</sub> (Aldrich) with *t*BuOH in benzene. The entire preparation procedure was carried out in an inert atmosphere using a Schlenk line. 20 g of V<sub>2</sub>O<sub>5</sub> in a 1-L round-bottom flask was connected to a Dean–Stark trap to capture the water from the reaction and the reflux condenser. 300-mL of benzene and later 165 ml of *t*-BuOH were added to the benzene

suspension of  $V_2O_5$ . The temperature was increased to ca. 373 K for 48 h. After reaction, the color of the solution changed to orange from red. The solution was filtered away from unreacted  $V_2O_5$ . White crystals were observed after distillation of the solvent. The crystals were dried under high vacuum line and purified by sublimation. After purification, the compound was identified by the presence of a strong  $^1H$  NMR resonance at 1.44 ppm for the protons of  $CH_3$  and two signals in  $^{13}C\{H\}$  NMR at 31.4 ppm corresponding to  $CH_3$  and 86 ppm for quaternary C of tert-butoxide ligand.

**Preparation and characterization of  $V(=O)(OtBu)_3/SiO_{2-200}$  (I).** Prior to the grafting reaction, the molecular precursor,  $[V(=O)(OtBu)_3]$ , was synthesized as reported above. A mixture of  $[V(=O)(OtBu)_3]$  (120 mg) and  $SiO_{2-200}$  (1 g) in pentane (10 mL) was stirred at 25 °C for 4 hours. After filtration, the solid, was washed 4 times with pentane and the liquid was transferred into another reactor in order to identify *t*-BuOH evolved during grafting. The resulting white powder was dried under vacuum ( $10^{-5}$  mbar). Elemental analysis: V 1.6 wt% C 1.5 wt%. The catalyst was characterized by DRIFT, solid state NMR, UV-Vis and XANES.

**Preparation and characterization of  $V(=O)(OtBu)_3/Al_2O_{3-500}$  (II).** Prior to the grafting reaction, the molecular precursor,  $[V(=O)(OtBu)_3]$ , was synthesized as reported. A mixture of  $[V(=O)(OtBu)_3]$  (120 mg) and  $Al_2O_{3-500}$  (1 g) in pentane (10 mL) was stirred at 25 °C for 4 hours. After filtration, the solid, was washed 4 times with pentane. The resulting white powder was dried under vacuum ( $10^{-5}$  mbar). Elemental analysis: V 1.3 wt% 1.5 C wt%. The catalyst was characterized by DRIFT, solid state NMR, UV-Vis and XANES.

**Catalyst evaluation.** Catalytic performances for trans-2-butenes (Air Liquide, 99.4%) conversion were tested in a stainless-steel continuous flow reactor ( $P_{total} = 1$  bar,  $T = 540$  °C, total flow rate = 5 mL.min $^{-1}$  (20% of trans-2-butene in argon 99.999%), with 0.5 g of (I) or (II) diluted in 2 g of CSi. The gases were purified with a column of molecular sieve and activated  $Cu_2O/Al_2O_3$  and controlled by Brooks mass flow controllers. The catalyst was charged in the glovebox. A 4-way valve allowed isolation of the charged catalyst in the reactor from the environment and extensive purging of the tubes before the reaction. The products were determined by an online HP 6890 GC equipped with 50 m KCl/ $Al_2O_3$  column and FID.

## Results and Discussions

### Preparation and characterization of $[V(=O)(OtBu)_3]$ on silica dehydroxylated at 200 °C (**I**)

$[V(=O)(OtBu)_3]$  was easily synthesized from a commercially available compounds  $V_2O_5$  and *t*-BuOH in benzene at 100 °C for 48 h with a good yield (70 %). After purification, the  $^1H$  NMR spectrum of this complex consisted in an intense signal at 1.43 ppm attributed to the protons of the methyl fragment, and  $^{13}C$  NMR revealed two signals at 31.4 ppm corresponding to  $CH_3$  and 86 ppm for quaternary  $CCH_3$  (Figure S1). In addition, the  $^{51}V$  NMR spectrum of  $[V(=O)(OtBu)_3]$  showed a signal at - 642 ppm (Figure S2), corresponding to a tetrahedral vanadium complex bearing an oxo and trialkoxy ligand [23].

$SiO_{2-200}$  support was obtained from Degussa Aerosil200 by dehydroxylation of this amorphous flame-silica at 200 °C under a high vacuum ( $10^{-5}$ mbar), with a density of silanols of ca. 2.5 OH per  $nm^2$  ( $0.86 \text{ mmol OH}\cdot g^{-1}$ ). The grafting reaction of  $[V(=O)(OtBu)_3]$  on  $SiO_{2-200}$  was carried out by impregnation in pentane at room temperature. The *t*-BuOH emitted during the grafting reaction was qualitatively identified by GC after reaction. The resulting powder was extensively washed (four times) with dry pentane in order to remove the excess of complex, affording  $V(=O)(OtBu)_3/SiO_{2-200}$  (**I**) as a white material. DRIFT spectroscopy of (**I**) revealed the total consumption of isolated silanols at  $3747 \text{ cm}^{-1}$ , while the band at  $3600 \text{ cm}^{-1}$ , attributed to the silanols in interaction through hydrogen bonds, remained (Figure 1). The low reactivity of these vicinals silanols was already observed during the reactivity of metal complexes of group IV, V and VI with  $SiO_{2-200}$  [24]. Simultaneously, two groups of bands appear in the  $3000\text{-}2700 \text{ cm}^{-1}$  and  $1500\text{-}1300 \text{ cm}^{-1}$  regions, assigned respectively to  $\nu(CH)$ , and  $\delta(CH)$  and C-C vibrations from the *tert*-butoxide ligands. These results confirm the grafting of  $[V(=O)(OtBu)_3]$  on  $SiO_{2-200}$  by protonolysis of V-*Ot*Bu bonds by surface silanols.

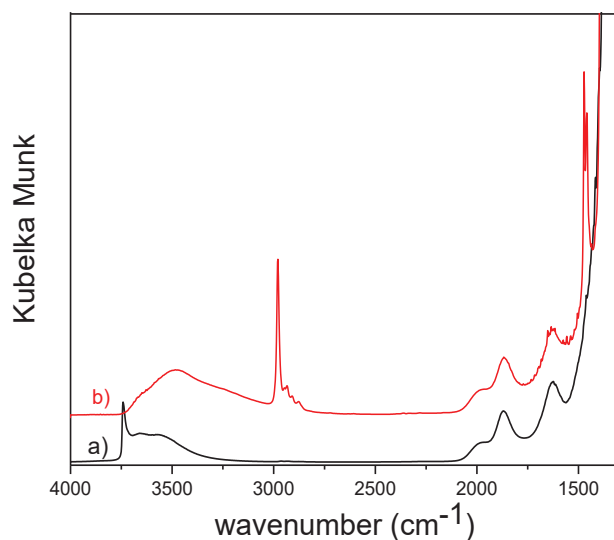
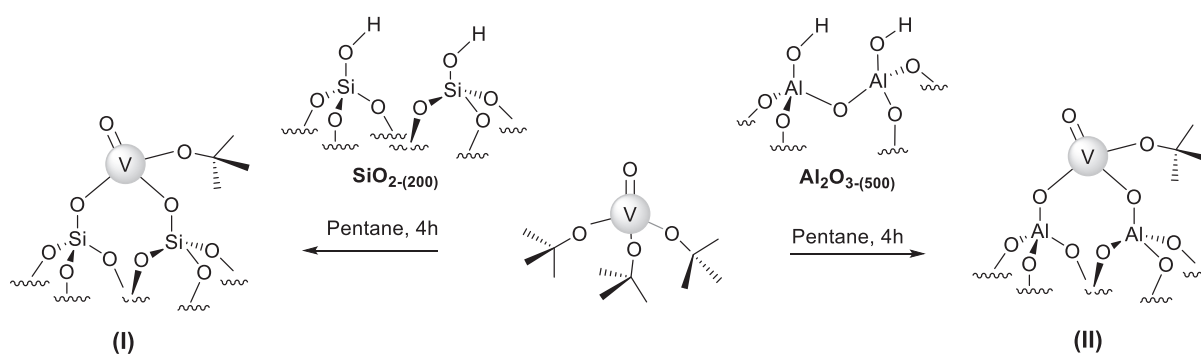


**Figure 1.** IR-spectra of a)  $\text{SiO}_2\text{-200}$  (black) and b) after the grafting of  $[\text{V}(=\text{O})(\text{OtBu})_3]$  on  $\text{SiO}_2\text{-200}$  (red)

Elemental analysis of  $\text{V}(=\text{O})(\text{OtBu})_3/\text{SiO}_2\text{-200}$  (**I**) revealed 1.6 wt% and 1.5 wt % of V and C respectively, corresponding to an atomic ratio of 4.0 C/V. On the other hand, 0.31 mmol of V/g of silica was grafted, although the concentration of silanols on  $\text{SiO}_2\text{-200}$  was about 0.86 mmol OH/g [19] which gives a V/OH ratio of 0.37. Thus, current characterizations are in line with the formation of a major bipodal species bearing a tert-butoxide ligand  $[(\equiv\text{SiO})_2\text{V}(=\text{O})(\text{OtBu})]$  (**I**) (Scheme 1).



**Scheme 1.** The formation of bipodal species after grafting  $[\text{V}(=\text{O})(\text{OtBu})_3]$  on  $\text{SiO}_2\text{-200}$  affording (**I**) and on  $\text{Al}_2\text{O}_3\text{-500}$  affording (**II**) at room temperature

Additional spectroscopic characterizations provided more information on the structure of the resulting species obtained after grafting  $[\text{V}(=\text{O})(\text{OtBu})_3]$  on  $\text{SiO}_2\text{-200}$ . The  $^1\text{H}$  MAS NMR

showed one signal at 1.4 ppm assigned to  $\text{CH}_3$  protons (Figure S3,a). The  $^{13}\text{C}$  CP MAS NMR revealed only one signal at 28.2 ppm attributed to the carbon of the methyl groups (Figure S3,b). The signal corresponding to the quaternary carbon of tert-butoxide ligand was not featured in the spectrum, due to the absence of proton bonded to this carbon. Such observation was also found in the case of supported titanium tert-butoxide [25].  $^{51}\text{V}$  MAS NMR in materials is known to be a sensitive method to investigate the local nuclear environment of vanadium. Therefore,  $^{51}\text{V}$  NMR spectroscopy was used to study the structure of the surface complexes of several catalysts [26].  $^{51}\text{V}$  MAS NMR spectrum of (**I**) consisted in a signal with an isotropic chemical shift of -693 ppm (Figure 2), as determined by the variation of the spinning frequency, which represented an upfield shift of 51 ppm in comparison to the spectrum of  $[\text{V}(=\text{O})(\text{OtBu})_3]$  (Figure S2), which showed a signal at -642 ppm. This result is consistent with the formation of a bipodal surface species on silica-200. In fact, the upfield shift was already described in the literature. The  $^{51}\text{V}$  MAS NMR chemical shift in the supported species was shifted to high fields compared to vanadium molecular complexes [19,23,27].

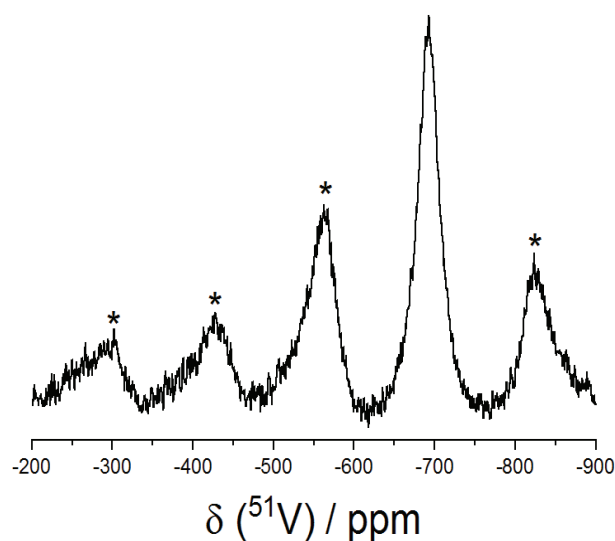


**Figure 2.**  $^{51}\text{V}$  MAS NMR spectrum of  $\text{V}(=\text{O})(\text{OtBu})_3/\text{SiO}_2\text{-200}$  (12 kHz MAS,  $d_1=1\text{s}$ )

UV-vis spectroscopy can provide information about the local coordination environment, the polymerization degree, and the oxidation state of supported vanadium oxo species [28]. The UV-Vis spectrum of  $[(\equiv\text{SiO})_2\text{V}(=\text{O})(\text{OtBu})]$  (**I**), comprised several absorption bands between 200 and 400 nm (Figure S4). The absence in the spectrum of any absorption in the  $d \rightarrow d$

transition part, suggested that for **(I)**,  $[(\equiv\text{SiO})_2\text{V}(=\text{O})(\text{OtBu})]$ , vanadium was in its highest oxidation state [29]. The broad peak ( $\lambda_{\text{max}} = 259 \text{ nm}$ ) can be assigned to a ligand to metal charge transfer (LMCT) originated from the tert-butoxide ligand. The energy edge ( $E_g$ ) derived from  $\text{O} \rightarrow \text{V}$  charge transfer peak (determined from the intercept of the  $[F(R_\infty)h\nu]^2$  vs  $h\nu$  plot in the low energy rise) reflects the degree of vanadia polymerization ( $\text{VO}_x$ ) [30]. This value is extrapolated to be 3.58 eV for **(I)**, strongly suggesting that the vanadium sites are present as monomers on the surface in a distorted tetrahedral geometry [31].

X-Ray absorption spectroscopy has been used to clarify the environmental structure around vanadium atoms in silica-supported vanadium oxo catalysts. Normalized V K-edge XANES spectra of the molecular complex,  $[\text{V}(=\text{O})(\text{OtBu})_3]$  and of **(I)**, obtained from the grafting of  $[\text{V}(=\text{O})(\text{OtBu})_3]$  onto  $\text{SiO}_2\text{-}200$  are shown in Figure S5. In both spectra, there is a prominent pre-edge peak. This pre-edge feature arises from electronic transitions from 1s core levels to the empty 3d levels, more or less 4p hybridized by the ligands of vanadium. These electronic transitions become electric-dipolar allowed in the absence of an inversion center. In this case, the loss of symmetry permits partial overlapping and mixing of the unfilled d states of the metal with the 4p orbital of the metal. Several studies of the V K-edge XANES features have considered the pre-edge intensity as well as its absolute position to determine both the vanadium oxidation state and its symmetry [32,33]. The only position of the pre-edge peak is generally insufficient to evaluate accurately the vanadium oxidation state. The position and intensity of the main pre-edge peak along with the position of the edge of different vanadium compounds studied are reported in Table 1. For both samples mentioned above, the position of the pre-edge peak at ca. 5470.3 eV and its high intensity (0.81 to 0.83) are consistent with those observed in other complexes or materials containing V(V) in a tetrahedral symmetry [33]. Moreover, the position of the K-edge of both samples, shifted by more than 18 eV to higher energy relative to the foil, are within the range of K-edge energies reported for known V(V) compounds [32].

**Table 1.** Positions and intensities of the pre-edge signal and edge positions in the V K-edge XANES of several vanadium samples.

Samples	Pre-edge signal position <sup>a</sup> (eV)	Pre-edge signal intensity <sup>b</sup> (a.u.)	Edge position <sup>a</sup> (eV)
$\text{V}^{(0)}$ (metal foil)			5465.1

$[V^{III}(\text{Mes})_3 \cdot \text{THF}]$	5466.6	0.55	5481.2
$[V^{IV}(=\text{O})\text{SO}_4(\text{H}_2\text{O})_x]$	5469.8	0.48	5480.7
$[V^V(=\text{O})(\text{OtBu})_3]$	5470.3	0.81	5481.9
$[(\equiv\text{SiO})_2\text{V}(=\text{O})(\text{OtBu})]$	5470.3	0.83	5483.4
$[(\equiv\text{AlO})_2\text{V}(=\text{O})(\text{OtBu})]$	5470.5	0.82	5482.7

<sup>a</sup> Relative to a calibration with a vanadium foil (5465.1 eV);  $A \pm 0.3$  eV error is estimated on the energy. <sup>b</sup> Intensity normalized to the step height of the K-edge.

### Preparation and characterization of $[V(=\text{O})(\text{OtBu})_3]$ on alumina dehydroxylated at 500 °C (**II**)

The effect of the support on single site V species has been studied by employing alumina as support.  $\gamma$ -alumina was dehydroxylated at 500 °C under high vacuum ( $10^{-5}$  mbar), with a density of ca. 3.7 OH per  $\text{nm}^2$  (0.65 mmol OH. $\text{g}^{-1}$ ), denoted as  $\text{Al}_2\text{O}_{3-500}$ . The reaction of  $[V(=\text{O})(\text{OtBu})_3]$  with  $\text{Al}_2\text{O}_{3-500}$  in a pentane solution and at room temperature provided a light yellow powder. The latter was extensively washed with pentane to remove the excess of the complex and dried using a high vacuum line. The *t*-BuOH evolved during grafting reaction was qualitatively identified by GC after reaction. IR spectrum of  $[V(=\text{O})(\text{OtBu})_3]$  on  $\text{Al}_2\text{O}_{3-500}$  (**II**) showed that the grafting occurs at least partially on the surface hydroxyl groups (Figure S6). Moreover, a band observed at around  $3600\text{ cm}^{-1}$  was probably attributed to the strong interaction of *tert*-butanol on the surface of alumina compared to silica. Concomitantly, two groups of bands appeared in the  $3200\text{-}2700\text{ cm}^{-1}$  and  $1500\text{-}1300\text{ cm}^{-1}$  regions, assigned to C-H stretching and bending bands respectively. According to elemental analysis, (**II**) contained 1.3 wt% and 1.5 wt % of V and C respectively, corresponding to an atomic ratio of 4.9 C/V. Theoretically, the atomic C/V ratio of the resulting species should be 4. This result may reveal that the excess of carbon was due to the presence of physisorbed *tert*-butanol, in agreement with the DRIFT spectrum. Thus, with the current evidence, the major surface species can tentatively be proposed as a bipodal species,  $[(\equiv\text{AlO})_2\text{V}(=\text{O})(\text{OtBu})]$  (**II**) (Scheme 1). In addition, the spectrum of  $^1\text{H}$  MAS NMR of (**II**) exhibited a signal at 1.2 ppm attributed to the methyl groups of the *tert*-butoxide ligand (Figure S7,a). Moreover, a minor peak was observed at 4.6 ppm, probably corresponding to residual hydroxyl groups, more specifically to  $\text{HO}-\mu^3\text{-Al}$  [34]. Concerning the  $^{13}\text{C}$  CP MAS spectrum, a main signal appeared at 29.2 ppm

assigned to methyl groups (Figure S7,b). Similarly to the case of vanadium supported onto SiO<sub>2-200</sub>, the signal assigned to the quaternary carbon of *tert*-butoxide ligand (at 80 ppm) was not observed in the spectrum. Normalized V K-edge XANES spectrum of **(II)** obtained after the grafting of [V(=O)(*Ot*Bu)<sub>3</sub>] onto Al<sub>2</sub>O<sub>3-500</sub> is shown in (Figure S5). The XANES data is very similar to the previously described [(≡SiO)<sub>2</sub>V(=O)(*Ot*Bu)] **(I)**, featuring comparable pre-edge position, pre-edge intensity and edge position (Table 1). Hence, the tetrahedral configuration as well as the oxidation state of vanadium is maintained and the proposed structure, [(≡AlO)<sub>2</sub>V(=O)(*Ot*Bu)], **(II)**, is quite similar to the one of **(I)**.

### Catalytic properties

The catalytic behavior of species [(≡SiO)<sub>2</sub>V(=O)(*Ot*Bu)], **(I)** was evaluated for trans-2-butene conversion in a continuous fixed-bed type reactor. The operating conditions used were P = 1 bar, with a total flow of 5 mL·min<sup>-1</sup> (20 % of trans-2-butene in Ar). The reactor was heated from room temperature to the required temperature under a flow of 4 mL·min<sup>-1</sup> of argon before trans-2-butene was introduced in the feed. The catalytic performance of **(I)**, has been evaluated at different temperatures (500, 540 and 580 °C). According to the best result obtained, the effect of the support was studied at the most promising temperature.

The conversion profile and the relative selectivities in monomers obtained with [(≡SiO)<sub>2</sub>V(=O)(*Ot*Bu)], **(I)**, are shown in Figure 3. The global selectivities toward all the products at 500, 540 and 580 °C are provided in supporting information (Figure S8, S9 and S10, respectively). At a lower temperature (500 °C), the initial conversion was 11.3 % and it decreased with time on stream to 7 % after 850 min (Figure 3, Left). At that time, the global selectivity of butadiene was 27.9 %, with 21.2 % propylene, 9.4 % ethylene, 21.5 % butane, 18.2 % methane and 1.8 % ethane. At 540 °C, the initial conversion increased to 20.5 % followed by a gradual deactivation to 14 % after 850 min. The selectivities toward different products were: 24 % in butadiene, 24.3 % in propylene, 11.2 % in ethylene, 24.9 % in methane, 12.4 % in butane and 3.2 % in ethane. At 580 °C, the initial conversion increased furthermore to 34.7 % and gradually decreased to 25.1 % after 850 min. The selectivity toward butadiene was the lowest with 17 % at 580 °C, while that of propylene increased to 28.1 % and that of ethylene increased to 12.2 %. Methane became the major product with a selectivity of 33 % and other products were also produced such as butane and ethane with selectivities of 5.7 % and 4 % respectively.

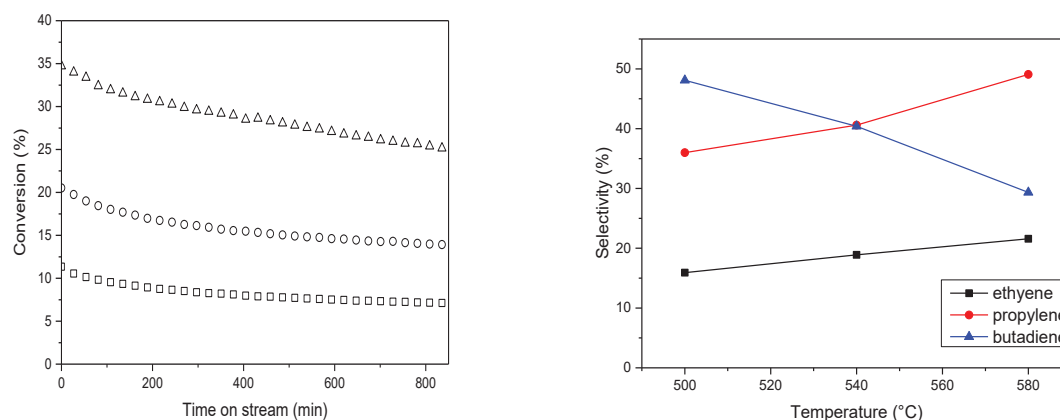
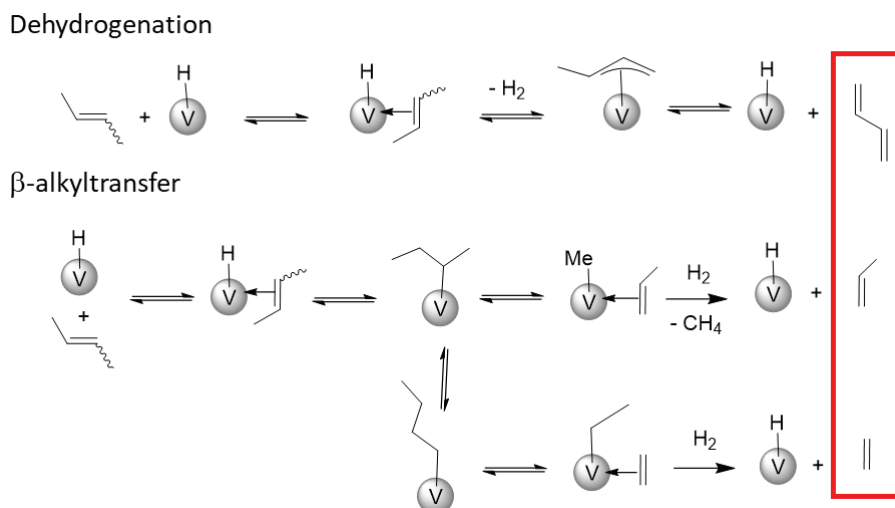


**Figure 3. Left:** trans-2-butene conversion catalyzed by  $V(=O)(OtBu)_3/SiO_{2-200}$  (**I**) at 500 °C (□), 540 °C (○) and 580 °C (△), **Right:** Relative selectivities in ethylene, propylene and butadiene ; P= 1 bar, Total Flow= 5 mL.min<sup>-1</sup> (20 % 2 trans-2-butene in Ar)

Importantly, we observed the formation of all the targeted monomers with different relative selectivities according to the operating temperature (Figure 3, Right). The relative selectivity in butadiene decreased with temperature, whereas the relative selectivity toward  $\alpha$ -olefins increased with temperature. These results showed that using a vanadium supported on silica catalyst (**I**), we can control the proportion of monomers in the gas produced (butadiene, propylene and ethylene), allowing to obtain a variety of elastomers with different butadiene content by terpolymerization reaction. In the case of alumina, a working temperature of 540 °C was selected since catalyst (**I**) exhibited a more stable conversion than at 580 °C by keeping an important selectivity toward butadiene and propylene. An initial conversion of 24.4 % was obtained with  $V(=O)(OtBu)_3/Al_2O_{3-500}$  catalyst, followed by a fast deactivation leading to a conversion of 12.4 % after 215 min (Figure S11). After this time, the conversion with catalyst (**II**) showed a high stability with time on stream. Interestingly, the selectivities vary with time on stream (Figure S11). Initially, the produced mixture composition consisted in 2.4 % butadiene, 23.8 % propylene, 7.3 % ethylene, 33.7 % methane, 23.8 % butane and 7.5 % ethane. After 850 min, the selectivity toward butadiene increased to 40.4 %, while the selectivity toward propylene and ethylene decreased to 18.7 and 4.8 %, respectively. The amounts of produced alkanes decreased as well, to 19.8 % for methane, 11.6 % for butane and 4.7 % for ethane.

In fact, for short times on stream, the conversion dropped quickly in the case of  $V(=O)(OtBu)_3/Al_2O_{3-500}$  due to the generation of acidic sites that leads to coke formation and a substantial amount of  $H_2$ . Consequently, at this stage with the availability of excess  $H_2$ , the dominating reactions are described by Eq. 2 and Eq. 3 in Scheme S1 yielding to saturated hydrocarbons, notably methane (Figure S11). Upon time on stream, the generated acidic sites started to deactivate, and the 2-butenes are mainly converted over single site V species (Scheme S1) like in the case of silica, giving significantly butadiene (Eq. 1 in Scheme S1) and to smaller extend, the other products described by Eq. 2 and Eq. 3 (Scheme S1). The relative selectivity toward butadiene was higher in the case of vanadium species supported on alumina (63 %) than on silica (40.4 %). This change in selectivity in the case of alumina toward butadiene from 2.4 % initially to 35 % after 400 min, are indicative of a modification in the reaction mechanism and in the nature of the active sites during 2-butenes conversion. In fact, the formation of coke at the beginning of the reaction, is known to be catalyzed by the presence of acid sites on the support and the carbonaceous deposits can enhance the catalytic activity as already reported in literature using  $VO_x/Al_2O_3$  prepared by classical method.[35] This phenomenon is not observed in the case of  $V(=O)(OtBu)_3/SiO_{2-200}$  where the acid sites are very weak.

Hence, in addition to the temperature, the support can as well influence directly the proportion of the monomers (Figure S12), allowing the formation of a variety of elastomers by terpolymerization with different butadiene content. These results showed that using supported vanadium oxo species, 2-butenes are converted for the first time into a mixture of important monomers (butadiene, ethylene and propylene) with different proportions. The mechanisms of the formation of these products are based on two elementary steps, namely  $\beta$ -H dehydrogenation and  $\beta$ -alkyl transfer. In fact, as reported recently for a vanadium catalyst [36], the proposed structure of the active sites is a vanadium tripodal species  $[(\equiv MO)_3V]$ , with  $M = Si$  or  $Al$ , generated after C-H activation of 2-butenes. The activation of C-H bond in allylic position of 2-butenes on V-O of tripodal active species leads to the formation of M-OH ( $M = Si$  or  $Al$ ) from the support and a bipodal vanadium  $\eta^3$ -methylallyl intermediate (Scheme S2). The latter species gives butadiene by  $\beta$ -H elimination and bipodal vanadium hydride  $[(\equiv MO)_2V-H]$ , that can lead to the formation of  $H_2$  after a second C-H activation of 2-butenes (Scheme S2). This mechanism represents the catalytic cycle for the conversion of 2-butenes into butadiene (Scheme 2).



**Scheme 2.** Mechanism proposed for the formation of monomers (butadiene, propylene and ethylene) by dehydrogenation and  $\beta$ -alkyl transfer reactions.

The 1,2-insertion of 2-butenes on V-H intermediate species, leads to the formation of V-*sec*-butyl that releases propylene and V-Me via  $\beta$ -alkyl transfer. The latter species (V-Me) leads to the V-H and methane by hydrogenolysis using hydrogen released during the dehydrogenation of 2-butenes into butadiene (Scheme 2). The V-*sec*-butyl can be isomerized to V-*n*-butyl fragment by  $\beta$ -H elimination followed by the 2,1-insertion of 1-butene intermediate. The formation of ethylene can be explained by  $\beta$ -alkyl transfer from V-*n*-butyl species resulting in a V-Et intermediate and ethylene. The hydrogenolysis of V-Et leads to the formation of a V-H and ethane (Scheme 2) using hydrogen released from dehydrogenation of 2-butenes to butadiene. The excess of hydrogen is also responsible for the hydrogenolysis of V-*sec*-butyl into butane by  $\sigma$ -bond metathesis, observed during the catalytic conversion of 2-butenes to monomers.

## Conclusion

The modification of dehydroxylated  $\text{SiO}_{2-200}$  and  $\text{Al}_2\text{O}_{3-500}$  by  $[\text{V}(=\text{O})(\text{OtBu})_3]$  using surface organometallic chemistry led to the formation of bipodal species,  $[(\equiv\text{MO})_2\text{V}(=\text{O})(\text{OtBu})]$ , M= Si or Al. The resulting materials were characterized by several techniques such as IR, solid-state NMR, UV-vis, XANES and elemental analysis. Although a higher conversion was obtained in the case of  $[(\equiv\text{SiO})_2\text{V}(=\text{O})(\text{OtBu})]$ , the relative selectivity toward monomers, more specifically for butadiene, was higher for  $[(\equiv\text{AlO})_2\text{V}(=\text{O})(\text{OtBu})]$ . Vanadium supported on silica favors  $\beta$ -H elimination at lower temperature over  $\beta$ -alkyl transfer, which leads to a

higher selectivity in butadiene compared to propylene and ethylene. At higher temperatures, the selectivity in  $\alpha$ -olefins increased due to the ability of vanadium to favor butenes conversion via  $\beta$ -alkyl transfer, resulting therefore in a lower selectivity toward butadiene. The catalytic behavior of these species in 2-butenes conversion revealed a difference in the monomer's distribution due to the nature of the support and the working temperature. The 2-butenes conversion on supported vanadium single site, allow the formation of a mixture of monomers with different butadiene content for direct terpolymerization use. This process can be extended to light alkanes such as butane for the production of monomers.

## Acknowledgements

This work was carried out as a part of BIZEOLCAT project, which has received funding from the European Union's Horizon 2020 research and innovation program under grant agreement No. 814671. In particular, J. A. N. is grateful for her PhD grant. AdM thanks Olivier Mathon and Kiril Lomachenko for their help during the recording of the X-ray absorption spectra at ESRF, on beam line BM23.

## References

- [1] M. Monai, M. Gambino, S. Wannakao, B. M. Weckhuysen, Propane to olefins tandem catalysis: a selective route towards light olefins production, *Chem. Soc. Rev.* 50 (2021) 11503–11529. <https://doi.org/10.1039/D1CS00357G>.
- [2] D. Gong, W. Pan, T. Zhu, H. Chen, Z. Zhou, F. Jiang, Y. Hu, X. Zhang, Polymerization of 1,3-butadiene catalyzed by a thermal robust, high selective and active iron catalyst: An applicable recipe for producing syndiotactic 1,2-polybutadiene, *Polymer*. 98 (2016) 136–142. <https://doi.org/10.1016/j.polymer.2016.06.026>.
- [3] P. Tian, Y. Wei, M. Ye, Z. Liu, Methanol to Olefins (MTO): From Fundamentals to Commercialization, *ACS Catal.* 5 (2015) 1922–1938. <https://doi.org/10.1021/acscatal.5b00007>.
- [4] I. Amghizar, L.A. Vandewalle, K.M. Van Geem, G.B. Marin, New Trends in Olefin Production, *Engineering*. 3 (2017) 171–178. <https://doi.org/10.1016/J.ENG.2017.02.006>.
- [5] Z. Nawaz, Light alkane dehydrogenation to light olefin technologies: a comprehensive review, *Rev. Chem. Eng.* 31 (2015) 413–436. <https://doi.org/10.1515/revce-2015-0012>.
- [6] J. Mol, Industrial applications of olefin metathesis, *J. Mol. Catal. Chem.* 213 (2004) 39–45. <https://doi.org/10.1016/j.molcata.2003.10.049>.
- [7] E. V. Makshina, M. Dusselier, W. Janssens, J. Degrève, P. A. Jacobs, B. F. Sels, Review of old chemistry and new catalytic advances in the on-purpose synthesis of butadiene, *Chem. Soc. Rev.* 43 (2014) 7917–7953. <https://doi.org/10.1039/C4CS00105B>.
- [8] D.W. Sauter, M. Taoufik, C. Boisson, Polyolefins, a Success Story, *Polymers*. 9 (2017) 185. <https://doi.org/10.3390/polym9060185>.

- [9] A.S. Mohite, Y.D. Rajpurkar, A.P. More, Bridging the gap between rubbers and plastics: a review on thermoplastic polyolefin elastomers, *Polym. Bull.* 79 (2022) 1309–1343. <https://doi.org/10.1007/s00289-020-03522-8>.
- [10] L. McKeen, 13 - Elastomers, in: L. McKeen (Ed.), *Eff. Steriliz. Plast. Elastomers Third Ed.*, William Andrew Publishing, Boston, 2012: pp. 319–353. <https://doi.org/10.1016/B978-1-4557-2598-4.00013-7>.
- [11] J.G. Drobny, *Handbook of Thermoplastic Elastomers*, Elsevier, 2014.
- [12] A. Ali, M.K. Tufail, M.I. Jamil, W. Yaseen, N. Iqbal, M. Hussain, A. Ali, T. Aziz, Z. Fan, L. Guo, Comparative Analysis of Ethylene/Diene Copolymerization and Ethylene/Propylene/Diene Terpolymerization Using Ansa-Zirconocene Catalyst with Alkylaluminum/Borate Activator: The Effect of Conjugated and Nonconjugated Dienes on Catalytic Behavior and Polymer Microstructure, *Molecules*. 26 (2021) 2037. <https://doi.org/10.3390/molecules26072037>.
- [13] R.A. Alberty, C.A. Gehrig, Standard Chemical Thermodynamic Properties of Alkene Isomer Groups, *J. Phys. Chem. Ref. Data*. 14 (1985) 803–820. <https://doi.org/10.1063/1.555737>.
- [14] E. Mazoyer, K.C. Szeto, J.-M. Basset, C.P. Nicholas, M. Taoufik, High selectivity production of propylene from 2-butene: non-degenerate pathways to convert symmetric olefins via olefin metathesis, *Chem. Commun.* 48 (2012) 3611–3613. <https://doi.org/10.1039/C2CC30172E>.
- [15] K.C. Szeto, N. Merle, C. Rios, P. Rouge, J.L. Castelbou, M. Taoufik, Tailoring the selectivity in 2-butene conversion over supported d0 group 4, 5 and 6 metal hydrides: from dimerization to metathesis, *Catal. Sci. Technol.* 5 (2015) 4765–4771. <https://doi.org/10.1039/C5CY00582E>.
- [16] M. Bender, An Overview of Industrial Processes for the Production of Olefins – C4 Hydrocarbons, *ChemBioEng Rev.* 1 (2014) 136–147. <https://doi.org/10.1002/cben.201400016>.
- [17] N. Popoff, E. Mazoyer, J. Pelletier, R.M. Gauvin, M. Taoufik, Expanding the scope of metathesis: a survey of polyfunctional, single-site supported tungsten systems for hydrocarbon valorization, *Chem. Soc. Rev.* 42 (2013) 9035–9054. <https://doi.org/10.1039/C3CS60115C>.
- [18] S. Norsic, C. Larabi, M. Delgado, A. Garron, A. de Mallmann, C. Santini, K. C. Szeto, J.-M. Basset, M. Taoufik, Low temperature hydrogenolysis of waxes to diesel range gasoline and light alkanes: Comparison of catalytic properties of group 4, 5 and 6 metal hydrides supported on silica – alumina, *Catal. Sci. Technol.* 2 (2012) 215–219. <https://doi.org/10.1039/C1CY00256B>.
- [19] K.C. Szeto, B. Loges, N. Merle, N. Popoff, A. Quadrelli, H. Jia, E. Berrier, A. De Mallmann, L. Delevoye, R.M. Gauvin, M. Taoufik, Vanadium Oxo Organometallic Species Supported on Silica for the Selective Non-oxidative Dehydrogenation of Propane, *Organometallics*. 32 (2013) 6452–6460. <https://doi.org/10.1021/om400795s>.
- [20] D.M. Kaphan, M.S. Ferrandon, R.R. Langeslay, G. Celik, E.C. Wegener, C. Liu, J. Niklas, O.G. Poluektov, M. Delferro, Mechanistic Aspects of a Surface Organovanadium(III) Catalyst for Hydrocarbon Hydrogenation and Dehydrogenation, *ACS Catal.* 9 (2019) 11055–11066. <https://doi.org/10.1021/acscatal.9b02800>.
- [21] O. Mathon, A. Beteva, J. Borrel, D. Bugnazet, S. Gatla, R. Hino, I. Kantor, T. Mairs, M. Munoz, S. Pasternak, F. Perrin, S. Pascarelli, The time-resolved and extreme conditions XAS (TEXAS) facility at the European Synchrotron Radiation Facility: the general-purpose EXAFS bending-magnet beamline BM23, *J. Synchrotron Radiat.* 22 (2015) 1548–1554. <https://doi.org/10.1107/S1600577515017786>.

- [22] B. Ravel, M. Newville, ATHENA, ARTEMIS, HEPHAESTUS: data analysis for X-ray absorption spectroscopy using IFEFFIT, *J. Synchrotron Radiat.* 12 (2005) 537–541. <https://doi.org/10.1107/S0909049505012719>.
- [23] M. P. Högerl, L.M.S. Goh, E. Abou-Hamad, S. Barman, O. Dachwald, F. Ahmad Pasha, J. Pelletier, K. Köhler, V. D’Elia, L. Cavallo, J.-M. Basset, SOMC grafting of vanadium oxytriisopropoxide (VO(O i Pr) 3 ) on dehydroxylated silica; analysis of surface complexes and thermal restructuring mechanism, *RSC Adv.* 8 (2018) 20801–20808. <https://doi.org/10.1039/C8RA02419G>.
- [24] J.-M. Basset, A. Baudouin, F. Bayard, J.-P. Candy, C. Copéret, A. De Mallmann, G. Godard, E. Kuntz, F. Lefebvre, C. Lucas, S. Norsic, K. Pelzer, A. Quadrelli, C. Santini, D. Soulivong, F. Stoffelbach, M. Taoufik, C. Thieuleux, J. Thivolle-Cazat, L. Veyre, Preparation of Single Site Catalysts on Oxides and Metals Prepared via Surface Organometallic Chemistry, in: *Mod. Surf. Organomet. Chem.*, John Wiley & Sons, Ltd, 2009: pp. 23–73. <https://doi.org/10.1002/9783527627097.ch2>.
- [25] F. Bini, C. Rosier, R.P. Saint-Arroman, E. Neumann, C. Dablemont, A. de Mallmann, F. Lefebvre, G.P. Niccolai, J.-M. Basset, M. Crocker, J.-K. Buijink, Surface Organometallic Chemistry of Titanium: Synthesis, Characterization, and Reactivity of ( $Si-O$ )<sub>n</sub>Ti(CH<sub>2</sub>C(CH<sub>3</sub>)<sub>3</sub>)<sub>4-n</sub> (n = 1, 2) Grafted on Aerosil Silica and MCM-41, *Organometallics.* 25 (2006) 3743–3760. <https://doi.org/10.1021/om050675g>.
- [26] H. Eckert, I.E. Wachs, Solid-state vanadium-51 NMR structural studies on supported vanadium(V) oxide catalysts: vanadium oxide surface layers on alumina and titania supports, *J. Phys. Chem.* 93 (1989) 6796–6805. <https://doi.org/10.1021/j100355a043>.
- [27] G.L. Rice, S.L. Scott, Characterization of Silica-Supported Vanadium(V) Complexes Derived from Molecular Precursors and Their Ligand Exchange Reactions, *Langmuir.* 13 (1997) 1545–1551. <https://doi.org/10.1021/la960679d>.
- [28] DR UV–vis Study of the Supported Vanadium Oxide Catalysts | *The Journal of Physical Chemistry C*, (n.d.). <https://pubs.acs.org/doi/abs/10.1021/jp112206c> (accessed January 26, 2022).
- [29] G. Catana, R.R. Rao, B.M. Weckhuysen, P. Van Der Voort, E. Vansant, R.A. Schoonheydt, Supported Vanadium Oxide Catalysts: Quantitative Spectroscopy, Preferential Adsorption of V<sup>4+</sup>/V<sup>5+</sup>, and Al<sub>2</sub>O<sub>3</sub> Coating of Zeolite Y, *J. Phys. Chem. B.* 102 (1998) 8005–8012. <https://doi.org/10.1021/jp981482s>.
- [30] X. Gao, I.E. Wachs, Investigation of Surface Structures of Supported Vanadium Oxide Catalysts by UV–vis–NIR Diffuse Reflectance Spectroscopy, *J. Phys. Chem. B.* 104 (2000) 1261–1268. <https://doi.org/10.1021/jp992867t>.
- [31] S.L. Wegener, H. Kim, T.J. Marks, P.C. Stair, Precursor Nuclearity Effects in Supported Vanadium Oxides Prepared by Organometallic Grafting, *J. Phys. Chem. Lett.* 2 (2011) 170–175. <https://doi.org/10.1021/jz101490p>.
- [32] J. Wong, F.W. Lytle, R.P. Messmer, D.H. Maylotte, K-edge absorption spectra of selected vanadium compounds, *Phys. Rev. B.* 30 (1984) 5596–5610. <https://doi.org/10.1103/PhysRevB.30.5596>.
- [33] M. Nabavi, F. Taulelle, C. Sanchez, M. Verdagner, Xanes and 51V Nmr study of vanadium-oxygen compounds, *J. Phys. Chem. Solids.* 51 (1990) 1375–1382. [https://doi.org/10.1016/0022-3697\(90\)90020-G](https://doi.org/10.1016/0022-3697(90)90020-G).
- [34] M. Taoufik, K.C. Szeto, N. Merle, I.D. Rosal, L. Maron, J. Trébosc, G. Tricot, R.M. Gauvin, L. Delevoye, Heteronuclear NMR Spectroscopy as a Surface-Selective Technique: A Unique Look at the Hydroxyl Groups of  $\gamma$ -Alumina., *Chem. – Eur. J.* 20 (2014) 4038–4046. <https://doi.org/10.1002/chem.201304883>.

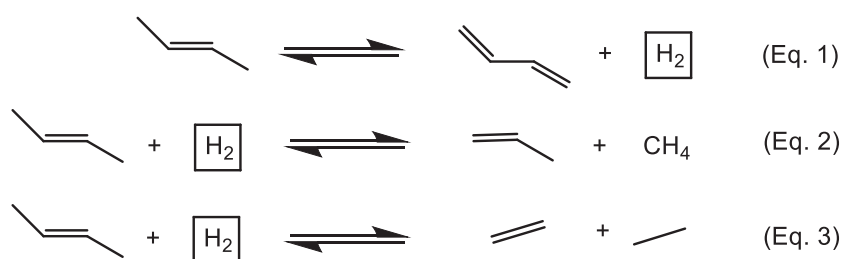
- [35] J. McGregor, Z. Huang, E.P.J. Parrott, J.A. Zeitler, K.L. Nguyen, J.M. Rawson, A. Carley, T.W. Hansen, J.-P. Tessonnier, D.S. Su, D. Teschner, E.M. Vass, A. Knop-Gericke, R. Schlögl, L.F. Gladden, Active coke: Carbonaceous materials as catalysts for alkane dehydrogenation, *J. Catal.* 269 (2010) 329–339. <https://doi.org/10.1016/j.jcat.2009.11.016>.
- [36] Y.-L. Wu, Z.-F. Han, X. Yan, W.-Z. Lang, Y.-J. Guo, Effective synthesis of vanadium-doped mesoporous silica nanospheres by sol-gel method for propane dehydrogenation reaction, *Microporous Mesoporous Mater.* 330 (2022) 111616. <https://doi.org/10.1016/j.micromeso.2021.111616>.

## Supplementary Material

### Direct conversion of 2-butenes into a mixture of monomers with different composition over vanadium supported catalysts

Abou Nakad Jessy,<sup>a</sup> Berthet Nicolas,<sup>a</sup> Szeto Kai,<sup>a</sup> De Mallman Aimery,<sup>a</sup> Taoufik Mostafa<sup>a</sup>

<sup>a</sup> Université de Lyon 1, CPE Lyon, CNRS-UMR 5128 – laboratoire Catalyse, Polymérisation, Procédés et Matériaux (CP2M), F-69616 Villeurbanne, France. Email: [mostafa.taoufik@univ-lyon1.fr](mailto:mostafa.taoufik@univ-lyon1.fr)



**Scheme S1.** Direct conversion of trans-2-butene to monomers through dehydrogenation and β-alkyl transfer steps.

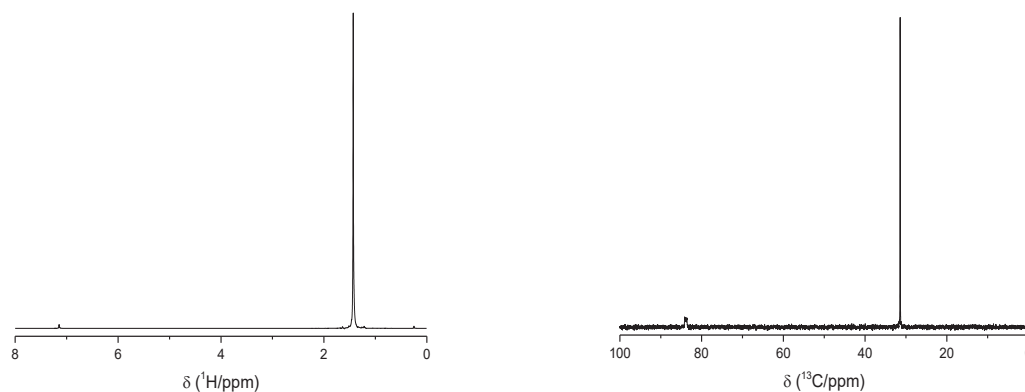


**Figure S1.** NMR spectra of [V(=O)(OtBu)<sub>3</sub>] molecular complex: Left: <sup>1</sup>H (d<sub>1</sub>=1 s) and Right: <sup>13</sup>C {<sup>1</sup>H} (d<sub>1</sub>=10 s).

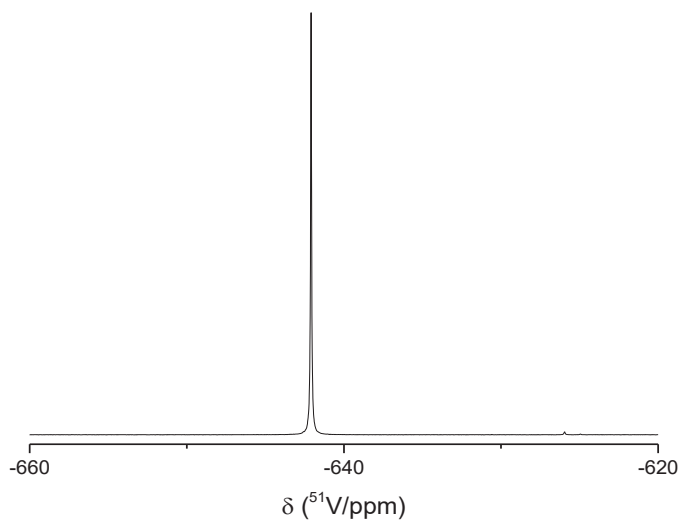
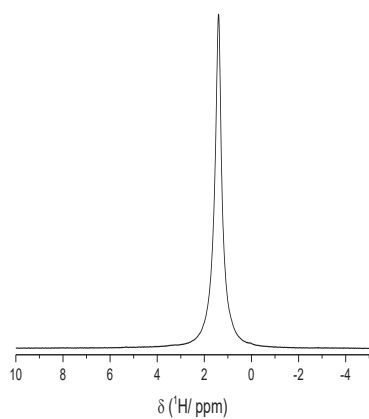


**Figure S2.**  $^{51}\text{V}$  NMR spectrum of  $[\text{V}(=\text{O})(\text{OtBu})_3]$  molecular complex ( $d_1 = 1\text{ s}$ ).

a)



b)

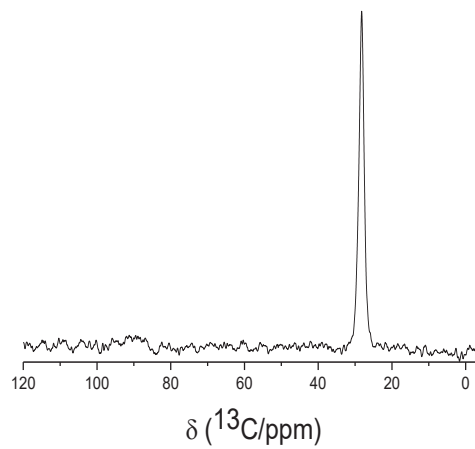


**Figure S3.** MAS NMR spectra of  $\text{V}(=\text{O})(\text{OtBu})_3/\text{SiO}_2\text{-200}$ : **a)**  $^1\text{H}$  and **b):**  $^{13}\text{C}$  CP (10 kHz MAS,  $d_1 = 5\text{ s}$ ).

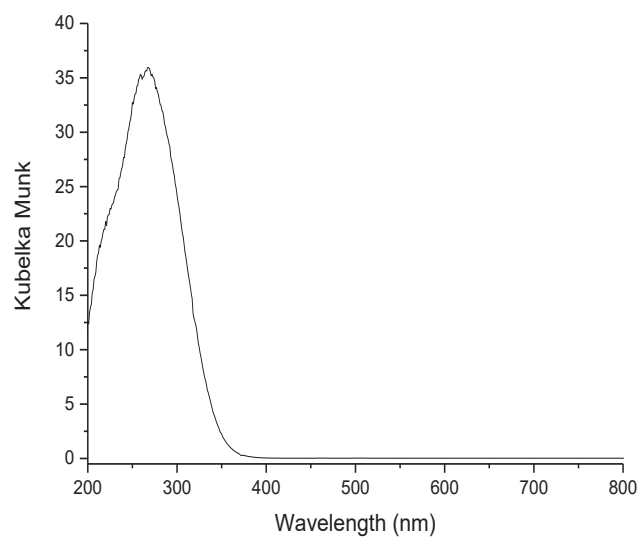


**Figure S4.** UV-Vis spectrum of **(I)**,  $V(=O)(OtBu)_3/SiO_{2-200}$

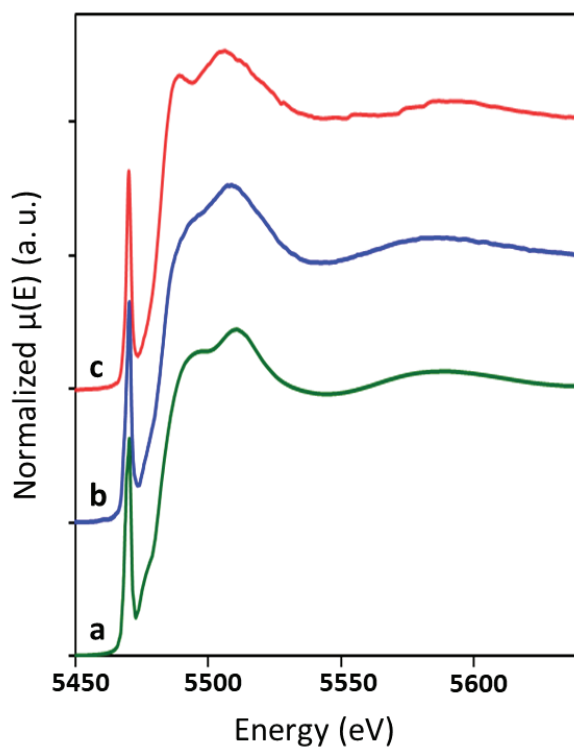


**Figure S5.** XANES: of (a)  $[V(=O)(OtBu)_3]$  molecular complex; (b)  $V(=O)(OtBu)_3/SiO_{2-200}$ ; (c)  $V(=O)(OtBu)_3/Al_2O_{3-500}$

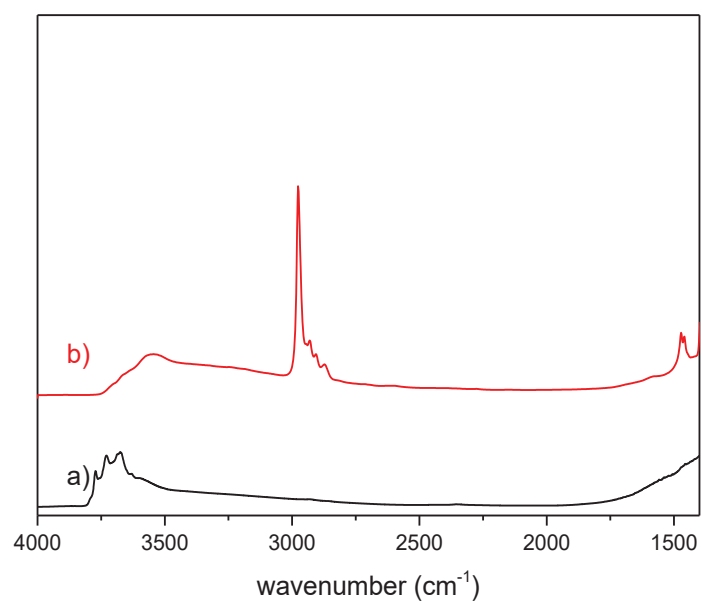


**Figure S6.** IR-spectra of a) Al<sub>2</sub>O<sub>3-500</sub> (black) and of **(II)**, b) after the grafting of [V(=O)(OtBu)<sub>3</sub>] on Al<sub>2</sub>O<sub>3-500</sub> (red)

a)

b)

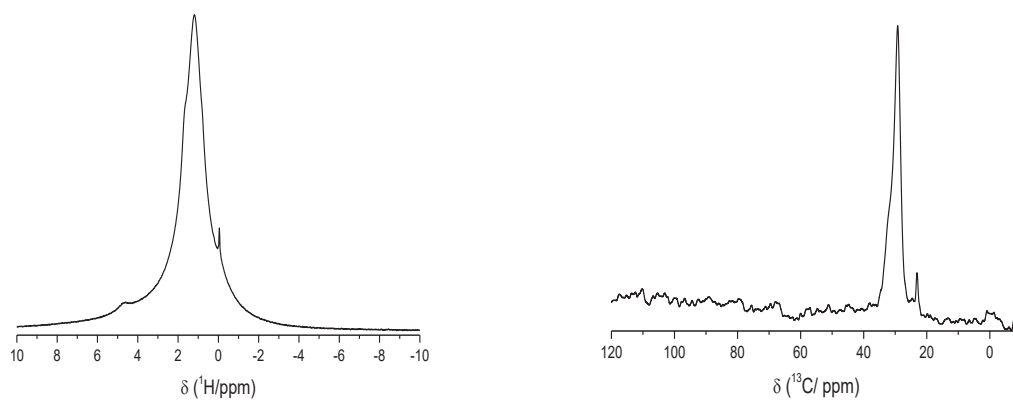


**Figure S7.** MAS NMR spectra of V(=O)(OtBu)<sub>3</sub>/Al<sub>2</sub>O<sub>3-500</sub> **(II)**, a) <sup>1</sup>H (10 kHz MAS, d<sub>1</sub>= 5 s) and b) <sup>13</sup>C {<sup>1</sup>H} (10 kHz MAS, d<sub>1</sub>= 10 s).

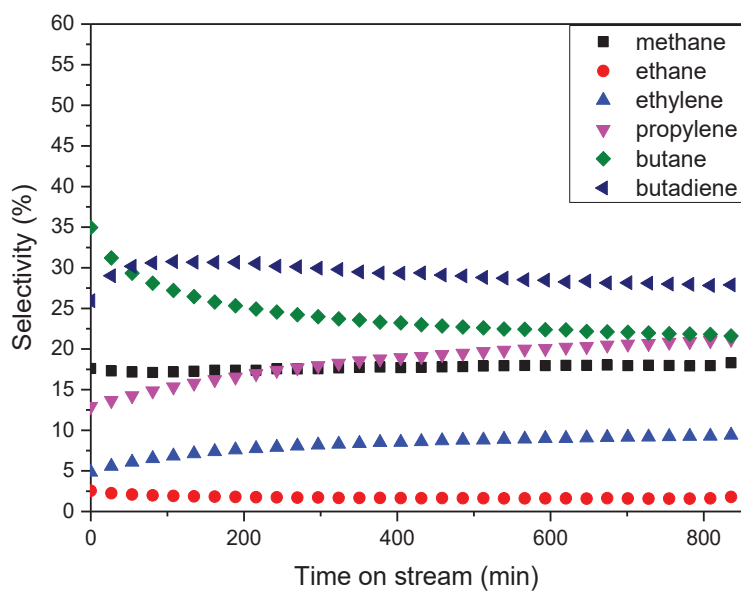


**Figure S8.** Selectivity of  $V(=O)(OtBu)_3/SiO_{2-200}$ , (I), catalyst in trans-2-butene conversion at 500 °C, with 1 bar pressure and 5 mL.min<sup>-1</sup> as a total flow = (20 % of trans-2-butene in Ar)

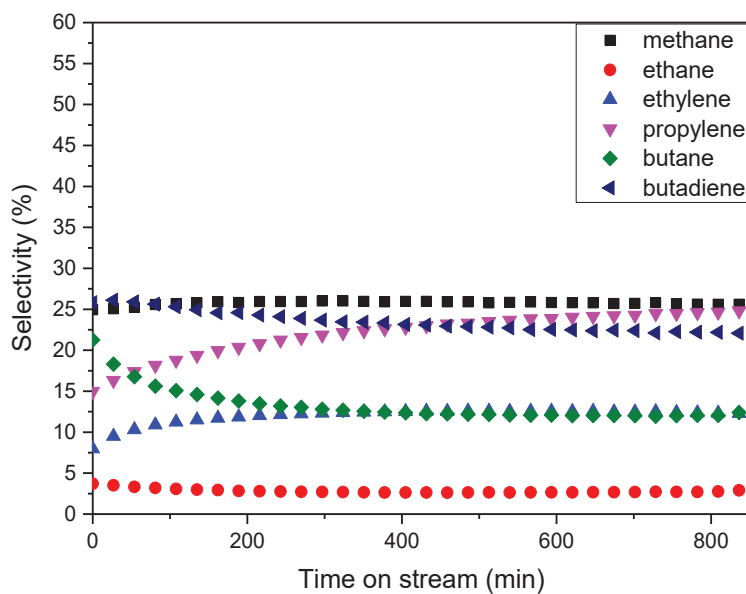


**Figure S9.** Selectivity of  $V(=O)(OtBu)_3/SiO_{2-200}$ , (I), catalyst in trans-2-butene conversion at 540 °C, with 1 bar pressure and 5 mL.min<sup>-1</sup> as a total flow = (20 % of trans-2-butene in Ar)

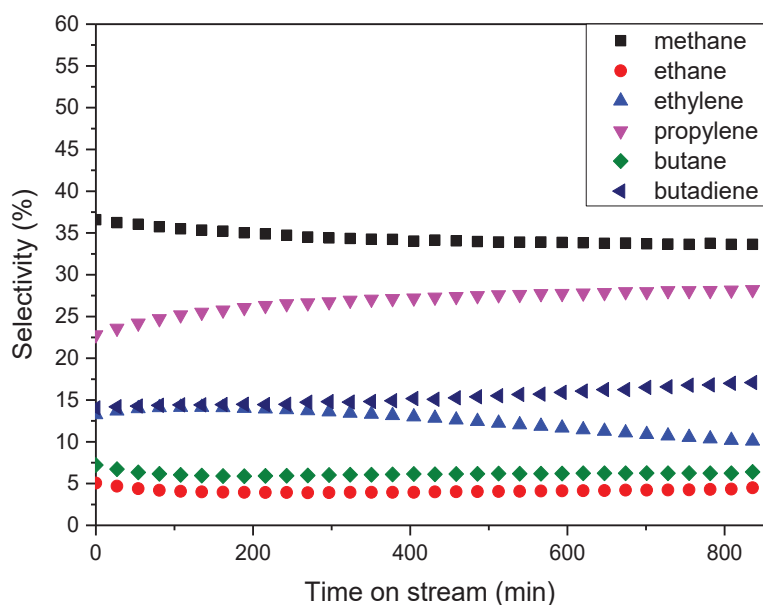


**Figure S10.** Selectivity of  $V(=O)(OtBu)_3/SiO_2-200$ , **(I)**, catalyst in trans-2-butene conversion at 580 °C, with 1 bar pressure and 5 mL.min<sup>-1</sup> as a total flow = (20 % of trans-2-butene in Ar)

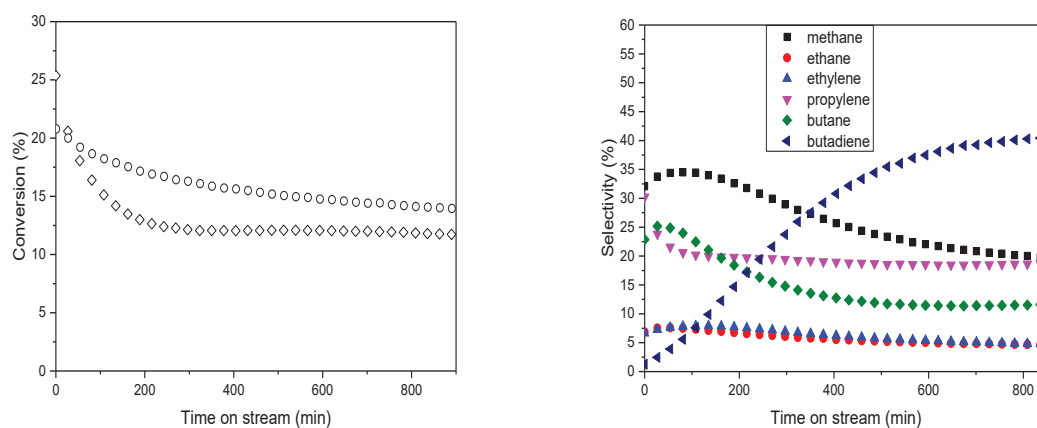


**Figure S11. Left:** conversion of trans-2-butene obtained with **(I)**:  $V(=O)(OtBu)_3/SiO_2-200$  ( $\circ$ ) or **(II)**:  $V(=O)(OtBu)_3/Al_2O_3-500$  ( $\diamond$ ) as catalysts and **Right:** Selectivity of  $V(=O)(OtBu)_3/Al_2O_3-500$ , **(II)** in trans-2-butene conversion at 540 °C, 1 bar, total flow= 5 mL.min<sup>-1</sup> (20 % trans-2-butene in Ar).

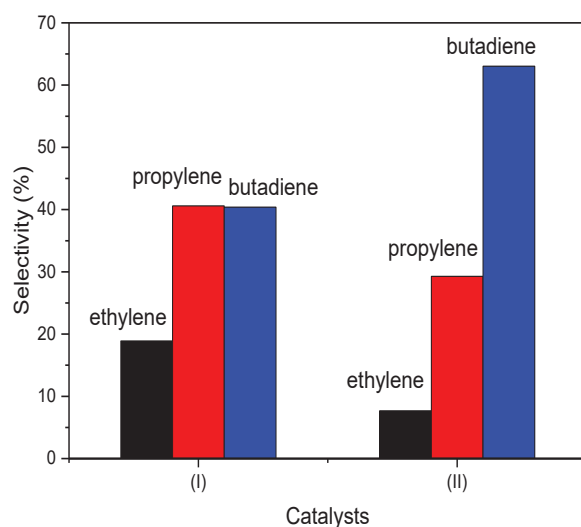
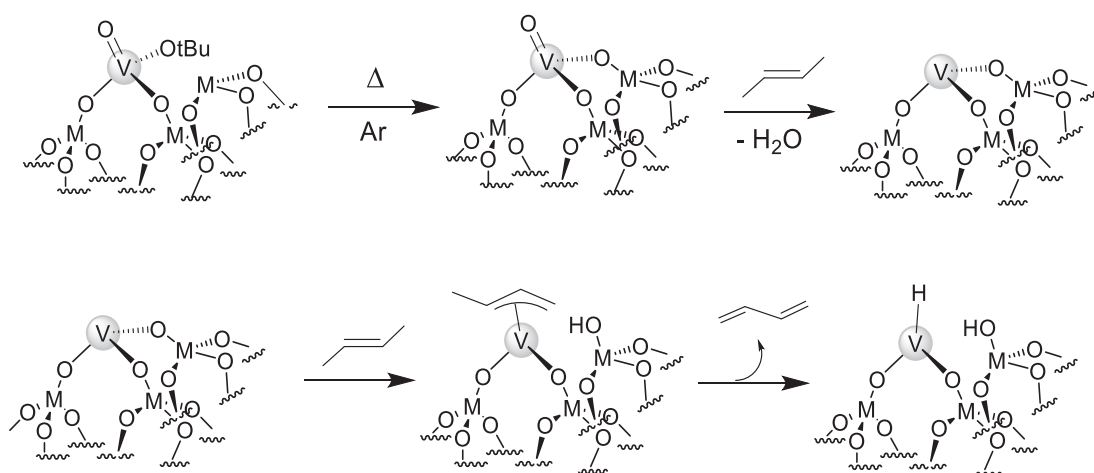


**Figure S12.** Relative selectivities toward monomers obtained with **(I)** and **(II)** catalysts in trans-2-butene conversion at 540 °C, with 1 bar pressure and 5 mL.min<sup>-1</sup> as a total flow = (20 % of trans-2-butene in Ar) after 850 min time on stream.



**Scheme S2.** Proposed mechanism for the formation of the supported bipodal V-H active species for the conversion of trans-2-butene (M= Si or Al)

## CHAPTER II. PART B

---

### Preparation of tripodal Vanadium Oxo-Organometallic Species Supported on Silica, $[(\equiv\text{SiO})_3\text{V}(=\text{O})]$ , for Selective Non-Oxidative Dehydrogenation of Propane

---



Jessy Abou Nakad,<sup>a</sup> Remy Rajapaksha,<sup>a</sup> Kai Szeto,<sup>a</sup> Aimery De Mallmann,<sup>a</sup> Mostafa Taoufik  
\*<sup>a</sup>

<sup>a</sup> Université Lyon 1, Institut de Chimie Lyon, CPE Lyon, CNRS, UMR 5128 CP2M, 43 Bd du 11 Novembre 1918, F-69616 Villeurbanne Cedex, France. E-mail: Mostafa.Taoufik@univ-lyon1.fr; Fax: +33 (0)472 431 798; Tel: +33 (0)472 431 795

## Abstract

In this work, a new strategy based on the grafting of a vanadium molecular complex,  $[V(=O)(OtBu)_3]$ , (**1**), bearing tert-butoxide ligands, on a partially dehydroxylated silica, followed by a thermal treatment has been used for the preparation of supported tripodal V complex,  $[(\equiv SiO)_3V(=O)]$ , active species, for important chemical processes. The molecular complex reacts with a silica partially dehydroxylated at 200 °C ( $SiO_{2-200}$ ) to lead to bipodal  $[(\equiv SiO)_2V(=O)(OtBu)]$  (**2**) as major surface species, while monopodal surface species  $[(\equiv SiO)V(=O)(OtBu)_2]$  (**3**) are obtained on  $SiO_{2-700}$ . These materials were thermally treated to form active supported tripodal vanadium species by releasing isobutene via a  $\beta$ -H transfer, leading to V-OH intermediate. The latter species lead to the targeted tripodal species  $[(\equiv SiO)_3V(=O)]$  after restructuration of the support and will be represented as materials (**2a**) and (**3a**). All the supported vanadium complexes were characterized by DRIFT, UV-Vis., solid-state NMR and XANES spectroscopies. In particular, the structure of isolated vanadium tripodal species,  $[(\equiv SiO)_3V(=O)]$ , was confirmed by  $^{51}V$  NMR with a major peak at -670 ppm, as reported in literature. The catalytic performances of (**2a**) and (**3a**) were evaluated for the direct propane dehydrogenation. A better conversion and selectivity to propylene was observed with the isolated species compared to the results reported in literature using conventional catalysts prepared by impregnation.

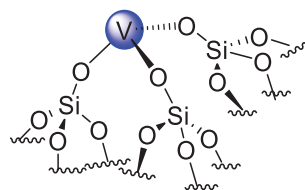
## Introduction

Propylene is an important intermediate in the chemical industry and is used for the synthesis of several key products such as polypropylene, acrylonitrile and propylene oxide.<sup>2,3</sup> It is mainly produced by steam cracking (SC) and fluid catalytic cracking (FCC) of hydrocarbon feedstocks.<sup>1,2</sup> With the increasing demand for propylene globally, SC and FCC will be unable to satisfy the market need. Hence, alternative routes such as on-purpose technologies have been developed, like olefin metathesis,<sup>4-6</sup> methanol to olefin process,<sup>7</sup> and more recently, the direct  $CO_2$  conversion to light olefins<sup>8,9</sup> as well as catalytic propane dehydrogenation.<sup>2,10</sup> The latter uses catalysts that can operate under oxidative or non-oxidative conditions. The main issue of the oxidative dehydrogenation is the low selectivity to olefins as  $CO_2$  can easily be produced from a total oxidation of light hydrocarbons. Non-oxidative dehydrogenation of propane (PDH) is widely used at industrial scale as it offers many advantages, such as a high selectivity toward the desired alkene (propylene) and the production of valuable dihydrogen. This reaction is highly endothermic ( $\Delta H^\circ = 124 \text{ kJ}\cdot\text{mol}^{-1}$ ) and requires high operating

temperatures (above 550 °C), resulting in undesired side-reactions (cracking) and deactivation of the catalyst due to the formation of coke and degradation/restructuring of the active phase. Two PDH processes dominate the market, known as Oleflex® and Catofin®. The first one employs supported hetero-bimetallic particles based on a noble metal Pt, alloyed with toxic Sn as a promoter, to enhance the selectivity to propylene, and to avoid cracking reactions and the fast deactivation of the catalyst at high temperature. However, despite the presence of promoters, high operating temperatures lead to a slow deactivation as a function of time on stream, which requires frequent regeneration treatments in order to maintain the catalytic performances. The Catofin® technology employs a cheap catalyst based on chromium oxides (typically 18-20 wt% Cr) supported on alumina with working temperatures ranging from 575 to 625 °C at reduced pressures (0.2 to 0.5 bar). The high temperature required to improve catalytic activity toward the desired product, leads inevitably to the formation of coke. Consequently, the regeneration cycles occurring every 15-30 min, decrease the activity, and therefore a replacement of the catalyst every two years is needed. In addition to coke formation, the process conditions lead to aging of the catalyst. This causes: i) a decrease of the dispersion of chromium species on the surface; ii) an incorporation of the Cr active species within alumina, resulting in an increase of the catalyst's acidity that reduces propylene selectivity; iii) an increase of the surface  $\text{Cr}^{6+}/\text{Cr}^{3+}$  ratio after each regeneration cycle by calcination.<sup>11</sup>

To overcome these challenges, other metal oxides such as  $\text{VO}_x$ ,  $\text{GaO}_x$ ,  $\text{InO}_x$  or  $\text{MoO}_x$  have been widely explored in the literature for PDH.<sup>2</sup> Supported vanadium oxides catalysts have been intensively studied for the oxidative dehydrogenation of propane and showed promising results, while few examples were reported in the case of the non-oxidative propane dehydrogenation. Vanadium(V) oxide supported on silica, alumina or titanium oxide shows promising activities for the catalytic dehydrogenation of light alkane.<sup>12-17</sup> The conventional synthesis methods of these catalysts described in literature involve various processes such as aqueous impregnation, sol-gel, chemical vapor deposition, to name a few.<sup>2</sup> However, depending on the nature of the vanadium precursor and the support used, these synthesis methods of supported vanadium oxo complexes, lead to a distribution of monomeric, dimeric and oligomeric  $\text{VO}_x$  species on the surface or even to particles of oxide.<sup>18,19</sup> Several studies in this area have been reported and suggest that the structure of the supported precursor of the active species, for example onto silica, is postulated as an isolated vanadium center bearing an

oxo and three siloxy ligands. In the case of vanadium systems, it is reasonable to propose that the active species is  $V^{3+}$  trisiloxy (Scheme 1) obtained during the initiation step, after an activation of propane on  $V^{5+}$  oxo tripodal species<sup>20</sup>, similar to chromium and gallium catalytic systems.



**Scheme 1.** Proposed tripodal  $V^{(III)}$  active species for PDH

Based on DFT calculations and Operando studies, the mechanism of propane dehydrogenation in the case of metal oxides has been proposed to occur via a heterolytic C-H bond cleavage via activation on a surface M-O- bond, leading to a coordinated alkyl, M-R and a surface hydroxyl, -OH or via a  $\sigma$ -bond metathesis on a M-H intermediate.<sup>2,21</sup> The low concentration of active sites hampers their characterization and thus limited information is available on their role in catalysis and the understanding of the elementary steps. In fact, many attempts to characterize the surface-active sites of supported  $VO_x$  species, prepared by conventional methods, using spectroscopic techniques for bulk systems such as XAFS and  $^{51}V$  MAS-NMR led to inconsistent results.<sup>22-29</sup> An obvious strategy to access to the real model of the active species and to increase the activity in PDH, is to control the number of active sites and to eliminate presumably inactive oligomeric  $VO_x$  sites. Regarding the preparation of well-defined functional materials at a molecular scale, especially single-site catalysts for PDH, surface organometallic chemistry has proven to be a powerful approach. This methodology involves a controlled grafting of a reactive organometallic precursor on a pretreated support. With a judicious choice of the precursor in combination with the pre-treatment of the support, supported species with a desired podality, oxidation state and coordination environment around the metal center can be designed.<sup>30</sup> This approach has resulted in highly active catalysts associated with the propylene chemistry, mainly through olefin metathesis,<sup>4-6,31-38</sup> but also for PDH.<sup>39-45</sup> Therefore, we intend to apply surface organometallic chemistry for the synthesis of a silica material containing supported trisiloxy vanadium oxo species as pre-catalyst for propane dehydrogenation reaction. We recently

developed a new synthetic method for the preparation of supported active sites, by using a molecular complex of group VI bearing tert-butoxide ligands  $[M(=O)(OtBu)_4]$  ( $M = Mo$  or  $W$ ). After a grafting reaction of these complexes onto silica followed by a thermolysis,  $[(\equiv SiO)_2M(=O)_2]$  species were obtained and showed high activities for the metathetic oxidation or the metathesis of olefins.<sup>42,47</sup> In the case of vanadium, we expect that this strategy would result in the formation of a well-defined tripodal vanadium oxo species after the grafting of  $[V(=O)(OtBu)_3]$ , (**1**), onto silica supports (dehydroxylated at 200 and 700 °C). A thermal treatment at high temperature of the resulting surface species, bearing one or two tert-butoxide ligands, leads to the targeted active species by a  $\beta$ -H elimination of isobutene from  $V-OtBu$ , resulting in a hydroxy ligand  $\sigma$ -coordinated to vanadium,  $V-OH$ . This reaction can be followed by a ring opening of a neighboring siloxane ( $\equiv Si-O-Si\equiv$ ) which forms a new  $V-OSi\equiv$  bond and a surface hydroxyl group,  $\equiv Si-OH$ . These well-defined surface species have been further characterized by elemental analysis and different spectroscopic techniques as DRIFT, Solid-State NMR of different nuclei ( $^1H$ ,  $^{13}C$ ,  $^{51}V$ ), UV-Vis, XAS and studied as catalysts for the non-oxidative dehydrogenation of propane in a continuous flow reactor.

## Experimental Section

### General Procedure.

All experiments were carried out using standard air-free methodology within an argon-filled glovebox, on a Schlenk line or in a Schlenk-type apparatus interfaced to a high-vacuum line ( $10^{-5}$  mbar). Solvents were purified and dried according to standard procedures.  $[V(=O)(OtBu)_3]$  was synthesized in one step followed by purification. Elemental analyses were performed at Mikroanalytisches Labor Pascher. Diffuse reflectance infrared spectra were collected with a Nicolet 6700 FT-IR spectrophotometer, with a  $4\text{ cm}^{-1}$  resolution with a SMART module. An air-tight IR cell equipped with  $CaF_2$  windows was employed and the final spectra comprise 64 scans. Diffuse reflectance UV-Vis spectra in the range of 200-850 nm were recorded on a Perkin Elmer  $\lambda 1050$  UV-Vis-NIR spectrophotometer adapted with the Praying Mantis optical unit provided by Harrick. The samples were diluted in dry  $BaSO_4$  and the spectra were recorded against a  $BaSO_4$  baseline. An air-tight cell equipped with quartz windows was used.

Solution NMR spectra were recorded on an Avance-300 Bruker spectrometer. All chemical shifts were measured relative to residual  $^1H$  or  $^{13}C$  resonance of the deuterated  $C_6D_6$  solvent:  $\delta$

7.15 ppm for  $^1\text{H}$  and 128 ppm for  $^{13}\text{C}$ . Solid-state NMR spectra were acquired with a Bruker Avance 500 spectrometer ( $^1\text{H}$ : 500.1 MHz,  $^{13}\text{C}$ : 125.7 MHz). For  $^1\text{H}$  experiments, the spinning frequency was 10 kHz, the recycle delay was 5 s and 8 scans were collected using a  $90^\circ$  pulse excitation of 3  $\mu\text{s}$ . The  $^{13}\text{C}$  CP MAS spectra were obtained at a spinning frequency of 10 kHz, with a recycle delay of 5 s and 12288 scans were collected. Chemical shifts were given in ppm with respect to TMS as external reference for  $^1\text{H}$  and  $^{13}\text{C}$  NMR. The  $^{51}\text{V}$  MAS NMR spectrum was acquired in a Bruker DSX 300 spectrometer ( $^{51}\text{V}$ : 78.9 MHz) using a single pulse excitation. The signal was optimized with crystalline  $\text{V}_2\text{O}_5$  ( $\delta = -609$  ppm) as external standard with a pulse angle of  $\pi/2$ . Two spinning rates were used in order to determine the isotropic chemical shift (10 kHz and 12 kHz).

X-ray absorption spectra were acquired at ESRF on BM23 beam-line, at room temperature at the vanadium K edge. A double Si(111) crystal was used as monochromator and a system based on a total reflection through a double X-ray mirror with an incidence angle variable from 2 to 5 mrad allowed harmonic rejection to a level better than  $10^{-5}$ .<sup>48</sup> The spectra were recorded in the transmission mode between 5.3 to 6.44 KeV at room temperature (295 K). Each data set was collected simultaneously with a V metal foil reference and was later aligned according to that reference (first maximum of the derivative of the V foil spectrum set at 5465.1 eV). The molecular complexes and vanadyl sulfate were homogeneously mixed with dry BN and the supported V samples were packaged as pellets within an argon filled glove-box in a double air-tight sample holder equipped with kapton windows. The data analyses were performed by standard procedures using in particular the program "Athena".<sup>49</sup>

### **Preparation of the complex.**

The vanadium precursor  $[\text{V}(=\text{O})(\text{O}t\text{Bu})_3]$ , (**1**), was synthesized by the reaction of  $\text{V}_2\text{O}_5$  (Aldrich) with  $t\text{BuOH}$  in benzene. The entire preparation procedure was carried out in an inert atmosphere using a Schlenk line. 20 grams of  $\text{V}_2\text{O}_5$  was first placed in a 1-L round-bottom flask and connected to a Dean–Stark trap in order to capture the water from the reaction, coming through the reflux condenser. After adding 300-mL of dry benzene, 165 ml of dry  $t\text{BuOH}$  was added to the benzene suspension of  $\text{V}_2\text{O}_5$ . The temperature was increased to ca. 368 K and maintained overnight. The solution was filtered away from unreacted  $\text{V}_2\text{O}_5$ . After removing the solvent by distillation, white crystals were observed. This product was further dried overnight under reduced pressure. In order to purify the freshly formed product,

[V(=O)(OtBu)<sub>3</sub>], a sublimation was conducted under vacuum at 313 K. <sup>1</sup>H NMR (C<sub>6</sub>D<sub>6</sub>): δ=1.44 ppm (CH<sub>3</sub>); <sup>13</sup>C{H} NMR (C<sub>6</sub>D<sub>6</sub>) δ= 31.4 ppm (CH<sub>3</sub>) and 86 ppm (C-CH<sub>3</sub>).

### **Preparation and characterization of (2), (2a), (3) and (3a) materials.**

A mixture of [V(=O)(OtBu)<sub>3</sub>] (in excess with respect to total amount of Si-OH groups) and SiO<sub>2-(200)</sub> (1 g) in pentane (10 mL) was stirred at 25 °C for 4 hours. After filtration, the solid was washed 4 times with pentane and the liquid was transferred into another reactor in order to quantify the *t*BuOH evolved during the grafting reaction by GC and using an internal standard. The resulting material, **(2)**, is a white powder that was dried under vacuum (10<sup>-5</sup> mbar). Elemental analysis: V 1.6 wt% C 1.5 wt%. The catalyst was characterized by DRIFT, Solid-State NMR, UV-Vis and XANES.

The same procedure was employed with SiO<sub>2-700</sub> to yield **(3)**, which was also characterized as **(2)**. Elemental analysis: V 1.12 wt%, C 2.23 wt%.

Both materials, **(2)** and **(3)** were heated to form tripodal V species leading to the synthesis of **(2a)** and **(3a)** materials, respectively. These species were characterized by DRIFT, Solid-State NMR UV-Vis, and XANES and their catalytic performances evaluated for propane dehydrogenation.

**Catalysts evaluation.** Catalytic propane conversion was carried out in a stainless-steel continuous flow reactor (P<sub>total</sub> = 1 bar, T = 540 °C, total flow rate = 5 mL.min<sup>-1</sup>: 20% propane in argon) mass of the catalyst = 500 mg diluted in 2.5 of CSi. The gases were purified with a column of molecular sieves and activated Cu<sub>2</sub>O/Al<sub>2</sub>O<sub>3</sub> and controlled by Brooks mass flow controllers. The catalyst was charged in the glovebox. A 4-way valve allowed the isolation of the charged catalyst in the reactor from the environment and extensive purging of the tubes before the reaction. The products were determined by an online HP 6890 GC equipped with a 50 m KCl/Al<sub>2</sub>O<sub>3</sub> column and a FID detector.

## **Results and Discussions**

### **Preparation and characterization of [V(=O)(OtBu)<sub>3</sub>], (1)**

The precursor, [V(=O)(OtBu)<sub>3</sub>], was easily synthesized using commercially available compounds V<sub>2</sub>O<sub>5</sub> and *t*BuOH in benzene at 100 °C for 48 h. After purification, this complex was identified by intense <sup>1</sup>H NMR signal at 1.43 ppm, attributed to proton of methyl fragments and <sup>13</sup>C NMR signals at 31.4 ppm, corresponding to carbons of methyl groups,

CH<sub>3</sub>, and at 86 ppm attributed to the quaternary C of the tert-butyl ligand (Figure S1). In addition, <sup>51</sup>V NMR showed a signal at -642 ppm, corresponding to a tetrahedral vanadium supported complex, bearing an oxo and three alkoxy ligands (Figure S2).<sup>42</sup>

### Reactivity of [V(=O)(OtBu)<sub>3</sub>], (1), with a silica dehydroxylated at 200 °C, synthesis of material (2)

Amorphous silica, Aerosil 200 from Degussa was partially dehydroxylated at 200 °C under high vacuum (10<sup>-5</sup> mbar) to afford SiO<sub>2-200</sub> with a density of silanols ca. 2.5 OH per nm<sup>2</sup> (0.86 mmol OH.g<sup>-1</sup>).<sup>40</sup> The grafting of [V(=O)(OtBu)<sub>3</sub>] on SiO<sub>2-200</sub> was carried out by an anhydrous impregnation in pentane at 25 °C. Then, the powder was washed four times with dry pentane in order to remove the excess of complex affording V(=O)(OtBu)<sub>3</sub>/SiO<sub>2-200</sub> (2) as a colorless material. The reaction of [V(=O)(OtBu)<sub>3</sub>] proceeds with the consumption of almost all the surface free (or “isolated”) silanols of SiO<sub>2-200</sub>, as shown from the irreversible disappearance of the ν<sub>O-H</sub> stretching band at 3747 cm<sup>-1</sup> (Figure 1, Left). Importantly, the intensity of the other large ν<sub>O-H</sub> band centered at 3600 cm<sup>-1</sup>, attributed to vicinal silanols, did not decrease after reaction with the complex due to the low reactivity of these vicinal silanols. This phenomenon was already observed for the reaction of SiO<sub>2-200</sub>, with several complexes of metal of groups IV, V and VI.<sup>50</sup> Concomitantly, two groups of bands appear in the 3200-2700 cm<sup>-1</sup> and 1500-1300 cm<sup>-1</sup> region, assigned respectively to ν(CH) and δ(CH) vibrations of the methyl groups of the per hydrocarbyl ligands.

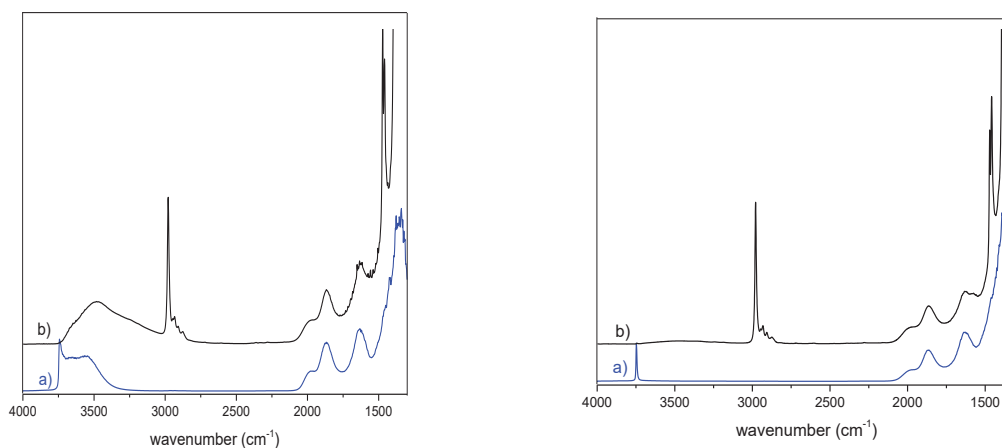


**Figure 1. Left:** IR-spectra of a) SiO<sub>2-200</sub> and b) after grafting of [V(=O)(OtBu)<sub>3</sub>] on SiO<sub>2-200</sub> (2), and **Right:** IR-spectra of a) SiO<sub>2-700</sub> and b) after grafting of [V(=O)(OtBu)<sub>3</sub>] on SiO<sub>2-700</sub> (3)

The amounts of vanadium and carbon, as quantified by elemental analysis of  $V(=O)(OtBu)_3/SiO_{2-200}$  material, (**2**), are 1.6 wt% V and 1.5 wt % C, which accounts for an atomic ratio of ca. 4.0 C/V. The vanadium loading of the material is thus  $0.315 \text{ mmol.g}^{-1}$  and since the concentration of silanols is ca.  $0.86 \text{ mmol OH/g}$  on  $SiO_{2-200}$ ,<sup>40</sup> this gives a V/OH ratio of 0.365. The quantification of the *t*BuOH evolved during the grafting reaction, was carried out by GC analysis, using octane as an internal standard. It leads to a release of 1.8 *t*BuOH/V. Thus, the results of these characterizations are in line with the formation of a major bipodal species bearing one tert-butoxide ligand,  $[(\equiv SiO)_2V(=O)(OtBu)]$ .

Further spectroscopic characterizations provided additional information on the grafting of  $[V(=O)(OtBu)_3]$  on  $SiO_{2-200}$ .  $^1H$  MAS NMR shows one signal at 1.4 ppm assigned to  $CH_3$  protons (Figure S3) and one signal in  $^{13}C$  CP MAS NMR at 28 ppm attributed to the carbon of the methyl groups (Figure 2). The lack of a significant signal for the quaternary carbon of the tert-butoxide ligand is most probably due to the larger chemical shift anisotropy, owing to a lower mobility of the surface species compared to the case of  $SiO_{2-700}$  support (material (**3**)), as previously observed.<sup>51,52</sup> No improvement for the  $^{13}C$  signal of the quaternary carbon was shown under the  $^{13}C\{^1H\}$  MAS mode.

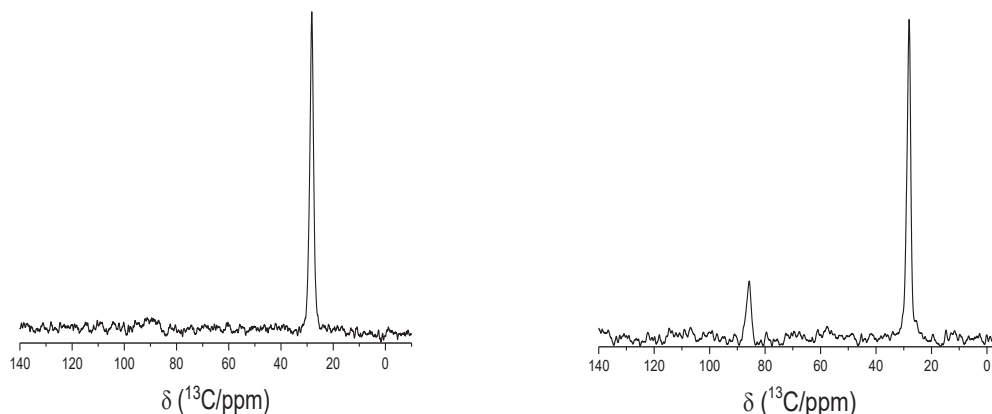


**Figure 2.**  $^{13}C$  CP MAS NMR of **Left:**  $V(=O)(OtBu)_3/SiO_{2-200}$  and **Right:**  $V(=O)(OtBu)_3/SiO_{2-700}$  (11.7 T, 10 kHz,  $d_1=5$  s)

$^{51}V$  NMR is a powerful technique that brings additional information on the coordination sphere and geometry of the vanadium centers in supported catalysts.<sup>53,54</sup> The  $^{51}V$  MAS NMR of (**2**) reveals a signal with an isotropic chemical shift of -693 ppm (Figure 3, top), which

represents an upfield shift of 51 ppm in comparison to  $[V(=O)(OtBu)_3]$  molecular complex, **(1)**, which shows a signal at -642 ppm (Figure S2). This result is consistent with the formation of a bipodal surface species on silica-200. In fact, the upfield shift was also reported in literature, for a  $[V(=O)(OiPr)_3]$  complex with a  $^{51}V$  NMR signal at -630 ppm, that shifts to -650 ppm when two *OiPr* ligands of this complex are exchanged by two siloxy groups from the silica surface, leading to  $[(\equiv SiO)_2V(=O)(OiPr)]$  supported species.<sup>55</sup>

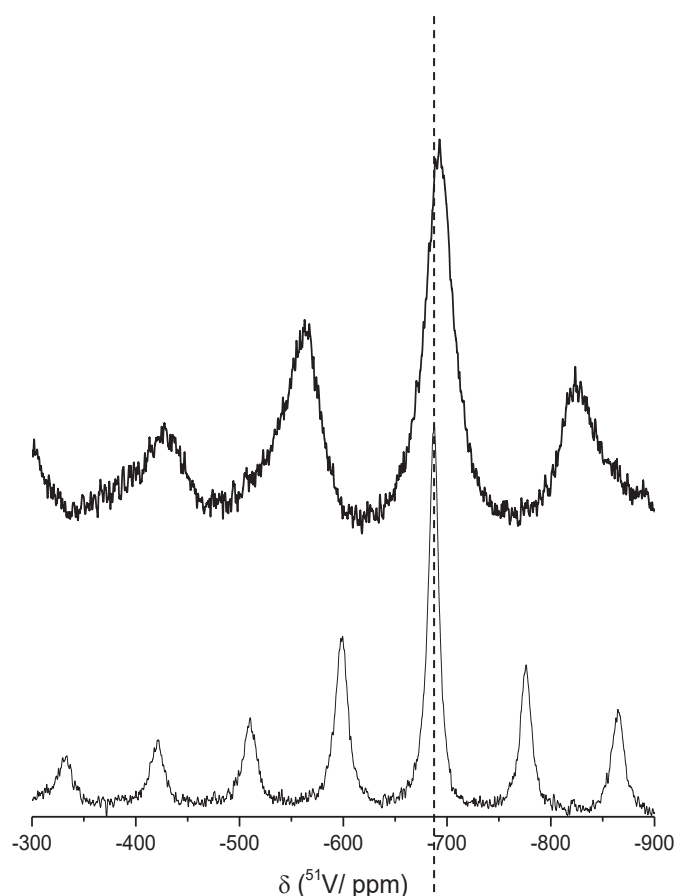


**Figure 3.**  $^{51}V$  MAS NMR spectra of:  $V(=O)(OtBu)_3/SiO_{2-200}$ , **(2)** (7.1 T, 12 kHz,  $d_1 = 1$  s) and  $V(=O)(OtBu)_3/SiO_{2-700}$ , **(3)** (7.1 T, 10 kHz,  $d_1 = 1$  s)

The UV-Vis spectrum of **(2)**, comprises absorption bands starting from 200-400 nm (Figure 4). The absence in the spectrum of any absorption in the  $d \rightarrow d$  transition part, suggests that the supported vanadium is in its highest oxidation state.<sup>56</sup> The broad peak in the UV region ( $\lambda_{max} = 267$  nm) can be assigned to a ligand to metal charge transfer (LMCT) originated from the tert-butoxide ligands. The energy edge ( $E_g$ ) derived from the  $O \rightarrow V$  charge transfer

peak (determined from the intercept of the  $[F(R_\infty)h\nu]^2$  vs  $h\nu$  plot in the low energy rise) reflects the degree of vanadia polymerization.<sup>57</sup> This value is extrapolated to be 3.58 eV for **(2)**, suggesting that the vanadium sites are present as monomer on the surface.<sup>58</sup>

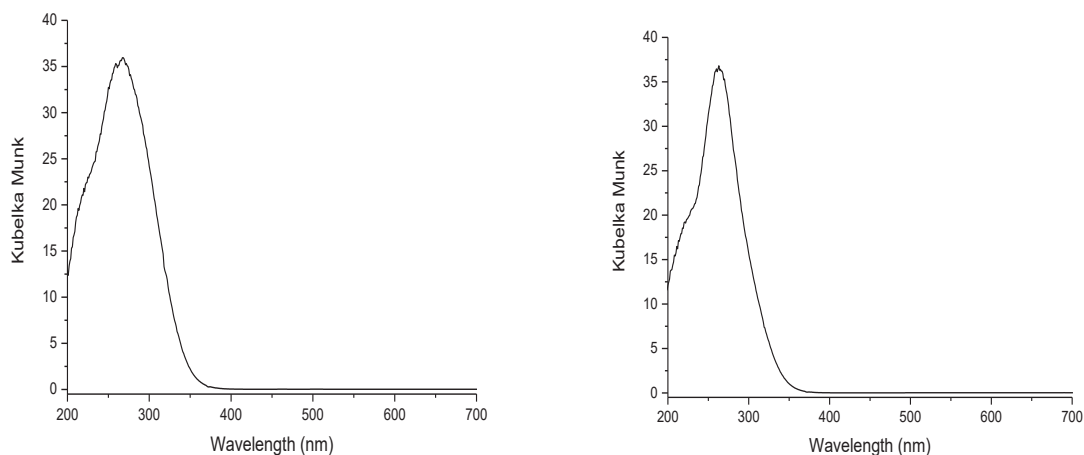


**Figure 4.** UV-Vis spectrum of **(2)** (left) and **(3)** (right)

#### **XANES analysis of the molecular complex on SiO<sub>2-200</sub>.**

Additional information on the vanadium coordination geometry, its structural environment and oxidation state in the case of the molecular complex, **(1)**, and materials **(2)** and **(3)** were given by X-ray absorption spectroscopy. Normalized V K-edge XANES spectra of the molecular complex,  $[V(=O)(OtBu)_3]$ , of the presumed  $[(\equiv SiO)_2V(=O)(OtBu)]$  complex in material **(2)**, obtained from the grafting of  $[V(=O)(OtBu)_3]$  onto SiO<sub>2-200</sub> are shown in Figure 5. In the two spectra (a and b), there is a prominent pre-edge peak. This pre-edge feature arises from electronic transitions from 1s core levels to the empty 3d levels, more or less 4p hybridized by the ligands of vanadium. These electronic transitions become electric-dipolar allowed in the absence of an inversion center. In this case, the loss of symmetry allows partial overlapping and mixing of the unfilled d states of the metal with its 4p orbitals. Several studies of the V K-edge XANES features have considered the pre-edge intensity as well as its absolute position to determine both the vanadium oxidation state and its symmetry.<sup>59-61</sup> The position of the pre-edge peak on its own is generally insufficient to evaluate accurately the vanadium oxidation state.

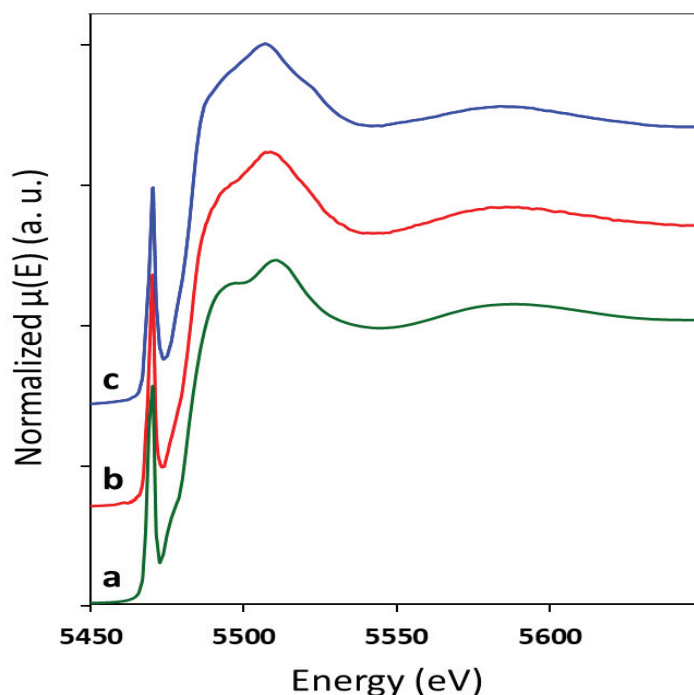


**Figure 5.** XANES: of (a)  $[V(=O)(OtBu)_3]$  molecular complex, **(1)**; (b)  $V(=O)(OtBu)_3/SiO_{2-200}$  **(2)**; (c)  $V(=O)(OtBu)_3/SiO_{2-200}$  heated at  $500^\circ C$  **(2a)**.

The position and intensity of the main pre-edge peak along with the position of the edge of different vanadium compounds studied are reported in Table 1. For the molecular complex, **(1)** and material **(2)** referenced above, the position of the pre-edge peak at ca. 5470.4 eV and its high intensity (0.79 to 0.85) are consistent with those observed in other complexes or materials containing  $V^{(V)}$  in a tetrahedral symmetry.<sup>60</sup> Moreover, the position of the K-edge of the three samples, shifted by 16 to more than 18 eV to higher energy relative to the metal foil, are within the range of K-edge energies reported for known  $V^{(V)}$  compounds.<sup>59</sup>

**Table 1.** Positions and intensities of the pre-edge signal and edge positions in the V K-edge XANES of several vanadium samples.

Sample	Pre-edge signal position <sup>a</sup> (eV)	Pre-edge signal intensity <sup>b</sup> (a.u.)	Edge position <sup>a</sup> (eV)
$V^{(0)}$ (metal foil)			5465.1
$[V^{III}(Mes)_3 \cdot THF]$	5466.6	0.55	5481.2

[V <sup>IV</sup> (=O)SO <sub>4</sub> (H <sub>2</sub> O) <sub>x</sub> ]	5469.8	0.48	5480.7
[V <sup>V</sup> (=O)( <i>Ot</i> Bu) <sub>3</sub> ] ( <b>1</b> )	5470.4	0.79	5481.9
V(=O)( <i>Ot</i> Bu) <sub>3</sub> /SiO <sub>2-200</sub> ( <b>2</b> )	5470.3	0.85	5483.4
V(=O)( <i>Ot</i> Bu) <sub>3</sub> /SiO <sub>2-200</sub> heated at 500°C ( <b>2a</b> )	5470.5	0.81	5483.5
V(=O)( <i>Ot</i> Bu) <sub>3</sub> /SiO <sub>2-700</sub> ( <b>3</b> )	5470.3	0.85	5483.2
V(=O)( <i>Ot</i> Bu) <sub>3</sub> /SiO <sub>2-700</sub> heated at 500°C ( <b>3a</b> )	5470.4	0.81	5483.6

<sup>a</sup> Relative to a calibration with a vanadium foil (5465.1 eV); A ± 0.3 eV error is estimated on the energy. <sup>b</sup> Intensity normalized to the step height of the K-edge.

### Reactivity of [V(=O)(*Ot*Bu)<sub>3</sub>] with a silica dehydroxylated at 700 °C, material (**3**) synthesis

The same amorphous silica support was partially dehydroxylated at 700 °C (SiO<sub>2-700</sub>) under high vacuum (10<sup>-5</sup> mbar) in order to compare the structure of the supported species on the resulting material, (**3**), to those obtained on material (**2**), after the grafting of [V(=O)(*Ot*Bu)<sub>3</sub>] on SiO<sub>2-200</sub>. SiO<sub>2-700</sub> presents a density of ca. 0.70 OH per nm<sup>2</sup> corresponding to 0.27 mmol OH.g<sup>-1</sup>.<sup>39</sup> The impregnation of [V(=O)(*Ot*Bu)<sub>3</sub>] on SiO<sub>2-700</sub> in a pentane solution occurred at room temperature for 4h. After an intensive washing with pentane to remove the excess of the complex and a drying under high vacuum, a white powder was obtained (**3**). The infrared spectroscopy of V(=O)(*Ot*Bu)<sub>3</sub>/SiO<sub>2-700</sub> (**3**) revealed the consumption of all the isolated silanols initially present on SiO<sub>2-700</sub>, shown by the disappearance of the ν<sub>O-H</sub> band at 3747 cm<sup>-1</sup> (Figure 1, Right). Simultaneously, alkyl bands in the range of 3000-2800 cm<sup>-1</sup> (ν<sub>C-H</sub>) and 1500-1300 cm<sup>-1</sup> (δ<sub>CH<sub>2</sub></sub> and δ<sub>CH<sub>3</sub></sub>) appeared, confirming the grafting of the vanadium complex on the silica surface. Elemental analysis of material (**3**) indicates V and C wt% contents of 1.12 and 2.23 wt%, respectively, corresponding to an atomic ratio of 7.9 C/V. The V/OH ratio is ca. 0.815, since 0.220 mmol of V/g of silica are grafted on the surface. GC analysis of *t*BuOH released during the grafting revealed a release of 0.88 *t*BuOH/V after reaction. The comparison of the mass balance analyses obtained after the grafting of [V(=O)(*Ot*Bu)<sub>3</sub>] on

SiO<sub>2-200</sub> and SiO<sub>2-700</sub> are resumed in Table 2. It is obvious from these results that the structure of the resulting species in materials **(2)** and **(3)** depends on the dehydroxylation temperature of the support. Thus, the characterization results suggest the formation of a major monopodal species, [(≡SiO)V(=O)(OtBu)<sub>2</sub>] for **(3)**, from SiO<sub>2-700</sub>, and a bipodal species [(≡SiO)<sub>2</sub>V(=O)(OtBu)] for **(2)**, from SiO<sub>2-200</sub>.

**Table 2.** Mass balance analysis for the grafting of [V(=O)(OtBu)<sub>3</sub>], **(1)**, onto silica.

Supports	% <sub>wt</sub> V <sup>c</sup>	% <sub>wt</sub> C <sup>d</sup>	C/V ratio	tBuOH/V
SiO <sub>2-200</sub>	1.6	1.5	4	1.8
SiO <sub>2-700</sub>	1.12	2.23	7.9	0.88

<sup>c</sup>The error on V is < 5 %.<sup>d</sup>The error on the C elemental analyses is ±1 a.m.u.

The characterization of material **(3)** by <sup>1</sup>H MAS NMR shows a similar result to the one observed for material **(2)**. The spectrum also consists in a main signal at 1.4 ppm corresponding to CH<sub>3</sub> protons of tert-butoxide ligands (Figure S3). The <sup>13</sup>C CP MAS spectrum of V(=O)(OtBu)<sub>3</sub>/SiO<sub>2-700</sub>, **(3)**, shows two signals at 86 ppm and 28 ppm, assigned to quaternary carbon and CH<sub>3</sub> terminal groups, respectively (Figure 2, Right). It is important to note that the signal attributed for the quaternary carbon at 86 ppm is visible compared to **(2)**. This is either due to the presence of two tert-butoxide ligands on the surface (higher concentration), compared to the main surface complex of **(2)**, or to a higher mobility of the surface species in **(3)**, leading to a narrower chemical anisotropy. A signal centered at -687 ppm appears in the <sup>51</sup>V MAS NMR spectrum, attributed to the monopodal complex [(≡SiO)V(=O)(OtBu)<sub>2</sub>] (Figure 3, down). This chemical shift corresponds to an up-field shift of -45 ppm compared to the precursor [V(=O)(OtBu)<sub>3</sub>] (-642 ppm). Nevertheless, the observed chemical shift is rather similar to the bipodal [(≡SiO)<sub>2</sub>V(=O)(OtBu)] (-693 ppm).<sup>42,55</sup> Taking into consideration the peak broadening (FWHM ≈ 70 ppm), the podality of supported [V(=O)(OtBu)<sub>3</sub>] is indistinguishable by <sup>51</sup>V MAS NMR spectroscopy. The UV-vis spectrum of [(≡SiO)V(=O)(OtBu)<sub>2</sub>] consists in an absorption band between 200 and 400 nm with a λ<sub>max</sub> = 262 nm, corresponding to ligand to metal charge transfer (LMCT O<sup>2-</sup> → V<sup>5+</sup>) (Figure 4). Similarly to the bipodal species, no absorption band at 650 nm was observed, hence, the vanadium adsorbed on the surface has the highest oxidation state (+V).<sup>56</sup> The

energy edge ( $E_g$ ) is 3.6 eV (compared to 3.58 eV in the case of  $V(=O)(OtBu)_3/SiO_{2-200}$ ), which is in line with the formation of monomers vanadium sites on the surface.<sup>58</sup>

### XANES analysis of the molecular complex on $SiO_{2-700}$ .

The normalized V K-edge XANES spectra of the molecular complex,  $[V(=O)(OtBu)_3]$ , of  $[(\equiv SiO)V(=O)(OtBu)_2]$  complex, obtained from the grafting of  $[V(=O)(OtBu)_3]$  onto  $SiO_{2-700}$  are shown in Figure 6. The position and intensity of the main pre-edge peak along with the position of the edge of these vanadium compounds are also reported in Table 1. For  $V(=O)(OtBu)_3/SiO_{2-700}$  supported species, the position of the pre-edge peak (5470.3 eV), its relative intensity (0.85) and the position of the edge (5483.2 eV) are also indicative of V(V) tetrahedral species.

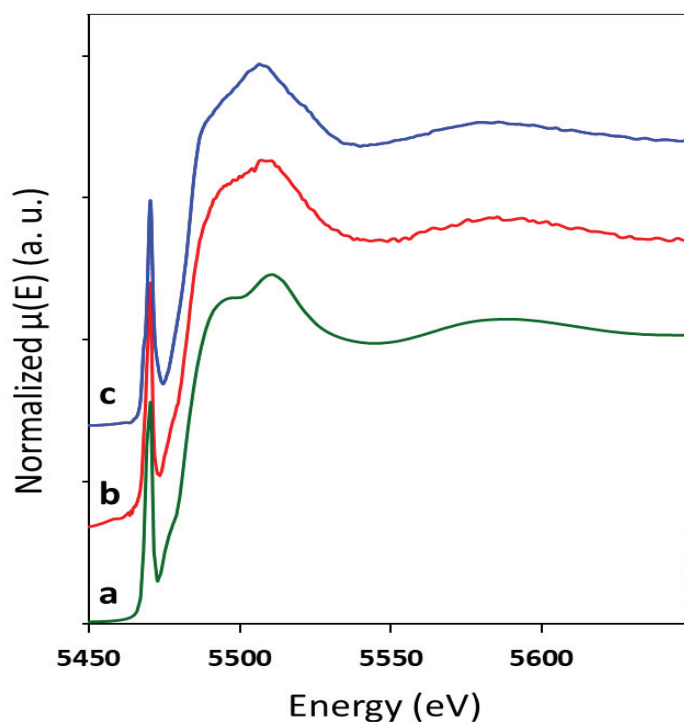
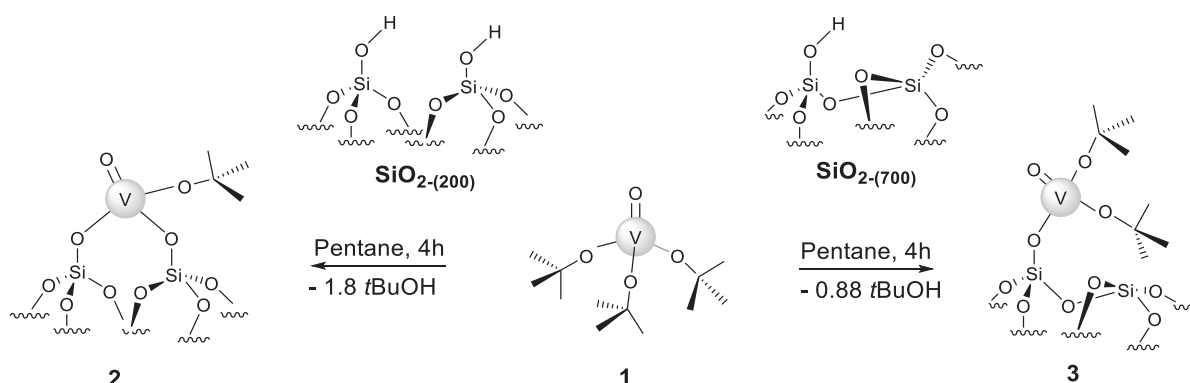


**Figure 6.** XANES of (a)  $[V(=O)(OtBu)_3]$  molecular complex (**1**); (b)  $V(=O)(OtBu)_3/SiO_{2-700}$ , (**3**); (c)  $V(=O)(OtBu)_3/SiO_{2-700}$  heated at 500°C, (**3a**).

In conclusion, well-defined single site catalysts with low loading of vanadium were obtained by grafting  $[V(=O)(OtBu)_3]$  onto  $SiO_{2-200}$  and  $SiO_{2-700}$ . A bipodal as major species was formed

on SiO<sub>2-200</sub> surface noted as [(≡SiO)<sub>2</sub>V(=O)(OtBu)] (**2**). The grafting of [V(=O)(OtBu)<sub>3</sub>] on SiO<sub>2-700</sub> led to monopodal species represented by [(≡SiO)V(=O)(OtBu)<sub>2</sub>] (**3**) (Scheme 2).



**Scheme 2.** Grafting of [V(=O)(OtBu)<sub>3</sub>] on SiO<sub>2-200</sub> and SiO<sub>2-700</sub> leading to structurally distinct surface species

### Tripodal species

Controlled thermolyses of [(≡SiO)V(=O)(OtBu)<sub>2</sub>], (**2**) from 25 to 300 °C (for 2 h), 400 °C (for 2 h) as well as 500 °C (for 2 h) were conducted under vacuum in a reactor equipped with a cold trap (liquid N<sub>2</sub>) in order to collect the gas phase evolved during the process. The analysis of the gas phase by GC after thermal treatment at 300 °C revealed the formation 0.88 isobutene/V for (**2**), and some traces of *t*BuOH were observed. As reported in the case of silica supported Mo and W complexes bearing oxo tert-butoxide ligands,<sup>42,47</sup> the formation of isobutene is triggered by the elimination from a methyl group of a H in β-position of the oxygen coordinated to the metal, M-O-C(Me)<sub>2</sub>-CH<sub>2</sub>-H, to form a hydroxy intermediate, M-OH. This step can be assisted by the presence of an oxo ligand in the coordination sphere of vanadium.

The DRIFT analysis of the resulting materials from bipodal [(≡SiO)<sub>2</sub>V(=O)(OtBu)] species after heating at 300 °C revealed the total disappearance of the alkyl vibrational bands in the range of 3000–2800 cm<sup>-1</sup> and 1500-1300 cm<sup>-1</sup>, assigned respectively to ν(CH), δ(CH) vibrations from the perhydrocarbyl ligands (Figure 7, Left). At 300 °C (after 2h), we observed the reappearance of isolated silanol groups at 3747 cm<sup>-1</sup> as well as the appearance of a new band at 3660 cm<sup>-1</sup> attributed to ν<sub>VO-H</sub>.<sup>62,63</sup> At 400 °C, the intensity of the band characteristic of ν<sub>SiO-H</sub> increases while the one of ν<sub>VO-H</sub> band decreases. At 500 °C, we observed the absence of the vibration band attributed to VO-H elongation vibration, accompanied by the decrease in

intensity of the  $\equiv\text{SiO-H}$  silanols vibration band. This phenomenon could be explained by a partial condensation of V-OH with the remaining silanols, leading to the formation of water and V-OSi bonds and thus tripodal V surface species (Scheme S1).

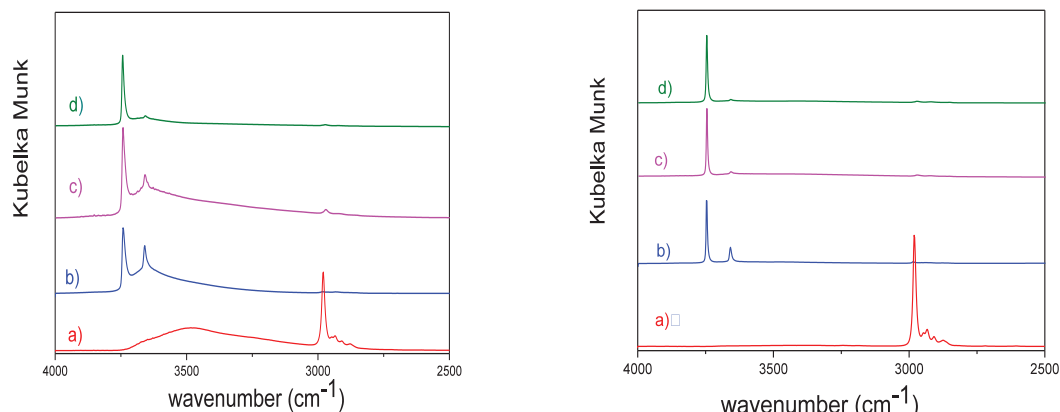


**Figure 7. Left.** IR-spectra of **a)**  $\text{V(=O)(OtBu)}_3/\text{SiO}_{2-200}$  (**2**), and then thermally treated at: **b)** 300 °C, **c)** 400 °C, and **d)** 500 °C; **Right.** IR-spectra of **a)**  $\text{V(=O)(OtBu)}_3/\text{SiO}_{2-700}$  (**3**), and then thermally treated at: **b)** 300 °C, **c)** 400 °C and **d)** 500 °C

Similarly, these phenomena were also observed by  $^1\text{H}$  MAS NMR of (**2**) thermally treated from 25 to 500 °C (Figure 8, Left). The intense signal at 1.3 ppm attributed to the methyl groups of tert-butoxide ligands decreased, and almost disappeared at 300 °C. Simultaneously, a signal at 1.8 ppm corresponding to isolated silanol groups appears at 300 °C and increases during the thermolysis (up to 500 °C). The release of isobutene during the thermolysis reaction and the appearance of silanol groups along with the disappearance of vanadium hydroxy intermediates, suggests that supported surface species in (**2**), lead to the formation of the targeted tripodal species  $[(\equiv\text{SiO})_3\text{V(=O)}]$  (**2a**) upon a thermal treatment under vacuum.

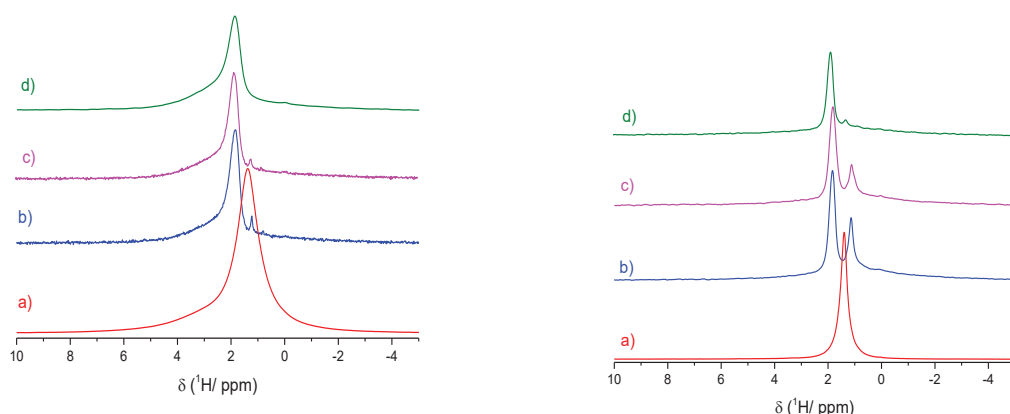


**Figure 8.** Left.  $^1\text{H}$  NMR spectra of **a)**  $\text{V}(=\text{O})(\text{OtBu})_3/\text{SiO}_{2-200}$  (**2**), and then thermally treated at: **b)** 300 °C, **c)** 400 °C, and **d)** 500 °C; Right.  $^1\text{H}$  NMR spectra of **a)**  $\text{V}(=\text{O})(\text{OtBu})_3/\text{SiO}_{2-700}$  (**3**), and then thermally treated at: **b)** 300 °C, **c)** 400 °C and **d)** 500 °C

The same procedure including a thermal treatment under vacuum at progressively increasing temperatures, has been applied to surface species of (**3**). This leads to similar observations from DRIFT and  $^1\text{H}$  MAS NMR data (right parts of Figure 7 and Figure 8, respectively), allowing to the formation of a tripodal vanadium oxo on  $\text{SiO}_{2-700}$  (**3a**) with a release of 1.9 isobutene/V. The resulting vanadium surface species (**2a**) and (**3a**) were further characterized by XANES, UV-vis and  $^{51}\text{V}$  MAS NMR.

### XANES of the tripodal species

Both tripodal vanadium systems obtained on silica were characterized by XANES spectroscopy to provide additional details on the vanadium structural environment after thermal treatment of the grafted species. Normalized V K-edge XANES spectra of tripodal systems on  $\text{SiO}_{2-200}$  (**2a**) and  $\text{SiO}_{2-700}$  (**3a**), in contrast with  $[\text{V}(=\text{O})(\text{OtBu})_3]$  and species (**2**) and (**3**) are shown in Figure 5,c and Figure 6,c. The position and intensity of the main pre-edge peak along with the position of the edge of targeted species  $[(\equiv\text{SiO})_3\text{V}(=\text{O})]$  is compared to molecular complex  $[\text{V}(=\text{O})(\text{OtBu})_3]$ , surface species (**2**)  $[(\equiv\text{SiO})_2\text{V}(=\text{O})(\text{OtBu})]$  and (**3**)  $[(\equiv\text{SiO})\text{V}(=\text{O})(\text{OtBu})_2]$  (Table 1). Similar to the complex and to the grafted species, the XANES spectra of tripodal species (**2a**) and (**3a**) displayed a pre-edge peak located at ca. 5470.4 eV. The relative intensities of these pre-edges are high and range from 0.85 (for grafted species (**2**) and (**3**)) to 0.81 for tripodal species (**2a**) and (**3a**). These results are consistent with those observed for other complexes or materials containing V(V) in a

tetrahedral symmetry.<sup>60</sup> Moreover, the position of the K-edge of the samples, shifted from 16 to more than 18 eV to higher energy relative to the metal foil, are within the range of K-edge energies reported for known V(V) compounds.<sup>59</sup>

Additional characterizations of the surface tripodal species **(2a)** and **(3a)** were given by UV-vis spectroscopy (Figure 9). This method allows the detection of isolated V(IV), V(V) and vanadium oligomeric species. The UV-vis spectra of **(2a)**,  $[(\equiv\text{SiO})_3\text{V}(=\text{O})]$  species on  $\text{SiO}_2\text{-200}$  exhibited a band at 253 nm along with a shoulder at 286 nm attributed to  $\pi(\text{t}2)\rightarrow\text{d}(\text{e})$  and  $\pi(\text{t}1)\rightarrow\text{d}(\text{e})$  oxygen-to-tetrahedral V(V) charge transfer transitions, involving oxygen in bridging (V-O-Si) and terminal (V=O) positions, respectively, in agreement with reported literature.<sup>64</sup> A similar result was obtained in the UV-vis spectrum of **(3a)**,  $[(\equiv\text{SiO})_3\text{V}(=\text{O})]$  on  $\text{SiO}_2\text{-700}$  with two bands at 256 and 287 nm. The absence of (d-d) transitions in the 600-800 nm range indicates that V(IV) species are not significantly present. Indeed, the energy edge ( $E_g$ ) of the tripodal V species on  $\text{SiO}_2\text{-200}$  and  $\text{SiO}_2\text{-700}$  are ca. 3.50 and 3.35 eV, respectively (compared to 3.58 and 3.6 eV in the case of **(2)**,  $\text{V}(=\text{O})(\text{OtBu})_3/\text{SiO}_2\text{-200}$  and **(3)**,  $\text{V}(=\text{O})(\text{OtBu})_3/\text{SiO}_2\text{-700}$ , respectively). The slight red-shift in the energy edge when transforming the grafted complexes into the tripodal species may be due to the creation of supplementary restrains around the deformed tetrahedral vanadium centers. These results are in agreement with the formation of monomeric vanadium sites on the surface, as supported by XANES and  $^{51}\text{V}$  MAS NMR.

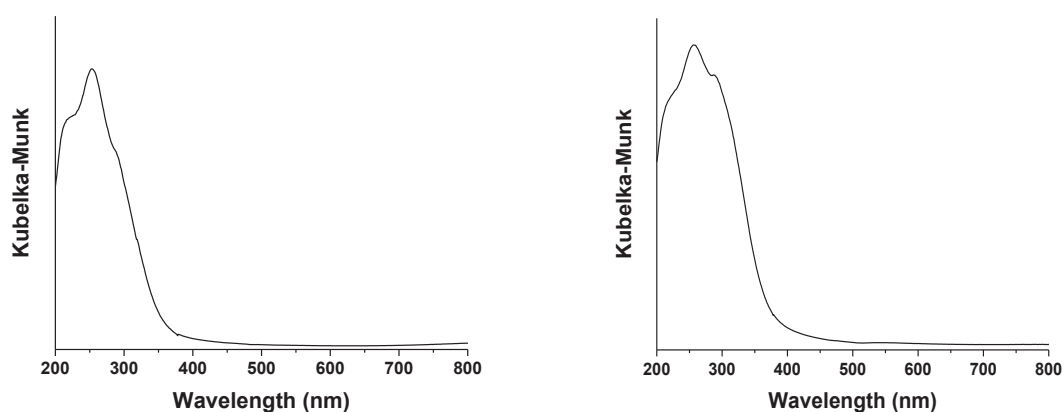


**Figure 9.** UV-vis of **Left: (2a)** and **Right: (3a)**

$^{51}\text{V}$  MAS NMR is a complementary technique to IR,  $^1\text{H}$  MAS NMR, XANES and UV-vis used to identify the surface vanadia species on the supported catalysts. Due to the importance

in catalysis of the isolated tetrahedral vanadium complexes on various supports, the intensive  $^{51}\text{V}$  soli-state NMR characterization of these types of catalysts by several groups showed that the chemical shift is generally in the range of -460 to -700 ppm.<sup>53,65-67</sup> The attribution of the signals in the  $^{51}\text{V}$  NMR spectrum of these materials remains challenging due to the lack of supporting models (such as  $(\text{Ph}_3\text{SiO})_3\text{V}(=\text{O})$  and vanadium oxo containing POMSS)<sup>68,69</sup> and to the variety of experimental conditions during the NMR acquisition.<sup>70,71</sup> Grant et al.<sup>72</sup> have studied by  $^{51}\text{V}$  MAS NMR silica-supported vanadia catalysts prepared by impregnation with a surface coverage between 1.3 to 15.4  $\text{V}\cdot\text{nm}^{-2}$ . In the  $^{51}\text{V}$  NMR spectra obtained, the authors observed two different isotropic shifts, depending on the surface coverage of vanadium. For the materials prepared with the highest vanadium content (13.4 and 15.4  $\text{V}\cdot\text{nm}^{-2}$ ), a sharp peak appeared at -614 ppm, corresponding to the distorted trigonal bipyramidal geometry of crystalline  $\text{V}_2\text{O}_5$ , which is in line with previous work revealing close isotropic shift of crystalline  $\text{V}_2\text{O}_5$  at -612 ppm<sup>73</sup> or -610 ppm.<sup>53</sup> In parallel, another signal was also observed at -675 ppm in all samples, but its intensity in the case of catalysts prepared with lower coverage of vanadium, in particular for 1.3  $\text{V}\cdot\text{nm}^{-2}$ , was very low. This signal is attributed to dispersed monomeric species,  $[(\equiv\text{SiO})_3\text{V}(=\text{O})]$ .<sup>74</sup> Recently, Jaegers. et al.,<sup>70</sup> confirmed these MAS NMR attributions, by employing faster spinning rates (above 30 kHz) at a higher field (19.975 T), and reported a better resolution of the signal assigned to tripodal V species (at -675 ppm), even at low V content (0.6  $\text{V}\cdot\text{nm}^{-2}$ ). In the case of the supported species of **(2a)** and **(3a)**, with low V coverages, ca. 1.1 and 0.8  $\text{V}\cdot\text{nm}^{-2}$ , respectively,  $^{51}\text{V}$  MAS NMR revealed a similar signal with a chemical shift of -670 ppm for both samples (Figure 10), attributed to  $[(\equiv\text{SiO})_3\text{V}(=\text{O})]$  isolated vanadium surface species, on  $\text{SiO}_2\text{-200}$  and  $\text{SiO}_2\text{-700}$  (Scheme 3).

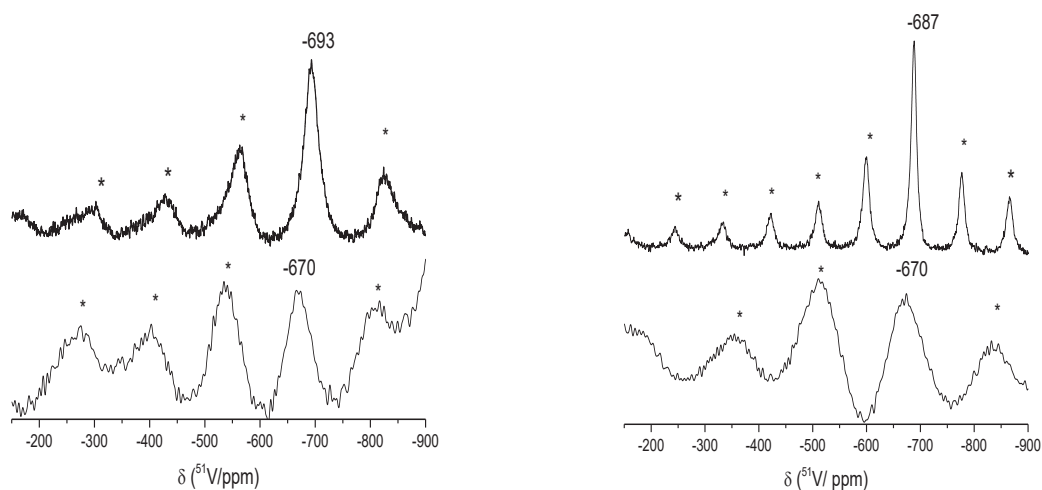
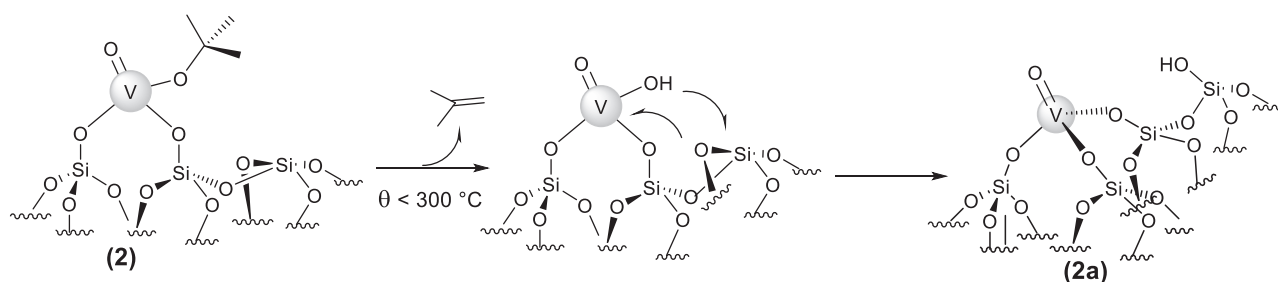


**Figure 10.** Solid-state  $^{51}\text{V}$  NMR spectra of: **Left:**  $\text{V(=O)(OtBu)}_3/\text{SiO}_{2-200}$  (**2**) (top) and  $[(\equiv\text{SiO})_3\text{V(=O)}]$  (**2a**) (down) (7.1 T, 12 kHz,  $d_1 = 1$  s), and **Right:**  $\text{V(=O)(OtBu)}_3/\text{SiO}_{2-700}$  (**3**) (top) and  $[(\equiv\text{SiO})_3\text{V(=O)}]$  (**3a**) (down) (7.1 T, 12 kHz,  $d_1 = 1$  s). Grafted species in (**2**) and (**3**) revealed a major peak at -693 and -687 ppm respectively. Tripodal species in (**2a**) and (**3a**) exhibited a major peak at -670 ppm.

The above characterization by DRIFT,  $^1\text{H}$  and  $^{51}\text{V}$  MAS NMR, XANES, mass balance analysis, UV-vis of the resulting species after a thermal treatment of bipodal (**2**) and monopodal (**3**) vanadium species, revealed the formation of tripodal vanadium species,  $[(\equiv\text{SiO})_3\text{V(=O)}]$  in (**2a**) and (**3a**) materials.

The mechanism of the formation of these active species would be similar on  $\text{SiO}_{2-200}$  and  $\text{SiO}_{2-700}$ . It has been proposed that a hydrogen transfer from a methyl group of a *tert*-butoxy ligand to the vanadyl oxygen occurs, leading to a V-OH fragment. The latter reacts with a siloxane bridge from the support by a Si-O-Si ring opening, leading to the formation of new isolated silanols as described in Scheme 3 (e.g on  $\text{SiO}_{2-200}$ ). The hydrogen transfer to the vanadyl oxygen can occur either by a transfer of one hydrogen to the oxo ligand, or by direct migration of one hydrogen from a methyl group to the oxygen of a *tert*-butoxide ligand, thus releasing a *t*BuOH molecule. It was indeed demonstrated that the thermal treatment of metal derivatives of  $-\text{OSi}(\text{OtBu})_3$  led to the direct elimination of isobutylene, even at low temperatures (100 - 150 °C) to form silanols without any assistance of other ligands.<sup>75</sup>



**Scheme 3.** Proposed mechanism for the formation of  $[(\equiv\text{SiO})_3\text{V(=O)}]$  species

### Catalytic properties

The catalytic behavior of the tripodal V species supported on  $\text{SiO}_{2-200}$  and  $\text{SiO}_{2-700}$  was evaluated in the non-oxidative dehydrogenation of propane. A continuous fixed-bed type reactor was used, under the following operating conditions:  $\theta = 540$  °C,  $P = 1$  bar and a total

flow of 5 mL.min<sup>-1</sup> (20 % of C<sub>3</sub>H<sub>8</sub> in Ar). The reactor was heated from room temperature to 540 °C under a flow of 4 mL.min<sup>-1</sup> of argon and then propane was introduced at 540°C.

When propane was fed to the catalytic bed of tripodal V obtained on SiO<sub>2-200</sub> (**2a**), a conversion of 19 % was reached at early times on stream and slightly decreased to 17 % after 1000 min (Figure 11). At that time, the selectivity toward propene was 84.5 %, and the by-products included methane (6.8 %), ethene (4.7 %) and ethane (2.5 %) as well as traces of C<sub>4</sub> (< 2%) (Figure 12, Left). On the other hand, tripodal V on SiO<sub>2-700</sub> (**3a**) exhibited a different behavior in function of time on stream. A lower initial conversion of 15 % followed by a gradual deactivation was observed, leading to 10.4 % after 1000 min (Figure 11). Initially, the products comprised propene (88.4 %), methane (6.8 %), ethane (2.4 %) and ethane (2.4 %). However, after 1000 min, the selectivity toward methane increased to 11.4 % and propene decreased to 81.7 % while ethane and ethene slightly increased to 3.6 % and 3.2 %, respectively (Figure 12, Right). The activity and selectivity observed with (**2a**), composed of tripodal V species on SiO<sub>2-200</sub> seems better than those with (**3a**), composed of tripodal V species on SiO<sub>2-700</sub>. This result was previously obtained in the case of vanadium species resulting from the grafting of O=V(mesityl)<sub>3</sub> complex on SiO<sub>2-200</sub> and on SiO<sub>2-700</sub>.<sup>40</sup> This is probably due to the difference in the local structure of the tripodal V on a silica pretreated at different temperature. This difference in terms of structure has been also observed in the <sup>51</sup>V solid-state NMR of the tripodal species [(≡SiO)<sub>3</sub>V(=O)] obtained on SiO<sub>2-200</sub> and SiO<sub>2-700</sub> after a thermal treatment. In fact, the larger signal observed in the case of vanadium supported on SiO<sub>2-700</sub> (**3a**), is attributed to the presence of different tetrahedral vanadium species, with the same coordination sphere but different local environment, which could explain the difference in terms of catalytic activity.

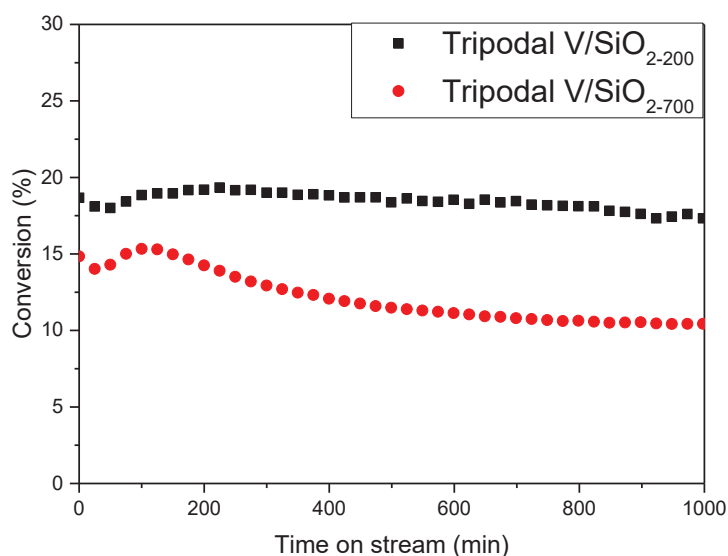


**Figure 11.** Propane conversion catalysed by vanadium tripodal species supported on  $\text{SiO}_{2-200}$ , (**2a**) and on  $\text{SiO}_{2-700}$ , (**3a**). Conditions:  $P=1$  bar;  $\theta=540$  °C; Total flow =  $5 \text{ mL}\cdot\text{min}^{-1}$  (20 %  $\text{C}_3\text{H}_8$  in Ar)

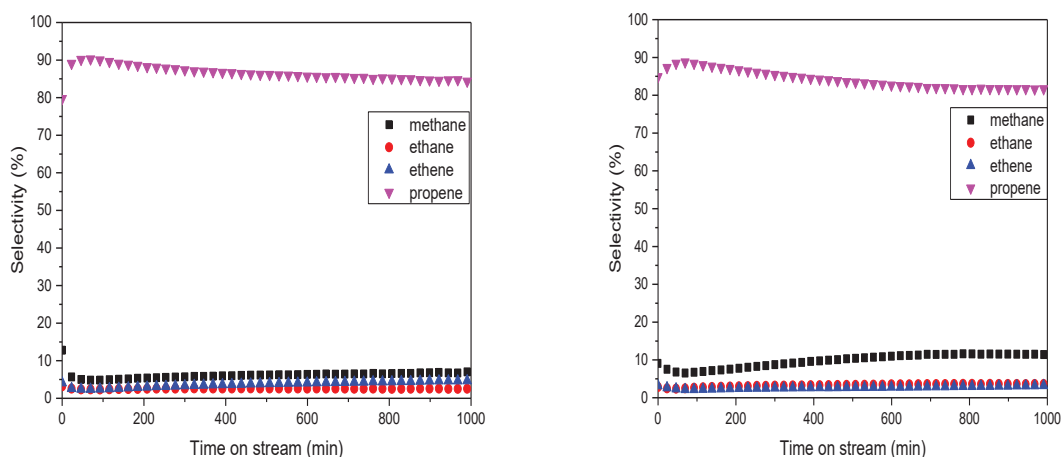


**Figure 12.** Selectivities obtained for propane conversion with vanadium tripodal species supported on  $\text{SiO}_{2-200}$ , (**2a**) (Left) and  $\text{SiO}_{2-700}$ , (**3a**) (Right). Conditions:  $P=1$  bar;  $\theta=540$  °C; Total flow =  $5 \text{ mL}\cdot\text{min}^{-1}$  (20 %  $\text{C}_3\text{H}_8$  in Ar)

These results demonstrate that the resulting materials containing silica supported tripodal species prepared by SOMC revealed a better activity and selectivity toward propane dehydrogenation compared to a  $\text{V}_2\text{O}_5$  catalyst supported on silica.<sup>13</sup> This is potentially due to the formation of oligomeric vanadia species on the surface of the catalyst prepared by aqueous impregnation and the presence of a lower concentration of tripodal active species.

The determination of the mechanism and of the nature of the active species in each step is of high interest. However, these key-issues cannot be addressed with our current ex-situ characterization techniques. As reported for chromium, it is reasonable to assume that the structure of the active species in PDH, is a tripodal  $V^{(III)}$ ,  $[(\equiv SiO)_3V]$ . In fact, at the initiation step, the first hydrogen abstraction of propane occurs on  $V=O$  ligand of  $[(\equiv SiO)_3V(=O)]$ , yielding an intermediate  $V^{(V)}$  bearing an alkyl and a hydroxy ligand. This latter species would then undergo a  $\beta$ -H elimination of the  $V$  coordinated propyl ligand, leading to the formation of  $V$  hydrido hydroxyl species and the release of one propylene. The reductive elimination of the water from the  $V$  hydrido hydroxyl species, would then lead to the formation of the active species,  $[(\equiv SiO)_3V^{(III)}]$ , during propane dehydrogenation (Scheme S2).

The full catalytic cycle can be described by two mechanistic pathways. Both involve an initialization of a  $V-O$  bond of  $[(\equiv SiO)_3V]$  by a  $C-H$  activation of propane, giving  $V$ -propyl species and an adjacent  $SiOH$  group. The next step is comprised by a  $\beta$ -H transfer to give a  $V-H$  and a coordinated propylene. Following a new activation of  $C-H$  of propane, the products (propylene and hydrogen) are released. The latter reaction scheme has previously been reported for supported metal hydride catalysts.<sup>76,77</sup> The second mechanistic pathway may involve cleavage and reconstruction of the  $V-H$  species with propylene coordinated, resulting in direct product release and regeneration of the tripodal species, as described for the chromium(III) system.<sup>78</sup> This mechanism has been earlier proposed in several reports. Firstly, Harlin *et al.* who observed that the reduced  $V_2O_5$  based catalyst has an enhanced activity in non-oxidative dehydrogenation of *n*-butane and *i*-butane, suggested that the reduced states of vanadium ( $V^{(IV)}$  or  $V^{(III)}$ ) are more active.<sup>79</sup> Moreover, Chen *et al.* have revealed the presence of  $V^{(III)}$  as a  $V_2O_3$  phase by XRD after the dehydrogenation of ethylbenzene under nitrogen at 550 °C.<sup>80</sup> In addition, Takahara *et al.* have studied the hydrogen treatment of silica supported  $V_2O_5$ , and suggested that a cleavage of  $V-O$  bonds has occurred with the formation of  $V-O-H$  sites adjacent to the  $V^{(IV)}/V^{(III)}$ , possible hydrides.<sup>81</sup> Hence, the  $V^{(IV)}/V^{(III)}$  species are most likely responsible for the dehydrogenation whereas  $VO-H$  acidic sites are believed to trigger the formation of carbonaceous deposit which increases with time on stream. Advanced operando techniques and theoretical calculations should offer additional insights on the reaction mechanism (Scheme S3).

## Conclusion

In conclusion, supported oxovanadium(V) complexes were prepared by surface organometallic chemistry from the grafting of the molecular complex  $[V(=O)(OtBu)_3]$ , (**1**), onto  $SiO_{2-200}$  and  $SiO_{2-700}$ , leading to materials exhibiting bipodal species  $[(\equiv SiO)_2V(=O)(OtBu)]$  on  $SiO_{2-200}$  (**2**) and monopodal species  $[(\equiv SiO)V(=O)(OtBu)_2]$  on  $SiO_{2-700}$  (**3**). They were fully characterized by elemental analysis, IR, UV-Vis, solid state NMR ( $^1H$ ,  $^{13}C$ ,  $^{51}V$ ) and XANES. A new original method has been developed in this work for the preparation of supported tetrahedral vanadium oxo tripodal species  $[(\equiv SiO)_3V(=O)]$  via a thermal treatment of the grafted species, triggering  $\beta$ -H transfer and isobutene release. In addition to the characterization of all these tripodal species by mass balance analysis, IR, UV-Vis, solid-state NMR ( $^1H$ ) and XANES spectroscopy, the characterization by  $^{51}V$  MAS NMR allowed the confirmation of the chemical isotropic shift of tripodal V at -670 ppm, which is in agreement with recently reported results. The catalytic behavior of the resulting tripodal species was evaluated in the direct dehydrogenation of propane to propene, with a high activity and propene selectivity compared to a classical  $V_2O_5/SiO_2$  catalyst, prepared by aqueous impregnation of vanadium salts. Thus, site isolation proved to have a beneficial impact on the catalytic performances of these materials when compared to conventional catalysts. In particular, regarding the gradual deactivation of the catalyst generally reported and attributed to the formation of carbonaceous species, this phenomenon was barely observed in our case compared to the conventional  $V_2O_5$  supported on silica catalyst, which presents V-O-H acidic sites responsible for the coke formation.

## Acknowledgements

This work was carried out as a part of the BIZEOLCAT project, which has received funding from the European Union's Horizon 2020 research and innovation program under grant agreement No. 814671. In particular, J. A. is grateful for her PhD grant. AdM thanks Olivier Mathon and Kiril Lomachenko for their help during the recording of the X-ray absorption spectra at ESRF, on beam line BM23.

## References

- (1) Akah, A.; Al-Ghrami, M. Maximizing Propylene Production via FCC Technology. *Appl. Petrochem. Res.* **2015**, 5 (4), 377–392. <https://doi.org/10.1007/s13203-015-0104-3>.

- (2) Sattler, J. J. H. B.; Ruiz-Martinez, J.; Santillan-Jimenez, E.; Weckhuysen, B. M. Catalytic Dehydrogenation of Light Alkanes on Metals and Metal Oxides. *Chem. Rev.* **2014**, *114* (20), 10613–10653. <https://doi.org/10.1021/cr5002436>.
- (3) Hu, Z.-P.; Yang, D.; Wang, Z.; Yuan, Z.-Y. State-of-the-Art Catalysts for Direct Dehydrogenation of Propane to Propylene. *Chin. J. Catal.* **2019**, *40* (9), 1233–1254. [https://doi.org/10.1016/S1872-2067\(19\)63360-7](https://doi.org/10.1016/S1872-2067(19)63360-7).
- (4) Mazoyer, E.; Szeto, K. C.; Norsic, S.; Garron, A.; Basset, J.-M.; Nicholas, C. P.; Taoufik, M. Production of Propylene from 1-Butene on Highly Active “Bi-Functional Single Active Site” Catalyst: Tungsten Carbene-Hydride Supported on Alumina. *ACS Catal.* **2011**, *1* (12), 1643–1646. <https://doi.org/10.1021/cs2004054>.
- (5) Mazoyer, E.; Szeto, K. C.; Basset, J.-M.; Nicholas, C. P.; Taoufik, M. High Selectivity Production of Propylene from 2-Butene: Non-Degenerate Pathways to Convert Symmetric Olefins via Olefin Metathesis. *Chem. Commun.* **2012**, *48* (30), 3611–3613. <https://doi.org/10.1039/C2CC30172E>.
- (6) Mazoyer, E.; Szeto, K. C.; Merle, N.; Norsic, S.; Boyron, O.; Basset, J.-M.; Taoufik, M.; Nicholas, C. P. Study of Ethylene/2-Butene Cross-Metathesis over W-H/Al<sub>2</sub>O<sub>3</sub> for Propylene Production: Effect of the Temperature and Reactant Ratios on the Productivity and Deactivation. **2013**. <https://doi.org/10.1016/j.jcat.2013.01.016>.
- (7) Svelle, S.; Olsbye, U.; Joensen, F.; Bjørgen, M. Conversion of Methanol to Alkenes over Medium- and Large-Pore Acidic Zeolites: Steric Manipulation of the Reaction Intermediates Governs the Ethene/Propene Product Selectivity. *J. Phys. Chem. C* **2007**, *111* (49), 17981–17984. <https://doi.org/10.1021/jp077331j>.
- (8) Liu, X.; Wang, M.; Zhou, C.; Zhou, W.; Cheng, K.; Kang, J.; Zhang, Q.; Deng, W.; Wang, Y. Selective Transformation of Carbon Dioxide into Lower Olefins with a Bifunctional Catalyst Composed of ZnGa<sub>2</sub>O<sub>4</sub> and SAPO-34. *Chem. Commun.* **2018**, *54* (2), 140–143. <https://doi.org/10.1039/c7cc08642c>.
- (9) Pawelec, B.; Guil-Lopez, R.; Mota, N.; Fierro, J. L. G.; Navarro Yerga, R. M. Catalysts for the Conversion of CO<sub>2</sub> to Low Molecular Weight Olefins-A Review. *Materials* **2021**, *14* (22), 6952. <https://doi.org/10.3390/ma14226952>.
- (10) Nawaz, Z. Light Alkane Dehydrogenation to Light Olefin Technologies: A Comprehensive Review. *Rev. Chem. Eng.* **2015**, *31* (5), 413–436. <https://doi.org/10.1515/revce-2015-0012>.
- (11) Fridman, V. Z.; Xing, R. Deactivation Studies of the CrO<sub>x</sub>/Al<sub>2</sub>O<sub>3</sub> Dehydrogenation Catalysts under Cyclic Redox Conditions. *Ind. Eng. Chem. Res.* **2017**, *56* (28), 7937–7947. <https://doi.org/10.1021/acs.iecr.7b01638>.
- (12) Chalupka, K.; Thomas, C.; Millot, Y.; Averseng, F.; Dzwigaj, S. Mononuclear Pseudo-Tetrahedral V Species of VSiBEA Zeolite as the Active Sites of the Selective Oxidative Dehydrogenation of Propane. *J. Catal.* **2013**, *305*, 46–55. <https://doi.org/10.1016/j.jcat.2013.04.020>.
- (13) Takahara, I.; Saito, M.; Inaba, M.; Murata, K. Dehydrogenation of Propane over a Silica-Supported Vanadium Oxide Catalyst. *Catal. Lett.* **2005**, *102* (3), 201–205. <https://doi.org/10.1007/s10562-005-5856-4>.
- (14) Rossetti, I.; Fabbrini, L.; Ballarini, N.; Oliva, C.; Cavani, F.; Cericola, A.; Bonelli, B.; Piumetti, M.; Garrone, E.; Dyrbeck, H.; Blekkan, E. A.; Forni, L. V–Al–O Catalysts Prepared by Flame Pyrolysis for the Oxidative Dehydrogenation of Propane to Propylene. *Catal. Today* **2009**, *141* (3), 271–281. <https://doi.org/10.1016/j.cattod.2008.05.020>.
- (15) Cheng, L.; Ferguson, G. A.; Zygmont, S. A.; Curtiss, L. A. Structure-Activity Relationships for Propane Oxidative Dehydrogenation by Anatase-Supported

- Vanadium Oxide Monomers and Dimers. *J. Catal.* **2013**, *302*, 31–36. <https://doi.org/10.1016/j.jcat.2013.02.012>.
- (16) Karakoulia, S. A.; Triantafyllidis, K. S.; Tsilomelekis, G.; Boghosian, S.; Lemonidou, A. A. Propane Oxidative Dehydrogenation over Vanadia Catalysts Supported on Mesoporous Silicas with Varying Pore Structure and Size. *Catal. Today* **2009**, *141* (3), 245–253. <https://doi.org/10.1016/j.cattod.2008.05.024>.
- (17) Routray, K.; Reddy, K. R. S. K.; Deo, G. Oxidative Dehydrogenation of Propane on V<sub>2</sub>O<sub>5</sub>/Al<sub>2</sub>O<sub>3</sub> and V<sub>2</sub>O<sub>5</sub>/TiO<sub>2</sub> Catalysts: Understanding the Effect of Support by Parameter Estimation. *Appl. Catal. Gen.* **2004**, *265* (1), 103–113. <https://doi.org/10.1016/j.apcata.2004.01.006>.
- (18) Carrero, C. A.; Schloegl, R.; Wachs, I. E.; Schomaecker, R. Critical Literature Review of the Kinetics for the Oxidative Dehydrogenation of Propane over Well-Defined Supported Vanadium Oxide Catalysts. *ACS Catal.* **2014**, *4* (10), 3357–3380. <https://doi.org/10.1021/cs5003417>.
- (19) Wegener, S. L.; Marks, T. J.; Stair, P. C. Design Strategies for the Molecular Level Synthesis of Supported Catalysts. *Acc. Chem. Res.* **2012**, *45* (2), 206–214. <https://doi.org/10.1021/ar2001342>.
- (20) Wu, Y.-L.; Han, Z.-F.; Yan, X.; Lang, W.-Z.; Guo, Y.-J. Effective Synthesis of Vanadium-Doped Mesoporous Silica Nanospheres by Sol-Gel Method for Propane Dehydrogenation Reaction. *Microporous Mesoporous Mater.* **2022**, *330*, 111616. <https://doi.org/10.1016/j.micromeso.2021.111616>.
- (21) Kaphan, D. M.; Ferrandon, M. S.; Langeslay, R. R.; Celik, G.; Wegener, E. C.; Liu, C.; Niklas, J.; Poluektov, O. G.; Delferro, M. Mechanistic Aspects of a Surface Organovanadium(III) Catalyst for Hydrocarbon Hydrogenation and Dehydrogenation. *ACS Catal.* **2019**, *9* (12), 11055–11066. <https://doi.org/10.1021/acscatal.9b02800>.
- (22) Muylaert, I.; Voort, P. V. D. Supported Vanadium Oxide in Heterogeneous Catalysis: Elucidating the Structure–Activity Relationship with Spectroscopy. *Phys. Chem. Chem. Phys.* **2009**, *11* (16), 2826–2832. <https://doi.org/10.1039/B819808J>.
- (23) Nielsen, U. G.; Topsøe, N.-Y.; Brorson, M.; Skibsted, J.; Jakobsen, H. J. The Complete 51V MAS NMR Spectrum of Surface Vanadia Nanoparticles on Anatase (TiO<sub>2</sub>): Vanadia Surface Structure of a DeNO<sub>x</sub> Catalyst. *J. Am. Chem. Soc.* **2004**, *126* (15), 4926–4933. <https://doi.org/10.1021/ja030091a>.
- (24) Izumi, Y.; Kiyotaki, F.; Yoshitake, H.; Aika, K.; Sugihara, T.; Tatsumi, T.; Tanizawa, Y.; Shido, T.; Iwasawa, Y. Structure of Low Concentrations of Vanadium on TiO<sub>2</sub> Determined by XANES and Ab Initio Calculations. *Chem. Commun.* **2002**, No. 20, 2402–2403. <https://doi.org/10.1039/B207159B>.
- (25) Kozłowski, R.; Pettifer, R. F.; Thomas, J. M. X-Ray Absorption Fine Structure Investigation of Vanadium(V) Oxide-Titanium(IV) Oxide Catalysts. 2. The Vanadium Oxide Active Phase. *J. Phys. Chem.* **1983**, *87* (25), 5176–5181. <https://doi.org/10.1021/j150643a023>.
- (26) Wolke, S. I.; Buffon, R.; Filho, U. P. R. Surface Organometallic Chemistry of Vanadium(V): Reactivity of (ButN□)VNp<sub>3</sub> towards Silica. *J. Organomet. Chem.* **2001**, *625* (1), 101–107. [https://doi.org/10.1016/S0022-328X\(00\)00908-6](https://doi.org/10.1016/S0022-328X(00)00908-6).
- (27) Ruitenbeek, M.; van Dillen, A. J.; de Groot, F. M. F.; Wachs, I. E.; Geus, J. W.; Koningsberger, D. C. The Structure of Vanadium Oxide Species on  $\gamma$ -Alumina; an in Situ X-Ray Absorption Study during Catalytic Oxidation. *Top. Catal.* **2000**, *10* (3), 241–254. <https://doi.org/10.1023/A:1019180504770>.

- (28) Weckhuysen, B. M.; Jehng, J.-M.; Wachs, I. E. In Situ Raman Spectroscopy of Supported Transition Metal Oxide Catalysts: 18O<sub>2</sub>–16O<sub>2</sub> Isotopic Labeling Studies. *J. Phys. Chem. B* **2000**, *104* (31), 7382–7387. <https://doi.org/10.1021/jp000055n>.
- (29) Tanaka, T.; Yamashita, H.; Tsuchitani, R.; Funabiki, T.; Yoshida, S. X-Ray Absorption (EXAFS/XANES) Study of Supported Vanadium Oxide Catalysts. Structure of Surface Vanadium Oxide Species on Silica and  $\gamma$ -Alumina at a Low Level of Vanadium Loading. *J. Chem. Soc. Faraday Trans. 1 Phys. Chem. Condens. Phases* **1988**, *84* (9), 2987–2999. <https://doi.org/10.1039/F19888402987>.
- (30) Pelletier, J. D. A.; Basset, J.-M. Catalysis by Design: Well-Defined Single-Site Heterogeneous Catalysts. *Acc. Chem. Res.* **2016**, *49* (4), 664–677. <https://doi.org/10.1021/acs.accounts.5b00518>.
- (31) Popoff, N.; Mazoyer, E.; Pelletier, J.; Gauvin, R. M.; Taoufik, M. Expanding the Scope of Metathesis: A Survey of Polyfunctional, Single-Site Supported Tungsten Systems for Hydrocarbon Valorization. *Chem. Soc. Rev.* **2013**, *42* (23), 9035–9054. <https://doi.org/10.1039/C3CS60115C>.
- (32) Mazoyer, E.; Merle, N.; Mallmann, A. de; Basset, J.-M.; Berrier, E.; Delevoye, L.; Paul, J.-F.; Nicholas, C. P.; Gauvin, R. M.; Taoufik, M. Development of the First Well-Defined Tungsten Oxo Alkyl Derivatives Supported on Silica by SOMC: Towards a Model of WO<sub>3</sub>/SiO<sub>2</sub> Olefin Metathesis Catalyst. *Chem. Commun.* **2010**, *46* (47), 8944–8946. <https://doi.org/10.1039/C0CC02507K>.
- (33) Bouhoute, Y.; Garron, A.; Grekov, D.; Merle, N.; Szeto, K. C.; De Mallmann, A.; Del Rosal, I.; Maron, L.; Girard, G.; Gauvin, R. M.; Delevoye, L.; Taoufik, M. Well-Defined Supported Mononuclear Tungsten Oxo Species as Olefin Metathesis Pre-Catalysts. *ACS Catal.* **2014**, *4* (11), 4232–4241. <https://doi.org/10.1021/cs501294j>.
- (34) Espinas, J.; Pelletier, J.; Szeto, K. C.; Merle, N.; Le Roux, E.; Lucas, C.; Mallmann, A. D.; Basset, J.-M.; Taoufik, M.; Thivolle-Cazat, J. Preparation and Characterization of Metallacalixarenes Anchored to a Mesoporous Silica SBA-15 LP as Potential Catalysts. *Microporous Mesoporous Mater.* **2014**, *188*, 77–85. <https://doi.org/10.1016/j.micromeso.2013.12.031>.
- (35) Garron, A.; Stoffelbach, F.; Merle, N.; Szeto, K.; Thivolle-Cazat, J.; Basset, J.-M.; Norsic, S.; Taoufik, M. Improved Direct Production of 2,3-Dimethylbutenes and 3,3-Dimethylbutene from 2-Methylpropene on Tungsten Hydride Based Catalysts. *Catal. Sci. Technol.* **2012**, *2* (12), 2453–2455. <https://doi.org/10.1039/C2CY20539D>.
- (36) Popoff, N.; Espinas, J.; Pelletier, J.; Szeto, K. C.; Thivolle-Cazat, J.; Delevoye, L.; Gauvin, R. M.; Taoufik, M. Design and Application of a Hybrid Material Featuring Well-Defined, Tuneable Grafting Sites for Supported Catalysis. *ChemCatChem* **2013**, *5* (7), 1971–1977. <https://doi.org/10.1002/cctc.201200850>.
- (37) Popoff, N.; Szeto, K. C.; Merle, N.; Espinas, J.; Pelletier, J.; Lefebvre, F.; Thivolle-Cazat, J.; Delevoye, L.; De Mallmann, A.; Gauvin, R. M.; Taoufik, M. Enforcing Z-Selectivity in Olefin Metathesis through Use of Catalysts Grafted on Well-Defined Phenolic Hybrid Material. *Catal. Today* **2014**, *235*, 41–48. <https://doi.org/10.1016/j.cattod.2014.02.036>.
- (38) Szeto, K. C.; Mazoyer, E.; Merle, N.; Norsic, S.; Basset, J.-M.; Nicholas, C. P.; Taoufik, M. Metallacyclobutane Substitution and Its Effect on Alkene Metathesis for Propylene Production over W–H/Al<sub>2</sub>O<sub>3</sub>: Case of Isobutene/2-Butene Cross-Metathesis. *ACS Catal.* **2013**, *3* (9), 2162–2168. <https://doi.org/10.1021/cs400508v>.
- (39) Szeto, K. C.; Jones, Z. R.; Merle, N.; Rios, C.; Gallo, A.; Le Quemener, F.; Delevoye, L.; Gauvin, R. M.; Scott, S. L.; Taoufik, M. A Strong Support Effect in Selective

- Propane Dehydrogenation Catalyzed by Ga(i-Bu)<sub>3</sub> Grafted onto  $\gamma$ -Alumina and Silica. *ACS Catal.* **2018**, *8* (8), 7566–7577. <https://doi.org/10.1021/acscatal.8b00936>.
- (40) Szeto, K. C.; Loges, B.; Merle, N.; Popoff, N.; Quadrelli, A.; Jia, H.; Berrier, E.; De Mallmann, A.; Delevoye, L.; Gauvin, R. M.; Taoufik, M. Vanadium Oxo Organometallic Species Supported on Silica for the Selective Non-Oxidative Dehydrogenation of Propane. *Organometallics* **2013**, *32* (21), 6452–6460. <https://doi.org/10.1021/om400795s>.
- (41) Love, A. M.; Carrero, C. A.; Chieragato, A.; Grant, J. T.; Conrad, S.; Verel, R.; Hermans, I. Elucidation of Anchoring and Restructuring Steps during Synthesis of Silica-Supported Vanadium Oxide Catalysts. *Chem. Mater.* **2016**, *28* (15), 5495–5504. <https://doi.org/10.1021/acs.chemmater.6b02118>.
- (42) P. Högerl, M.; Goh, L. M. S.; Abou-Hamad, E.; Barman, S.; Dachwald, O.; Ahmad Pasha, F.; Pelletier, J.; Köhler, K.; D’Elia, V.; Cavallo, L.; Basset, J.-M. SOMC Grafting of Vanadium Oxytriisopropoxide (VO(O i Pr) <sub>3</sub>) on Dehydroxylated Silica; Analysis of Surface Complexes and Thermal Restructuring Mechanism. *RSC Adv.* **2018**, *8* (37), 20801–20808. <https://doi.org/10.1039/C8RA02419G>.
- (43) Barman, S.; Maity, N.; Bhatte, K.; Ould-Chikh, S.; Dachwald, O.; Haessner, C.; Saih, Y.; Abou-Hamad, E.; Llorens, I.; Hazemann, J. L.; Kohler, K.; D’Elia, V.; Basset, J. M. Single-Site VO<sub>x</sub> Moieties Generated on Silica by Surface Organometallic Chemistry: A Way To Enhance the Catalytic Activity in the Oxidative Dehydrogenation of Propane. *ACS Catal.* **2016**, *6* (9), 5908–5921. <https://doi.org/10.1021/acscatal.6b01263>.
- (44) Schweitzer, N. M.; Hu, B.; Das, U.; Kim, H.; Greeley, J.; Curtiss, L. A.; Stair, P. C.; Miller, J. T.; Hock, A. S. Propylene Hydrogenation and Propane Dehydrogenation by a Single-Site Zn<sup>2+</sup> on Silica Catalyst. *ACS Catal.* **2014**, *4* (4), 1091–1098. <https://doi.org/10.1021/cs401116p>.
- (45) Hu, B.; Schweitzer, N. M.; Zhang, G.; Kraft, S. J.; Childers, D. J.; Lanci, M. P.; Miller, J. T.; Hock, A. S. Isolated Fe<sup>II</sup> on Silica As a Selective Propane Dehydrogenation Catalyst. *ACS Catal.* **2015**, *5* (6), 3494–3503. <https://doi.org/10.1021/acscatal.5b00248>.
- (46) Le Quéméner, F.; Barman, S.; Merle, N.; Aljuhani, M. A.; Samantaray, M. K.; Saih, Y.; Szeto, K. C.; De Mallmann, A.; Minenkov, Y.; Huang, K.-W.; Cavallo, L.; Taoufik, M.; Basset, J.-M. Metathetic Oxidation of 2-Butenes to Acetaldehyde by Molecular Oxygen Using the Single-Site Olefin Metathesis Catalyst ( $\equiv\text{SiO}$ )<sub>2</sub>Mo(=O)<sub>2</sub>. *ACS Catal.* **2018**, *8* (8), 7549–7555. <https://doi.org/10.1021/acscatal.8b01767>.
- (47) Larabi, C.; Merle, N.; Le Quéméner, F.; Rouge, P.; Berrier, E.; Gauvin, R. M.; Le Roux, E.; de Mallmann, A.; Szeto, K. C.; Taoufik, M. New Synthetic Approach towards Well-Defined Silica Supported Tungsten Bis-Oxo, Active Catalysts for Olefin Metathesis. *Catal. Commun.* **2018**, *108*, 51–54. <https://doi.org/10.1016/j.catcom.2018.01.031>.
- (48) Mathon, O.; Beteva, A.; Borrel, J.; Bugnazet, D.; Gatla, S.; Hino, R.; Kantor, I.; Mairs, T.; Munoz, M.; Pasternak, S.; Perrin, F.; Pascarelli, S. The Time-Resolved and Extreme Conditions XAS (TEXAS) Facility at the European Synchrotron Radiation Facility: The General-Purpose EXAFS Bending-Magnet Beamline BM23. *J. Synchrotron Radiat.* **2015**, *22*, 1548–1554. <https://doi.org/10.1107/S1600577515017786>.
- (49) Ravel, B.; Newville, M. ATHENA, ARTEMIS, HEPHAESTUS: Data Analysis for X-Ray Absorption Spectroscopy Using IFEFFIT. *J. Synchrotron Radiat.* **2005**, *12* (4), 537–541. <https://doi.org/10.1107/S0909049505012719>.
- (50) Basset, J.-M.; Baudouin, A.; Bayard, F.; Candy, J.-P.; Copéret, C.; De Mallmann, A.; Godard, G.; Kuntz, E.; Lefebvre, F.; Lucas, C.; Norsic, S.; Pelzer, K.; Quadrelli, A.; Santini, C.; Soulivong, D.; Stoffelbach, F.; Taoufik, M.; Thieuleux, C.; Thivolle-Cazat,

- J.; Veyre, L. Preparation of Single Site Catalysts on Oxides and Metals Prepared via Surface Organometallic Chemistry. In *Modern Surface Organometallic Chemistry*; John Wiley & Sons, Ltd, **2009**; pp 23–73. <https://doi.org/10.1002/9783527627097.ch2>.
- (51) Conte, P.; Spaccini, R.; Piccolo, A. State of the Art of CP/MAS <sup>13</sup>C-NMR Spectroscopy Applied to Natural Organic Matter. *Prog. Nucl. Magn. Reson. Spectrosc.* **2004**, *44* (3–4), 215–223.
- (52) Bini, F.; Rosier, C.; Saint-Arroman, R. P.; Neumann, E.; Dablemont, C.; de Mallmann, A.; Lefebvre, F.; Niccolai, G. P.; Basset, J.-M.; Crocker, M.; Buijink, J.-K. Surface Organometallic Chemistry of Titanium: Synthesis, Characterization, and Reactivity of (:Si–O)NTi(CH<sub>2</sub>C(CH<sub>3</sub>)<sub>3</sub>)<sub>4-n</sub> (n = 1, 2) Grafted on Aerosil Silica and MCM-41. *Organometallics* **2006**, *25* (15), 3743–3760. <https://doi.org/10.1021/om050675g>.
- (53) Hu, J. Z.; Xu, S.; Li, W.-Z.; Hu, M. Y.; Deng, X.; Dixon, D. A.; Vasiliu, M.; Craciun, R.; Wang, Y.; Bao, X.; Peden, C. H. F. Investigation of the Structure and Active Sites of TiO<sub>2</sub> Nanorod Supported VO<sub>x</sub> Catalysts by High-Field and Fast-Spinning 51V MAS NMR. *ACS Catal.* **2015**, *5* (7), 3945–3952. <https://doi.org/10.1021/acscatal.5b00286>.
- (54) McGregor, J. Solid-State NMR of Oxidation Catalysts. *Met. Oxide Catal.* **2008**, 195–242.
- (55) Rice, G. L.; Scott, S. L. Characterization of Silica-Supported Vanadium(V) Complexes Derived from Molecular Precursors and Their Ligand Exchange Reactions. *Langmuir* **1997**, *13* (6), 1545–1551. <https://doi.org/10.1021/la960679d>.
- (56) Catana, G.; Rao, R. R.; Weckhuysen, B. M.; Van Der Voort, P.; Vansant, E.; Schoonheydt, R. A. Supported Vanadium Oxide Catalysts: Quantitative Spectroscopy, Preferential Adsorption of V<sup>4+</sup>/V<sup>5+</sup>, and Al<sub>2</sub>O<sub>3</sub> Coating of Zeolite Y. *J. Phys. Chem. B* **1998**, *102* (41), 8005–8012. <https://doi.org/10.1021/jp981482s>.
- (57) Gao, X.; Wachs, I. E. Investigation of Surface Structures of Supported Vanadium Oxide Catalysts by UV–vis–NIR Diffuse Reflectance Spectroscopy. *J. Phys. Chem. B* **2000**, *104* (6), 1261–1268. <https://doi.org/10.1021/jp992867t>.
- (58) Wegener, S. L.; Kim, H.; Marks, T. J.; Stair, P. C. Precursor Nuclearity Effects in Supported Vanadium Oxides Prepared by Organometallic Grafting. *J. Phys. Chem. Lett.* **2011**, *2* (3), 170–175. <https://doi.org/10.1021/jz101490p>.
- (59) Wong, J.; Lytle, F. W.; Messmer, R. P.; Maylotte, D. H. K-edge Absorption Spectra of Selected Vanadium Compounds. *Phys. Rev. B* **1984**, *30* (10), 5596–5610. <https://doi.org/10.1103/PhysRevB.30.5596>.
- (60) Nabavi, M.; Taulelle, F.; Sanchez, C.; Verdagner, M. Xanes and 51V Nmr Study of Vanadium-Oxygen Compounds. *J. Phys. Chem. Solids* **1990**, *51* (12), 1375–1382. [https://doi.org/10.1016/0022-3697\(90\)90020-G](https://doi.org/10.1016/0022-3697(90)90020-G).
- (61) Chaurand, P.; Rose, J.; Briois, V.; Salome, M.; Proux, O.; Nassif, V.; Olivi, L.; Susini, J.; Hazemann, J.-L.; Bottero, J.-Y. New Methodological Approach for the Vanadium K-Edge X-Ray Absorption Near-Edge Structure Interpretation: Application to the Speciation of Vanadium in Oxide Phases from Steel Slag. *J. Phys. Chem. B* **2007**, *111* (19), 5101–5110. <https://doi.org/10.1021/jp063186i>.
- (62) Keller, D. E.; Visser, T.; Soulimani, F.; Koningsberger, D. C.; Weckhuysen, B. M. Hydration Effects on the Molecular Structure of Silica-Supported Vanadium Oxide Catalysts: A Combined IR, Raman, UV–Vis and EXAFS Study. *Vib. Spectrosc.* **2007**, *43* (1), 140–151. <https://doi.org/10.1016/j.vibspec.2006.07.005>.
- (63) Nguyen, L. D.; Loridant, S.; Launay, H.; Pigamo, A.; Dubois, J. L.; Millet, J. M. M. Study of New Catalysts Based on Vanadium Oxide Supported on Mesoporous Silica for the Partial Oxidation of Methane to Formaldehyde: Catalytic Properties and

- Reaction Mechanism. *J. Catal.* **2006**, *237* (1), 38–48. <https://doi.org/10.1016/j.jcat.2005.10.016>.
- (64) Lewandowska, A. E.; Banares, M. A.; Tielens, F.; Che, M.; Dzwigaj, S. Different Kinds of Tetrahedral V Species in Vanadium-Containing Zeolites Evidenced by Diffuse Reflectance UV–vis, Raman, and Periodic Density Functional Theory. *J. Phys. Chem. C* **2010**, *114* (46), 19771–19776. <https://doi.org/10.1021/jp107589d>.
- (65) Liu, Y.-M.; Cao, Y.; Yi, N.; Feng, W.-L.; Dai, W.-L.; Yan, S.-R.; He, H.-Y.; Fan, K.-N. Vanadium Oxide Supported on Mesoporous SBA-15 as Highly Selective Catalysts in the Oxidative Dehydrogenation of Propane. *J. Catal.* **2004**, *224* (2), 417–428. <https://doi.org/10.1016/j.jcat.2004.03.010>.
- (66) Luca, V.; Thomson, S.; Howe, R. F. Spectroscopic Investigation of Vanadium Speciation Invanadium-Doped Nanocrystalline Anatase. *J. Chem. Soc. Faraday Trans.* **1997**, *93* (12), 2195–2202. <https://doi.org/10.1039/A608569E>.
- (67) Keränen, J.; Auroux, A.; Ek, S.; Niinistö, L. Preparation, Characterization and Activity Testing of Vanadia Catalysts Deposited onto Silica and Alumina Supports by Atomic Layer Deposition. *Appl. Catal. Gen.* **2002**, *228* (1), 213–225. [https://doi.org/10.1016/S0926-860X\(01\)00975-9](https://doi.org/10.1016/S0926-860X(01)00975-9).
- (68) Das, N.; Eckert, H.; Hu, H.; Wachs, I. E.; Walzer, J. F.; Feher, F. J. Bonding States of Surface Vanadium (V) Oxide Phases on Silica: Structural Characterization by Vanadium-51 NMR and Raman Spectroscopy. *J. Phys. Chem.* **1993**, *97* (31), 8240–8243.
- (69) Feher, F. J.; Walzer, J. F. Synthesis and Characterization of Vanadium-Containing Silsesquioxanes. *Inorg. Chem.* **1991**, *30* (8), 1689–1694. <https://doi.org/10.1021/ic00008a005>.
- (70) Jaegers, N. R.; Wan, C.; Hu, M. Y.; Vasiliu, M.; Dixon, D. A.; Walter, E.; Wachs, I. E.; Wang, Y.; Hu, J. Z. Investigation of Silica-Supported Vanadium Oxide Catalysts by High-Field 51V Magic-Angle Spinning NMR. *J. Phys. Chem. C* **2017**, *121* (11), 6246–6254. <https://doi.org/10.1021/acs.jpcc.7b01658>.
- (71) Miller, J. M.; Lakshmi, L. J. V2O5 Catalysts Supported on Al2O3–SiO2 Mixed Oxide: 51V, 1H MAS Solid-State NMR, DRIFTS and Methanol Oxidation Studies. *Appl. Catal. Gen.* **2000**, *190* (1), 197–206. [https://doi.org/10.1016/S0926-860X\(99\)00296-3](https://doi.org/10.1016/S0926-860X(99)00296-3).
- (72) Grant, J. T.; Carrero, C. A.; Love, A. M.; Verel, R.; Hermans, I. Enhanced Two-Dimensional Dispersion of Group V Metal Oxides on Silica. *ACS Catal.* **2015**, *5* (10), 5787–5793. <https://doi.org/10.1021/acscatal.5b01679>.
- (73) McGregor, J. Solid-State NMR of Oxidation Catalysts. In *Metal Oxide Catalysis*; John Wiley & Sons, Ltd, 2008; pp 195–242. <https://doi.org/10.1002/9783527626113.ch5>.
- (74) Das, N.; Eckert, H.; Hu, H.; Wachs, I. E.; Walzer, J. F.; Feher, F. J. *Bonding states of surface vanadium(V) oxide phases on silica: structural characterization by vanadium-51 NMR and Raman spectroscopy*. ACS Publications. <https://pubs.acs.org/doi/pdf/10.1021/j100133a020> (accessed 2022-05-17). <https://doi.org/10.1021/j100133a020>.
- (75) Terry, K. W.; Lugmair, C. G.; Tilley, T. D. Tris(Tert-Butoxy)Siloxo Complexes as Single-Source Precursors to Homogeneous Zirconia- and Hafnia-Silica Materials. An Alternative to the Sol-Gel Method. *J. Am. Chem. Soc.* **1997**, *119* (41), 9745–9756. <https://doi.org/10.1021/ja971405v>.
- (76) Niccolai, G. P.; Basset, J.-M. Primary Selectivity in the Activation of the Carbon-Hydrogen Bonds of Propane by Silica Supported Zirconium Hydride. *Appl. Catal. Gen.* **1996**, *146* (1), 145–156. [https://doi.org/10.1016/0926-860X\(96\)00120-2](https://doi.org/10.1016/0926-860X(96)00120-2).

- (77) C. Szeto, K.; Hardou, L.; Merle, N.; Basset, J.-M.; Thivolle-Cazat, J.; Papaioannou, C.; Taoufik, M. Selective Conversion of Butane into Liquid Hydrocarbon Fuels on Alkane Metathesis Catalysts. *Catal. Sci. Technol.* **2012**, *2* (7), 1336–1339. <https://doi.org/10.1039/C2CY20150J>.
- (78) Olsbye, U.; Virnovskaia, A.; Prytz, Ø.; Tinnemans, S.; Weckhuysen, B. Mechanistic Insight in the Ethane Dehydrogenation Reaction over Cr/Al<sub>2</sub>O<sub>3</sub> Catalysts. *Catal. Lett.* **2005**, *103*, 143–148. <https://doi.org/10.1007/s10562-005-6521-7>.
- (79) Harlin, M. E.; Niemi, V. M.; Krause, A. O. I. Alumina-Supported Vanadium Oxide in the Dehydrogenation of Butanes. *J. Catal.* **2000**, *195* (1), 67–78. <https://doi.org/10.1006/jcat.2000.2969>.
- (80) Chen, S.; Qin, Z.; Wang, G.; Dong, M.; Wang, J. Promoting Effect of Carbon Dioxide on the Dehydrogenation of Ethylbenzene over Silica-Supported Vanadium Catalysts. *Fuel* **2013**, *109*, 43–48. <https://doi.org/10.1016/j.fuel.2012.06.004>.
- (81) Takahara, I.; Saito, M.; Inaba, M.; Murata, K. Dehydrogenation of Propane over a Silica-Supported Vanadium Oxide Catalyst. *Catal. Lett.* **2005**, *102* (3), 201–205. <https://doi.org/10.1007/s10562-005-5856-4>.

## Supporting information

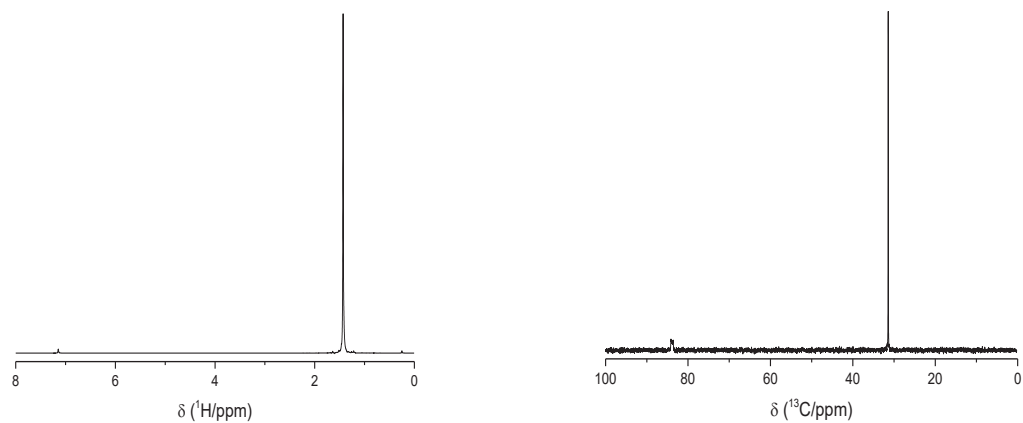


**Figure S1.** NMR spectra of  $[\text{V}(=\text{O})(\text{OtBu})_3]$  molecular complex: Left:  $^1\text{H}$  ( $d_1=1$  s) and Right:  $^{13}\text{C}$   $\{^1\text{H}\}$  ( $d_1=10$  s).

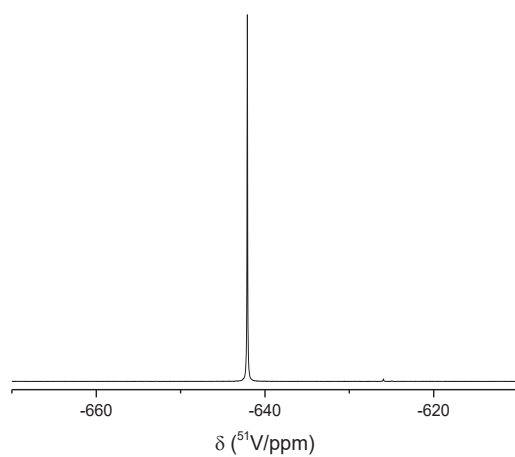


**Figure S2.**  $^{51}\text{V}$  NMR spectrum of  $[\text{V}(=\text{O})(\text{OtBu})_3]$  molecular complex ( $d_1=1$  s).

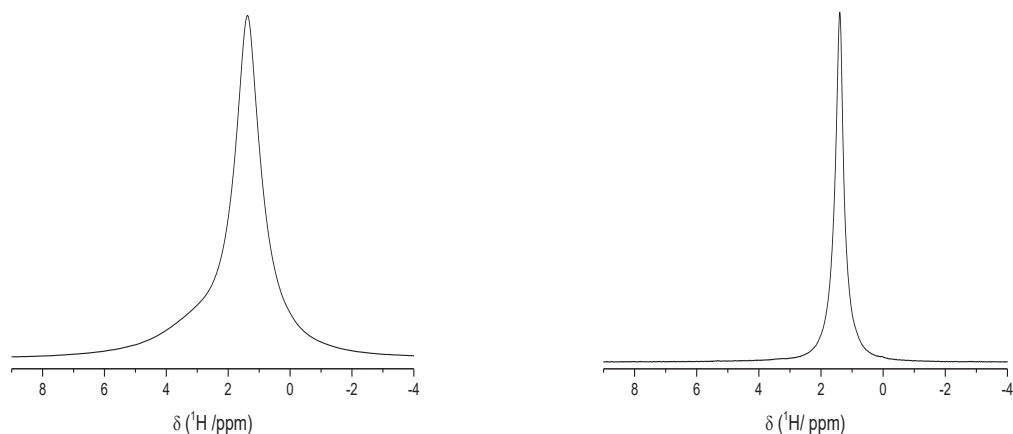
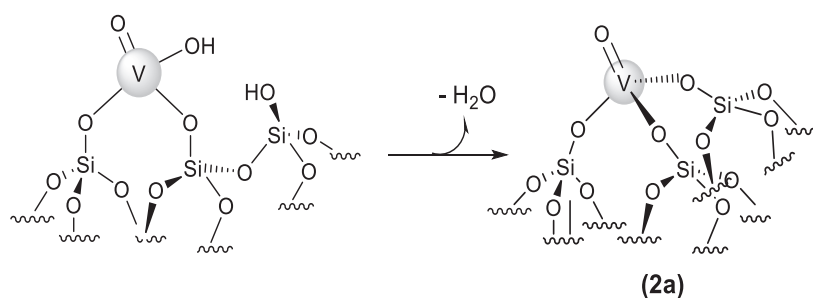
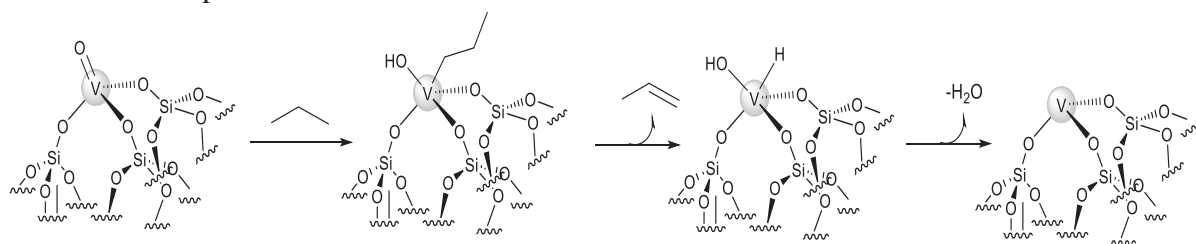


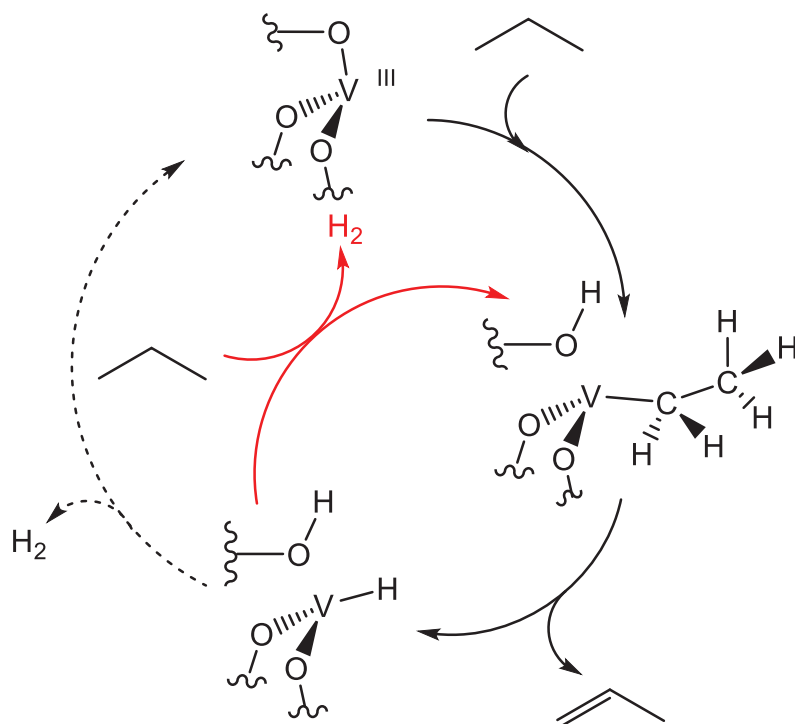
**Figure S3.**  $^1\text{H}$  MAS NMR spectra, **Left:**  $\text{V}(=\text{O})(\text{OtBu})_3/\text{SiO}_2\text{-200}$  and **Right:**  $\text{V}(=\text{O})(\text{OtBu})_3/\text{SiO}_2\text{-700}$  (11.7 T, 10 kHz MAS,  $d_1=5$  s)



**Scheme S1.** Partial condensation of V-OH with the remaining silanols, leading to the formation of tripodal V oxo and water



**Scheme S2.** Formation of tripodal active species after activation of propane and release of water



**Scheme S3.** Proposed mechanism for propane dehydrogenation based on V

## CHAPTER III. PART A

---

# Non-oxidative propane dehydrogenation over well-defined gallium catalysts prepared by surface organometallic chemistry

---



Jessy Abou Nakad,<sup>a</sup> Li Li,<sup>b</sup> Kai C. Szeto,<sup>a</sup> Aimery De Mallman,<sup>a</sup> Susannah L. Scott,<sup>\*b,c</sup>  
Mostafa Taoufik <sup>\*a</sup>

<sup>a</sup> Université de Lyon 1, CPE Lyon, CNRS-UMR 5128 – laboratoire Catalyse, Polymérisation, Procédés et Matériaux (CP2M), F-69616 Villeurbanne, France. Email: [mostafa.taoufik@univ-lyon1.fr](mailto:mostafa.taoufik@univ-lyon1.fr)

<sup>b</sup> Department of Chemistry & Biochemistry, University of California, Santa Barbara 93106-9510 USA.

<sup>c</sup> Department of Chemical Engineering, University of California, Santa Barbara 93106-5080 USA. Email: [sscott@uscb.edu](mailto:sscott@uscb.edu)

## Abstract

$\text{Ga}_2\text{O}_3$  supported on alumina is reported to be an effective catalyst in propane dehydrogenation (PDH). Its catalytic activity is attributed to the presence of isolated Ga sites, while Ga oligomers are reported to be less active and their formation responsible for deactivation of the catalyst. In this work, we report the preparation and characterization of a highly active and stable single-site catalyst for propane dehydrogenation consisting of Ga ions dispersed on alumina using surface organometallic chemistry. Supported  $\text{Ga}^{\text{III}}$  complexes were prepared by grafting  $[\text{Ga}(\text{O}^t\text{Bu})_3]_2$  onto  $\text{Al}_2\text{O}_{3-500}$  and  $\text{SiO}_{2-700}$ . On alumina, the surface reaction leads to monopodal  $[(\equiv\text{AlO})\text{Ga}(\text{O}^t\text{Bu})_2]$  (**I**), while on silica a dimeric site  $[(\equiv\text{SiO})_2\text{Ga}_2(\text{O}^t\text{Bu})_4]$  (**II**) is formed. Species **I** and **II** were fully characterized by elemental analysis, IR, solid-state NMR ( $^1\text{H}$  and  $^{13}\text{C}$ ) and XAS. The catalytic PDH activity and stability of **I** was better than that of **II**, showing that isolated Ga sites are more active and stable than dimeric Ga sites. Thermal treatment of **I** leads to the formation of tripodal  $[(\equiv\text{AlO})_3\text{Ga}]$  (**III**), proposed in the literature to be the active species in propane dehydrogenation. Its structure was confirmed by DRIFTS,  $^1\text{H}$  MAS NMR and XAS. The catalyst showed much better stability as function of time on stream compared to  $[(\equiv\text{AlO})\text{Ga}(\text{O}^t\text{Bu})_2]$ , suggesting that the isolated sites and tripodal structure of **III** limit deactivation by coke formation and/or Ga reduction. The structural evolution of  $[(\equiv\text{AlO})\text{Ga}(\text{O}^t\text{Bu})_2]$  monitored by *operando* XAS during PDH confirmed that it is more susceptible to reduction of  $\text{Ga}(\text{III})$  to  $\text{Ga}(\text{I})$ , compared to **III**.

## Introduction

The petrochemical and polymer industries are experiencing increased demand for propylene. The worldwide demand for propylene is expected to surge to 135 million tons in 2025, due to its diverse use in the large-scale production of polypropylene, acrylonitrile, and propylene oxide.<sup>1-3</sup> Steam cracking (SC) of light naphtha and fluid catalytic cracking (FCC) are the main traditional routes to produce propylene. The increased demand for propylene currently exceeds the capacity of these existing processes to satisfy the prediction expansion of growth in coming years.<sup>2,4</sup> This situation has inspired the development of alternative approaches for these processes. Hence, on-purpose technologies (OPT)<sup>5</sup> are used to boost propylene's production such as olefin metathesis<sup>6</sup>, methanol to olefins<sup>7</sup> and propane dehydrogenation (PDH).<sup>8,9</sup> Among them, PDH is of a paramount importance from the industrial point of view due to its high selectivity toward propylene obtained from a cheap feedstock of saturated

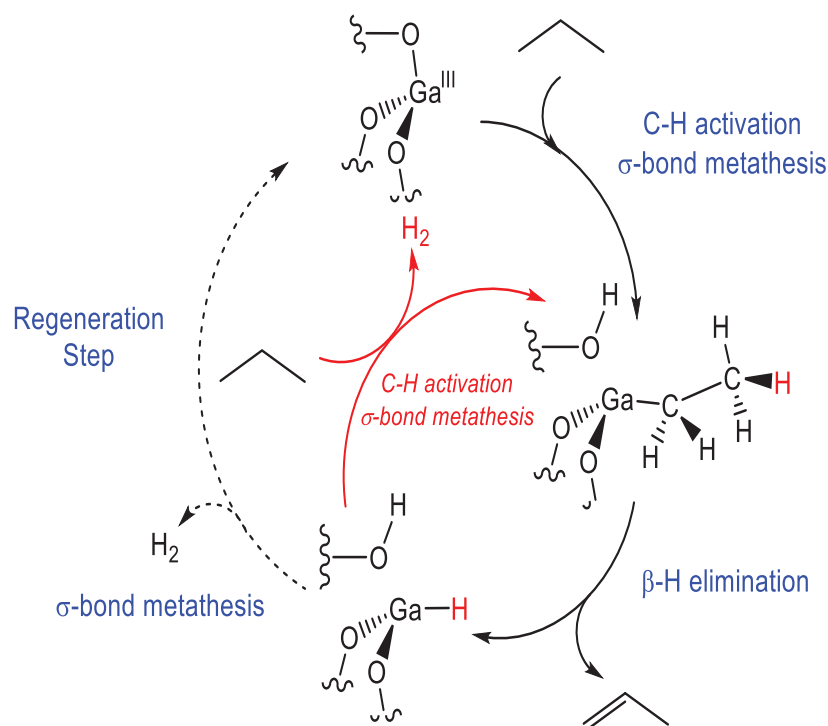
hydrocarbons, in particular propane from shale gas.<sup>9,10</sup> Indeed, many catalysts were widely studied for both oxidative and non-oxidative propane dehydrogenation reaction. Oxidative dehydrogenation reaction is exothermic where an oxidant, should be present during the reaction.<sup>11</sup> This process suffers from a low selectivity for propene compared to the non-oxidative dehydrogenation due to the formation of oxygenated molecules like CO<sub>2</sub> and CO.<sup>11-13</sup> The non-oxidative dehydrogenation reaction is known to be endothermic and requires therefore, high operating temperature (> 550°C) in order to obtain a high conversion.<sup>14-16</sup> Increasing the temperature usually leads to undesired reactions such as cracking, coke formation and restructuring of the catalyst (incorporation of the metal in the support or change in the oxidation state of the metal).<sup>17,18</sup> To date, the market is dominated by two industrial processes for non-oxidative dehydrogenation, Oleflex® (UOP) and Catofin® (ABB Lummus), using Pt-Sn/Al<sub>2</sub>O<sub>3</sub> and CrO<sub>x</sub>/Al<sub>2</sub>O<sub>3</sub>, respectively.<sup>19,20</sup> Oleflex®, employs low loading of noble metal Pt and operates at very high T °C and P (520 to 700 °C with 1-3 bar). In order to access a high selectivity toward propene and afford a high stability, Pt catalysts must be alloyed with promoters such as Sn. However, the deactivation is still observed and a frequent regeneration is required which results in a gradual loss of the catalyst's activity and stability.<sup>21</sup> On the other hand, Catofin® technology explores high loading of chromium oxides (18-20 wt%) supported on alumina, which operates at high temperatures ranging from 575 to 625 °C at reduced pressures (0.2 to 0.5 bar). The catalyst is often regenerated to overcome the deactivation from coke formation due to the high operating temperature and the presence of acidic sites (CrO<sub>x</sub>). The short lifetime of the catalyst is also affected by the incorporation of Cr in alumina, the formation of clusters on the surface and the change of Cr<sup>6+</sup>/Cr<sup>3+</sup> ratio on the surface.<sup>22</sup> To overcome the aforementioned issues, it is important to develop catalysts based on non-noble and non-toxic metals with low loading. Regarding the catalyst composition and preparation as well the operating conditions, many catalysts based on non-noble metals<sup>23-26</sup> have been evaluated for light alkane dehydrogenation. Supported metal oxide species, such as GaO<sub>x</sub>,<sup>27,28</sup> VO<sub>x</sub>,<sup>29,30</sup> FeO<sub>x</sub>,<sup>31</sup> CoO<sub>x</sub>,<sup>32</sup> SnO<sub>x</sub>,<sup>33</sup> ZnO<sub>x</sub>,<sup>34</sup> and ZrO<sub>x</sub><sup>23</sup> were widely studied in that manner. The catalyst composition of these metal oxides is highly dependent of the metal loading, the nature of the support and the preparation methods. The classical preparation methods including impregnation and sol-gel processes using salt precursors, leads to the formation of mono, di or oligomeric species that can under high temperature become volatile and poisoning for the catalyst's activity and lifetime.<sup>35-38</sup> In classical heterogeneous catalysts, it has been reported in literature a low concentration of the active sites resulting from these

preparations methods, hampering their characterization, as well as mechanistic analysis of the catalytic reaction, including the initiation and deactivation steps. This was confirmed in the case of GaOx-based catalysts prepared from gallium nitrate, especially with high loading of metal, that deactivates due to the reducibility of Ga (III) to Ga (I) and coke formation resulting in a low stability.<sup>9</sup> Recently, it has been reported that the presence of CO<sub>2</sub> or H<sub>2</sub>O in co-feed during PDH, can lead to high stability of the catalyst, attributed to the re-oxidation of Ga(I) sites and removal of coke formation.<sup>39-41</sup> Hence, to overcome this issue, it is of a paramount importance to immobilize isolated Ga species on the support with low loading of metal and different coordination sphere, that can lead to high active and stable catalyst, with high concentration of active sites.

Recently, we developed a strategy to access to well-defined single-site Ga catalyst using surface organometallic chemistry (SOMC). Previously, [Ga(*i*Bu)<sub>3</sub>] was grafted onto alumina and silica and the structures of the resulting species were characterized by various techniques. Their PDH activity showed that the monomeric species obtained on Al<sub>2</sub>O<sub>3</sub> is more active than the dimeric species obtained on SiO<sub>2</sub>. Both of them showed high selectivity (90%) in propene.<sup>42</sup> These results revealed that the Ga isolated sites on alumina are more promising than the supported GaOx prepared by classical methods. However, a gradual deactivation was observed in the case of [Ga(*i*Bu)<sub>3</sub>] on alumina, probably due to the formation of Ga (I), since there was no evidence of coke formation.

Although the PDH mechanism is still debated,<sup>43</sup> the active sites are suggested to be isolated tripodal (M<sup>3+</sup>) species.<sup>44-46</sup> The mechanism proposed was based on the work reported on Cr based catalysts by Sindre et al.,<sup>44</sup> involving a C-H activation of propane on the Ga-O pair site, leading to the formation of a Ga-propyl intermediate and an OH group by  $\sigma$ -bond metathesis, followed by a  $\beta$ -hydride elimination, resulting in a Ga-H site and propylene. The tripodal Ga active sites is regenerated after release of propene and H<sub>2</sub> (Scheme 1). Hence, it is believed that C-H activation happens across Ga-O bond,<sup>47</sup> and is probably more favorable at [-Ga-O-Al-] sites relative to [-Ga-O-Si-] sites, which can explain the difference in the catalytic results between [Ga(*i*Bu)<sub>3</sub>] on alumina and silica. In fact, the C-H bond activation of propane can take place via heterolytic splitting on highly reactive and ionic Ga-OAl and is more favorable compared to neutral Ga-OSi. Another parallel pathway was proposed based on C-H bond activation of propane on the generated Ga-H, intermediate active species, followed by a  $\beta$ -H elimination leading to the release of H<sub>2</sub> and propylene. The latter intermediate species (Ga-H) can undergo a reductive elimination leading to the formation of HO-Al and Ga

with oxidation state (I), inactive species in PDH. This pathway can be responsible for the deactivation observed during the catalytic dehydrogenation of propane on Ga based catalysts.



**Scheme 1.** Proposed PDH mechanism based on Ga

Since Ga tripodal species is proposed as an intermediate in the mechanism, we suggested the preparation of this surface species by using an appropriate molecular precursor that would allow us to generate well-defined isolated active sites of gallium. Hence, preparing an isolated gallium species with three oxygen atoms in its environment would decrease the possibility of reduction and would inhibit the gradual deactivation during PDH, a phenomenon previously seen in the case of  $[\text{Ga}(i\text{Bu})_3]$  on alumina. Thus, using SOMC on oxides combined to thermolysis has proven to be a powerful method to generate isolated well-defined surface species.<sup>48,49</sup>

In this context, we describe the synthesis of tris-alkoxide gallium precursor,  $[\text{Ga}(\text{O}t\text{Bu})_3]_2$  followed by a grafting on alumina and silica for the generation of isolated single site species. The resulting species were characterized by DRIFT, solid-state NMR ( $^1\text{H}$  and  $^{13}\text{C}$ ), XAS and mass balance analysis. After comparison between the effect of supports, a better catalytic performance was obtained on alumina than on silica. Thus, the grafted  $[\text{Ga}(\text{O}t\text{Bu})_3]$  on alumina was then treated by thermal treatment to afford Ga tripodal species, and was characterized as well by DRIFT, solid-state NMR ( $^1\text{H}$  and  $^{13}\text{C}$ ), XAS and mass balance

analysis. In order to compare the effect of ligand and local structure of Ga on the surface,  $[\text{Ga}(i\text{Bu})_3]$  on alumina was also prepared and similar results were obtained compared to the previous work.<sup>42</sup> The catalytic performance of the tripodal Ga on alumina was furthermore compared to  $[\text{Ga}(i\text{Bu})_3]$  and  $[\text{Ga}(\text{OtBu})_3]_2$  on alumina in PDH using the same conditions. XAFS Operando has been used in order to understand the high stability of Ga tripodal,  $(\equiv\text{AlO})_3\text{Ga}$ , compared to  $[\text{Ga}(i\text{Bu})_3]$  on alumina,  $[(\equiv\text{AlO})\text{Ga}(i\text{Bu})_2]$ .

## Experimental Methods

### General procedures

All experiments were carried out under a controlled atmosphere, using Schlenk and glove box techniques for organometallic synthesis. The synthesis and handling of supported species were carried out using high-vacuum lines (ca. 1 mPa) and glove boxes. Pentane was distilled from Na-benzophenone and NaK-benzophenone and degassed using freeze-pump-thaw cycles. OH titration was performed by reaction between the support and excess  $\text{Al}^i\text{Bu}_3$ , (which reacts quantitatively with surface hydroxyl groups on  $\text{Al}_2\text{O}_{3-500}$ <sup>50</sup> and on  $\text{SiO}_{2-700}$ )<sup>51</sup> followed by GC quantification of the liberated *t*-BuOH and isobutene.

### Preparation and characterization of $\text{Ga}(i\text{Bu})_3/\gamma\text{-Al}_2\text{O}_{3-500}$

Following a previously reported protocol,<sup>42</sup> a mixture of  $[\text{Ga}(i\text{Bu})_3]$  (200 mg, 0.80 mmol) and  $\gamma\text{-Al}_2\text{O}_{3-500}$  (1.0 g) in pentane (10 mL) was stirred at 25 °C for 4 h. After filtration, the solid was washed 5 times with pentane. The washing fractions and volatiles were transferred to another reactor to quantify *i*-BuH evolved during grafting by GC. The resulting white powder was dried under vacuum (1 mPa) at 25 °C for 15 h. Elemental analysis: Ga 1.97 wt%, C 2.85 wt%.

### Preparation and characterization of $[\text{Ga}(\text{OtBu})_3]_2$

The synthesis of the (tert-butoxy)gallium(III) dimer was achieved in 68 % yield from a mixture of  $[\text{Ga}(\text{NMe}_2)_3]$  and *t*-BuOH in hexane for 48 h, as described in the literature.<sup>52</sup> After purification in  $\text{CH}_2\text{Cl}_2$ , its dimeric structure was confirmed by the <sup>1</sup>H NMR signal at 1.6 ppm and two <sup>13</sup>C NMR signals at 78.5 and 32.1 ppm, characteristic of the bridging  $\mu\text{-OCMe}_3$  ligand (Figure S1).

### Preparation and characterization of $\text{Ga}(\text{OtBu})_3/\gamma\text{-Al}_2\text{O}_{3-500}$ (I)

A mixture of  $[\text{Ga}(\text{OtBu})_3]_2$  (200 mg, 0.70 mmol Ga) and  $\gamma\text{-Al}_2\text{O}_{3-500}$  (1.0 g) in pentane (10

mL) was stirred at 25 °C for 4 h. After filtration, the solid was washed 5 times with pentane. The washing fractions and volatiles were transferred to another reactor in order to quantify the *t*-BuOH evolved during grafting by GC using *n*-octane as an internal standard. The resulting white powder was dried under vacuum (1 mPa) at 25 °C for 15 h. Elemental analysis: Ga 1.97 wt%, C 2.85 wt%.

### **Preparation and characterization of [Ga(*O**t*Bu)<sub>3</sub>]<sub>2</sub>/SiO<sub>2-700</sub> (II)**

A mixture of [Ga(*O**t*Bu)<sub>3</sub>]<sub>2</sub> (200 mg, 0.70 mmol Ga) and SiO<sub>2-700</sub> (1.0 g) in pentane (10 mL) was stirred at 25 °C for 4 h. After filtration, the solid was washed 5 times with pentane. The washing fractions and volatiles were transferred to another reactor in order to quantify *t*-BuH evolved during grafting by GC using *n*-octane as an internal standard. The resulting white powder was dried under vacuum (1 mPa) at 25 °C for 15 h. Elemental analysis: Ga 3.7 wt%, C 6.1 wt%.

### **Preparation and characterization of tripodal Ga/Al<sub>2</sub>O<sub>3-500</sub> (III)**

Tripodal Ga species on Al<sub>2</sub>O<sub>3-500</sub> (III) was obtained by thermal treatment of Ga(*O**t*Bu)<sub>3</sub>/Al<sub>2</sub>O<sub>3-500</sub> (I) under vacuum at 300 °C for 2 h. Isobutene evolved during the process was collected in liquid N<sub>2</sub> cold trap for characterization by GC using *n*-octane as an internal standard

### **Analytical and Spectroscopic Procedures.**

Elemental analyses were carried out under air-free conditions by Mikroanalytisches Labor Pascher, Remagen (Germany). Gas analyses were performed on a Hewlett-Packard 5890 series II gas chromatograph, equipped with a flame ionization detector and an HP PLOT KCl/Al<sub>2</sub>O<sub>3</sub> column (50 m × 0.32 mm). Diffuse reflectance IR spectra were collected in an air-tight IR cell equipped with CaF<sub>2</sub> windows, using a Nicolet 6700 FT-IR spectrophotometer and recording 64 scans at 4 cm<sup>-1</sup> resolutions.

Solid-state NMR spectra were acquired on Bruker Avance 500 and Bruker Avance III 800 spectrometers (<sup>1</sup>H: 800.13 MHz, <sup>27</sup>Al: 208.50 MHz). For <sup>1</sup>H NMR experiments (18.8 T), the spinning frequency was 20 kHz, the recycle delay was 10 s, and 16 scans were collected using a 90 ° pulse excitation of 2.25 μs. The <sup>13</sup>C CP-MAS NMR spectrum was obtained at 11.74 T using the CP-MAS pulse sequence and high power <sup>1</sup>H decoupling at an RF field amplitude of 70 kHz. The spinning frequency was set to 10 kHz.

Ex situ XAS (EXAFS and XANES) spectra at the Ga K-edge (10,367 keV), were acquired at room temperature at ESRF on beamline BM23. A pair of Si(111) crystals was used as

monochromator and a system based on total reflection through a double X-ray mirror with an incidence angle variable from 2 to 5 mrad for harmonic rejection.<sup>53</sup> Spectra were recorded in transmission mode, between 10.1 and 11.4 keV. Four scans were collected for each sample. Each data set was collected simultaneously with a W metal foil reference ( $L_{III}$  edge at 10,206.8 keV: maximum in the first derivative), for energy calibration. Supported Ga materials were loaded in an Ar-filled glovebox into a sample holder equipped with air-tight Kapton windows. Data analyses were carried out using the program “Athena”<sup>54</sup> and the EXAFS fitting program “RoundMidnight”, from the “MAX” package,<sup>55</sup> using spherical waves. The program FEFF8 was used to calculate theoretical phases, amplitudes and  $S_0^2$  value based on model clusters of atoms.<sup>56</sup> Refinements were carried out by fitting the structural parameters  $N_i$ ,  $R_i$ , and  $\sigma_i$  for each shell, and the energy shift,  $\Delta E_0$  (constrained to be the same for all shells).

Quick XAS spectra were recorded at the Ga K-edge (10,367 eV) on beamline 2-2 at the Stanford Synchrotron Radiation Lightsource. It operates at 3.0 GeV with a current of 500 mA. Data were acquired in transmission mode, using a double crystal monochromator (Si(220)  $\phi = 90^\circ$ ) and  $N_2$ -filled ionization chambers as detectors. For energy calibration, a W foil ( $L_{III}$ -edge, 10,207 eV) was placed after the second ionization chamber following the incident beam direction.  $Ga^iBu_3/Al_2O_3$  (approx. 33 mg, Ga 1.97 wt%)<sup>42</sup> was loaded into an air-free *in-situ* XAS cell consisting of a thin-walled quartz capillary (Hilgenberg GmbH, 100 mm length, 3 mm O.D.) and held in place using quartz wool, inside an Ar-filled glove box.<sup>57</sup> The sample was pretreated thermally in flowing He (30 mL/min) and cooled in the same atmosphere. Four consecutive Quick XAS scans (92 s each) were recorded at 550 °C in flowing propane (2 mL/min, diluted in 8 mL/min He) to improve S/N.

XAS data were processed and analyzed using the Demeter software package.<sup>54</sup> A linear function was subtracted from the pre-edge region, then the edge jump was normalized using the Athena program. The  $\chi(k)$  data were isolated by subtracting a smooth, third-order polynomial approximating the absorption background of an isolated atom. The  $k^3$ -weighted  $\chi(k)$  data were treated with a Hanning window function, then Fourier-transformed. The distances to the scattering atoms ( $R_i$ ) and mean-squared displacements ( $\sigma_i^2$ ) were obtained by non-linear fitting with least-squares refinement of the EXAFS equation to the Fourier-transformed data in  $R$ -space, using the Artemis program. To simulate the EXAFS spectra of individual paths, crystallographic information files were imported into Artemis. EXAFS

spectra were generated using FEFF6.<sup>54</sup> Principal component analysis and linear combination fitting were conducted using the Athena software.

**Online Mass Spectroscopy.** An online mass spectrometer (Hiden QGA) was connected after the *in-situ* XAS cell to monitor the gas products released during the reaction. Ions with  $m/z = 2, 4, 17, 28, 30, 32, 41,$  and  $44$  were scanned using a Faraday detector, while ions with  $m/z = 16, 39$  and  $43$  were scanned using a SEM detector. The temperature was measured and recorded simultaneously.

### Reactivity testing

The reactivity of the supported catalysts in propane dehydrogenation was evaluated in a stainless steel, continuous flow reactor. The catalysts (50-100 mg) were diluted in SiC (Strem), affording a final catalyst bed mass of 2.5 g. Catalysts were loaded into the reactor inside a glovebox, and protected from the ambient atmosphere by a 4-way valve. Lines were purged extensively with the reaction gas prior to its introduction into the reactor. The catalyst bed was heated to 540 °C in flowing Ar (4 mL/min) before admitting propane (99.95 % Air Liquide, < 20 ppm propene). The molar flow rate was constant at  $1.7 \text{ mol}_{\text{C}_3} \cdot \text{mol}_{\text{Ga}}^{-1} \cdot \text{min}^{-1}$ , at  $P_{\text{total}} = 1 \text{ bar}$ ,  $T = 540 \text{ °C}$ , total flow rate =  $5 \text{ mL min}^{-1}$  (20 vol% propane in Ar). The feed gas was purified by passage through a column containing molecular sieves and activated  $\text{Cu}_2\text{O}/\text{Al}_2\text{O}_3$ , and the flow rate controlled by a Brooks mass flow controller. Products were determined by online GC (HP 6890, equipped with 50 m KCl/ $\text{Al}_2\text{O}_3$  column and an FID). Conversion was calculated based on calibration curve of all elements.

## Results and discussion

### Grafting $[\text{Ga}(\text{OtBu})_3]_2$ with alumina dehydroxylated at 500 °C (I)

In order to leverage our previous results on extensive characterization of alumina and alumina-supported catalysts, we selected a  $\gamma$ -alumina partially dehydroxylated at 500 °C to afford  $\text{Al}_2\text{O}_{3-500}$ . It has a B.E.T. surface area of  $200 \text{ m}^2 \cdot \text{g}^{-1}$  and a surface hydroxyl density of ca.  $2.0 \text{ nm}^{-2}$  ( $0.65 \text{ mmol g}^{-1}$ ).<sup>50</sup> These hydroxyl groups are potential sites for protonolysis of organometallic complexes. In addition, the thermal treatment of  $\gamma$ -alumina generates coordinatively-unsaturated, Lewis acidic Al sites that are electrophilic and therefore, potentially reactive towards organometallics either during grafting or in subsequent surface

reactions. For example, grafted fragments such as  $(\text{AlO})_{3-n}\text{Al}(i\text{-Bu})_n$  ( $n = 1, 2$ ) undergo isobutyl group transfer to neighboring cus sites.<sup>51</sup>

Partial consumption of surface hydroxyl groups was observed when either  $[\text{Ga}(i\text{Bu})_3]^{42}$  or  $[\text{W}(\equiv\text{C}t\text{Bu})(\text{CH}_2t\text{Bu})_3]^{51}$  were grafted onto this alumina. In these cases, only the terminal hydroxyls present on tetrahedral aluminum sites reacted with the W and Ga complexes, while with aluminium complex, all hydroxyl groups react. Hence, the reactivity of the surface hydroxyls of alumina is highly dependent on the nature of the organometallic complex.<sup>58</sup> It is reasonable to believe that this reactivity is related to the oxophilicity of the metal. Thus, gallium complexes bearing different ligands (e.g., alkyl or alkoxide) may show the same reactivity towards alumina.

Grafting of dimeric  $[\text{Ga}(\text{O}t\text{Bu})_3]_2$  onto  $\text{Al}_2\text{O}_{3-500}$  was carried out by impregnation from pentane at room temperature to give  $\text{Ga}(\text{O}t\text{Bu})_3/\text{Al}_2\text{O}_{3-500}$  (**I**). As for  $[\text{Ga}(i\text{Bu})_3]$  grafting,<sup>42</sup> DRIFT spectroscopy reveals a partial consumption of the hydroxyl groups (Figure 1). The remaining hydroxyls groups are probably due to their lower reactivity with Ga complexes as observed in the case of  $\text{Ga}(i\text{Bu})_3$  on alumina. Simultaneously, new bands appeared in the ranges  $3000\text{-}2800$  and  $1500\text{-}1300\text{ cm}^{-1}$ , corresponding to vibrational modes typical of the C-H stretching and bending modes of tert-butoxy ligands.

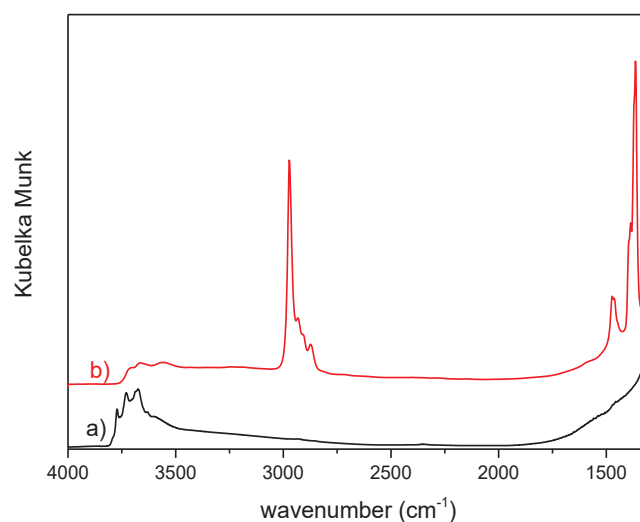


**Figure 1.** DRIFT spectra of  $\text{Al}_2\text{O}_{3-500}$ : (a) before, and (b) after reaction with  $[\text{Ga}(\text{O}t\text{Bu})_3]_2$  in pentane at  $25\text{ }^\circ\text{C}$ , affording  $\text{Ga}(\text{O}t\text{Bu})_3/\text{Al}_2\text{O}_{3-500}$  (**I**)

Elemental analysis of **I** revealed Ga and C contents of 1.97 and 2.78 wt%, respectively, corresponding to a C/Ga molar ratio of 8.2. Since the amount of grafted Ga corresponds to 0.28 mmol/g  $\gamma$ -alumina, and the original surface hydroxyl concentration was ca. 0.65 mmol/g,<sup>50</sup> the grafting stoichiometry Ga/OH is 0.43. Similar to  $[\text{Ga}(i\text{Bu})_3]$ , the reactivity of  $[\text{Ga}(\text{OtBu})_3]_2$  toward the various surface hydroxyls is lower than that of  $\text{Al}(i\text{Bu})_3$ , confirming that the reactivity of Ga complexes is independent of the nature of the ligands. GC analysis confirmed the release of 0.8 *t*-BuOH/Ga. Hence, the results suggest formation of monomeric  $[(\equiv\text{AlO})\text{Ga}(\text{OtBu})_2]$  via the protonolysis of a Ga-O*t*Bu bond by a surface hydroxyl group. A similar surface reaction was reported for  $\text{Ga}(i\text{Bu})_3/\text{Al}_2\text{O}_{3-500}$ .

More detailed information about the Ga coordination environment in **I** was obtained using solid-state NMR techniques. The  $^1\text{H}$  MAS NMR spectrum shows one intense, broad signal at 1.3 ppm assigned to  $\text{CH}_3$  protons (Figure 2, a). The  $^{13}\text{C}$  CP/MAS spectrum consists of two signals at 72 and 31.1 ppm. They are assigned to quaternary C and  $\text{CH}_3$ , respectively,<sup>52</sup> of the tert-butoxide ligands (Figure 2, b). The broad intensity between 65 and 80 ppm in  $^{13}\text{C}$  signal of quaternary carbon of tert-butoxide ligand does not allow to conclude about the structure of the resulting species. To gain additional information on this structure, **I** was then characterized using Ga K-edge EXAFS.

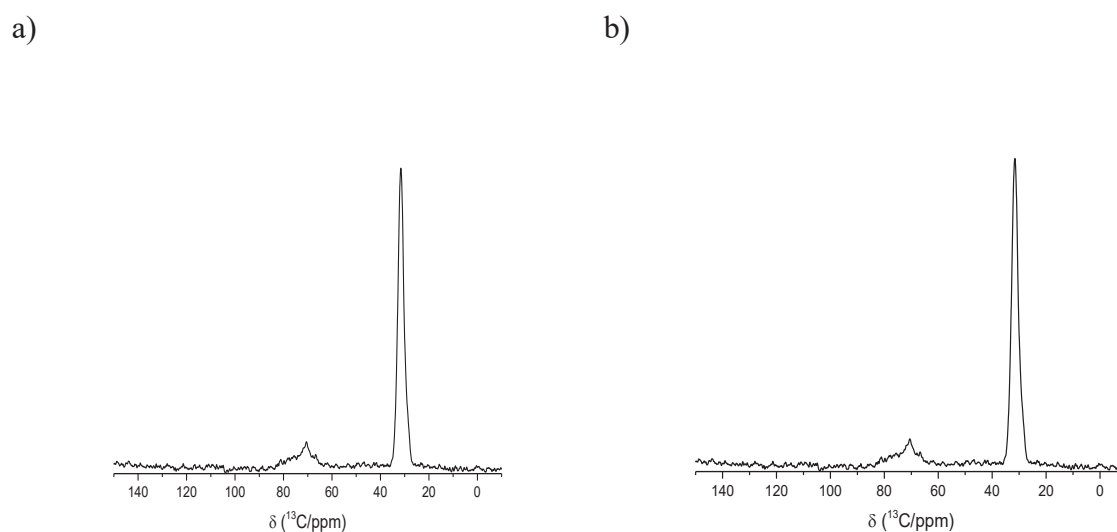


**Figure 2.** Solid-state NMR spectra of  $\text{Ga}(\text{OtBu})_3/\text{Al}_2\text{O}_{3-500}$ : (a)  $^1\text{H}$  MAS NMR (11.8 T, 10 kHz,  $d_1 = 10$  s), and (b)  $^{13}\text{C}$  CP-MAS NMR (11.7 T, 10 kHz,  $d_1 = 2$  s).

The XANES of  $[\text{Ga}(\text{OtBu})_3]_2$  supported on alumina is shown in Figure 3. The edge, at 10374.5 eV and the intense white line at 10376.5 eV, are characteristic of Ga(III) surrounded

by oxygen donor atoms.<sup>47</sup> For comparison,  $[\text{Ga}(i\text{Bu})_3]$  grafted on alumina, with one oxygen donor atom and two carbon donor atoms, has a lower Ga K-edge at 10,370.5 eV, followed by a broad, unstructured peak with a maximum at 10,371.5 eV. The XANES is therefore sensitive to the nature of the ligands around Ga.

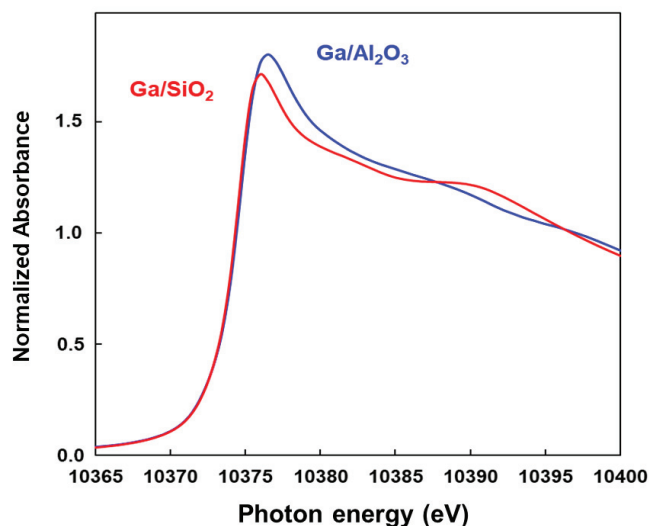


**Figure 3.** Comparison of Ga K-edge XANES for  $[\text{Ga}(\text{OtBu})_3]_2/\text{SiO}_{2-700}$  (red) and  $\text{Ga}(\text{OtBu})_3/\text{Al}_2\text{O}_{3-500}$  (blue).

The EXAFS of **I** agree with a monomeric structure (Figure 4, Table 1). The second peak in the Fourier transform (maximum in  $R-\delta$  at ca. 2.55 Å) is satisfactorily fitted with a combination Ga-C and Ga-Al paths. This contrasts with the EXAFS of **II** on silica (see below).

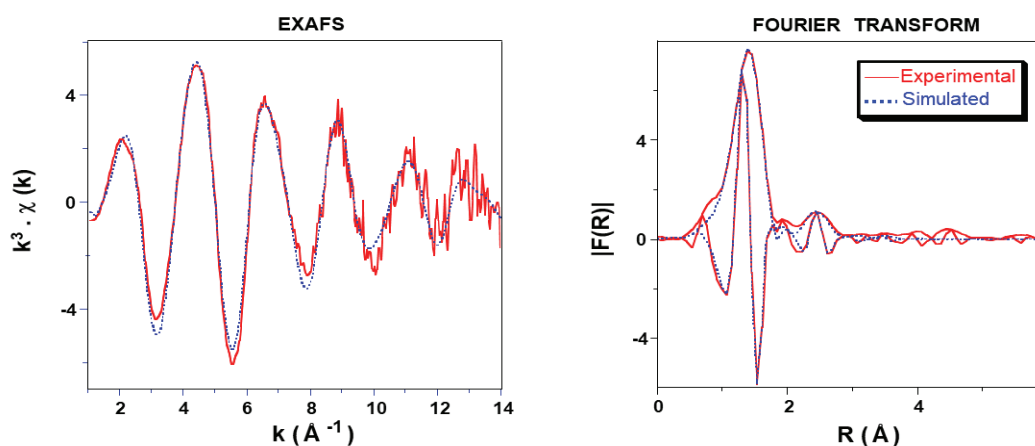


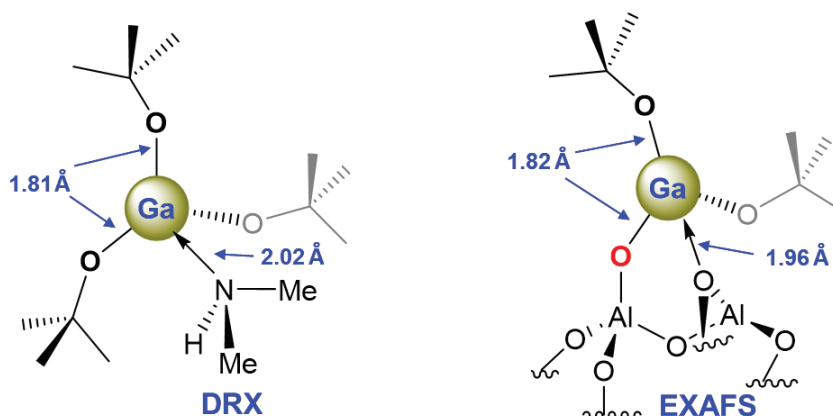
**Figure 4.** Ga K-edge EXAFS of  $\text{Ga}(\text{OtBu})_3/\text{Al}_2\text{O}_{3-500}$  in  $k^3$ -weighted  $k$ -space (left) and Fourier transformed  $R$ -space (right). Solid lines: data; Dashed lines: curvefit (spherical wave theory).

**Table 1.** Ga K-edge EXAFS curvefit parameters<sup>a</sup> for Ga(*O**t*Bu)<sub>3</sub>/Al<sub>2</sub>O<sub>3-500</sub>

Type of neighbor	N number of neighbors	R (Å)	σ <sup>2</sup> (Å <sup>2</sup> )
<b>Ga-O<sub>1</sub></b>	3.3(4)	1.825(12)	0.0057(11)
<b>Ga-O<sub>2</sub></b>	0.5(2)	1.96(7)	0.0059(36)
<b>Ga-C</b>	1.6(9)	2.98(5)	0.0048(35)
<b>Ga-Al</b>	1	3.60(28)	0.069(62)

<sup>a</sup> Single-scattering theory; values in parentheses represent the errors generated in RoundMidnight). Δk: [1.2 - 14.0 Å<sup>-1</sup>] - ΔR: [0.3 - 3.4 Å]; S<sub>0</sub><sup>2</sup> = 0.96; ΔE<sub>0</sub> = 4.7 ± 0.7 eV (global fit parameter); Fit residual: ρ = 5.8 %; Quality factor: (Δχ)<sup>2</sup>/ν = 3.09 (ν = 15/27).

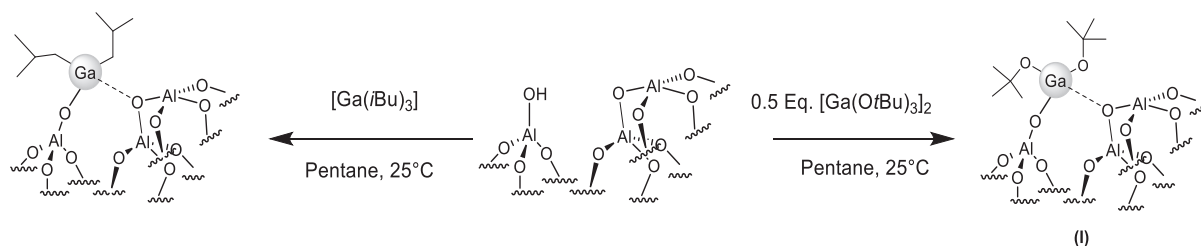
The curvefit is consistent with ca. three short Ga-O distances at 1.825(12) Å and less than one longer Ga-O distance at 1.96(7) Å. This agrees with a structure similar to that of monomeric molecular [Ga(*O**t*Bu)<sub>3</sub>(HNMe<sub>2</sub>)], characterized by single-crystal XRD. This complex has a Ga center coordinated by three O atoms at distances in the range [1.797 - 1.824 Å] and one N atom at 2.022(2) Å (Scheme 2).<sup>52</sup> The fit was improved by including more backscatterers, namely ca. two C atoms at 2.98(5) Å and one Al atom at 3.60(28) Å.



**Scheme 2.** Comparison of the structure of monomeric molecular Ga(*O**t*Bu)<sub>3</sub>(HNMe<sub>2</sub>), determined by single crystal XRD,<sup>47</sup> and the structure of Ga(*O**t*Bu)<sub>3</sub>/Al<sub>2</sub>O<sub>3-500</sub> consistent with the EXAFS.

Previously we reported that grafting of mononuclear [Ga(*t*Bu)<sub>3</sub>] onto Al<sub>2</sub>O<sub>3-500</sub> results in a similar mononuclear surface species by protonolysis. Hence, the structure on alumina is

monomeric, independent of the nuclearity of the molecular precursor or the type of ligand (alkyl or alkoxide), Scheme 3.



**Scheme 3.** Grafting of either  $[Ga(iBu)_3]$  or  $[Ga(OtBu)_3]_2$  onto  $Al_2O_{3-500}$  leads to monomeric species.

### Grafting $[Ga(OtBu)_3]_2$ onto silica dehydroxylated at 700 °C (II)

We also investigated the reactivity of  $[Ga(OtBu)_3]_2$  towards silica. This amorphous silica was partially dehydroxylated at 700 °C under high vacuum ( $10^{-5}$  mbar). The resulting  $SiO_{2-700}$  features non-interacting silanols (IR peak at  $3747\text{ cm}^{-1}$ , Figure 5) with an average density of  $0.70\text{ nm}^{-2}$ , corresponding to  $0.27\text{ mmol}_{OH}\text{ g}^{-1}$ .<sup>59</sup> The reaction of  $[Ga(OtBu)_3]_2$  with  $SiO_{2-700}$  completely consumes the silanols. The retention of some tert-butoxide ligands in **II** is evidenced by the appearance of characteristic C-H stretching and bending bands in the range  $3000\text{-}2800\text{ cm}^{-1}$  and  $1500\text{-}1300\text{ cm}^{-1}$ , respectively. The amounts of Ga and C, quantified by elemental analysis, are 3.7 and 6.1 wt %, respectively, representing a molar ratio of 9.6 C/Ga. The amount of Ga corresponds to  $0.528\text{ mmol}_{Ga}/\text{g}_{silica}$ , relative to an initial silanol surface density of  $0.27\text{ mmol}_{OH}/\text{g}$ , for a Ga/OH ratio of 1.95. Furthermore, GC analysis confirmed the release of  $0.47\text{ t-BuOH}/\text{Ga}$  during grafting. DRIFTS and the mass balance therefore suggest that, while protonolysis leads to a dinuclear site as the major surface species on  $SiO_{2-700}$ . Consequently, the structure resulting from grafting  $[Ga(OtBu)_3]_2$  onto silica differs from that obtained on alumina (*vide supra*).

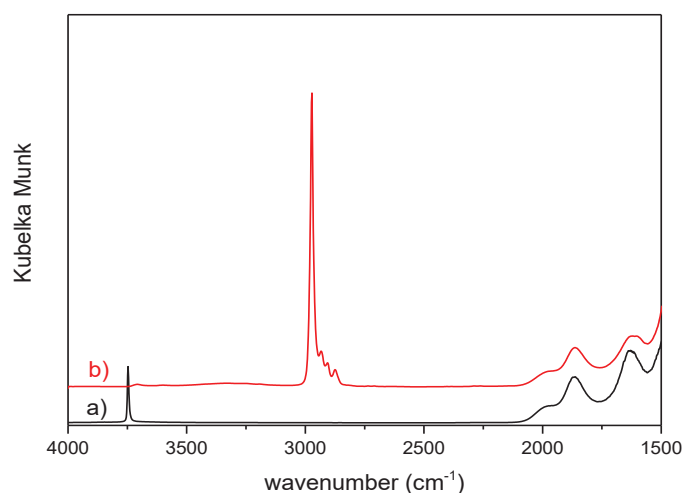


**Figure 5.** DRIFT spectra of SiO<sub>2-700</sub>: (a) before, and (b) after reaction with [Ga(O*t*Bu)<sub>3</sub>]<sub>2</sub> in pentane at 25°C.

The <sup>1</sup>H MAS NMR of **II** is similar to that obtained for **I**, consisting of a signal at 1.4 ppm corresponding to the CH<sub>3</sub> protons of the *tert*-butoxide ligands (Figure 6, a). The <sup>13</sup>C CP MAS spectrum of **II** is more informative about the local Ga environment. In addition to the signal at 31.1 ppm attributed to the methyl group of *tert*-butoxide ligand, the spectrum contains two resolved peaks at 71.6 and 78.6 ppm, attributed to the quaternary carbons (OCMe<sub>3</sub>) of terminal and bridging *tert*-butoxide ligands, respectively (Figure 6, b). Thus <sup>13</sup>C MAS NMR supports a dimeric structure for the product of grafting [Ga(O*t*Bu)<sub>3</sub>]<sub>2</sub> onto SiO<sub>2-700</sub>.

a)

b)

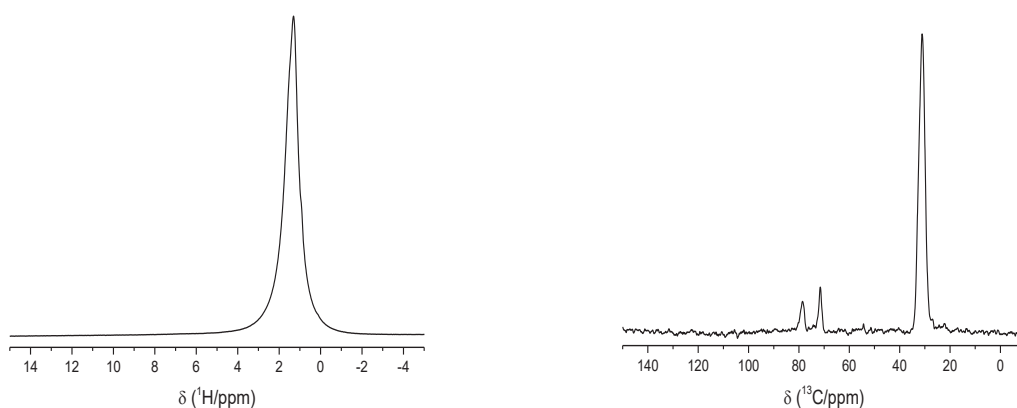


**Figure 6.** MAS NMR of [Ga(O*t*Bu)<sub>3</sub>]<sub>2</sub>/SiO<sub>2-700</sub>: **Left:** <sup>1</sup>H (11.8 T, 10 kHz, d<sub>1</sub>= 10 s) and **Right:** <sup>13</sup>C CP, revealing the retention of the ligands on the surface. (11.7 T, 10 kHz, d<sub>1</sub>= 2 s)

The average Ga coordination environment in  $[\text{Ga}(\text{OtBu})_3]_2/\text{SiO}_{2-700}$  was further studied by XAS spectroscopy. The Ga K-edge at 10374.4 eV (maximum in the first derivative), with a first maximum (intense white line) at 10376.1 eV, is characteristic of Ga(III) surrounded by oxygen atoms (Figure 3).<sup>47</sup> The EXAFS of  $\text{Ga}(\text{OtBu})_3/\text{SiO}_{2-700}$  is shown in Figure 7 and Table 2. The prominent second peak in the Fourier transform (maximum in  $R - \delta$  at ca. 2.55 Å) was modeled as a Ga-Ga path, since a fit using a combination of long (non-bonded) Ga-O, Ga-C and Ga-Si paths was unsatisfactory.

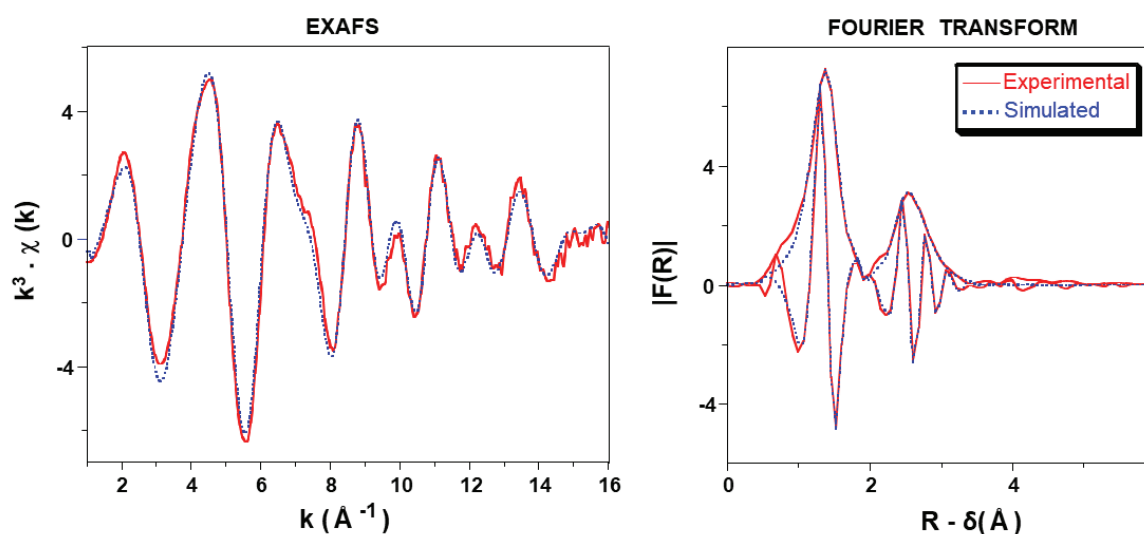


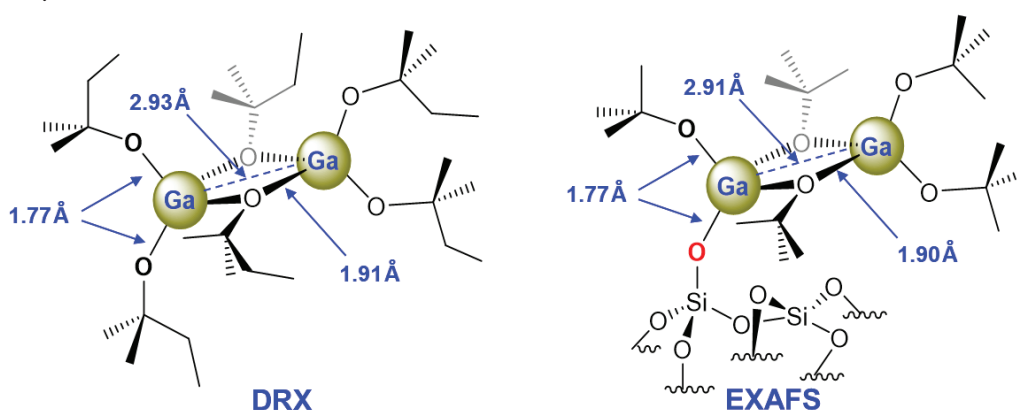
**Figure 7.** Ga K-edge EXAFS in  $k^3$ -weighted  $k$ -space (left), and Fourier transform (right, modulus and imaginary part; distances uncorrected by the phase shift), for  $[\text{Ga}(\text{OtBu})_3]_2/\text{SiO}_{2-700}$ . Solid lines: Experimental data; Dashed lines: Fit (spherical wave theory).

**Table 2.** Fit parameters for the EXAFS of  $[\text{Ga}(\text{O}^t\text{Bu})_3]_2/\text{SiO}_{2-700}$ .<sup>a</sup>

Path	$N^b$ number of neighbors	$R$ (Å)	$\sigma^2$ (Å <sup>2</sup> )
<b>Ga-O<sub>t</sub></b>	2.0	1.773(7)	0.0033(9)
<b>Ga-O<sub>b</sub></b>	2.0	1.90(1)	0.0048(14)
<b>Ga-Ga</b>	1.2(3)	2.91(1)	0.0063(8)
<b>Ga-C</b>	3.1(12)	3.15(6)	0.020(12)

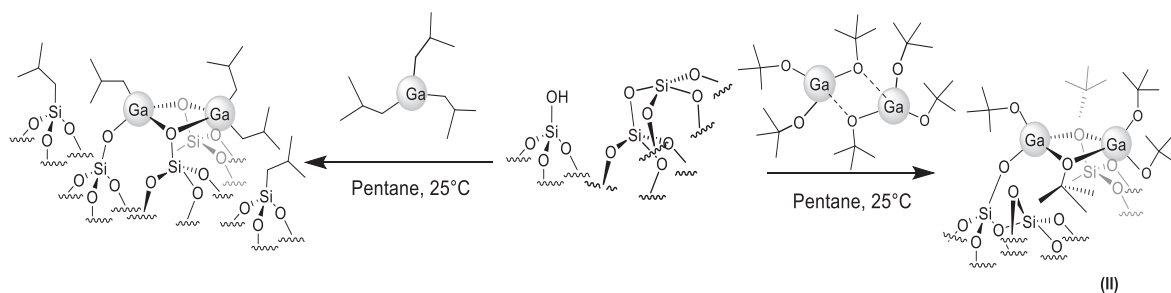
<sup>a</sup> Errors generated by the fitting program “RoundMidnight” are indicated in parentheses for each variable parameter.  $\Delta k$ : [1.2 - 16.0 Å<sup>-1</sup>] -  $\Delta R$ : [0.4 - 3.6 Å];  $S_0^2 = 0.96$ ;  $\Delta E_0 = 4.7 \pm 0.5$  eV (global fit parameter); Fit residual:  $\rho = 2.8$  %; Quality factor:  $(\Delta\chi)^2/\nu = 2.33$  ( $\nu = 19/32$ ).

The EXAFS curvefit gives a short Ga-O path at 1.773(7) Å ( $N = 2$ ), a longer Ga-O path at 1.90(1) Å ( $N = 2$ ), and a Ga-Ga path at 2.91(1) Å ( $N \sim 1$ ). The distances resemble those for dimeric  $[\text{Ga}(\mu\text{-OCMe}_2\text{Et})(\text{OCMe}_2\text{Et})_2]_2$ , a molecular compound characterized by XRD, in which the average  $\text{Ga-O}_{\text{terminal}}$  and  $\text{Ga-O}_{\text{bridging}}$  distances are  $1.773 \pm 0.007$  Å and  $1.914 \pm 0.004$  Å, respectively, and the  $\text{Ga-Ga}$  distance is  $2.927 \pm 0.004$  Å (Scheme 4).<sup>52</sup> Moreover, the EXAFS curvefit was improved by including a Ga-C path at 3.15(6) Å and a Ga-Si path at 3.41(5) Å. The latter presumably arises from one of the two Ga atoms which is anchored onto silica.



**Scheme 4.** Comparison of the dimeric structure of molecular  $[\text{Ga}(\mu\text{-OCMe}_2\text{Et})(\text{OCMe}_2\text{Et})_2]_2$ , determined by XRD,<sup>60</sup> with the structure of  $[\text{Ga}(\text{O}t\text{Bu})_3]_2/\text{SiO}_{2-700}$  proposed by EXAFS.

Recently, we reported the grafting of  $[\text{Ga}(i\text{Bu})_3]$  onto  $\text{SiO}_{2-700}$ , leading to a dinuclear species with the empirical formula  $[(\equiv\text{SiO})_3\text{Ga}_2(i\text{Bu})_3]$ , via a combination of ligand protonolysis by surface hydroxyls and isobutyl group transfer from Ga to Si via reactions with strained siloxane bridges. Thus, the materials obtained by grafting Ga complexes bearing either isobutyl or tert-butoxide ligands are both dinuclear, but have slightly different coordination spheres (Scheme 5). Indeed,  $[\text{Ga}(\text{O}t\text{Bu})_3]_2$  with Ga-O bonds but not Ga-C bonds does not transfer ligands to silicon.



**Scheme 5.** Grafting of  $[\text{Ga}(i\text{Bu})_3]$  or  $[\text{Ga}(\text{OtBu})_3]_2$  onto  $\text{SiO}_{2-700}$  leads to slightly different dinuclear species.

In conclusion, mass balance analysis, DRIFTS, solid-state NMR and EXAFS show that dimeric  $[\text{Ga}(\text{OtBu})_3]_2$  exhibits different reactivity towards  $\text{Al}_2\text{O}_{3-500}$  and  $\text{SiO}_{2-700}$ , leading to structurally distinct surface sites (monomeric on alumina, dinuclear on silica). The unexpected formation of monomeric species on alumina is attributed to the greater basicity of oxygen atoms on alumina, compared to silica. These oxygens are better ligands to Ga, stabilizing the tetrahedral monomeric surface species.<sup>60</sup>

### Catalytic propane dehydrogenation

The catalytic behavior of  $\text{Ga}(\text{OtBu})_3/\text{Al}_2\text{O}_{3-500}$  (**I**) and  $[\text{Ga}(\text{OtBu})_3]_2/\text{SiO}_{2-700}$  (**II**) was evaluated in propane dehydrogenation. **II** exhibits low activity, with an initial conversion of 12 % (Figure S2). Fast deactivation occurs starting immediately, and ending with stable conversion of 4.2 % after 400 min. After 1000 min, the major product is propene (87 %), accompanied by the formation of methane (6.8 %), ethene (6 %) and traces of benzene (<1 %, Figure S2). The by-products originate from propane cracking (*vide infra*) and a small degree of aromatization. Similar activity and selectivity were reported for the dimeric species obtained by grafting  $[\text{Ga}(i\text{Bu})_3]$  onto silica.<sup>42</sup> A previously reported<sup>61</sup> Ga/silica catalyst prepared by grafting of  $\text{Ga}[\text{OSi}(\text{OtBu})_3]_3$  onto silica followed by thermal decomposition was found to have mononuclear Ga sites. However, it showed virtually the same low propane dehydrogenation activity, independent of ligand type or Ga nuclearity.

In contrast, the behavior of **I** is different from that of **II**. The initial conversion is 16 % at early times on stream (Figure 8). However, after 1000 min, the conversion had decreased only slightly to 14 %. The products consisted mainly of propene (90 %), with minor amounts of methane (3 %), ethene (4 %),  $\text{C}_4$  (2 %) as well as traces (< 1 %) of ethane and benzene (Figure S4). Thus, the alumina-supported catalyst is much more stable than the silica-

supported catalyst. In order to study the ligand effect, we prepared  $[\text{Ga}(i\text{Bu})_3]$  on alumina as previously reported,<sup>42</sup> and tested its performance in propane dehydrogenation. Monomeric  $\text{Ga}(i\text{Bu})_3/\text{Al}_2\text{O}_{3-500}$  exhibited an initial propane conversion of 22 % and gradually deactivated, eventually stabilizing at 10 % conversion with a selectivity of 88 % toward propene (Figure 8). The global selectivity is shown as a function of time on stream in Figure S5. Thus  $\text{Ga}(i\text{Bu})_3/\text{Al}_2\text{O}_{3-500}$  is less stable than **I** under reaction conditions.

In addition, we observed a better catalytic performance for monomeric Ga species on alumina compared to dimeric Ga species on silica. This was previously reported in the case of  $[\text{Ga}(i\text{Bu})_3]$  on silica and alumina and could be attributed to the environment of the metal depending on the support and Ga-M bond (M= Al or Si). In other terms, the presence of Al around Ga seems more favorable than the presence of Si, resulting in an easier C-H activation on  $[\text{Ga}-\text{O}-\text{Al}]$  site than on strongest sites  $[\text{Ga}-\text{O}-\text{Si}]$ . The effect of the support showed that the selectivity in propylene is higher in the case of alumina compared to silica. This is probably due to the formation of coke in the case of dimeric species on silica, resulting in the formation of high amount of hydrogen leading to cracking and the formation of undesired products. This was observed in the selectivity in the case of silica, revealing a decrease in the propylene, while an increase of methane and ethene was observed.

a)

b)

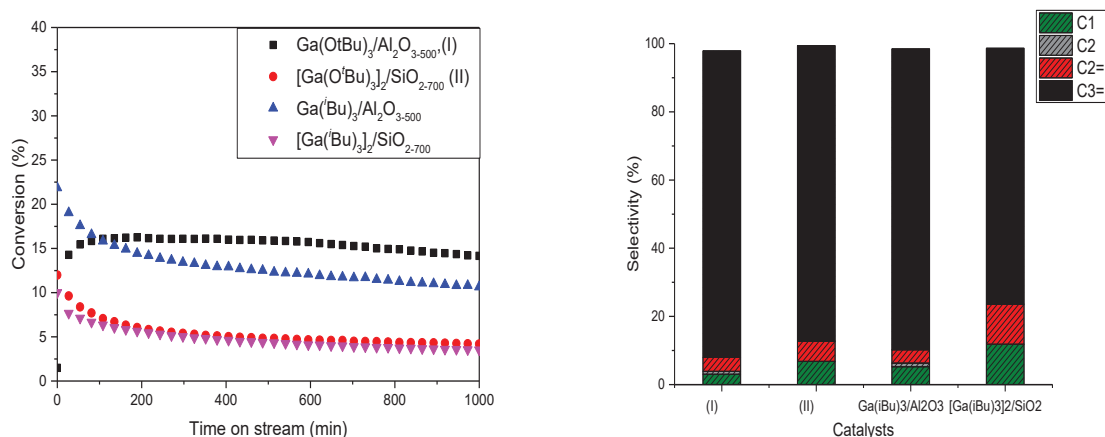


**Figure 8.** Comparison of (a) propane conversion, and (b) selectivity after 1000 min, in the reactions of  $\text{Ga}(\text{O}t\text{Bu})_3/\text{Al}_2\text{O}_{3-500}$ , **I** (■),  $[\text{Ga}(\text{O}t\text{Bu})_3]_2/\text{SiO}_{2-700}$ , **II** (●),  $\text{Ga}(i\text{Bu})_3/\text{Al}_2\text{O}_{3-500}$  (p) and  $[\text{Ga}(i\text{Bu})_3]_2/\text{SiO}_{2-700}$  (q). Reaction conditions: 1 bar, 540 °C, total flow rate 5 mL.min<sup>-1</sup> (20 % propane in Ar)

In conclusion, Ga-based pre-catalysts supported on alumina give better results in propane

dehydrogenation than Ga-based pre-catalysts supported on silica. The monomeric pre-catalyst sites on alumina are more active and selective compared to the dimeric pre-catalyst sites on silica. In addition, the ligands (alkyl vs. alkoxide) of the Ga pre-catalysts also affect the catalytic activity and stability. To further understand the origin of this difference, we synthesized the species proposed to be the PDH active site, tripodal  $[(\equiv\text{AlO})_3\text{Ga}]$ . This species (**III**) was characterized by DRIFTS, solid-state NMR, XAFS, and mass balance, and its PDH activity was tested in the same reaction conditions.

### Thermal treatment

Monomeric  $[(\equiv\text{AlO})_2\text{Ga}(\text{OtBu})]$  was heated at progressively higher temperatures under vacuum. The gas phase evolved was collected in a liquid  $\text{N}_2$  cold trap. DRIFTS reveals the total disappearance of vibrations in the range  $3000\text{--}2800\text{ cm}^{-1}$  and  $1500\text{--}1300\text{ cm}^{-1}$ , assigned to the  $\nu(\text{CH})$ , and  $\delta(\text{CH}_x)$  vibrations, respectively, of the perhydrocarbyl ligands, by  $300\text{ }^\circ\text{C}$  (Figure 9). Silanol vibrations at  $3800\text{--}3600\text{ cm}^{-1}$  reappear and become more intense at higher temperatures.

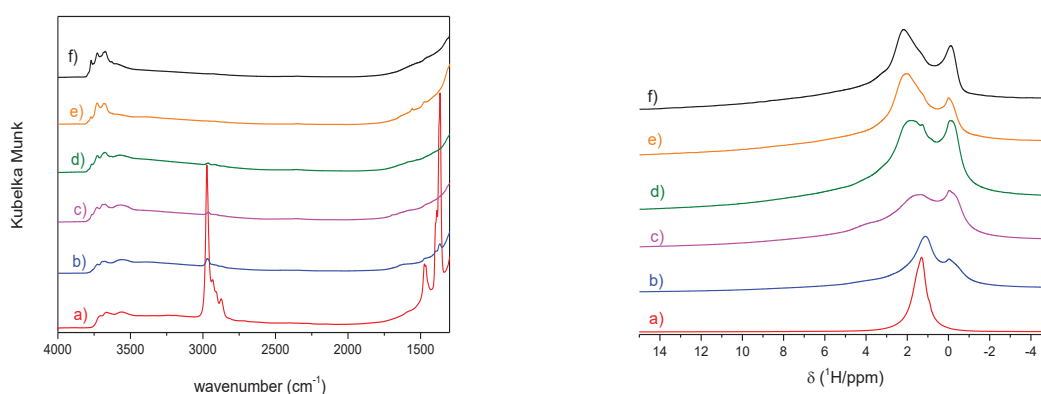
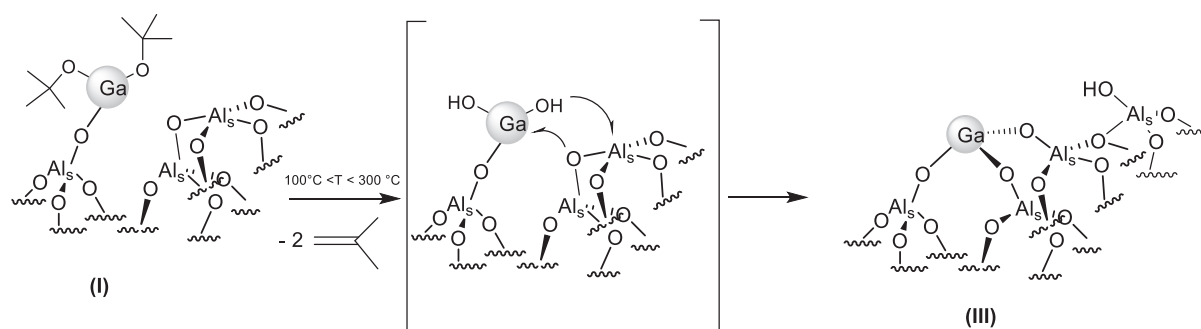


**Figure 9.** Spectra of  $\text{Ga}(\text{OtBu})_3/\text{Al}_2\text{O}_{3-500}$  (**I**) during controlled thermolysis at (a) room temperature, and after heating for 2 h at (b)  $100\text{ }^\circ\text{C}$ , (c)  $200\text{ }^\circ\text{C}$ , (d)  $300\text{ }^\circ\text{C}$ , and (e)  $500\text{ }^\circ\text{C}$ , as well as (f)  $\text{Al}_2\text{O}_{3-500}$ . **Left:** IR spectra. **Right:**  $^1\text{H}$  MAS NMR spectra (11.7 T, 10 kHz,  $d_1=10$  s).

The  $^1\text{H}$  MAS NMR spectrum of **I** show a similar evolution (Figure 9). The intense signal at 1.3 ppm attributed to the methyl groups of tert-butoxide ligands decreases in intensity upon heating, and almost disappears by  $300\text{ }^\circ\text{C}$ . At high temperatures, there are two main features: a rather sharp, high-field signal at  $-0.2$  ppm, and a broader signal resulting from several

overlapping signals at about 1.8 ppm. The latter has a low field shoulder from 3 to 4 ppm. These signals are characteristic of surface hydroxyl groups of alumina.<sup>50</sup>

The gas phase analysis by GC after thermal treatment at 300 °C revealed the formation of 1.9 isobutene/Ga, and traces of *t*-BuOH. Formation of isobutene is triggered by  $\beta$ -H elimination from a methyl group to form a hydroxygallium intermediate, followed by OH transfer from Ga to Al with cleavage of Al-O-Al bonds, leading to Al-OH formation. These new surface hydroxyls are associated with Al atoms having a variety of coordination numbers (Al<sub>IV</sub>, Al<sub>V</sub>, Al<sub>VI</sub>, Scheme 6) as revealed by DRIFTS and <sup>1</sup>H NMR. Thermal treatment of metal complexes bearing -OSi(O*t*Bu)<sub>3</sub> ligands was reported to lead to isobutene elimination at even lower temperatures (100 - 150 °C) to form silanols, without assistance from other ligands.<sup>62</sup> Recently, this strategy was used to prepare a tripodal oxovanadium on silica, which is a highly active PDF catalyst.



**Scheme 6.** Formation of tripodal gallium species **III** on alumina by elimination of tert-butoxide ligands.

Based on characterization of **III** by DRIFTS, <sup>1</sup>H MAS NMR, and mass balance, we infer that thermal treatment of **I** leads to a tripodal Ga species, ( $\equiv$ AlO)<sub>3</sub>Ga, which is an intermediate in the PDH catalytic cycle. Its structure was further investigated by Ga K-edge EXAFS (Figure 10, Table 3). The weak second peak in the Fourier Transform (maximum in R -  $\delta$  at ca. 2.75 Å) was satisfactorily fitted using only Ga-O and Ga-Al paths.

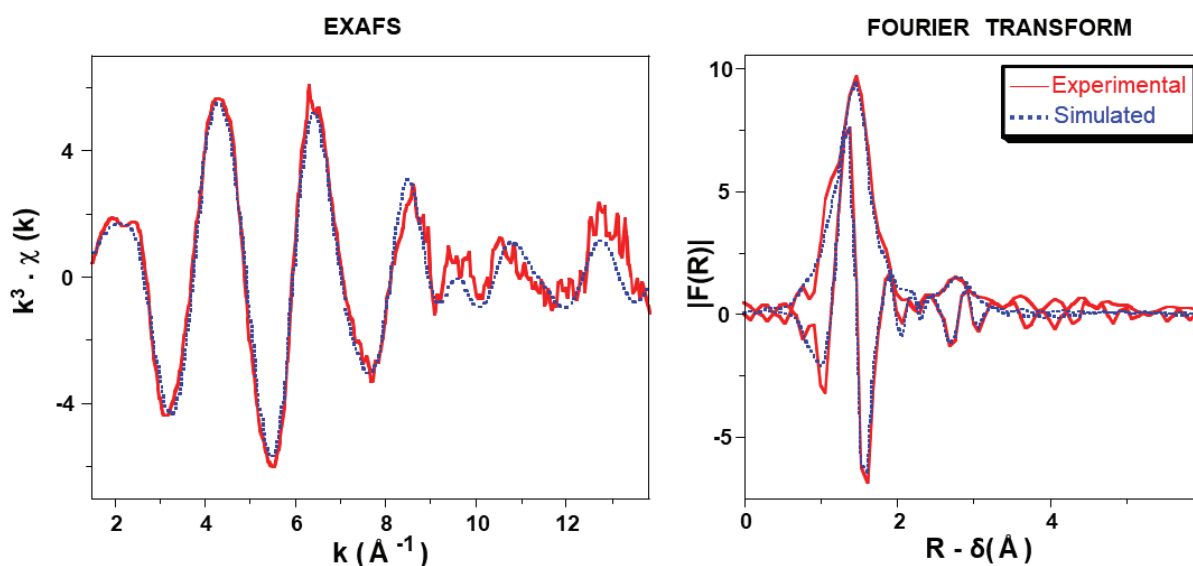


**Figure 10.** Ga K-edge EXAFS of  $\text{Ga}(\text{OtBu})_3/\text{Al}_2\text{O}_{3-500}$ , after a thermal treatment at  $300\text{ }^\circ\text{C}$ , in  $k^3$ -weighted  $k$ -space (left) and its Fourier transform (right, modulus and imaginary part; distances uncorrected for phase shift). Solid lines: Experimental data; Dashed lines: Fit (spherical wave theory).

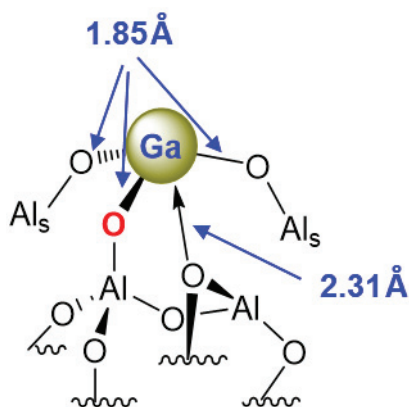
**Table 3.** Curvefit parameters for the EXAFS of  $\text{Ga}(\text{OtBu})_3/\text{Al}_2\text{O}_{3-500}$  after thermal treatment at  $300\text{ }^\circ\text{C}$ <sup>a</sup>

Path	N number of neighbors	R (Å)	$\sigma^2$ (Å <sup>2</sup> )
<b>Ga-O<sub>1</sub></b>	3	1.853(9)	0.0058(8)
<b>Ga-O<sub>2</sub></b>	1	2.31(2)	0.0023(16)
<b>Ga-O<sub>3</sub></b>	1	3.01(7)	0.0074(57)
<b>Ga-Al</b>	2	3.24(4)	0.0094(37)
<b>Ga-Al</b>	1	3.56(7)	0.0094 <sup>(b)</sup>

<sup>(a)</sup> Errors generated by the fitting program “RoundMidnight” are indicated for each variable parameter in parentheses.  $\Delta k$ : [1.5 - 13.8 Å<sup>-1</sup>] -  $\Delta R$ : [0.4 - 3.6 Å];  $S_0^2 = 0.96$ ;  $\Delta E_0 = 4.6 \pm 0.9$  eV (global fit parameter); Fit residual:  $\rho = 4.8\%$ ; Quality factor:  $(\Delta\chi)^2/\nu = 3.39$  ( $\nu = 17/27$ ). <sup>(b)</sup> Parameter constrained to the value of the one above.

The fit returns a short Ga-O distance at 1.853(9) Å ( $N = 3$ ) and a Ga-O longer distance at 2.31(2) Å ( $N = 1$ ). This result is reminiscent of the structure of monomeric molecular  $\text{Ga}(\text{OtBu})_3(\text{HNMe}_2)$ , characterized by XRD. In this complex, Ga is coordinated by three O

atoms at distances in the range [1.797 - 1.824 Å] and one N atom from the basic dimethylamine at 2.022(2) Å (Scheme 7).<sup>60</sup> The EXAFS fit was improved by including another Ga-O path at 3.01(7) Å and two Ga-Al paths, at 3.24(4) and 3.56(4) Å.



**Scheme 7.** Proposed structure of  $\text{Ga}(\text{OtBu})_3/\text{Al}_2\text{O}_{3-500}$  after thermal treatment at 300 °C, based on EXAFS.

### Catalytic performance of $(\equiv\text{AlO})_3\text{Ga}$

The PDH activity of **III** was evaluated and showed similar behavior to **I**, with a maximum conversion of 17 % at early times on stream (Figure 11) and minor deactivation resulting in 14.6 % conversion after 1000 min. The selectivity toward propene is high at 90 %, with small amounts of the by-products methane (3.3 %), ethene (4.1 %), C4 (2%) as well as traces of ethane and benzene (<1 %) (Figure S6). Thus it appears that when  $\text{Ga}(\text{OtBu})_3/\text{Al}_2\text{O}_{3-500}$  is heated under Ar up to 540 °C, at a rate of 4 °C/min, active sites similar to tripodal Ga (**III**) are formed. Furthermore, **III** exhibits similar catalytic performance (activity, selectivity and stability), even after exposure to air (Figure 11, Figure S7). Similar to  $\text{Ga}(\text{iBu})_3/\text{Al}_2\text{O}_{3-500}$  and  $\text{Ga}(\text{OtBu})_3/\text{Al}_2\text{O}_{3-500}$  (Figure 8), tripodal  $\text{Ga}/\text{Al}_2\text{O}_{3-500}$  exhibits some initial deactivation (Figure 12). The rate of deactivation slows significantly after 200 min. A high selectivity of 90 % toward propylene was recorded after 1000 min.

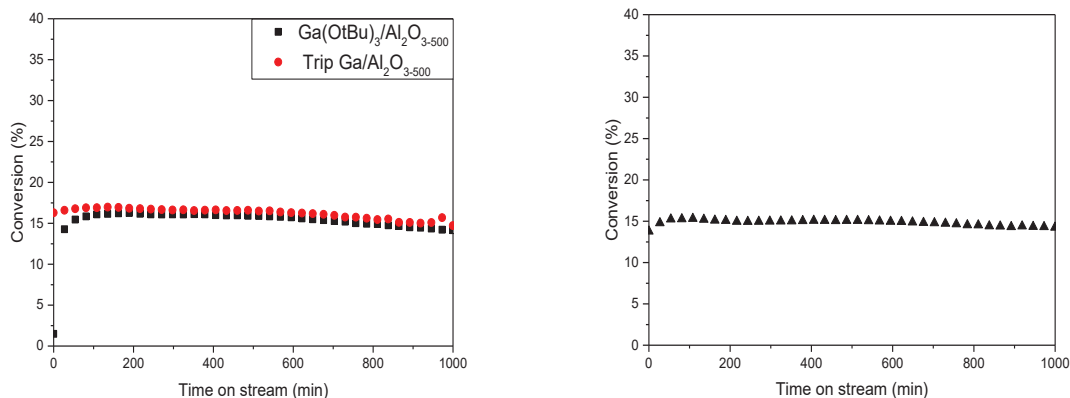


**Figure 11. Left:** Comparison of propane conversion catalyzed by Ga(OtBu)<sub>3</sub>/Al<sub>2</sub>O<sub>3-500</sub> (■) and tripodal Ga/Al<sub>2</sub>O<sub>3-500</sub> (●), **Right:** Propane conversion by tripodal Ga/Al<sub>2</sub>O<sub>3-500</sub> after exposure to air at room temperature for 20 min. Reaction conditions: 1 bar, 540 °C, total flow rate 5 mL. min<sup>-1</sup> (20 % propane in Ar)

Heating Ga(*i*Bu)<sub>3</sub>/Al<sub>2</sub>O<sub>3-500</sub> under Ar prior to introducing propane was expected to lead to the same active Ga tripodal sites, by transfer of isobutyl ligand on alumina. However, the catalytic behavior of Ga(*i*Bu)<sub>3</sub>/Al<sub>2</sub>O<sub>3-500</sub> differs from that of tripodal Ga/Al<sub>2</sub>O<sub>3-500</sub>. Thus Ga(*i*Bu)<sub>3</sub>/Al<sub>2</sub>O<sub>3-500</sub> may contain a mixture of Ga active sites. A site with higher activity may deactivate faster, while another, less active site may be more stable. In contrast, **III** appears to be a single site, based on its stability as a function of time. In order to confirm these hypotheses, we studied the structural evolution of Ga(*i*Bu)<sub>3</sub>/Al<sub>2</sub>O<sub>3-500</sub> using *operando* XAS during thermal treatment of the pre-catalyst under Ar, and during propane dehydrogenation.

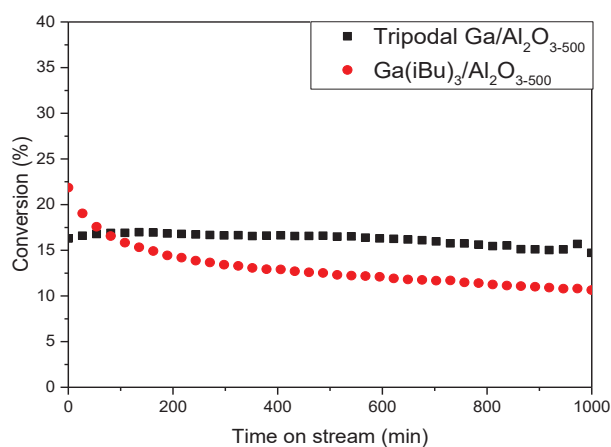
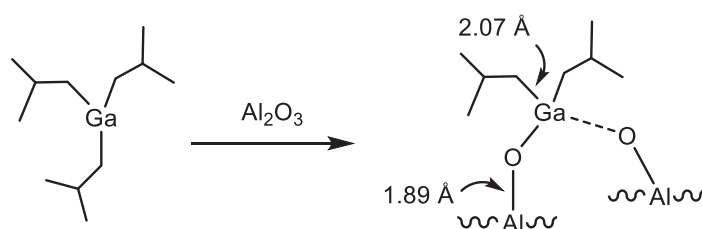


**Figure 12.** Comparison of propane conversion catalyzed by tripodal Ga/Al<sub>2</sub>O<sub>3-500</sub> (■) and Ga(*i*Bu)<sub>3</sub>/Al<sub>2</sub>O<sub>3-500</sub> (●) at 1 bar, 540 °C, total flow rate 5 mL min<sup>-1</sup> (20 % propane in Ar)

### EXAFS analysis of as-prepared Ga(*i*Bu)<sub>3</sub>/Al<sub>2</sub>O<sub>3-500</sub>

Previously, the reaction of [Ga(*i*Bu)<sub>3</sub>] with alumina was reported to remove one isobutyl ligand per Ga, resulting in attachment of the complex to the support via a Ga-O-Al linkage. The EXAFS data, acquired at 10 K, were analyzed using a simple four-coordinate model, [(≡AlO)Ga(*i*Bu)<sub>2</sub>], Scheme 8.<sup>42</sup> In the first coordination sphere, a shorter path ( $N = 1$ ) is associated with the Ga-O bond at  $(1.89 \pm 0.01) \text{ \AA}$ , in addition to a longer Ga-C1 path ( $N = 2$ ) at  $(2.07 \pm 0.02) \text{ \AA}$ .<sup>42</sup> Longer paths that may contribute FT magnitude intensity from 2-3  $\text{\AA}$  include weakly-bonded surface O, as well as non-bonded Ga-C2 and Ga-Al back-scattering.



**Scheme 8.** Proposed reaction of [Ga(*i*Bu)<sub>3</sub>] with partially dehydroxylated Al<sub>2</sub>O<sub>3-500</sub>, resulting in mononuclear, four-coordinate grafted Ga sites.<sup>42</sup>

In this work, the EXAFS of as-prepared Ga(*i*Bu)<sub>3</sub>/Al<sub>2</sub>O<sub>3-500</sub> was acquired at room temperature. The data are consistent with the previously reported cryogenic data, Figure 13 and Figure S8, and the curvefit parameters are similar, Table 4. However, the Ga-C1 distance,  $(2.00 \pm 0.01) \text{ \AA}$ , is slightly shorter in the fit of the room temperature data. It is still in the range of Ga-CH<sub>2</sub>R distances, 1.97 – 2.06  $\text{\AA}$ , found in molecular organogallium complexes.<sup>63,64</sup> A long Ga-O path at ca. 2.5  $\text{\AA}$ , previously attributed to a weakly coordinated oxygen from the Al<sub>2</sub>O<sub>3</sub>, was again included in the curvefit. When the fit was performed without this path, the result is visually less satisfying and the R-factor increased from 1.7 to 3.5%, Figure S9 and Table S1.

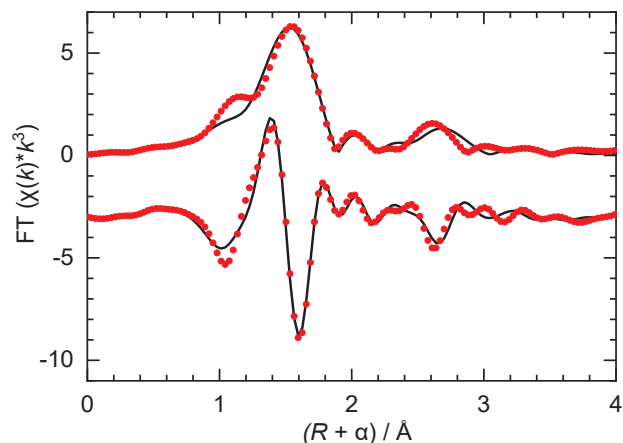


**Figure 13.** Ga K-edge EXAFS (point) for Ga(*i*Bu)<sub>3</sub>/Al<sub>2</sub>O<sub>3-500</sub> recorded at room temperature under He. The curvefit (line) includes a Ga-O path at ca. 2.5 Å.

**Table 4.** Curvefit Parameters<sup>a</sup> for Ga K-edge EXAFS of Ga(*i*Bu)<sub>3</sub>/Al<sub>2</sub>O<sub>3-500</sub>, recorded at room temperature under He

Path	$d^b / \text{Å}$	$N^c$	$R / \text{Å}$	$\sigma^2 / \text{Å}^2$
Ga – O1	1.863	1	1.86(2)	0.002(1) <sup>d</sup>
Ga – C1	2.066	2	2.00(1)	0.002(1) <sup>d</sup>
Ga – O2	2.585	1	2.49(3)	0.008(2) <sup>e</sup>
Ga – C2	2.976	2	2.96(3)	0.008(2) <sup>e</sup>
Ga – Al	3.325	1	3.24(4)	0.008(2) <sup>e</sup>

<sup>a</sup>  $S_0^2$  was fixed at 1.  $\Delta E_0$  was refined as a global fit parameter, returning a value of  $(4 \pm 1)$  eV. Data ranges:  $3.0 \leq k \leq 13.0 \text{ Å}^{-1}$ ,  $1.0 \leq R \leq 3.2 \text{ Å}$ . The number of variable parameters is 8, out of a total of 13.8 independent data points. The R-factor for this fit is 1.7 %. <sup>b</sup> The Ga-O1 and Ga-O2 reference distances are from the crystal structure of Ga<sub>2</sub>O<sub>3</sub> and SrGa<sub>2</sub>B<sub>2</sub>O<sub>7</sub>, respectively.<sup>65,66</sup> The Ga-C and Ga-Al distances are from crystal structures of organogallium compounds.<sup>67,68</sup> <sup>c</sup> The coordination numbers were constrained to integer values, based on the model. <sup>d</sup> Constrained to the same value. <sup>e</sup> Constrained to the same value.

### Evolution of the organogallium sites observed by *operando* XAS

The Ga K-edge XAS of Ga(*i*Bu)<sub>3</sub>/Al<sub>2</sub>O<sub>3-500</sub> was recorded as the sample was heated from room temperature to 540 °C at 10 °C/min in flowing He, Figure 14, a. The initial edge position is 10,372.5 eV, with a maximum at 10,374.7 eV. For temperatures below 200 °C, the XANES shows only minor changes, Figure 15, a. However, above 200 °C, the edge position shifts to

higher energy, as the maximum at 10,374.7 eV is gradually replaced by a more intense peak at 10,376.8 eV, Figure 15, b. As the temperature approaches 450 °C, the edge position stabilizes at 10,375.3 eV, Figure 15, c. Since Ga is initially in its maximum oxidation state, this edge shift of nearly 3 eV must arise due to a change in ligand environment, such as replacing isobutyl ligands with O-donor ligands derived from the alumina surface.

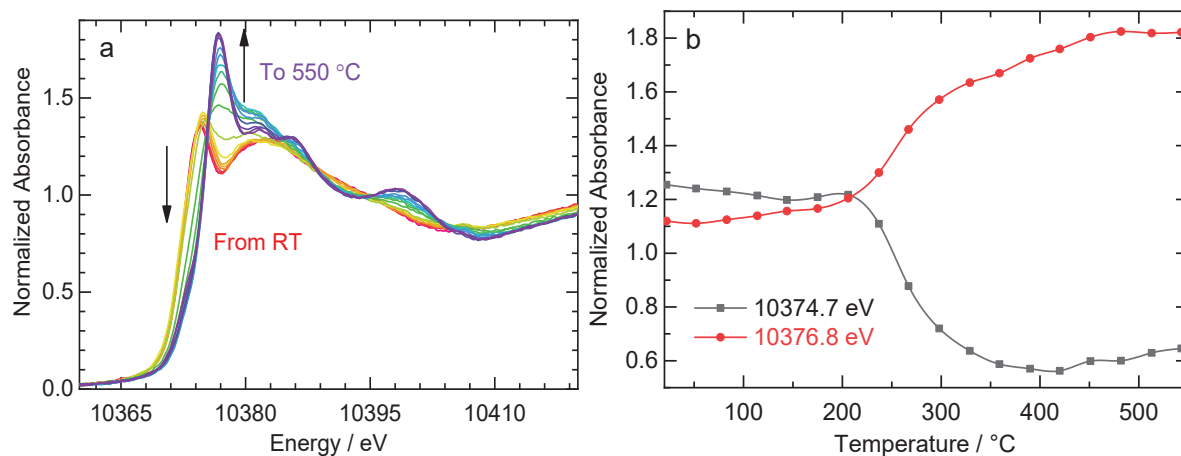


**Figure 14.** (a) Evolution of the Ga K-edge XANES for  $\text{Ga}(i\text{Bu})_3/\text{Al}_2\text{O}_{3-500}$ , recorded in flowing He while ramping the temperature from 23 °C (red) to 550 °C (purple) at 10 °C/min. Spectra in different temperature ranges are displayed in Figure 15 (b) Evolution of the Ga K-edge absorbance with temperature

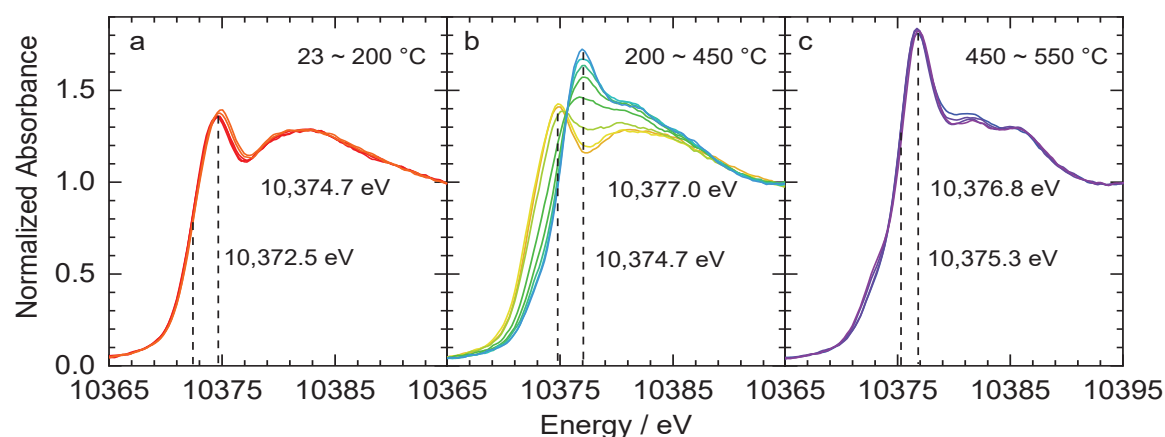


**Figure 15.** Evolution of the Ga K-edge XANES for  $\text{Ga}(i\text{Bu})_3/\text{Al}_2\text{O}_{3-500}$ , recorded in flowing He while ramping the temperature from 23 to 550 °C at 10 °C/min: (a) 23 – 200 °C (red to orange); (b) 200 – 450 °C (from orange to blue); (c) 450 – 550 °C (blue to purple).

The volatile products released during heating were analyzed by online mass spectrometry. From 100 – 450 °C, the major hydrocarbons include the expected isobutane ( $m/z = 43$ ) and isobutene ( $m/z = 39$ ), as well as propane ( $m/z = 29$ ) and propene ( $m/z = 41$ ), Figure 16. All appear simultaneously in this temperature range. Isobutane presumably forms by protonolysis involving residual surface protons. Isobutene may form by  $\beta$ -H elimination, in a reaction resembling the thermal decomposition of  $\text{GaR}_3$  ( $\text{R} = \text{Et}, ^n\text{Pr}, ^n\text{Bu}$ ),<sup>69,70</sup> and the reaction of Et groups on the GaAs(100) surface.<sup>71</sup> The resulting hydride may also contribute to isobutane formation by reductive elimination, although the edge position is not consistent with this being a major pathway. Homolytic cleavage of the Ga-C bond is also known in organogallium decomposition mechanisms, particularly at higher temperatures. One study reported slightly lower barriers for homolysis relative to  $\beta$ -H elimination for larger alkyl groups on GaAs(100).<sup>71</sup> However, these reactions also imply a reduction in oxidation state for Ga, which is inconsistent with the XANES.

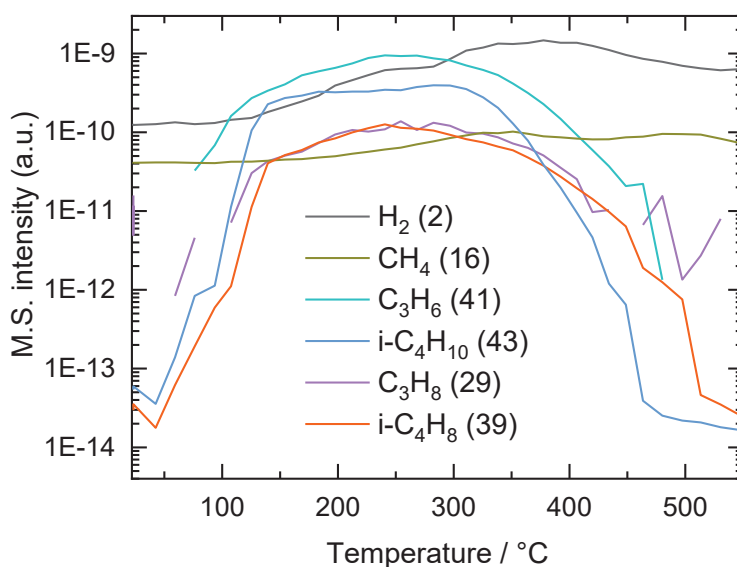


**Figure 16.** Evolution of gas products released from  $\text{Ga}(i\text{Bu})_3/\text{Al}_2\text{O}_{3-500}$  as a function of temperature recorded by mass spectroscopy in flowing He and while ramping the temperature from 23 °C to 550 °C at 10 °C/min.

Above 420 °C, few additional changes occur in the XANES, Figure 15,c. However, a weak shoulder superimposed on the edge appears at 10,372.4 eV, seen more clearly in Figure S10 and Figure S11. Its emergence causes the intensity at 10,376.8 eV to rise slightly. In the gas phase, signals for  $\text{H}_2$  ( $m/z = 2$ ) and methane ( $m/z = 16$ ) appear at higher temperatures, Figure 17. In principle, these products may arise via reductive elimination from  $[\text{Ga}^{\text{III}}\text{H}_2]$  and

[Ga<sup>III</sup>(H)(Me)] sites, respectively. However, such reactions would generate Ga(I) sites,<sup>72</sup> and since the edge position (10,375.3 eV) does not change significantly, it is unlikely that much Ga(III) is reduced.

The non-phase-corrected FT-EXAFS for Ga(*i*Bu)<sub>3</sub>/Al<sub>2</sub>O<sub>3-500</sub> recorded at room temperature contains two prominent peaks, at ca. 1.5 and 2.6 Å, Figure 18. The peak intensity at ca. 1.5 Å initially decreases slightly as the temperature rises from 23 – 200 °C, then increases gradually and shifts to a slightly shorter distance (ca. 1.3 Å) as the temperature is raised to 450 °C, Figure S12. These changes are consistent with the replacement of isobutyl ligands by oxygen-donor ligands, since the value of  $d(\text{Ga-O}) = 1.89 \text{ \AA}$  is shorter than  $d(\text{Ga-C}_a) = 2.00 \text{ \AA}$ . Above 100 °C, the peak at ca. 2.6 Å becomes broader, then new features appear between 2.5 and 3.5 Å. The wavelet-transform EXAFS reveals that the signal in the region 2.5 – 3.5 Å becomes stronger and more complex as the temperature is raised, Figure S13.

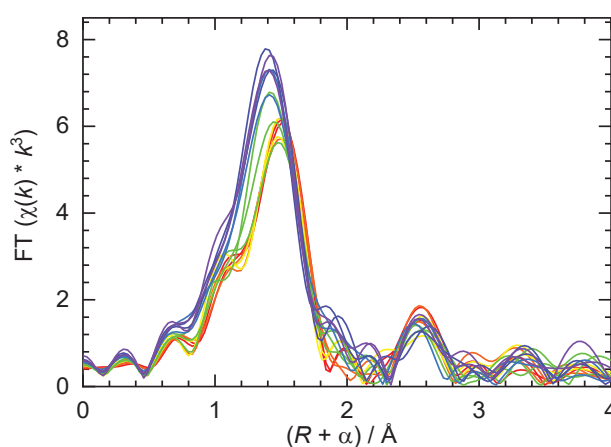


**Figure 17.** Evolution of the Ga K-edge EXAFS for Ga(*i*Bu)<sub>3</sub>/Al<sub>2</sub>O<sub>3-500</sub>, recorded in flowing He while ramping the temperature from 23 °C (red) to 550 °C (purple) at 10 °C/min.

### Principal Component Analysis

The evolution of the XANES region for Ga(*i*Bu)<sub>3</sub>/Al<sub>2</sub>O<sub>3-500</sub> from 23 to 550 °C was assessed via principal component analysis (PCA). All 18 XANES spectra from 23 to 550 °C, covering the region between 10,322 and 10,522 eV, were used to find the principal components. Just two components account for 0.9990 cumulative variance (Figure 18, a). The first component (variance 0.9776) consists of a rising edge followed by oscillations, similar to a XANES

spectrum. Its primary role is to reproduce the edge jump. The second component (variance 0.0214) is predominantly a simple oscillation at 10,368 – 10,381 eV. The contributions of the other components are minimal.

The spectra were reconstructed by linear combination fitting (LCF) of the first two PCA components. Changes in the contributions of each component are shown as a function of temperature in Figure 18, b. The contribution of the first component is unchanged over the whole temperature range. The contribution of the second component decreases slightly from 23 – 200 °C, becomes negative at higher temperatures, then starts to increase again above 400 °C. These changes create variations in absorbance at 10,374.7 and 10,376.8 eV in Figure 14, b.

The XANES reconstructions suggest that the evolution of  $\text{Ga}(i\text{Bu})_3/\text{Al}_2\text{O}_3\text{-500}$  from 23 to 550 °C can be represented primarily by a single, gradual process, i.e., the replacement of isobutyl ligands with oxygen-donor ligands derived from the alumina surface. It occurs mostly between 200 and 350 °C. The reconstructed XANES at 23 °C is a good match for the experimental spectrum, Figure S14. However, the reconstructed XANES at 550 °C lacks sufficient intensity at 10,378.6 eV and some of the post-edge oscillations. These discrepancies indicate contributions from minor sites not represented by the 2-component PCA. Being a bulk technique, XAS generally lacks sensitivity for minor sites.

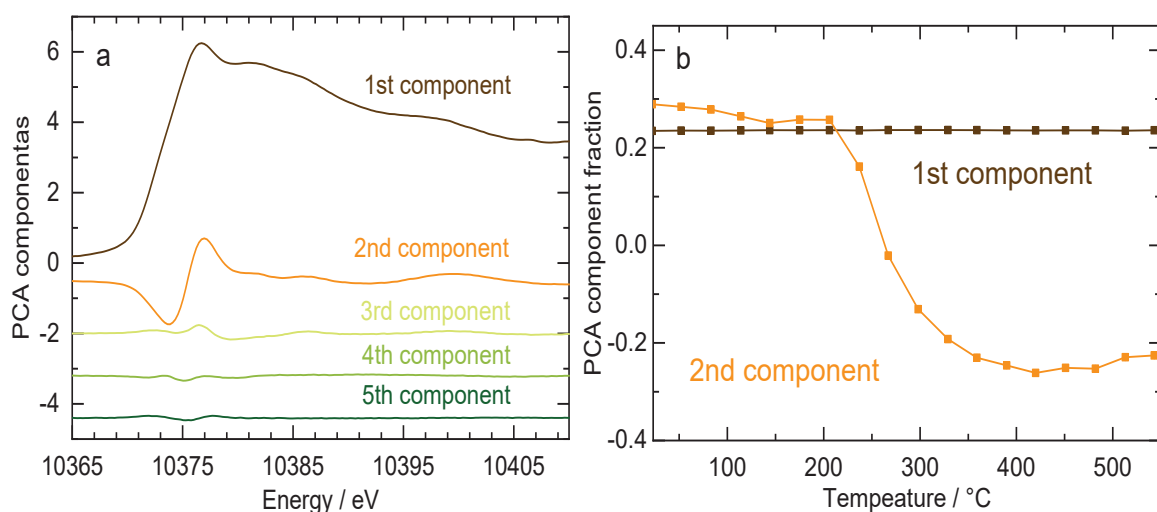


**Figure 18.** (a) The first five components extracted from principal component analysis of the XANES for  $\text{Ga}(i\text{Bu})_3/\text{Al}_2\text{O}_3\text{-500}$ , recorded as a function of temperature from 23 to 550 °C in He. (b) Contributions of the first and second components used to reconstruct the experimental XANES.

## EXAFS analysis of Ga(*i*Bu)<sub>3</sub>/Al<sub>2</sub>O<sub>3-500</sub> after thermal treatment

The structure of Ga(*i*Bu)<sub>3</sub>/Al<sub>2</sub>O<sub>3-500</sub> was reassessed after heating to 550 °C in flowing He. During cooling to room temperature, the XANES of Ga(*i*Bu)<sub>3</sub>/Al<sub>2</sub>O<sub>3-500</sub> almost remains unchanged, while the EXAFS amplitude in *k*-space increases with no other changes in appearance, Figure S15. Thus, the EXAFS after cooling reflects structural information about the Ga species present at 550 °C under He. Two prominent signals appear in the *k*<sup>3</sup>-weighed FT-EXAFS after the thermal treatment, Figure 19. In particular, the signal at 2.5 – 3.5 Å is much stronger than the one in as-prepared Ga(*i*Bu)<sub>3</sub>/Al<sub>2</sub>O<sub>3-500</sub>, implying new features in the interaction between Ga and the Al<sub>2</sub>O<sub>3</sub> support. To simplify the model, we consider that no Ga-C paths remain. The EXAFS curvefit of the region below 2 Å suggests that Ga is 3-coordinate with  $R(\text{Ga-O}) = 1.85$  Å, Figure 20, Figure S16 and Table 5. Including a second, slightly longer Ga – O path did not improve the fit.

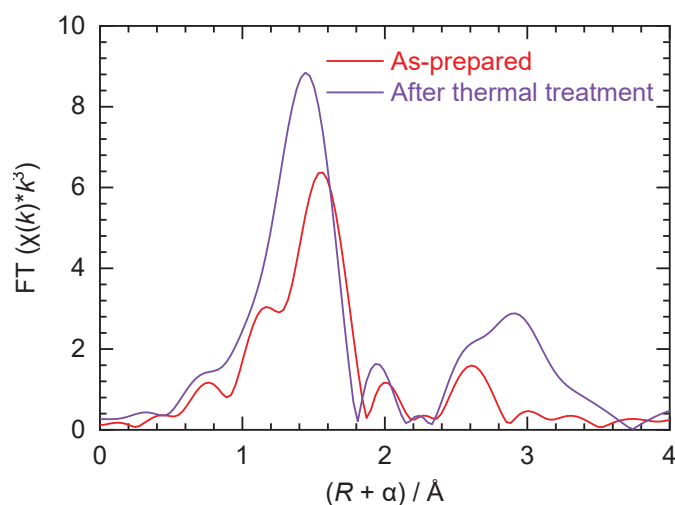


**Figure 19.** Comparison of Mo K-edge FT-EXAFS for Ga(*i*Bu)<sub>3</sub>/Al<sub>2</sub>O<sub>3-500</sub>, before (red) and after (purple) treatment at 550 °C in flowing He. Both spectra were recorded at 23 °C.

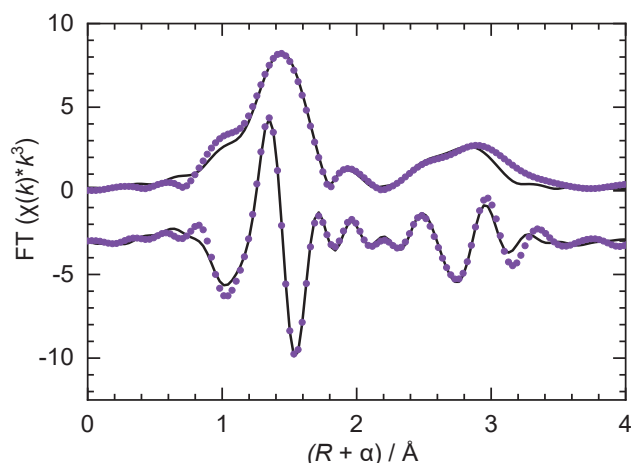


**Figure 20.** EXAFS (point) and curvefit (line) for Ga(*i*Bu)<sub>3</sub>/Al<sub>2</sub>O<sub>3-500</sub> after heating to 550 °C under He and cooling to room temperature.

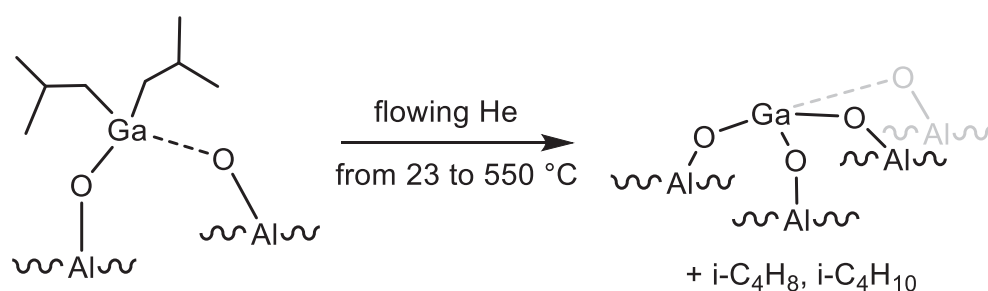
**Table 5.** Curvefit parameters<sup>a</sup> for Ga K-edge EXAFS of Ga(*i*Bu)<sub>3</sub>/Al<sub>2</sub>O<sub>3-500</sub> after heating to 550 °C in He and cooling to room temperature.

Path	$d^b / \text{Å}$	$N$	$R / \text{Å}$	$\sigma^2 / \text{Å}^2$
Ga – O1	1.803	3.0(2) <sup>c</sup>	1.85(1)	0.004(1)
Ga – O2	2.772	1 <sup>c</sup>	2.97(4)	0.006(1) <sup>d</sup>
Ga – Al	3.511	3.0(2) <sup>c</sup>	3.30(2)	0.006(1) <sup>d</sup>

<sup>a</sup>  $S_0^2$  was fixed at 1. Data ranges:  $3.0 \leq k \leq 13.0 \text{ Å}^{-1}$ ,  $1.0 \leq R \leq 4.0 \text{ Å}$ . The number of independent data points is 18.9.  $\Delta E_0$  was refined as a global fit parameter, returning a value of  $(-1 \pm 2) \text{ eV}$ . The number of variable parameters is 8. The R-factor for this fit is 1.7 %. <sup>b</sup> The Ga-O and Ga-Al distances were extracted from a computational model for 3-coordinate Ga dispersed in Al<sub>2</sub>O<sub>3</sub>.<sup>73</sup> <sup>c</sup>  $N(\text{Ga-O1})$  and  $N(\text{Ga-Al})$  were constrained to the same value.  $N(\text{Ga-O2})$  was fixed at 1, based on the computational model.<sup>73</sup> <sup>d</sup> Constrained to the same value to reduce the number of variables in the fit.

The broad signals from 2.5 – 3.5 Å (Figure 19) suggest contributions from more than one path in this region. Candidates include Ga-O, Ga-Al, and Ga-Ga single-scattering, as well as multiple-scattering paths. Since surface heterogeneity complicates curvefitting in this region, we attempted to use the fewest paths possible to describe the average environment of the major Ga species. Including just one path (Ga-O, Ga-Al, or Ga-Ga) led to the conclusion that the broad feature at ca. 2.9 Å arises principally from a Ga-Al path ( $N = 3.0$ ) at 3.30 Å, Table 5. A computational model for Ga doped into Al<sub>2</sub>O<sub>3</sub> has a long (non-bonded) Ga-O path at

2.77 Å.<sup>73</sup> Including a similar Ga-O path in the curvefit (with  $N$  fixed at 1) resulted in a much longer distance, 2.97 Å. The Ga<sub>2</sub>O<sub>3</sub> crystal structure has several Ga-Ga paths at ca. 2.9 Å.<sup>66</sup> An attempt to include such a path (with  $N$  fixed at 1) in the curvefit returned a distance of 2.95 Å and a large  $\sigma^2$ , 0.011 Å<sup>2</sup>, Figure S17 and Table S2. Since the major contribution in this region arises from the Ga-Al path, EXAFS curvefitting cannot definitely identify other contributions. However, it seems unlikely that the initially mononuclear Ga site becomes dinuclear during thermal treatment in an inert atmosphere, particularly since the Ga loading is low (2 wt%).<sup>53</sup> Therefore, we conclude that thermal treatment of Ga(*i*Bu)<sub>3</sub>/Al<sub>2</sub>O<sub>3-500</sub> in an inert atmosphere forms primarily mononuclear 3-coordinate Ga sites, Scheme 9.



**Scheme 9.** Proposed evolution of Ga(*i*Bu)<sub>3</sub>/Al<sub>2</sub>O<sub>3-500</sub> during heating to 550 °C in flowing He

### XAS of Ga(*i*Bu)<sub>3</sub>/Al<sub>2</sub>O<sub>3-500</sub> during propane dehydrogenation

The propane conversion by Ga(*i*Bu)<sub>3</sub>/Al<sub>2</sub>O<sub>3-500</sub> at 550 °C was reported to decrease gradually from 24 to 14% over 200 min.<sup>53</sup> Ga(*i*Bu)<sub>3</sub>/Al<sub>2</sub>O<sub>3-500</sub> heated to 550 °C under He was exposed to 20 vol% C<sub>3</sub>H<sub>8</sub>/He at the same temperature, and Ga K-edge XAS spectra were recorded while flowing propane for 200 min to monitor structural change in the Ga sites. Both XANES and EXAFS show small changes during this period, Figure 21 and Figure S18. Specifically, the intensity of the XANES shoulder at 10,371.0 eV decreases, while the intensity of the EXAFS peak at 1.4 Å in  $R$ -space increases slightly. The broad peaks at 2.5 – 3.5 Å remain essentially unchanged.

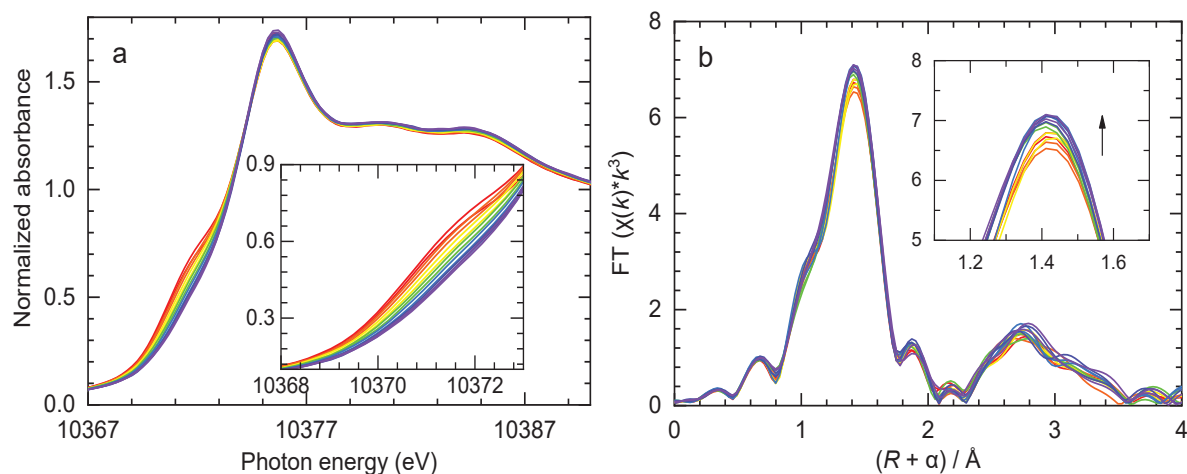


**Figure 21.** Evolution of the Ga K-edge XAS of Ga(*i*Bu)<sub>3</sub>/Al<sub>2</sub>O<sub>3-500</sub>, recorded in flowing 20 vol% C<sub>3</sub>H<sub>8</sub>/He at 550 °C for 200 min, in two regions: (a) XANES, and (b) EXAFS. The colors from red to purple show the time course (with inset showing the major spectrum changes).

These small changes may be linked to the minor Ga species generated by the thermal treatment above 450 °C (see above). Significantly, a XANES shoulder in a similar location (10374.2 eV) appeared in flowing He as the temperature was raised from 450 to 550 °C. The negative correlation between the XANES intensity at ca. 10,371 eV and the EXAFS peak intensity at ca. 1.4 Å (corresponding to Ga-O paths) has been reported for several Ga dehydrogenation catalysts upon H<sub>2</sub>-treatment.<sup>47,74–78</sup> However, the assignment of the low energy peak (ca. 10371 eV) in Ga K-edge XANES is controversial. Suggestions include Ga(I), Ga(III)-hydride or 3-coordinate Ga(III) sites.<sup>47,79,80</sup> The formation of Ga(III)-hydrides seems unlikely in our system since thermal treatment was performed in He rather than H<sub>2</sub> (although the isobutyl ligands may be a source of H). Three-coordinate Ga sites, with a XANES peak at ca. 10379 eV, are formed under He before introducing C<sub>3</sub>H<sub>8</sub>. It is possible that the shoulder at 10,371 eV arises from a small amount of Ga(I), possibly resulting from the reductive elimination of the isobutyl ligands.

The previously observed decline in catalytic activity suggests that the minority species such as Ga(I) may be responsible for much of the initial dehydrogenation activity, although they deactivate quickly. However, redox mechanisms for Ga(I) sites involve interconversion with Ga(III) sites. For example, oxidative addition of propane would form the ethyl hydride site [Ga(H)(C<sub>3</sub>H<sub>7</sub>)]<sup>+</sup>.<sup>81,82</sup> Alternatively, protonation of Ga(I) could give rise to a Ga(III) hydride.<sup>79</sup> The amplitude increase in the first coordination sphere is consistent with these two proposed

activation mechanisms. Meanwhile, 3-coordinate Ga oxide species remain to catalyze propane dehydrogenation at a slower rate. Although the 3-coordinate Ga sites appear to be less active, they are more robust.<sup>83</sup> DFT simulations predicted that a 3-coordinate Ga oxide site can undergo concerted (simultaneous formation of alkene) or stepwise mechanisms (forming alkylGa sites) to catalyze propane dehydrogenation.<sup>73,83</sup>

## Conclusion

Recent investigations of supported metal oxides show that isolated surface species with uniform local structures are more active and selective in PDH compared to oligomeric surface species. In this contribution, we report the first alumina-supported isolated tetra-coordinated gallium sites. They are highly active and selective in propane dehydrogenation. The catalyst was prepared from a molecular gallium tert-butoxide precursor by a surface organometallic chemistry method with thermolysis of the resulting species. The first step consists of grafting the molecular precursor onto Al<sub>2</sub>O<sub>3-500</sub>, leading to a monopodal species, [(≡AlO)Ga(O*t*Bu)<sub>2</sub>], **(I)**. Subsequent thermal treatment gives a tripodal Ga species, [(≡AlO)<sub>3</sub>Ga], **(III)**. DRIFTS, NMR (<sup>1</sup>H, <sup>13</sup>C), EXAFS and mass balance analysis were used to characterize this well-defined Ga surface species. It shows high activity and selectivity in propane dehydrogenation in a continuous flow reactor, with remarkable stability as a function of time on stream compared to a previously reported catalyst made by grafting [Ga(*i*Bu)<sub>3</sub>] onto alumina as [(≡AlO)Ga(*i*Bu)<sub>2</sub>]. In order to understand the difference in stability we studied the evolution of [(≡AlO)Ga(*i*Bu)<sub>2</sub>] during its thermal treatment and during propane dehydrogenation using *operando* XAS.

Ga(*i*Bu)<sub>3</sub>/Al<sub>2</sub>O<sub>3-500</sub> undergoes step-wise ligand removal from 23 to 550 °C in flowing He, as it is transformed primarily to 3-coordinate Ga(III). Replacement of the isobutyl ligands by O-donor ligands in the first coordination sphere alters the edge position and white line intensity in the XANES, without a change in oxidation state. Principal component analysis of the XANES during thermal treatment suggests that a minor fraction of Ga sites forms above 400 °C, presumably Ga(I). These minor sites are more effective catalysts for propane dehydrogenation, but they deactivate rapidly. The remaining Ga(III) tripodal sites show a lower but more stable catalytic performance by avoiding the reduction to Ga(I).

Supported organometallic catalysts allow us to connect the structures of dispersed Ga sites to their catalytic activity. Previous studies of Ga/Al<sub>2</sub>O<sub>3</sub> prepared by classical methods were

complicated by the presence of Ga<sub>2</sub>O<sub>3</sub> clusters, which also show measurable catalytic activity. *Operando* X-ray absorption spectroscopy enables the direct observation of even dilute metal sites under reaction conditions.

## Acknowledgments

This work was carried out as a part of BIZEOLCAT project, with funding from the European Union's Horizon 2020 research and innovation program under grant agreement No. 814671. In particular, J.A.N is grateful for her PhD grant. A.d.M. thanks Olivier Mathon and Kiril Lomachenko for assistance during the recording of the X-ray absorption spectra at ESRF. L.L. and S.L.S. acknowledge financial support from the U.S. Department of Energy, Office of Science, Division of Basic Energy Sciences, under the Catalysis Science Initiative (DE-FG-02-03ER15467). Use of the Stanford Synchrotron Radiation Lightsource, SLAC National Accelerator Laboratory, is supported by the U.S. Department of Energy, Office of Science, Office of Basic Energy Sciences, under Contract DE-AC02-76SF00515.

## References

- (1) Liu, Q.; Luo, M.; Zhao, Z.; Zhao, Q. K-Modified Sn-Containing Dendritic Mesoporous Silica Nanoparticles with Tunable Size and SnO<sub>x</sub>-Silica Interaction for the Dehydrogenation of Propane to Propylene. *Chem. Eng. J.* **2020**, *380*, 122423. <https://doi.org/10.1016/j.cej.2019.122423>.
- (2) The Role of Acidity, Side Pocket, and Steam on Maximizing Propylene Yield from Light Naphtha Cracking over One-Dimensional Zeolites: Case Studies of EU-1 and Disordered ZSM-48. *Fuel* **2019**, *258*, 116034. <https://doi.org/10.1016/j.fuel.2019.116034>.
- (3) Corma, A.; Melo, F. V.; Sauvanaud, L.; Ortega, F. Light Cracked Naphtha Processing: Controlling Chemistry for Maximum Propylene Production. *Catal. Today* **2005**, *107–108*, 699–706. <https://doi.org/10.1016/j.cattod.2005.07.109>.
- (4) Ali, M. A.; Ahmed, S.; Al-Baghli, N.; Malaibari, Z.; Abutaleb, A.; Yousef, A. A Comprehensive Review Covering Conventional and Structured Catalysis for Methanol to Propylene Conversion. *Catal. Lett.* **2019**, *149* (12), 3395–3424. <https://doi.org/10.1007/s10562-019-02914-4>.
- (5) *Tullo: Propylene on demand-A tight market for propylene...* - Google Scholar. [https://scholar-google-com.docelec.univ-lyon1.fr/scholar\\_lookup?author=A%20Tullo&atitle=Propylene%20on%20demand%20-%20A%20tight%20market%20for%20propylene%20globally%20is%20breathing%20new%20life%20into%20propane%20dehydrogenation&publication\\_year=2003&hl=en&journal=CHEMICAL%20&%20ENGINEERING%20NEWS=&volume=81&issue=50&pages=15-16&issn=0009-2347](https://scholar-google-com.docelec.univ-lyon1.fr/scholar_lookup?author=A%20Tullo&atitle=Propylene%20on%20demand%20-%20A%20tight%20market%20for%20propylene%20globally%20is%20breathing%20new%20life%20into%20propane%20dehydrogenation&publication_year=2003&hl=en&journal=CHEMICAL%20&%20ENGINEERING%20NEWS=&volume=81&issue=50&pages=15-16&issn=0009-2347) (accessed 2020-03-25).
- (6) Mol, J. Industrial Applications of Olefin Metathesis. *J. Mol. Catal. Chem.* **2004**, *213* (1), 39–45. <https://doi.org/10.1016/j.molcata.2003.10.049>.

- (7) Olsbye, U.; Svelle, S.; Bjørgen, M.; Beato, P.; Janssens, T. V. W.; Joensen, F.; Bordiga, S.; Lillerud, K. P. Conversion of Methanol to Hydrocarbons: How Zeolite Cavity and Pore Size Controls Product Selectivity. *Angew. Chem. Int. Ed.* **2012**, *51* (24), 5810–5831. <https://doi.org/10.1002/anie.201103657>.
- (8) Nawaz, Z. Light Alkane Dehydrogenation to Light Olefin Technologies: A Comprehensive Review. *Rev. Chem. Eng.* **2015**, *31* (5), 413–436. <https://doi.org/10.1515/revce-2015-0012>.
- (9) Sattler, J. J. H. B.; Ruiz-Martinez, J.; Santillan-Jimenez, E.; Weckhuysen, B. M. Catalytic Dehydrogenation of Light Alkanes on Metals and Metal Oxides. *Chem. Rev.* **2014**, *114* (20), 10613–10653. <https://doi.org/10.1021/cr5002436>.
- (10) Wang, G.; Zhu, X.; Li, C. Recent Progress in Commercial and Novel Catalysts for Catalytic Dehydrogenation of Light Alkanes. *Chem. Rec.* **2020**, *20* (6), 604–616. <https://doi.org/10.1002/tcr.201900090>.
- (11) Barsan, M. M.; Thyrion, F. C. Kinetic Study of Oxidative Dehydrogenation of Propane over Ni-Co Molybdate Catalyst. *Catal. Today* **2003**, *81* (2), 159–170. [https://doi.org/10.1016/S0920-5861\(03\)00109-3](https://doi.org/10.1016/S0920-5861(03)00109-3).
- (12) Siahvashi, A.; Chesterfield, D.; Adesina, A. A. Nonoxidative and Oxidative Propane Dehydrogenation over Bimetallic Mo–Ni/Al<sub>2</sub>O<sub>3</sub> Catalyst. *Ind. Eng. Chem. Res.* **2013**, *52* (11), 4017–4026. <https://doi.org/10.1021/ie302392h>.
- (13) Ballarini, N.; Battisti, A.; Cavani, F.; Cericola, A.; Cortelli, C.; Ferrari, M.; Trifirò, F.; Arpentinier, P. The Combination of Propane Partial Oxidation and of WGS Reaction in a Single Catalytic Bed, and the Self-Adapting Catalytic Properties of Vanadium Oxide Catalyst. *Appl. Catal. Gen.* **2006**, *307* (1), 148–155. <https://doi.org/10.1016/j.apcata.2006.03.016>.
- (14) Li, J.; Li, J.; Zhao, Z.; Fan, X.; Liu, J.; Wei, Y.; Duan, A.; Xie, Z.; Liu, Q. Size Effect of TS-1 Supports on the Catalytic Performance of PtSn/TS-1 Catalysts for Propane Dehydrogenation. *J. Catal.* **2017**, *352*, 361–370. <https://doi.org/10.1016/j.jcat.2017.05.024>.
- (15) Sokolov, S.; Stoyanova, M.; Rodemerck, U.; Linke, D.; Kondratenko, E. V. Comparative Study of Propane Dehydrogenation over V-, Cr-, and Pt-Based Catalysts: Time on-Stream Behavior and Origins of Deactivation. *J. Catal.* **2012**, *293*, 67–75. <https://doi.org/10.1016/j.jcat.2012.06.005>.
- (16) Xiong, H.; Lin, S.; Goetze, J.; Pletcher, P.; Guo, H.; Kovarik, L.; Artyushkova, K.; Weckhuysen, B. M.; Datye, A. K. Thermally Stable and Regenerable Platinum–Tin Clusters for Propane Dehydrogenation Prepared by Atom Trapping on Ceria. *Angew. Chem.* **2017**, *129* (31), 9114–9119. <https://doi.org/10.1002/ange.201701115>.
- (17) Sattler, J. J. H. B.; Mens, A. M.; Weckhuysen, B. M. Real-Time Quantitative Operando Raman Spectroscopy of a CrOx/Al<sub>2</sub>O<sub>3</sub> Propane Dehydrogenation Catalyst in a Pilot-Scale Reactor. *ChemCatChem* **2014**, *6* (11), 3139–3145. <https://doi.org/10.1002/cctc.201402649>.
- (18) Lian, Z.; Ali, S.; Liu, T.; Si, C.; Li, B.; Su, D. S. Revealing the Janus Character of the Coke Precursor in the Propane Direct Dehydrogenation on Pt Catalysts from a KMC Simulation. *ACS Catal.* **2018**, *8* (5), 4694–4704. <https://doi.org/10.1021/acscatal.8b00107>.
- (19) Wang, G.; Zhang, H.; Wang, H.; Zhu, Q.; Li, C.; Shan, H. The Role of Metallic Sn Species in Catalytic Dehydrogenation of Propane: Active Component Rather than Only Promoter. *J. Catal.* **2016**, *344*, 606–608. <https://doi.org/10.1016/j.jcat.2016.11.003>.
- (20) Gascón, J.; Téllez, C.; Herguido, J.; Menéndez, M. Propane Dehydrogenation over a Cr<sub>2</sub>O<sub>3</sub>/Al<sub>2</sub>O<sub>3</sub> Catalyst: Transient Kinetic Modeling of Propene and Coke Formation.

- Appl. Catal. Gen.* **2003**, *248* (1), 105–116. [https://doi.org/10.1016/S0926-860X\(03\)00128-5](https://doi.org/10.1016/S0926-860X(03)00128-5).
- (21) Cai, W.; Mu, R.; Zha, S.; Sun, G.; Chen, S.; Zhao, Z.-J.; Li, H.; Tian, H.; Tang, Y.; Tao, F. (Feng); Zeng, L.; Gong, J. Subsurface Catalysis-Mediated Selectivity of Dehydrogenation Reaction. *Sci. Adv.* **4** (8), eaar5418. <https://doi.org/10.1126/sciadv.aar5418>.
- (22) Fridman, V. Z.; Xing, R. Deactivation Studies of the CrOx/Al<sub>2</sub>O<sub>3</sub> Dehydrogenation Catalysts under Cyclic Redox Conditions. *Ind. Eng. Chem. Res.* **2017**, *56* (28), 7937–7947. <https://doi.org/10.1021/acs.iecr.7b01638>.
- (23) Otroshchenko, T.; Sokolov, S.; Stoyanova, M.; Kondratenko, V. A.; Rodemerck, U.; Linke, D.; Kondratenko, E. V. ZrO<sub>2</sub>-Based Alternatives to Conventional Propane Dehydrogenation Catalysts: Active Sites, Design, and Performance. *Angew. Chem. Int. Ed.* **2015**, *54* (52), 15880–15883. <https://doi.org/10.1002/anie.201508731>.
- (24) Cheng, M.; Zhao, H.; Yang, J.; Zhao, J.; Yan, L.; Song, H.; Chou, L. Synthesis and Catalytic Performance of a Dual-Sites Fe–Zn Catalyst Based on Ordered Mesoporous Al<sub>2</sub>O<sub>3</sub> for Isobutane Dehydrogenation. *Catal. Lett.* **2019**, *149* (5), 1326–1336. <https://doi.org/10.1007/s10562-019-02686-x>.
- (25) Tan, S.; Kim, S.-J.; Moore, J. S.; Liu, Y.; Dixit, R. S.; Pendergast, J. G.; Sholl, D. S.; Nair, S.; Jones, C. W. Propane Dehydrogenation over In<sub>2</sub>O<sub>3</sub>–Ga<sub>2</sub>O<sub>3</sub>–Al<sub>2</sub>O<sub>3</sub> Mixed Oxides. *ChemCatChem* **2016**, *8* (1), 214–221. <https://doi.org/10.1002/cctc.201500916>.
- (26) Xie, Y.; Luo, R.; Sun, G.; Chen, S.; Zhao, Z.-J.; Mu, R.; Gong, J. Facilitating the Reduction of V–O Bonds on VO<sub>x</sub>/ZrO<sub>2</sub> Catalysts for Non-Oxidative Propane Dehydrogenation. *Chem. Sci.* **2020**. <https://doi.org/10.1039/D0SC00690D>.
- (27) Shao, C.-T.; Lang, W.-Z.; Yan, X.; Guo, Y.-J. Catalytic Performance of Gallium Oxide Based-Catalysts for the Propane Dehydrogenation Reaction: Effects of Support and Loading Amount. *RSC Adv.* **2017**, *7* (8), 4710–4723. <https://doi.org/10.1039/C6RA27204E>.
- (28) Choi, S.-W.; Kim, W.-G.; So, J.-S.; Moore, J. S.; Liu, Y.; Dixit, R. S.; Pendergast, J. G.; Sievers, C.; Sholl, D. S.; Nair, S.; Jones, C. W. Propane Dehydrogenation Catalyzed by Gallosilicate MFI Zeolites with Perturbed Acidity. *J. Catal.* **2017**, *345*, 113–123. <https://doi.org/10.1016/j.jcat.2016.11.017>.
- (29) Hu, P.; Lang, W.-Z.; Yan, X.; Chu, L.-F.; Guo, Y.-J. Influence of Gelation and Calcination Temperature on the Structure-Performance of Porous VOX-SiO<sub>2</sub> Solids in Non-Oxidative Propane Dehydrogenation. *J. Catal.* **2018**, *358*, 108–117. <https://doi.org/10.1016/j.jcat.2017.12.004>.
- (30) Zhao, Z.-J.; Wu, T.; Xiong, C.; Sun, G.; Mu, R.; Zeng, L.; Gong, J. Hydroxyl-Mediated Non-Oxidative Propane Dehydrogenation over VO<sub>x</sub>/γ-Al<sub>2</sub>O<sub>3</sub> Catalysts with Improved Stability. *Angew. Chem. Int. Ed.* **2018**, *57* (23), 6791–6795. <https://doi.org/10.1002/anie.201800123>.
- (31) Sun, Y.; Tao, L.; You, T.; Li, C.; Shan, H. Effect of Sulfation on the Performance of Fe<sub>2</sub>O<sub>3</sub>/Al<sub>2</sub>O<sub>3</sub> Catalyst in Catalytic Dehydrogenation of Propane to Propylene. *Chem. Eng. J.* **2014**, *244*, 145–151. <https://doi.org/10.1016/j.cej.2014.01.047>.
- (32) Hu, B.; “Bean” Getsoian, A.; Schweitzer, N. M.; Das, U.; Kim, H.; Niklas, J.; Poluektov, O.; Curtiss, L. A.; Stair, P. C.; Miller, J. T.; Hock, A. S. Selective Propane Dehydrogenation with Single-Site CoII on SiO<sub>2</sub> by a Non-Redox Mechanism. *J. Catal.* **2015**, *322*, 24–37. <https://doi.org/10.1016/j.jcat.2014.10.018>.
- (33) Wang, G.; Zhang, H.; Zhu, Q.; Zhu, X.; Li, X.; Wang, H.; Li, C.; Shan, H. Sn-Containing Hexagonal Mesoporous Silica (HMS) for Catalytic Dehydrogenation of

- Propane: An Efficient Strategy to Enhance Stability. *J. Catal.* **2017**, *351*, 90–94. <https://doi.org/10.1016/j.jcat.2017.04.018>.
- (34) Camacho-Bunquin, J.; Aich, P.; Ferrandon, M.; “Bean” Getsoian, A.; Das, U.; Dogan, F.; Curtiss, L. A.; Miller, J. T.; Marshall, C. L.; Hock, A. S.; Stair, P. C. Single-Site Zinc on Silica Catalysts for Propylene Hydrogenation and Propane Dehydrogenation: Synthesis and Reactivity Evaluation Using an Integrated Atomic Layer Deposition-Catalysis Instrument. *J. Catal.* **2017**, *345*, 170–182. <https://doi.org/10.1016/j.jcat.2016.10.017>.
- (35) Barman, S.; Maity, N.; Bhatte, K.; Ould-Chikh, S.; Dachwald, O.; Haessner, C.; Saih, Y.; Abou-Hamad, E.; Llorens, I.; Hazemann, J. L.; Kohler, K.; D’Elia, V.; Basset, J. M. Single-Site VO<sub>x</sub> Moieties Generated on Silica by Surface Organometallic Chemistry: A Way To Enhance the Catalytic Activity in the Oxidative Dehydrogenation of Propane. *ACS Catal.* **2016**, *6* (9), 5908–5921. <https://doi.org/10.1021/acscatal.6b01263>.
- (36) Fukudome, K.; Ikenaga, N.; Miyake, T.; Suzuki, T. Oxidative Dehydrogenation of Propane Using Lattice Oxygen of Vanadium Oxides on Silica. *Catal. Sci. Technol.* **2011**, *1* (6), 987–998. <https://doi.org/10.1039/C1CY00115A>.
- (37) Fukudome, K.; Ikenaga, N.; Miyake, T.; Suzuki, T. Oxidative Dehydrogenation of Alkanes over Vanadium Oxide Prepared with V(t-BuO)<sub>3</sub>O and Si(OEt)<sub>4</sub> in the Presence of Polyethyleneglycol. *Catal. Today* **2013**, *203*, 10–16. <https://doi.org/10.1016/j.cattod.2012.04.042>.
- (38) Gao, X.; Bare, S. R.; Weckhuysen, B. M.; Wachs, I. E. In Situ Spectroscopic Investigation of Molecular Structures of Highly Dispersed Vanadium Oxide on Silica under Various Conditions. *J. Phys. Chem. B* **1998**, *102* (52), 10842–10852. <https://doi.org/10.1021/jp9826367>.
- (39) Pidko, E. A.; Santen, R. A. van; Hensen, E. J. M. Multinuclear Gallium-Oxide Cations in High-Silica Zeolites. *Phys. Chem. Chem. Phys.* **2009**, *11* (16), 2893–2902. <https://doi.org/10.1039/B815943B>.
- (40) Hensen, E. J. M.; Pidko, E. A.; Rane, N.; van Santen, R. A. Water-Promoted Hydrocarbon Activation Catalyzed by Binuclear Gallium Sites in ZSM-5 Zeolite. *Angew. Chem. Int. Ed.* **2007**, *46* (38), 7273–7276. <https://doi.org/10.1002/anie.200702463>.
- (41) Pidko, E. A.; van Santen, R. A. Structure–Reactivity Relationship for Catalytic Activity of Gallium Oxide and Sulfide Clusters in Zeolite. *J. Phys. Chem. C* **2009**, *113* (11), 4246–4249. <https://doi.org/10.1021/jp8113607>.
- (42) Szeto, K. C.; Jones, Z. R.; Merle, N.; Rios, C.; Gallo, A.; Le Quemener, F.; Delevoye, L.; Gauvin, R. M.; Scott, S. L.; Taoufik, M. A Strong Support Effect in Selective Propane Dehydrogenation Catalyzed by Ga(i-Bu)<sub>3</sub> Grafted onto  $\gamma$ -Alumina and Silica. *ACS Catal.* **2018**, *8* (8), 7566–7577. <https://doi.org/10.1021/acscatal.8b00936>.
- (43) Cheng, L.; Ferguson, G. A.; Zygmunt, S. A.; Curtiss, L. A. Structure-Activity Relationships for Propane Oxidative Dehydrogenation by Anatase-Supported Vanadium Oxide Monomers and Dimers. *J. Catal.* **2013**, *302*, 31–36. <https://doi.org/10.1016/j.jcat.2013.02.012>.
- (44) Lillehaug, S.; Børve, K. J.; Sierka, M.; Sauer, J. Catalytic Dehydrogenation of Ethane over Mononuclear Cr(III) Surface Sites on Silica. Part I. C–H Activation by  $\sigma$ -Bond Metathesis. *J. Phys. Org. Chem.* **2004**, *17* (11), 990–1006. <https://doi.org/10.1002/poc.842>.
- (45) Olsbye, U.; Virnovskaia, A.; Prytz, Ø.; Tinnemans, S.; Weckhuysen, B. Mechanistic Insight in the Ethane Dehydrogenation Reaction over Cr/Al<sub>2</sub>O<sub>3</sub> Catalysts. *Catal. Lett.* **2005**, *103*, 143–148. <https://doi.org/10.1007/s10562-005-6521-7>.

- (46) Weckhuysen, B. M.; Schoonheydt, R. A. *Alkane dehydrogenation over supported chromium oxide catalysts*. *Catalysis Today*. <http://localhost/handle/1874/21356> (accessed 2020-03-31).
- (47) Getsoian, A. “Bean”; Das, U.; Camacho-Bunquin, J.; Zhang, G.; Gallagher, J. R.; Hu, B.; Cheah, S.; Schaidle, J. A.; Ruddy, D. A.; Hensley, J. E.; Krause, T. R.; Curtiss, L. A.; Miller, J. T.; Hock, A. S. Organometallic Model Complexes Elucidate the Active Gallium Species in Alkane Dehydrogenation Catalysts Based on Ligand Effects in Ga K-Edge XANES. *Catal. Sci. Technol.* **2016**, *6* (16), 6339–6353. <https://doi.org/10.1039/C6CY00698A>.
- (48) Le Quéméner, F.; Barman, S.; Merle, N.; Aljuhani, M. A.; Samantaray, M. K.; Saih, Y.; Szeto, K. C.; De Mallmann, A.; Minenkov, Y.; Huang, K.-W.; Cavallo, L.; Taoufik, M.; Basset, J.-M. Metathetic Oxidation of 2-Butenes to Acetaldehyde by Molecular Oxygen Using the Single-Site Olefin Metathesis Catalyst  $(\equiv\text{SiO})_2\text{Mo}(=\text{O})_2$ . *ACS Catal.* **2018**, *8* (8), 7549–7555. <https://doi.org/10.1021/acscatal.8b01767>.
- (49) Mazoyer, E.; Merle, N.; Mallmann, A. de; Basset, J.-M.; Berrier, E.; Delevoye, L.; Paul, J.-F.; Nicholas, C. P.; Gauvin, R. M.; Taoufik, M. Development of the First Well-Defined Tungsten Oxo Alkyl Derivatives Supported on Silica by SOMC: Towards a Model of  $\text{WO}_3/\text{SiO}_2$  Olefin Metathesis Catalyst. *Chem. Commun.* **2010**, *46* (47), 8944–8946. <https://doi.org/10.1039/C0CC02507K>.
- (50) Mazoyer, E.; Trébosc, J.; Baudouin, A.; Boyron, O.; Pelletier, J.; Basset, J.-M.; Vitorino, M. J.; Nicholas, C. P.; Gauvin, R. M.; Taoufik, M.; Delevoye, L. Heteronuclear NMR Correlations To Probe the Local Structure of Catalytically Active Surface Aluminum Hydride Species on  $\gamma$ -Alumina. *Angew. Chem. Int. Ed.* **2010**, *49* (51), 9854–9858. <https://doi.org/10.1002/anie.201004310>.
- (51) Pelletier, J.; Espinas, J.; Vu, N.; Norsic, S.; Baudouin, A.; Delevoye, L.; Trébosc, J.; Roux, E. L.; Santini, C.; Basset, J.-M.; Gauvin, R. M.; Taoufik, M. A Well-Defined Silica-Supported Aluminium Alkyl through an Unprecedented, Consecutive Two-Step Protonolysis–Alkyl Transfer Mechanism. *Chem. Commun.* **2011**, *47* (10), 2979–2981. <https://doi.org/10.1039/C0CC04986G>.
- (52) Valet, M.; Hoffman, D. M. Synthesis of Homoleptic Gallium Alkoxide Complexes and the Chemical Vapor Deposition of Gallium Oxide Films. *Chem. Mater.* **2001**, *13* (6), 2135–2143. <https://doi.org/10.1021/cm0014177>.
- (53) Mathon, O.; Beteva, A.; Borrel, J.; Bugnazet, D.; Gatla, S.; Hino, R.; Kantor, I.; Mairs, T.; Munoz, M.; Pasternak, S.; Perrin, F.; Pascarelli, S. The Time-Resolved and Extreme Conditions XAS (TEXAS) Facility at the European Synchrotron Radiation Facility: The General-Purpose EXAFS Bending-Magnet Beamline BM23. *J. Synchrotron Radiat.* **2015**, *22*, 1548–1554. <https://doi.org/10.1107/S1600577515017786>.
- (54) Ravel, B.; Newville, M. ATHENA, ARTEMIS, HEPHAESTUS: Data Analysis for X-Ray Absorption Spectroscopy Using IFEFFIT. *J. Synchrotron Radiat.* **2005**, *12* (4), 537–541. <https://doi.org/10.1107/S0909049505012719>.
- (55) Alain, M.; Jacques, M.; Diane, M.-B.; Karine, P. MAX: Multiplatform Applications for XAFS. *J. Phys. Conf. Ser.* **2009**, *190*, 012034. <https://doi.org/10.1088/1742-6596/190/1/012034>.
- (56) Modrow, H.; Bucher, S.; Rehr, J. J.; Ankudinov, A. L. Calculation and Interpretation of  $\text{K}$ -Shell x-Ray Absorption near-Edge Structure of Transition Metal Oxides. *Phys. Rev. B* **2003**, *67* (3), 035123. <https://doi.org/10.1103/PhysRevB.67.035123>.
- (57) Hoffman, A. S.; Singh, J. A.; Bent, S. F.; Bare, S. R. In Situ Observation of Phase Changes of a Silica-Supported Cobalt Catalyst for the Fischer–Tropsch Process by the Development of a Synchrotron-Compatible in Situ/Operando Powder X-Ray

- Diffraction Cell. *J. Synchrotron Radiat.* **2018**, *25* (6), 1673–1682. <https://doi.org/10.1107/S1600577518013942>.
- (58) Larabi, C.; Norsic, S.; Khrouz, L.; Boyron, O.; Szeto, K. C.; Lucas, C.; Taoufik, M.; De Mallmann, A. Oxide-Supported Titanium Catalysts: Structure–Activity Relationship in Heterogeneous Catalysis, with the Choice of Support as a Key Step. *Organometallics* **2020**, *39* (24), 4608–4617. <https://doi.org/10.1021/acs.organomet.0c00650>.
- (59) Millot, N.; Santini, C. C.; Lefebvre, F.; Basset, J.-M. Surface Organometallic Chemistry: A Route to Well-Defined Boron Heterogeneous Co-Catalyst for Olefin Polymerisation. *Comptes Rendus Chim.* **2004**, *7* (8), 725–736. <https://doi.org/10.1016/j.crci.2004.03.011>.
- (60) and, M. V.; Hoffman\*, D. M. *Synthesis of Homoleptic Gallium Alkoxide Complexes and the Chemical Vapor Deposition of Gallium Oxide Films.* <https://pubs.acs.org/doi/pdf/10.1021/cm0014177> (accessed 2020-04-03). <https://doi.org/10.1021/cm0014177>.
- (61) Searles, K.; Siddiqi, G.; V. Safonova, O.; Copéret, C. Silica-Supported Isolated Gallium Sites as Highly Active, Selective and Stable Propane Dehydrogenation Catalysts. *Chem. Sci.* **2017**, *8* (4), 2661–2666. <https://doi.org/10.1039/C6SC05178B>.
- (62) Terry, K. W.; Lugmair, C. G.; Tilley, T. D. Tris(Tert-Butoxy)Siloxy Complexes as Single-Source Precursors to Homogeneous Zirconia- and Hafnia-Silica Materials. An Alternative to the Sol-Gel Method. *J. Am. Chem. Soc.* **1997**, *119* (41), 9745–9756. <https://doi.org/10.1021/ja971405v>.
- (63) Banks, M. A.; Beachley, O. T.; Maloney, J. D.; Rogers, R. D. The Chemistry of Diphenylphosphine Adducts of Tris(Neopentyl) and Tris(Trimethylsilyl-Methyl)Gallium and -Indium Including the Crystal and Molecular Structure of (Me<sub>3</sub>CCH<sub>2</sub>)<sub>3</sub>Ga·P(H)Ph<sub>2</sub>. *Polyhedron* **1990**, *9* (2), 335–342. [https://doi.org/10.1016/S0277-5387\(00\)80588-4](https://doi.org/10.1016/S0277-5387(00)80588-4).
- (64) Beachley, O. T.; Noble, M. J.; Churchill, M. R.; Lake, C. H. The Dihydronaphthalene Elimination Reaction as a Route to Gallium–Nitrogen Compounds. Crystal and Molecular Structure of [(PhMe<sub>2</sub>CCH<sub>2</sub>)<sub>2</sub>GaNHPh]<sub>2</sub>. *Organometallics* **1998**, *17* (15), 3311–3315. <https://doi.org/10.1021/om9801249>.
- (65) Park, H.; Barbier, J. Crystal Structures of New Gallo-Borates MGa<sub>2</sub>B<sub>2</sub>O<sub>7</sub>, M=Sr, Ba. *J. Solid State Chem.* **2000**, *154* (2), 598–602. <https://doi.org/10.1006/jssc.2000.8901>.
- (66) Åhman, J.; Svensson, G.; Albertsson, J. A Reinvestigation of β-Gallium Oxide. *Acta Crystallogr. C* **1996**, *52* (6), 1336–1338. <https://doi.org/10.1107/S0108270195016404>.
- (67) Mason, M. R.; Song, B.; Han, Y.; Hu, X. Reaction of Carbon Monoxide with Tri-Tert-Butylgallium: The First Example of CO Insertion into a Gallium–Carbon Bond. *Inorganica Chim. Acta* **2008**, *361* (11), 3332–3337. <https://doi.org/10.1016/j.ica.2007.11.021>.
- (68) Robinson, G. H.; Pennington, W. T.; Lee, B.; Self, M. F.; Hrcir, D. C. Isolation of Unusual Conformations of the [14]AneN<sub>4</sub> Aza Crown Ether: Syntheses and Molecular Structures of [M(CH<sub>3</sub>)<sub>3</sub>]<sub>2</sub>[14]AneN<sub>4</sub> (M = Aluminum, Gallium) and the Group 13 Heterobimetallic Complex [Al(CH<sub>3</sub>)]<sub>2</sub>[14]AneN<sub>4</sub>[Ga(CH<sub>3</sub>)<sub>3</sub>]<sub>2</sub>. *Inorg. Chem.* **1991**, *30* (4), 809–812. <https://doi.org/10.1021/ic00004a037>.
- (69) Aleksandrov, Y. A.; Makin, G. I.; Druzhkov, O. N.; Baryshnikov, Y. Y.; Postnikova, T. K.; Kozyrkin, B. I. Thermal Decomposition of Triatkyl Compounds of Gallium. *Russ J Gen Chem* **1981**, *51*, 61.
- (70) Aleksandrov, Y. A.; Druzhkov, O. N.; Baryshnikov,... - Google Scholar. [https://scholar.google.fr/scholar?hl=fr&as\\_sdt=0%2C5&q=Aleksandrov%2C+Y.+A.%3B+Druzhkov%2C+O.+N.%3B+Baryshnikov%2C+Y.+Y.%3B+Postnikova%2C+T.+](https://scholar.google.fr/scholar?hl=fr&as_sdt=0%2C5&q=Aleksandrov%2C+Y.+A.%3B+Druzhkov%2C+O.+N.%3B+Baryshnikov%2C+Y.+Y.%3B+Postnikova%2C+T.+)

- K.%3B+Makin%2C+G.+I.%3B+Kozyrkin%2C+B.+I.+Russ.+J.+Gen.+Chem+1980%2C+50%2C+2129.&btnG= (accessed 2022-05-15).
- (71) Wong, K. C.; McBurnett, B. G.; Culp, R. D.; Cowley, A. H.; Ekerdt, J. G. Homolysis versus  $\beta$ -Hydride Elimination in the Decomposition of Trialkylgallium on GaAs(100). *Surf. Sci.* **1998**, *416* (3), 480–487. [https://doi.org/10.1016/S0039-6028\(98\)00641-4](https://doi.org/10.1016/S0039-6028(98)00641-4).
- (72) Hensen, E. J. M.; Pidko, E. A.; Rane, N.; van Santen, R. A. Modification of Brønsted Acidity of Zeolites by Ga<sup>+</sup>, GaO<sup>+</sup> and AlO<sup>+</sup>: Comparison for Alkane Activation. In *Studies in Surface Science and Catalysis*; Xu, R., Gao, Z., Chen, J., Yan, W., Eds.; From Zeolites to Porous MOF Materials - The 40th Anniversary of International Zeolite Conference; Elsevier, 2007; Vol. 170, pp 1182–1189. [https://doi.org/10.1016/S0167-2991\(07\)80976-1](https://doi.org/10.1016/S0167-2991(07)80976-1).
- (73) Batchu, S. P.; Wang, H.-L.; Chen, W.; Zheng, W.; Caratzoulas, S.; Lobo, R. F.; Vlachos, D. G. Ethane Dehydrogenation on Single and Dual Centers of Ga-Modified  $\gamma$ -Al<sub>2</sub>O<sub>3</sub>. *ACS Catal.* **2021**, *11* (3), 1380–1391. <https://doi.org/10.1021/acscatal.0c03536>.
- (74) Cybulskis, V. J.; Pradhan, S. U.; Lovón-Quintana, J. J.; Hock, A. S.; Hu, B.; Zhang, G.; Delgass, W. N.; Ribeiro, F. H.; Miller, J. T. The Nature of the Isolated Gallium Active Center for Propane Dehydrogenation on Ga/SiO<sub>2</sub>. *Catal. Lett.* **2017**, *147* (5), 1252–1262. <https://doi.org/10.1007/s10562-017-2028-2>.
- (75) Phadke, N. M.; Van der Mynsbrugge, J.; Mansoor, E.; Getsoian, A. B.; Head-Gordon, M.; Bell, A. T. Characterization of Isolated Ga<sup>3+</sup> Cations in Ga/H-MFI Prepared by Vapor-Phase Exchange of H-MFI Zeolite with GaCl<sub>3</sub>. *ACS Catal.* **2018**, *8* (7), 6106–6126. <https://doi.org/10.1021/acscatal.8b01254>.
- (76) Mansoor, E.; Head-Gordon, M.; Bell, A. T. Computational Modeling of the Nature and Role of Ga Species for Light Alkane Dehydrogenation Catalyzed by Ga/H-MFI. *ACS Catal.* **2018**, *8* (7), 6146–6162. <https://doi.org/10.1021/acscatal.7b04295>.
- (77) Hensen, E. J. M.; García-Sánchez, M.; Rane, N.; Magusin, P. C. M. M.; Liu, P.-H.; Chao, K.-J.; van Santen, R. A. In Situ Ga K Edge XANES Study of the Activation of Ga/ZSM-5 Prepared by Chemical Vapor Deposition of Trimethylgallium. *Catal. Lett.* **2005**, *101* (1–2), 79–85. <https://doi.org/10.1007/s10562-004-3753-x>.
- (78) LiBretto, N. J.; Xu, Y.; Quigley, A.; Edwards, E.; Nargund, R.; Vega-Vila, J. C.; Caulkins, R.; Saxena, A.; Gounder, R.; Greeley, J.; Zhang, G.; Miller, J. T. Olefin Oligomerization by Main Group Ga<sup>3+</sup> and Zn<sup>2+</sup> Single Site Catalysts on SiO<sub>2</sub>. *Nat. Commun.* **2021**, *12* (1), 2322. <https://doi.org/10.1038/s41467-021-22512-6>.
- (79) Schreiber, M. W.; Plaisance, C. P.; Baumgärtl, M.; Reuter, K.; Jentys, A.; Bermejo-Deval, R.; Lercher, J. A. Lewis–Brønsted Acid Pairs in Ga/H-ZSM-5 To Catalyze Dehydrogenation of Light Alkanes. *J. Am. Chem. Soc.* **2018**, *140* (14), 4849–4859. <https://doi.org/10.1021/jacs.7b12901>.
- (80) Meitzner, G. D.; Iglesia, E.; Baumgartner, J. E.; Huang, E. S. The Chemical State of Gallium in Working Alkane Dehydrocyclodimerization Catalysts. In Situ Gallium K-Edge X-Ray Absorption Spectroscopy. *J. Catal.* **1993**, *140* (1), 209–225. <https://doi.org/10.1006/jcat.1993.1079>.
- (81) Rane, N.; Overweg, A. R.; Kazansky, V. B.; van Santen, R. A.; Hensen, E. J. M. Characterization and Reactivity of Ga<sup>+</sup> and GaO<sup>+</sup> Cations in Zeolite ZSM-5. *J. Catal.* **2006**, *239* (2), 478–485. <https://doi.org/10.1016/j.jcat.2006.03.004>.
- (82) Pidko, E. A.; Kazansky, V. B.; Hensen, E. J. M.; van Santen, R. A. A Comprehensive Density Functional Theory Study of Ethane Dehydrogenation over Reduced Extra-Framework Gallium Species in ZSM-5 Zeolite. *J. Catal.* **2006**, *240* (1), 73–84. <https://doi.org/10.1016/j.jcat.2006.03.011>.

- (83) Abdelgaid, M.; Dean, J.; Mpourmpakis, G. Improving Alkane Dehydrogenation Activity on  $\gamma$ -Al<sub>2</sub>O<sub>3</sub> through Ga Doping. *Catal. Sci. Technol.* **2020**, *10* (21), 7194–7202. <https://doi.org/10.1039/D0CY01474E>.

## Supporting Information

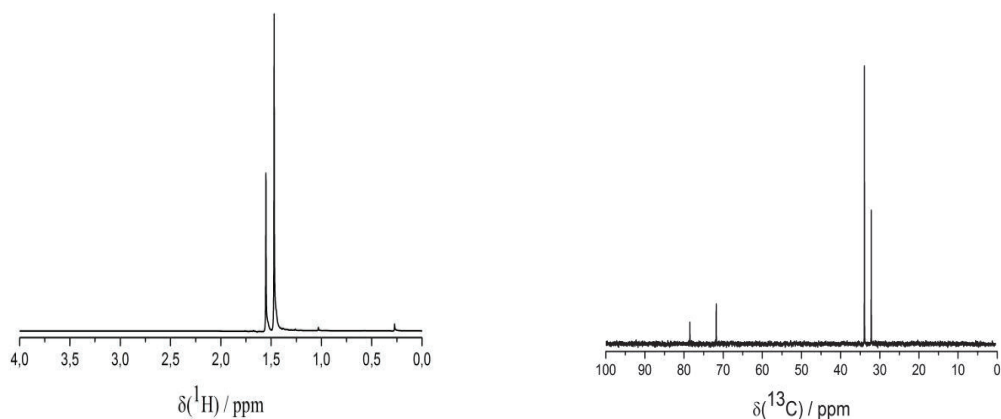


**Figure S1.** NMR spectra of  $[\text{Ga}(\text{OtBu})_3]_2$  molecular complex **Left:**  $^1\text{H}$  MAS NMR and **Right:**  $^{13}\text{C}$   $\{^1\text{H}\}$  ( $d_1=1$  s)

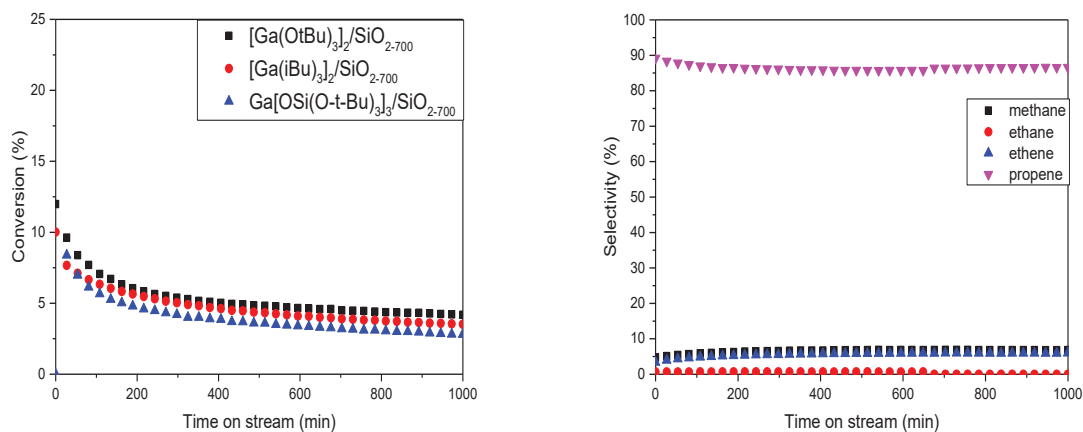


**Figure S2.** **Left:** Comparison of propane conversion catalyzed by  $[\text{Ga}(\text{OtBu})_3]_2/\text{SiO}_{2-700}$  (II) (■),  $[\text{Ga}(\text{iBu})_3]_2/\text{SiO}_{2-700}$  (●) and  $\text{Ga}[\text{OSi}(\text{O-t-Bu})_3]_3/\text{SiO}_{2-700}$  (▲), and **Right:** Selectivity of (II) at  $P=1$  bar,  $T=540$  °C, total flow =  $5 \text{ mL}\cdot\text{min}^{-1}$  (20 % of C3 in Ar)

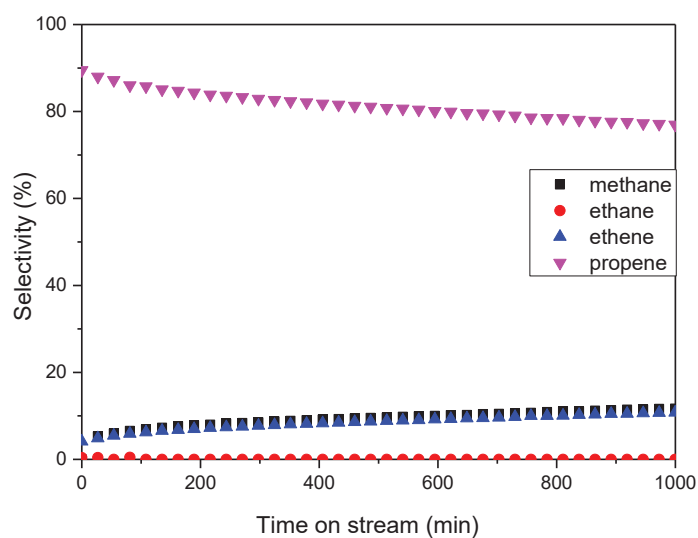


**Figure S3.** Selectivity of  $[\text{Ga}(i\text{Bu})_3]_2/\text{SiO}_2\text{-700}$  at  $P= 1$  bar,  $T= 540$  °C, total flow=  $5 \text{ mL}\cdot\text{min}^{-1}$  (20 % of C3 in Ar)

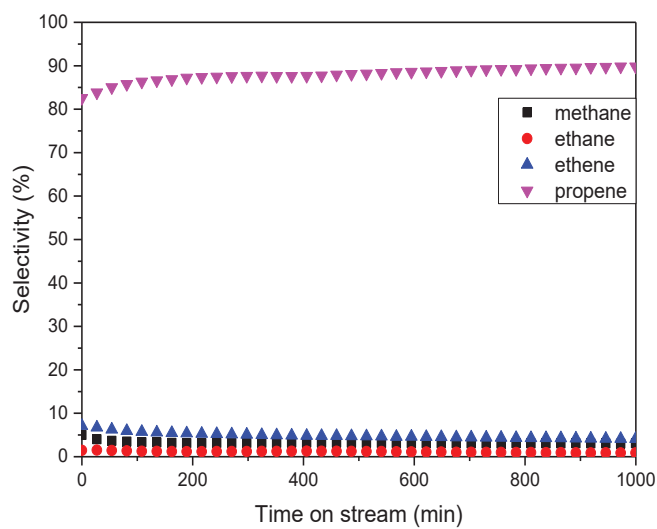


**Figure S4.** Selectivity of **(I)** in propane dehydrogenation;  $P= 1$  bar,  $T= 540$  °C, total flow=  $5 \text{ mL}\cdot\text{min}^{-1}$  (20 % of C3 in Ar)

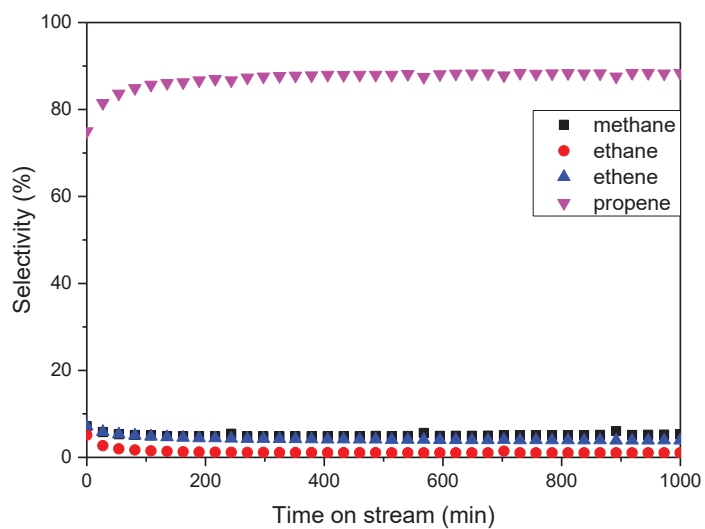


**Figure S5.** Selectivity of  $\text{Ga}(i\text{Bu})_3/\text{Al}_2\text{O}_3\text{-500}$  in propane dehydrogenation;  $P= 1$  bar,  $T= 540$  °C, total flow=  $5 \text{ mL}\cdot\text{min}^{-1}$  (20 % of C3 in Ar)

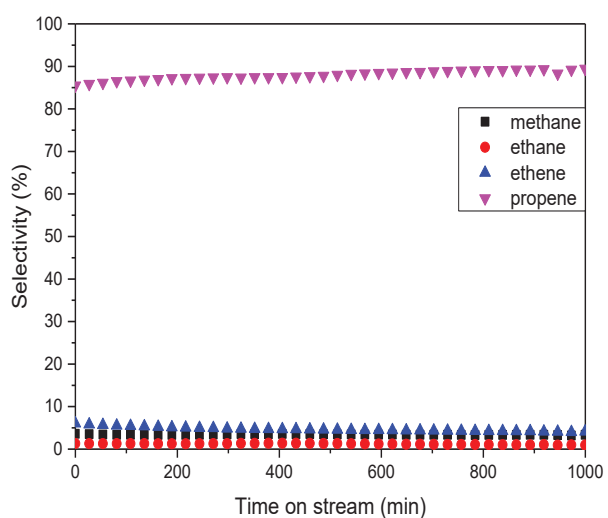


**Figure S6.** Selectivity of **(III)** in propane dehydrogenation;  $P= 1$  bar,  $T= 540$  °C, total flow=  $5 \text{ mL}\cdot\text{min}^{-1}$  (20 % of C3 in Ar)

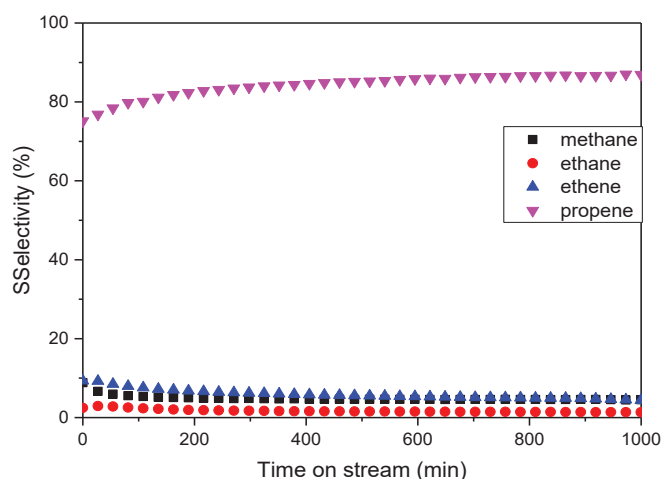


**Figure S7.** Selectivity of (III) in propane dehydrogenation; P= 1 bar, T= 540 °C, total flow= 5 mL.min<sup>-1</sup> (20 % of C3 in Ar)

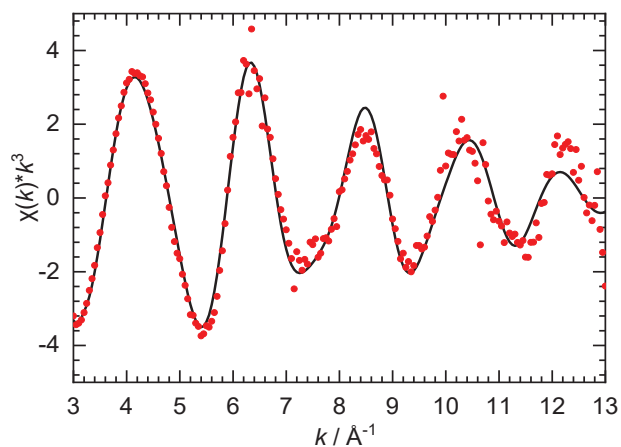


**Figure S8.** Curvefits (line) of the Mo K-edge EXAFS (points) in k<sup>3</sup>-weighted k-space for Ga(*i*Bu)<sub>3</sub>/Al<sub>2</sub>O<sub>3-500</sub>.

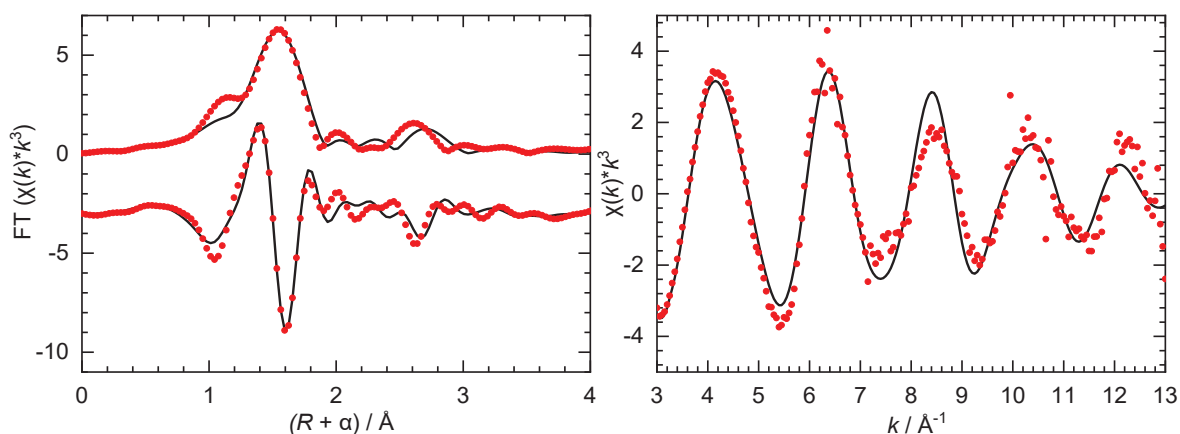


**Figure S9.** Ga K-edge EXAFS (point) for Ga(*i*Bu)<sub>3</sub>/Al<sub>2</sub>O<sub>3-500</sub> recorded at room temperature under He. The curvefit (line) DOES NOT include a Ga-O path at ca. 2.5 Å.

**Table S1.** Curvefit Parameters<sup>a</sup> for Ga K-edge EXAFS of Ga(*i*Bu)<sub>3</sub>/Al<sub>2</sub>O<sub>3-500</sub> without a Ga-O path at ca. 2.5 Å, recorded at room temperature under He

Path	$d^b / \text{Å}$	$N^c$	$R / \text{Å}$	$\sigma^2 / \text{Å}^2$
Ga – O1	1.863	1	1.87(3)	0.002(2) <sup>d</sup>
Ga – C1	2.066	2	2.01(2)	0.002(2) <sup>d</sup>
Ga – C2	2.976	2	3.03(5)	0.010(5) <sup>e</sup>
Ga – Al	3.325	1	3.24(6)	0.010(5) <sup>e</sup>

<sup>a</sup>  $S_0^2$  was fixed at 1.  $\Delta E_0$  was refined as a global fit parameter, returning a value of  $(6 \pm 1)$  eV. Data ranges:  $3.0 \leq k \leq 13.0 \text{ Å}^{-1}$ ,  $1.0 \leq R \leq 3.2 \text{ Å}$ . The number of variable parameters is 7, out of a total of 13.8 independent data points. The R-factor for this fit is 3.5 %. <sup>b</sup> The Ga-O1 and Ga-O2 reference distances are from the crystal structure of Ga<sub>2</sub>O<sub>3</sub> and SrGa<sub>2</sub>B<sub>2</sub>O<sub>7</sub>, respectively.<sup>65,66</sup> The Ga-C and Ga-Al distances are from crystal structures of organogallium compounds.<sup>67,68</sup> <sup>c</sup> These coordination numbers were constrained to integer values, based on the model. <sup>d</sup> Constrained to the same value. <sup>e</sup> Constrained to the same value.

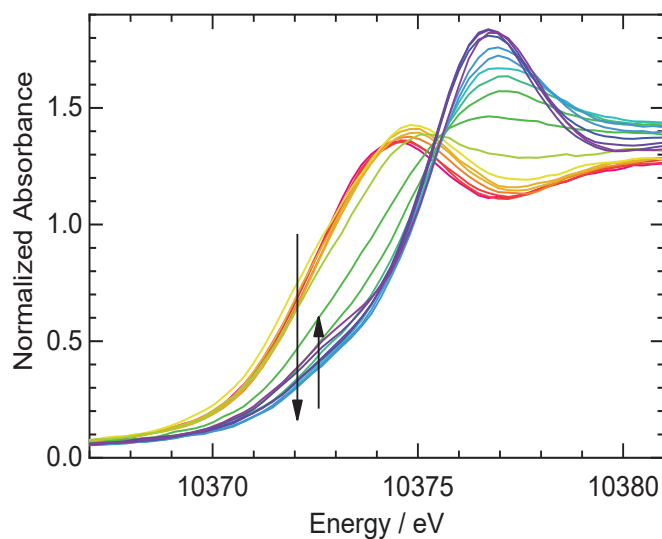


**Figure S10.** Closeup of the Ga K-edge XANES for Ga(*i*Bu)<sub>3</sub>/Al<sub>2</sub>O<sub>3-500</sub>, recorded in flowing He while ramping the temperature from 23 °C (red) to 550 °C (purple) at 10 °C/min.

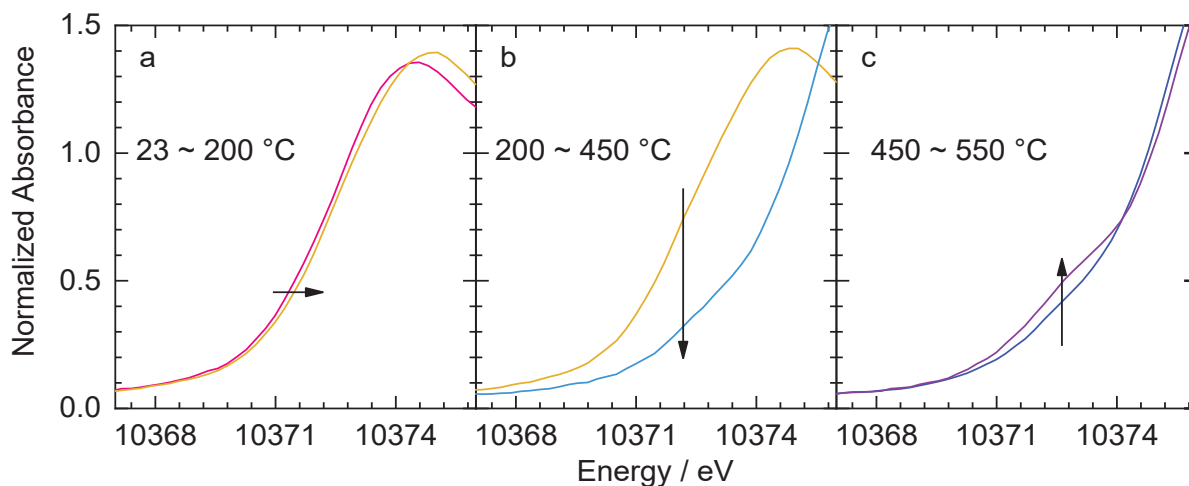


**Figure S11.** Closeup of the Ga K-edge XANES for  $\text{Ga}(i\text{Bu})_3/\text{Al}_2\text{O}_{3-500}$ , recorded in flowing He while ramping the temperature from 23 °C to 550 °C at 10 °C/min: (a) 23 – 200 °C (red to orange); (b) 200 – 450 °C (from orange to blue); (c) 450 – 550 °C (blue to purple).

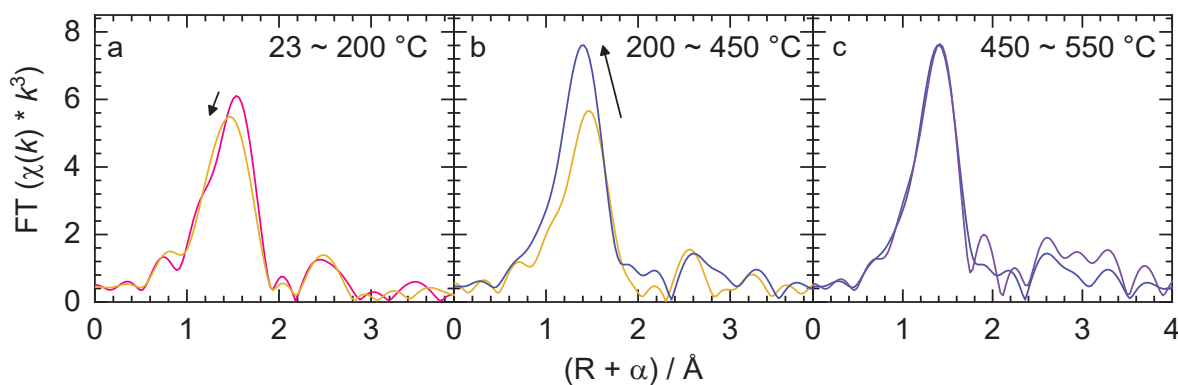


**Figure S12.** Evolution of the Ga K-edge EXAFS for  $\text{Ga}(i\text{Bu})_3/\text{Al}_2\text{O}_{3-500}$ , recorded in flowing He while ramping the temperature from 23 °C (red) to 550 °C (purple) at 10 °C/min. Left: 22 °C (red) and 83 °C (orange); Middle: 114 °C (orange) and 420 °C (blue); Right: 451 °C (blue) and 543 °C (purple).

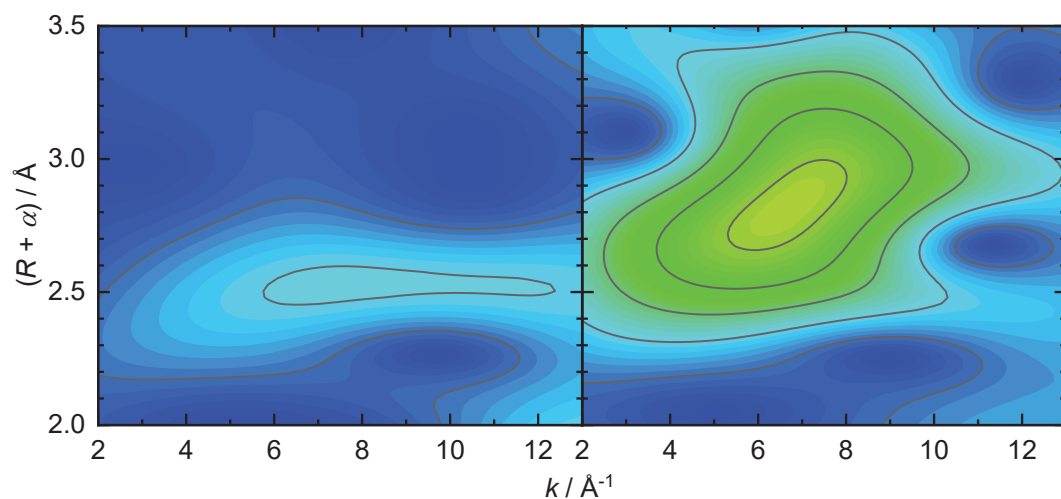


**Figure S13.** Wavelet-transform EXAFS of  $\text{Ga}(i\text{Bu})_3/\text{Al}_2\text{O}_{3-500}$ , at 23 °C (left) and 550 °C (right).

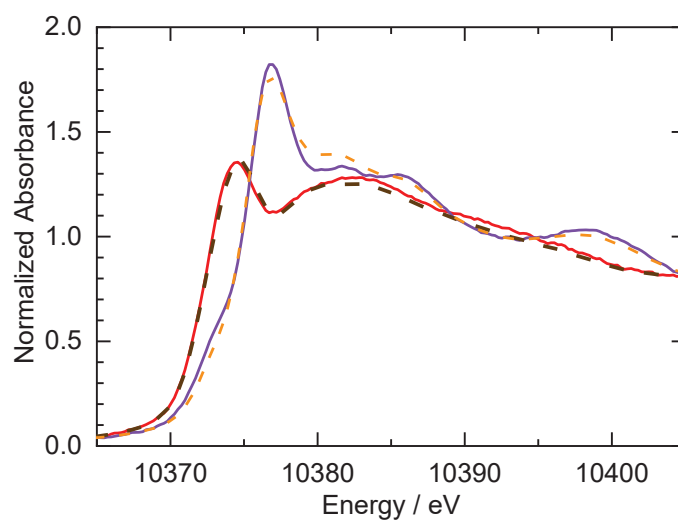


**Figure S14.** Ga K-edge XANES for  $\text{Ga}(i\text{Bu})_3/\text{Al}_2\text{O}_{3-500}$  at 23 °C (red line) and 550 °C (purple line), in comparison with the reconstructed XANES from PCA components at 23 °C (brown dash line) and 550 °C (orange dash line).

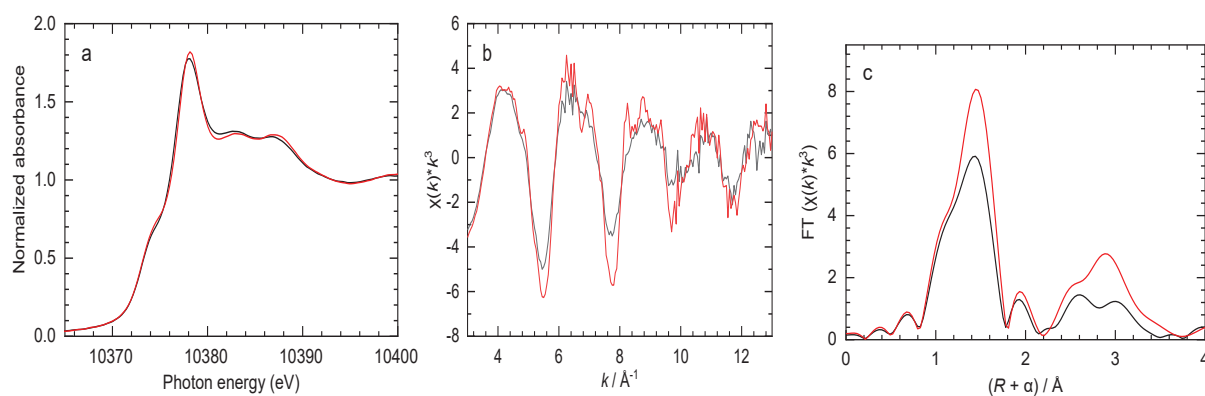


**Figure S15.** The comparison of Ga K-edge (a) XANES, (b) EXAFS in  $k^3$ -weighted  $k$ -space, and (c)  $k^3$ -weighted FT-EXAFS for Ga(*i*Bu)<sub>3</sub>/Al<sub>2</sub>O<sub>3-500</sub> at 550 °C (black line) and cool down to 23 °C (red line).

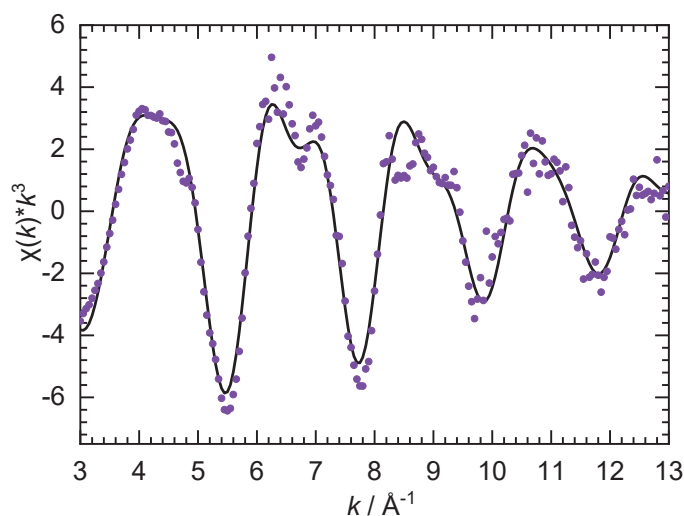


**Figure S16.** Curvefits (red) of the Ga K-edge EXAFS (points) in  $k^3$ -weighted  $k$ -space for Ga(*i*Bu)<sub>3</sub>/Al<sub>2</sub>O<sub>3-500</sub> after heating to 550 °C under He and cooling to room temperature.

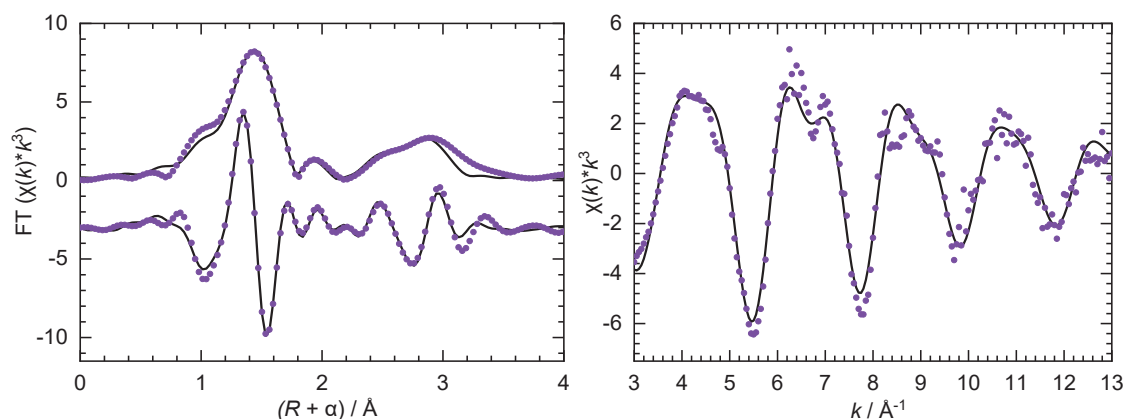


**Figure S17.** Curvefits (line) of the Ga K-edge EXAFS (points) in  $k^3$ -weighted  $k$ -space for Ga(*i*Bu)<sub>3</sub>/Al<sub>2</sub>O<sub>3-500</sub> after heating to 550 °C under He and cooling to room temperature, with a dinuclear Ga model.

**Table S2.** Curvefit parameters<sup>a</sup> for Ga K-edge EXAFS of Ga(*i*Bu)<sub>3</sub>/Al<sub>2</sub>O<sub>3-500</sub> after heating to 550 °C under He and cooling to room temperature, with a dinuclear Ga model.

Path	$d^b / \text{Å}$	$N$	$R / \text{Å}$	$\sigma^2 / \text{Å}^2$
Ga – O1	1.803	3.0(3)	1.85(1)	0.004(1)
Ga – Ga1	3.037	1 <sup>c</sup>	2.95(4)	0.011(4)

Ga – Al1 3.511 3<sup>c</sup> 3.31(2) 0.007(2)

<sup>a</sup>  $S_0^2$  was fixed at 1. Data ranges:  $3.0 \leq k \leq 13.0 \text{ \AA}^{-1}$ ,  $1.0 \leq R \leq 4.0 \text{ \AA}$ . The total independent data point is 18.9.  $\Delta E_0$  was refined as a global fit parameter, returning a value of  $(-1 \pm 1) \text{ eV}$ . The number of variable parameters is 8. The R-factor for this fit is 1.7 %. <sup>b</sup> The Ga-O and Ga-Al distances are extracted from a 3-coordinate doped mononuclear Ga on  $\text{Al}_2\text{O}_3$  model.<sup>73</sup> The Ga-Ga distance is extracted from the crystal structure of  $\text{Ga}_2\text{O}_3$ .<sup>66</sup> <sup>c</sup>  $N$  was fixed based the dinuclear Ga structure.

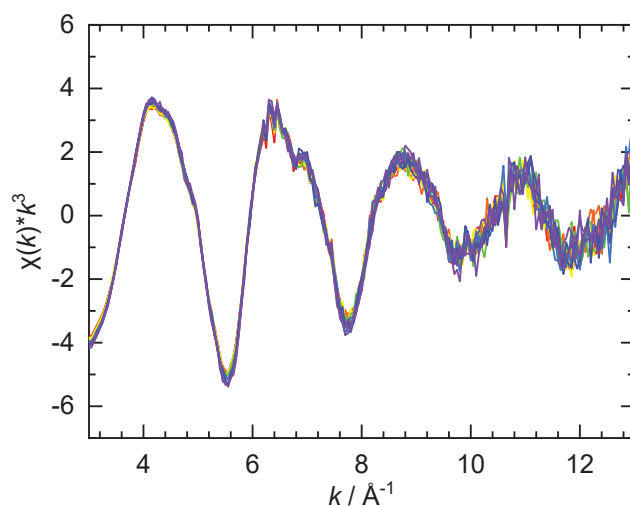


**Figure S18.** Evolution of the Ga K-edge EXAFS for  $\text{Ga}(i\text{Bu})_3/\text{Al}_2\text{O}_{3-500}$  in  $k^3$ -weighted  $k$  space, recorded in flowing 20 vol%  $\text{C}_3\text{H}_8/\text{He}$  at  $550 \text{ }^\circ\text{C}$  for 3 h.

## CHAPTER III. PART B

---

# Influence of coke formation on supported Ga tripodal species during trans-2-butene conversion to butadiene

---



Jessy Abou Nakad,<sup>a</sup> Kai C. Szeto,<sup>a</sup> Aimery De Mallmann,<sup>a</sup> and Mostafa Taoufik <sup>\*a</sup>

<sup>a</sup> Université Lyon 1, Institut de Chimie Lyon, CPE Lyon, CNRS, UMR 5128 CP2M, 43 Bd du 11 Novembre 1918, F-69616 Villeurbanne Cedex, France. E-mail: Mostafa.Taoufik@univ-lyon1.fr; Fax: +33 (0)472 431 798; Tel: +33 (0)472 431 795

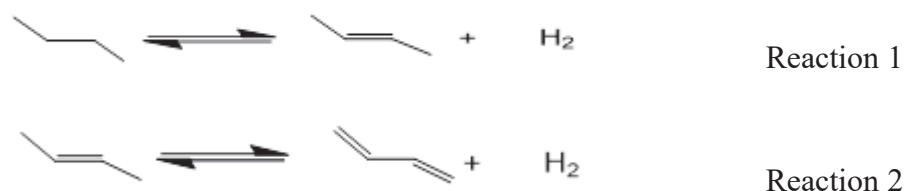
## Abstract

The modification of an alumina partially dehydroxylated at 500°C, Al<sub>2</sub>O<sub>3-500</sub>, by [Ga(O*t*Bu)<sub>3</sub>]<sub>2</sub>, (**1**), using surface organometallic chemistry leads to the formation of material (**2**), bearing a monopodal [(≡AlO)Ga(O*t*Bu)<sub>2</sub>] complex, as major surface species. (**2**) was further thermally treated at 300 °C leading to (**2'**), forming most probably tripodal Ga species, [(≡AlO)<sub>3</sub>Ga], an intermediate proposed in the mechanism of hydrocarbons dehydrogenation reaction. (**2**) and (**2'**) were characterized by mass balance analysis, DRIFT, <sup>1</sup>H and <sup>13</sup>C solid-state NMR, and X-ray absorption spectroscopies. The EXAFS results, were in agreement with the presence of [(≡AlO)<sub>3</sub>Ga] species in (**2'**) with three Ga-O, bond distances at 1.85 Å. The catalytic activity of (**2'**) for trans-2-butene dehydrogenation revealed a butadiene selectivity of 51 % after 300 min on stream. The low selectivity in butadiene observed at short times on stream is related to the formation of cracking products and coke deposition on the surface of the catalyst. These changes are indicative of a modification in the reaction mechanism and in the nature of the active sites during 2-butenes conversion, where in addition to gallium sites, the carbonaceous phase on the materials is also active for this reaction. The catalytic activity of (**2'**) for 2-butenes conversion was also evaluated in the presence of CO<sub>2</sub> as a co-feed. It was shown that, when introduced in the feed, CO<sub>2</sub> reacts with H<sub>2</sub>, due to RWGS reaction, thus limiting the formation of undesired products and leading to a higher selectivity toward butadiene (65 %), similarly to what was reported for Catadiene® process.

## Introduction

From an industrial point of view, 1,3-butadiene (1,3-BD) is considered as an important chemical building block due to its several uses as an intermediate to produce important industrial products. The major uses of 1,3-BD are for the production of styrene-butadiene rubbers and polybutadienes,<sup>1,2</sup> hence, the demand is estimated to increase in the upcoming years. The existing routes to produce butadiene are i) steam cracking (SC), as a coproduct of ethylene, ii) the catalytic conversion of ethanol to butadiene (ETB), iii) the dehydration of butanediol into butadiene, iv) the oxidative dehydrogenation of n-butene (Oxo-D or OX-D process), v) the catalytic dehydrogenation of n-butane and n-butene (Houdry process). Among these processes, SC is holding the largest share of the global butadiene production (95%). Butadiene is obtained as a co-product in SC followed by a purification process and the selectivity is highly dependent of the feedstock used.<sup>3</sup> Although two processes known as

Lebedev® and Ostromislensky® are employed for ETB reaction, the productivity with this technology is insufficient to insure its economic viability.<sup>4</sup> The dehydration of butanediol (BDO) to butadiene (BD) was also proposed as an alternative route to produce BD, however, this reaction undergoes two steps: a dehydration of 2,3 BDO into 3-buten-2-ol at 350 °C and a further dehydration of the butenol at a higher temperature is required to produce 1,3-BD.<sup>5</sup> Oxidative dehydrogenation routes have been widely studied due to the low operating temperature required during this reaction. However, many undesired reactions are possible with oxygen, leading to the formation of oxygenated products (for example CO<sub>2</sub>) resulting in a lower selectivity toward 1,3-BD.<sup>6</sup> The non-oxidative dehydrogenation of butane and/or butane/butene (BDH) mixtures is an important route, since it reduces the dependency on steam cracking of naphtha from one part, and from another part, it produces H<sub>2</sub>, a valuable product to the market. A chromium-based catalyst supported on alumina was developed to convert butane into butene followed by a dimerization and hydrogenation to produce octane. To date, Catadiene® is the only commercial technology available for on-purpose production of n-butylenes and butadiene from n-butane by BDH which is used in the industry. This process employs a highly loaded chromium catalyst supported on alumina with operating conditions of 600-620 °C and 0.2-0.4 bar. The catalyst must be regenerated after a few minutes by injecting air to burn off the coke layer formed at such high operating temperatures. Apart from the coke, the catalyst deactivates due to the decrease in the concentration of chromium active sites, after their incorporation within the alumina framework. A butane conversion of 30-40% is obtained in the process and butadiene selectivity can reach up to 65%. However, this selectivity is obtained after two steps: the first one consists in the dehydrogenation of butane into n-butenes as an intermediate species, whereas the second, requires further dehydrogenation of n-butenes into butadiene (Scheme 1).<sup>7</sup> Thermodynamically, the dehydrogenation of n-butenes is more challenging than the dehydrogenation of n-butane.<sup>8</sup>



**Scheme 1.** Proposed reactions during butane/butenes dehydrogenation

Consequently, butane dehydrogenation has been occasionally explored and can be catalyzed by several metal oxides such as  $\text{VOx}/\text{Al}_2\text{O}_3$ ,<sup>9,10</sup>  $\text{CrOx}/\text{SiO}_2$ ,<sup>11</sup> and  $\text{Ga}_2\text{O}_3/\text{ZSM-5}$ ,<sup>12</sup> as well as noble metal-based catalysts.<sup>13-16</sup> A general inconvenience appearing in these studies is the low selectivity toward 1,3-BD due to side reactions.<sup>17</sup> On the other hand, the dehydrogenation of n-butenes, thermodynamically more challenging and which will principally lead to a high selectivity in 1,3-BD) is far less exploited.

We hereby aim to develop heterogeneous catalysts carefully designed to readily undergo the dehydrogenation of n-butenes to 1,3-BD. From an environmental context, it is highly desirable to replace the toxic chromium-based catalyst by an environmental friendly element. Sticking to non-noble elements (for economical reason), supported gallium and vanadium catalysts have shown promising activities in propane dehydrogenation and are evidently the elements of choice. The mechanism for alkane or alkene dehydrogenation over supported metal oxide catalysts as well as the active sites responsible for this reaction are still unclear. Former studies were inspired by the state of the art on chromium systems for dehydrogenation reactions (notably of propane), where the active site is postulated to be an isolated tripodal Cr(III) species based on theoretical calculations.<sup>18</sup> Obtaining strong evidences of the active site from experimental data are rather challenging, due to the preparation methods that are usually based on aqueous impregnation followed by calcination. The latter step will inevitably generate a variety of monomeric, dimeric and oligomeric MOx species on the surface, hampering the characterization of the real active sites. Thus, a prerequisite to access supported catalysts suitable for active site investigations lies on innovative preparation methods that uniquely give the postulated tripodal surface species. Furthermore, such materials are expected to strongly enhance the catalytic activity with respect to the metal content. We expected that the mechanism of the conversion of 2-butenes occurs via an isomerization of 2-butenes into 1-butene by an insertion of 2-butene, for instance in a MO-H bond (M= Al, Ga), followed by a  $\beta$ -H elimination (Scheme 2). The C-H bond in an allylic position of 1-butene intermediate can then be activated on the Ga-O of tripodal species, leading to the formation of a gallium  $\eta^3$ -methalallyl intermediate and a surfacic Al-OH. The  $\eta^3$ -methalallyl gallium intermediate in equilibrium with  $\eta^1$ -methalallyl gallium may then undergo a  $\beta$ -H elimination, which leads to the release of butadiene and the generation of a bipodal Ga-H species. The latter species, proposed as an intermediate in Scheme 2, can either release hydrogen and regenerate the tripodal species, activate a C-H bond or react with the double bond of butenes through insertion reactions. Another mechanism would occur via coordination of 2-butenes



experiments, the spinning frequency was 10 kHz, the recycle delay was 5 s and 8 scans were collected using a 90° pulse excitation of 3 μs. The <sup>13</sup>C CP MAS spectrum was obtained at a spinning frequency of 10 kHz, with a recycle delay of 5 s and 10312 scans were collected. Chemical shifts were given in ppm with respect to TMS as an external reference for <sup>1</sup>H and <sup>13</sup>C NMR. **X-ray absorption spectra** were acquired at ESRF on BM23 beam-line, at room temperature at the gallium K edge (10.37 keV). A double Si(111) crystal was used as monochromator and a system based on a total reflection through a double X-ray mirror with an incidence angle variable from 2 to 5 mrad allowed harmonic rejection to better than the 10<sup>-5</sup> level.<sup>20</sup> The spectra were recorded in the transmission mode between 10.1 and 11.4 keV. Four scans were collected for each sample. Each data set was collected simultaneously with a W metal foil (L<sub>III</sub> edge at 10.2068 keV) and was later aligned according to that reference. Samples were packaged with dry BN as pellets within an argon filled glove box in a double air-tight sample holder equipped with kapton windows. The data analyses were performed by standard procedures using in particular the program “Athena”.<sup>21</sup>

#### **Preparation of the molecular complex [Ga(O*t*Bu)<sub>3</sub>]<sub>2</sub>, (1):**

The gallium precursor [Ga(O*t*Bu)<sub>3</sub>]<sub>2</sub> was synthesized by reaction of [Ga(NMe<sub>3</sub>)<sub>2</sub>]<sub>2</sub> (Strem, used as received) with *t*BuOH in hexane.<sup>19</sup> The entire preparation procedure was carried out in an inert atmosphere, using a Schlenk line. A mass of 2 g of [Ga(NMe<sub>3</sub>)<sub>2</sub>]<sub>2</sub> was dissolved in 55 mL hexane in a Schlenk flask. Then, a solution made of 2.33 g of dried *t*BuOH in 25 mL hexane was gradually added in the Schlenk flask and the resulting solution was stirred at room temperature for 48 hours. After removing the solvent by distillation, a white solid was observed. This product was further dried under reduced pressure and crystallized in dry CH<sub>2</sub>Cl<sub>2</sub>. <sup>1</sup>H NMR, C<sub>6</sub>D<sub>6</sub>: δ (ppm) = 1.48 (OCCH<sub>3</sub>), 1.56 (μ-OCCH<sub>3</sub>); <sup>13</sup>C{<sup>1</sup>H} NMR, C<sub>6</sub>D<sub>6</sub>: δ (ppm) = 32.2 (μ-OCCH<sub>3</sub>), 33.9 (OCCH<sub>3</sub>), 71.8 (OCCH<sub>3</sub>), 78.5 (μ-OCCH<sub>3</sub>)

#### **Preparation of the supported Ga tripodal species (2’).**

The tripodal species were prepared in two steps: First, the grafting of the organometallic precursor onto the desired support and second, a thermolysis of the resulting material under a high vacuum at 300 °C. Typically, [Ga(O*t*Bu)<sub>3</sub>]<sub>2</sub> (170 mg) was dissolved in pentane and brought in contact with 1 g of Al<sub>2</sub>O<sub>3</sub> (AluC, Evonik) previously dehydroxylated at 500 °C, Al<sub>2</sub>O<sub>3-500</sub>. The suspension was stirred for 4 hours at room temperature and was then filtered. The resulting solid was extensively washed with pentane and dried under high vacuum at room temperature, affording (2). The dried material was then thermally treated at 300 °C under a high vacuum for 2 hours to finally afford the tripodal species, (2’).

### **Preparation of the supported Ga tripodal species (3'). Article in preparation**

The tripodal species were prepared in two steps: First, the grafting of the organometallic precursor onto the desired support and second, a thermolysis of the resulting material under a high vacuum at 300 °C. Typically,  $[\text{Ga}(\text{O}t\text{Bu})_3]_2$  (170 mg) was dissolved in pentane and brought in contact with 1 g of  $\text{Al}_2\text{O}_3$  (with a B.E.T of  $200 \text{ m}^2.\text{g}^{-1}$ ) previously dehydroxylated at 500 °C,  $\text{Al}_2\text{O}_{3-500}$ . The suspension was stirred for 4 hours at room temperature and was then filtered. The resulting solid was extensively washed with pentane and dried under high vacuum at room temperature, affording (3). The dried material was then thermally treated at 300 °C under a high vacuum for 2 hours to finally afford the tripodal species, (3').

**Catalyst evaluation.** The performances of (2') for trans-2-butene (Air Liquide, 99.5%) and (3') for propane (99.95 % Air Liquide, < 20 ppm propene). conversion was carried out in a stainless-steel continuous flow reactor ( $P_{\text{total}} = 1 \text{ bar}$ ,  $\theta = 540 \text{ °C}$ , total flow rate =  $5 \text{ mL}\cdot\text{min}^{-1}$  (20% trans-2-butenes or propane in argon). The catalytic mass varied between 80-170 mg and was diluted in 2 g of CSi. The gases were purified on a column of molecular sieve and activated  $\text{Cu}_2\text{O}/\text{Al}_2\text{O}_3$  catalyst, and their flow controlled by Brooks mass-flow controllers. The catalyst was charged within the reactor inside the glovebox. A 4-way valve allowed the isolation of the catalyst from the environment and extensive purging of the tubes before the reaction. In each experiment, the catalyst was heated under a flow of Ar ( $4 \text{ mL}\cdot\text{min}^{-1}$ ) until the targeted temperature was reached and then the gas containing 20 % of trans-2-butene or propane was introduced, resulting in a total flow of  $5 \text{ mL}\cdot\text{min}^{-1}$ . The products were determined by an online HP 6890 GC equipped with a 50 m  $\text{KCl}/\text{Al}_2\text{O}_3$  column and a FID detector. The conversion was calculated directly from the data given by the FID detector, without considering the isomerization of trans-2-butene.

## **Results and Discussions**

### **Preparation and characterization of tripodal species**

The isolated surface tripodal Ga species,  $[(\equiv\text{AlO})_3\text{Ga}]$ , is prepared by using an innovative synthetic method based on two steps, combining a grafting reaction, according to surface organometallic chemistry (SOMC) procedures and a thermolysis of the grafted surface species. Surface organometallic chemistry on oxides is a powerful, flexible and sustainable approach to prepare isolated surface species.<sup>22</sup> It involves the controlled grafting of a suitable organometallic precursor onto the surface hydroxyl groups of oxides supports. The structure

of the surface species depends on the dehydroxylation temperature of the support, allowing to control the density of surface hydroxyl groups that serve as anchoring points. Hence, the resulted material will contain firmly bonded surface organometallic fragments being highly dispersed.

A judicious selection of the organometallic precursor is the most important part of the process. In order to access to surface tripodal species, it turns out that *tert*-butoxide metal complexes are suitable precursors. Previously, we have employed molybdenum and tungsten oxo *tert*-butoxide complexes to produce silica supported single sites, bis-oxo species, for olefin metathetic oxidation or metathesis.<sup>23,24</sup> During the thermolysis under vacuum, the metal coordinated *tert*-butoxide ligand undergoes a  $\beta$ -H elimination, resulting in an *isobutene* release and an OH group coordinated to the metal, M-OH. The bis-oxo species of Mo and W are formed after a subsequent  $\alpha$ -H abstraction releasing water. For the preparation of Ga tripodal systems,  $[\text{Ga}(\text{O}t\text{Bu})_3]_2$  is grafted on  $\text{Al}_2\text{O}_3$  (AluC, Evonik,  $100 \text{ m}^2\cdot\text{g}^{-1}$ ) previously dehydroxylated at  $500 \text{ }^\circ\text{C}$ ,  $\text{Al}_2\text{O}_{3-500}$  by a protonolysis, reaction affording material **(2)**, bearing alumina supported gallium *tert*-butoxide intermediates.

Elemental analysis of material **(2)** indicated Ga and C contents of 1.07 and 1.51 wt%, respectively, which corresponds to a C/Ga molar ratio of 8.23. The identification of the *tert*-butanol evolved during the grafting reaction and its quantification by GC using octane as an internal standard, revealed an amount of 0.8 *t*BuOH/Ga. These results suggest the formation of  $[(\equiv\text{AlO})\text{Ga}(\text{O}t\text{Bu})_2]$  monomeric species. The resulting material, **(2)**, was characterized by DRIFT, solid-state NMR and X-ray absorption spectroscopies. The DRIFT spectrum of  $\text{Ga}(\text{O}t\text{Bu})_3/\text{Al}_2\text{O}_{3-500}$ , **(2)**, exhibits a partial consumption of the hydroxyl groups (a in Figure 1 Left). Consequently, we observed new bands in the range of 3000-2800 and 1500-1300  $\text{cm}^{-1}$ , assigned to C-H stretching and  $\text{CH}_x$  bending and scissoring of *tert*-butoxide ligands.

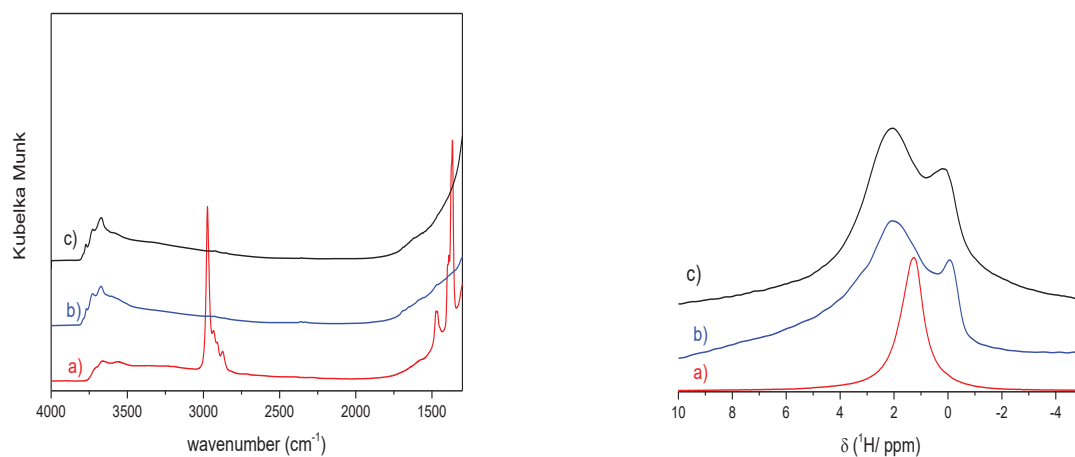
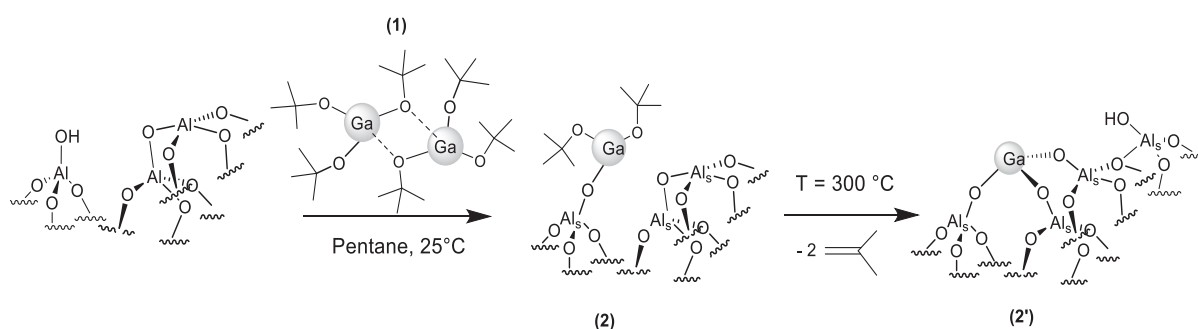


**Figure 1. Left.** DRIFT and **Right.** <sup>1</sup>H MAS NMR (11.7 T, 10 kHz,  $d_1 = 10$  s) of a) Material **(2)**, Ga(O*t*Bu)<sub>3</sub>/Al<sub>2</sub>O<sub>3-500</sub> ; b) Material **(2')**, obtained from **(2)** after a thermal treatment of [Ga(O*t*Bu)<sub>3</sub>]<sub>2</sub>/ Al<sub>2</sub>O<sub>3-500</sub> at 300 °C and c) Al<sub>2</sub>O<sub>3-500</sub> support.

Additional information on the Ga coordination environment were provided by solid-state NMR techniques. The <sup>1</sup>H MAS NMR spectrum consists in an intense and large signal at 1.3 ppm, attributed to CH<sub>3</sub> protons of the tert-butoxide ligand (a in Figure 1, Right), while in the <sup>13</sup>C CP/MAS spectrum of **(2)** exhibited two signals centered at 72 ppm and 31.1 ppm corresponding to quaternary C and CH<sub>3</sub> of the tert-butoxide ligands,<sup>19</sup> respectively (Figure S1, b). The formation of this Ga species has been confirmed by the study of the EXAFS of **(2)** at the Ga K-edge. From the fit of the EXAFS, an average Ga coordination sphere can be specified with the distances of Ga to its neighbouring atoms. For **(2)**, the EXAFS and the fit are shown in Figure 2 (top: A1 and B1) with the corresponding Fourier transforms and the structural parameters obtained from this fit are given in the right part of Table 1. This gives ca. three Ga-O short distances at 1.823(9) Å and less than one Ga-O longer distance at 1.95(3) Å, which agrees with a structure similar to the one of Ga(O*t*Bu)<sub>3</sub>(HNMe<sub>2</sub>) monomeric molecular compound, characterized by DRX. In this complex, Ga is coordinated by three O atoms at distances in the range of [1.797 - 1.824 Å] and one N atom from the basic dimethylamine at 2.022(2) Å.<sup>19</sup> Moreover, the fit was improved when considering further layers of backscatterers, ca. two C atoms at 3.01(5) Å and a one Al atom at 3.61(14) Å. Thus, all of the above results agree with the the formation of a monopodal species on the Evonik AluC alumina support, (species **(2)** in Scheme 3) similarly to what was reported in the case of an alumina with a higher surface area (200 m<sup>2</sup>.g<sup>-1</sup>). Article in preparation

A thermal treatment of **(2)** under vacuum at 300 °C affords **(2')**, which is also a white solid, along with the release of 1.9 equivalents of isobutene per gallium. Isobutene is presumably formed by a  $\beta$ -H elimination with the formation of Ga-OH bonds in intermediate species (Scheme 3). DRIFT analysis indicates that part of the Al-OH groups has been restored (b in the left part of Figure 1). The reappearance of Al-OH groups is most likely due to a Ga-OH transfer by the opening of an adjacent Al-O-Al bridge, resulting in the gallium tripodal surface species along with formation of a surface Al-OH group (from **(2)** to **(2')** in Scheme 3). A similar feature is observed by  $^1\text{H}$  MAS NMR since the spectrum of **(2')** strongly resembles the one of the dehydroxylated alumina, with several unresolved signals between 2.2 to 0 ppm (b and c in the right part of Figure 1).<sup>25</sup>



**Scheme 3.** Formation of tripodal **(2')**,  $[(\equiv\text{AlO})_3\text{Ga}]$  from **(2)**,  $[(\equiv\text{AlO})\text{Ga}(\text{OtBu})_2]$ , after a thermal treatment at 300 °C which releases isobutene

The fit of the EXAFS obtained for **(2')** at the Ga K-edge also agrees with a tripodal Ga structure in this material, with three oxygen atoms at 1.86 Å and three aluminium atoms, two at 3.23 Å and one at 3.56 Å (Figure 2 and Table 1). Beside the fit could be improved by considering two other O backscatterers at distances of 2.30 and 2.98 Å that may correspond to oxygen from the support. Thus, this is in accordance with the formation of a tripodal monomeric species.

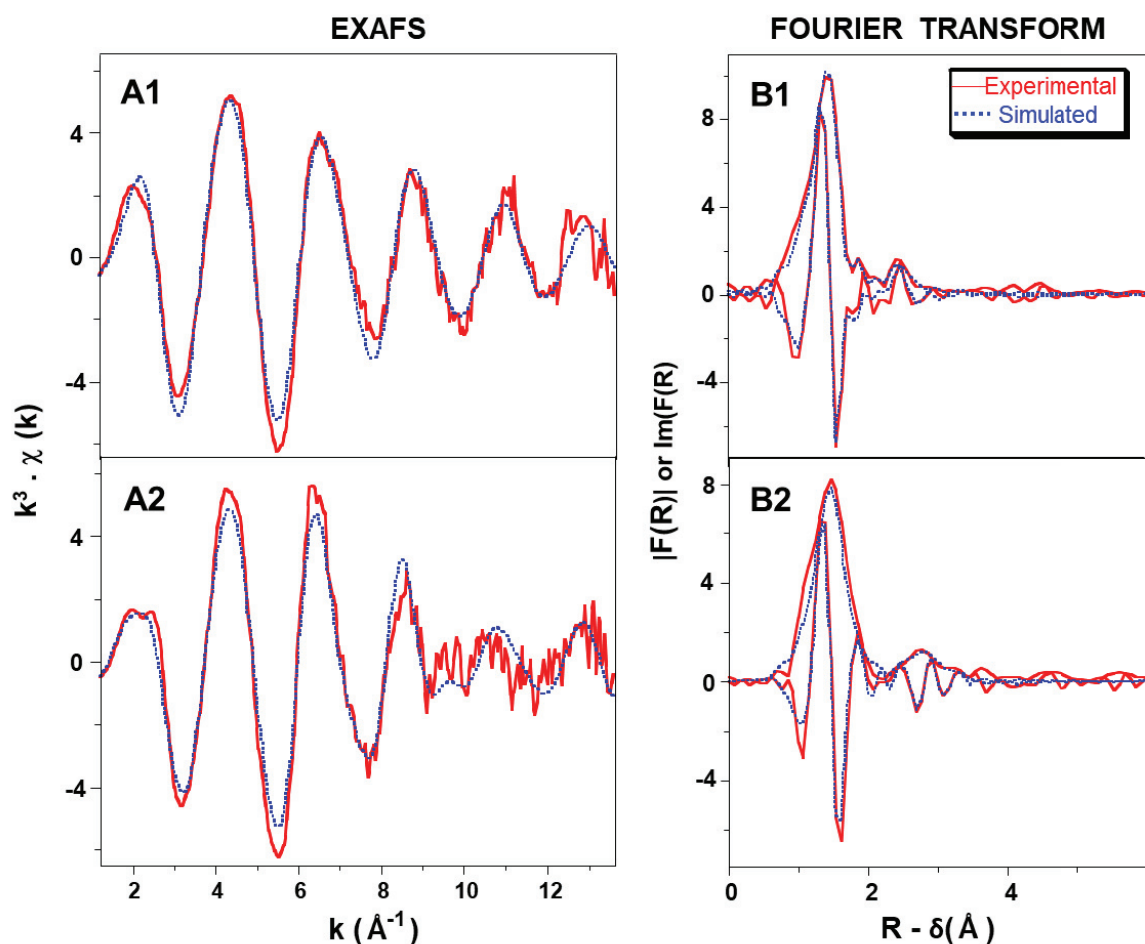


**Figure 2.** Ga K-edge  $k^3$ -weighted EXAFS of (**2**) and (**2'**) (left: A1 and A2 respectively) and corresponding Fourier transform (right: B1 and B2; moduli and imaginary parts;  $R - \delta$ : distance uncorrected from phase shifts). Solid red lines: Experimental; Dashed blue lines: Fit (spherical wave theory).

**Table 1.** Parameters obtained from the fit of the EXAFS spectra of (**2**) and (**2'**). The error interval generated by the fitting program “RoundMidnight” is between parentheses for each variable parameter.

Type of neighbors	Material <b>2</b> ( $[(\equiv\text{AlO})\text{Ga}(\text{OtBu})_2]^{(a)}$ )			Material <b>2'</b> ( $[(\equiv\text{AlO})_3\text{Ga}]^{(b)}$ )		
	Number of neighbors	Distance ( $\text{\AA}$ )	$\sigma^2$ ( $\text{\AA}^2$ )	Number of neighbors	Distance ( $\text{\AA}$ )	$\sigma^2$ ( $\text{\AA}^2$ )
Ga- <u>O</u> <sub>1</sub>	3	1.823(9)	0.0049(8)	3	1.86(1)	0.0061(10)
Ga- <u>O</u> <sub>2</sub>	1	1.95(3)	0.0069(30)	1	2.30(2)	0.0024(15)
Ga- <u>C</u>	2	3.01(5)	0.0075(35)	-	-	-
Ga- <u>O</u> <sub>3</sub>	-	-	-	1	2.98(7)	0.0054(50)

<b>Ga--Al<sub>s</sub></b>	-	-	-	2	3.23(5)	0.0114(35)
<b>Ga--Al<sub>s</sub></b>	1	3.61(14)	0.060(50)	1	3.56(7)	0.0114 <sup>(c)</sup>

<sup>(a)</sup>  $\Delta k$ : [1.2 - 13.6 Å<sup>-1</sup>] -  $\Delta R$ : [0.3 - 3.2 Å];  $S_0^2 = 0.96$ ;  $\Delta E_0 = 5.2 \pm 0.6$  eV (the same for all shells); Fit residue:  $\rho = 4.6$  %; Quality factor:  $(\Delta\chi)^2/\nu = 2.86$  ( $\nu = 15/24$ ). <sup>(b)</sup>  $\Delta k$ : [1.2 - 13.6 Å<sup>-1</sup>] -  $\Delta R$ : [0.5 - 3.6 Å];  $S_0^2 = 0.96$ ;  $\Delta E_0 = 4.7 \pm 0.9$  eV (the same for all shells); Fit residue:  $\rho = 4.9$  %; Quality factor:  $(\Delta\chi)^2/\nu = 3.36$  ( $\nu = 16/26$ ). <sup>(c)</sup> parameter constrained to the one above.

The characterization of (**2'**) by DRIFT, NMR, mass balance analysis and EXAFS reveals a similar structure, with supported tripodal Ga species, independently on the nature and the surface area of the employed alumina (100 vs 200 m<sup>2</sup>.g<sup>-1</sup>). In fact, this synthetic method was indeed already extended to an alumina with a higher surface area of 200 m<sup>2</sup>.g<sup>-1</sup> (**3'**), leading to similar structures for (**2**) and (**2'**).

## Catalytic properties

In order to study the effect of the nature of alumina on the dehydrogenation reaction, material (**2'**) containing supported Ga tripodal, catalyst (was initially tested for propane dehydrogenation at 540 °C, and the results compared to those obtained with a similar material containing tripodal Ga species but supported on an alumina presenting a higher surface area (200 m<sup>2</sup>.g<sup>-1</sup>), (**3'**). Article in preparation.

The catalysts (**2'**) and (**3'**) showed a similar activity in PDH in the same conditions, however, a very slow deactivation was observed in the case of (**3'**) compared to the high stability for (**2'**) (Figure S2). This result suggests that with a non-porous alumina (100 m<sup>2</sup>.g<sup>-1</sup>) used as support, higher catalytic performances are obtained compared to a porous alumina (200 m<sup>2</sup>.g<sup>-1</sup>), most probably due to the deactivation of gallium sites located within the pores by the formation of coke. The initial propylene selectivity obtained with catalyst (**3'**) was higher (86 %) (Figure S3) compared to (**2'**) (73 %) (Figure S4). However, after 1000 min, the selectivity in propene was *ca.* 89 % for both catalysts.

Since the catalytic behavior of (**2'**) and (**3'**) are similar for PDH, the conversion of trans-2-butene was also studied with catalyst (**2'**) in a continuous flow reactor. The trans-2-butene isomer is more stable than *n*-butene isomer,<sup>26</sup> but is far less exploited compared to 1-butene due to its lower reactivity. Apart from industrial processes where 2-butenes (trans and cis isomers) are used for the production of alkylated gasoline and propylene (through olefin cross-metathesis),<sup>27,28</sup> other valorization of 2-butenes is rare,<sup>29,30</sup> even in academic research. We reported the best unprecedented single-site catalyst, WH<sub>3</sub>/Al<sub>2</sub>O<sub>3-500</sub> for the direct conversion of trans-2-butene to propylene. This catalyst operates as a “bi-functional single

active site”, a tungsten carbene-hydride catalyst opening up the non-degenerate pathway via 2-butene isomerization to 1-butene and a tungsten carbene catalyst for 2-butenes/1-butene cross-metathesis. This example was described as a novel process to utilize 2-butene feedstock to produce propylene with a promising productivity.<sup>29</sup> Gallium catalyst on alumina can also play the role of a bifunctional catalyst for the isomerization of trans-2-butenes into 1-butenes on Ga-H intermediate species (Scheme 2), followed by a dehydrogenation from an allylic gallium species, leading to the formation of butadiene.

The catalytic performance of  $[(\equiv\text{AlO})_3\text{Ga}]$ , (**2'**), for trans-2-butene conversion has been evaluated at 540 °C, 1 bar and in a total flow of 5 mL.min<sup>-1</sup> (20 % trans-2-butene in Ar). An initial conversion of 13.3 % was obtained followed by a gradual deactivation as a function of time on stream, leading to 6.2 % after 2400 min (Figure 3, a). After 2400 min, the selectivities were 47 % in butadiene, 18.8 % in methane, 14.6 % in butane, 14.2 % in propene, 2.75 % in ethane and 2.3 % in ethylene, with traces of propane (<1 %). Butadiene is observed as a product at early times on stream but with a low selectivity (ca. 22 % at 60 min) (Figure 3, b). However, after 300 min, the selectivity toward 1,3-butadiene reaches its maximum, ca. 51.4 %. At 60 min, butadiene is accompanied with the formation of ca. 20.2 % ethylene, 19.3 % methane, 19 % propene, 13.3 % butane, 5.2 % ethane and traces of propane (< 1%). It is noticeable that a substantial formation of light C<sub>1</sub>-C<sub>3</sub> hydrocarbons from the cracking of the feed's molecule is seen at the beginning of the catalytic reaction and decreases after 300 min. This formation of coke at the beginning of the reaction, is known to be catalyzed by the presence of acid sites on the support.<sup>31</sup> These changes are indicative of a modification in the reaction mechanism and in the nature of the active sites during 2-butenes conversion.

Similar phenomena of carbonaceous deposits allowing an enhancement of the catalytic activity are already reported in literature. McGregor et al.<sup>31</sup> were the first to demonstrate by using advanced techniques that carbonaceous materials, coke, deposited over VO<sub>x</sub>/Al<sub>2</sub>O<sub>3</sub> can also convert *n*-butane into butadiene. This active material was produced on the surface of a vanadium catalyst supported on alumina at the beginning of the dehydrogenation reaction, where the selectivity in butenes is very low. The authors claim that organic radicals detected by EPR associated with the carbonaceous material may play a role in the reaction mechanism. These findings are not restricted to dehydrogenation reactions,<sup>32</sup> interestingly, the catalytic activity related to the formation of carbonaceous over layers was also observed during Fisher-Tropsch reaction. Another example describing the key role of carbon deposits forming a Pd-Cx catalytic active phase during the selective hydrogenation of alkynes, was reported in

literature.<sup>33,34</sup> From all these results, we can conclude that butenes dehydrogenation can be also considered as a reaction in which carbonaceous materials associated to gallium tripodal species supported on alumina can offer a high activity and selectivity.

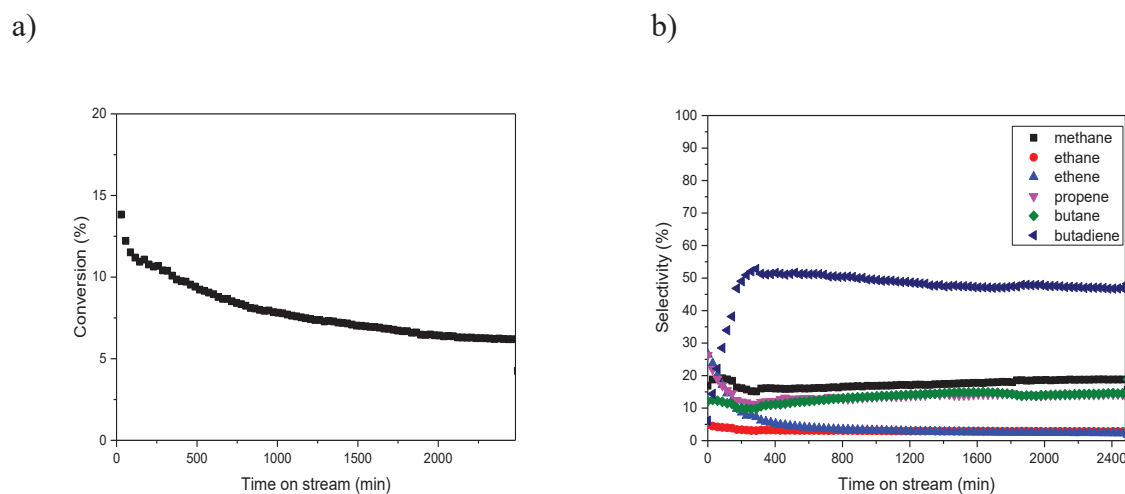


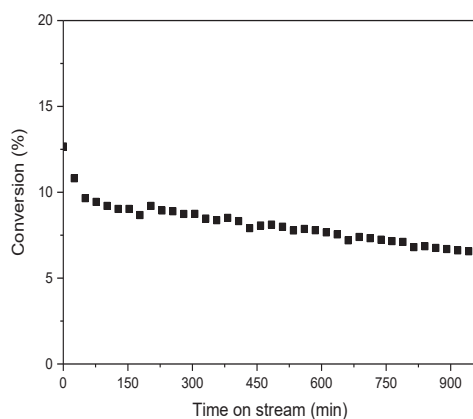
**Figure 3.**  $[(\equiv\text{AlO})_3\text{Ga}]$ , (**2'**), for trans-2-butene transformation, a) conversion and b) selectivity (%) at 540 °C, 1 bar and with a total flow = 5 mL.min<sup>-1</sup> (20 % trans-2-butene in Ar)

In order to increase the 2-butene conversion and the selectivity in butadiene, material (**2'**) was tested in the presence of CO<sub>2</sub>. In that manner, the hydrogen produced can be removed by the RWGS reaction, which would be beneficial, resulting in better catalytic performances, allowing the decrease of the formation of light hydrocarbons by cracking reaction. In fact, studies recently reported the use of CO<sub>2</sub> as a mild oxidant during the non-oxidative dehydrogenation reaction, in order to shift the equilibrium toward the production of olefins.<sup>35-37</sup> Liu et al. demonstrated that the use of CO<sub>2</sub> as a mild oxidant with Ga<sub>2</sub>O<sub>3</sub>/SiO<sub>2</sub> catalyst would minimize the carbonaceous deposition and improve the stability of the catalyst and propene selectivity during propane dehydrogenation.<sup>35</sup> Hence, using this information, catalyst (**2'**), containing tripodal gallium species supported on alumina was tested for trans-2-butene conversion in the presence of CO<sub>2</sub> in the feed.

Exposing (**2'**) to trans-2-butene (20% in Ar) in a fixed-bed reactor at 540 °C gives an initial conversion of 13% followed by a rapid decay towards 7 % after approximately 900 min on stream (Figure 4). The selectivity is altered during the first hours on stream and starts to stabilize after ca. 320 min on stream. After 900 min, the main products are butadiene (64.6 %), methane (13.1 %), propylene (9.5 %), butane (6.8 %), ethene (3.4 %) and ethane (2.6 %). Although the conversion does not vary in the presence of CO<sub>2</sub>, the formation of secondary

reaction was limited and led to a higher selectivity toward butadiene, 64.6 % instead of 50 % in the absence of CO<sub>2</sub>. These results are in accordance with those reported in literature, showing that using an oxidant in order to limit hydrogen production can decrease the formation of cracking products.

a)



b)

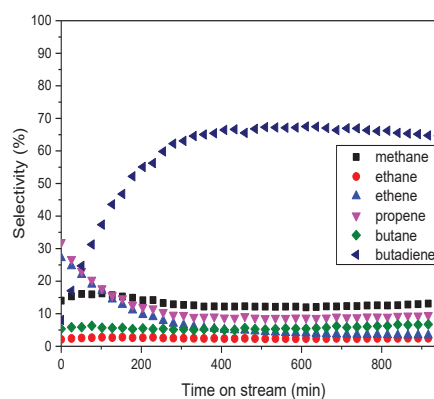


**Figure 4.** a) trans-2-butene conversion and b) selectivity obtained with (**2'**) ( $(\equiv\text{AlO})_3\text{Ga}$  species) in trans-2-butene conversion at 540 °C, 1 bar, total flow= 5 mL.min<sup>-1</sup> (Ar/2-C<sub>4</sub>=/CO<sub>2</sub> = 3.5/1/0.5).

## Conclusion

The grafting by SOMC methodology of an organometallic gallium precursor,  $[\text{Ga}(\text{OtBu})_3]_2$ , (**1**), on an alumina dehydroxylated at 500 °C, Al<sub>2</sub>O<sub>3-500</sub>, leads to the formation of a monopodal gallium species,  $[(\equiv\text{AlO})\text{Ga}(\text{OtBu})_2]$ , (**2**), on the surface. The formation of this species was confirmed by DRIFT, solid-state NMR (<sup>1</sup>H and <sup>13</sup>C), EXAFS and mass balance analyses. A controlled thermolysis of (**2**) releases an amount of 1.9 isobutene from the two tert-butoxide ligands by a β-H elimination resulting in a Ga-OH intermediate species. The transfer of these gallium hydroxy ligands from gallium to surface aluminum atoms by the opening of Al-O-Al bridges leads to the regeneration of Al-OH groups on the surface and results in new gallium-based species,  $[(\equiv\text{AlO})_3\text{Ga}]$ , in (**2'**) catalyst, proposed as the active phase during dehydrogenation reactions. These species were characterized by DRIFT, solid-state NMR (<sup>1</sup>H and <sup>13</sup>C), EXAFS and mass balance analysis. The tripodal Ga species were tested for trans-2-butene dehydrogenation to butadiene in a continuous flow reactor and showed an initial conversion of 13.3 % with a 51 % selectivity in butadiene after 300 min on stream. The selectivity in butadiene was related to the combination of the gallium sites and coke deposition produced by acidic sites at the beginning of the catalytic test. Importantly,

introducing CO<sub>2</sub> as a co-feed resulted in a very high selectivity toward butadiene (65 %), similar to what was reported in the case of Catadiene® process. Coke deposit can be also considered as an active phase in the material for dehydrogenation reactions and can provide high selectivities toward mono or di-olefins.

## Acknowledgements

This work was carried out as a part of BIZEOLCAT project, which has received funding from the European Union's Horizon 2020 research and innovation program under grant agreement No. 814671. In particular, J. A. is grateful for her PhD grant. AdM thanks Olivier Mathon and Kiril Lomachenko for their help during the recording of the X-ray absorption spectra at ESRF, on beam line BM23

## References

- (1) Shylesh, S.; Gokhale, A. A.; Scown, C. D.; Kim, D.; Ho, C. R.; Bell, A. T. From Sugars to Wheels: The Conversion of Ethanol to 1,3-Butadiene over Metal-Promoted Magnesia-Silicate Catalysts. *ChemSusChem* **2016**, *9* (12), 1462–1472. <https://doi.org/10.1002/cssc.201600195>.
- (2) Pomalaza, G.; Ponton, P. A.; Capron, M.; Dumeignil, F. Ethanol-to-Butadiene: The Reaction and Its Catalysts. *Catal. Sci. Technol.* **2020**, *10* (15), 4860–4911. <https://doi.org/10.1039/D0CY00784F>.
- (3) White, Wm. C. Butadiene Production Process Overview. *Chem. Biol. Interact.* **2007**, *166* (1), 10–14. <https://doi.org/10.1016/j.cbi.2007.01.009>.
- (4) Makshina, E. V.; Janssens, W.; Sels, B. F.; Jacobs, P. A. Catalytic Study of the Conversion of Ethanol into 1,3-Butadiene. *Catal. Today* **2012**, *198* (1), 338–344. <https://doi.org/10.1016/j.cattod.2012.05.031>.
- (5) Duan, H.; Yamada, Y.; Sato, S. Efficient Production of 1,3-Butadiene in the Catalytic Dehydration of 2,3-Butanediol. *Appl. Catal. Gen.* **2015**, *491*, 163–169. <https://doi.org/10.1016/j.apcata.2014.12.006>.
- (6) Madeira, L. M.; Portela, M. F. Catalytic Oxidative Dehydrogenation of N-Butane. *Catal. Rev.* **2002**, *44* (2), 247–286. <https://doi.org/10.1081/CR-120001461>.
- (7) CATADIENE® n-Butane Dehydrogenation to Butadiene | Lummus Technology. <https://www.lummustechnology.com/Process-Technologies/Petrochemicals/Butadiene-Butylene-Production/CATADIENE-n-Butane-Dehydrogenation-to-Butadiene> (accessed 2020-12-09).
- (8) Zhang, Y.; Qi, L.; Leonhardt, B.; Bell, A. T. Mechanism and Kinetics of N-Butane Dehydrogenation to 1,3-Butadiene Catalyzed by Isolated Pt Sites Grafted onto ≡SiOZn–OH Nests in Dealuminated Zeolite Beta. *ACS Catal.* **2022**, *12* (6), 3333–3345. <https://doi.org/10.1021/acscatal.2c00059>.
- (9) Rodemerck, U.; Sokolov, S.; Stoyanova, M.; Bentrup, U.; Linke, D.; Kondratenko, E. V. Influence of Support and Kind of VO<sub>x</sub> Species on Isobutene Selectivity and Coke Deposition in Non-Oxidative Dehydrogenation of Isobutane. *J. Catal.* **2016**, *338*, 174–183. <https://doi.org/10.1016/j.jcat.2016.03.003>.

- (10) Harlin, M. E.; Niemi, V. M.; Krause, A. O. I. Alumina-Supported Vanadium Oxide in the Dehydrogenation of Butanes. *J. Catal.* **2000**, *195* (1), 67–78. <https://doi.org/10.1006/jcat.2000.2969>.
- (11) Hakuli, A.; Harlin, M. E.; Backman, L. B.; Krause, A. O. I. Dehydrogenation of I-Butane on CrOx/SiO<sub>2</sub> Catalysts. *J. Catal.* **1999**, *184* (2), 349–356. <https://doi.org/10.1006/jcat.1999.2468>.
- (12) Han, J.; Jiang, G.; Han, S.; Liu, J.; Zhang, Y.; Liu, Y.; Wang, R.; Zhao, Z.; Xu, C.; Wang, Y.; Duan, A.; Liu, J.; Wei, Y. The Fabrication of Ga<sub>2</sub>O<sub>3</sub>/ZSM-5 Hollow Fibers for Efficient Catalytic Conversion of n-Butane into Light Olefins and Aromatics. *Catalysts* **2016**, *6* (1), 13. <https://doi.org/10.3390/catal6010013>.
- (13) Ma, Z.; Mo, Y.; Li, J.; An, C.; Liu, X. Optimization of PtSnK/Al<sub>2</sub>O<sub>3</sub> Isobutane Dehydrogenation Catalyst Prepared by an Impregnation-Reduction Method. *J. Nat. Gas Sci. Eng.* **2015**, *27*, 1035–1042. <https://doi.org/10.1016/j.jngse.2015.09.047>.
- (14) Lee, J. K.; Seo, H.; Kim, J. K.; Seo, H.; Cho, H.-R.; Lee, J.; Chang, H.; Song, I. K. Direct Dehydrogenation of N-Butane Over Pt/Sn/Zn–K/Al<sub>2</sub>O<sub>3</sub> Catalyst: Effect of Hydrogen in the Feed. *J. Nanosci. Nanotechnol.* **2016**, *16* (5), 4580–4586. <https://doi.org/10.1166/jnn.2016.10985>.
- (15) Gu, B.; He, S.; Rong, X.; Shi, Y.; Sun, C. Dehydrogenation of I-Butane over Tunable Mesoporous Alumina Supported Pt–Sn Catalyst. *Catal. Lett.* **2016**, *146* (8), 1415–1422. <https://doi.org/10.1007/s10562-016-1767-9>.
- (16) Furukawa, S.; Tamura, A.; Ozawa, K.; Komatsu, T. Catalytic Properties of Pt-Based Intermetallic Compounds in Dehydrogenation of Cyclohexane and n-Butane. *Appl. Catal. Gen.* **2014**, *469*, 300–305. <https://doi.org/10.1016/j.apcata.2013.10.012>.
- (17) Chu, M.; Liu, Y.; Gong, J.; Zhang, C.; Wang, X.; Zhong, Q.; Wu, L.; Xu, Y. Suppressing Dehydroisomerization Boosts N-Butane Dehydrogenation with High Butadiene Selectivity. *Chem. – Eur. J.* **2021**, *27* (45), 11643–11648. <https://doi.org/10.1002/chem.202101087>.
- (18) Lillehaug, S.; Jensen, V. R.; Børve, K. J. Catalytic Dehydrogenation of Ethane over Mononuclear Cr(III)–Silica Surface Sites. Part 2: C–H Activation by Oxidative Addition. *J. Phys. Org. Chem.* **2006**, *19* (1), 25–33. <https://doi.org/10.1002/poc.990>.
- (19) Valet, M.; Hoffman, D. M. Synthesis of Homoleptic Gallium Alkoxide Complexes and the Chemical Vapor Deposition of Gallium Oxide Films. *Chem. Mater.* **2001**, *13* (6), 2135–2143. <https://doi.org/10.1021/cm0014177>.
- (20) Mathon, O.; Beteva, A.; Borrel, J.; Bugnazet, D.; Gatla, S.; Hino, R.; Kantor, I.; Mairs, T.; Munoz, M.; Pasternak, S.; Perrin, F.; Pascarelli, S. The Time-Resolved and Extreme Conditions XAS (TEXAS) Facility at the European Synchrotron Radiation Facility: The General-Purpose EXAFS Bending-Magnet Beamline BM23. *J. Synchrotron Radiat.* **2015**, *22* (6), 1548–1554. <https://doi.org/10.1107/S1600577515017786>.
- (21) Ravel, B.; Newville, M. ATHENA, ARTEMIS, HEPHAESTUS: Data Analysis for X-Ray Absorption Spectroscopy Using IFEFFIT. *J. Synchrotron Radiat.* **2005**, *12* (4), 537–541. <https://doi.org/10.1107/S0909049505012719>.
- (22) Samantaray, M. K.; Mishra, S. K.; Saidi, A.; Basset, J.-M. Surface Organometallic Chemistry: A Sustainable Approach in Modern Catalysis. *J. Organomet. Chem.* **2021**, *945*, 121864. <https://doi.org/10.1016/j.jorganchem.2021.121864>.
- (23) Le Quémener, F.; Barman, S.; Merle, N.; Aljuhani, M. A.; Samantaray, M. K.; Saih, Y.; Szeto, K. C.; De Mallmann, A.; Minenkov, Y.; Huang, K.-W.; Cavallo, L.; Taoufik, M.; Basset, J.-M. Metathetic Oxidation of 2-Butenes to Acetaldehyde by Molecular Oxygen Using the Single-Site Olefin Metathesis Catalyst (≡SiO)<sub>2</sub>Mo(=O)<sub>2</sub>. *ACS Catal.* **2018**, *8* (8), 7549–7555. <https://doi.org/10.1021/acscatal.8b01767>.

- (24) Larabi, C.; Merle, N.; Le Quéméner, F.; Rouge, P.; Berrier, E.; Gauvin, R. M.; Le Roux, E.; de Mallmann, A.; Szeto, K. C.; Taoufik, M. New Synthetic Approach towards Well-Defined Silica Supported Tungsten Bis-Oxo, Active Catalysts for Olefin Metathesis. *Catal. Commun.* **2018**, *108*, 51–54. <https://doi.org/10.1016/j.catcom.2018.01.031>.
- (25) Mazoyer, E.; Trébosc, J.; Baudouin, A.; Boyron, O.; Pelletier, J.; Basset, J.-M.; Vitorino, M. J.; Nicholas, C. P.; Gauvin, R. M.; Taoufik, M.; Delevoeye, L. Heteronuclear NMR Correlations To Probe the Local Structure of Catalytically Active Surface Aluminum Hydride Species on  $\gamma$ -Alumina. *Angew. Chem. Int. Ed.* **2010**, *49* (51), 9854–9858. <https://doi.org/10.1002/anie.201004310>.
- (26) Alberty, R. A.; Gehrig, C. A. Standard Chemical Thermodynamic Properties of Alkene Isomer Groups. *J. Phys. Chem. Ref. Data* **1985**, *14* (3), 803–820. <https://doi.org/10.1063/1.555737>.
- (27) Bender, M. An Overview of Industrial Processes for the Production of Olefins – C4 Hydrocarbons. *ChemBioEng Rev.* **2014**, *1* (4), 136–147. <https://doi.org/10.1002/cben.201400016>.
- (28) Mazoyer, E.; Szeto, K. C.; Merle, N.; Norsic, S.; Boyron, O.; Basset, J.-M.; Taoufik, M.; Nicholas, C. P. Study of Ethylene/2-Butene Cross-Metathesis over W-H/Al<sub>2</sub>O<sub>3</sub> for Propylene Production: Effect of the Temperature and Reactant Ratios on the Productivity and Deactivation. **2013**. <https://doi.org/10.1016/j.jcat.2013.01.016>.
- (29) Mazoyer, E.; Szeto, K. C.; Basset, J.-M.; Nicholas, C. P.; Taoufik, M. High Selectivity Production of Propylene from 2-Butene: Non-Degenerate Pathways to Convert Symmetric Olefins via Olefin Metathesis. *Chem. Commun.* **2012**, *48* (30), 3611–3613. <https://doi.org/10.1039/C2CC30172E>.
- (30) Szeto, K. C.; Merle, N.; Rios, C.; Rouge, P.; Castelbou, J. L.; Taoufik, M. Tailoring the Selectivity in 2-Butene Conversion over Supported D<sub>0</sub> Group 4, 5 and 6 Metal Hydrides: From Dimerization to Metathesis. *Catal. Sci. Technol.* **2015**, *5* (10), 4765–4771. <https://doi.org/10.1039/C5CY00582E>.
- (31) McGregor, J.; Huang, Z.; Parrott, E. P. J.; Zeitler, J. A.; Nguyen, K. L.; Rawson, J. M.; Carley, A.; Hansen, T. W.; Tessonier, J.-P.; Su, D. S.; Teschner, D.; Vass, E. M.; Knop-Gericke, A.; Schlögl, R.; Gladden, L. F. Active Coke: Carbonaceous Materials as Catalysts for Alkane Dehydrogenation. *J. Catal.* **2010**, *269* (2), 329–339. <https://doi.org/10.1016/j.jcat.2009.11.016>.
- (32) Bychko, I.; Abakumov, A.; Nikolenko, A.; Selyshchev, O. V.; Zahn, D. R. T.; Khavrus, V. O.; Tang, J.; Strizhak, P. Ethane Direct Dehydrogenation over Carbon Nanotubes and Reduced Graphene Oxide. *ChemistrySelect* **2021**, *6* (34), 8981–8984. <https://doi.org/10.1002/slct.202102493>.
- (33) Teschner, D.; Vass, E.; Hävecker, M.; Zafeiratos, S.; Schnörch, P.; Sauer, H.; Knop-Gericke, A.; Schlögl, R.; Chamam, M.; Wootsch, A.; Canning, A. S.; Gamman, J. J.; Jackson, S. D.; McGregor, J.; Gladden, L. F. Alkyne Hydrogenation over Pd Catalysts: A New Paradigm. *J. Catal.* **2006**, *242* (1), 26–37. <https://doi.org/10.1016/j.jcat.2006.05.030>.
- (34) Teschner, D.; Borsodi, J.; Wootsch, A.; Révay, Z.; Hävecker, M.; Knop-Gericke, A.; Jackson, S. D.; Schlögl, R. The Roles of Subsurface Carbon and Hydrogen in Palladium-Catalyzed Alkyne Hydrogenation. *Science* **2008**, *320* (5872), 86–89. <https://doi.org/10.1126/science.1155200>.
- (35) Liu, Y.; Zhang, G.; Wang, J.; Zhu, J.; Zhang, X.; Miller, J. T.; Song, C.; Guo, X. Promoting Propane Dehydrogenation with CO<sub>2</sub> over Ga<sub>2</sub>O<sub>3</sub>/SiO<sub>2</sub> by Eliminating Ga-

- Hydrides. *Chin. J. Catal.* **2021**, *42* (12), 2225–2233. [https://doi.org/10.1016/S1872-2067\(21\)63900-1](https://doi.org/10.1016/S1872-2067(21)63900-1).
- (36) Xu, B.; Zheng, B.; Hua, W.; Yue, Y.; Gao, Z. Support Effect in Dehydrogenation of Propane in the Presence of CO<sub>2</sub> over Supported Gallium Oxide Catalysts. *J. Catal.* **2006**, *239* (2), 470–477. <https://doi.org/10.1016/j.jcat.2006.02.017>.
- (37) Michorczyk, P.; Kuśtrowski, P.; Kolak, A.; Zimowska, M. Ordered Mesoporous Ga<sub>2</sub>O<sub>3</sub> and Ga<sub>2</sub>O<sub>3</sub>–Al<sub>2</sub>O<sub>3</sub> Prepared by Nanocasting as Effective Catalysts for Propane Dehydrogenation in the Presence of CO<sub>2</sub>. *Catal. Commun.* **2013**, *35*, 95–100. <https://doi.org/10.1016/j.catcom.2013.01.019>.

## Supporting information

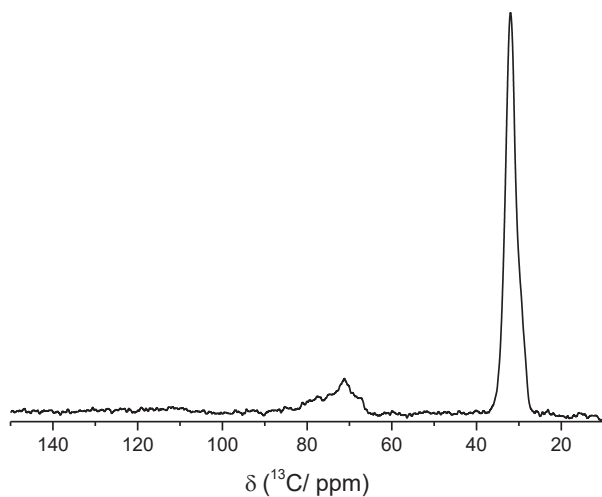


**Figure S1.**  $^{13}\text{C}$  CP NMR spectrum of **(2)**,  $\text{Ga}(\text{OtBu})_3/\text{Al}_2\text{O}_3\text{-500}$  (11.7 T, 10 kHz,  $d_1=5$  s)

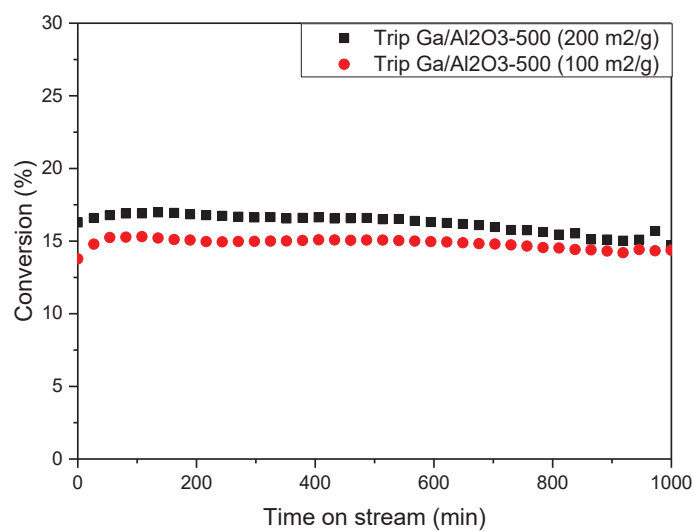


**Figure S2.** Propane conversion obtained with **(3')**, tripodal Ga species supported on an alumina  $\text{Al}_2\text{O}_3\text{-500}$  presenting a high surface area,  $200 \text{ m}^2\cdot\text{g}^{-1}$ , ( $\blacksquare$ ) and **(2')**, tripodal Ga species supported on an Evonik alumina, presenting a lower surface area,  $100 \text{ m}^2\cdot\text{g}^{-1}$ , ( $\bullet$ ). Conditions:  $540^\circ\text{C}$ , 1 bar and  $5 \text{ mL}\cdot\text{min}^{-1}$  (20 % propane in argon)

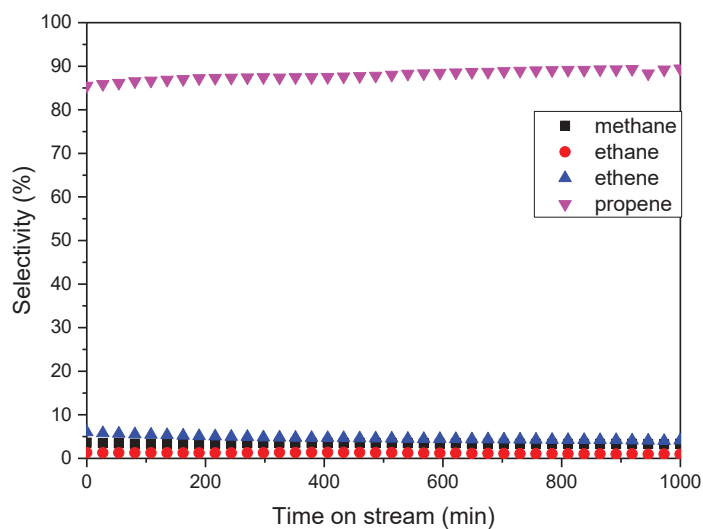


**Figure S3.** Selectivities observed for propane conversion with (**3'**), tripodal Ga species supported on an alumina  $\text{Al}_2\text{O}_3\text{-500}$  presenting a high surface area,  $200 \text{ m}^2 \cdot \text{g}^{-1}$ . Conditions:  $540 \text{ }^\circ\text{C}$ , 1 bar and  $5 \text{ mL} \cdot \text{min}^{-1}$  (20 % propane in argon).

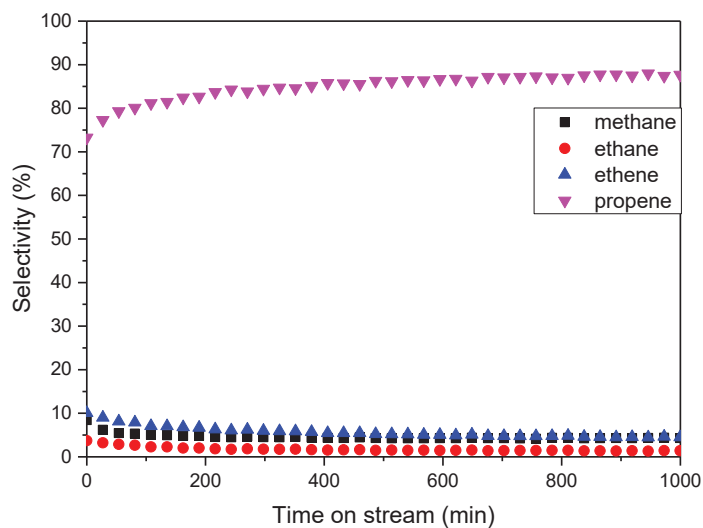


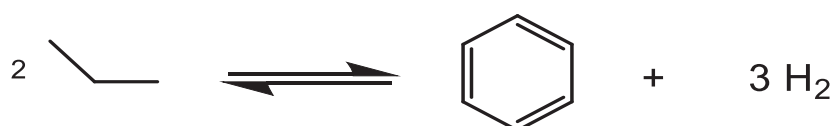
**Figure S4.** Selectivities observed for propane conversion with (**2'**), tripodal Ga species supported on an Evonik alumina  $\text{Al}_2\text{O}_3\text{-500}$ , presenting a lower surface area,  $100 \text{ m}^2 \cdot \text{g}^{-1}$ . Conditions:  $540 \text{ }^\circ\text{C}$ , 1 bar at  $5 \text{ mL} \cdot \text{min}^{-1}$  (20 % propane in argon).

## CHAPTER IV. PART A

---

# The effect of local structure of Ga supported on meso H-ZSM-5 on the activity, stability, and selectivity in propane aromatization

---



Jessy Abou Nakad,<sup>a</sup> Daniel Firth,<sup>b</sup> Kai C. Szeto,<sup>a</sup> Nicolas Merle,<sup>c</sup> Aimery De Mallmann,<sup>a</sup> Régis Gauvin,<sup>d</sup> Laurent Delevoye,<sup>c</sup> Unni Olsbye,<sup>\*b</sup> and Mostafa Taoufik<sup>\*a</sup>

<sup>a</sup> Université Lyon 1, Institut de Chimie Lyon, CPE Lyon, CNRS, UMR 5128 CP2M, 43 Bd du 11 Novembre 1918, F-69616 Villeurbanne Cedex, France. E-mail: Mostafa.Taoufik@univ-lyon1.fr; Fax: +33 (0)472 431 798; Tel: +33 (0)472 431 795

<sup>b</sup> Centre for Materials Science and Nanotechnology (SMN), Department of Chemistry, University of Oslo, N-0371 Oslo, Norway. E-mail: unni.olsbye@kjemi.uio.no

<sup>c</sup> UCCS (CNRS-UMR 8181), Université Lille Nord de France, USTL, 59652 Villeneuve d'Ascq, France

<sup>d</sup> Institut de Recherche de Chimie Paris, IRCP - UMR CNRS 8247, Chimie ParisTech, Paris, France

## Abstract

Hierarchical gallium meso zeolites catalyst that combines both the unique pore structure and the strong acidity is proven to be a powerful bi-functional catalyst for propane aromatization. The aim of this work is to investigate the influence of the Ga structure (monomeric or dimeric) in the mesopores of meso H-ZSM-5-250 (Si/Al= 40) on the catalytic activity during propane aromatization. In that manner, dimeric Ga species supported on meso H-ZSM-5-250 (Si/Al= 40) (**II**) were obtained by the grafting of  $[\text{Ga}(\text{OtBu})_3]_2$  followed by a thermal treatment at 300 °C. Moreover, monomeric Ga species on meso zeolite were prepared by grafting  $[\text{Ga}(i\text{Bu})_3]$  on meso H-ZSM-5-250 (Si/Al= 40) (**III**). The selective grafting of the Ga precursors on the silanols groups in the mesopores and the resulting structures of (**II**) and (**III**) were confirmed by DRIFT, solid-state NMR, elemental analysis,  $\text{N}_2$  adsorption/desorption and EXAFS. The catalytic activity of species (**II**) and (**III**) were also compared to the bare meso zeolite for propane aromatization in order to highlight the effect of the structure of Ga species. A highly active, more stable and selective catalyst was obtained in the case of monomeric species (**III**) compared to dimeric Ga species (**II**). The deactivation observed in the case of (**II**) is attributed to coke formation by the Ga dimeric species, blocking the access to acidic sites in the micropores and hence lower selectivity toward aromatics.

## Introduction

Regarding the wide range of applications of BTX (benzene, toluene and xylene), the conversion of light hydrocarbons into these aromatic compounds has become a central process in petrochemistry. These products have for a while been used in gasoline blend to increase the octane number and remain actual.<sup>1</sup> In chemical industry, toluene is employed for the production of adhesives,<sup>2</sup> while benzene is used as starting material for the production of styrene and phenol.<sup>3</sup> Xylenes are converted by oxidation reaction into terephthalic and isophthalic acids.<sup>4</sup> Traditionally, BTX can be produced by catalytic reforming or by steam cracking plants, or alternatively from methanol (MTA),<sup>5,6</sup> syngas (STA)<sup>7,8</sup> and  $\text{CO}_2$  hydrogenation.<sup>9,10</sup> Recently, several efforts are focused on the development of alternative routes for BTX production, notably from methane,<sup>11</sup> but also from other light alkanes. The main drawback in methane aromatization lies on the thermodynamic barrier that limit the aromatics yield, even at 700 °C. Moreover, a quick deactivation is observed due to the high accumulation of coke on the surface of the most used catalyst, Mo/H-ZSM-5. From another part, the discovery of new shale gas reserves recently resulted in an abundant amount of

propane. Thus, propane aromatization has attracted a lot of attention and many investigations are made in order to optimize the catalytic system.<sup>12</sup> On purpose propane aromatization is believed to happen in two main steps: dehydrogenation occurring on the metal sites and aromatization occurring on the acidic sites of a zeolitic material. Although the latter is widely employed as catalyst or support, their catalytic activity suffer from diffusional limitations, leading to undesired reactions such as cracking (into C1 and C2 products) and coke formation and hence a deactivation. Creation of mesopores in microporous zeolite seems to be a solution in order to overcome diffusion issue. In fact, the preparation of a composite bearing micropores and mesopores allowing to enhance the dispersion of the metal through the crystallite and to ensure a high acidity in proximity. Hierarchical meso zeolites have been extensively used by several research groups for propane aromatization, in particular by hosting Zn, Ga and Pt as dehydrogenating metals. For example, Dauda et al. have reported recently the desilication of ZnO on microporous ZSM-5 with 2 wt% of ZnO which results in a hierarchical ZnO on meso ZSM-5.<sup>13</sup> This catalyst displays a high selectivity in aromatics (61 %) compared to the parent microporous catalyst (25.2 %). The corresponding Ga system has been expansively investigated, notably in the preparation part, such as hydrothermal in-situ synthesis and post synthesis treatment (impregnation, ion-exchange, chemical vapor deposition (CVD), and reduction–oxidation treatments). However, controlling the dispersion of active gallium and its structure remain a great challenge due to the tendency to form bulky Ga<sub>2</sub>O<sub>3</sub>, known to be responsible of the deactivation of the catalyst. Hence, efforts have been made to increase the Ga dispersion by using several methods such as: desilication of microporous Ga/H-ZSM-5 or by using surfactant-mediated hydrolysis approach. These approaches resulted in an improvement in the activity and selectivity in BTX of 58.3 %.<sup>14</sup> Another strategy is reported in our laboratory, consisting in the use of surface organometallic chemistry (SOMC) of [Ga(*i*Bu)<sub>3</sub>] on meso H-ZSM-5 (Si/Al = 20) prepared by desilication. This approach leads to the formation of a bifunctional monopodal catalyst confirmed by DRIFT, solid state NMR and EXAFS, where Ga was located in the mesopores and responsible for dehydrogenation, while the acidic Brønsted sites were preserved in the micropores for oligomerization and aromatization of propylene intermediate.<sup>15</sup> The high activity and selectivity in this case is related to the use of highly dispersed Ga (as dehydrogenation phase) in the meso-porous zeolites. Recently, further research on gallium-based propane dehydrogenation catalysts have been conducted, and we discovered that the alumina supported Ga tripod species is even more active and stable than the grafted gallium

isobutyl fragment. This catalyst is prepared through surface organometallic chemistry using  $[\text{Ga}(\text{OtBu})_3]_2$  as precursor. Thermolysis under vacuum triggers  $\beta$ -H elimination, giving an alumina supported Ga-OH species and isobutene. Consecutively, a transfer of the Ga-OH groups to the alumina support occurs, resulting in the regeneration of Al-OH groups and a surface species of Ga linked to three O-Al surface moieties, hence, a tripodal species. Current aim is to integrate the tripodal gallium species into a meso porous H-ZSM-5, yielding a new hierarchical material which is expected to enhance the activity of propane aromatization. For this target, we selected H-ZSM-5 as support with a ratio Si/Al = 40, known to be highly acidic material. This zeolite was prepared by combining the procedure described by Jacobs and Martens for the preparation of microporous zeolites using different concentration of  $\text{NaAlO}_2$  and post-synthesis (treatment by NaOH) in order to create the mesopores followed by ion exchange method.<sup>16</sup> In addition, this catalyst will be compared to the  $[\text{Ga}(i\text{Bu})_3]$  supported on meso H-ZSM-5 (Si/Al= 40) in order to draw the structure-reactivity relationship and enhance fundamental comprehension in propane aromatization. All the catalytic materials were characterized by DRIFT, solid state NMR,  $\text{N}_2$  adsorption/desorption, EXAFS and mass balance analysis.

## Experimental section

**General procedures.** All experiments were carried out under a controlled atmosphere, using Schlenk and glovebox techniques for organometallic synthesis. For the synthesis and treatment of supported species, reactions were carried out using high-vacuum lines (ca. 1 mPa) and gloveboxes. Benzene and pentane were distilled from Na-benzophenone and NaK, respectively, and degassed using freeze-pump-thaw cycles.

### Preparation of Meso H-ZSM-5-250.

#### Synthesis of microporous zeolites supports

Meso H-ZSM-5 was synthesized following procedures previously reported by Jacobs and Martens.<sup>16</sup> First, fumed silica was combined with NaOH and water and stirred until homogenous (Solution 1). Then, a premixed solution of tetrapropylammonium bromide and water (Solution 2) was added and the gel allowed to stir until homogenous. This was then followed by the addition of a premixed aqueous solution of sodium aluminate (Solution 3) to achieve the desired Si/Al gel ratio and the gel was stirred until homogeneous. The gel was then transferred to an autoclave and crystalized at 150 °C for 3 days. The resulting solid was

then filtered and washed with water and dried at 50 °C overnight. The template was then removed from the zeolite by calcination at 550 °C for 6 hours in air.

### **Desilication treatment**

The calcined microporous ZSM-5 sample was placed in a 0.1 M NaOH solution that had been preheated to 70 °C (20 mL of solutions per gram of zeolite). The slurry was then stirred at 70 °C after which the reaction was cooled with ice to prevent further desilication. The mixture was then centrifuged and washed with water three times and dried at 50 °C overnight.

### **Ion exchange of support**

Mesoporous ZSM-5 (Si/Al= 40) sample was ion exchanged by adding 1 g of zeolite in 20 mL of 1 M ammonium nitrate aqueous solution and stirring the solution at 80 °C for 2 h. The sample was then centrifuged, the solution decanted and replaced with additional 1M ammonium nitrate aqueous solution. The process was then repeated three times while the last ion exchange was carried out overnight. Afterwards, the solid was separated from the liquid by centrifugation, washed with water and dried in the oven for 12 h at 80 °C. The final solids were calcined at 550 °C for 6 h in air to achieve protonated ZSM-5. Finally, the material was calcined by heating under flow of air from room temperature to 500 °C at a heating rate of 2 °C/min, with a hold time of 16 h. The support was further dehydroxylated at 250 °C (2 °C/min) for 16 h under high vacuum (1 mPa).

### **Preparation and characterization of [Ga(O*t*Bu)<sub>3</sub>]<sub>2</sub>/meso H-ZSM-5-250 (I)**

[Ga(O*t*Bu)<sub>3</sub>]<sub>2</sub> was synthesized according to a published method.<sup>17</sup> A mixture of [Ga(O*t*Bu)<sub>3</sub>]<sub>2</sub> (250 mg) and meso-H-ZSM-5-250 (Si/Al= 40) (1 g) in pentane (10 mL) was stirred at 25 °C for 4 h. After filtration, the solid was washed 4 times with pentane. The resulting powder (I) was dried under vacuum (1 mPa) at 70 °C.

### **Preparation and characterization of tripodal Ga species supported on meso H-ZSM-5-250, (II)**

(II) was obtained via thermal treatment of (I) under vacuum equipped with a cold trap (liquid N<sub>2</sub>) to collect the isobutene evolved during the process.

### **Preparation and characterization of Ga(*i*Bu)<sub>3</sub>/meso H-ZSM-5-250 (III)**

[Ga(*i*Bu)<sub>3</sub>] was synthesized according to a published method.<sup>18</sup> A mixture of [Ga(*i*Bu)<sub>3</sub>] (200 mg) and meso-H-ZSM-5-250 (Si/Al= 40) (1 g) in pentane (10 mL) was stirred at 25 °C for 4 h. After filtration, the solid was washed 4 times with pentane and the washing fractions were

transferred to another reactor in order to quantify isobutane evolved during grafting. The resulting powder (**III**) was dried under vacuum (1 mPa) at 70 °C.

### **Analytical and Spectroscopic Procedures.**

Elemental analyses were carried out at Mikroanalytisches Labor Pascher, Remagen (Germany). Gas-phase analyses were performed on a Hewlett-Packard 5890 series II gas chromatograph, equipped with a flame ionization detector and HP PLOT KCl/Al<sub>2</sub>O<sub>3</sub> column (50 m × 0.32 mm) or HP5 column (30 m × 0.32 mm). Diffuse reflectance IR spectra were collected in an airtight IR cell equipped with CaF<sub>2</sub> window, using a Nicolet 6700 FT-IR spectrophotometer and recording 64 scans at 4 cm<sup>-1</sup> resolutions. Nitrogen adsorption/desorption experiments were performed in Micrometrics ASAP 2020 instrument. X-ray diffraction patterns were recorded in a Bruker D8 diffractometer in Bragg-Bretano geometry, using monochromatic Cu K $\alpha$ 1 radiation.

Solid-state NMR spectra were acquired on Bruker Avance 500 and Bruker Avance III 800 spectrometers. For <sup>1</sup>H experiments, the spinning frequency was 20 kHz, the recycle delay was 30 s for meso-H-ZSM-5<sub>250</sub> and 10 s for Ga(<sup>*i*</sup>Bu)<sub>3</sub>/meso-H-ZSM-5<sub>250</sub>, and 16 scans were collected using a 90° pulse excitation of 2.25  $\mu$ s. The <sup>13</sup>C CP-MAS NMR spectrum was obtained at 11.74 T using the CP-MAS pulse sequence and a high-power <sup>1</sup>H decoupling at an RF field amplitude of 70 kHz. The spinning frequency was set to 10 kHz.

EXAFS spectra were acquired at ESRF, using BM23 beam-line, at room temperature at the gallium K-edge (10.37 keV). A pair of Si(111) crystals was used as monochromator and a system based on a total reflection through a double X-ray mirror with an incidence angle variable from 2 to 5 mrad allowed harmonic rejection to better than the 10<sup>-5</sup> level.<sup>19</sup> The spectra were recorded in the transmission mode between 10.1 and 11.4 keV. Four scans were collected for each sample. Each data set was collected simultaneously with a W metal foil (L<sub>III</sub> edge at 10.206.8 keV) and was later aligned according to that reference. The Ga supported samples were packaged within an argon filled glovebox in a double air-tight sample holder equipped with kapton windows. The data analyses were carried out using the program “Athena”<sup>20</sup> and the EXAFS fitting program “RoundMidnight”, from the “MAX” package,<sup>21,22</sup> using spherical waves. The program FEFF8 was used to calculate S<sub>0</sub><sup>2</sup> and theoretical files for the total central atom loss factor, r<sub>c</sub>, the electron mean free path,  $\lambda$ , the phases,  $\phi_i$ ,  $\phi_c$  and amplitudes, F<sub>i</sub>, based on model clusters of atoms.<sup>23</sup> The refinements were carried out by fitting the structural parameters N<sub>i</sub>, R<sub>i</sub>,  $\sigma_i$  and the energy shift,  $\Delta E_0$  (the same for all shells of a same structure was used):

$$\chi(k) \cong S_0^2 * r_c(k) * \sum_{i=1}^n \frac{N_i F_i(k, R_i)}{k R_i^2} * \exp\left(\frac{-2R_i}{\lambda(k)}\right) * \exp(-2\sigma_i^2 k^2) * \sin[2kR_i + \Phi_i(k, R_i) + \Phi_c(k)]$$

### Reactivity testing

The reactivity of the supported catalysts in propane dehydrogenation was evaluated in a stainless steel, continuous flow reactor. The catalysts (500 mg) were diluted in 2 g of SiC (Strem), affording a final catalyst bed mass of 2.5 g. Catalysts were loaded into the reactor inside a glovebox, and protected from the ambient atmosphere by a 4-way valve. Lines were purged extensively with the reaction gas prior to its introduction into the reactor. The catalyst bed was heated to 580 °C in flowing Ar (9.5 mL.min<sup>-1</sup>) before admitting 5 % of propane (99.95 % Air Liquide, < 20 ppm propene), affording a total flow of 10 mL.min<sup>-1</sup>, at P<sub>total</sub> = 1 bar. The feed gas was purified by passage through a column containing molecular sieves and activated Cu<sub>2</sub>O/Al<sub>2</sub>O<sub>3</sub>, and the flow rate controlled by a Brooks mass flow controller. Products were determined by online GC (HP 6890, equipped with 50 m KCl/Al<sub>2</sub>O<sub>3</sub> column and an FID). Conversion was calculated based on peak areas normalized by carbon number.

## Results and discussion

### Preparation and characterization of [Ga(O*t*Bu)<sub>3</sub>]<sub>2</sub> supported on meso H-ZSM-5-250 (I)

Meso-H-ZSM-5 with Si/Al= 40 was dehydroxylated at 250 °C under high vacuum (10<sup>-5</sup> mbar), affording meso H-ZSM-5-250 (Si/Al= 40). The DRIFT spectroscopy of meso H-ZSM-5-250 (Si/Al= 40) revealed two main bands at 3743 and 3608 cm<sup>-1</sup>, characteristic of isolated silanols and Brønsted acidic sites, respectively. The other weak and unresolved bands between 3700 and 3650 cm<sup>-1</sup> correspond to extra-framework alumina (EFA), generated during desilication (Figure 1, a). Additional information was obtained by using solid state <sup>1</sup>H MAS NMR technique. In fact, the presence of these groups was indicated by the characteristic peaks in <sup>1</sup>H MAS NMR spectrum at 3.9, 2.5, and 1.6 ppm (Figure 2, a). They are attributed to Brønsted acidic sites, EFA hydroxyls, and isolated silanol groups, respectively.<sup>24,25</sup> Two other minor signals at 4.7 and 0 ppm, are already assigned in literature to another type of acid sites and aluminum hydroxyls (Al<sub>IV</sub>), respectively.<sup>26,27</sup> The textural properties of meso H-ZSM-5-250 were evaluated using N<sub>2</sub> physisorption measurements and revealed a type IV isotherm behavior (Figure S2). A large surface area of 381.6 m<sup>2</sup>.g<sup>-1</sup> was obtained with a total volume pores of 0.27 cm<sup>3</sup>.g<sup>-1</sup>, consistent with the retention of the desired properties (Table 1).

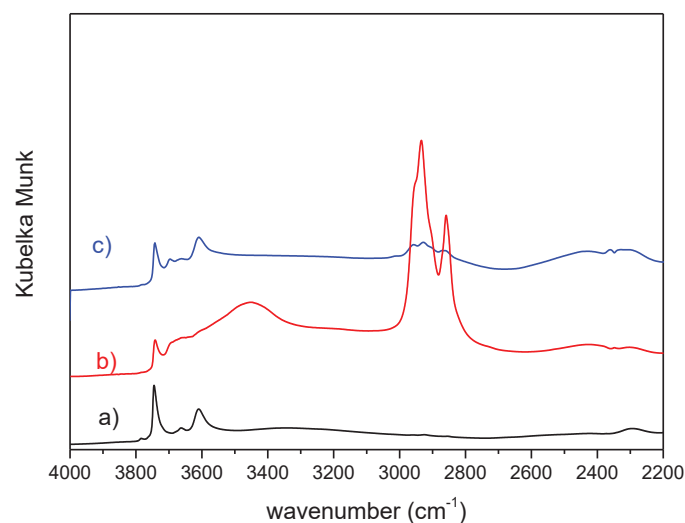


**Figure 1.** DRIFT spectra of a) meso H-ZSM-5-250 (Si/Al= 40), b)  $[\text{Ga}(\text{O}t\text{Bu})_3]_2$  on meso H-ZSM-5-250 (Si/Al= 40) (**I**) and c)  $[\text{Ga}(\text{O}t\text{Bu})_3]_2$  on meso H-ZSM-5-250 (Si/Al= 40) treated at 300 °C (**II**)

The grafting reaction of dimeric complex  $[\text{Ga}(\text{O}t\text{Bu})_3]_2$ <sup>17</sup> in pentane on meso H-ZSM-5-250 (Si/Al= 40) was carried out at room temperature. The solid (**I**) was washed extensively with pentane and dried under vacuum (1 mPa) at 70 °C for 12 h. The resulting material was characterized by IR, solid state NMR (<sup>1</sup>H and <sup>13</sup>C), EXAFS, BET and mass balance analysis. DRIFT was used to monitor the grafting reaction (Figure 1, b). Evidently, the peak belonged to isolated silanol (at 3743 cm<sup>-1</sup>) has degraded, indicating that the grafting occurred via protonolysis. There was still sign to the bands originated to EFA. Conversely, a large peak centered at 3420 cm<sup>-1</sup> appeared and was assigned to Brønsted acidic sites in interaction with probably organic fragments. Moreover, adsorption at 2800-3000 cm<sup>-1</sup> corresponded to typically  $\nu(\text{C-H})$  vibrations of alkyl moieties, supporting the presence of surface organometallic fragments. Due to the dimeric structure of  $[\text{Ga}(\text{O}t\text{Bu})_3]_2$  and its steric hindrance, the grafting reaction occurs selectively on the isolated silanol groups located in the mesopores, while the Brønsted acidic sites in the micropores remained unreacted. Further information about the Ga coordination environment in (**I**) were provided using solid-state NMR techniques. The data obtained from the characterization of  $[\text{Ga}(\text{O}t\text{Bu})_3]_2$  on meso H-ZSM-5-250 (Si/Al= 40) by <sup>1</sup>H MAS NMR showed two resolved, but fairly broad signals at 1.0 and 1.7 ppm (Figure 2, b), assigned respectively to alkyl fragments and remaining silanol groups (consistent with DRIFT). The protons belonged to EFA and Brønsted acid became unresolved and partially masked by the dominating resonances, though a weak shoulder

centered at 4.0 ppm (Brønsted proton) was visible. The  $^{13}\text{C}$  CPMAS spectrum was dominating by two signals at 32.7 and 29.7 ppm (Figure S1), attributed to  $\text{OCMe}_3$  and  $\mu\text{-OCMe}_3$ , respectively.<sup>17</sup> The minor peaks corresponded to strongly adsorbed pentane being difficult to remove at low temperature.<sup>15</sup> Indeed, no signal of the quaternary carbon of tert-butoxide ligand was observed, probably due to the absence of proton bonded to this carbon. Such observation was also found in the case of supported titanium *tert*-butoxide.<sup>28</sup>

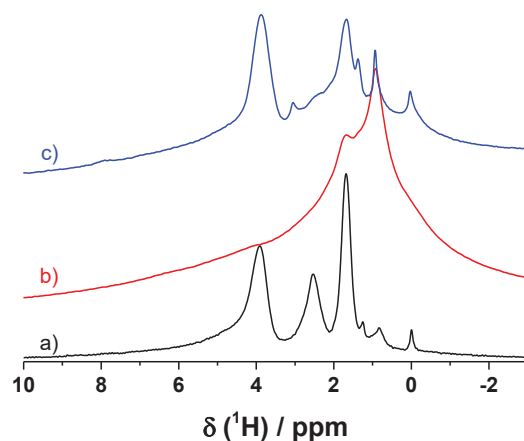


**Figure 2.**  $^1\text{H}$  MAS NMR of a): meso H-ZSM-5-250 (Si/Al= 40), (18.8 T, 20 kHz,  $d_1= 10$  s); b): **(I)** and c): **(II)** (11.7 T, 10 kHz,  $d_1= 10$  s)

$\text{N}_2$  adsorption/desorption isotherms of **(I)** displayed a significant decrease in the surface area from 381.6 (for meso H-ZSM-5-250 (Si/Al= 40)) to 104.4  $\text{m}^2\cdot\text{g}^{-1}$  and the total pore volume was also reduced to 0.10  $\text{cm}^3\cdot\text{g}^{-1}$  (Table 1). Such decrease was previously seen while grafting organogallium compounds and was attributed to the pore blockage.<sup>29</sup> Moreover, elemental analysis of this catalyst revealed 2.37 wt% of Ga and 4.25 wt% of C, corresponding to an atomic ratio C/Ga of 10.6. The loading of Ga in **(I)** was higher than what we previously reported in the case of  $[\text{Ga}(i\text{Bu})_3]$  on meso H-ZSM-5-250 (Si/Al= 20) (1.36 wt%), which suggested the formation of a dimeric Ga surface species when using  $[\text{Ga}(\text{O}t\text{Bu})_3]_2$  as precursor.

**Table 1.** Characterization of meso H-ZSM-5-250 (Si/Al= 40), **(I)**, **(II)** and **(III)** by  $\text{N}_2$  desorption.  $V_{\text{micro}}$  is calculated from the t-plot method.  $V_{\text{total}}$  is calculated from single-point adsorption at  $P/P_0 = 0.985$ ;  $V_{\text{meso}} = V_{\text{total}} - V_{\text{micro}}$

Samples	$S_{\text{BET}}^{\text{a}}$ ( $\text{m}^2\cdot\text{g}^{-1}$ )	$S_{\text{micro}}^{\text{b}}$ ( $\text{m}^2\cdot\text{g}^{-1}$ )	$S_{\text{ext}}^{\text{c}}$ ( $\text{m}^2\cdot\text{g}^{-1}$ )	$V_{\text{total}}^{\text{e}}$ ( $\text{cm}^3\cdot\text{g}^{-1}$ )	$V_{\text{micro}}^{\text{f}}$ ( $\text{cm}^3\cdot\text{g}^{-1}$ )	$V_{\text{meso}}^{\text{g}}$ ( $\text{cm}^3\cdot\text{g}^{-1}$ )
Meso H-ZSM-5-250	381.6	241.5	140.1	0.27	0.11	0.16
<b>(I)</b>	104.4	35.5	68.9	0.10	0.02	0.08

(II)	377	111.3	265.8	0.21	0.05	0.16
(III)	143.1	51.34	91.77	0.14	0.02	0.11

A study of the EXAFS, evaluating the average Ga coordination environment of  $[\text{Ga}(\text{OtBu})_3]_2$  on meso H-ZSM-5-250 (Si/Al= 40) confirmed the former findings on the formation of a dimeric species. The Fourier-transformed magnitude and imaginary component of the EXAFS for  $[\text{Ga}(\text{OtBu})_3]_2$  grafted onto meso-H-ZSM-5-250 (Si/Al= 40) are shown in Figure 3. For this species, the results from the EXAFS studies agree with a dimeric structure (Figure 3, Table 2). The first peak observed in the Fourier transform (FT) (maximum in R-  $\delta$  at ca. 1.6 Å) could be fitted by two levels of oxygen back-scatterers, ca. two O at 1.83 and two O at 1.93 Å. Moreover, the second peak (maximum in R-  $\delta$  at ca. 2.55 Å) could be fitted including a Ga--Ga contribution from a Ga back-scatterer at ca. 2.96 Å while a fit with only a combination of long (non-bonded) Ga-O, Ga-C and Ga-Si paths gave a really less satisfactory fit in the region 2.1 - 3.6 Å in R-space. A dimeric structure was suggested regarding the results obtained from elemental analysis of Ga (2.37 wt%, compared to 1.36 wt% for monomeric species obtained with  $[\text{Ga}(i\text{Bu})_3]$  on meso H-ZSM-5-250 (Si/Al= 20)). This agrees with a structure similar to the one of  $[\text{Ga}(\mu\text{-OCMe}_2\text{Et})(\text{OCMe}_2\text{Et})_2]_2$ , dimeric molecular compound characterized by XRD, where  $\text{O}_{\text{terminal}}$  and  $\text{O}_{\text{bridged}}$  atoms are at average distances of  $1.773 \pm 0.007$  Å and  $1.914 \pm 0.004$  Å respectively and with a Ga--Ga distance of ca.  $2.927 \pm 0.004$  Å (Scheme 1).<sup>17</sup> Hence, all these results are in agreement with the formation of a dimeric structure  $[(\equiv\text{SiO})\text{Ga}_2(\text{OtBu})_5]$ , as depicted below in Scheme 1.

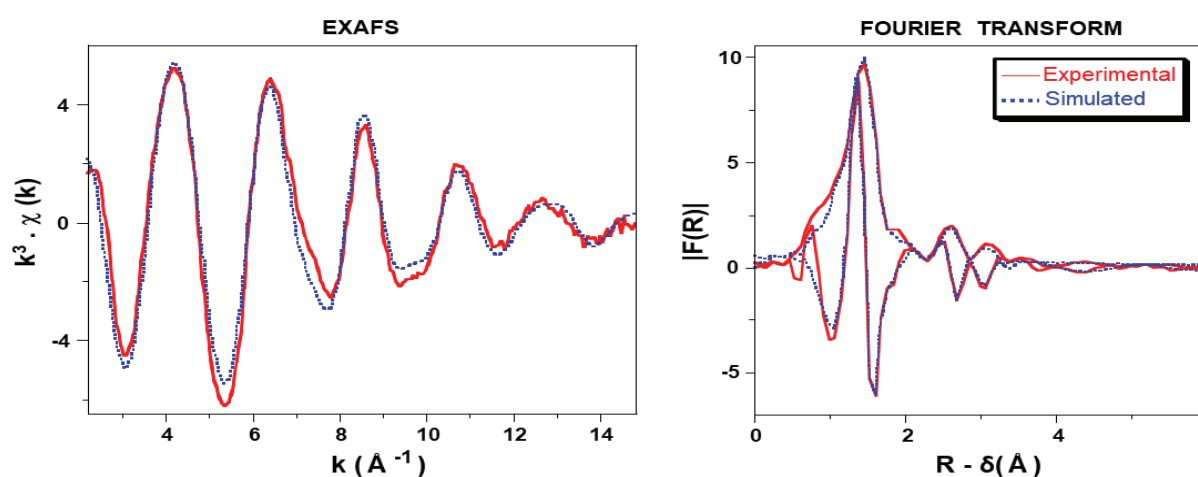
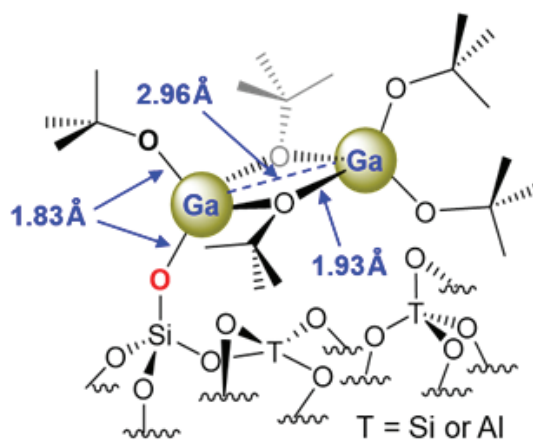


**Figure 3.** Ga K-edge  $k^3$ -weighted EXAFS (left) and Fourier transform (right, modulus and imaginary part; distances uncorrected from phase shifts) of  $[\text{Ga}(\text{OtBu})_3]_2$  on meso H-ZSM-5-250 (Si/Al=40) Solid lines: Experimental; Dashed lines: Fit (spherical wave theory).

**Table 2.** Parameters obtained from the fit of the EXAFS spectrum for  $[\text{Ga}(\text{OtBu})_3]_2/\text{H-ZSM-5-250}$  ( $\text{Si}/\text{Al} = 40$ ).<sup>(a)</sup> The error interval generated by the fitting program “RoundMidnight” is indicated between parentheses for each variable parameter.

Type of neighbor	Number of neighbors	Distance (Å)	$\sigma^2$ (Å <sup>2</sup> )
<b><i>Ga-O<sub>f</sub></i></b>	2.1(4)	1.829(14)	0.0039(9)
<b><i>Ga-O<sub>b</sub></i></b>	1.9 <sup>b</sup>	1.93(2)	0.0053(22)
<b><i>Ga-Ga</i></b>	1.0(2)	2.96(3)	0.0103(30)
<b><i>Ga-C</i></b>	4(3)	2.88(8)	0.087(63)
<b><i>Ga-Si</i></b>	0.5(8)	3.54(8)	0.0048(43)

<sup>(a)</sup> $\Delta k$ : [2.2 - 14.8 Å<sup>-1</sup>] -  $\Delta R$ : [0.4 - 3.9 Å];  $S_0^2 = 0.96$ ;  $\Delta E_0 = 5.1 \pm 0.8$  eV (the same for all shells); Fit residue:  $\rho = 4.7\%$ ; Quality factor:  $(\Delta\chi)^2/\nu = 3.83$  ( $\nu = 15/30$ ). (b) Parameter constrained to the parameter above.



**Scheme 1.** Formation of a dimeric species after grafting  $[\text{Ga}(\text{OtBu})_3]_2$  on meso H-ZSM-5-250 ( $\text{Si}/\text{Al} = 40$ )

## Preparation and characterization of supported tripodal Ga on meso H-ZSM-5-250 (II)

Controlled thermolysis of  $[(\equiv\text{SiO})\text{Ga}_2(\text{OtBu})_5]$ , (**I**), from 25 to 300 °C (for 2 h), was conducted under vacuum equipped with a cold trap (liquid N<sub>2</sub>) to collect the gas evolved during the process. The analysis of the gas phase by GC after thermal treatment at 300 °C revealed the formation of isobutene and traces of *t*-BuOH. As reported in the case of supported tripodal V, the formation of isobutene is generated via a  $\beta$ -H elimination from the methyl groups to form a hydroxy gallium intermediate justified by a band at 3680 cm<sup>-1</sup> in the DRIFT spectrum.<sup>30</sup> Simultaneously, a significant decrease of the alkyl vibrational bands between 3000–2800 cm<sup>-1</sup> of tert-butoxy ligand after heating was observed (Figure 1, c). Interestingly, the free silanol groups have been partial regenerated and was due to a transfer of OH groups from gallium by ring opening of Si-O-Si fragments, leading to the formation of Si-OH and creation of Ga-O bond. Similarly, this phenomenon was also evidenced by <sup>1</sup>H MAS

NMR (Figure 2, c). The spectrum obtained was similar to that of pristine meso H-ZSM-5-250 (Si/Al= 40), with signals at 1.7, 2.5, 3.9 ppm attributed for the regenerated isolated silanol, the EFA hydroxyls and the Brønsted acid sites, respectively. Moreover, three other bands were observed at 0, 0.9 and 1.4 ppm, corresponding to tetrahedral aluminum hydroxy, residual alkyl groups and Ga-OH, respectively. The attribution of Ga-OH at 1.4 ppm was previously reported in literature.<sup>31</sup> Analysis of **(II)** (Si/Al= 40) by N<sub>2</sub> adsorption/desorption showed that the BET surface area and the total pore volume (377.0 m<sup>2</sup>/g and 0.21 cm<sup>3</sup>/g) have almost been restored with respect to the bare support (Table 1). Regains in surface area and pore volume were expected as the alkyl ligands, causing partial blockage of the pores, have been removed. **(II)** has further been submitted to EXAFS analysis in order to confirm the local structure. Further evidence supporting the formation of a dimeric structure was obtained from Ga K-edge X-ray absorption spectroscopy. The k<sup>3</sup>-weighted Ga K-edge EXAFS corresponding Fourier transform of tripodal Ga/meso H-ZSM-5-250 (Si/Al= 40) obtained from a [Ga(OtBu)<sub>3</sub>]<sub>2</sub> precursor after grafting and heating are shown in Figure 4. The results from the fit are in accordance with the formation of a dimeric structure (Figure 4, Table 3). The peaks observed in the Fourier transform could be fitted by two levels of oxygen back-scatterers, ca. two O at 1.80 and two O at 1.93 Å and a Ga--Ga contribution from a Ga back-scatterer at ca. 2.88 Å. In addition, the spectrum is also fitted with a Ga-Si contribution at ca. 3.52 Å. This result is in agreement with DRIFT and solid state NMR, resulting in a dimeric structure where each Ga is bonded to a silicon, bearing a terminal and a bridged hydroxy ligand, [(≡SiO)Ga(OH)<sub>2</sub>]<sub>2</sub>, as depicted below in Scheme 2.

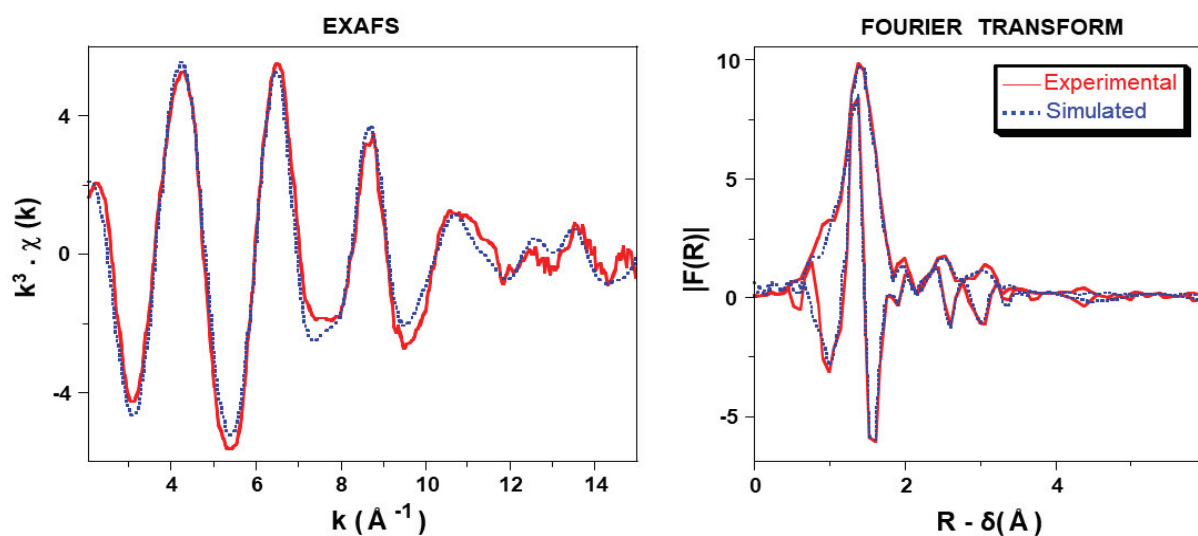


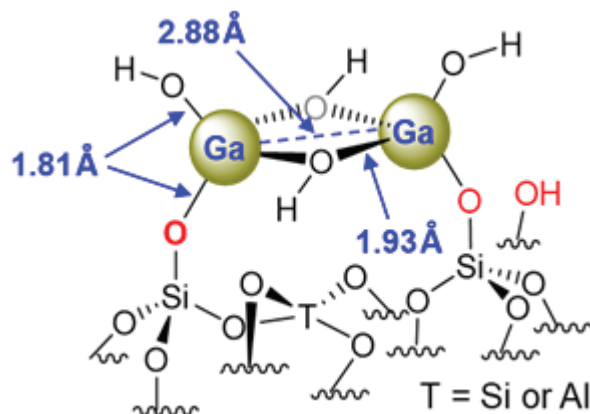
**Figure 4.** Ga K-edge k<sup>3</sup>-weighted EXAFS (left) and Fourier transform (right, modulus and imaginary part; distances uncorrected from phase shifts) of obtained from a [Ga(OtBu)<sub>3</sub>]<sub>2</sub>

precursor after grafting on meso H-ZSM-5-250 (Si/Al= 40), followed by a thermal treatment at 300 °C. Solid lines: Experimental; Dashed lines: Fit (spherical wave theory).

**Table 3.** Parameters obtained from the fit of the EXAFS spectrum of obtained from a  $[\text{Ga}(\text{OtBu})_3]_2$  precursor after grafting on meso H-ZSM-5-250 (Si/Al= 40), followed by a thermal treatment at 300 °C.<sup>(a)</sup> The error interval generated by the fitting program “RoundMidnight” is indicated between parentheses for each variable parameter.

Type of neighbor	Number of neighbors	Distance (Å)	$\sigma^2$ (Å <sup>2</sup> )
<i>Ga-Q<sub>t</sub></i>	2.0	1.805(8)	0.0025(8)
<i>Ga--Q<sub>b</sub></i>	2.0	1.93(1)	0.0053(22)
<i>Ga--Ga</i>	1.0	2.88(3)	0.0103(30)
<i>Ga--Si</i>	1.0	3.52(4)	0.0052(35)

<sup>a</sup> $\Delta k$ : [2.1 - 15.0 Å<sup>-1</sup>] -  $\Delta R$ : [0.4 - 3.9 Å];  $S_0^2 = 0.96$ ;  $\Delta E_0 = 5.5 \pm 0.7$  eV (the same for all shells); Fit residue:  $\rho = 4.1$  %; Quality factor:  $(\Delta\chi)^2/\nu = 2.87$  ( $\nu = 20/30$ ).



**Scheme 2.** Formation of a dimeric species after thermal treatment of  $[\text{Ga}(\text{OtBu})_3]_2/\text{meso H-ZSM-5-250}$  (Si/Al= 40) at 300 °C

### Preparation and characterization of $[\text{Ga}(i\text{Bu})_3]$ supported on meso H-ZSM-5-250 (III)

$[\text{Ga}(i\text{Bu})_3]$ , being a monomeric complex in solution was immobilized onto meso H-ZSM-5-250 (Si/Al= 40) in the same manner as described for (I), offering material (III). The grafting reaction was monitored by IR spectroscopy. Grafting of  $[\text{Ga}(i\text{Bu})_3]$  proceeded via protonolysis on the silanol groups, as indicated in the DRIFT spectrum where isolated silanols at 3743  $\text{cm}^{-1}$  has been partially consumed. On the other hand, the Brønsted acid sites at 3601  $\text{cm}^{-1}$  remained intact during the grafting (Figure 5). Presence of surface alkyl groups associated to iso-butyl ligands were evidenced by the  $\nu(\text{C-H})$  vibration bands appearing in the range between 2800–3000  $\text{cm}^{-1}$ . These results were similar to the ones observed in the case of

catalyst **(I)**, consistent with a selective grafting on the silanol groups in the mesopores, while the Brønsted sites in micropores were conserved.

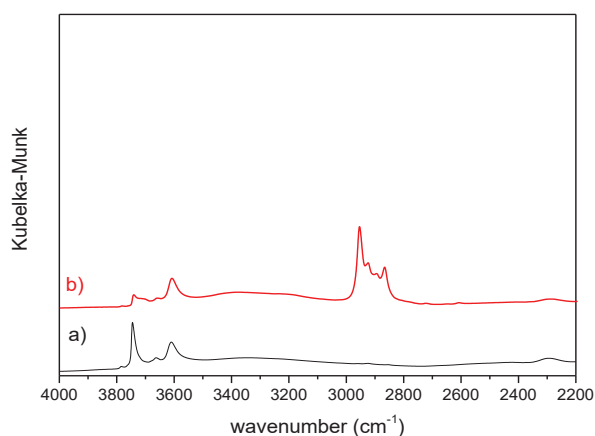


**Figure 5.** DRIFT spectra a) of meso H-ZSM-5-250 (Si/Al= 40) before (black), b) after reaction with  $[Ga(iBu)_3]$  in pentane at 25 °C and thermal treatment at 70 °C and high vacuum for 12 h (red)

The  $^1H$  MAS NMR spectrum of **(III)** exhibited signals at 0.9, around 2 and 4.0 ppm corresponding to methyl groups of isobutyl fragments, to the Al-OH (EFA) and to the Brønsted acid sites, respectively (Figure 6, a). The peak around 2 ppm was particularly large due to the presence of different Al-OH types, as well as the presence of  $Ga-CH_2-CH-(CH_3)_2$  having an expected resonance at 2.0 ppm.<sup>15</sup> Moreover, two signals are observed in the  $^{13}C$  CP MAS spectrum at 25.6 and 30.9 ppm, attributed to  $CH_3$  and  $CH$  from the isobutyl groups, respectively (Figure 6, b). Hence, DRIFT and NMR techniques suggest the formation of a bifunctional  $[Ga(iBu)_3]$  on meso H-ZSM-5-250 (Si/Al= 40) catalyst like in the case of catalyst **(I)**.

a)

b)

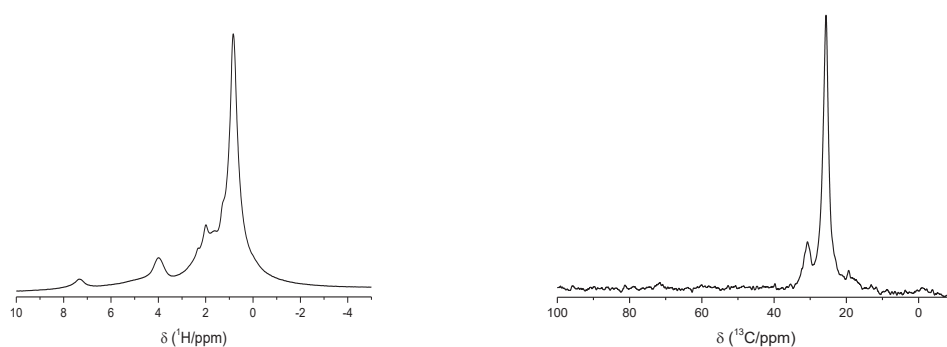


**Figure 6.** MAS NMR spectra of a)  $^1H$  and b)  $^{13}C$  CP of  $Ga(iBu)_3/meso$  H-ZSM-5-250 (Si/Al= 40) (11.7 T, 10 kHz,  $d_1=5s$ )

The N<sub>2</sub> adsorption/desorption of species **(III)** revealed a decrease in the surface area from 381.6 to 143.11 m<sup>2</sup>.g<sup>-1</sup> and in the volume of the total pores (Table 1). According to elemental analysis, **(III)** contained 0.92 and 1.7 wt% of Ga and C, respectively, corresponding to an atomic ratio 10.8. In addition, the isobutane evolved during the grafting and detected by GC was 0.9/Ga. The Ga loading in species **(III)** (0.92 wt%) was lower than what we observed in the species **(I)** (2.37 wt%). Since the Ga content is practically governed by the available Si-OH for grafting, such low Ga loading in **(III)** suggested a monomeric surface organometallic fragment, like the one reported earlier.<sup>15</sup> It is important to note that the structure of [Ga(*i*Bu)<sub>3</sub>] depends on the nature of the support. In the case of silica, we recently observed the formation of a dimeric species while a monomeric species was obtained on alumina.<sup>32</sup> The local structure of the catalyst Ga(*i*Bu)<sub>3</sub>/meso H-ZSM-5-250 (Si/Al= 40) was furthermore investigated by EXAFS to confirm the previous findings. In Figure 7, the first maxima between 0.8 and 2.0 Å, corresponds to scattering from light (O, C) atoms in the first coordination sphere of Ga, hence two carbon atoms from the isobutyl ligands are bonded to Ga with a distance of 1.98 Å. In fact, terminal Ga-C bonds in [HGa(*i*-Pr)<sub>2</sub>]<sub>3</sub> were reported to be between 2.004-2.129 Å,<sup>33</sup> similar to the case of catalyst **(III)**. Moreover, one oxygen atom distanced at 1.80 Å derived from the support (Si-O-Ga). The Ga-O distance (1.80 Å) falls in the range expected for terminal Ga-OR bond lengths (1.79-1.89 Å).<sup>34,35</sup> This is in accordance with the mass balance analysis (*vide supra*), suggesting the formation of a monopodal species **(III)** (Table 4). From the other maxima in the FT magnitude (2.2 and 3.0 Å) corresponding to non-bonded atoms in the second coordination sphere of the Ga, the presence of two non-bonded C atoms at a distance of 3.0 Å were seen, as Ga is surrounded by secondary carbon from the two iso-butyl ligands. Two other long contributions Ga-O (2.47 Å) attributed to an O from the surface coordinated to the metal, and a Si, second neighbor of Ga, located at 3.25 Å, allowing to obtain a good fit with experimental spectrum. Hence, all these data from EXAFS agrees with the formation of a monopodal species, [(≡SiO)Ga(*i*Bu)<sub>2</sub>], depicted in Scheme 3. A judicious choice of the nature of the ligand in the Ga precursor can lead to a catalyst bearing monomeric, dimeric or oligomeric species after grafting on meso H-ZSM-5-250 (Si/Al= 40). Hence, the variety of the catalyst with different surface species permit to establish a relationship structure-activity in propane aromatization and to provide more information about the best active sites and the sites responsible for deactivation.

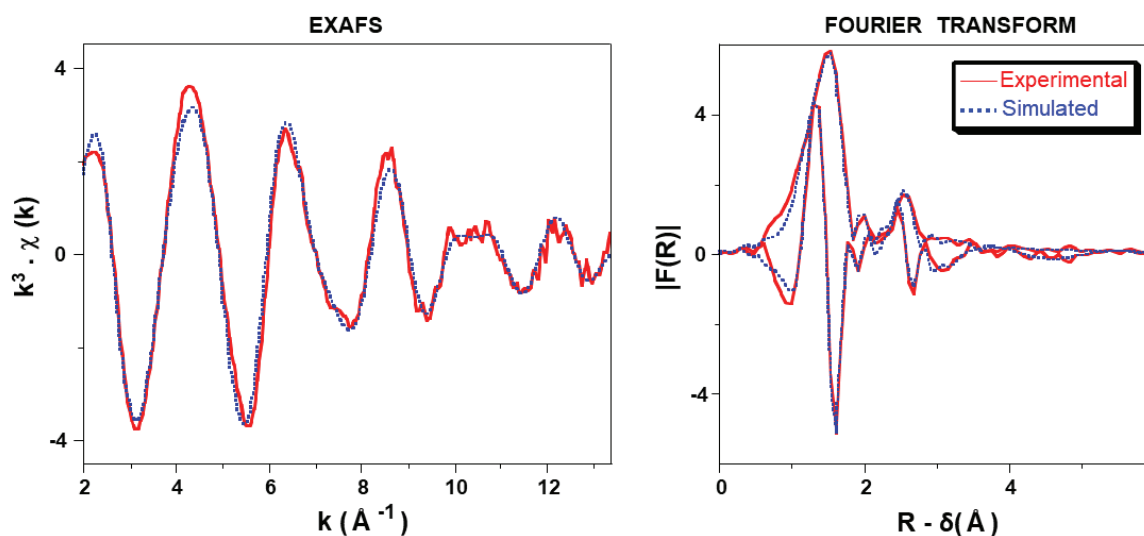
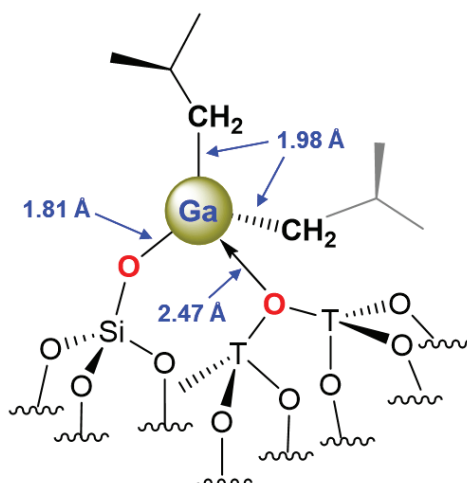


**Figure 7.** Ga K-edge  $k^3$ -weighted EXAFS (left) and Fourier transform (right, modulus and imaginary part; distances uncorrected from phase shifts) of  $\text{Ga}(i\text{Bu})_3/\text{H-ZSM-5-250}$  (Si/Al=40). Solid lines: Experimental; Dashed lines: Fit (spherical wave theory).

**Table 4.** Parameters obtained from the fit of the EXAFS spectrum for  $\text{Ga}(i\text{Bu})_3/\text{H-ZSM-5-250}$  (Si/Al=40).<sup>(a)</sup> The error interval generated by the fitting program “RoundMidnight” is indicated for each variable parameter between parentheses.

Path <sup>a</sup>	$N^b$	$R$ (Å)	$10^3 \sigma^2$ (Å <sup>2</sup> )
<b><i>Ga-O</i></b>	1	1.807(12)	0.0042(16)
<b><i>Ga-C1</i></b>	2	1.98 (2)	0.0025(10)
<b><i>Ga-O&lt;</i></b>	1	2.47(7)	0.017(8)
<b><i>Ga-C2</i></b>	2	3.00(2)	0.0036(18)
<b><i>Ga-Si</i></b>	1	3.25(10)	0.057(75)

(a)  $\Delta k$ : [2.0 - 13.4 Å<sup>-1</sup>] -  $\Delta R$ : [0.4 - 3.9 Å];  $S_0^2 = 0.96$ ;  $\Delta E_0 = 7.0 \pm 0.7$  eV (the same for all shells); Fit residue:  $\rho = 3.4$  %; Quality factor:  $(\Delta\chi)^2/\nu = 2.57$  ( $\nu = 15/26$ ).



**Scheme 3.** Formation of a monomeric species after grafting  $\text{Ga}(i\text{Bu})_3/\text{meso H-ZSM-5-250}$  (Si/Al=40)

## Reactivity toward propane aromatization

As mentioned earlier, propane aromatization requires a bifunctional catalyst supported on a zeolite, where the first step (dehydrogenation) is known to be favored on the metal sites whereas the acidic sites in the zeolites undergo aromatization of propylene, the primary product. Additionally, it is important to note that the aromatization process include a series of reaction between dehydrogenation and aromatization such as oligomerization and cyclization ensured by the Brønsted acid sites.<sup>36</sup> Thus, dehydrogenation is the limiting step during the propane aromatization. It is then preferable to incorporate a more active Ga phase for dehydrogenation in the zeolite giving higher concentration in propylene. Based on our recent results obtained in propane dehydrogenation, we expected by using a high active Ga species obtained from a  $[\text{Ga}(\text{OtBu})_3]_2$  precursor after grafting and heating, located in the mesopores, to access to a high catalytic activity in propane aromatization with catalyst **(II)**. The catalytic performance of **(II)** in propane aromatization was evaluated in a continuous flow reactor at 580 °C with a total flow of 10 mL.min<sup>-1</sup> (5 % of C3 in Ar) and was compared to  $\text{Ga}(i\text{Bu})_3/\text{meso H-ZSM-5-250}$  (Si/Al= 40) and meso H-ZSM-5-250 (Si/Al= 40). The purpose of this section is to assess the effect of the presence of Ga in the mesopores, as well as the effect of the structure (monomeric vs dimeric) on the activity and selectivity in propane aromatization.

The initial propane conversion obtained at 580 °C on tripodal Ga/meso H-ZSM-5-250 (Si/Al= 40) was high (74%), followed by a gradual deactivation over the time leading to 38% after 900 min (Figure 8, a). The selectivity toward aromatics was around 60 wt% at early times on stream and dropped to 50.5 wt% (23.4 wt% of benzene and 27.1 wt% of toluene) after 900 min (Figure 8, b). The light products (methane, ethane and ethylene) resulting from the cracking reactions and the propylene obtained from the dehydrogenation reaction increase as function of time while the aromatics products decrease. At 900 min, the selectivity toward propene was 19.9 wt% (initially 3.5 wt%) with 12.9 wt% of ethene, 11.6 wt% of ethane and 5.1 wt% of methane (Figure S3). Thus, the presence of Ga in the mesopores promoted the formation of 60 wt% of aromatics compared to 40 wt% in the case of pristine meso H-ZSM-5-250 (Si/Al= 40) tested in the same conditions (Figure S4). Surprisingly, meso H-ZSM-5-250 (Si/Al= 40) exhibited a high stability with a conversion of 67% compared to tripodal Ga catalyst. However, **(II)** exhibited fairly high activity and selectivity at early time on stream, indicating that the combination of these tripodal Ga supported species and meso H-ZSM-5 was efficient for propane aromatization. These tripodal Ga species were incapable of

accomplishing propane aromatization without the simultaneous presence of strong acidic sites that appeared to be involved as well in the activation of C-H bond of propane. In fact, this was supported from the results obtained in the case of the bare zeolite in propane aromatization. Additionally, the decrease in the conversion observed after 100 min in the case of (II) was probably due to limited diffusion of propylene (primary product that increases as function of time) into the acidic sites located in the micropores. The constantly increase in propene selectivity as function of time on stream in the case of species (II) implied that the dehydrogenation phase was still active, but the limited step lies on the acid sites which seemed to become less accessible due to coke formation and blocking the micropores. In fact, the material (II) turned into black after catalytic performance, revealing the formation of 4 % of coke, evidenced by TGA (Figure S5). However, in the case of meso zeolite (Si/Al= 40), the deactivation by coke formation was not observed. This result revealed that the dimeric tripodal Ga supported species also accelerate coke formation. In order to confirm this hypothesis, we evaluated the catalytic activity of monomeric  $[Ga(iBu)_3]$  on meso H-ZSM-5-250 (Si/Al= 40).

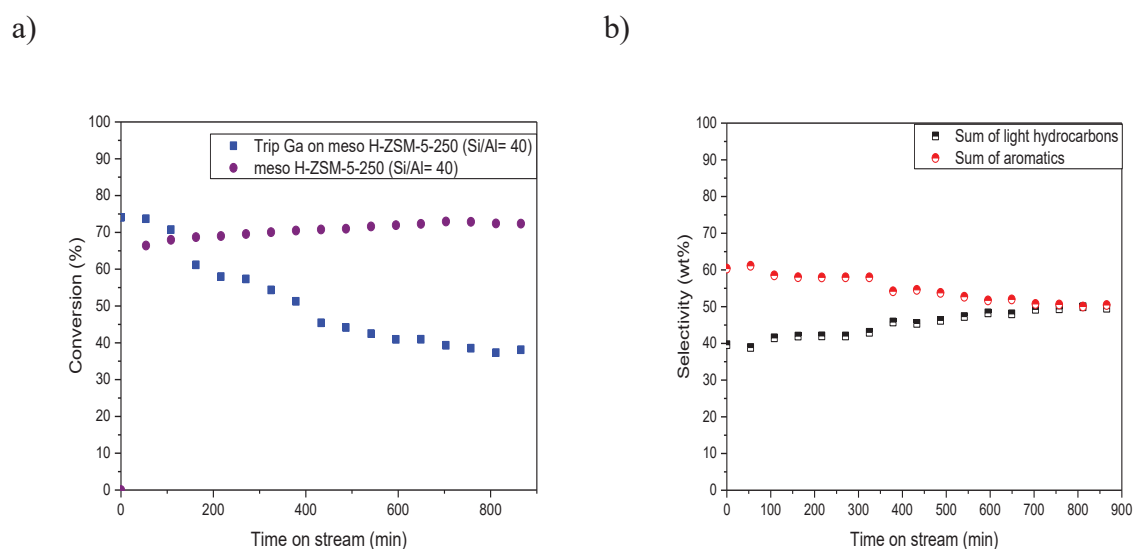


**Figure 8.** a) propane conversion with meso H-ZSM-5-250 (Si/Al= 40) (●) and tripodal Ga/meso H-ZSM-5-250 (Si/Al= 40) (■) and b) selectivity of light hydrocarbons and aromatics in wt% with Ga/meso H-ZSM-5 (Si/Al= 40) for propane aromatization; Conditions: T = 580 °C, total flow = 10 mL.min<sup>-1</sup> (5 % C3 in Ar)

Compared to (II), a high stability was observed with a conversion of around 88 % in the case of monomeric  $Ga(iBu)_3$ /meso H-ZSM-5-250 (Si/Al= 40) (III), with a high selectivity toward aromatics 64 wt% along with 36 wt% of light hydrocarbons (Figure 9). After 900 min, the products consisted in 36.6 wt% of benzene, 26.1 wt% of toluene, 13 wt% of methane, 10.5

wt% of ethene, 7 wt% of ethane and 5.7 wt% of propene, along with traces of C4. In addition, the global selectivity in aromatics for **(III)** was far higher than what we observed in the case of meso H-ZSM-5-250 (Si/Al= 40) alone (Figure S6). These results showed that the monomeric Ga species in the mesopores was more appropriate to perform propane dehydrogenation/aromatization compared to Ga dimeric species without remarkable deactivation of the catalyst. In fact, the low deactivation of this catalyst was related to the absence of coke formation and pore blockage of micropores containing the acidic Brønsted sites during the catalytic test. Based on current results, the isolated Ga species in meso zeolite **(III)** was more suitable for propane aromatization than dimeric Ga species. The low catalytic performance of **(II)** was attributed to the dimeric Ga species that may lead to the formation of coke due to its high acidity. In fact, it was reported in literature that the Ga oligomeric species on alumina were less active and stable than isolated Ga species due to the formation of coke during catalytic test at high temperature. The difference in the catalytic activity between **(II)** and **(III)** is thus ascribed by the different Ga structure (monomeric or dimeric) on the surface. Hence, current data suggested that it was essential to obtain isolated species on the surface in the mesopores of meso zeolites in order to avoid the quick deactivation due to the formation and migration of coke into the micropores as well as to access to a highly active, stable and selective catalyst for propane aromatization.

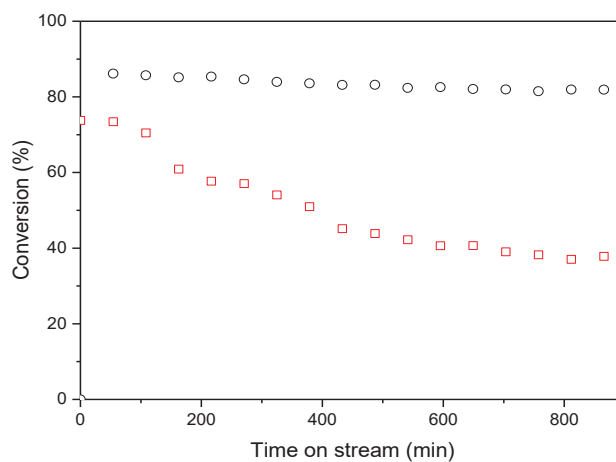


**Figure 9.** Propane conversion with monopodal Ga(*i*Bu)<sub>3</sub>/meso H-ZSM-5-250 (Si/Al= 40) (○) and tripodal Ga/meso H-ZSM-5-250 (Si/Al= 40) (□) ; Conditions: T= 580 °C, total flow= 10 mL.min<sup>-1</sup> (5 % C3 in Ar)

## Conclusion

The present investigation reports the catalytic activity of a tripodal dimeric species supported on a meso H-ZSM-5-250 (Si/Al= 40), from a  $[\text{Ga}(\text{OtBu})_3]_2$  precursor after grafting and heating at 300 °C, and monomeric species supported on a the same zeolite and obtained from  $[\text{Ga}(i\text{Bu})_3]$  molecular precursor for propane aromatization. Meso H-ZSM-5-250 (Si/Al= 40) was prepared by desilication of microporous H-ZSM-5 (Si/Al= 40), dehydroxylated at 250 °C and characterized by DRIFT,  $^1\text{H}$  NMR and  $\text{N}_2$  adsorption/desorption. Material **(I)** was prepared by using an original method based on the selective grafting of a dimeric complex  $[\text{Ga}(\text{OtBu})_3]_2$  on the silanols in the mesopores of meso H-ZSM-5-250 (with Si/Al= 40). This leads to dimeric gallium supported species  $[(\equiv\text{SiO})\text{Ga}_2(\text{OtBu})_5]$  **(I)**, evidenced by DRIFT, high field solid-state NMR ( $^1\text{H}$  and  $^{13}\text{C}$ ),  $\text{N}_2$  adsorption/desorption, EXAFS as well as mass balance analysis. Tripodal Ga species supported on meso H-ZSM-5-250 (Si/Al= 40) **(II)** were then obtained by a thermal treatment, triggering  $\beta$ -H elimination leading to gallium hydroxy intermediate followed by a hydroxy transfer to Si-O-Si or Si-O-Al fragments. This catalyst **(II)** was fully characterized by DRIFT,  $^1\text{H}$  MAS NMR,  $\text{N}_2$  adsorption/desorption. In addition, EXAFS confirmed the formation of a Ga dimeric species after the thermal treatment. A Ga monomeric species on meso H-ZSM-5-250 (Si/Al= 40) using  $[\text{Ga}(i\text{Bu})_3]$  was prepared and characterized by the same techniques as **(I)**. Importantly, in all cases, the immobilization of Ga occurred selectively on the silanol groups located in the mesopores, leading to a bifunctional catalyst affording Ga sites for dehydrogenation and Brønsted acid sites for cyclization, oligomerization, and aromatization. A better activity and stability for propane aromatization were obtained on monomeric Ga species in the case of species **(III)** compared to the dimeric species **(II)**. A fast deactivation was observed in the case of **(II)** with a decrease in the selectivity toward aromatics as function of time on stream. This deactivation was attributed to coke formation due to the presence of acidic Ga-OH-Ga sites in the case of a dimeric structure. This resulted in the blockage of the micropores and made the Brønsted acidic sites inaccessible. Thus, the difference in reactivity observed for species **(II)** and **(III)** was hence attributed to the structurally distinct gallium surface sites in these catalysts. We can conclude that isolated Ga species in the mesopores of the meso zeolite was crucial in order to avoid a quick deactivation due to the formation and migration of coke into the micropores and thus to access to a highly active, stable and selective catalyst for propane aromatization.

## Acknowledgments

This work was carried out as a part of BIZEOLCAT project, which has received funding from the European Union's Horizon 2020 research and innovation program under grant agreement No. 814671. In particular, J. A. is grateful for her PhD grant. AdM thanks Olivier Mathon and Kiril Lomachenko for their help during the recording of the X-ray absorption spectra at ESRF, on beam line BM23.

## References

- (1) Knop, V.; Loos, M.; Pera, C.; Jeuland, N. A Linear-by-Mole Blending Rule for Octane Numbers of n-Heptane/Iso-Octane/Toluene Mixtures. *Fuel* **2014**, *115*, 666–673. <https://doi.org/10.1016/j.fuel.2013.07.093>.
- (2) Mirzaei, A.; Kim, J.-H.; Woo Kim, H.; Sub Kim, S. Resistive-Based Gas Sensors for Detection of Benzene, Toluene and Xylene (BTX) Gases: A Review. *J. Mater. Chem. C* **2018**, *6* (16), 4342–4370. <https://doi.org/10.1039/C8TC00245B>.
- (3) Marshall, A.-L.; Alaimo, P. J. Useful Products from Complex Starting Materials: Common Chemicals from Biomass Feedstocks. *Chem. – Eur. J.* **2010**, *16* (17), 4970–4980. <https://doi.org/10.1002/chem.200903028>.
- (4) Fishbein, L. An Overview of Environmental and Toxicological Aspects of Aromatic Hydrocarbons III. Xylene. *Sci. Total Environ.* **1985**, *43* (1), 165–183. [https://doi.org/10.1016/0048-9697\(85\)90039-7](https://doi.org/10.1016/0048-9697(85)90039-7).
- (5) Li, N.; Jiao, F.; Pan, X.; Chen, Y.; Feng, J.; Li, G.; Bao, X. High-Quality Gasoline Directly from Syngas by Dual Metal Oxide–Zeolite (OX-ZEO) Catalysis. *Angew. Chem.* **2019**, *131* (22), 7478–7482. <https://doi.org/10.1002/ange.201902990>.
- (6) Wang, K.; Dong, M.; Li, J.; Liu, P.; Zhang, K.; Wang, J.; Fan, W. Facile Fabrication of ZSM-5 Zeolite Hollow Spheres for Catalytic Conversion of Methanol to Aromatics. *Catal. Sci. Technol.* **2017**, *7* (3), 560–564. <https://doi.org/10.1039/C6CY02476A>.
- (7) Zhang, P.; Tan, L.; Yang, G.; Tsubaki, N. One-Pass Selective Conversion of Syngas to Para -Xylene. *Chem. Sci.* **2017**, *8* (12), 7941–7946. <https://doi.org/10.1039/C7SC03427J>.
- (8) Wei, Z.; Chen, L.; Cao, Q.; Wen, Z.; Zhou, Z.; Xu, Y.; Zhu, X. Steamed Zn/ZSM-5 Catalysts for Improved Methanol Aromatization with High Stability. *Fuel Process. Technol.* **2017**, *162*, 66–77. <https://doi.org/10.1016/j.fuproc.2017.03.026>.
- (9) Zhang, J.; Zhang, M.; Chen, S.; Wang, X.; Zhou, Z.; Wu, Y.; Zhang, T.; Yang, G.; Han, Y.; Tan, Y. Hydrogenation of CO<sub>2</sub> into Aromatics over a ZnCrO<sub>x</sub>–Zeolite Composite Catalyst. *Chem. Commun.* **2019**, *55* (7), 973–976. <https://doi.org/10.1039/C8CC09019J>.
- (10) Zhou, W.; Zhou, C.; Yin, H.; Shi, J.; Zhang, G.; Zheng, X.; Min, X.; Zhang, Z.; Cheng, K.; Kang, J.; Zhang, Q.; Wang, Y. Direct Conversion of Syngas into Aromatics over a Bifunctional Catalyst: Inhibiting Net CO<sub>2</sub> Release. *Chem. Commun.* **2020**, *56* (39), 5239–5242. <https://doi.org/10.1039/D0CC00608D>.
- (11) J. Spivey, J.; Hutchings, G. Catalytic Aromatization of Methane. *Chem. Soc. Rev.* **2014**, *43* (3), 792–803. <https://doi.org/10.1039/C3CS60259A>.
- (12) Sharifi, K.; Halladj, R.; Royae, S. J.; Towfighi, F.; Firoozi, S.; Yousefi, H. Effective Factors on Performance of Zeolite Based Metal Catalysts in Light Hydrocarbon Aromatization. *Rev. Chem. Eng.* **2022**. <https://doi.org/10.1515/revce-2020-0082>.

- (13) Dauda, I. B.; Yusuf, M.; Gbadamasi, S.; Bello, M.; Atta, A. Y.; Aderemi, B. O.; Jibril, B. Y. Highly Selective Hierarchical ZnO/ZSM-5 Catalysts for Propane Aromatization. *ACS Omega* **2020**, *5* (6), 2725–2733. <https://doi.org/10.1021/acsomega.9b03343>.
- (14) Al-Yassir, N.; Akhtar, M. N.; Ogunronbi, K.; Al-Khattaf, S. Synthesis of Stable H-Galloaluminosilicate MFI with Hierarchical Pore Architecture by Surfactant-Mediated Base Hydrolysis, and Their Application in Propane Aromatization. *J. Mol. Catal. Chem.* **2012**, *360*, 1–15. <https://doi.org/10.1016/j.molcata.2012.04.005>.
- (15) Szeto, K. C.; Gallo, A.; Hernández-Morejudo, S.; Olsbye, U.; De Mallmann, A.; Lefebvre, F.; Gauvin, R. M.; Delevoye, L.; Scott, S. L.; Taoufik, M. Selective Grafting of Ga(i-Bu)<sub>3</sub> on the Silanols of Mesoporous H-ZSM-5 by Surface Organometallic Chemistry. *J. Phys. Chem. C* **2015**, *119* (47), 26611–26619. <https://doi.org/10.1021/acs.jpcc.5b09289>.
- (16) Chapter I: Synthesis of ZSM-5 Zeolites in the Presence of Tetrapropylammonium Ions. In *Studies in Surface Science and Catalysis*; Jacobs, P. A., Martens, J. A., Eds.; Synthesis of High-Silica Aluminosilicate Zeolites; Elsevier, 1987; Vol. 33, pp 47–111. [https://doi.org/10.1016/S0167-2991\(09\)60467-5](https://doi.org/10.1016/S0167-2991(09)60467-5).
- (17) Valet, M.; Hoffman, D. M. Synthesis of Homoleptic Gallium Alkoxide Complexes and the Chemical Vapor Deposition of Gallium Oxide Films. *Chem. Mater.* **2001**, *13* (6), 2135–2143. <https://doi.org/10.1021/cm0014177>.
- (18) Kovar, R. A.; Derr, Henry.; Brandau, Duane.; Callaway, J. O. Preparation of Organogallium Compounds from Organolithium Reagents and Gallium Chloride. Infrared, Magnetic Resonance, and Mass Spectral Studies of Alkylgallium Compounds. *Inorg. Chem.* **1975**, *14* (11), 2809–2814. <https://doi.org/10.1021/ic50153a042>.
- (19) Mathon, O.; Beteva, A.; Borrel, J.; Bugnazet, D.; Gatla, S.; Hino, R.; Kantor, I.; Mairs, T.; Munoz, M.; Pasternak, S.; Perrin, F.; Pascarelli, S. The Time-Resolved and Extreme Conditions XAS (TEXAS) Facility at the European Synchrotron Radiation Facility: The General-Purpose EXAFS Bending-Magnet Beamline BM23. *J. Synchrotron Radiat.* **2015**, *22*, 1548–1554. <https://doi.org/10.1107/S1600577515017786>.
- (20) Ravel, B.; Newville, M. ATHENA, ARTEMIS, HEPHAESTUS: Data Analysis for X-Ray Absorption Spectroscopy Using IFEFFIT. *J. Synchrotron Radiat.* **2005**, *12* (4), 537–541. <https://doi.org/10.1107/S0909049505012719>.
- (21) Alain, M.; Jacques, M.; Diane, M.-B.; Karine, P. MAX: Multiplatform Applications for XAFS. *J. Phys. Conf. Ser.* **2009**, *190*, 012034. <https://doi.org/10.1088/1742-6596/190/1/012034>.
- (22) Michalowicz, A. “EXAFS Pour Le MAC”: A New Version of an EXAFS Data Analysis Code for the Macintosh. *J. Phys. IV* **1997**, *7* (C2), C2-236. <https://doi.org/10.1051/jp4/1997178>.
- (23) Ankudinov, A. L.; Ravel, B.; Rehr, J. J.; Conradson, S. D. Real-Space Multiple-Scattering Calculation and Interpretation of x-Ray-Absorption near-Edge Structure. *Phys. Rev. B* **1998**, *58* (12), 7565–7576. <https://doi.org/10.1103/PhysRevB.58.7565>.
- (24) Deng, F.; Yue, Y.; Ye, C. <sup>1</sup>H/<sup>27</sup>Al TRAPDOR NMR Studies on Aluminum Species in Dealuminated Zeolites. *Solid State Nucl. Magn. Reson.* **1998**, *10* (3), 151–160. [https://doi.org/10.1016/S0926-2040\(97\)00028-3](https://doi.org/10.1016/S0926-2040(97)00028-3).
- (25) Beck, L. W.; Haw, J. F. *Multinuclear NMR Studies Reveal a Complex Acid Function for Zeolite Beta*. ACS Publications. <https://pubs.acs.org/doi/pdf/10.1021/j100004a004> (accessed 2021-11-09). <https://doi.org/10.1021/j100004a004>.
- (26) HUNGER, M. Brønsted Acid Sites in Zeolites Characterized by Multinuclear Solid-State NMR Spectroscopy. *Catal. Rev.* **1997**, *39* (4), 345–393. <https://doi.org/10.1080/01614949708007100>.

- (27) Mazoyer, E.; Trébosc, J.; Baudouin, A.; Boyron, O.; Pelletier, J.; Basset, J.-M.; Vitorino, M. J.; Nicholas, C. P.; Gauvin, R. M.; Taoufik, M.; Delevoye, L. Heteronuclear NMR Correlations To Probe the Local Structure of Catalytically Active Surface Aluminum Hydride Species on  $\gamma$ -Alumina. *Angew. Chem. Int. Ed.* **2010**, *49* (51), 9854–9858. <https://doi.org/10.1002/anie.201004310>.
- (28) Conte, P.; Spaccini, R.; Piccolo, A. State of the Art of CPMAS  $^{13}\text{C}$ -NMR Spectroscopy Applied to Natural Organic Matter. *Prog. Nucl. Magn. Reson. Spectrosc.* **2004**, *44* (3–4), 215–223.
- (29) Kazansky, V. B.; Subbotina, I. R.; van Santen, R. A.; Hensen, E. J. M. DRIFTS Study of the Nature and Chemical Reactivity of Gallium Ions in Ga/ZSM-5: II. Oxidation of Reduced Ga Species in ZSM-5 by Nitrous Oxide or Water. *J. Catal.* **2005**, *233* (2), 351–358. <https://doi.org/10.1016/j.jcat.2005.05.004>.
- (30) Pal, P.; Quartararo, J.; Abd Hamid, S. B.; Derouane, E. G.; Védrine, J. C.; Magusin, P. C.; Anderson, B. G. A MAS NMR and DRIFT Study of the Ga Species in Ga/H-ZSM5 Catalysts and Their Effect on Propane Ammoxidation. *Can. J. Chem.* **2005**, *83* (6–7), 574–580. <https://doi.org/10.1139/v05-073>.
- (31) Gao, P.; Wang, Q.; Xu, J.; Qi, G.; Wang, C.; Zhou, X.; Zhao, X.; Feng, N.; Liu, X.; Deng, F. Brønsted/Lewis Acid Synergy in Methanol-to-Aromatics Conversion on Ga-Modified ZSM-5 Zeolites, As Studied by Solid-State NMR Spectroscopy. *ACS Catal.* **2018**, *8* (1), 69–74. <https://doi.org/10.1021/acscatal.7b03211>.
- (32) Szeto, K. C.; Jones, Z. R.; Merle, N.; Rios, C.; Gallo, A.; Le Quemener, F.; Delevoye, L.; Gauvin, R. M.; Scott, S. L.; Taoufik, M. A Strong Support Effect in Selective Propane Dehydrogenation Catalyzed by Ga(*i*-Bu) $_3$  Grafted onto  $\gamma$ -Alumina and Silica. *ACS Catal.* **2018**, *8* (8), 7566–7577. <https://doi.org/10.1021/acscatal.8b00936>.
- (33) Uhl, W.; Cuypers, L.; Geiseler, G.; Harms, K.; Massa, W. Synthesen und Kristallstrukturen von Dialkylgalliumhydriden — dimere versus trimere Formeleinheiten. *Z. Für Anorg. Allg. Chem.* **2002**, *628* (5), 1001–1006. [https://doi.org/10.1002/1521-3749\(200206\)628:5<1001::AID-ZAAC1001>3.0.CO;2-N](https://doi.org/10.1002/1521-3749(200206)628:5<1001::AID-ZAAC1001>3.0.CO;2-N).
- (34) Duchateau, R.; Dijkstra, T. W.; van Santen, R. A.; Yap, G. P. A. Silsesquioxane Models for Silica Surface Silanol Sites with Adjacent Siloxide Functionalites and Olefin Polymerization Catalysts Thereof. *Chem. – Eur. J.* **2004**, *10* (16), 3979–3990. <https://doi.org/10.1002/chem.200400206>.
- (35) Basharat, S.; Betchley, W.; Carmalt, C. J.; Barnett, S.; Tocher, D. A.; Davies, H. O. Synthesis of Group 13 Sesquialkoxides and Their Application as Precursors to Crystalline Oxide Films. *Organometallics* **2007**, *26* (2), 403–407. <https://doi.org/10.1021/om0608657>.
- (36) Liu, R.; Zhu, H.; Wu, Z.; Qin, Z.; Fan, W.; Wang, J. Aromatization of Propane over Ga-Modified ZSM-5 Catalysts. *J. Fuel Chem. Technol.* **2015**, *43* (8), 961–969. [https://doi.org/10.1016/S1872-5813\(15\)30027-X](https://doi.org/10.1016/S1872-5813(15)30027-X).

## Supporting information

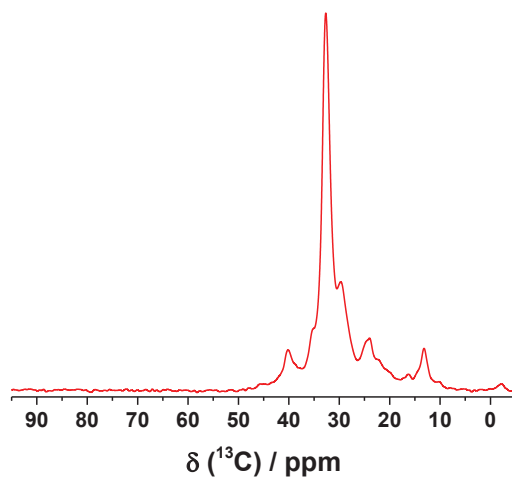


**Figure S1.**  $^{13}\text{C}$  CPMAS NMR (II) (11.7 T, 10 kHz,  $d_1=5\text{s}$ )

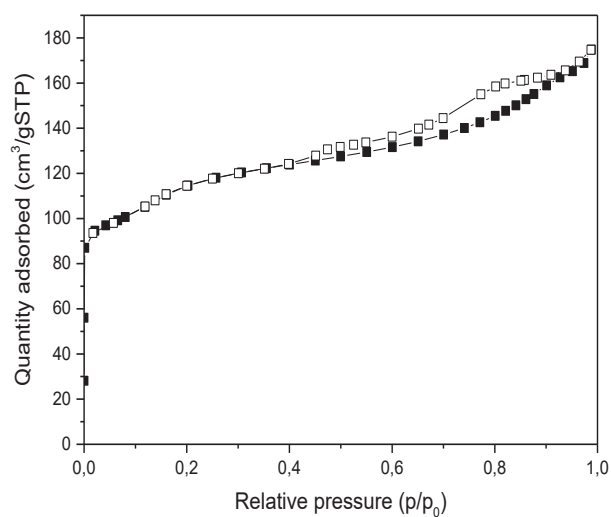


**Figure S2.** BJH desorption profile of meso H-ZSM-5-250 (Si/Al= 40)

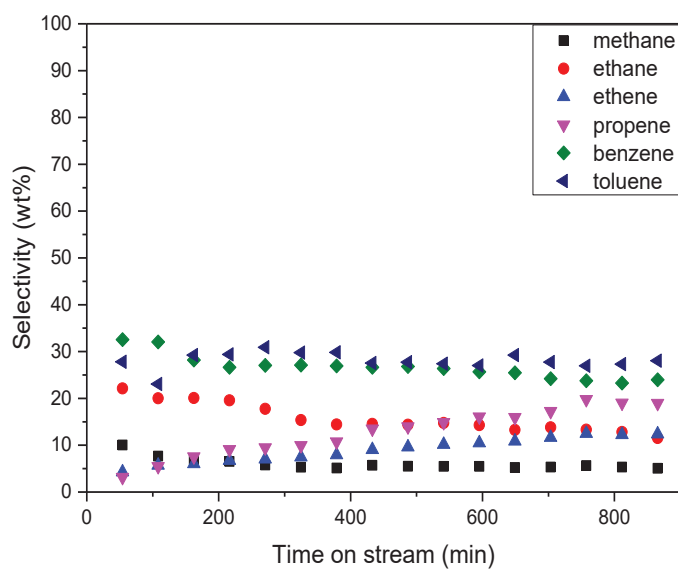


**Figure S3.** Selectivity in wt% of (II) in propane aromatization

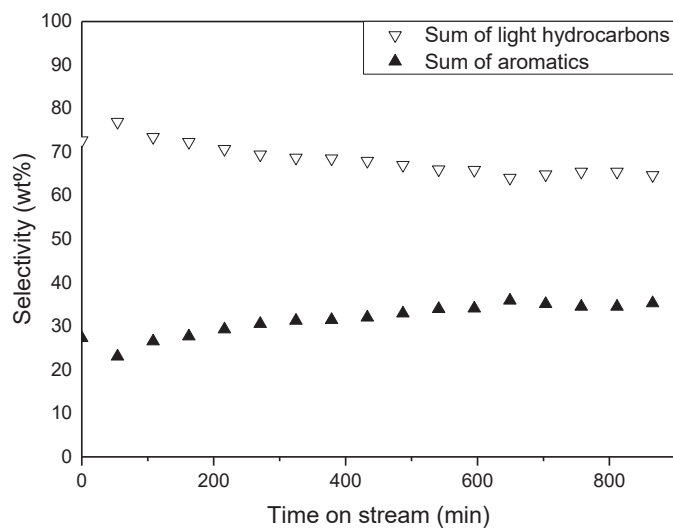


**Figure S4.** Selectivity in wt% in light hydrocarbons and in aromatics for meso H-ZSM-5-250 (Si/Al =40) at T= 580 °C with a total flow= 10 mL.min<sup>-1</sup> (5 % of C3 in Ar)

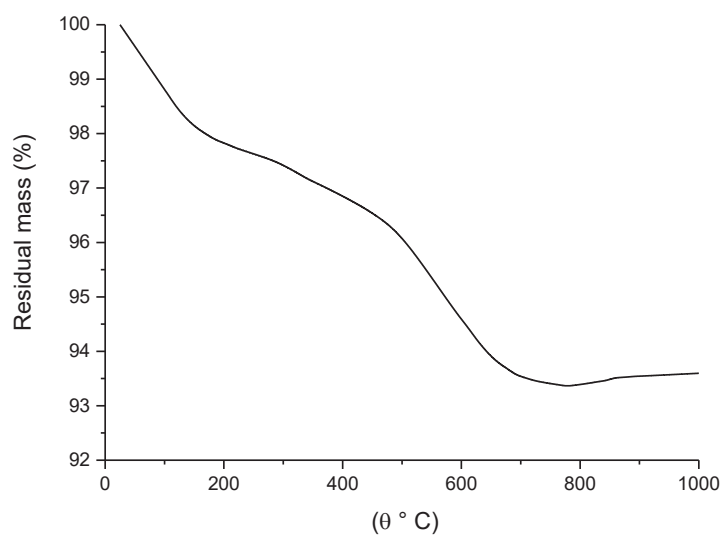


**Figure S5.** TGA of tripodal Ga on meso H-ZSM-5-250 (Si/Al= 40)

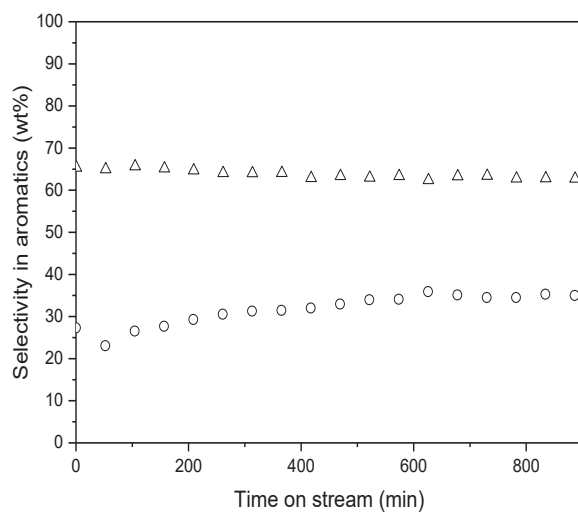


**Figure S6.** Selectivity in wt% in aromatics of meso H-ZSM-5-250 (Si/Al= 40) (○), and Ga(*i*Bu)<sub>3</sub>/meso H-ZSM-5-250 (Si/Al= 40) (Δ); Conditions: T= 580 °C, total flow= 10 mL.min<sup>-1</sup> (5 % C3 in Ar)

## CHAPTER IV. PART B

---

### Ga(*i*Bu)<sub>3</sub> supported on meso H-ZSM-5: Effect of Si/Al ratio on the activity and selectivity in propane aromatization

---



Jessy Abou Nakad,<sup>a</sup> Daniel Firth,<sup>b</sup> Kai C. Szeto,<sup>a</sup> Nicolas Merle,<sup>c</sup> Aimery De Mallmann,<sup>a</sup> Régis Gauvin,<sup>d</sup> Laurent Delevoye,<sup>c</sup> Unni Olsbye,<sup>\*b</sup> and Mostafa Taoufik<sup>\*a</sup>

<sup>a</sup> Université Lyon 1, Institut de Chimie Lyon, CPE Lyon, CNRS, UMR 5128 CP2M, 43 Bd du 11 Novembre 1918, F-69616 Villeurbanne Cedex, France. E-mail: Mostafa.Taoufik@univ-lyon1.fr; Fax: +33 (0)472 431 798; Tel: +33 (0)472 431 795

<sup>b</sup> Centre for Materials Science and Nanotechnology (SMN), Department of Chemistry, University of Oslo, N-0371 Oslo, Norway. E-mail: unni.olsbye@kjemi.uio.no

<sup>c</sup> UCCS (CNRS-UMR 8181), Université Lille Nord de France, USTL, 59652 Villeneuve d'Ascq, France

<sup>d</sup> Institut de Recherche de Chimie Paris, IRCP - UMR CNRS 8247, Chimie ParisTech, Paris, France

## Abstract

Tri-isobutyl gallium has been immobilized on a series of mesoporous H-ZSM5 prepared by desilication with different Si/Al ratio (25, 40, 100, 200 and  $\infty$ ). The resulted materials have been characterized by IR, solid state NMR, BET, elemental analysis and EXAFS. In all cases, the organometallic precursor reacts selectively with silanol groups, yielding a monopodal surface species located in the mesopores. Importantly, the Brønsted acidic sites remain intact in the micropores of the materials, as revealed by IR and high field solid state NMR. This series of materials can be regarded as bifunctional catalysts containing isolated Ga site and Brønsted sites in proximity, suitable for propane aromatization. Catalytic investigations show that the materials are highly active and the activity and selectivity towards aromatics are favorable for low Si/Al ratio. Different conditions have been studied for Ga(*i*Bu)<sub>3</sub>/meso-H-ZSM-5-250 (Si/Al = 40), such as temperature and feed composition. The optimal conditions are found to be 580 °C and 5% propane in the feed.

## Introduction

Light aromatic compounds such as benzene, toluene and xylene (BTX), are considered as essential raw materials for the petrochemical industry and important intermediates to high value-added chemicals. They are also used as blending mixture to enhance the octane number of gasolines. The increasing demand of BTX led to a higher interest toward the transformation of light alkanes into aromatics, since light alkanes became abundant with the discovery of new shale gas reserves.<sup>1</sup> BTX are mainly produced by catalytic reforming or by steam cracking processes,<sup>2</sup> however, other methods can be used like methanol (MTA),<sup>3,4</sup> syngas (STA)<sup>5,6</sup> and CO<sub>2</sub> hydrogenation.<sup>7,8</sup> Although these technologies are still the dominating sources to produce BTX, those “by-product” technologies are less flexible to align with the market evolution. Hence, on-purpose technology is a promising alternative to conventional cracking and reforming processes that has the potential to secure the market supply. The advantage of on-purpose aromatization is the use of cheap and abundant feedstock (light alkanes).<sup>2,9</sup> For example, methane aromatization has been studied, however, due to the low selectivity and the high temperature required during the reaction,<sup>10</sup> the use of propane is preferable in this reaction. On-purpose propane aromatization requires generally a bifunctional catalyst, where the metal sites are responsible for its dehydrogenation into propylene, followed by an oligomerization and cyclization leading to aromatics over the Brønsted acid sites present in the zeolitic support.<sup>11–14</sup> Beside the main reaction, coking and

cracking may also occur resulting in undesired products. Due to the complexity of this process, many studies were conducted to find a suitable high-performing catalyst. Several metals such as Ga, Pt, Zn and others, have been hosted on zeolites and studied for the aromatization reaction.<sup>15-20</sup> Economically, Ga and Zn are more preferred over the expensive noble metal Pt. However, Zn supported on H-ZSM-5 zeolites exhibited a high volatility of the metal under the reaction conditions (high temperature > 500 °C).<sup>9,21,22</sup> To date, Ga is the most promising metal due to its ability to dehydrogenate and aromatize propane into BTX with a high selectivity and marginal leaching of metal species,<sup>23,24</sup> and hence is the only metal used in industry for propane aromatization. UOP and BP commercialized the Cyclar® process, using a bifunctional catalyst based on Ga supported on H-ZSM-5.<sup>2,25</sup> The main drawback of propane aromatization is the production of large amounts of light hydrocarbons by cracking reaction on acidic sites.<sup>21</sup> In addition, these cracking reactions can be also favored by the presence of different gallium oxide phases, clusters or agglomerates on the surface. In fact, the catalysts described in the literature are generally obtained via classical synthesis methods such as wetness impregnation by using Ga salts, chemical vapor deposition of GaCl<sub>3</sub>, followed by thermal activation or reduction, and even mechanical mixing with Ga<sub>2</sub>O<sub>3</sub>.<sup>24,26-34</sup> These methods hamper the highly dispersion and characterization of the isolated active sites, reported to be responsible for the aromatization reaction. In fact, Ga-based catalysts prepared by impregnation with gallium nitrate on zeolite followed by successive calcination, reduction in hydrogen and reoxidation in air and with high loading of metal, lead to the formation of segregated Ga<sub>2</sub>O<sub>3</sub> phase on the surface, responsible for the cracking reaction. The latter facilitates the formation of clusters as well with four gallium centers that were confirmed by EXAFS.<sup>35</sup> The reduction of active sites numbers can also result from the catalyst pretreatment, like water, leading to a low dispersion of Ga. In fact, during the preparation of Ga on zeolites through the ion exchange method, a substantial quantity of metal may still remain on the external surface of the H-ZSM-5 after calcination, due the high-volume size of hydrated Ga<sup>3+</sup> that inhibits its access to the intracrystalline volume of the zeolite. Such low dispersity of Ga leads to the formation of undesired Ga oxide. To overcome these challenges, an anhydrous route for the incorporation of Ga into pores of the zeolites associated to the creation of mesoporous zeolites connected to the zeolite micropores has been proposed. Santen et al. described the chemical vapor deposition of trimethylgallium on meso zeolite, with subsequent removal of the methyl groups by treatment with H<sub>2</sub> or O<sub>2</sub>.<sup>36-38</sup> The obtained catalyst revealed a high selectivity in propane dehydrogenation without the formation of any

aromatic compounds, due to the total absence of acid sites which have been consumed during the preparation of the catalyst. This is due to the diffusion of the low-sized trimethylgallium through the micropores.<sup>37,39,40</sup> Hence, it is essential to control the size of the selected precursor. In that context, using a mesoporous H-ZSM-5, we developed recently a bifunctional catalyst through a selective grafting of [Ga(*i*Bu)<sub>3</sub>] containing moderately bulky ligands. Essentially, the Ga precursor was successfully attached into the mesopores, while the acidic sites in the micropores remained intact. The resulting bifunctional catalyst exhibited a high propane conversion of 74 % at early times on stream with 64 wt% of BTX at 500 °C.<sup>41</sup> The formation of aromatic compounds occurs via two steps: dehydrogenation of propane on Ga isolated sites in the mesopores, while the aromatization of the propylene intermediate on the acidic sites takes place in the micropores. Hence, further improvements can eventually be achieved by tuning the acidity of the meso-porous H-ZSM-5 using different Si/Al ratio. It is important to note that a highly active and stable site for propane dehydrogenation is needed to access high productivity in BTX. We propose to study the effect of the ratio Si/Al of meso ZSM-5 by using [Ga(*i*Bu)<sub>3</sub>] as a precursor on the activity and selectivity in propane aromatization.

The aim of the present work is to prepare a bifunctional Ga catalyst by immobilizing [Ga(*i*Bu)<sub>3</sub>] on meso H-ZSM-5-250 (Si/Al= 25, 40, 100, 200 and ∞). The resulting materials were evaluated in propane aromatization in order to select the most promising support. The catalysts were characterized by DRIFT, solid-state NMR, BET, XAFS and mass balance analysis.

## Experimental Section

**General procedures.** All experiments were carried out under a controlled atmosphere, using Schlenk and glovebox techniques for organometallic synthesis. For the synthesis and treatment of supported species, reactions were carried out using high-vacuum lines (ca. 1 mPa) and gloveboxes. Benzene and pentane were distilled from Na-benzophenone and NaK-benzophenone, respectively, and degassed using freeze-pump-thaw cycles. [Ga(*i*Bu)<sub>3</sub>] was synthesized according to a published method.<sup>42</sup>

### Preparation of Meso H-ZSM-5-250.

#### Synthesis of microporous zeolites supports

Samples were synthesized following procedures previously reported by Jacobs and Martens.<sup>43</sup> First fumed silica was combined with NaOH and water and stirred until homogenous (Solution 1). Then a premixed solution of tetrapropylammonium bromide and water (Solution 2) was added and the gel allowed to stir until homogenous. This step was followed by the addition of a premixed solution of sodium aluminate and water (Solution 3) to achieve the desired Si/Al gel ratio and the gel was stirred until homogeneous (Table E1). The gel was then transferred to an autoclave and crystallized at 150 °C for 3 days. The resulting solid was filtered and washed with water and dried at 50 °C overnight. The template was removed from the zeolite by calcination at 550 °C for 6 hours in air.

**Table E1.** Synthesis ratios and amounts

Target Si/Al ratio	Gel Si/Al ratio	Solution 1			Solution 2		Solution 3	
		Fumed Silica (g)	NaOH (g)	Water (mL)	TPABr (g)	Water (mL)	NaAlO <sub>2</sub> (g)	Water (mL)
25	18	66.60	9.60	192	15.00	468	5.04	84
40	36	66.60	9.60	192	15.00	468	2.52	42
100	74	66.60	9.60	192	15.00	468	1.260	21
200	144	66.60	9.60	192	15.00	468	0.63	10.5
∞	∞	66.60	9.60	192	15.00	468	0	60

### Desilication treatment

The calcined microporous ZSM-5 samples were placed in a preheated 0.1 M NaOH solution at 70 °C (20 mL of solutions per gram of zeolite). The slurry was then stirred at 70 °C after which the reaction was cooled with ice to prevent further desilication. The mixture was then centrifuged and washed with water three times and dried at 50 °C overnight.

### Ion exchange of supports

Mesoporous ZSM-5 samples were ion exchanged by adding 1 g of zeolite in 20 ml of 1 M ammonium nitrate aqueous solution and stirring the solution at 80 °C for 2 h. The samples

were centrifuged, the solution decanted and replaced with additional 1M ammonium nitrate aqueous solution. The process was repeated three times while the last ion exchange was carried out overnight. Afterwards, the solid was separated from the liquid by centrifugation, washed with water and dried in the oven for 12 h at 80 °C. The final solids were calcined at 550 °C for 6 h in air to achieve protonated ZSM-5.

Finally, the material was calcined by heating in air from room temperature to 500 °C at a heating rate of 2 °C/min, with a hold time of 16 h. The supports were further dehydroxylated at 250 °C (2 °C/min) for 16 h under high vacuum (1 mPa).

### **Preparation and characterization of Ga(*i*Bu)<sub>3</sub>/meso H-ZSM-5-250.**

A mixture of [Ga(*i*Bu)<sub>3</sub>] (200 mg, 0.80 mmol) and meso-H-ZSM-5-250 (1 g) in pentane (10 mL) was stirred at 25 °C for 4 h. After filtration, the solid was washed 4 times with pentane and the washing fractions were transferred to another reactor in order to quantify isobutane evolved during grafting. The resulting powder was dried under vacuum (1 mPa) at 70 °C.

### **Analytical and Spectroscopic Procedures.**

Elemental analyses were carried out at Mikroanalytisches Labor Pascher, Remagen (Germany). Gas-phase analyses were performed on a Hewlett-Packard 5890 series II gas chromatograph, equipped with a flame ionization detector and HP PLOT KCl/Al<sub>2</sub>O<sub>3</sub> column (50 m × 0.32 mm). Diffuse reflectance IR spectra were collected in an airtight IR cell equipped with CaF<sub>2</sub> window, using a Nicolet 6700 FT-IR spectrophotometer recording 64 scans at 4 cm<sup>-1</sup> resolutions. Nitrogen adsorption/desorption experiments were performed in Micrometrics ASAP 2020 instrument. X-ray diffraction patterns were recorded in a Bruker D8 diffractometer in Bragg-Bretano geometry, using monochromatic Cu Kα<sub>1</sub> radiation.

Solid-state NMR spectra were acquired on Bruker Avance 500 and Bruker Avance III 800 spectrometers (<sup>1</sup>H: 800.13 MHz;). For <sup>1</sup>H experiments, the spinning frequency was 20 kHz, the recycle delay was 30 s for meso-H-ZSM-5<sub>250</sub> and 10 s for Ga(*i*Bu)<sub>3</sub>/meso-H-ZSM-5<sub>250</sub>, and 16 scans were collected using a 90° pulse excitation of 2.25 μs. The <sup>13</sup>C CP-MAS NMR spectrum was obtained at 11.74 T using the CP-MAS pulse sequence and a high-power 1H decoupling at an RF field amplitude of 70 kHz. The spinning frequency was set to 10 kHz.

EXAFS spectra were measured at ESRF, using BM23 beam-line, at room temperature at the gallium K-edge (10.37 keV). A pair of Si(111) crystals was used as monochromator and a

system based on a total reflection through a double X-ray mirror with an incidence angle variable from 2 to 5 mrad allowed harmonic rejection close to  $10^{-5}$  level.<sup>44</sup> The spectra were recorded in the transmission mode between 10.1 and 11.4 keV. Four scans were collected for each sample. Each data set was collected simultaneously with a W metal foil ( $L_{III}$  edge at 10.207 keV) and was later aligned according to that reference. The Ga supported samples were packaged within an argon filled glovebox in a double air-tight sample holder equipped with kapton windows. The data analyses were carried out using the program “Athena”<sup>45</sup> and the EXAFS fitting program “RoundMidnight”, from the “MAX” package,<sup>46</sup> using spherical waves. The program FEFF8 was used to calculate theoretical files for the total central atom loss factor,  $r_c$ , the electron mean free path,  $\lambda$ , the phases,  $\phi_i$ ,  $\phi_c$  and amplitudes,  $F_i$ , based on model clusters of atoms.<sup>47</sup> The refinements were carried out by fitting the structural parameters  $N_i$ ,  $R_i$ ,  $\sigma_i$  and the energy shift,  $\Delta E_0$  (the same for all shells of a same structure was used):

$$\chi(k) \cong S_0^2 * r_c(k) * \sum_{i=1}^n \frac{N_i F_i(k, R_i)}{k R_i^2} * \exp\left(\frac{-2R_i}{\lambda(k)}\right) * \exp(-2\sigma_i^2 k^2) * \sin[2kR_i + \Phi_i(k, R_i) + \Phi_c(k)]$$

## Reactivity testing

The reactivity of the supported catalysts in propane dehydrogenation was evaluated in a stainless steel, continuous flow reactor. The catalysts (500 mg) were diluted in 2 g of SiC (Strem), affording a final catalyst bed mass of 2.5 g. Catalysts were loaded into the reactor inside a glovebox, and protected from the ambient atmosphere by a 4-way valve. Lines were purged extensively with the reaction gas prior to its introduction into the reactor. The catalyst bed was heated to 580 °C in flowing Ar (9.5 mL.min<sup>-1</sup>) before admitting 5 % of propane (99.95 % Air Liquide, < 20 ppm propene), thus affording a total flow of 10 mL.min<sup>-1</sup>, at  $P_{total} = 1$  bar. The feed gas was purified by passage through a column containing molecular sieves and activated Cu<sub>2</sub>O/Al<sub>2</sub>O<sub>3</sub>, and the flow rate controlled by a Brooks mass flow controller. Products were determined by online GC (HP 6890, equipped with 50 m KCl/Al<sub>2</sub>O<sub>3</sub> column and an FID). Conversion was calculated based on peak areas normalized by carbon number.

## Results and discussion

### Preparation and characterization of meso-H-ZSM-5 with Si/Al ratio (from 25 to $\infty$ )

Zeolites are well-defined crystalline, thermally stable, aluminosilicate materials with regular pores and channels, and a high specific surface area, ranging typically from 300 to 700 m<sup>2</sup>/g.<sup>48</sup>

These materials are widely used in the industry as heterogeneous catalysts for a wide range of processes, due to their strong acidity and uniform micropores (<2 nm in diameter).<sup>49,50</sup> However, their catalytic activity suffers from diffusional limitations in the presence of bulky reactants or products, resulting in pore blocking.<sup>51-53</sup> The creation of mesopores connected to the zeolite micropores is a promising solution to minimize and to overcome the diffusion limitation.<sup>14,54-56</sup> In this way, the micropores of the zeolite are effectively shortened while the formation of mesopores increases the external surface area of the zeolite, allowing the accessibility of the reactants to a larger number of pores. Several synthesis routes have been reported in the literature, such as post-treatment and template assembly for the preparation of hierarchically porous zeolites.<sup>57</sup> Jacobs and Martens reported a synthesis process to produce hierarchical zeolites (H-ZSM-5) by combining TPABr as template, fumed SiO<sub>2</sub> and different concentrations of NaAlO<sub>2</sub> followed by solid state crystallization. In order to establish the correlation between the acidity of the zeolites with the catalytic activity in propane aromatization in presence or absence of Ga, we synthesized a series of meso zeolites (meso H-ZSM-5) with different ratios (Si/Al = 25, 40, 100, 200, ∞). Using the procedure described by Jacobs and Martens for the preparation of micropores using different concentrations of NaAlO<sub>2</sub> and a post-synthesis (treatment by NaOH), the mesopores were created followed by ion exchange method (see experimental section). The zeolites (H-ZSM-5 and meso H-ZSM-5) have been characterized before and after post-synthesis by XRD, SEM, EDX and BET. The meso zeolites with different Si/Al obtained after calcination and dehydroxylation at 250 °C were characterized by DRIFT, solid state NMR and BET before grafting of gallium organometallic complex.

The change in crystalline structure of ZSM-5 before and after NaOH treatment was evaluated using Powder X-ray diffraction patterns (PXRD patterns) technique (Figure S1). The corresponding peaks for crystalline ZSM-5 are observed in both cases confirming the expected MFI framework. However, a slight difference between phases was observed when the Si/Al ratio increased and after post-treatment with NaOH. Similar results were also reported by Xue et al.<sup>58</sup> In addition to XRD, SEM images of the H-ZSM-5 crystals confirmed the formation of the expected coffin-like crystals typically seen for ZSM-5 (Figure 1). SEM images also showed that typical crystal sizes are within the required range of 1-5 μm. It was noted that with increasing aluminum content of the synthesized gel (Si/Al ratio lower than 50) a slight change in the morphology of the H-ZSM-5 was observed with the crystals becoming

less well defined and more polycrystalline in nature. The morphology of the crystals remained unchanged following the NaOH treatment of the microporous H-ZSM-5 to form the mesoporous supports (meso H-ZSM-5, Si/Al= 25, 40, 100, 200,  $\infty$ ) (Figure 2).



**Figure 1.** SEM images of the as-synthesized microporous ZSM-5 with Si/Al ratios of 25, 50, 100, 200 and infinite (from left to right).

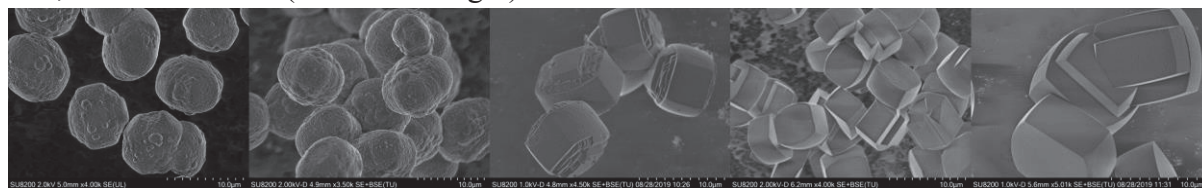


**Figure 2.** SEM images of the mesoporous ZSM-5 supports with Si/Al ratios of 25, 50, 100, 200 and infinite (from left to right).

Moreover, EDX analysis (Table S1) of these samples confirmed that the increase of Si/Al ratio of the samples was maintained in the Si/Al content of the synthesized H-ZSM-5 and remained relatively unchanged for meso H-ZSM-5 after the NaOH treatment. To gain more information about the porous property of the mesoporous ZSM-5, we performed  $N_2$  physisorption measurements. Figures S2 show the  $N_2$  adsorption/desorption isotherms of H-ZSM-5 and meso H-ZSM-5 with the different Si/Al ratio. In figures S2.a, H-ZSM-5 adsorption/desorption behavior is attributed to a type I isotherm, typical of a microporous zeolite, with the adsorption being slightly higher for those samples with higher Si/Al ratios. In comparison with Figure S2.b, the post-treatment of these samples with NaOH solution resulting in meso H-ZSM-5 exhibited a type IV behavior and greater adsorption capacity associated with the production of mesopores. It should be noted that as the Si/Al ratio of the parent ZSM-5 samples increased, treated samples (meso H-ZSM-5) were less mesoporous in character and showed decreased adsorption capacity (Table S1). This is likely due to the increasing crystallinity (with increasing Si content) of the samples making the crystals less susceptible to the desilication process. The pore volumes and surface areas of the meso H-ZSM-5 samples were also evaluated using  $N_2$  physisorption measurements (Table S1). The post treatment with NaOH of H-ZSM-5 led to an increase in the total pore volumes and

specifically in the mesopores volume. A slight increase in the BET surface area was observed (for Si/Al= 25 and 40), as calculated by BJH method. The above results confirmed that mesopores formation in the synthesized ZSM-5 samples depends on Si/Al ratios.

In order to control the structure of Ga surface species on the mesoporous zeolites, meso-H-ZSM-5 with different ratio (Si/Al= 25, 40, 100, 200 and  $\infty$ ) were obtained by dehydroxylation of the material at 250 °C under high vacuum (1 mPa), affording meso H-ZSM-5-<sub>250</sub>. The resulting materials were characterized by N<sub>2</sub> adsorption/desorption, DRIFT and <sup>1</sup>H MAS NMR and were tested in propane aromatization. Table 1 summarizes the results obtained on the meso zeolites using N<sub>2</sub> adsorption/desorption. A high specific surface area between 350 and 400 m<sup>2</sup>/g was obtained with large total pores volume in the range of 0.21 to 0.27 cm<sup>3</sup>/g. For example, Figure 3, Left displays the N<sub>2</sub> adsorption/desorption feature of meso H-ZSM-5-<sub>250</sub> with Si/Al= 40, revealing a BET surface of 381.6 m<sup>2</sup>/g with large pore volumes of 0.27 cm<sup>3</sup>/g. These results confirm the conservation of the zeolite properties (large BET surface and pore volumes) even after thermal treatment under vacuum. The highest total pores volume was obtained for meso-zeolites with the lowest Si/Al ratios (Si/Al= 25 and 40) and decreases with the increase of silicon proportion in the support. A similar result was obtained for the volume of mesopores, which was reduced when the Si/Al ratio increases from 25 to  $\infty$  along with the increase of the micropores volume.

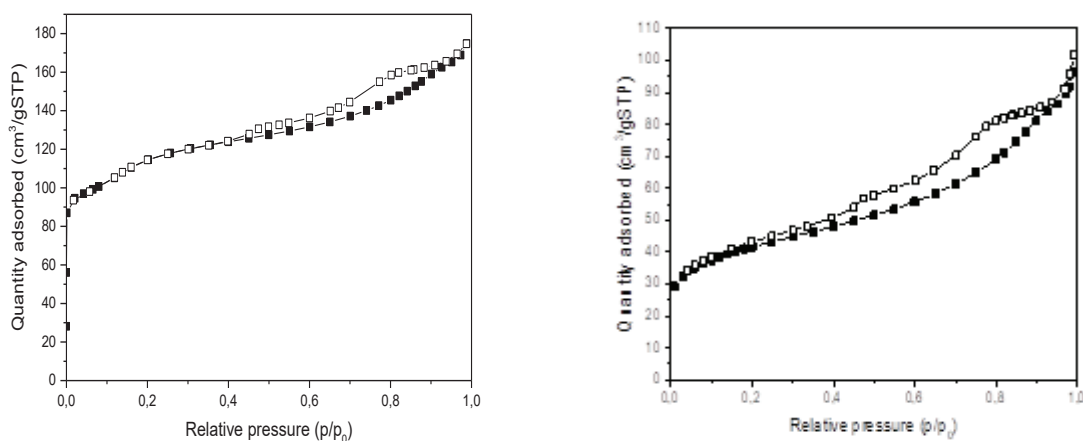


**Figure 3. Left:** N<sub>2</sub> adsorption (closed symbols) /desorption (open symbols) isotherms for meso-H-ZSM-5-<sub>250</sub> (Si/Al =40). **Right:** N<sub>2</sub> adsorption (closed symbols) /desorption (open symbols) isotherms for Ga(*i*Bu)<sub>3</sub>/meso-H-ZSM-5-<sub>250</sub> (Si/Al =40).

**Table 1.** Characterization of meso H-ZSM-5-250 by N<sub>2</sub> desorption. V<sub>micro</sub> is calculated from the t-plot method. V<sub>total</sub> is calculated from single-point adsorption at P/P<sub>0</sub> = 0.985  
 $V_{\text{meso}} = V_{\text{total}} - V_{\text{micro}}$

Samples	S <sub>BET</sub> <sup>a</sup> (m <sup>2</sup> .g <sup>-1</sup> ) 1)	S <sub>micro</sub> <sup>b</sup> (m <sup>2</sup> .g <sup>-1</sup> )	S <sub>ext</sub> <sup>c</sup> (m <sup>2</sup> .g <sup>-1</sup> )	V <sub>total</sub> <sup>e</sup> (cm <sup>3</sup> .g <sup>-1</sup> )	V <sub>micro</sub> <sup>f</sup> (cm <sup>3</sup> .g <sup>-1</sup> )	V <sub>meso</sub> <sup>g</sup> (cm <sup>3</sup> .g <sup>-1</sup> )
Si/Al= 25	386.7	307.6	126.1	0.27	0.10	0.17
Si/Al= 40	381.6	241.5	140.1	0.27	0.11	0.16
Si/Al= 100	402.2	277.4	143.8	0.23	0.11	0.12
Si/Al= 200	374.8	248.6	126.2	0.21	0.11	0.10
Si/Al= ∞	345.8	255.2	90.6	0.22	0.13	0.09

Further spectroscopic characterizations provided more detailed information on the neutral or Brønsted acidic sites present on the meso H-ZSM-5-250. The presence of both isolated silanols ( $\equiv\text{SiOH}$ ) and Brønsted acid sites ( $\equiv\text{Si}(\text{OH})\text{Al}$ ) was reflected by the characteristic bands in the DRIFT spectrum of meso H-ZSM-5-250 (Si/Al= 40) at 3743 and 3608 cm<sup>-1</sup>, respectively. The other weak and unresolved band centered at 3663 cm<sup>-1</sup> corresponded to AlOH species associated with extra-framework alumina (EFA), generated during desilication (Figure 4). For the comparison of all the meso H-ZSM-5-250 with different ratio, we observed that the vibration band at 3740 cm<sup>-1</sup> characteristics of isolated silanols and the band at 3608 cm<sup>-1</sup> attributed to the acidity decreased with increasing Si/Al. Consequently, the acidity of the support decreases when Si/Al ratio rises.<sup>59</sup> However, the large band centered at 3450 cm<sup>-1</sup> attributed to vicinal silanols increased when Si/Al ratio increased, in particular for Si/Al= 200 and ∞. These silanols were already observed in the case of SiO<sub>2</sub> dehydroxylated at low temperatures (200 °C) and have been reported to be unreactive with organometallic complexes.<sup>60,61</sup> Additionally, no band at 3608 cm<sup>-1</sup> attributed to Brønsted acidic protons was observed in the spectrum of meso H-ZSM-250 (Si/Al= ∞).

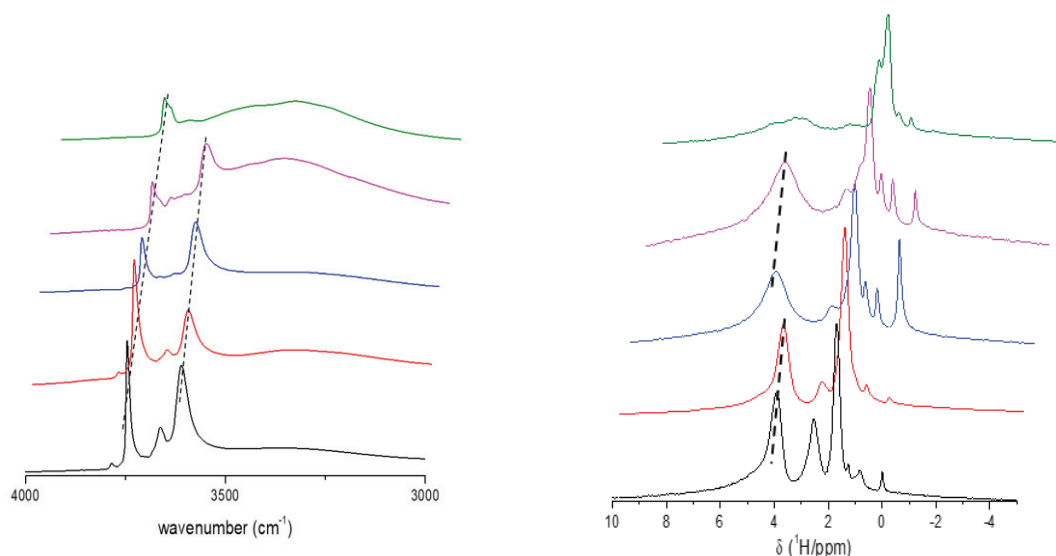


**Figure 4. Left:** DRIFT and **Right:** NMR  $^1\text{H}$  spectra of meso H-ZSM-5-250: Si/Al=25 (black), Si/Al= 40 (red), Si/Al= 100 (blue), Si/Al= 200 (magenta), Si/Al=  $\infty$  (olive) (18.8 T, 20 kHz,  $d_1=20$  s)

Accordingly, the characterization of these materials using high field solid-state NMR spectroscopy confirmed the previous result. The spectra obtained after dehydroxylation of meso H-ZSM-5 with different ratios in Figure 4, Right were in agreement with the large number of H-ZSM-5 spectra reported in literature, in which three main signals were distinguished.<sup>62–65</sup> The aromatization activity is reported to be located on the bridging acid site (BAS), indicated by a peak at around 4 ppm. It was observed that the intensity of this peak decreased as the Si/Al ratio increased from 25 to 40, due to the decreasing incorporation of Al into the framework and concomitant charge balance by the Brønsted proton. For example, the  $^1\text{H}$  NMR spectra of meso-H-ZSM-5-250 (Si/Al = 25 and 40) showed three major signals at 3.9, 2.5, and 1.6 ppm (Figure 4, black and red line). Those are attributed to Brønsted acidic protons ( $\equiv\text{Si}(\text{OH})\text{Al}$ -type),<sup>66</sup> extraframework alumina (EFA) hydroxyls,<sup>67</sup> and non-interacting silanol protons,<sup>66</sup> respectively. Minor signals at 4.7 and 0 ppm were assigned to another type of acid sites and aluminum hydroxyls ( $\text{Al}_{\text{IV}}$ ), respectively (Figure 4). In fact, the peak obtained at 3.9 ppm corresponds to a range of bridging hydroxyl groups attached to more than one aluminum ion and likely also to those between Si and Al atoms. Whereas the signal at 4.7 ppm could be attributed to bridging hydroxyl groups attached to a lower number of aluminums, resulting in a different acidity and hence in another chemical shift in  $^1\text{H}$  NMR. However, in the case of meso H-ZSM-5-250 (Si/Al= 100 and 200), the same signals were

obtained but with a shift of the peak from 3.9 to 4.7 ppm (Figure 4), which was assigned in the literature to another type of acid sites, where the hydroxyl groups were attached to one Al ion.<sup>68,69</sup> The <sup>1</sup>H NMR spectrum of meso H-ZSM-5-250 (Si/Al= ∞) featured two intense signals, namely a sharp, asymmetric contribution at 1.6 ppm for non-interacting silanols, accompanied with a peak at 2 ppm probably due to the presence of H-bonded vicinal silanol (Figure 4). These results confirmed that the meso zeolites with ratio of Si/Al from 25 to 200 show Brønsted acidity compared to non-acidic meso H-ZSM-5-250 (Si/Al= ∞). This is in agreement with the work reported by Shirazi et al. who demonstrated by using NH<sub>3</sub>-TPD profile that the total acidity of the meso zeolites decreases when Si/Al ratio increases.<sup>59</sup> This tendency was furthermore confirmed during the catalytic testing of these meso zeolites in propane aromatization.

### **Catalytic properties of meso H-ZSM-5-250 in propane aromatization**

In order to evaluate the catalytic activity of the zeolites as function of their acidity related to their Si/Al ratio, meso H-ZSM-5-250 (Si/Al= 25, 40, 100, 200 and ∞) supports were exposed to propane in a continuous flow reactor at T = 580 °C, P = 1 bar and with a total flow of 10 mL.min<sup>-1</sup> (5 % C<sub>3</sub> in Ar). The propane conversion obtained on the bare meso zeolites with several ratio of Si/Al as well as the average selectivity of light hydrocarbons and aromatics are depicted in Figure 5. Both meso H-ZSM-5-250 with lowest ratio of Si/Al = 25 and 40 exhibited an important C<sub>3</sub> conversion of 87 and 67%, respectively. The average selectivity in aromatics for meso H-ZSM-5-250 (Si/Al= 25 and 40) was significant in that case with 45 and 31 wt%, along with 55 and 69 wt% of light hydrocarbons, respectively. The formation of aromatics in large quantity confirmed that these supports were highly acidic and capable to convert propene intermediate into the targeted products, and hence justifying the low amount of propene observed in the gas phase during catalytic test (3.1 and 8 wt% for Si/Al = 25 and 40, respectively). The lighter compounds were produced from protolytic cracking, via a penta-coordinated carbonium ion transition state.<sup>70</sup> For Si/Al= 100 and 200, the C<sub>3</sub> conversion (38 and 28 %, respectively) and the selectivity toward aromatics (9 and 7 wt%) were lower compared to the previously described zeolites at lower Si/Al ratio, attributed to the low amount and the nature of Brønsted acid sites in the zeolite. It is important to note that the relative selectivity toward propene was higher compared to the previous zeolites, with 16.3 and 22.3 wt% for meso H-ZSM-5-250 (Si/Al= 100 and 200), respectively. The role of the acid sites in producing aromatics was confirmed when meso H-ZSM-5-250 with no Brønsted site (Si/Al= ∞) was tested in propane aromatization and produced only light products with

propene as a major component (59.1 wt%) at 2% conversion. All these results revealed that the meso H-ZSM-5-250 with low ratio (Si/Al= 25 and 40) were more selective and more acidic than the other meso H-ZSM-5-250 with higher ratio (Figure 5, Right).

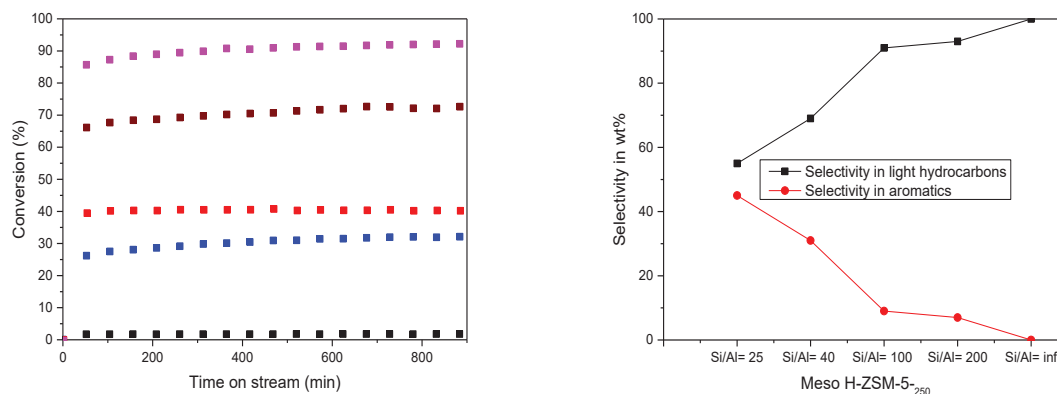


**Figure 5. Left:** propane conversion of meso H-ZSM-5-250: (Si/Al = 25) in magenta, (Si/Al = 40) in brown, (Si/Al = 100) in red, (Si/Al = 200) in blue and (Si/Al =  $\infty$ ) in black. **Right:** Average selectivity in wt% of meso H-ZSM-5-250 with different ratio Conditions: T = 580 °C, total flow = 10 mL.min<sup>-1</sup> (5 % C3 in Ar)

## Preparation and characterization of [Ga(*i*Bu)<sub>3</sub>] supported on meso H-ZSM-5-250

The grafting reaction of meso H-ZSM-5-250 with different ratio was carried out with an excess of [Ga(*i*Bu)<sub>3</sub>] in pentane at room temperature. The resulting materials were extensively washed with pentane. The washing fractions and the gas evolved were transferred to another reactor in order to quantify the isobutane released upon grafting by GC. The white powders were dried under vacuum (1 mPa) at room temperature for 3 h and characterized by DRIFT, solid-state NMR, EXAFS, BET and mass balance analysis.

The grafted supports were characterized by IR spectroscopy. For example, the DRIFT spectrum of catalyst Ga(*i*Bu)<sub>3</sub>/meso H-ZSM-5-250 (Si/Al = 40) (**B**) revealed significant consumption of isolated silanols, supported by the attenuation of the intensity of the band at 3743 cm<sup>-1</sup> (Figure 6, red line). The bands appearing at 2800–3000 cm<sup>-1</sup> are attributed to  $\nu$ (C–H) vibrations of alkyl moieties. The large and intense band centered at 3475 cm<sup>-1</sup> is due to Brønsted acidic protons in interactions with pentane causing a red shift.<sup>71</sup> Upon thermal treatment of the sample at 70 °C under high vacuum for 12h, the band at 3601 cm<sup>-1</sup> reappears confirming the resistance of such sites during the grafting. This result further

demonstrated that the grafting occurred selectively on the silanol groups located in the mesopores, while the Brønsted acidic sites in the micropores remained unreacted. Similar behaviors were also observed in the case of catalysts Ga(*i*Bu)<sub>3</sub>/meso H-ZSM-5-250 (Si/Al= 25) (A), Ga(*i*Bu)<sub>3</sub>/meso H-ZSM-5-250 (Si/Al= 100) (C), Ga(*i*Bu)<sub>3</sub>/meso H-ZSM-5-250 (Si/Al= 200) (D) and Ga(*i*Bu)<sub>3</sub>/meso H-ZSM-5-250 (Si/Al= ∞) (E) (Figure S3-6, respectively). Contrarily to (A) and (B), we observed in the spectra of (C), (D) and (E) a partial consumption of isolated silanol groups at 3743 cm<sup>-1</sup>.

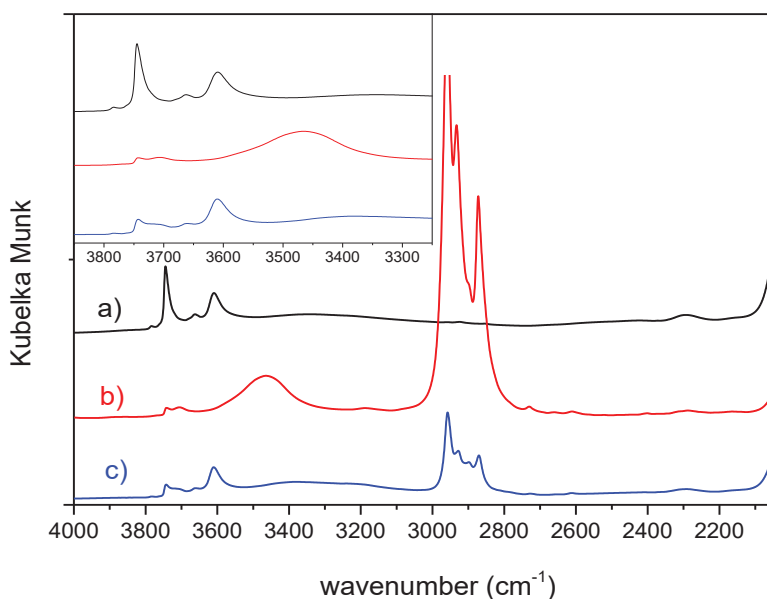


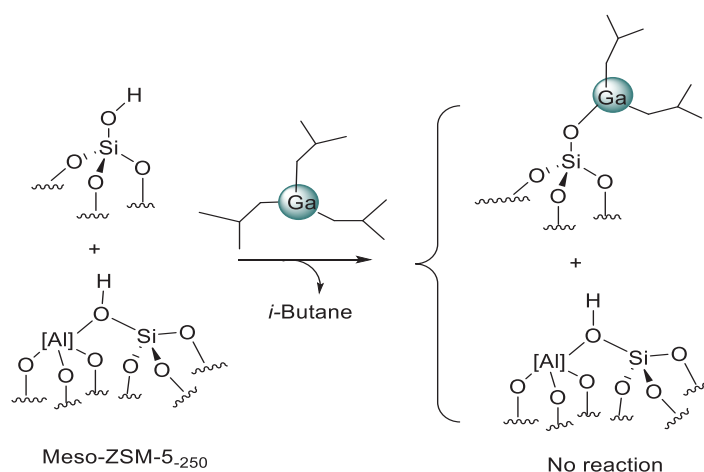
**Figure 6.** DRIFT spectra a) of meso H-ZSM-5-250 (Si/Al= 40) before (black), b) after reaction with [Ga(*i*Bu)<sub>3</sub>] in pentane at 25 °C (red) and Ga(*i*Bu)<sub>3</sub>/meso H-ZSM-5-250 (Si/Al= 40) after thermal treatment at 70 °C and high vacuum for 12 h

According to elemental analysis, the capability to graft gallium at room temperature varies on the different supports and depends strongly on the Si/Al ratio. When the latter increased from 25 to infinite, the grafted amount of Ga decreased from 1 to 0.08 wt% (Table 2). This is in accordance with the decrease in the volume of the mesopores when the Si/Al ratio increases, as shown in Table 1. The low Ga loading obtained on meso H-ZSM-5-250 (Si/Al= 100, 200 and ∞) can be explained by the blockage of the mesopores by the organometallic complex at the beginning of the grafting reaction, thus limiting the diffusion of the complex into the mesopores. These results are in agreement with the DRIFT spectra of (C), (D) and (E) that showed a partial consumption of silanols.

**Table 2.** Mass balance analysis of catalysts **(A)**, **(B)**, **(C)**, **(D)** and **(E)**

Samples	% <sub>wt</sub> Ga	% <sub>wt</sub> C	<sup>i</sup> -BuH/Ga
Ga( <i>i</i> Bu) <sub>3</sub> /meso H-ZSM-5-250 (Si/Al= 25) <b>(A)</b>	1	1.75	0.9
Ga( <i>i</i> Bu) <sub>3</sub> /meso H-ZSM-5-250 (Si/Al= 40) <b>(B)</b>	0.92	1.7	0.89
Ga( <i>i</i> Bu) <sub>3</sub> /meso H-ZSM-5-250 (Si/Al= 100) <b>(C)</b>	0.25	0.45	0.85
Ga( <i>i</i> Bu) <sub>3</sub> /meso H-ZSM-5-250 (Si/Al= 200) <b>(D)</b>	0.11	0.2	0.87
Ga( <i>i</i> Bu) <sub>3</sub> /meso H-ZSM-5-250 (Si/Al= ∞) <b>(E)</b>	0.08	n.d	0.82

The quantification of the gas evolved during grafting by GC analysis method displayed the release of 0.9 isobutane in the case of [Ga(*i*Bu)<sub>3</sub>] on meso H-ZSM-5-250 (Si/Al= 40) **(B)**. Additionally, elemental analysis of **(B)**, contains 0.92 wt% of Ga and 1.7 wt% of C. These results suggested that the surface gallium species was predominantly monopodal, bearing two isobutyl fragments, as reported in the case of [Ga(*i*Bu)<sub>3</sub>] on meso H-ZSM-5-250 (Si/Al= 20).<sup>41</sup> Same features were obtained for the other materials (Scheme 1), independently of the Si/Al ratio (see Table 2), suggesting the same surface species were formed.

**Scheme 1.** Grafting of [Ga(*i*Bu)<sub>3</sub>] onto meso H-ZSM-5-250 (Si/Al= 25, 40, 100, 200 and ∞)

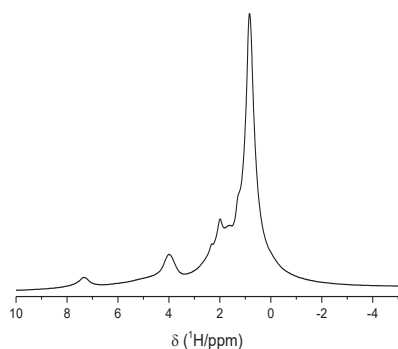
Additional information concerning the meso H-ZSM-5-250 after grafting were obtained via N<sub>2</sub> physisorption measurements. Catalysts **(A)** and **(B)** obtained on meso H-ZSM-5-250 with low Si/Al ratio (25 and 40) revealed an important decrease in the surface area as well as in the total pore volume (Table 3 and Figure 3). This decrease was previously seen while grafting organogallium compounds and was attributed to the pore blockage.<sup>37</sup> Consequently, it is expected that [Ga(*i*Bu)<sub>3</sub>] was grafted mainly in the mesopores and is unable to access the 10-membered ring system of the ZSM-5 bearing the Brønsted acid sites (in micropores). For the rest of the supports (Si/Al= 100, 200 and ∞), a slight decrease in the surface area and in the total volume pores was observed which is in agreement with the partial grafting of [Ga(*i*Bu)<sub>3</sub>] in the mesopores as revealed by elemental analysis and DRIFT spectra.

**Table 3.** Characterization of catalysts by N<sub>2</sub> desorption. V<sub>micro</sub> is calculated from t-plot method. V<sub>total</sub> is calculated from single-point adsorption at p/p<sub>0</sub>= 0.985  
 $V_{\text{meso}} = V_{\text{total}} - V_{\text{micro}}$

Samples	S <sub>BET</sub> <sup>a</sup> (m <sup>2</sup> .g <sup>-1</sup> ) 1)	S <sub>micro</sub> <sup>b</sup> (m <sup>2</sup> .g <sup>-1</sup> )	S <sub>ext</sub> <sup>c</sup> (m <sup>2</sup> .g <sup>-1</sup> )	V <sub>total</sub> <sup>e</sup> (cm <sup>3</sup> .g <sup>-1</sup> )	V <sub>micro</sub> <sup>f</sup> (cm <sup>3</sup> .g <sup>-1</sup> )	V <sub>meso</sub> <sup>g</sup> (cm <sup>3</sup> .g <sup>-1</sup> )
<b>(A)</b>	140.6	56.82	83.79	0.15	0.03	0.12
<b>(B)</b>	143.11	51.34	91.77	0.14	0.02	0.11
<b>(C)</b>	302.90	25.95	276.95	0.17	0.01	0.16
<b>(D)</b>	322.65	104.20	218.45	0.18	0.05	0.13
<b>(E)</b>	300.23	222.41	77.82	0.18	0.11	0.07

Complementary evidence on the grafting was obtained by using solid-state NMR technique. In the <sup>1</sup>H MAS NMR spectrum of Ga(*i*Bu)<sub>3</sub>/meso H-ZSM-5-250 (Si/Al= 40), several signals appeared at 0.88, 2 and 4 ppm corresponding to methyl groups of isobutyl fragments, to the Al-OH (EFA) and to the Brønsted acid sites, respectively (Figure 7). The <sup>13</sup>C CP MAS spectrum consisted in two signals at 25.6 and 30.9 ppm, attributed to CH<sub>3</sub> and CH from the isobutyl groups, respectively. These findings supported the results obtained with DRIFT spectroscopy, revealing that the grafting occurs selectively on the silanol groups in the mesopores leaving the Brønsted acid sites intact in the micropores. Similar behavior was observed in the NMR spectra for the rest of the catalysts **(A)**, **(C)**, **(D)** and **(E)** (Figure S7-10).

a)



b)

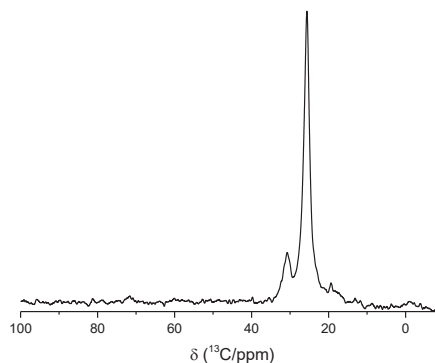


**Figure 7.** MAS NMR spectra of a)  $^1\text{H}$  (11.7 T, 10 kHz,  $d_1 = 5$  s) and b)  $^{13}\text{C}$  CP of  $\text{Ga}(i\text{Bu})_3/\text{meso H-ZSM-5-250}$  (Si/Al= 40) (11.7 T, 10 kHz,  $d_1 = 3$  s)

To conclude, DRIFT, solid-state NMR and mass balance analysis are in agreement with the formation of a monopodal species on the different meso H-ZSM-5-250 (Scheme 1).

The local structure of the catalyst  $\text{Ga}(i\text{Bu})_3/\text{meso H-ZSM-5-250}$  (Si/Al= 40) was investigated by X-ray absorption spectroscopy at the Ga K-edge. The Fourier-transformed magnitude and imaginary component of the EXAFS for  $[\text{Ga}(i\text{Bu})_3]$  grafted onto meso-H-ZSM-5-250 (Si/Al= 40) are shown in Figure 8. In this spectrum, we observed two principal maxima. A peak between 0.8 and 2.0 Å, corresponds to scattering from light (O, C) atoms in the first coordination sphere of Ga. In fact, Ga is bonded to 2 C atoms of the isobutyl ligands, as well as 1 O atom derived from the support, in agreement with the mass balance analysis (*vide supra*), in which monopodal species were proposed (Table 4). The fitted Ga-O (1.80 Å) and Ga-C (1.98 Å) bond distances are both slightly shorter than values previously reported by our laboratory for grafted  $[\text{Ga}(i\text{Bu})_3]$  on meso H-ZSM-5-250 (Si/Al= 20) (for  $\text{Ga}(\text{CH}_3)_3$  grafted on H-ZSM-5 (1.88 and 2.07 Å, respectively).<sup>41</sup> Indeed, the Ga-C distance reported for terminal Ga-C bonds in  $[\text{HGa}(i\text{-Pr})_2]_3$ , 2.004-2.129 Å, which is close to what we observed in the case of catalyst (**B**).<sup>72</sup> However, the Ga-O distance (1.80 Å) falls in the range expected for terminal Ga-OR bond lengths (1.79-1.89 Å).<sup>73,74</sup>

The other maxima in the FT magnitude between 2.2 and 3.0 Å is assigned to non-bonded atoms in the second coordination sphere of the Ga. The curvefit is compatible with the presence of 2 non-bonded C atoms at a distance of 3.0 Å, as Ga is surrounded by two iso-

butyl ligands, each bearing a secondary carbon. In addition, two other long paths: Ga-O (2.47 Å) and Ga-Si (3.25 Å), allow to obtain a good fit with experimental spectrum. In summary, all the above contributions from EXAFS are consistent with the presence of grafted monopodal species, [(≡SiO)Ga(*i*Bu)<sub>2</sub>].

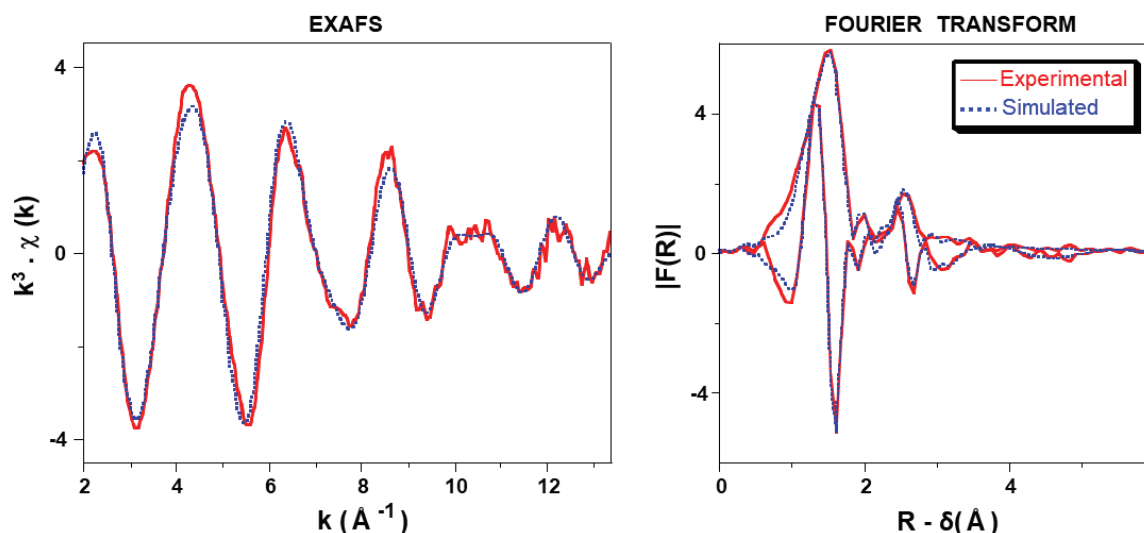


**Figure 8.** Ga K-edge  $k^3$ -weighted EXAFS (left) and Fourier transform (right, modulus and imaginary part; distances uncorrected from phase shifts) of Ga(*i*Bu)<sub>3</sub>/H-ZSM-5-250 (Si/Al=40). Solid lines: Experimental; Dashed lines: Fit (spherical wave theory).

**Table 4.** Parameters obtained from the fit of the EXAFS spectrum for Ga(*i*Bu)<sub>3</sub>/H-ZSM-5-250 (Si/Al=40).<sup>(a)</sup> The error interval generated by the fitting program “RoundMidnight” is indicated for each variable parameter between parentheses.

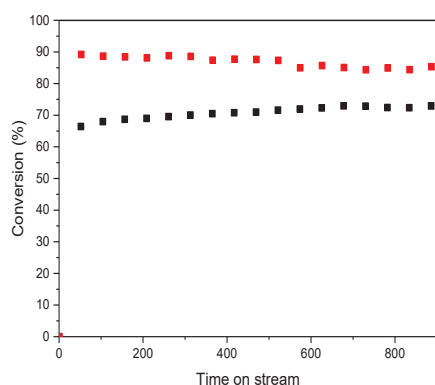
Path <sup>a</sup>	$N^b$	$R$ (Å)	$10^3 \sigma^2$ (Å <sup>2</sup> )
<i>Ga-O</i>	1	1.807(12)	0.0042(16)
<i>Ga-C1</i>	2	1.98 (2)	0.0025(10)
<i>Ga-O&lt;</i>	1	2.47(7)	0.017(8)
<i>Ga-C2</i>	2	3.00(2)	0.0036(18)
<i>Ga-Si</i>	1	3.25(10)	0.057(75)

(a)  $\Delta k$ : [2.0 - 13.4 Å<sup>-1</sup>] -  $\Delta R$ : [0.4 - 3.9 Å];  $S_0^2 = 0.96$ ;  $\Delta E_0 = 7.0 \pm 0.7$  eV (the same for all shells); Fit residue:  $\rho = 3.4$  %; Quality factor:  $(\Delta\chi)^2/\nu = 2.57$  ( $\nu = 15/26$ ).

## Catalytic activity of [Ga(*i*Bu)<sub>3</sub>] catalysts on meso H-ZSM-5-250

In order to evaluate the effect of the Si/Al ratio in propane aromatization, the resulting grafted materials were tested in the same conditions as the bare zeolitic support. Ga(*i*Bu)<sub>3</sub>/meso H-ZSM-5-250 (Si/Al= 40) revealed a higher conversion (88% vs 67%) than the bare meso zeolite (Si/Al= 40) at early times on stream (Figure 9, a). At 900 min, the products consisted in 36.6 wt% of benzene, 26.1 wt% of toluene, 13 wt% of methane, 10.5 wt% of ethene, 7 wt% of ethane and 5.7 wt% of propene, along with traces of C4 (Figure S12). It is important to note that the selectivity toward aromatics remains constant over the time on stream. The low amount of propene indicates the capacity of this catalyst, more specifically of the Brønsted acid sites located in the micropores of the zeolite, to catalyze oligomerization and aromatization of the olefins intermediates.<sup>27</sup> Moreover, the presence of Ga in the zeolite resulted in an increase toward the selectivity of aromatics to 64 wt% along with 36 wt% of light hydrocarbons. Figure 9, b highlights the importance of Ga in the mesopores of the zeolite. The presence of Ga led to a considerable difference in the product distribution. The essential features were reduction of the cracking products observed earlier in the bare zeolite and promotion of aromatization reactions. The average selectivity of aromatics doubled (64 wt%) when gallium was grafted on the meso zeolite (Si/Al= 40) compared to 32 wt% of aromatics for the bare support. These results confirm the formation of a stable and highly selective bifunctional catalyst for propane aromatization where Ga is mainly responsible for propane dehydrogenation reaction while Brønsted acid sites located in the micropores drive the aromatization of primary product, propylene.

a)



b)

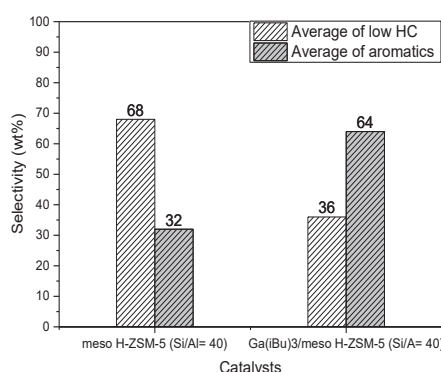
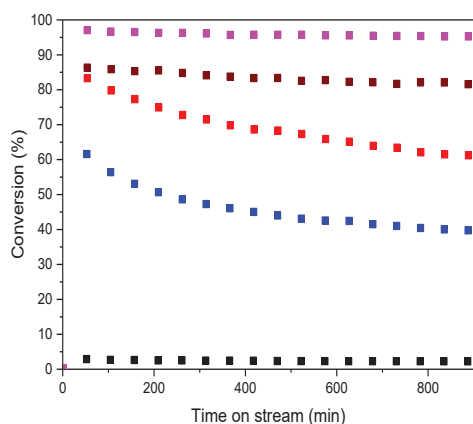


**Figure 9.** a) Propane conversion of meso H-ZSM-5-250 (Si/Al= 40) in black symbols, and Ga(*i*Bu)<sub>3</sub>/meso H-ZSM-5-250 (Si/Al= 40) in red symbols; b) Comparison between the

selectivity (wt%) of meso H-ZSM-5-250 (Si/Al = 40) and Ga(*i*Bu)<sub>3</sub>/meso H-ZSM-5-250 (Si/Al = 40); Conditions: T= 580 °C, total flow= 10 mL.min<sup>-1</sup> (5 % C3 in Ar)

The catalytic performance of all the catalysts is summarized in Figure 10 and the selectivities are shown in Figure S11-S15. Catalyst **(A)** revealed also a high conversion of 97 % with an important selectivity toward aromatics of 66 wt% along with 34 wt% of light hydrocarbons. The lowest amount of propene was observed with the most acidic catalyst **(A)** and **(B)** with lowest ratio of Si/Al (25 and 40), exhibiting only 2.2 and 5.3 wt% (Figure 10, b). Catalysts **(C)** and **(D)** prepared on higher ratio of Si/Al (100 and 200) showed a quick deactivation and a lower amount of BTX compounds produced (Figure 10), due to the low acidity of the used supports. Consequently, the amount of propene produced in these catalysts increased (10 wt% for **(C)** and 16.2 wt% for **(D)**), compared to catalysts **(A)** and **(B)**. The deactivation was more pronounced with the increase of silica amount in the support. Hence, Ga(*i*Bu)<sub>3</sub>/meso H-ZSM-5-250 (Si/Al = ∞) possessed a very low conversion of 2.5 % and the major product was propene (71.8 wt%) along with methane (11.4 wt%) and ethene (16.8 wt%). The absence of aromatics in this case was due to the total absence of Brønsted acid sites in this support as shown by DRIFT and <sup>1</sup>H MAS NMR. In conclusion, the selectivity in aromatics is related to the Si/Al ratio of the [Ga(*i*Bu)<sub>3</sub>] on meso H-ZSM-5-250, that decreases when Si/Al ratio increases. This observation was also reported earlier for GaOx supported on microporous H-ZSM-5 prepared by incipient wetness impregnation.<sup>27</sup>

a)



b)

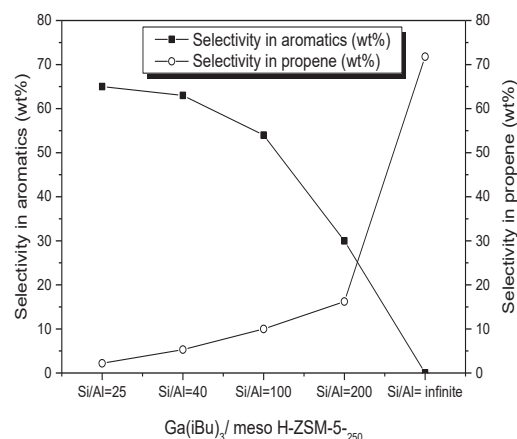


**Figure 10.** a) propane conversion of [Ga(*i*Bu)<sub>3</sub>] on meso H-ZSM-5-250: (Si/Al=25) in magenta, (Si/Al=40) in brown, (Si/Al= 100) in red, (Si/Al= 200) in blue and (Si/Al= ∞) in

black. b) Selectivity in wt% of aromatics of Ga(*i*Bu)<sub>3</sub>/meso H-ZSM-5-250  
Conditions: T= 580 °C, total flow= 10 mL.min<sup>-1</sup> (5 % of C3 in Ar)

On meso H-ZSM-5-250 (Si/Al= 40), we observed a high selectivity of aromatics accompanied with the formation of light hydrocarbons. These findings showed that several reactions like cracking, dehydrogenation, aromatization and hydrogenolysis occurred simultaneously during propane aromatization. These reactions are expected to be somewhat tuned by thermodynamic parameters such as the reaction temperature. Choudhary et al. demonstrated that the selectivity and distribution of the aromatic products were highly affected by the operating temperature.<sup>75,76</sup> Therefore, supplementary efforts were made to investigate the influence of temperature and propane concentration with respect to the product selectivity and distribution of aromatics during propane aromatization over Ga(*i*Bu)<sub>3</sub>/meso H-ZSM-5-250 (Si/Al= 40). Based on the data obtained at 580 °C, we studied the propane aromatization on catalyst **(B)** at 500 and 540 °C in the same conditions (total flow of 10 mL.min<sup>-1</sup> (5 % of C3 in Ar)). Decreasing the temperature to 500 °C led to the lowest conversion (Figure 11, black curve) and selectivity toward aromatics among the three temperatures. Propane conversion decreased to 38% but seemed to be more stable over the time compared to the conversion at 580 °C, while the selectivity toward aromatics decreased slightly from 64 wt% to 56.7 wt%. At 540 °C, the C3 conversion was about 57% (Figure 11, blue curve) with high stability as function of time on stream and high selectivity toward aromatics with 62 wt%. The variation of the temperature from 500 to 580 °C showed that the best compromise between activity and selectivity to aromatics (high activity (88 %) and selectivity toward BTX (64 wt%)) was obtained at 580 °C. Therefore, this temperature was selected to investigate the influence of the gas composition on the conversion and selectivity of Ga(*i*Bu)<sub>3</sub>/meso H-ZSM-5-250 (Si/Al= 40) in propane aromatization.

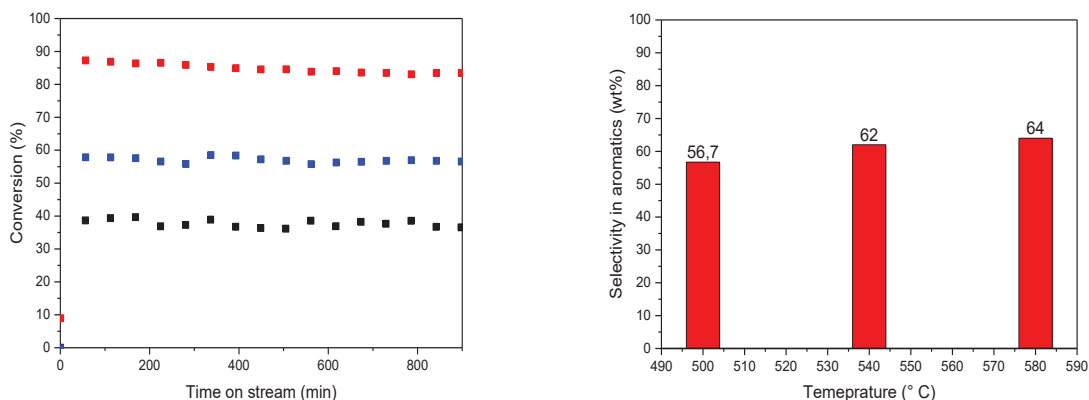
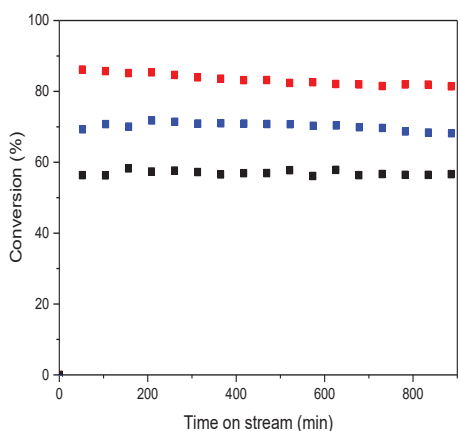


**Figure 11.** Propane conversion and selectivity in aromatics (in wt%) of Ga(*i*Bu)<sub>3</sub>/meso H-ZSM-5-250 (Si/Al= 40); Conditions: black curve at T = 500 °C, blue curve at T = 540 °C and red curve at T = 580 °C with a total flow= 10 mL.min<sup>-1</sup> (5 % of C3 in Ar)

When propane concentration in the feed was increased from 5 to 10%, the conversion decreased from 88% to around 72% (Figure 12). The selectivity toward aromatics decreased as well from 64 wt% to 58 wt%. Increasing the propane concentration to 20% in Ar, the conversion reached its lowest (58%) and the selectivity toward aromatics decreased to 51.4 wt%.

To sum up, optimizing thermodynamic and kinetic parameters such as temperature and propane concentration in the feed shows that the most promising results were obtained at 580 °C with 5 % of propane in the feed.

a)



b)

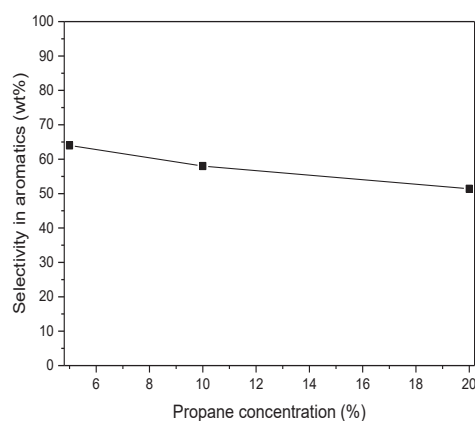


**Figure 12.** a) Propane conversion and b) selectivity in aromatics (in wt%) of Ga(*i*Bu)<sub>3</sub>/meso H-ZSM-5-<sub>250</sub> (Si/Al= 40); Conditions: red curve at 5 % of C3, blue curve at 10 % of C3 and black curve at 20 % of C3 in total flow of 10 mL.min<sup>-1</sup> at  $\theta = 580$  °C

## Conclusion

The main objective of this work is to investigate the effect of the Brønsted acidity over gallium immobilized H-ZSM-5 for propane aromatization and to determine the most promising reaction conditions. The first stage involves preparation of a series of H-ZSM-5 with different Si/Al ratio (Si/Al = 25, 40, 100, 200 and  $\infty$ ) followed by desilication to create the meso-pores. The Si/Al ratio was tuned by the control addition desired amount of NaAlO<sub>2</sub> on fumed silica. These materials were characterized by XRD, N<sub>2</sub> adsorption/desorption and EDX and served as support for gallium immobilization. Prior to grafting of the gallium precursor on the support, these materials were dehydroxylated at 250 °C and characterized by DRIFT, solid-state <sup>1</sup>H MAS NMR and N<sub>2</sub> adsorption/desorption. The grafting of [Ga(*i*Bu)<sub>3</sub>] occurred on silanol of these meso H-ZSM-5-<sub>250</sub> (with Si/Al= 25, 40, 100, 200 and  $\infty$ ) and led to a monopodal gallium species [(≡SiO)Ga(*i*Bu)<sub>2</sub>], evidenced by DRIFT, high field solid-state NMR (<sup>1</sup>H and <sup>13</sup>C), N<sub>2</sub> adsorption/desorption, EXAFS as well as mass balance analysis. Importantly, the immobilization of Ga occurred selectively on the silanol groups located in the mesopores. Thus, a bifunctional catalyst including Ga sites for dehydrogenation and Brønsted acid sites for aromatization was obtained and tested in propane aromatization. The gallium functionalized materials exhibited higher activity and selectivity compared to the bare zeolites support. This result confirmed the role of Ga and its high capacity of dehydrogenating propane into propene. The effect of Si/Al ratio on the catalytic performance of the catalyst as well as the distribution in the reaction products were evaluated. At low Si/Al ratio of meso H-ZSM-5-<sub>250</sub> (25 and 40), a very high activity and selectivity toward the aromatics was obtained compared to Ga(*i*Bu)<sub>3</sub>/meso H-ZSM-5-<sub>250</sub> (Si/Al= 100 and 200). Simultaneously, the lack of acidity in high ratios of Si/Al led to low formation of aromatics compounds. On non-acidic meso H-ZSM-5-<sub>250</sub> (Si/Al=  $\infty$ ), aromatic compounds were absent, and a very low activity was obtained. Operating at lower temperature results in a considerably lower conversion and selectivity toward aromatics. The variation of the gas composition in the feed affected the activity and the formation of products; the most promising results were obtained at lower concentration of propane in the feed. Supplementary studies and characterization techniques are required to further investigate the Ga species under the operating conditions.

## Acknowledgments

This work was carried out as a part of BIZEOLCAT project, which has received funding from the European Union's Horizon 2020 research and innovation program under grant agreement No. 814671. In particular, J. A. is grateful for her PhD grant. AdM thanks Olivier Mathon and Kiril Lomachenko for their help during the recording of the X-ray absorption spectra at ESRF, on beam line BM23

## References

- (1) Chen, Z.; Rodriguez, E.; Agrawal, R. Toward Carbon Neutrality for Natural Gas Liquids Valorization from Shale Gas. *Ind. Eng. Chem. Res.* **2022**, *61* (12), 4469–4474. <https://doi.org/10.1021/acs.iecr.1c04913>.
- (2) Hajimirzaee, S.; Soleimani Mehr, A.; Kianfar, E. Modified ZSM-5 Zeolite for Conversion of LPG to Aromatics. *Polycycl. Aromat. Compd.* **2020**, *0* (0), 1–14. <https://doi.org/10.1080/10406638.2020.1833048>.
- (3) Li, N.; Jiao, F.; Pan, X.; Chen, Y.; Feng, J.; Li, G.; Bao, X. High-Quality Gasoline Directly from Syngas by Dual Metal Oxide–Zeolite (OX-ZEO) Catalysis. *Angew. Chem.* **2019**, *131* (22), 7478–7482. <https://doi.org/10.1002/ange.201902990>.
- (4) Wang, K.; Dong, M.; Li, J.; Liu, P.; Zhang, K.; Wang, J.; Fan, W. Facile Fabrication of ZSM-5 Zeolite Hollow Spheres for Catalytic Conversion of Methanol to Aromatics. *Catal. Sci. Technol.* **2017**, *7* (3), 560–564. <https://doi.org/10.1039/C6CY02476A>.
- (5) Zhang, P.; Tan, L.; Yang, G.; Tsubaki, N. One-Pass Selective Conversion of Syngas to Para -Xylene. *Chem. Sci.* **2017**, *8* (12), 7941–7946. <https://doi.org/10.1039/C7SC03427J>.
- (6) Wei, Z.; Chen, L.; Cao, Q.; Wen, Z.; Zhou, Z.; Xu, Y.; Zhu, X. Steamed Zn/ZSM-5 Catalysts for Improved Methanol Aromatization with High Stability. *Fuel Process. Technol.* **2017**, *162*, 66–77. <https://doi.org/10.1016/j.fuproc.2017.03.026>.
- (7) Zhang, J.; Zhang, M.; Chen, S.; Wang, X.; Zhou, Z.; Wu, Y.; Zhang, T.; Yang, G.; Han, Y.; Tan, Y. Hydrogenation of CO<sub>2</sub> into Aromatics over a ZnCrO<sub>x</sub>–Zeolite Composite Catalyst. *Chem. Commun.* **2019**, *55* (7), 973–976. <https://doi.org/10.1039/C8CC09019J>.
- (8) Zhou, W.; Zhou, C.; Yin, H.; Shi, J.; Zhang, G.; Zheng, X.; Min, X.; Zhang, Z.; Cheng, K.; Kang, J.; Zhang, Q.; Wang, Y. Direct Conversion of Syngas into Aromatics over a Bifunctional Catalyst: Inhibiting Net CO<sub>2</sub> Release. *Chem. Commun.* **2020**, *56* (39), 5239–5242. <https://doi.org/10.1039/D0CC00608D>.
- (9) Bhan, A.; Nicholas Delgass, W. Propane Aromatization over HZSM-5 and Ga/HZSM-5 Catalysts. *Catal. Rev.* **2008**, *50* (1), 19–151. <https://doi.org/10.1080/01614940701804745>.
- (10) J. Spivey, J.; Hutchings, G. Catalytic Aromatization of Methane. *Chem. Soc. Rev.* **2014**, *43* (3), 792–803. <https://doi.org/10.1039/C3CS60259A>.
- (11) Schulz, P.; Baerns, M. Aromatization of Ethane over Gallium-Promoted H-ZSM-5 Catalysts. *Appl. Catal.* **1991**, *78* (1), 15–29. [https://doi.org/10.1016/0166-9834\(91\)80086-C](https://doi.org/10.1016/0166-9834(91)80086-C).
- (12) Price, G. L.; Kanazirev, V.; Dooley, K. M.; Hart, V. I. On the Mechanism of Propane Dehydrocyclization over Cation-Containing, Proton-Poor MFI Zeolite. *J. Catal.* **1998**, *173* (1), 17–27. <https://doi.org/10.1006/jcat.1997.1891>.

- (13) Raad, M.; Astafan, A.; Hamieh, S.; Toufaily, J.; Hamieh, T.; Comparot, J. D.; Canaff, C.; Daou, T. J.; Patarin, J.; Pinard, L. Catalytic Properties of Ga-Containing MFI-Type Zeolite in Cyclohexane Dehydrogenation and Propane Aromatization. *J. Catal.* **2018**, *365*, 376–390. <https://doi.org/10.1016/j.jcat.2018.06.029>.
- (14) Raad, M.; Hamieh, S.; Toufaily, J.; Hamieh, T.; Pinard, L. Propane Aromatization on Hierarchical Ga/HZSM-5 Catalysts. *J. Catal.* **2018**, *366*, 223–236. <https://doi.org/10.1016/j.jcat.2018.07.035>.
- (15) Caeiro, G.; Carvalho, R. H.; Wang, X.; Lemos, M. A. N. D. A.; Lemos, F.; Guisnet, M.; Ramôa Ribeiro, F. Activation of C2–C4 Alkanes over Acid and Bifunctional Zeolite Catalysts. *J. Mol. Catal. Chem.* **2006**, *255* (1), 131–158. <https://doi.org/10.1016/j.molcata.2006.03.068>.
- (16) Guisnet, M.; Gnep, N. S.; Vasques, H.; Ribeiro, F. R. Zn-Doped HZSM-5 Catalysts for Propane Aromatization. In *Studies in Surface Science and Catalysis*; Jacobs, P. A., Jaeger, N. I., Kubelková, L., Wichterlov', B., Eds.; Zeolite Chemistry and Catalysis; Elsevier, 1991; Vol. 69, pp 321–329. [https://doi.org/10.1016/S0167-2991\(08\)61584-0](https://doi.org/10.1016/S0167-2991(08)61584-0).
- (17) Rodrigues, V. de O.; Faro Júnior, A. C. On Catalyst Activation and Reaction Mechanisms in Propane Aromatization on Ga/HZSM-5 Catalysts. *Appl. Catal. Gen.* **2012**, *435–436*, 68–77. <https://doi.org/10.1016/j.apcata.2012.05.036>.
- (18) Zhou, W.; Liu, J.; Wang, J.; Lin, L.; Zhang, X.; He, N.; Liu, C.; Guo, H. Enhancing Propane Aromatization Performance of Zn/H-ZSM-5 Zeolite Catalyst with Pt Promotion: Effect of the Third Metal Additive-Sn. *Catal. Lett.* **2019**, *149* (8), 2064–2077. <https://doi.org/10.1007/s10562-019-02832-5>.
- (19) Meriaudeau, P.; Sapaly, G.; Naccache, C. Dual Function Mechanism of Alkane Aromatization over H-HZSM-5 Supported Ga, Zn, Pt Catalysts: Respective Role of Acidity and Additive. In *Studies in Surface Science and Catalysis*; Inui, T., Namba, S., Tatsumi, T., Eds.; Chemistry of Microporous Crystals; Elsevier, 1991; Vol. 60, pp 267–279. [https://doi.org/10.1016/S0167-2991\(08\)61904-7](https://doi.org/10.1016/S0167-2991(08)61904-7).
- (20) Samanta, A.; Bai, X.; Robinson, B.; Chen, H.; Hu, J. Conversion of Light Alkane to Value-Added Chemicals over ZSM-5/Metal Promoted Catalysts. *Ind. Eng. Chem. Res.* **2017**, *56* (39), 11006–11012. <https://doi.org/10.1021/acs.iecr.7b02095>.
- (21) Aromatization of Short Chain Alkanes on Zeolite Catalysts. *Appl. Catal. Gen.* **1992**, *89* (1), 1–30. [https://doi.org/10.1016/0926-860X\(92\)80075-N](https://doi.org/10.1016/0926-860X(92)80075-N).
- (22) Joshi, Y. V.; Thomson, K. T. The Roles of Gallium Hydride and Brønsted Acidity in Light Alkane Dehydrogenation Mechanisms Using Ga-Exchanged HZSM-5 Catalysts: A DFT Pathway Analysis. *Catal. Today* **2005**, *105* (1), 106–121. <https://doi.org/10.1016/j.cattod.2005.04.017>.
- (23) Xiao, H.; Zhang, J.; Wang, X.; Zhang, Q.; Xie, H.; Han, Y.; Tan, Y. A Highly Efficient Ga/ZSM-5 Catalyst Prepared by Formic Acid Impregnation and in Situ Treatment for Propane Aromatization. *Catal. Sci. Technol.* **2015**, *5* (8), 4081–4090. <https://doi.org/10.1039/C5CY00665A>.
- (24) Krishnamurthy, G.; Bhan, A.; Delgass, W. N. Identity and Chemical Function of Gallium Species Inferred from Microkinetic Modeling Studies of Propane Aromatization over Ga/HZSM-5 Catalysts. *J. Catal.* **2010**, *271* (2), 370–385. <https://doi.org/10.1016/j.jcat.2010.02.026>.
- (25) R, L. V. M.; J, Y.; R, C. Gallium Containing Hybrid Catalysts for the Aromatization of N-Butane. *Appl. Catal. Gen.* **1992**, *86* (2), 127–138.
- (26) Dooley, K. M.; Chang, C.; Price, G. L. Effects of Pretreatments on State of Gallium and Aromatization Activity of Gallium/ZSM-5 Catalysts. *Appl. Catal. Gen.* **1992**, *84* (1), 17–30. [https://doi.org/10.1016/0926-860X\(92\)80336-B](https://doi.org/10.1016/0926-860X(92)80336-B).

- (27) Choudhary, V. R.; Mantri, K.; Sivadinarayana, C. Influence of Zeolite Factors Affecting Zeolitic Acidity on the Propane Aromatization Activity and Selectivity of Ga/H-ZSM-5. *Microporous Mesoporous Mater.* **2000**, *37* (1), 1–8. [https://doi.org/10.1016/S1387-1811\(99\)00185-7](https://doi.org/10.1016/S1387-1811(99)00185-7).
- (28) Price, G. L.; Kanazirev, V. Ga<sub>2</sub>O<sub>3</sub>/HZSM-5 Propane Aromatization Catalysts: Formation of Active Centers via Solid-State Reaction. *J. Catal.* **1990**, *126* (1), 267–278. [https://doi.org/10.1016/0021-9517\(90\)90065-R](https://doi.org/10.1016/0021-9517(90)90065-R).
- (29) Kwak, B. S.; Sachtler, W. M. H. Effect of Ga/Proton Balance in Ga/HZSM-5 Catalysts on C<sub>3</sub> Conversion to Aromatics. *J. Catal.* **1994**, *145* (2), 456–463. <https://doi.org/10.1006/jcat.1994.1056>.
- (30) Meitzner, G. D.; Iglesia, E.; Baumgartner, J. E.; Huang, E. S. The Chemical State of Gallium in Working Alkane Dehydrocyclodimerization Catalysts. In Situ Gallium K-Edge X-Ray Absorption Spectroscopy. *J. Catal.* **1993**, *140* (1), 209–225. <https://doi.org/10.1006/jcat.1993.1079>.
- (31) El-Malki, E.-M.; van Santen, R. A.; Sachtler, W. M. H. Introduction of Zn, Ga, and Fe into HZSM-5 Cavities by Sublimation: Identification of Acid Sites. *J. Phys. Chem. B* **1999**, *103* (22), 4611–4622. <https://doi.org/10.1021/jp990116l>.
- (32) Mériaudeau, P.; Naccache, C. Gallium Based MFI Zeolites for the Aromatization of Propane. *Catal. Today* **1996**, *31* (3), 265–273. [https://doi.org/10.1016/S0920-5861\(96\)00017-X](https://doi.org/10.1016/S0920-5861(96)00017-X).
- (33) Tshabalala, T. E.; Scurrrell, M. S. Aromatization of N-Hexane over Ga, Mo and Zn Modified H-ZSM-5 Zeolite Catalysts. *Catal. Commun.* **2015**, *72*, 49–52. <https://doi.org/10.1016/j.catcom.2015.06.022>.
- (34) Xin, M.; Xing, E.; Gao, X.; Wang, Y.; Ouyang, Y.; Xu, G.; Luo, Y.; Shu, X. Ga Substitution during Modification of ZSM-5 and Its Influences on Catalytic Aromatization Performance. *Ind. Eng. Chem. Res.* **2019**, *58* (17), 6970–6981. <https://doi.org/10.1021/acs.iecr.9b00295>.
- (35) Rodrigues, V. de O.; Eon, J.-G.; Faro, A. C. Correlations between Dispersion, Acidity, Reducibility, and Propane Aromatization Activity of Gallium Species Supported on HZSM5 Zeolites. *J. Phys. Chem. C* **2010**, *114* (10), 4557–4567. <https://doi.org/10.1021/jp910642p>.
- (36) Gao, P.; Xu, J.; Qi, G.; Wang, C.; Wang, Q.; Zhao, Y.; Zhang, Y.; Feng, N.; Zhao, X.; Li, J.; Deng, F. A Mechanistic Study of Methanol-to-Aromatics Reaction over Ga-Modified ZSM-5 Zeolites: Understanding the Dehydrogenation Process. *ACS Catal.* **2018**, *8* (10), 9809–9820. <https://doi.org/10.1021/acscatal.8b03076>.
- (37) Kazansky, V. B.; Subbotina, I. R.; van Santen, R. A.; Hensen, E. J. M. DRIFTS Study of the Nature and Chemical Reactivity of Gallium Ions in Ga/ZSM-5: II. Oxidation of Reduced Ga Species in ZSM-5 by Nitrous Oxide or Water. *J. Catal.* **2005**, *233* (2), 351–358. <https://doi.org/10.1016/j.jcat.2005.05.004>.
- (38) Hensen, E. J. M.; García-Sánchez, M.; Rane, N.; Magusin, P. C. M. M.; Liu, P.-H.; Chao, K.-J.; van Santen, R. A. In Situ Ga K Edge XANES Study of the Activation of Ga/ZSM-5 Prepared by Chemical Vapor Deposition of Trimethylgallium. *Catal. Lett.* **2005**, *101* (1–2), 79–85. <https://doi.org/10.1007/s10562-004-3753-x>.
- (39) Fleischman, S. D.; Scott, S. L. Evidence for the Pairwise Disposition of Grafting Sites on Highly Dehydroxylated Silicas via Their Reactions with Ga(CH<sub>3</sub>)<sub>3</sub>. *J. Am. Chem. Soc.* **2011**, *133* (13), 4847–4855. <https://doi.org/10.1021/ja108905p>.
- (40) Taha, Z. A.; Deguns, E. W.; Chattopadhyay, S.; Scott, S. L. Formation of Digallium Sites in the Reaction of Trimethylgallium with Silica. *Organometallics* **2006**, *25* (8), 1891–1899. <https://doi.org/10.1021/om051034o>.

- (41) Szeto, K. C.; Gallo, A.; Hernández-Morejudo, S.; Olsbye, U.; De Mallmann, A.; Lefebvre, F.; Gauvin, R. M.; Delevoye, L.; Scott, S. L.; Taoufik, M. Selective Grafting of Ga(i-Bu)<sub>3</sub> on the Silanols of Mesoporous H-ZSM-5 by Surface Organometallic Chemistry. *J. Phys. Chem. C* **2015**, *119* (47), 26611–26619. <https://doi.org/10.1021/acs.jpcc.5b09289>.
- (42) Kovar, R. A.; Derr, Henry.; Brandau, Duane.; Callaway, J. O. Preparation of Organogallium Compounds from Organolithium Reagents and Gallium Chloride. Infrared, Magnetic Resonance, and Mass Spectral Studies of Alkylgallium Compounds. *Inorg. Chem.* **1975**, *14* (11), 2809–2814. <https://doi.org/10.1021/ic50153a042>.
- (43) Chapter I: Synthesis of ZSM-5 Zeolites in the Presence of Tetrapropylammonium Ions. In *Studies in Surface Science and Catalysis*; Jacobs, P. A., Martens, J. A., Eds.; Synthesis of High-Silica Aluminosilicate Zeolites; Elsevier, 1987; Vol. 33, pp 47–111. [https://doi.org/10.1016/S0167-2991\(09\)60467-5](https://doi.org/10.1016/S0167-2991(09)60467-5).
- (44) Mathon, O.; Beteva, A.; Borrel, J.; Bugnazet, D.; Gatla, S.; Hino, R.; Kantor, I.; Mairs, T.; Munoz, M.; Pasternak, S.; Perrin, F.; Pascarelli, S. The Time-Resolved and Extreme Conditions XAS (TEXAS) Facility at the European Synchrotron Radiation Facility: The General-Purpose EXAFS Bending-Magnet Beamline BM23. *J. Synchrotron Radiat.* **2015**, *22*, 1548–1554. <https://doi.org/10.1107/S1600577515017786>.
- (45) Ravel, B.; Newville, M. ATHENA, ARTEMIS, HEPHAESTUS: Data Analysis for X-Ray Absorption Spectroscopy Using IFEFFIT. *J. Synchrotron Radiat.* **2005**, *12* (4), 537–541. <https://doi.org/10.1107/S0909049505012719>.
- (46) Alain, M.; Jacques, M.; Diane, M.-B.; Karine, P. MAX: Multiplatform Applications for XAFS. *J. Phys. Conf. Ser.* **2009**, *190*, 012034. <https://doi.org/10.1088/1742-6596/190/1/012034>.
- (47) Ankudinov, A. L.; Ravel, B.; Rehr, J. J.; Conradson, S. D. Real-Space Multiple-Scattering Calculation and Interpretation of x-Ray-Absorption near-Edge Structure. *Phys. Rev. B* **1998**, *58* (12), 7565–7576. <https://doi.org/10.1103/PhysRevB.58.7565>.
- (48) Auerbach, S. M.; Carrado, K. A.; Dutta, P. K. *Handbook of Zeolite Science and Technology*; CRC Press, 2003.
- (49) Davis, M. E. Ordered Porous Materials for Emerging Applications. *Nature* **2002**, *417* (6891), 813–821. <https://doi.org/10.1038/nature00785>.
- (50) Corma, A. State of the Art and Future Challenges of Zeolites as Catalysts. *J. Catal.* **2003**, *216* (1), 298–312. [https://doi.org/10.1016/S0021-9517\(02\)00132-X](https://doi.org/10.1016/S0021-9517(02)00132-X).
- (51) He, T.; Wang, Y.; Miao, P.; Li, J.; Wu, J.; Fang, Y. Hydrogenation of Naphthalene over Noble Metal Supported on Mesoporous Zeolite in the Absence and Presence of Sulfur. *Fuel* **2013**, *106*, 365–371. <https://doi.org/10.1016/j.fuel.2012.12.025>.
- (52) Wang, Y.; He, T.; Liu, K.; Wu, J.; Fang, Y. From Biomass to Advanced Bio-Fuel by Catalytic Pyrolysis/Hydro-Processing: Hydrodeoxygenation of Bio-Oil Derived from Biomass Catalytic Pyrolysis. *Bioresour. Technol.* **2012**, *108*, 280–284. <https://doi.org/10.1016/j.biortech.2011.12.132>.
- (53) Wang, Y.; Fang, Y.; He, T.; Hu, H.; Wu, J. Hydrodeoxygenation of Dibenzofuran over Noble Metal Supported on Mesoporous Zeolite. *Catal. Commun.* **2011**, *12* (13), 1201–1205. <https://doi.org/10.1016/j.catcom.2011.04.010>.
- (54) van Donk, S.; Janssen, A. H.; Bitter, J. H.; de Jong, K. P. Generation, Characterization, and Impact of Mesopores in Zeolite Catalysts. *Catal. Rev.* **2003**, *45* (2), 297–319. <https://doi.org/10.1081/CR-120023908>.
- (55) Tsai, T.-C.; Liu, S.-B.; Wang, I. Disproportionation and Transalkylation of Alkylbenzenes over Zeolite Catalysts. *Appl. Catal. Gen.* **1999**, *181* (2), 355–398. [https://doi.org/10.1016/S0926-860X\(98\)00396-2](https://doi.org/10.1016/S0926-860X(98)00396-2).

- (56) Song, C. Shape-Selective Isopropylation of Naphthalene over H-Mordenite Catalysts for Environmentally Friendly Synthesis of 2,6-Dialkyl-naphthalene. *Comptes Rendus Académie Sci. - Ser. IIC - Chem.* **2000**, 3 (6), 477–496. [https://doi.org/10.1016/S1387-1609\(00\)01164-6](https://doi.org/10.1016/S1387-1609(00)01164-6).
- (57) Ji, Y.; Yang, H.; Yan, W. Strategies to Enhance the Catalytic Performance of ZSM-5 Zeolite in Hydrocarbon Cracking: A Review. *Catalysts* **2017**, 7 (12), 367. <https://doi.org/10.3390/catal7120367>.
- (58) Xue, L.; Cheng, K.; Zhang, H.; Deng, W.; Zhang, Q.; Wang, Y. Mesoporous H-ZSM-5 as an Efficient Catalyst for Conversions of Cellulose and Cellobiose into Methyl Glucosides in Methanol. *Catal. Today* **2016**, 274, 60–66. <https://doi.org/10.1016/j.cattod.2016.01.055>.
- (59) Shirazi, L.; Jamshidi, E.; Ghasemi, M. R. The Effect of Si/Al Ratio of ZSM-5 Zeolite on Its Morphology, Acidity and Crystal Size. *Cryst. Res. Technol.* **2008**, 43 (12), 1300–1306. <https://doi.org/10.1002/crat.200800149>.
- (60) Bouhoute, Y.; Grekov, D.; Szeto, K. C.; Merle, N.; De Mallmann, A.; Lefebvre, F.; Raffa, G.; Del Rosal, I.; Maron, L.; Gauvin, R. M.; Delevoye, L.; Taoufik, M. Accessing Realistic Models for the WO<sub>3</sub>-SiO<sub>2</sub> Industrial Catalyst through the Design of Organometallic Precursors. *ACS Catal.* **2016**, 6 (1), 1–18. <https://doi.org/10.1021/acscatal.5b01744>.
- (61) Riollet, V.; Taoufik, M.; Basset, J.-M.; Lefebvre, F. Reactivity of Silica-Supported Zirconium Neopentyl Fragments with Trimethylphosphine and Acetone: Formation of Unexpected Reaction Products. *J. Organomet. Chem.* **2007**, 692 (19), 4193–4195. <https://doi.org/10.1016/j.jorganchem.2007.06.038>.
- (62) Harris, K. D. M.; Xu, M.; Thomas, J. M. Probing the Evolution of Water Clusters during Hydration of the Solid Acid Catalyst H-ZSM-5. *Philos. Mag.* **2009**, 89 (33), 3001–3012. <https://doi.org/10.1080/14786430903164606>.
- (63) Brunner, E.; Ernst, H.; Freude, D.; Hunger, M.; Krause, C. B.; Prager, D.; Reschetilowski, W.; Schwieger, W.; Bergk, K.-H. Solid-State n.m.r. and Catalytic Studies of Mildly Hydrothermally Dealuminated HZSM-5. *Zeolites* **1989**, 9 (4), 282–286. [https://doi.org/10.1016/0144-2449\(89\)90072-9](https://doi.org/10.1016/0144-2449(89)90072-9).
- (64) Huo, H.; Peng, L.; Grey, C. P. Low Temperature <sup>1</sup>H MAS NMR Spectroscopy Studies of Proton Motion in Zeolite HZSM-5. *J. Phys. Chem. C* **2009**, 113 (19), 8211–8219. <https://doi.org/10.1021/jp900313y>.
- (65) Chen, K.; Abdolrhamani, M.; Sheets, E.; Freeman, J.; Ward, G.; White, J. L. Direct Detection of Multiple Acidic Proton Sites in Zeolite HZSM-5. *J. Am. Chem. Soc.* **2017**, 139 (51), 18698–18704. <https://doi.org/10.1021/jacs.7b10940>.
- (66) Deng, F.; Yue, Y.; Ye, C. <sup>1</sup>H/<sup>27</sup>Al TRAPDOR NMR Studies on Aluminum Species in Dealuminated Zeolites. *Solid State Nucl. Magn. Reson.* **1998**, 10 (3), 151–160. [https://doi.org/10.1016/S0926-2040\(97\)00028-3](https://doi.org/10.1016/S0926-2040(97)00028-3).
- (67) Beck, L. W.; Haw, J. F. Multinuclear NMR Studies Reveal a Complex Acid Function for Zeolite Beta. *J. Phys. Chem.* **1995**, 99 (4), 1076–1079.
- (68) HUNGER, M. Brønsted Acid Sites in Zeolites Characterized by Multinuclear Solid-State NMR Spectroscopy. *Catal. Rev.* **1997**, 39 (4), 345–393. <https://doi.org/10.1080/01614949708007100>.
- (69) Hensen, E. J. M.; Poduval, D. G.; Degirmenci, V.; Ligthart, D. A. J. M.; Chen, W.; Maugé, F.; Rigutto, M. S.; Veen, J. A. R. van. Acidity Characterization of Amorphous Silica-Alumina. *J. Phys. Chem. C* **2012**, 116 (40), 21416–21429. <https://doi.org/10.1021/jp309182f>.

- (70) Lercher, J. A.; van Santen, R. A.; Vinek, H. Carbonium Ion Formation in Zeolite Catalysis. *Catal. Lett.* **1994**, *27* (1), 91–96. <https://doi.org/10.1007/BF00806981>.
- (71) Piccini, G.; Alessio, M.; Sauer, J.; Zhi, Y.; Liu, Y.; Kolvenbach, R.; Jentys, A.; Lercher, J. A. Accurate Adsorption Thermodynamics of Small Alkanes in Zeolites. Ab Initio Theory and Experiment for H-Chabazite. *J. Phys. Chem. C* **2015**, *119* (11), 6128–6137. <https://doi.org/10.1021/acs.jpcc.5b01739>.
- (72) Uhl, W.; Cuypers, L.; Geiseler, G.; Harms, K.; Massa, W. Synthesen und Kristallstrukturen von Dialkylgalliumhydriden — dimere versus trimere Formeleinheiten. *Z. Für Anorg. Allg. Chem.* **2002**, *628* (5), 1001–1006. [https://doi.org/10.1002/1521-3749\(200206\)628:5<1001::AID-ZAAC1001>3.0.CO;2-N](https://doi.org/10.1002/1521-3749(200206)628:5<1001::AID-ZAAC1001>3.0.CO;2-N).
- (73) Duchateau, R.; Dijkstra, T. W.; van Santen, R. A.; Yap, G. P. A. Silsesquioxane Models for Silica Surface Silanol Sites with Adjacent Siloxide Functionalites and Olefin Polymerization Catalysts Thereof. *Chem. – Eur. J.* **2004**, *10* (16), 3979–3990. <https://doi.org/10.1002/chem.200400206>.
- (74) Basharat, S.; Betchley, W.; Carmalt, C. J.; Barnett, S.; Tocher, D. A.; Davies, H. O. Synthesis of Group 13 Sesquialkoxides and Their Application as Precursors to Crystalline Oxide Films. *Organometallics* **2007**, *26* (2), 403–407. <https://doi.org/10.1021/om0608657>.
- (75) Choudhary, V. R.; Devadas, P. Product Selectivity and Aromatics Distribution in Aromatization of Propane over H-GaMFI Zeolite: Influence of Temperature. *Microporous Mesoporous Mater.* **1998**, *23* (3), 231–238. [https://doi.org/10.1016/S1387-1811\(98\)00112-7](https://doi.org/10.1016/S1387-1811(98)00112-7).
- (76) Choudhary, T. V.; Kinage, A. K.; Banerjee, S.; Choudhary, V. R. Effect of Temperature on the Product Selectivity and Aromatics Distribution in Aromatization of Propane over H-GaAlMFI Zeolite. *Microporous Mesoporous Mater.* **2004**, *70* (1), 37–42. <https://doi.org/10.1016/j.micromeso.2004.01.010>.

## Supporting information

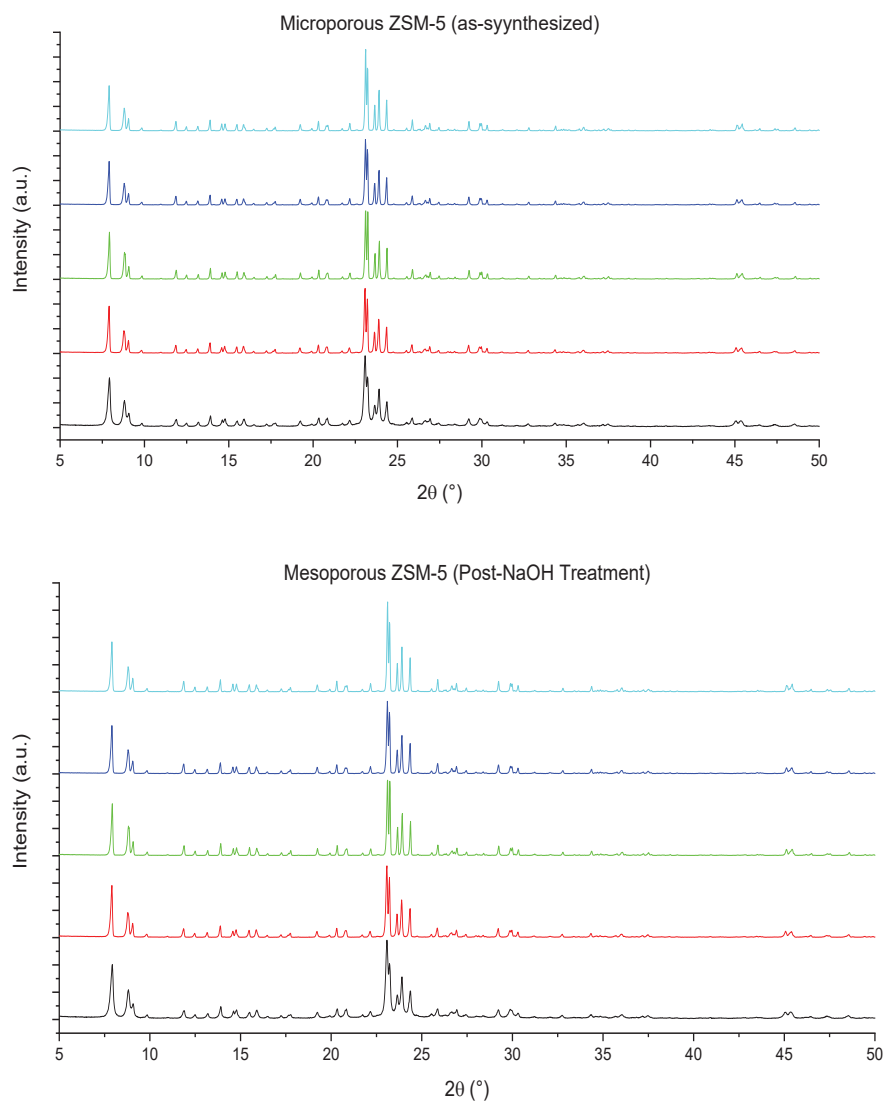


**Figure S1.** PXRD patterns of as-synthesized microporous ZSM-5 (left) and mesoporous ZSM-5 supports (right) in increasing Si/Al ratios of 25 (black), 50 (red), 100 (green) 200 (blue) infinite (cyan).

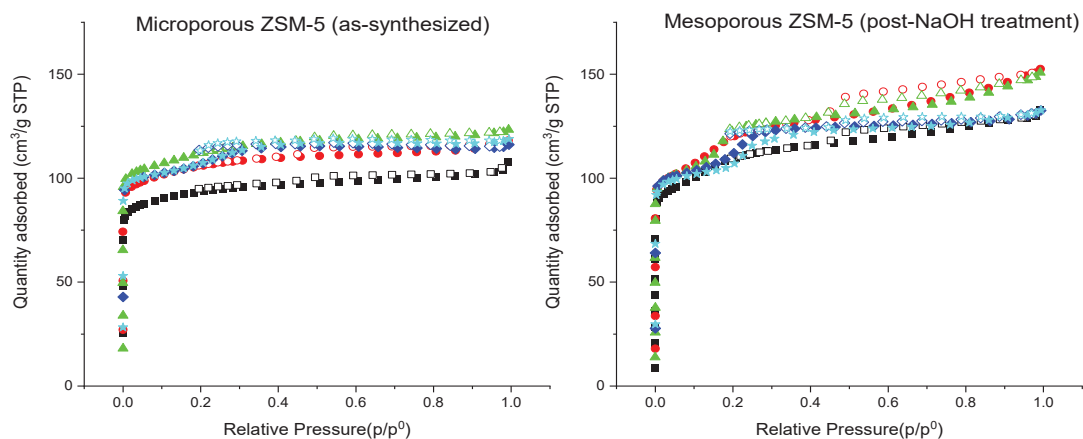


**Figure S2.** Adsorption/desorption (filled and unfilled symbols respectively) profiles of the as-synthesized microporous ZSM-5 (left) and mesoporous supports (right) with increasing Si/Al ratios of 25 (black), 50 (red), 100 (green) 200 (blue) infinite (cyan).

**Table S1.** BET and EDX characterization of the synthesized and post treated zeolites

Sample Name	BET surface area (m <sup>2</sup> /g)	Total pore volume (cm <sup>3</sup> /g)	Mesopore volume (cm <sup>3</sup> /g)	Micropore volume (cm <sup>3</sup> /g)	Si/Al ratio (by EDX)
As-Synthesized ZSM-5					
Si/Al=25	362.54	0.166	0.033	0.160	21.8-25.5
Si/Al=40	407.72	0.182	0.032	0.182	49.1-54.0
Si/Al=100	433.23	0.190	0.034	0.194	98.4-102.7
Si/Al=200	414.85	0.179	0.033	0.193	190-199
Si/Al=∞	419.17	0.183	0.039	0.195	>400
Post-NaOH treatment					
Si/Al=25	395.86	0.205	0.062	0.188	22.9-23.9
Si/Al=40	420.70	0.236	0.088	0.204	48.4-52.4
Si/Al=100	419.48	0.233	0.092	0.200	97.0-103.9
Si/Al=200	392.83	0.205	0.065	0.203	188-196
Si/Al=∞	413.02	0.205	0.071	0.195	>400

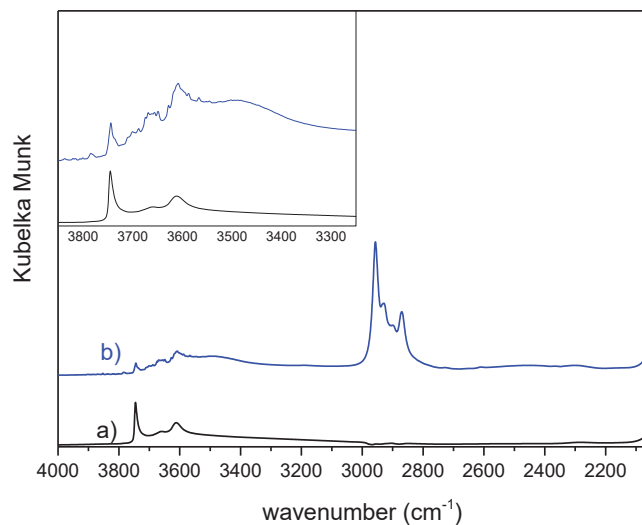


**Figure S3.** DRIFT spectra of a) meso H-ZSM-5-250 (Si/Al= 25) before (black) and b) after reaction with  $[Ga(iBu)_3]$  in pentane at 25 °C (blue) after thermal treatment at 70 °C and high vacuum for 12 h

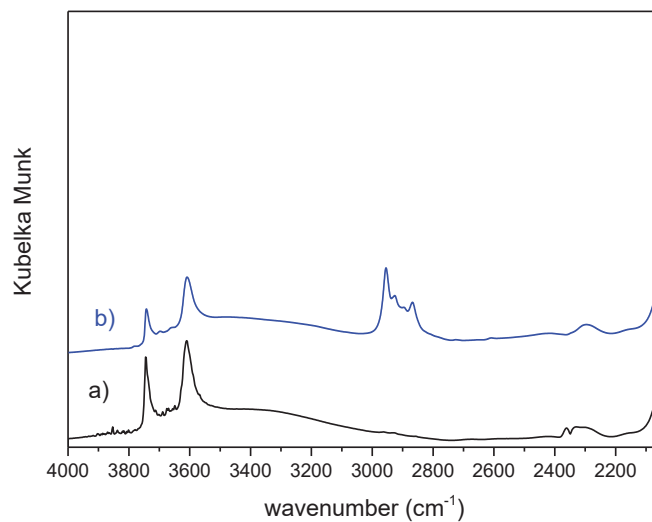


**Figure S4.** DRIFT spectra of a) meso H-ZSM-5-250 (Si/Al= 100) before (black) and b) after reaction with  $[Ga(iBu)_3]$  in pentane at 25 °C (blue) after thermal treatment at 70 °C and high vacuum for 12 h

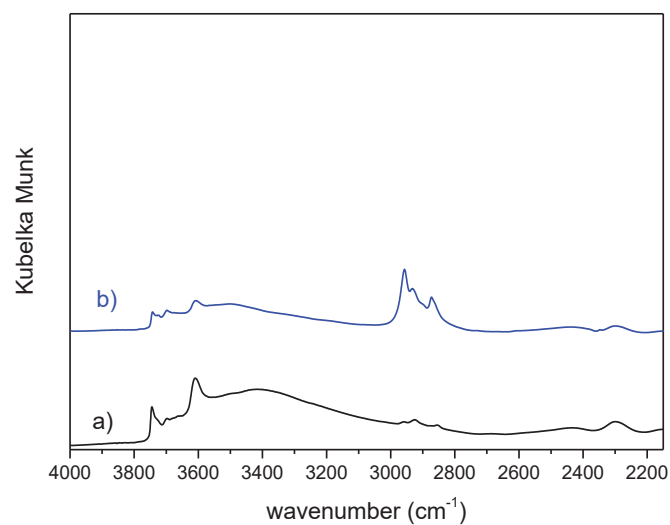


**Figure S5.** DRIFT spectra of a) meso H-ZSM-5-250 (Si/Al= 200) before (black) and b) after reaction with [Ga(*i*Bu)<sub>3</sub>] in pentane at 25 °C (blue) after thermal treatment at 70 °C and high vacuum for 12 h

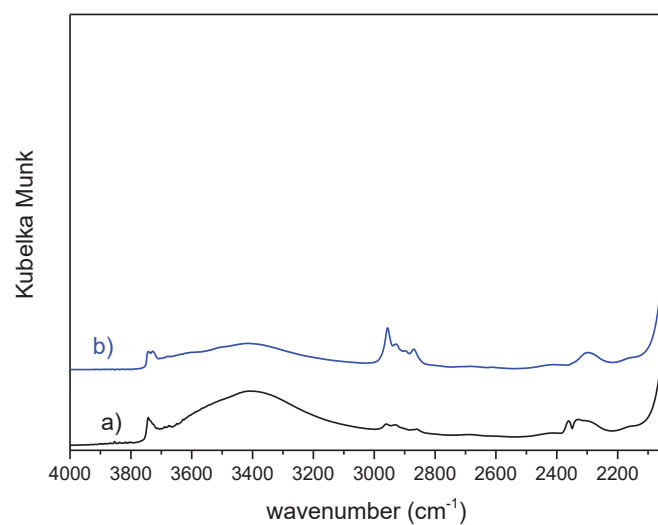
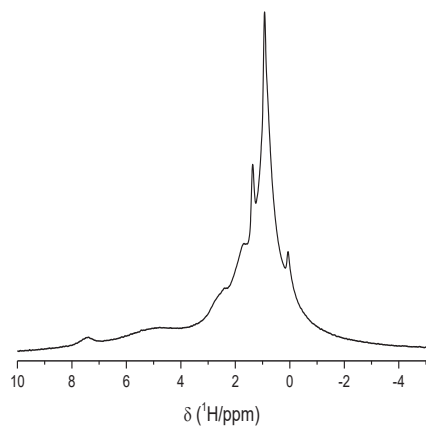


**Figure S6.** DRIFT spectra of a) meso H-ZSM-5-250 (Si/Al= ∞) before (black) and b) after reaction with [Ga(*i*Bu)<sub>3</sub>] in pentane at 25 °C (blue) after thermal treatment at 70 °C and high vacuum for 12 h

a)



b)

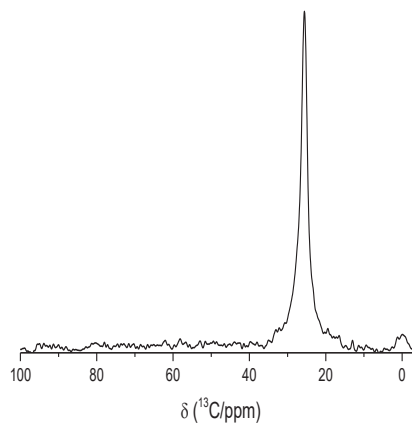
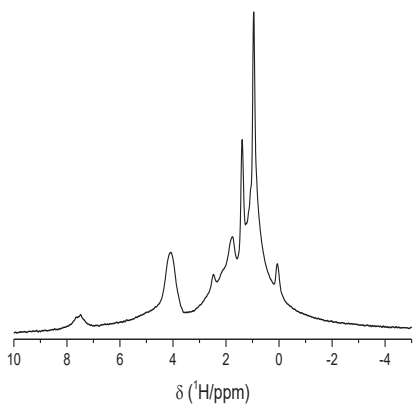


**Figure S7.** Nuclear Magnetic resonance spectra of Ga(*i*Bu)<sub>3</sub>/meso H-ZSM-5-250 (Si/Al=25): a) <sup>1</sup>H MAS NMR (11.7 T, 10 kHz, d<sub>1</sub> = 5 s) and b) <sup>13</sup>C CP MAS NMR (11.7 T, 10 kHz, d<sub>1</sub> = 3 s)

a)



b)

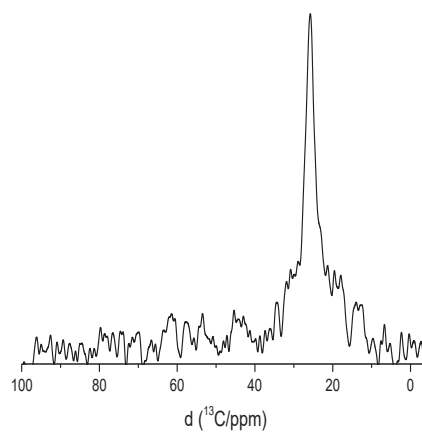
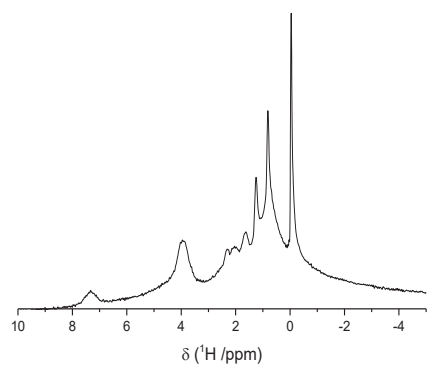


**Figure S8.** Nuclear Magnetic resonance spectra of Ga(*i*Bu)<sub>3</sub>/meso H-ZSM-5-250 (Si/Al=100): a) <sup>1</sup>H MAS NMR (11.7 T, 10 kHz, d<sub>1</sub> = 20 s) and b) <sup>13</sup>C CP MAS NMR (11.7 T, 10 kHz, d<sub>1</sub> = 5 s)

a)



b)

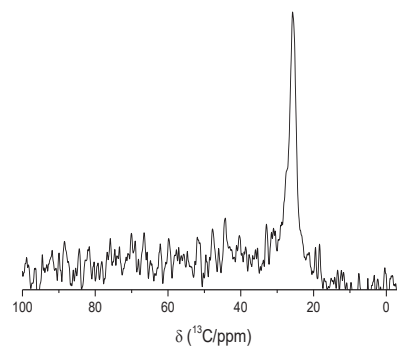
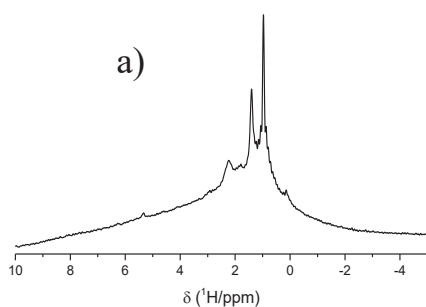


**Figure S9.** Nuclear Magnetic resonance spectra of  $\text{Ga}(i\text{Bu})_3/\text{meso H-ZSM-5-250}$  ( $\text{Si}/\text{Al}=200$ ): a)  $^1\text{H}$  MAS NMR (11.7 T, 10 kHz,  $d_1=10$  s) and b)  $^{13}\text{C}$  CP MAS NMR (11.7 T, 10 kHz,  $d_1=5$  s)

a)



b)

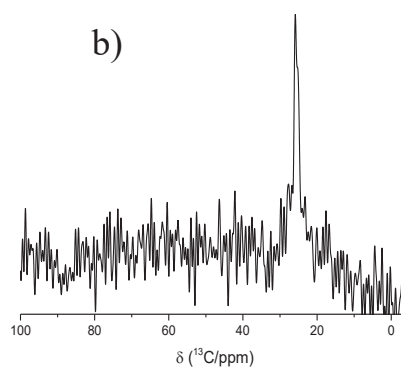


**Figure S10.** Nuclear Magnetic resonance spectra of  $\text{Ga}(i\text{Bu})_3/\text{meso H-ZSM-5-250}$  ( $\text{Si}/\text{Al}=\infty$ ): a)  $^1\text{H}$  MAS NMR (11.7 T, 10 kHz,  $d_1=30$  s) and b)  $^{13}\text{C}$  CP MAS NMR (11.7 T, 10 kHz,  $d_1=10$  s)

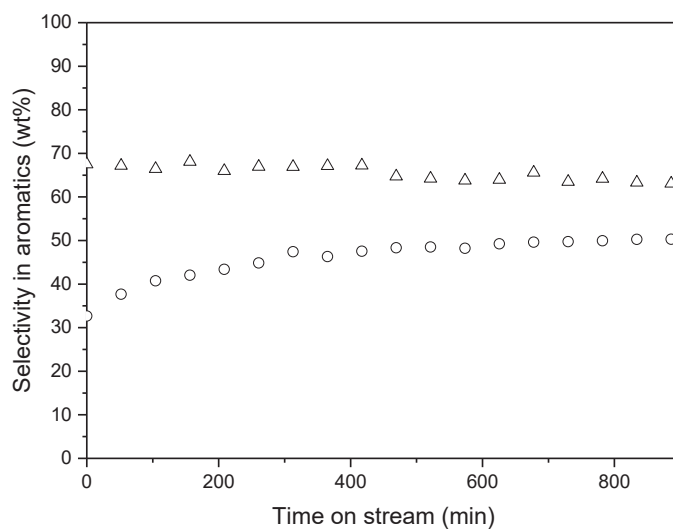


**Figure S11.** Selectivity in aromatics (in wt%) of meso H-ZSM-5-250 (Si/Al= 25) (○), and Ga(*i*Bu)<sub>3</sub>/meso H-ZSM-5-250 (Si/Al= 25) (△); Conditions: T= 580 °C, total flow= 10 mL.min<sup>-1</sup> (5 % C3 in Ar)

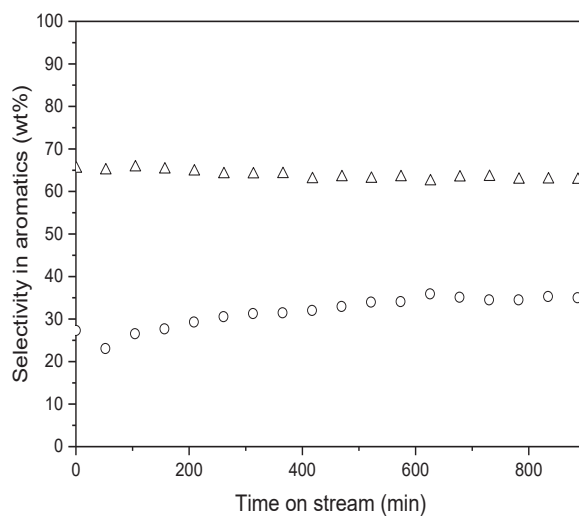


**Figure S12.** Selectivity in aromatics (in wt%) of meso H-ZSM-5-250 (Si/Al= 40) (○), and Ga(*i*Bu)<sub>3</sub>/meso H-ZSM-5-250 (Si/Al= 40) (△); Conditions: T= 580 °C, total flow= 10 mL.min<sup>-1</sup> (5 % C3 in Ar)

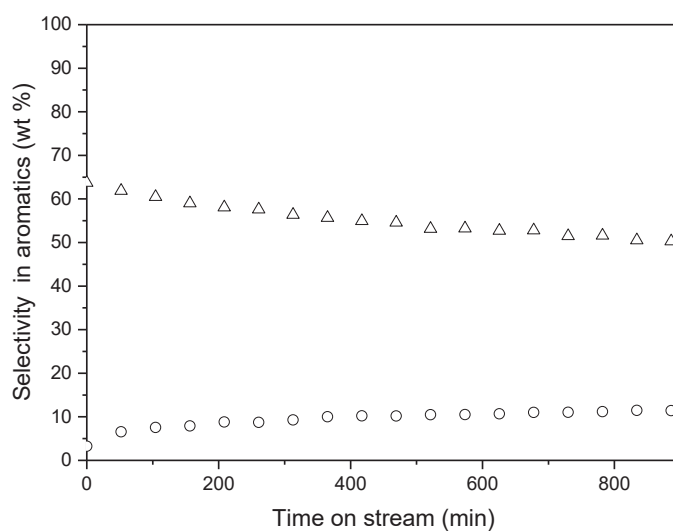


**Figure S13.** Selectivity in aromatics (in wt%) of meso H-ZSM-5-250 (Si/Al= 100) (○), and Ga(*i*Bu)<sub>3</sub>/meso H-ZSM-5-250 (Si/Al= 100) (△); Conditions: T= 580 °C, total flow= 10 mL.min<sup>-1</sup> (5 % C3 in Ar)

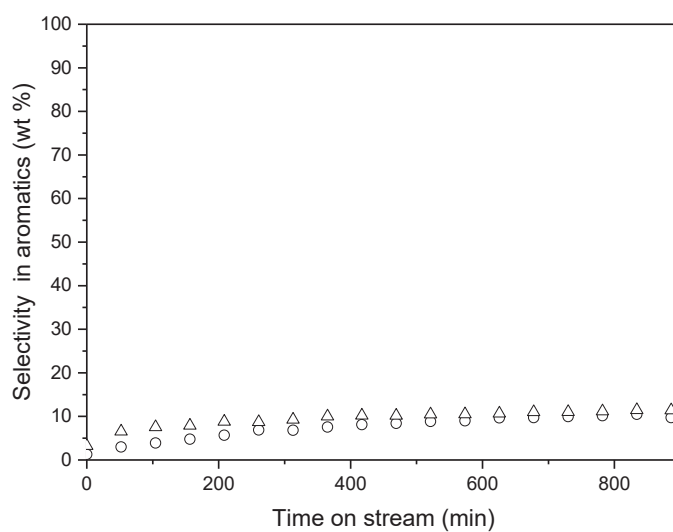


**Figure S14.** Selectivity in aromatics (in wt%) of meso H-ZSM-5-250 (Si/Al= 200) (○), and Ga(*i*Bu)<sub>3</sub>/meso H-ZSM-5-250 (Si/Al= 200) (△); Conditions: T= 580 °C, total flow= 10 mL.min<sup>-1</sup> (5 % C3 in Ar)

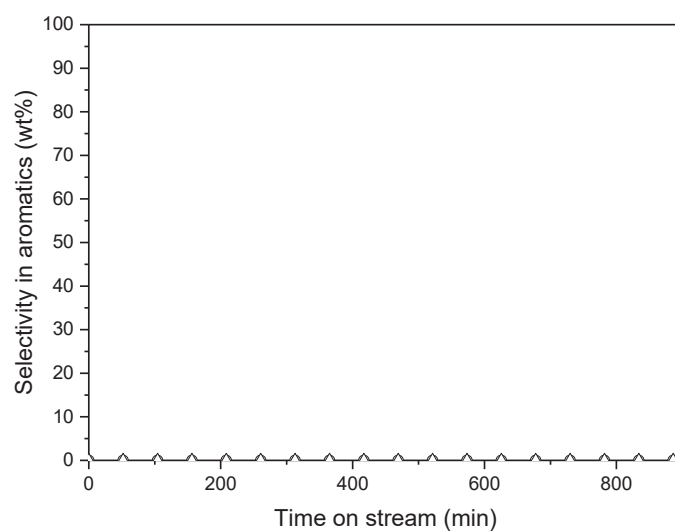


**Figure S15.** Selectivity in aromatics (in wt%) of meso H-ZSM-5-250 (Si/Al=  $\infty$ ) ( $\circ$ ), and Ga(*i*Bu)<sub>3</sub>/meso H-ZSM-5-250 (Si/Al=  $\infty$ ) ( $\Delta$ ); Conditions: T= 580 °C, total flow= 10 mL.min<sup>-1</sup> (5 % C3 in Ar)

## **CHAPTER V**

---

# **Conclusions and perspectives**

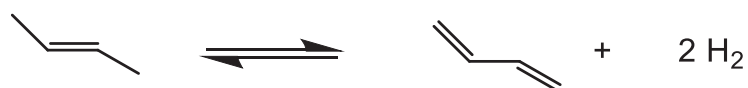
---

The demand toward propylene (PP), butadiene (BD) and aromatics (BTX: benzene, toluene and xylene) is growing due to their diverse consumptions. PP and BD products are mainly obtained from steam cracking and fluid catalytic cracking, whereas BTX are produced from steam catalytic cracking of naphta. These traditional routes seem inadequate to satisfy the market which results in an expanding gap between the demand and the production of these products. On-purpose technologies such as catalytic propane and butane/butenes dehydrogenation and propane aromatization were proposed as promising alternatives for the production of PP, BD and BTX. In fact, many processes have been commercialized due to the success of these reactions. Among them, Oleflex® and Catofin® processes are widely applied for PDH technology, Catadiene® is the most used for butane/butenes dehydrogenation and finally, Cyclar® technology is still applied for propane aromatization. The traditional catalysts used in these processes are based on either expensive platinum supported catalyst or toxic chromium supported on modified alumina, and both of them need frequent regeneration due to their fast deactivation by coke formation.

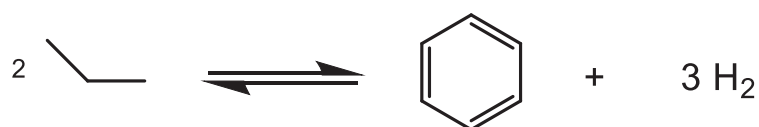
Propane dehydrogenation into propylene:



Butenes dehydrogenation into butadiene:



Propane aromatization:

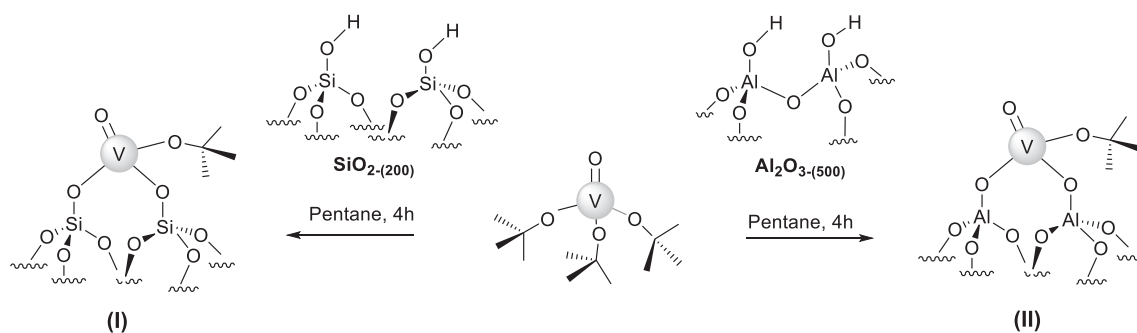


**Scheme 1.** Targeted reactions studied in this PhD

The aim of this thesis involved in the BiZeolCat European project was to develop innovative catalysts to obtain propylene, butadiene and aromatics using light hydrocarbons as feedstocks (Scheme 1). The first chapter in this work was dedicated to the state of art of these existing processes, the catalysts used and their proposed active sites and mechanisms. We then focused our bibliographic studies in particular on the reported alternative catalysts based on Ga and V

for propane dehydrogenation, considered as a common reaction for all these processes. From this study, we found that these traditional catalysts involve a mixture of monomeric, dimeric and oligomeric species on the surface due to their preparation by classical methods. This leaves many unanswered questions concerning the active sites identification and the establishment of a structure-activity relationship. Additionally, these surface species lead to undesired coking and cracking reactions, influencing the catalyst's stability, activity and selectivity toward the targeted products. However, it was proposed in literature that the high activity in PDH of supported vanadium and gallium oxides is related to the presence of a highly electrophilic isolated tripodal  $M^{3+}$  system. Due to the classical preparation methods used for the synthesis of these catalysts, these active species in low concentration are accompanied by oligomeric species, known to be responsible for the deactivation by coke formation. Thus, a judicious choice of the preparation method is highly desired in order to develop a unique tripodal species on the surface, with the aim to establish a structure-activity relationship, and access to the mechanism of PDH on isolated Ga and V on oxides. Surface organometallic chemistry (SOMC) has been used and demonstrated to be a powerful method for the immobilization of organometallic precursors based on Ga and V by protonolysis of a metal ligand bond via a surface hydroxyl group of the oxide, that after restructuration of the support, leads to the targeted active species. For propane and butenes dehydrogenation, alumina and silica are used as supports for gallium and vanadium, while a highly acidic mesoporous zeolite is employed in the case of propane aromatization, that requires a bifunctional catalyst (dehydrogenation on supported metal and aromatization on acidic sites).

The first part of Chapter II is devoted to the modification of a silica dehydroxylated at 200 °C ( $SiO_{2-200}$ ) and an alumina dehydroxylated at 500 °C ( $Al_2O_{3-500}$ ) by the grafting of  $[V(=O)(OtBu)_3]$  using SOMC. The grafting reaction resulted in the formation of bipodal species on the surface,  $[(\equiv MO)_2V(=O)(OtBu)]$ ,  $M = Si$  or  $Al$  (Scheme 2). These resulting catalysts were characterized using several techniques such as IR, solid-state NMR, UV-vis, XANES and elemental analysis.



**Scheme 2.** The formation of bipodal species after grafting  $[V(=O)(OtBu)_3]$  on  $SiO_2-200$  affording **(I)** and on  $Al_2O_3-500$  affording **(II)** at room temperature.

Species **(I)** and **(II)** were tested for the conversion of trans-2-butene in a continuous flow reactor and according to the results obtained, the support and the operating temperature have a large influence on the activity and the distribution of products. In fact, the catalytic performance of these two catalysts revealed that the silica supported species,  $[(\equiv SiO)_2V(=O)(OtBu)]$  **(I)** is more active and stable with time on stream. At different temperatures, this catalyst revealed a more stable conversion at lower temperature (500 and 540 °C) compared to a gradual deactivation observed at 580 °C (Figure 1, Left). Importantly, we observed a different relative selectivities according to the operating temperature (Figure 1, Right). At 500 °C, the relative selectivity in butadiene is 50 % accompanied with 36% propylene and 14 % ethylene. At high temperature (580 °C), the relative selectivity toward  $\alpha$ -olefins increased and consequently decreased for butadiene.

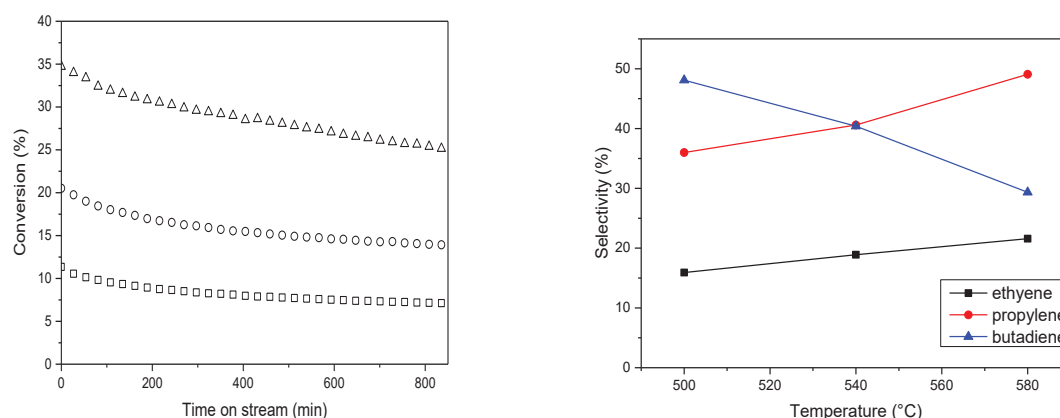
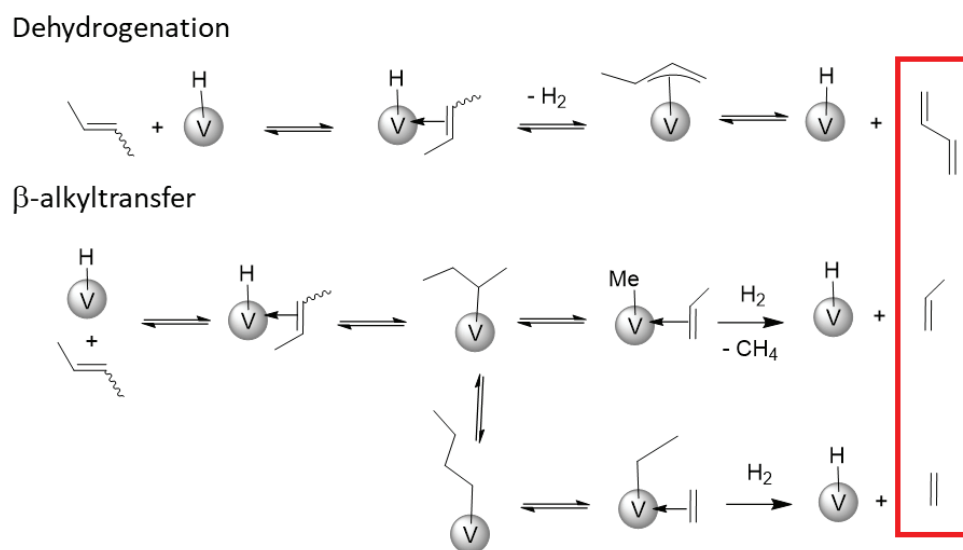


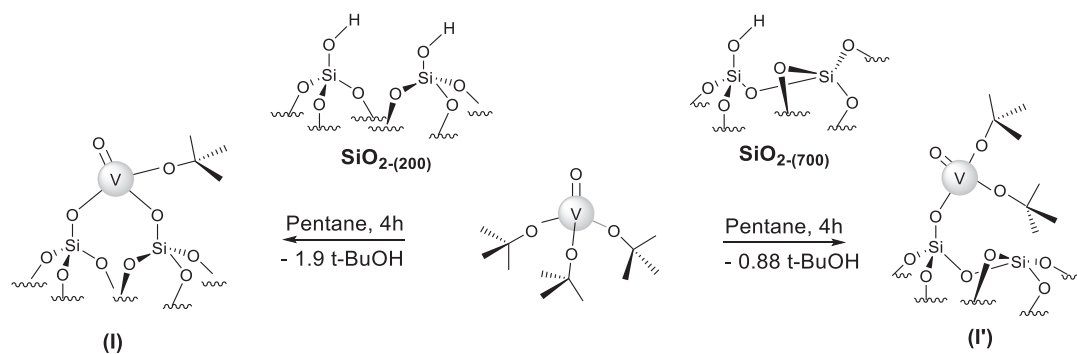
**Figure 1. Left:** trans-2-butene conversion catalyzed by  $V(=O)(OtBu)_3/SiO_2-200$  **(I)** at 500 °C (□), 540 °C (○) and 580 °C (△), **Right:** Relative selectivities in ethylene, propylene and butadiene  $P=1$  bar, Total Flow= 5 mL.min<sup>-1</sup> (20 % trans-2-butene in Ar)

Thus, the 2-butenes conversion on supported vanadium single sites catalysts, allows the formation of a mixture of monomers (butadiene, propylene and ethylene) with different butadiene contents that can be used for direct terpolymerization. In fact, for economical and safety reasons, it is preferable to simplify the process scheme of the terpolymerization reaction in gas or liquid phase, by starting with a mixture of these monomers instead of mixing three different monomers. The mechanism for the formation of these monomers has been proposed and the elementary steps are presented in Scheme 3.



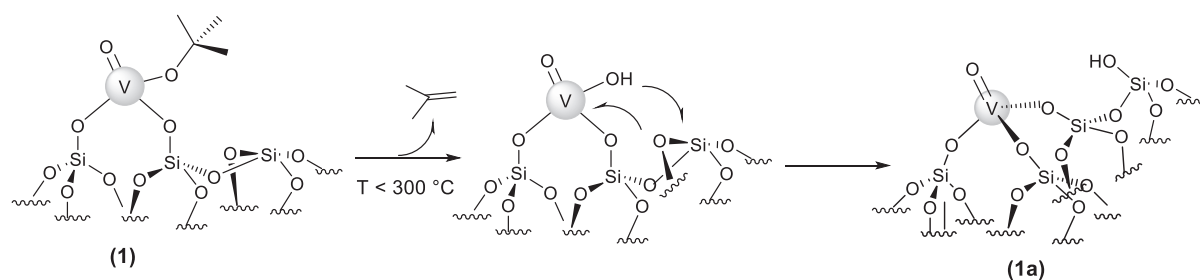
**Scheme 3.** Mechanism proposed for the formation of monomers (butadiene, propylene and ethylene) by dehydrogenation and  $\beta$ -alkyl transfer reactions.

The second part of chapter II is focused on the preparation of tripodal vanadium oxo species supported on silica for the non-oxidative dehydrogenation of propane. Two tripodal vanadium oxo catalysts were synthesized in two steps. The first step consists in the grafting by surface organometallic chemistry of  $[V(=O)(OtBu)_3]$  on  $SiO_{2-200}$  and  $SiO_{2-700}$ , leading to a bipodal  $[(\equiv SiO)_2V(=O)(OtBu)_2]$  on  $SiO_{2-200}$  and monopodal  $[(\equiv SiO)V(=O)(OtBu)_2]$  on  $SiO_{2-700}$  (Scheme 4) which were fully characterized by elemental analysis, IR, UV-Vis, solid-state NMR ( $^1H$ ,  $^{13}C$ ,  $^{51}V$ ) and XANES.



**Scheme 4.** Grafting of  $[\text{V}(=\text{O})(\text{OtBu})_3]$  on  $\text{SiO}_2\text{-}200$  and  $\text{SiO}_2\text{-}700$  leads to structurally distinct surface species

The second step is based on a new original method, involving an easy thermal treatment of  $[(\equiv\text{SiO})_2\text{V}(=\text{O})(\text{OtBu})_2]$  and  $[(\equiv\text{SiO})\text{V}(=\text{O})(\text{OtBu})_2]$  leading to the formation of tetrahedral vanadium oxo tripodal species  $[(\equiv\text{SiO})_3\text{V}(=\text{O})]$ . A mechanism for the formation of these active species similar on  $\text{SiO}_2\text{-}200$  and  $\text{SiO}_2\text{-}700$ , has been proposed based on DRIFT and  $^1\text{H}$  NMR studies. These results suggested that the formation of a tripodal V oxo species occurs via a tripodal V oxo species occurs via a  $\beta$ -H transfer of a proton of a methyl group to the vanadyl oxygen, which leads to evolved propene and a surface V-OH fragment. This fragment can then react by a ring opening with a siloxane bridge from the support, resulting in the formation of new isolated silanol, as depicted in Scheme 5 (e.g on  $\text{SiO}_2\text{-}200$ ). The  $\beta$ -H transfer to an oxygen can occur either by transfer of hydrogen to the oxo ligand, or by direct migration of hydrogen from a methyl group to the oxygen of a tert-butoxide ligand.



**Scheme 5.** Proposed mechanism for the formation of  $[(\equiv\text{SiO})_3\text{V}(=\text{O})]$  species

In particular,  $^{51}\text{V}$  MAS NMR allowed the confirmation of the formation of tetrahedral tripodal V oxo species, showing a chemical isotropic shift at -670 ppm, in agreement with recently

reported results. The catalytic behavior of the resulting tripodal species were tested for propane dehydrogenation to propene, with high selectivity and activity compared to classical  $V_2O_5/SiO_2$ , prepared by aqueous impregnation of vanadium salts. Thus, site isolation and tripodal structures proved to have a beneficial impact on the catalytic performances of these materials when compared to classical catalysts. The catalytic behavior of the most performant tripodal vanadium oxo species, supported on  $SiO_{2-200}$  for propane dehydrogenation is shown in Figure 2.

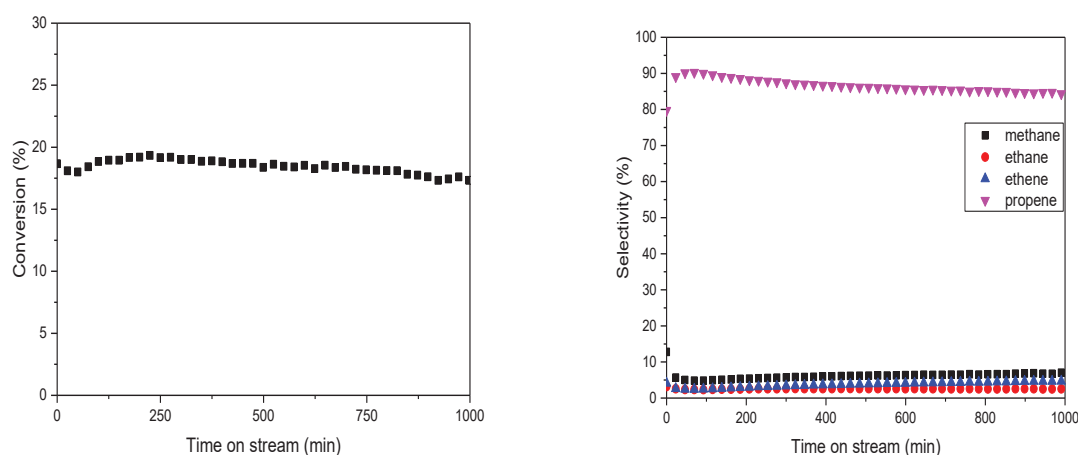
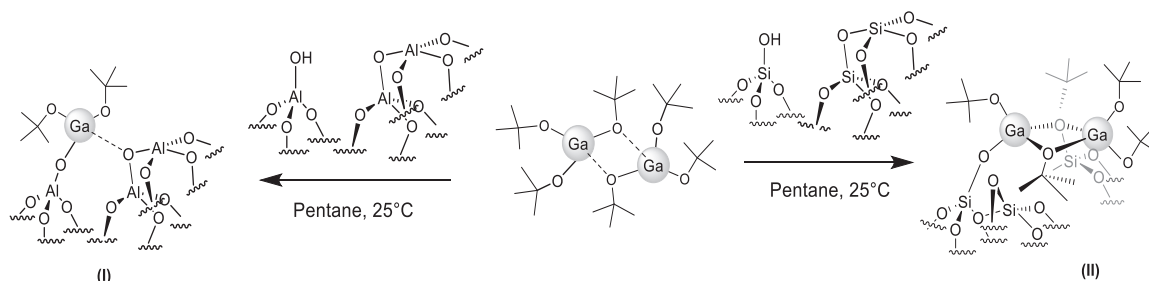


**Figure 2.** Propane conversion catalysed by tripodal  $V/SiO_{2-200}$  (■) and selectivities observed. Conditions:  $P = 1$  bar,  $T = 540$  °C and a total flow of  $5 \text{ mL}\cdot\text{min}^{-1}$  (20 % of  $C_3$  in Ar)

This innovative synthetic method has been applied in chapter III for the preparation of tripodal gallium single site catalysts for the non-oxidative propane dehydrogenation in the first part. The application of the best catalyst on PDH was extended for trans-2-butene conversion into butadiene.

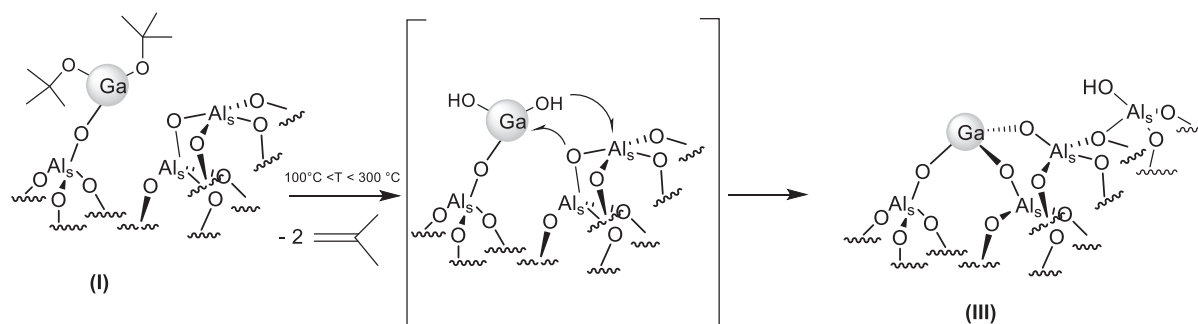
For the non-oxidative propane dehydrogenation, we reported the preparation and characterization of highly active and stable Ga single site catalyst supported on alumina by using surface organometallic chemistry methods. Supported  $Ga^{III}$  complexes were prepared by grafting of  $[Ga(O^tBu)_3]_2$  on  $Al_2O_{3-500}$  and  $SiO_{2-700}$ , leading to a monopodal surface compound,  $[(\equiv AlO)Ga(O^tBu)_2]$  (**I**) on alumina, while a dimeric species  $[(\equiv SiO)_2Ga_2(O^tBu)_4]$  (**II**) were grafted on silica (Scheme 6). These surface species have been fully characterized by elemental analysis, IR,  $^1H$  and  $^{13}C$  solid-state NMR and XAS (EXAFS and XANES). The study and fit of the Ga K-edge EXAFS of the silica supported species on confirmed the

presence of a Ga--Ga contribution from a neighbouring Ga back-scatterer at ca. 2.91 Å. A more active catalyst for PDH was obtained in the case of alumina supported species. In fact, a deactivation was observed in the case of the dimeric Ga silica supported species, which is in accordance with the observations reported in the literature.



**Scheme 6.** Grafting of  $[\text{Ga}(\text{O}t\text{Bu})_3]_2$  on  $\text{Al}_2\text{O}_3\text{-500}$  or  $\text{SiO}_2\text{-700}$  leads to different species

A thermal treatment of species **(I)** leads to the formation of tripodal Ga species **(III)**, proposed to be the active species in propane dehydrogenation (Scheme 7).



**Scheme 7.** Mechanism of the formation of gallium tripodal species on alumina

The structure of **(III)** has been characterized by DRIFT,  $^1\text{H}$  MAS NMR, XAS and mass balance analysis. For the first time, a well-defined tripodal gallium catalyst supported on alumina was obtained and it was confirmed by EXAFS spectroscopy (Figure 3). The result of the fit gives ca. three Ga-O distances at 1.853(9) Å and one Ga-O longer distance at 2.31(2) Å and three neighbouring aluminium atoms, two at 3.24(4) Å and one at 3.56(7) Å (Scheme 7).

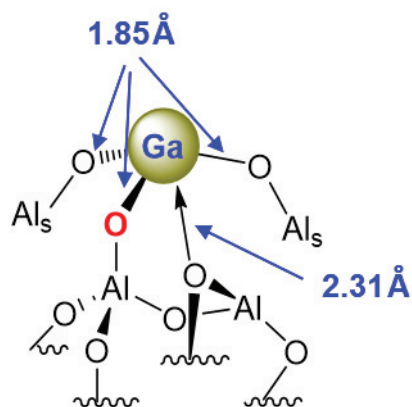


**Figure 3.** Structure of the surface species on  $\text{Ga}(\text{OtBu})_3/\text{Al}_2\text{O}_{3-500}$  thermally treated at  $350^\circ\text{C}$  proposed from a study of the EXAFS at the Ga K-edge.

The tripodal Ga catalytic species supported on alumina showed a higher activity and a remarkable stability as function of time on stream, compared to monopodal  $[\text{Ga}(\text{iBu})_3]$  supported on alumina (Figure 4) and to other catalysts based on Ga from literature. In fact,  $\text{Ga}(\text{iBu})_3/\text{Al}_2\text{O}_3$  deactivates with time on stream, due to the formation of inactive Ga(I) species as revealed by XAFS operando.

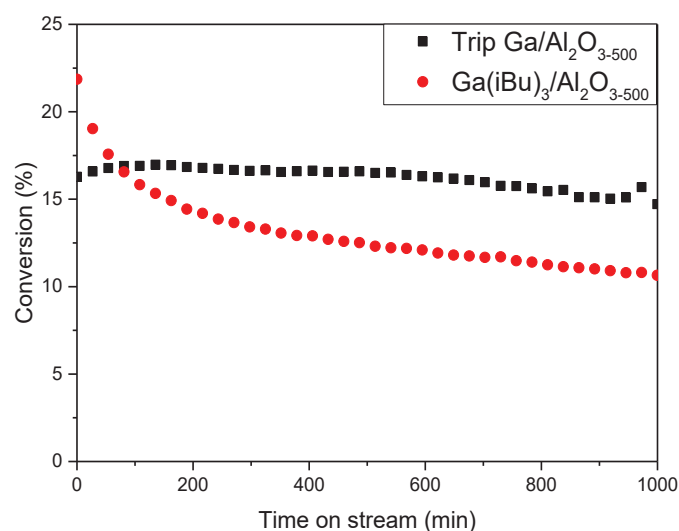
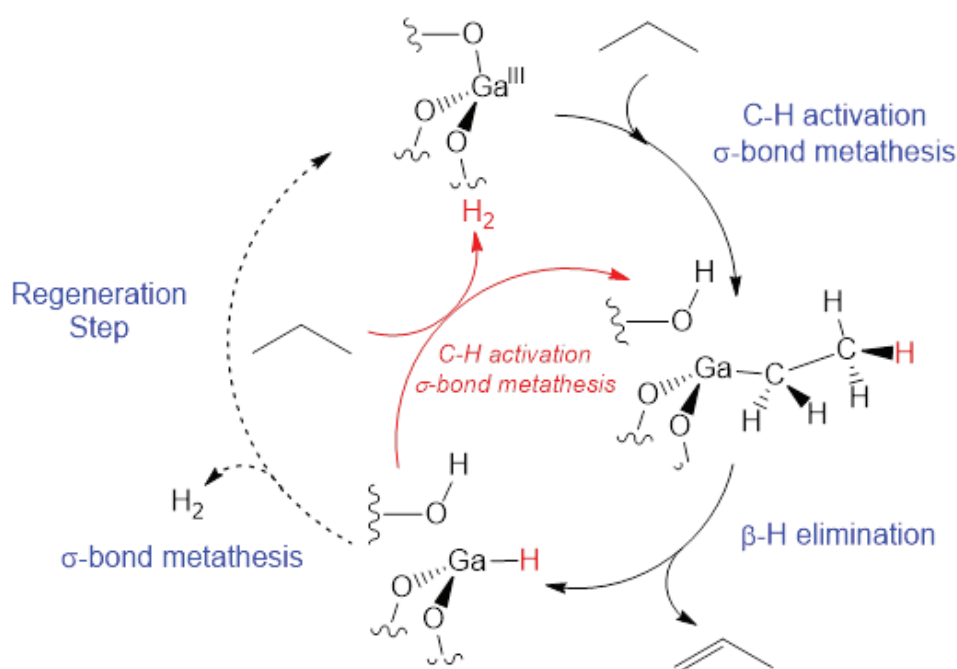


**Figure 4.** Comparison of propane conversion catalyzed by  $\text{Ga}(\text{OtBu})_3/\text{Al}_2\text{O}_{3-500}$  thermally treated at  $350^\circ\text{C}$  (■) or  $\text{Ga}(\text{iBu})_3/\text{Al}_2\text{O}_{3-500}$  (●). Conditions:  $P=1$  bar,  $T=540^\circ\text{C}$ , total flow =  $5\text{ mL}\cdot\text{min}^{-1}$  (20 % C3 in Ar)

XANES spectroscopy of  $\text{Ga}(\text{iBu})_3/\text{Al}_2\text{O}_{3-500}$  during thermal treatment suggests that a minor fraction of Ga(I) sites is formed above  $400^\circ\text{C}$ . These minor sites are more effective catalysts

for propane dehydrogenation, but they deactivate rapidly. The remaining Ga(III) sites show a lower but more stable catalytic performance. These results are in agreement with the curve's shape observed in Figure 4.

All these results revealed that the isolated nature of the Ga sites and their tripodal structure are essential in order to limit the deactivation by coke formation, and to access to a highly active catalyst for PDH, compared to the oligomeric Ga species obtained on conventional Ga catalysts that deactivate quickly over the time. This tripodal Ga species is reported as the active sites for propane dehydrogenation based on Horiuti-Polanyi (H-P) mechanism. The catalytic cycle involves a C-H activation of propane on a Ga-O pair site, leading to the formation of a Ga-propyl intermediate and an OH group by  $\sigma$ -bond metathesis, followed by a  $\beta$ -hydride elimination, resulting in a Ga-H intermediate and propylene. The tripodal Ga active sites can be regenerated after a release of  $H_2$  (Scheme 8). Another parallel and possible pathway of this mechanism is the activation of a C-H bond on the generated Ga-H species (possible intermediate active species), followed by a  $\beta$ -H elimination and leading to the release of  $H_2$  and propylene.



**Scheme 8.** Proposed mechanism in PDH for tripodal Ga catalyst

Tripodal Ga on  $Al_2O_{3-500}$  (**2'**) was also prepared by thermal treatment of  $[Ga(OtBu)_3]_2$  on alumina with lower surface area ( $100 \text{ m}^2 \cdot \text{g}^{-1}$ ) and was compared to tripodal Ga on alumina with higher surface area ( $200 \text{ m}^2 \cdot \text{g}^{-1}$ ), (**3'**) (or species **III**) from the previous part). The

characterization of (2') by mass balance analysis, DRIFT,  $^1\text{H}$  and  $^{13}\text{C}$  solid-state NMR, and X-ray absorption spectroscopies, revealed a monopodal Ga species, similar to the case of species (3'). After testing (2') and (3') in propane dehydrogenation and revealing a similar activity, (2') was also evaluated in trans-2-butene conversion. At 300 min, the selectivity toward butadiene was 51 %. The selectivity in butadiene obtained with species (2') was attributed to the presence of gallium sites and coke deposition produced from the acidity at the beginning of the catalytic test. In addition, using  $\text{CO}_2$  as a co-feed in the feed, limit the coke deposition by reacting with hydrogen as RWGS reaction, which leads to higher selectivity in butadiene (65 % compared to 51 % in the absence of  $\text{CO}_2$ ). The mechanism on  $[(\equiv\text{AlO})_3\text{Ga}]$ , (2'), in the conversion of trans-2-butene into butadiene is similar to the one proposed in the case of vanadium (chapter II part A).

Regarding the high activity and selectivity obtained in the case of tripodal Ga on alumina, the first part of chapter IV reported the preparation of Ga species obtained from the grafting of  $\text{Ga}(\text{O}t\text{Bu})_3$  on a meso H-ZSM-5-250 ( $\text{Si}/\text{Al} = 40$ ) followed by a thermal treatment in order to access to a bifunctional catalyst for propane aromatization. This catalyst was fully characterized by DRIFT,  $^1\text{H}$  MAS NMR,  $\text{N}_2$  adsorption/desorption, mass balance analysis and EXAFS. More importantly, all these techniques confirmed that the grafting occurs selectively on the silanols located in the mesopores while the acidic sites in the micropores remained intact. Additionally, EXAFS studies confirmed the formation of Ga dimeric species on mesoH-ZSM-5-250 after a grafting reaction followed by a thermal treatment. However, for propane aromatization, this catalyst revealed a quick deactivation with a decrease in the selectivity toward aromatics as a function of time on stream (Figure 5). This deactivation was attributed to coke formation due to the presence of acidic Ga-OH-Ga sites in the case of the dimeric structure of the surface species, blocking the access to the acid sites in the micropores.

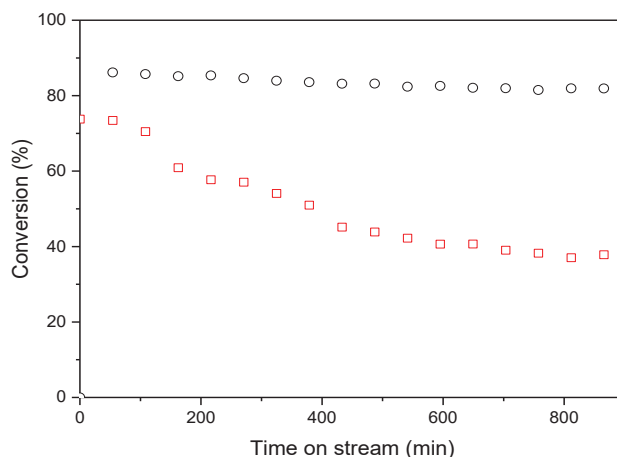
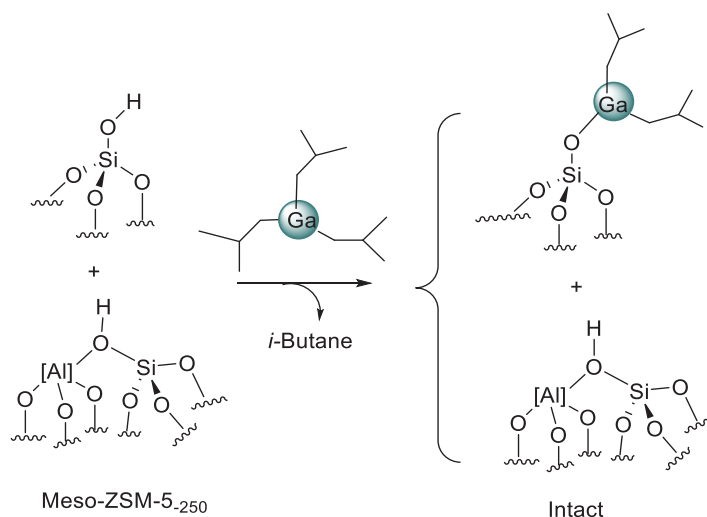


**Figure 5.** Propane conversion of monopodal species of  $\text{Ga}(i\text{Bu})_3/\text{meso H-ZSM-5-250}$  ( $\text{Si}/\text{Al}=40$ ) ( $\circ$ ) and tripodal  $\text{Ga}/\text{meso H-ZSM-5-250}$  ( $\text{Si}/\text{Al}=40$ ) ( $\square$ ); Conditions:  $T=580\text{ }^\circ\text{C}$ , total flow= $10\text{ mL}\cdot\text{min}^{-1}$  (5 %  $\text{C}_3$  in Ar)

Contrarily to the case of Ga species supported on a meso zeolite obtained from the grafting of  $\text{Ga}(\text{O}t\text{Bu})_3$ , supported species obtained from  $[\text{Ga}(i\text{Bu})_3]$  immobilized on the same acidic support, lead to monomeric species,  $[(\equiv\text{SiO})\text{Ga}(i\text{Bu})_2]$ , by a selective grafting in the mesopores. This was confirmed via DRIFT, solid-state NMR,  $\text{N}_2$  adsorption/desorption, mass balance analysis and EXAFS. Contrarily to Ga species obtained from  $\text{Ga}(\text{O}t\text{Bu})_3$ , EXAFS studies revealed the formation of monomeric species in the case of  $\text{Ga}(i\text{Bu})_3/\text{meso H-ZSM-250}$  ( $\text{Si}/\text{Al}=40$ ). The immobilization of Ga from  $[\text{Ga}(i\text{Bu})_3]$  on meso H-ZSM-250 ( $\text{Si}/\text{Al}=40$ ) leads as well to a bifunctional catalyst affording Ga single sites for propane dehydrogenation and intact acid sites for cyclization, oligomerization, and aromatization reactions. Importantly, a highly selective and stable catalyst was obtained in this case compared the catalyst obtained from  $\text{Ga}(\text{O}t\text{Bu})_3$  precursor (Figure 5). This result is also due to the fact that isolated Ga species are more active and stable for the propane dehydrogenation reaction, considered as the first step during propane aromatization.

The last part of this chapter was dedicated to the study of the effect of the acidity of the support, linked to  $\text{Si}/\text{Al}$  the ratio of the meso H-ZSM-250, on the activity and selectivity in propane aromatization. A series of meso H-ZSM-5 with several  $\text{Si}/\text{Al}$  ratios, 25, 40, 100, 200 and  $\infty$  were prepared by UiO laboratory in Oslo and were dehydroxylated at  $250\text{ }^\circ\text{C}$ , affording meso H-ZSM-250 zeolites. All these acidic supports were characterized by DRIFT and high

field solid-state NMR ( $^1\text{H}$  and  $^{13}\text{C}$ ), which revealed that the acid strength increases when the Si/Al ratio decreases. In addition, the structural properties of these materials were characterized by  $\text{N}_2$  adsorption/desorption and confirmed the retention of high surface areas and large pores after thermal treatment. The grafting of  $[\text{Ga}(i\text{Bu})_3]$  on the silanols of these meso H-ZSM-5- $_{250}$  (Si/Al = 25, 40, 100, 200 and  $\infty$ ) leads to monopodal gallium species  $[(\equiv\text{SiO})\text{Ga}(i\text{Bu})_2]$ , evidenced by DRIFT, high field solid-state NMR ( $^1\text{H}$  and  $^{13}\text{C}$ ),  $\text{N}_2$  adsorption/desorption, EXAFS studies as well as mass balance analyses (Scheme 9).



**Scheme 9.** Grafting of  $[\text{Ga}(i\text{Bu})_3]$  onto meso H-ZSM-5- $_{250}$  (Si/Al= 25, 40, 100, 200)

These bifunctional catalysts affording Ga sites for the dehydrogenation and intact acid sites for the aromatization were tested for propane aromatization and revealed higher activities and selectivities compared to the bare zeolite supports. The influence of the Si/Al ratio on the catalytic behavior of  $\text{Ga}(i\text{Bu})_3/\text{meso H-ZSM-5-}_{250}$  catalyst as well as the products distribution (aromatics vs hydrocarbons) was evaluated (Figure 6). At a low Si/Al ratio (25 or 40), very high activity and selectivity toward aromatics were obtained compared to those obtained with Si/Al = 100 or 200. Simultaneously, the lack of acidity for high Si/Al ratios of leads to a low formation of aromatics compounds. On a non-acidic meso H-ZSM-5- $_{250}$  (Si/Al=  $\infty$ ), no aromatic compounds and a very low activity for propane conversion were observed.

a)

b)

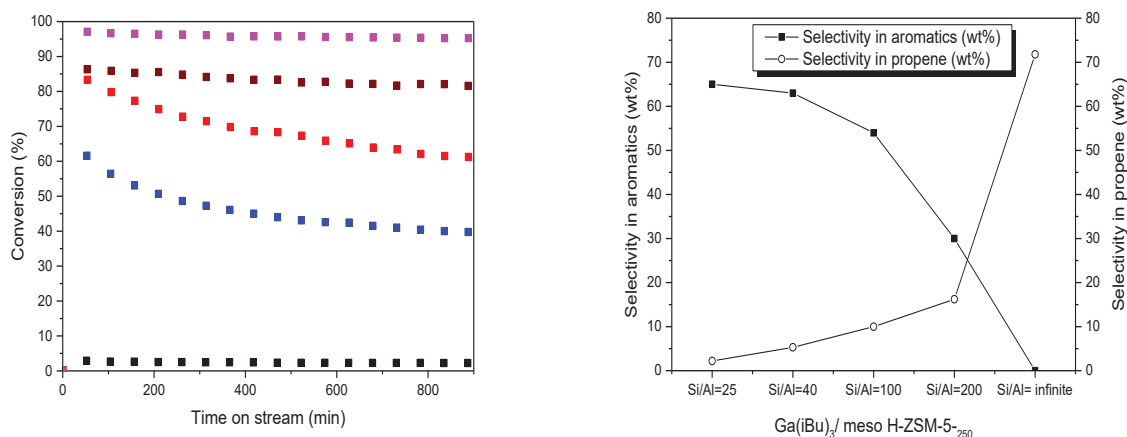


**Figure 6.** a) Propane conversion with  $[\text{Ga}(i\text{Bu})_3]/\text{meso H-ZSM-5-250}$ : (Si/Al=25), magenta; (Si/Al=40), brown; (Si/Al= 100), red; (Si/Al= 200), blue;(Si/Al=  $\infty$ ), black. b) Selectivity in wt% of aromatics of  $\text{Ga}(i\text{Bu})_3/\text{meso H-ZSM-5-250}$  Conditions:  $T = 580\text{ }^\circ\text{C}$ , total flow =  $10\text{ mL}\cdot\text{min}^{-1}$  (5 % C3 in Ar)

Operating at lower temperatures ( $500$  and  $540\text{ }^\circ\text{C}$ ) results in a considerably lower conversion and selectivity towards aromatics. The variation of the gas composition in the feed affects the activity and the formation of products; the highest performances were obtained at a lower concentration of propane in the feed.

## Perspectives

In order to confirm the mechanism of propane dehydrogenation, further studies of the catalysts by solid state NMR using labeled propane in order to characterize the different steps of the mechanism. This technique will be supported by Operando DRIFT and XAFS to identify the intermediates in the catalytic cycle and establish the reaction's mechanism of PDH. The deactivation of the catalyst will be also studied by using XPS and XAFS Operando, since it was suggested during this thesis that the reduction of Ga(III) into Ga(I) may be a factor responsible for the deactivation during PDH.

It was also proposed in literature that the reduced Ga during the catalytic test can be restored by using oxygenated substrates such as  $\text{CO}_2$ . We will study the effect of  $\text{CO}_2$  in the feed with different ratio during propane dehydrogenation. This investigation will be extended to the effect of  $\text{H}_2$  in the feed since hydrogen can oxidize Ga(I) to Ga(III).

Since the C-H activation of propane or butenes would occur on a M-O-S (M= metal and S= support) and depends on the polarity of O-S bond, we expect that the support will have a great effect on the catalytic performance of Ga and V tripodal species. Thus, the effect of redox and basic supports such as  $ZrO_2$ ,  $CeO_2$ ,  $CeZrO_4$  will be evaluated.

Supported tripodal Ga and V were obtained easily by thermal treatment of  $[Ga(OtBu)_3]_2$  on alumina and  $[V(=O)(OtBu)_3]$  on silica, respectively and they exhibited a high stability and selectivity in the targeted reactions. Similarly, we will extend our studies to prepare tripodal Cr catalysts with low loadings from thermal treatment of  $[Cr(OtBu)_3]$  on oxides.

Another important perspective is to use cheap and commercial gallium and vanadium precursors, such as gallium and vanadium nitrate by a combination of grafting low loading of metals on oxides followed by a decomposition at 300 °C in order to access to the same tripodal species.